Theoretical and numerical modeling of magnetorheological elastomers comprising magnetically soft and hard particles

Dipayan Mukherjee

INSTITUT POLYTECHNIQUE DE PARIS

NNT : 2020IPPAX047

Thèse de doctorat

Modélisation théorique et numérique des élastomères magnéto-rhéologiques contenant des particules ferromagnétiques douces et dures

Thèse de doctorat de l'Institut Polytechnique de Paris
préparée à École Polytechnique

École doctorale n°626, Ecole Doctorale de l'Institut Polytechnique de Paris
Spécialité de doctorat : Ingénierie, mécanique et énergétique

Thèse présentée et soutenue à Palaiseau, le 6 octobre 2020, par

DIPAYAN MUKHERJEE

Composition du Jury :

M. Nicolas TRIANTAFYLLIDIS Professor, LMS, C.N.R.S, École Polytechnique, IP Paris	Président
Mme. Laurence BRASSART Associate Professor, Department of Engineering Science, University of Oxford	Rapporteur
M. Noel LAHELLEC Maître de conférences, LMA, Aix-Marsaille Université	Rapporteur
M. Chad M. LANDIS Professor, Department of Aerospace Engineering and Applied Mechanics, The University of Texas at Austin	Examinateur
M. Victor LEFÈVRE Assistant Professor, Department of Mechanical Engineering, Northwestern University	Examinateur
M. Konstantinos DANAS Charge de Recherche, LMS, C.N.R.S, École Polytechnique, IP Paris	Directeur de thèse
Mme. Laurence BODELOT Maître de conférences, LMS, École Polytechnique, IP Paris	Co-directeur de thèse

Theoretical and numerical modeling of magnetorheological elastomers comprising magnetically soft and hard particles

Ph.D. Thesis

Submitted by

Dipayan MUKHERJEE

Thesis advisors: Konstantinos DANAS
Laurence BODELOT

Laboratoire de Mécanique des Solids

École Polytechnique

Institute Polytechnique de Paris

Abstract

Particle-filled magnetorheological elastomers (MREs) are essentially two-phase composites comprising magneto-active metallic inclusions in a mechanically soft elastomer matrix. This work provides a set of equivalent microstructurally-guided constitutive models for the isotropic MREs in the $\mathbf{F}-\mathbf{H}$, $\mathbf{F}-\mathbf{h}$, $\mathbf{F}-\mathbf{B}$ and $\mathbf{F}-\mathbf{b}$ variable spaces. Depending on the magnetic properties of the inclusion phases, the MREs are referred to as soft (s-MRE) or hard (h-MRE), in they contain, respectively, magneto-active (e.g., iron) or, permanently magnetizable (e.g., NdFeB) particles. In turn, the non-coercive, "soft" magneto-active particles exhibit a saturation-type magnetization response, whereas the highly coercive, permanently magnetizable "hard" magnetic particles exhibit ferromagnetic hysteresis.

Two equivalent, $\mathbf{h}$ and $\mathbf{b}$-based, thermodynamically consistent, rate-independent models for the ferromagnetic hysteresis are proposed herein. Furthermore, the non-hysteretic saturation-type soft magnetic response is observed to be a special case of the hysteresis response, in the limit of vanishing coercivity. A full-field numerical homogenization is subsequently carried out, in order to estimate the macroscopic response of the s- and h-MREs. In particular, an augmented, incremental numerical homogenization framework is proposed, that is suitable for the h-MREs. This proposed incremental framework simplifies further in the limit of vanishing particle coercivity, thus leading to a purely energetic homogenization problem for the s-MREs. Numerical homogenization estimates for both s- and h-MREs provide crucial insights into the particle rearrangements and rotations under various loading conditions.

Fully objective, explicit macroscopic models, that become exact to the analytical homogenization estimates in certain limits, are proposed for the s-MREs in both $\mathbf{F}-\mathbf{H}$ and $\mathbf{F}-\mathbf{B}$ variable spaces. Since most of the effective properties are estimated from the limiting cases of analytical homogenization, the number of model parameters to be estimated via model response fitting reduces to one. Similarly, fully objective, equivalent constitutive models in the $\mathbf{F}-\mathbf{H}$, $\mathbf{F}-\mathbf{h}$, $\mathbf{F}-\mathbf{B}$ and $\mathbf{F}-\mathbf{b}$ variable spaces are proposed for the h-MREs, where the internal variables in the Lagrangian $\mathbf{F}-\mathbf{H}$ and $\mathbf{F}-\mathbf{B}$-based formulations are considered to be in a stretch-free, intermediate configuration. Consequently, the total Cauchy stress derived from the Clausius-Duhem inequalities via employing the classical Coleman-Noll-Gurtin method is found to be consisting of the mechanical stress, the energetic and remanent Maxwell stresses, where the last is an additional stress contribution, obtained for the h-MREs. Furthermore, the evolution equation for the current internal variables are defined to be in terms of their objective Green-Naghdi rates. Here also, only one additional model parameter, to be identified via fitting the model response, is introduced.

Excellent agreements are obtained between the proposed models for the s- and h-MREs and the numerical homogenization estimates for all particle volume fractions of interest, i.e., up to 30%, and for moderately-soft to relatively stiff matrix phases having shear moduli $G_m \geqslant 0.3$ MPa. In turn, the proposed s-MRE models also perform very well for softer matrices having moduli $G_m < 0.1$ MPa.

Résumé

Les élastomères magnétorhéologiques (MREs) remplis de particules sont essentiellement des composites à deux phases comprenant des inclusions métalliques magnéto-actives dans une matrice d'élastomère mécaniquement souple. Ce travail fournit un ensemble de modèles constitutifs équivalents guidés microstructurellement pour les MREs isotropes dans les espaces de variables $\mathbf{F}-\mathbf{H}$, $\mathbf{F}-\mathbf{h}$, $\mathbf{F}-\mathbf{B}$ et $\mathbf{F}-\mathbf{b}$. En fonction des propriétés magnétiques des phases d'inclusion, les MREs sont appelés doux (s-MREs) ou durs (h-MREs), s'ils contiennent, respectivement, des particules magnéto-actives (par exemple, fer) ou des particules magnétisables de façon permanente (par exemple, NdFeB). À leur tour, les particules magnéto-actives "douces" non-coercitives présentent une réponse de magnétisation de type saturation, tandis que les particules magnétiques "dures" fortement coercitives et magnétisables de façon permanente présentent une hystérésis ferromagnétique.

Deux modèles équivalents, basés sur $\mathbf{h}$ et $\mathbf{b}$, thermodynamiquement cohérents et indépendants de la vitesse sont proposés ici pour l'hystérésis ferromagnétique. De plus, la réponse magnétique douce de type non-hystérétique à saturation apparaît comme un cas particulier de la réponse hystérétique lorsque la coercivité tend vers zéro. Une homogénéisation numérique à champ complet est ensuite réalisée afin d'estimer la réponse macroscopique des s- et h-MREs. En particulier, un cadre d'homogénéisation numérique incrémental augmenté est proposé, qui convient aux h-MREs. Ce cadre incrémental peut être davantage simplifié lorsque la coercivité des particules tend vers zéro, conduisant ainsi à un problème d'homogénéisation purement énergétique pour les s-MREs. Les estimations numériques d'homogénéisation pour les s- et h-MREs fournissent des informations cruciales sur les réarrangements et les rotations des particules dans diverses conditions de chargement.

Des modèles macroscopiques explicites et entièrement objectifs, qui deviennent identiques aux estimations analytiques d'homogénéisation dans certaines limites, sont proposés pour les s-MREs dans les deux espaces de variables $\mathbf{F}-\mathbf{H}$ et $\mathbf{F}-\mathbf{B}$. Étant donné que la plupart des propriétés effectives sont estimées à partir des cas limites d'homogénéisation analytique, le nombre de paramètres du modèle à estimer via l'ajustement de la réponse du modèle se réduit à un. De la même manière, des modèles constitutifs entièrement objectifs et équivalents dans les espaces de variables $\mathbf{F}-\mathbf{H}$, $\mathbf{F}-\mathbf{h}$, $\mathbf{F}-\mathbf{B}$ et $\mathbf{F}-\mathbf{b}$ sont proposés pour les h-MREs, où les variables internes dans le Lagrangien $\mathbf{F}-\mathbf{H}$ et $\mathbf{F}-\mathbf{B}$ sont considérées comme étant dans une configuration intermédiaire sans étirement. Par conséquent, la contrainte totale de Cauchy dérivée des inégalités de Clausius-Duhem via l'utilisation de la méthode classique de Coleman-Noll-Gurtin trouve être constituée de la contrainte mécanique et des contraintes énergétiques et rémanentes de Maxwell, la dernière contrainte étant une contribution supplémentaire obtenue pour les h-MREs. De plus, l'équation d'évolution des variables internes actuelles est définie en fonction de leurs taux objectifs de Green-Naghdi. Ici aussi, un seul paramètre supplémentaire, à identifier via l'ajustement de la réponse du modèle, est introduit.

D'excellents accords sont obtenus entre les modèles proposés pour les s- et h-MREs et les estima-

tions numériques d'homogénéisation pour toutes les fractions volumiques de particules considérées, c'est-à-dire jusqu'à 30%, et pour des matrices allant de modérément souples à relativement rigides ayant des modules de cisaillement $G_m > 0,3$ MPa. À leur tour, les modèles s-MREs proposés fonctionnent également très bien pour des matrices plus souples de modules $G_m < 0,1$ MPa.

Acknowledgments

I would like to extend my sincere gratitude towards my thesis advisors Prof. Kostas Danas and Prof. Laurence Bodelot for mentoring my growing up as a researcher at LMS. The long hours of discussion with them was never bounded by the narrow domain of my Ph.D. thesis. Rather, they were vibrant, open-ended and sometimes going beyond the general diaspora of physics and engineering. I consider all of these as a part of my growing up as a researcher. Also, I extend my gratitude towards the ERC starting grant MAGNETO, awarded to Prof. Kostas Danas, for funding my research.

I would also like to thank Prof. Nicolas Triantafyllidis for always encouraging my work and for very inciteful discussions on various topics of multiphysics modeling. The computation cluster facility, provided by LMS is also highly appreciated. Finally, I am thankful to all the members of LMS, who collectively contribute to make LMS such a center of excellence in the solid mechanics research.

On a personal note, it would not be complete if I don't acknowledge the constant support from my parents. I would also thank my excellent colleagues Dr. Matthias Rambausek and Dr. Othmane Zerhouni at LMS for helping me in sorting out a number of technical and non-technical issues in multiple times. Finally, I thank my friends Mr. Mainak Banerjee, Dr. Ritwik Bandyopadhyay, Mr. Alauddin Sk., Mr. Chandan Biswas and Mr. Soumik Ghatak for constantly helping me in navigating in between different terrains of my life during the past three years.

To my parents...

Contents

List of symbols

Volume, boundary and coordinate systems

$\mathcal{V}_0$	*Reference volume of a continuum*	$\mathcal{V}$	*Current volume of a continuum*
$\partial\mathcal{V}_0$	*Reference boundary of a continuum*	$\partial\mathcal{V}$	*Current boundary of a continuum*
$\mathcal{N}$	*Reference unit normal on* $\partial\mathcal{V}_0$	$\mathbf{n}$	*Current unit normal on* $\partial\mathcal{V}$
$\mathcal{V}_i$	*Stretch-free intermediate volume*	$\mathcal{V}_0^{\#}$	*Reference volume of a RVE*[1]
$\mathcal{V}^{\#}$	*Current volume of a RVE*	$\partial\mathcal{V}_0^{\#}$	*Reference boundary of a RVE*
$\mathbf{X}$	*Reference coordinate system*	$\mathbf{x}$	*Current coordinate system*
$\mathfrak{y}(\mathbf{X}, t)$	*Deformation map*	$\breve{\boldsymbol{\xi}}$	*Local coordinate system of a finite-element*

Vector and tensor operations and differential operators

$\mathbf{a}\cdot\mathbf{b} = a_i b_i$	*Vector inner product*	$\mathbf{A}\colon\mathbf{B} = A_{ij}B_{ij}$	*Tensor inner product*
$\mathbf{a}\times\mathbf{b} = \epsilon_{ijk}a_i b_j$	*Vector cross product*	$\mathbf{a}\wedge\mathbf{b}$	*Vector wedge product*
$\mathbf{a}\otimes\mathbf{b} = a_i b_j$	*Vector dyadic product*	Div	*Divergence with respect to* $\mathbf{X}$
Curl	*Curl with respect to* $\mathbf{X}$	Grad	*Gradient with respect to* $\mathbf{X}$
div	*Divergence with respect to* $\mathbf{x}$	curl	*Gradient with respect to* $\mathbf{x}$
grad	*Gradient with respect to* $\mathbf{x}$		

Accents and subscripts

$\widetilde{(\blacksquare)}$	*Microscopic fields and potentials*	$\widetilde{(\blacksquare)}$	*Periodic fluctuation fields in the RVE*
$\dot{(\blacksquare)}$	*Material time derivative*	$\overset{\triangle}{(\blacksquare)}$	*Green-Naghdi rate*
$(\blacksquare)_p$	*Properties/potentials of the particle phase*	$(\blacksquare)_m$	*Properties/potentials of the matrix phase*
$(\blacksquare)_{mech}$	*Mechanical part of* $(\blacksquare)$	$(\blacksquare)_{mag}$	*Magnetic part of* $(\blacksquare)$
$(\blacksquare)^{en}_{mag}$	*Energetic part of* $(\blacksquare)_{mag}$	$(\blacksquare)^{rem}_{mag}$	*Remanent part of* $(\blacksquare)_{mag}$

Magnetic and mechanical field variables

$\mathbf{b}$	*Current magnetic induction*	$\mathbf{h}$	*Current magnetic field*
$\mathbf{m}$	*Current magnetization*	$\mathbf{b}^r$	*Current remanent* $\mathfrak{b}$*-field*
$\mathbf{h}^r$	*Current remanent* $\mathfrak{h}$*-field*	$\mathbf{B}$	*Reference magnetic induction*
$\mathbf{H}$	*Reference magnetic field*	$\mathbf{B}^r$	*Reference remanent* $\mathfrak{b}$*-field*
$\mathbf{H}^r$	*Reference remanent* $\mathfrak{h}$*-field*	$\mathcal{B}^r$	*Intermediate remanent* $\mathfrak{b}$*-field*
$\mathcal{H}^r$	*Intermediate remanent* $\mathfrak{h}$*-field*	$\varphi(\mathbf{X})$	*Reference scalar potential*
$\mathcal{A}(\mathbf{X})$	*Reference vector potential*	$\mathbf{h}_a$	*Applied Eulerian magnetic field*
$\mathbf{F}$	*Mechanical deformation gradient*	$\mathbf{u}$	*Mechanical displacement field*

[1] Representative Volume Elements in the numerical homogenization.

$\mathbb{C}$	*Right Cauchy-Green tensor*	$\mathbb{B}$	*Left Cauchy-Green tensor*
$\mathbf{U}$	*Right stretch tensor*	$\mathbf{V}$	*Left stretch tensor*
$\mathbf{R}$	*Mechanical rotation tensor*	$\mathbf{l}$	*Mechanical deformation rate tensor*
$\mathbf{d}$	*Mechanical stretch rate tensor*	$\mathbf{\Omega}$	*Mechanical spin tensor*
$\lambda_i,\ i = 1-3$	*Principal mechanical stretches*	$\gamma_{ij},\ i \neq j$	*Mechanical shear strain*
$\mathbf{S}$	*Total first Piola-Kirchhoff (P-K) stress*	$\mathbf{S}_{mech}$	*Mechanical part of* 1^{st} *P-K stress*
$\mathbf{S}^{en}_{maxw}$	*Energetic Maxwell* 1^{st} *P-K stress*	$\mathbf{S}^{mech}_{a}$	*Applied mechanical* 1^{st} *P-K stress*
$\boldsymbol{\sigma}$	*Total Cauchy stress*	$\boldsymbol{\sigma}_{mech}$	*Mechanical part of Cauchy stress*
$\boldsymbol{\sigma}^{en}_{maxw}$	*Energetic Maxwell Cauchy stress*	$\boldsymbol{\sigma}^{rem}_{maxw}$	*Remanent Maxwell Cauchy stress*
$\mathbf{T}$	*Reference total traction vector*	$\mathbf{t}$	*Current total traction vector*
$\mathbf{q}$	*Current heat flux vector*	$\mathbf{p}$	*Current magnetic flux vector*

Potentials and switching surfaces

W^H	*Potential energy in the* $\mathbf{F}-\mathbf{H}$ *model*	w^h	*Potential energy in the* $\mathbf{F}-\mathbf{h}$ *model*
W^B	*Potential energy in the* $\mathbf{F}-\mathbf{B}$ *model*	w^b	*Potential energy in the* $\mathbf{F}-\mathbf{b}$ *model*
D^H	*Dissipation potential in the* $\mathbf{F}-\mathbf{H}$ *model*	$\mathscr{D}^h$	*Dissipation potential in the* $\mathbf{F}-\mathbf{h}$ *model*
D^B	*Dissipation potential in the* $\mathbf{F}-\mathbf{B}$ *model*	$\mathscr{D}^b$	*Dissipation potential in the* $\mathbf{F}-\mathbf{b}$ *model*
ψ^H	*Helmholtz free energy*[2] *in* $\mathbf{F}-\mathbf{H}$ *model*	ψ^B	*Helmholtz free energy in* $\mathbf{F}-\mathbf{B}$ *model*
Φ^H	*Switching surface in the* $\mathbf{F}-\mathbf{H}$ *model*	ϕ^h	*Switching surface in the* $\mathbf{F}-\mathbf{h}$ *model*
Φ^B	*Switching surface in the* $\mathbf{F}-\mathbf{B}$ *model*	ϕ^b	*Switching surface in the* $\mathbf{F}-\mathbf{b}$ *model*
$\mathcal{W}^H$	*Incremental potential in the* $\mathbf{F}-\mathbf{H}$ *model*	$\mathscr{P}^H$	*Augmented incremental potential*

Properties

ρ_0	*Reference material density*	ρ	*Current material density*
c	*Particle volume fraction*	μ_0	*Magnetic permeability of vacuum*
μ	*Magnetic permeability of a material*	μ^e	*Energetic permeability of a material*
χ	*Magnetic susceptibility*	χ^e	*Energetic magnetic susceptibility*
m^s	*Saturation magnetization*	b^c	*Coercive field*
κ^h	*Hysteresis shape parameter (*$\mathbf{h}$*-model)*	κ^b	*Hysteresis shape parameter (*$\mathbf{b}$*-model)*
G	*Mechanical shear modulus*	G'	*Mechanical bulk modulus*
β_1^H	*Coupling parameter in* $\mathbf{F}-\mathbf{H}/\mathbf{h}$ *s-MRE model*	β_1^B	*Coupling parameter in* $\mathbf{F}-\mathbf{B}/\mathbf{b}$ *s- model*
β^{Hr}	*Coupling parameter in* $\mathbf{F}-\mathbf{H}/\mathbf{h}$ *ħ-MRE model*	β^{Br}	*Coupling parameter in* $\mathbf{F}-\mathbf{B}/\mathbf{b}$ *ħ- model*
p, q	*Rate exponents in dissipation potentials*	ζ	*Penalty parameter in FE computations*

[2] specific Helmholtz free energy, i.e. per unit mass.

Chapter

1 Introduction

Chapter summary: *This chapter summarizes the key aspects in the fabrication and modeling of magnetorheological elastomers (MREs), reported in the literature. In particular, a comparison is drawn between the MREs comprising soft and hard ferromagnetic particles vis-a-vis different fabrication techniques and modeling approaches. Both microscopic and macroscopic modeling approaches for these soft and hard MREs are summarized subsequently. The detailing of the state-of-the-art is followed by a discussion on the scope of the present work and the organization of the thesis.*

Chapter content

Magneto-active particle-filled magnetorheological elastomers (MREs) are being explored since the last two decades due to its excellent magnetic field-driven mechanical tuning properties (Jolly et al., 1996; Ginder et al., 1999, 2000; Bodelot et al., 2017). This property of the MREs enable it to find its potential applications in vibration absorbers (Lerner and Cunefare, 2007; Li et al., 2014; Ahamed et al., 2018), active surface pattern controllers (Danas and Triantafyllidis, 2014; Huang et al., 2016a; Psarra et al., 2017, 2019), soft robotic actuators (Manti et al., 2016; Kim et al., 2018; Zhao et al., 2019; Sitti and Wiersma, 2020), microfluidic separators (Hilber and Jakoby, 2012; Royet et al., 2017; Zhou et al., 2020), bio-inspired magnetic sensors (Kaidarova et al., 2018), etc. The MREs are essentially two phase composites having metallic magneto-active particles suspended in a magnetically passive but mechanically soft elastomer matrix (see Fig. 1.1). Depending on the magnetic coercivity of the particle phase, the MREs are broadly classified under two heads listed in the following.

- *Soft magnetic* (e.g., carbonyl iron) particle-filled MREs, or s-MREs.
- *Hard magnetic* (e.g., NdFeB) particle-filled MREs, or h-MREs.

Figure 1.1 shows the typical microstructures of soft (Fig. 1.1a) and hard (Fig. 1.1b) MREs with commercially available carbonyl iron (CI) and MQP-S-11 NdFeB particles, respectively. We observe from Fig. 1.1 that, both the CI and NdFeB microstructures have spherical morphologies with the median

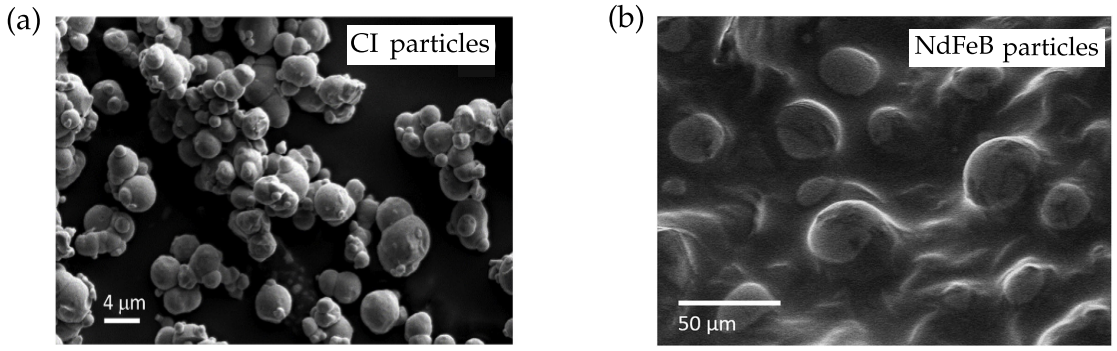

Figure 1.1: Scanning electron microscopy (SEM) images of (a) commercially available carbonyl iron (CI) particles from MilliporeSigma in silicone matrix (Perales-Martínez et al., 2017) and (b) magnetic MQP-S-11 NdFeB particles from Magnequench in PDMS matrix (Linke et al., 2016).

particle radius of ~ 4 μm and ~ 20 μm, respectively. Nevertheless, it should be noted that a number of commercially available NdFeB powders also exhibit highly amorphous, sometimes rod-like morphologies (Stepanov et al., 2017; Schümann and Odenbach, 2017; Schümann et al., 2017; Kim et al., 2018). Although, the average macroscopic responses of the *statistically isotropic* h-MREs do *not* exhibit a strong dependence on the morphology of the underlying NdFeB particles.

In contrast to the s-MREs (Danas et al., 2012b; Bodelot et al., 2017), the NdFeB particle-filled h-MREs (Kalina et al., 2017; Kim et al., 2018; Zhao et al., 2019) exhibit remanent magnetization, which is defined by the magnetization left after the initial loading and subsequent unloading of a demagnetized sample. Such magnetic properties of the s- and h-MREs are direct consequences of the different magnetic coercivities of the underlying micro-particles. Typical magnetization responses of commercial CI and NdFeB particles and their comparison are shown in Fig. 1.2. Notice from

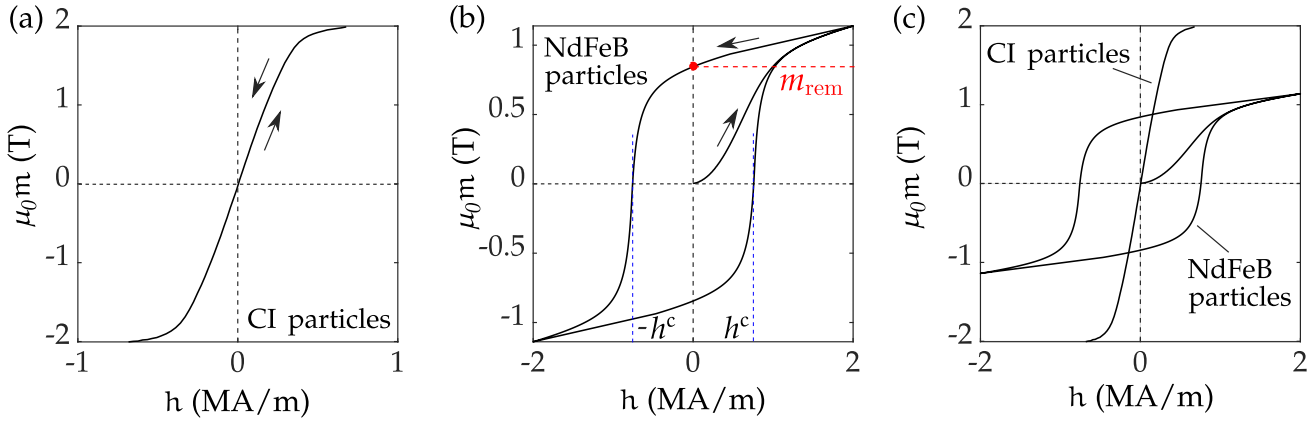

Figure 1.2: Measured magnetization responses of (a) carbonyl iron (CI) particles (Sugawa et al., 2013) and (b) NdFeB particles (Deng et al., 2015). (c) Comparison between CI and NdFeB magnetization responses.

Fig. 1.2a that the CI particles magnetize and demagnetize following almost the same path, thus, retain no remanent magnetization. The NdFeB particles, on the other hand, do not demagnetize on the removal of the applied external magnetic field, thus, exhibiting ferromagnetic hysteresis, as shown in Fig. 1.2b. In turn, this remanent magnetization is caused by a crucial property of the hard magnets, namely the coercivity, which is typically defined in terms of the *coercive field* associated with

a hard magnet. As indicated by h^c on Fig 1.2b, the coercive field is defined to be the reverse magnetic field that is needed to demagnetize a permanent magnet completely. Evidently, h^c is negligibly small for the soft CI particles and remains in the order of $0.8 - 1.2$ MA/m for the NdFeB particles (see the particles catalogs of Magnequench). Finally, a comparison between the magnetization responses of CI and NdFeB particles is shown in Fig. 1.2c, where we observe that, in spite of having a vanishingly small coercivity, the CI particles magnetize to a greater extent before its saturation as compared to the NdFeB particles. Hence, under external magnetic fields, the inter-particle attraction forces are greater in the s-MREs than in the h-MREs.

The choice for a suitable material for the elastomer matrix is not straightforward. In spite of having a number of commercially available curable elastomers, a many among them suffer from the particle debonding, excessive viscosity and other issues. Engineering stress-strain responses of a subset of these elastomers are shown in Fig. 1.3. In turn, the detailed investigations of Park et al.

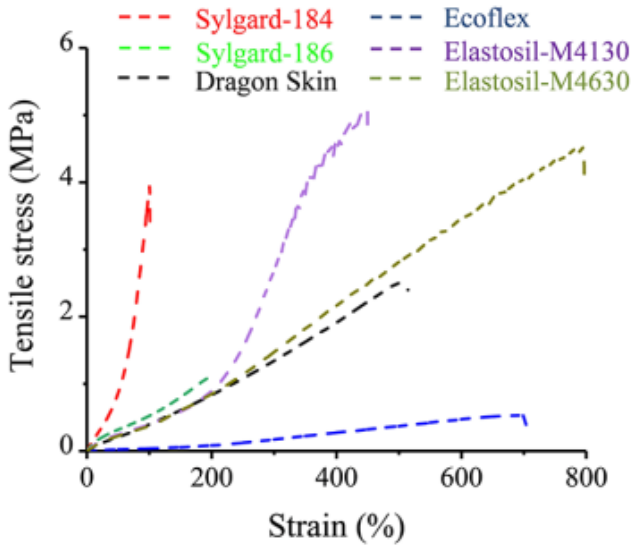

Figure 1.3: Engineering stress-strain responses of various commercially available elastomers (Park et al., 2018).

(2018) suggests that Sylgard-184, Elastosil-M4130 and Elastosil-M4630, having the shear moduli of ~ 1.0, 0.3 and 0.6 MPa, respectively, are the most suitable elastomers for the s- and h- MREs. Even though the Ecoflex elastomers also exhibit high stretchability, they are extremely soft and thus, are not suitable for most of the applications where an inherent structural strength is required to stay firm against the gravity. Recent work of Wang et al. (2019) show that depending on the composition and curing temperature, a range of different elastic properties of Sylgard-184 can be achieved. Specific details on the material selection for the s- and h- MREs and their testing methods are summarized in the following.

1.1 Fabrication and testing

The fabrication of both s- and h-MREs are mostly done by mixing the metallic fillers with the monomer of the elastomer and the curing agent, followed by curing the suitably-molded mixture at a temperature of $60^o - 120^o$C for $1 - 8$ hours (Jolly et al., 1996; Ginder et al., 1999; Danas et al., 2012b; Bodelot et al., 2017; Psarra et al., 2017; Zhao et al., 2019). More sophisticated 3D printing

techniques for the fabrication of s- and pre-magnetized h-MREs have been reported recently (Kim et al., 2018). However, the 3D printing technique imposes additional constraint on the choice of the elastomer matrix, since not all of the aforementioned elastomers are suitable for 3D printing (Kim et al., 2018). Thus, the standard mixing and curing technique still remains the primary technique for all the MREs (Linke et al., 2016; Stepanov et al., 2017; Schümann and Odenbach, 2017; Schümann et al., 2017). Specific material selections and testing techniques for the s- and h-MREs are discussed in the following.

1.1.1 MREs with iron particles

Fabrication of the iron particle-filled s-MREs were initiated by Rigbi and Jilkén (1983), who cured soft ferrite particles in a natural rubber matrix and consequently tested its mechanical properties under applied magnetic field. Since then, numerous fabrication techniques and experimental probes for the soft MREs have been reported (Jolly et al., 1996; Ginder et al., 1999, 2000; Lokander and Stenberg, 2003; Danas et al., 2012b; Bodelot et al., 2017). While the earlier fabrications of s-MREs mostly use the natural rubber-like materials to be the matrix (Jolly et al., 1996; Ginder et al., 1999, 2000; Danas et al., 2012b), the recent works consider the very soft Ecoflex (shear modulus $\sim 0.003 - 0.01$ MPa) to be the matrix material (Bodelot et al., 2017; Psarra et al., 2017). The latter provides highly compliant s-MREs, which also ensure high stretchability and high magneto-mechanical coupling.

Measurement of the coupled magneto-mechanical response of the s-MREs are not straightforward. In this context, the measurement techniques of Bodelot et al. (2017) employ highly sensitive hall probes to measure the magnetic **b** and **h** fields across the ellipsoidal specimens. Also, the associated magnetostrictions are measured via clever positioning of mirrors and sophisticated image processing techniques. The measured magnetization and magnetostriction responses by Bodelot et al. (2017) for isotropic s-MREs are shown in Fig 1.4, where we observe fully reversible magneti-

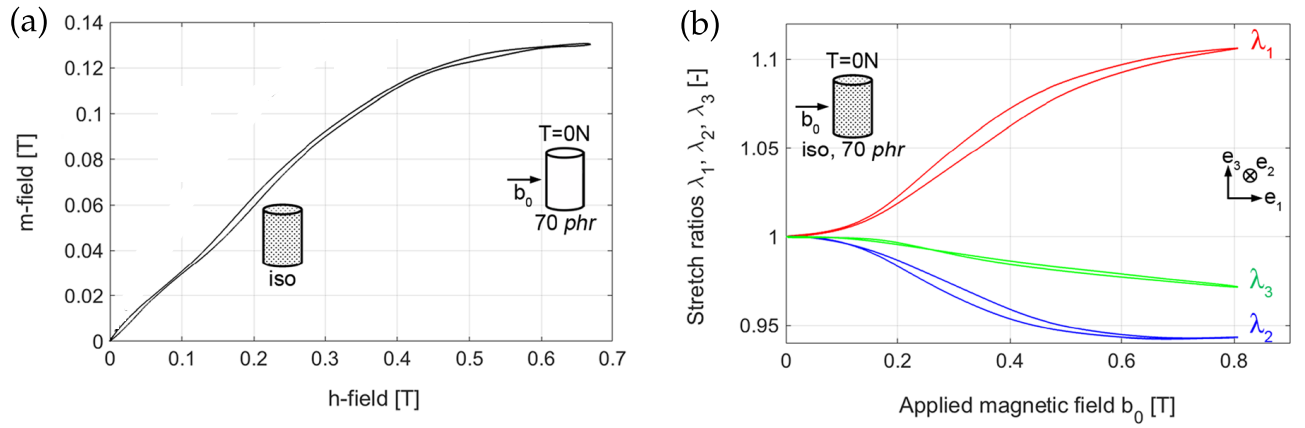

Figure 1.4: Measured (a) magnetization and (b) magnetostriction responses of a cylindrical specimen of s-MRE comprising CI particle in the Ecoflex matrix (Bodelot et al., 2017).

zation/demagnetization response in Fig 1.4a. The magnetostriction response in Fig 1.4b in terms of three orthogonal stretch ratios are, however, not representative of the local magnetostriction characteristics of the s-MREs. In fact, strong shape effects of the MRE samples play crucial roles in the measured magnetostriction response. On the other hand, Kankanala (2007) and Danas et al. (2012b) present an alternative method to measure the magnetization and magnetostriction responses of the

natural rubber-based s-MREs. Of course, the order of magnetostriction becomes less than 1% in these relatively stiff natural rubber-based MREs.

1.1.2 MREs with NdFeB particles

NdFeB particles bonded in polymers, on the other hand, are fabricated to replace the traditional permanent magnets in various applications (Garrell et al., 2003). The polymer matrix used by Garrell et al. (2003) and its contemporary investigations are highly stiff with negligible mechanical compliance. Thus, such composites are typically referred to be the "polymer bonded magnets" instead of h-MREs (Huber et al., 2017; Taylor et al., 2019; Lantean et al., 2019). Recently, a number of studies report various 3D printing methods to manufacture bonded NdFeB magnets, where highly stiff and brittle polymer matrix materials, such that epoxy resin, PEEK, etc. are used (Taylor et al., 2019; Lantean et al., 2019; Pigliaru et al., 2020).

The term h-MRE is coined since the fabrication and testing of the NdFeB particles suspended in the soft PDMS matrix are reported (Linke et al., 2016; Schümann and Odenbach, 2017; Kalina et al., 2017; Sánchez et al., 2018). However, the h-MREs made of such soft PDMS or silicone elastomers are often too soft to be used as a structural element. Moreover, the strongly magnetic NdFeB particles typically end-up damaging considerably such soft elastomeric matrices having shear modulus $G \sim 0.04 - 0.001$ MPa (Schümann and Odenbach, 2017). Thus, recent investigations on the coupled structural response of h-MREs use a *moderately soft* commercially available Sylgard-184 (10:1) PDMS matrix (Kim et al., 2018; Kaidarova et al., 2018; Zhao et al., 2019; Sitti and Wiersma, 2020). Such a flexible cured h-MRE sample made of the commercially available Magnequench MQP-16-7FP particles and Sylgard-184 is shown in Fig. 1.5a and various other shapes of the cured samples are shown

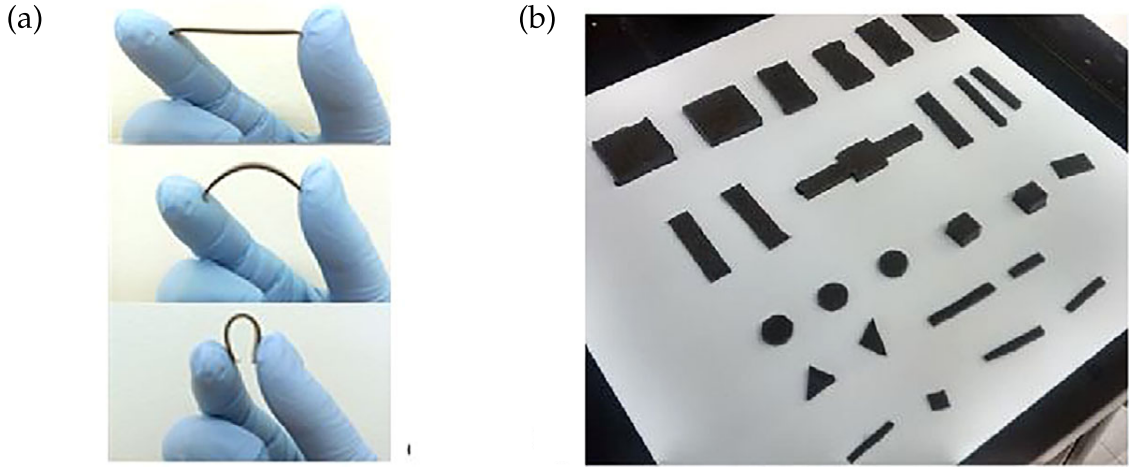

Figure 1.5: (a) Flexible h-MRE ribbon, cured Magnequench MQP-16-7FP NdFeB particles in Sylgard-184 (10:1) matrix at 90°C for 1 hour, bent by hand. (b) Examples of different shapes and sizes of cured h-MREs having the same particle-matrix combination (Kaidarova et al., 2018).

in Fig. 1.5b. Sylgard-184, having a mechanical shear modulus in the range of $G \sim 0.4 - 1.2$ MPa (Choi and Rogers, 2003; Johnston et al., 2014; Park et al., 2018; Wang et al., 2019) serves as an excellent matrix material that provides the perfect level of compliance in the h-MREs.

The magnetic hysteresis response of h-MREs are typically measured in the vibrating sample

magnetometers (VSMs), which require flat, cylindrical specimens (Linke et al., 2016; Stepanov et al., 2017). The commercially available VSMs (e.g., Lakeshore 7400), however, do not provide the setup to measure the magnetostriction responses. Thus, the measurement of magnetostrictions in the h-MREs still require rigorous investigations. In turn, Kim et al. (2018) and Zhao et al. (2019) measure structural deformations of the slender h-MRE structures under applied magnetic field having very small amplitude in the order of $\sim 20-200$ mT. This particular loading path ensures a perfectly reversible magneto-structural response and thus, one can repeat the experiments with the same samples without any pre/post treatment.

1.2 Theoretical and numerical modeling

The continuum magneto-elastic modeling of bulk metallic soft and hard magnets traces its way back to Brown (1966). Since then, a set of different continuum models for the static and dynamic response of the metallic magnets has been proposed (see the books by Hutter and van de Ven (1978); Kovetz (2000)). The MREs are, in contrast, two phase composites having both metallic magnetic and mechanically soft elastomeric phases. Thus, both microscopic (models for the individual phases) and macroscopic modeling of the MREs require finite strain-based continuum settings. In the following, we discuss such micro and macroscopic modeling and numerical computation frameworks developed in the context of s- and h-MREs.

1.2.1 s-MREs

The finite-strain framework of soft magneto-elasticity is a relatively recent development introduced by Dorfmann and Ogden (2003, 2004) and Kankanala and Triantafyllidis (2004, 2008). A continuum model for the anisotropic soft MREs is subsequently proposed by Danas et al. (2012b). These so called "top-down" phenomenological models propose the constitutive framework by observing macroscopic experimental observations.

On the other hand, a "bottom-up" approach towards the macroscopic response of the soft MREs has been developed via the variational homogenization of local microscopic potentials associated with the two phase composite. Analytical homogenization estimates for the "effective response" of mechanically incompressible, soft magnetic composites are provided by Ponte Castañeda and Galipeau (2011) and Lefèvre et al. (2017), while the numerical homogenization estimates for the same are provided by Kalina et al. (2016) and Danas (2017). In particular, Danas (2017) provides an augmented variational principle that ensures no boundary and specimen shape effects on the numerical resolutions of homogenization problems for s-MREs. Recently, Keip and Rambausek (2016, 2017) and Zabihyan et al. (2020) have developed a multi-scale (FE^2) computational technique for the soft MREs.

None of the aforementioned analytical or numerical homogenization framework provide an *explicit* macroscopic model that can be readily applied to a macroscopic boundary value problem. Thus, a "microstructure-guided" phenomenological models have been proposed recently by Mukherjee et al. (2020) and Lefèvre et al. (2019) that essentially leads exactly to the analytical homogenization model of Lefèvre et al. (2017) in some limiting cases. An alternative approach towards such microstructurally-guided models has been developed recently by Kalina et al. (2020), which however, requires expensive computations in order to fit a comparatively large set of model parameters. It

is noted that the top-down and bottom-up approaches employ either $\mathbf{F}-\mathbf{H}$ (Keip and Rambausek, 2016, 2017; Lefèvre et al., 2017; Lefèvre et al., 2019; Kalina et al., 2020) or $\mathbf{F}-\mathbf{B}$ (Kankanala and Triantafyllidis, 2004; Dorfmann and Ogden, 2004, 2005; Danas, 2017; Psarra et al., 2019) based modeling frameworks, where $\mathbf{F}$ is the mechanical deformation gradient, $\mathbf{H}$ and $\mathbf{B}$ are the magnetic field and induction, respectively. Here we indicate the independent primary variables of the modeling framework by the suffix $\mathbf{F}-\mathbf{H}$ or $\mathbf{F}-\mathbf{B}$. Of course, the relative advantage of one framework over the another depends on the objective of the study under consideration. In particular, the $\mathbf{F}-\mathbf{H}$ model leads to a scalar potential-based finite-element computation framework and thus, facilitates the computations by reducing the nodal degrees of freedom. On the other hand, the $\mathbf{F}-\mathbf{B}$-based models are advantageous when performing a stability and post-bifurcation analysis by the numerical FE method (Psarra et al., 2017, 2019).

1.2.2 Ferro-electric/magnetic switching

Thermodynamically consistent modeling of the remanent magnetization is typically carried out via introducing a *remanent internal variable*. Such thermodynamic formalism has been first introduced in the context of remanent polarization in ferroelectric ceramics (Huber et al., 1999; Huber and Fleck, 2001; McMeeking and Landis, 2002; Landis, 2002; Klinkel, 2006). Subsequently, this framework has been extended for the ferromagnetic materials as well (Linnemann et al., 2009; Mukherjee and Danas, 2019). All the aforementioned works, however, have been developed in a small strain setting. Miehe et al. (2011) provides a numerical implementation procedure for the general dissipative electro-magneto-elastic materials at small strains. Subsequently, Rosato and Miehe (2014) have proposed a "top-down" approach towards modeling the remanent polarization in a material at finite strains. Therein, the coupled polarization strain is modeled via constituting a *polarization tensor* that is defined to have the principal directions along the direction of the polarization vector. In their recent attempt to macro-model the $\mathfrak{h}$-MREs, Zhao et al. (2019) have considered a linearization of the hysteretic response near the zero applied $\mathfrak{h}$-field and subsequently carried out the coupled structural computations under a small applied magnetic field ($\sim 0.04-0.12$ T). However, this model remains relevant only for specific loading paths having small magnetic loading amplitudes.

Numerical computations for the effective response of the $\mathfrak{h}$-MREs via numerically resolving the local mechanical and magnetic fields in a representative volume element have not been investigated in detail. Although the numerical simulations of the internal particle rotations in the $\mathfrak{h}$-MREs have been carried out by Kalina et al. (2017), an incremental homogenization formalism for the hard magnetic microstructures yet needs to be stated. In this regard, it is noted that the incremental variational homogenization framework has already been employed to compute the effective response of elasto-plastic composites (Miehe, 2002; Miehe et al., 2002). Again, it is noted from Danas (2017) that the numerical homogenization for the MREs necessitates suitable augmentations to the variational homogenization problem, that, in turn, leads to a "pure" magneto-mechanical response, which is free from the geometric shape effects in the MRE sample.

1.3 Scope of the present work

Keeping in mind the variety of possible applications of the $\mathfrak{s}$- and $\mathfrak{h}$-MREs, the central idea of this work is to provide rigorous yet simple models for the macroscopic computations of the boundary

value problems (BVPs) that, in general, involve remanent (residual) magnetization and are subjected to arbitrary magneto-mechanical loading paths. Such macroscopic BVPs are of direct interest in the design of MRE-based sensors, actuators and other devices. In particular, the macroscopic models those are sought for, must reflect the effects from the underlying microstructure and its evolution sufficiently well. Thus, emphasis are given on both microscopic and macroscopic modeling of s- and h-MREs. Specifically, the present work provides the following ingredients towards an efficient micro and macroscale modeling for s- and h-MREs.

- Two equivalent **h** and **b**-based constitutive models for the metallic hard magnets with negligibly small strain are developed. These models involve suitable definitions of the *thermodynamic internal variables* and the associated constitutive laws from the Clausius-Duhem inequality and the generalized standard material (Halphen and Nguyen, 1975) framework. Moreover, we seek to have a non-hysteretic, saturation-type magnetization response from the proposed hysteresis models under the limit of vanishing coercivity (see Fig. 1.2a and b), so that the soft magnetic response can be treated to be a special case of the hard hysteresis response.

- We develop an incremental numerical homogenization method in order to compute the effective response of the h-MREs, so that the effective response of the s-MREs can also be estimated from the same model under the limit of vanishing coercivity. Such general incremental homogenization framework enables us to estimate the effective macroscopic responses emerging from a wide range of microstructures having different magnetic (hard/soft) and mechanical properties of the underlying constituents. We employ a fully Lagrangian finite-element method to locally resolve the microscopic magnetic and mechanical fields in a representative volume element (RVE) of the microstructure. The ensemble averages of these local field variables are then numerically computed to obtain the effective response of the composite as a whole.

- In order to bridge the gap between the explicit "top down" (Kankanala and Triantafyllidis, 2004) and implicit "bottom up" (Ponte Castañeda and Galipeau, 2011; Galipeau and Ponte Castañeda, 2013; Lefèvre et al., 2017) modeling approaches, we propose microstructurally-guided macroscopic phenomenological models for the s-MREs in both $\mathbf{F}-\mathbf{H}$ and $\mathbf{F}-\mathbf{B}$ modeling frameworks. The proposed models are designed to yield the exact analytical homogenization estimates in the limit of small magnetic field/induction.

- Finally, we propose macroscopic models for the h-MREs in both $\mathbf{F}-\mathbf{H}$ and $\mathbf{F}-\mathbf{B}$ variable spaces. The model is designed to take care of the underlying microstructure evolutions under different magneto-mechanical loading paths. The models are designed to satisfy various limiting conditions, that, in turn, enable us to reduce the number of model parameters in these models. Specifically, in the limit of a vanishing coercivity, the proposed models for h-MREs are set to approach the analytical homogenization model of Lefèvre et al. (2017) for the s-MREs.

As per the best of our knowledge, these aforementioned aspects in the modeling of s- and h-MREs did not receive sufficient attention in the literature, yet are of paramount interest in the theoretical and numerical modeling of them. This thesis is therefore dedicated towards addressing all these issues, step-by-step as listed in the above.

1.4 Organization of the thesis

Following this introduction, we divide the thesis in five chapters, which are dedicated towards the step-by-step development of the theoretical and numerical modeling of the effective response of MREs. The contents of these chapters are briefly described in the following.

- Local balance laws for the magnetic **b** and **h** fields, mass, linear and angular momentum are derived from the global balance laws in Chapter 2. The localized versions of the energy balance and the entropy imbalance are also developed therein and combining these two, we also derive the local Clausius-Duhem inequality. Specifically, Section 2.1 develops the local balance laws in the current configuration in terms of the current magnetic and mechanical variables. The current Clausius-Duhem inequality is also derived therein by combining the current energy balance and entropy imbalance laws. In turn, the referential counterparts of these balance laws and the Clausius-Duhem inequality are derived in Section 2.2.

- Chapter 3 is associated with the development of "switching surface"-type ferromagnetic hysteresis models both by considering **h** (Section 3.1) and **b** (Section 3.2) to be the primary variables. Important limiting cases, under which the hysteresis model yields the non-hysteretic saturation-type magnetization response, are discussed therein for both models. Finally, in Section 3.3, we identify the model parameters by fitting the model responses with the measured hysteresis loops for the NdFeB magnets.

- An incremental numerical homogenization framework for the computations of the effective response of $\mathfrak{h}$-MREs is developed in Chapter 4. Specifically, we derive the local constitutive relations in the microstructure from the Clausius-Duhem inequality and the generalized standard material relations in Section 4.2. This is followed by the definitions of the *incremental microscopic potential* and the effective (homogenized) incremental potential in Section 4.3 and 4.4, respectively. An augmented variational principle for the numerical homogenization fo the MREs is defined in Section 4.5. This variational principle ensures a magneto-mechanical response free from the specimen boundary and shape effects. Subsequently, a fully Lagrangian finite-element computation framework is developed in Section 4.6. Finally, the computed effective response for various $\mathfrak{s}$- and $\mathfrak{h}$-MREs under different loading conditions are provided in Section 4.7. In addition, the mesh convergence studies for both $\mathfrak{s}$- and $\mathfrak{h}$-MREs are presented therein.

- Chapter 5 provides microstructurally-guided explicit phenomenological models for the $\mathfrak{s}$-MREs in both $\mathbf{F}-\mathbf{H}$ and $\mathbf{F}-\mathbf{B}$ variable spaces. The model is proposed to replicate the response of the implicit, analytical homogenization model of Lefèvre et al. (2017), which is discussed in brief in Section 5.1. This is followed by the proposition of the $\mathbf{F}-\mathbf{H}$ and $\mathbf{F}-\mathbf{B}$ models in Section 5.2.1 and 5.2.2, respectively. Finally, the proposed models are probed against the full field numerical homogenization estimates and the analytical homogenization model in Section 5.3.

- Microstructurally-guided continuum modeling frameworks for the $\mathfrak{h}$-MREs are provided in Chapter 6. Specifically the Lagrangian and Eulerian modeling frameworks in, respectively, the $\mathbf{F}-\mathbf{H}$ and $\mathbf{F}-\mathbf{h}$ variable spaces are discussed in Section 6.1. The modeling is carried out in a step-by-step way by suitably defining the intermediate and current internal variables and then deriving the constitutive equations from the Clausius-Duhem inequalities and generalized

standard material relations. An equivalent set of $\mathbf{F}-\mathbf{B}$ and $\mathbf{F}-\mathbf{b}$-based constitutive models are proposed in Section 6.2, where we follow a similar procedure in deriving the constitutive relations. The magneto-mechanical coupling parameter is estimated via fitting the model responses with the numerically computed ones in Section 6.4. This is followed by a rigorous probe of the model performance against full-field microscopic numerical simulations under various non-proportional magneto-mechanical loading cycles.

- Key features of the developed numerical homogenization framework and the proposed models for s- and h-MREs are summarized in Section 7. Finally, we propose some improvement strategies of the proposed model performances and their numerical implementation schemes as the possible future directions of research.

- Appendix A provides an evolving switching surface model that enables the proposed switching surface model to model the magnetic minor loops under partially-reversed loading cycles. The evolution in the switching surface is defining via proposing suitable evolution laws for the coercive field in terms of various history-dependent, scalar variables. Finally, the proposed evolving switching surface model is fitted and probed against the experimentally measured minor loops and first-order reversal curves (FORCs).

These summarizes the organization of the thesis. We also use chapter wise appendices wherever necessary. Finally, specific concluding remarks are also provided by the ending of each chapter.

List of publications resulting from this thesis work

1. Mukherjee, D., Danas, K., 2019. An evolving switching surface model for ferromagnetic hysteresis. *J. Appl. Phys.* **125**, 033902. (doi)

2. Danas, K., Mukherjee, D., Haldar, K., Triantafyllidis, N., 2019. Bifurcation analysis of twisted liquid crystal bilayers. *J. Mech. Phys. Solids* **123**, 61-79. (doi)

3. Mukherjee, D., Bodelot, L., Danas, K., 2020. Microstructurally-guided explicit continuum models for isotropic magnetorheological elastomers with iron particles. *Int. J. Nonlin. Mech.* **120**, 103380. (doi)

Manuscripts in preparation

1. Mukherjee, D., Rambausek, M., Danas, K. Microstructurally-guided continuum models for NdFeB particle-filled, isotropic magnetorheological elastomers. *in preparation*.

2. Rambausek, M., Mukherjee, D., Danas, K. Numerical computation algorithms for dissipative magneto- visco- hyperelasticity. *in preparation*.

Chapter

2 Balance Laws and Dissipation Thermodynamic Frameworks

Chapter summary: *This chapter provides the set of balance laws along with the boundary/interface conditions and the thermodynamic Clausius-Duhem inequalities in the context of a general dissipative magneto-elastic solid. Both current (Eulerian) and reference (Lagrangian) formulations, provided herein, are derived via the direct formulation in terms of the balance laws of various field variables and the total specific energy along with the entropy inequality leading from the second law of thermodynamics.*

Chapter content

This section develops the governing equations and the constitutive laws for a magneto-active solid under finite strains. It is noted that a typical magneto-mechanical problem at the finite strains can be developed via considering either the current magnetic field $\mathbf{h}(\mathbf{x})$ or the magnetic induction $\mathbf{b}(\mathbf{x})$. Equivalently, the Lagrangian counterpart of the model can be developed via considering the referential $\mathbf{H}(\mathbf{X})$ or $\mathbf{B}(\mathbf{X})$ to be the primary magnetic variables. This chapter first derives the current

(Eulerian) version of the governing equations and thermodynamic inequalities. Their Lagrangian counterpart is subsequently provided by the end of this chapter.

We consider a deformable solid occupying a volume $\mathcal{V}_0 \in \mathbb{R}^3$ with boundary $\partial\mathcal{V}_0 \in \mathbb{R}^2$ in its reference configuration. The deformation of the solid from its reference configuration $\mathcal{V}_0$ to the current configuration $\mathcal{V}$ is defined in terms of a continuous and one-to-one mapping $\mathbf{y}(\mathbf{X})$. We assume $\mathbf{y}$ to be continuous and twice differentiable in $\mathcal{V}_0$, except at the material interfaces. Thus, the position vector of a material point in the current configuration is given by $\mathbf{x} = \mathbf{y}(\mathbf{X})$. The deformation gradient is therefore defined as $\mathbf{F}(\mathbf{X}) = \text{Grad}\,\mathbf{y}$ with $J = \det\mathbf{F} > 0$, where "Grad" denotes the gradient operator with respect to $\mathbf{X}$. We consider a *quasi-static* modeling with no inertial effects.

2.1 Current configuration (Eulerian) formulation

This formulation employs a direct approach, which, in turn, is associated with expressing the balance laws for the magnetic and mechanical quantities in the current configuration $\mathcal{V}$. The magneto-static balance laws for the current $\mathbf{h}$ and $\mathbf{b}$ along with the mechanical mass, momentum balance laws are developed via considering a closed current surface $\mathcal{S}$ and a current volume $\mathcal{V}$, both residing in a 3-dimensional Eucledian space $\mathbb{R}^3$. The current energy balance and entropy imbalance laws also follow an identical framework and thus are defined in the current volume $\mathcal{V}$. The present framework is developed by following closely the monograph of Kovetz (2000) and the articles by Dorfmann and Ogden (2004, 2005), and Kankanala and Triantafyllidis (2004).

2.1.1 Ampère's law

In the context of a magneto-active solid under the *quasi-static* loading and in absence of any space/surface charge, the sufficiently smooth magnetic induction $\mathbf{h}(\mathbf{x})$ satisfies the Ampère's law, which under the aforementioned condition is given by[1]

$$\int_{\partial\mathcal{S}} \mathbf{h}(\mathbf{x}) \cdot \mathbf{s}(\mathbf{x}) \mathrm{d}\ell = 0, \tag{2.1}$$

where $\mathbf{s}(\mathbf{x})$ is the direction of tangent to the path $\partial\mathcal{S}$ at the point $\mathbf{x}$ and $\mathrm{d}\ell$ is an infinitesimally small line element around $\mathbf{x}$. The path integral (2.1) upon applying the Stokes' theorem can be rephrased in terms of a surface integral, so that

$$\int_{\mathcal{S}} \text{curl}\,\mathbf{h} \cdot \mathbf{n}\, \mathrm{d}a = 0, \tag{2.2}$$

where "curl" represents the curl operation with respect $\mathbf{x}$, $\mathcal{S}$ is an arbitrary closed surface in $\mathbb{R}^3$ having an unit outward normal $\mathbf{n}$ at $\mathbf{x}$ and $\mathrm{d}a$ is an infinitesimal area around the point $\mathbf{x}$ on the surface $\mathcal{S}$. We henceforth suppress the $\mathbf{x}$-dependence of $\mathbf{h}$ for brevity. Applying subsequently the localization theorem we obtain the local (point-wise) form of the Ampère's law, such that

$$\text{curl}\,\mathbf{h} = \mathbf{0}, \qquad \forall\, \mathbf{x} \in \mathbb{R}^3 \tag{2.3}$$

[1] The vector inner product of two vectors $\boldsymbol{\alpha}$ and $\boldsymbol{\beta}$ is defined in terms of the index notation via $\boldsymbol{\alpha}\cdot\boldsymbol{\beta} = \alpha_i\beta_i$.

along with the interface/jump conditions

$$\mathbf{n} \times [\![\mathbf{h}]\!] = 0, \tag{2.4}$$

where $[\![\blacklozenge]\!]$ represents the jump in the field ($\blacklozenge$) across the boundary/interface $\partial\mathcal{V}$. The last is derived via applying equation (2.1) along a closed loop comprising parts just above and just below a boundary (see e.g. Kovetz (2000)). It is noted that in the jump condition (2.4), we have assumed no surface charge and electric displacement fields. Next, we set forth the balance law for the magnetic field **b**.

2.1.2 Absence of magnetic monopole

In absence of magnetic monopole, the normal component of the sufficiently smooth magnetic induction $\mathbf{b}(\mathbf{x})$ integrated over a closed surface $\partial\mathcal{V}$ vanishes identically, such that

$$\int_{\partial\mathcal{V}} \mathbf{b}(\mathbf{x}) \cdot \mathbf{n}(\mathbf{x}) \, \mathrm{d}a = 0, \tag{2.5}$$

where $\mathbf{n}(\mathbf{x})$ is an unit outward normal on $\partial\mathcal{V} \equiv \mathcal{S}$. The surface integral (2.5), upon applying the divergence theorem leads to

$$\int_{\mathcal{V}} \operatorname{div} \mathbf{b} \, \mathrm{d}v = 0, \tag{2.6}$$

where "div" denotes the divergence operator with respect to $\mathbf{x}$. Localizing (2.6) via considering a vanishing current volume $\mathcal{V}$, the point-wise form of the balance law for the **b** field is obtained to be

$$\operatorname{div} \mathbf{b} = 0, \qquad \forall\, \mathbf{x} \in \mathbb{R}^3. \tag{2.7}$$

The interface/jump condition for **b** across the surface $\partial\mathcal{V}$ is subsequently obtained via applying (2.5) in a "pill box" having its parts just above and just below an elementary boundary $\partial\mathcal{V}$, such that

$$\mathbf{n} \cdot [\![\mathbf{b}]\!] = 0, \tag{2.8}$$

Thus, the local governing equations and jump conditions for the two conjugate magnetic field variables **h** and **b** are derived from the global balance laws. Prior to the description of mechanical balance laws, it is crucial to introduce the notion of the magnetization **m** per unit current volume, which is defined in terms of the magnetic field variables via

$$\boxed{\mathbf{b} = \mu_0(\mathbf{h} + \mathbf{m}),} \tag{2.9}$$

where μ_0 is the magnetic permeability of the vacuum, whose value is given by $4\pi \times 10^{-7}$ N A^{-2}. Notably, the magnetization **m** vanishes identically in any non-magnetizable media, leading to the constitutive relation $\mathbf{b} = \mu_0\mathbf{h}$.

Remark 2.1. The magnetization **m**, unlike the magnetic field **h** or magnetic induction **b**, is a derived quantity and hence, is not subjected to any differential or boundary constraints. Nevertheless, **m** is a crucial quantity in magnetism that is used to represent the "magnetization response" of a material under externally applied magnetic **h** or **b** fields.

2.1.3 Balance of mass

The mass balance law postulates that the total mass associated with the current volume $\mathcal{V}$ remains unchanged in time, such that

$$\frac{d}{dt}\left[\int_{\mathcal{V}} \rho \, dv\right] = 0, \tag{2.10}$$

where ρ is the current density of the solid and the operator $d(\blacklozenge)/dt$ represents the material time derivative. Since the current volume element dv is related to the referential volume element dV via $dv = JdV$, (2.10) is now recast in the form

$$\frac{d}{dt}\left[\int_{\mathcal{V}} \rho J \, dV\right] = 0 \quad \Rightarrow \quad \int_{\mathcal{V}_0} \dot{\overline{\rho J}} \, dV = 0, \tag{2.11}$$

where the $\dot{(\blacklozenge)}$ symbol is introduced to be an alternative representation for the material time derivative $d(\blacklozenge)/dt$ for brevity. Due to the arbitrariness of the reference volume $\mathcal{V}_0$, one can express the localized (point-wise) mass balance law to be

$$\dot{\overline{\rho J}} = (\dot{\rho} + \rho \, \mathrm{grad}\dot{\mathbf{x}})J = 0, \tag{2.12}$$

where we utilize the relation $\dot{J} = J \, \mathrm{grad}\dot{\mathbf{x}}$, with the operator "grad" representing the gradient with respect to $\mathbf{x}$. Furthermore, the kinematic constraints on J leads to the condition $J > 0$. Thus, (2.12) can be recast to be

$$\dot{\rho}_0 = (\dot{\rho} + \rho \, \mathrm{grad}\dot{\mathbf{x}}) = 0 \qquad \forall \, \mathbf{x} \in \mathbb{R}^3, \tag{2.13}$$

where $\rho_0 = \rho J$ is the reference material density.

2.1.4 Balance of linear momentum

In the linear and angular momentum balance laws, we follow the approach of Kovetz (2000) and Kankanala and Triantafyllidis (2004) in terms of considering a "total" Cauchy stress $\boldsymbol{\sigma}$ in the solid that comprises both mechanical and magnetic stress contributions. The body force per unit mass $\mathbf{f}$, thus, does not contain any magnetic body force term. It is noted that the earlier formulations for magneto-elasticity starting from Brown (1966) have considered the magnetic body forces and couples explicitly in addition to the general asymmetric mechanical Cauchy stress $\boldsymbol{\sigma}_{\mathtt{mech}}$. Nevertheless, the present approach, as would be observed in the subsequent sections, takes the magnetic stress contributions into account due to its very construction.

For a non-accelerating solid, the mechanical force equilibrium equation in an arbitrary current volume element $\mathcal{V}$ reads

$$\int_{\mathcal{V}} \rho \mathbf{f} \, dv + \int_{\partial\mathcal{V}} \mathbf{t} \, da = 0, \tag{2.14}$$

where $\mathbf{t}$ is the boundary traction on the surface $\partial\mathcal{V}$. The current surface traction $\mathbf{t}$ on a surface element having unit normal $\mathbf{n}$ is related to the Cauchy stress at that point via the well-known Cauchy tetrahedron relation $\boldsymbol{\sigma} \cdot \mathbf{n} = \mathbf{t}$. Substituting this relation into (2.14) and subsequently applying the divergence theorem, we obtain

$$\int_{\mathcal{V}} (\rho \mathbf{f} + \mathrm{div}\boldsymbol{\sigma}) \, dv = 0, \tag{2.15}$$

which, owing to the arbitrariness of the volume element $\mathcal{V}$, readily leads to the point-wise form of the linear momentum balance law, such that

$$\rho\mathbf{f} + \operatorname{div}\boldsymbol{\sigma} = 0, \qquad \forall\, \mathbf{x} \in \mathbb{R}^3. \tag{2.16}$$

Notice that, the "total stress" $\boldsymbol{\sigma}$ is non-zero in both MRE and the surrounding air (Kankanala and Triantafyllidis, 2004). Applying (2.14) in a "pill box" across the boundary, the jump condition across an elementary boundary surface $\partial\mathcal{V}$ is obtained to be

$$[\![\boldsymbol{\sigma}]\!] \cdot \mathbf{n} + \mathbf{t}^{\mathtt{mech}} = 0, \tag{2.17}$$

where $\mathbf{t}^{\mathtt{mech}}$ is the applied traction on the boundary $\partial\mathcal{V}$. We assume no propagating discontinuity surface in the continuum.

2.1.5 Balance of angular momentum

During the quasi-static deformation of a solid, the balance law for the angular momentum postulates that the moment of all the forces with respect to a fixed point mush vanish. Without loss of generality, the fixed point is considered to be the origin of the coordinate system $\mathbf{x}$. Thus, in absence of body couples, the angular momentum balance in an elementary current volume $\mathcal{V}$ reads

$$\int_{\mathcal{V}} \mathbf{x} \wedge \rho\mathbf{f}\, \mathrm{d}v + \int_{\partial\mathcal{V}} \mathbf{x} \wedge (\boldsymbol{\sigma} \cdot \mathbf{n})\, \mathrm{d}a = 0, \tag{2.18}$$

where the wedge "$\wedge$" symbol denotes the exterior tensor product, such that $\boldsymbol{\alpha} \wedge \boldsymbol{\beta} = \boldsymbol{\alpha} \otimes \boldsymbol{\beta} - \boldsymbol{\beta} \otimes \boldsymbol{\alpha}$. Eq. (2.18) upon algebraic manipulations followed by the application of the divergence theorem leads to

$$\int_{\mathcal{V}} \mathbf{x} \wedge \rho\mathbf{f}\, \mathrm{d}v + \int_{\mathcal{V}} \left[\mathbf{x} \wedge (\operatorname{div}\boldsymbol{\sigma}) + \boldsymbol{\sigma} - \boldsymbol{\sigma}^{\mathsf{T}}\right] \mathrm{d}v = 0. \tag{2.19}$$

Substituting (2.15) into the last equation and due to the arbitrariness of $\mathcal{V}$, one obtains the point-wise form of the angular momentum balance given by

$$\boldsymbol{\sigma} = \boldsymbol{\sigma}^{\mathsf{T}}. \tag{2.20}$$

Thus, in absence of body couples, the angular momentum balance law dictates the Cauchy stress to remain identically symmetric. Again, the symmetry of $\boldsymbol{\sigma}$ is a direct consequence of considering it to be comprised of both mechanical and magnetic contributions (Robinson, 1975; Kovetz, 2000; Kankanala and Triantafyllidis, 2004). A different set of theories in magneto-elasticity considers $\boldsymbol{\sigma}$ to be purely $\boldsymbol{\sigma}_{\mathtt{mech}}$ and considers the magneto-mechanical interactions in terms of body forces and couples, leading to an asymmetric $\boldsymbol{\sigma}$ (Pao and Hutter, 1975).

2.1.6 Energy balance

The total energy associated with an arbitrary current volume $\mathcal{V}$ is given by $\rho\varepsilon$, where ε is the specific energy (per unit mass) associated with the system. The law of energy balance postulates that the rate of change of the total energy in an arbitrary volume $\mathcal{V}$ is a sum of three contributions, namely i) mechanical power associated with the body force $\mathbf{f}$ and surface traction $\mathbf{t}$, ii) thermal power

associated with the internal heat generation per unit mass r and the surface heat flux and iii) magnetic power associated with the surface magnetic flux. The energy balance law is therefore expressed to be

$$\frac{d}{dt}\left[\int_{\mathcal{V}} \rho\varepsilon dv\right] = \underbrace{\left[\int_{\mathcal{V}} \dot{\mathbf{x}}\cdot\rho\mathbf{f}\, dv + \int_{\partial\mathcal{V}} \dot{\mathbf{x}}\cdot\mathbf{t}\, da\right]}_{\text{mechanical power}} + \underbrace{\left[\int_{\mathcal{V}} \rho r\, dv - \int_{\partial\mathcal{V}} \mathbf{n}\cdot\mathbf{q}\, da\right]}_{\text{thermal power}} - \underbrace{\int_{\partial\mathcal{V}} \mathbf{n}\cdot\mathbf{p}\, da}_{\text{magnetic power}}, \tag{2.21}$$

where $\mathbf{q}$ is the heat flux vector and $\mathbf{p} = (\dot{\mathbf{x}}\times\mathbf{b})\times\mathbf{h}$ is the *Poynting vector* that denotes the magnetic energy flux. Both, the thermal and magnetic energy flowing outside the volume $\mathcal{V}$ are considered to be positive, which, in turn, justifies the negative signs associated with the energy flux associated to $\mathbf{q}$ and $\mathbf{p}$ in (2.21). Localizing subsequently (2.21) leads to the point-wise energy balance equation, so that

$$\rho\dot{\varepsilon} = \rho(\dot{\mathbf{x}}\cdot\mathbf{f} + r) + \operatorname{div}(\dot{\mathbf{x}}\boldsymbol{\sigma} - \mathbf{q} - \mathbf{p}). \tag{2.22}$$

The term $\operatorname{div}(\dot{\mathbf{x}}\boldsymbol{\sigma})$ in the last equation can be expanded further to be $\operatorname{div}(\dot{\mathbf{x}}\boldsymbol{\sigma}) = \dot{\mathbf{x}}\cdot\operatorname{div}(\boldsymbol{\sigma}) + \boldsymbol{\sigma}\colon \operatorname{grad}\dot{\mathbf{x}}$[2]. The divergence of the Poynting vector is further expanded, such that

$$\begin{aligned}\operatorname{div}[(\dot{\mathbf{x}}\times\mathbf{b})\times\mathbf{h}] &= \mathbf{h}\cdot\operatorname{curl}(\dot{\mathbf{x}}\times\mathbf{b}) - (\dot{\mathbf{x}}\times\mathbf{b})\cdot\operatorname{curl}\mathbf{h}\\ &= \mathbf{h}\cdot\left[\mathbf{b}\cdot(\operatorname{grad}\dot{\mathbf{x}}) - \mathbf{b}\,(\operatorname{div}\dot{\mathbf{x}}) - (\operatorname{grad}\mathbf{b})\cdot\dot{\mathbf{x}} + (\operatorname{div}\mathbf{b})\,\dot{\mathbf{x}}\right]\\ &= [\mathbf{h}\otimes\mathbf{b} - (\mathbf{h}\cdot\mathbf{b})\mathbf{I}]\colon\operatorname{grad}\dot{\mathbf{x}} - \mathbf{h}\cdot\operatorname{grad}\mathbf{b}\cdot\dot{\mathbf{x}},\end{aligned} \tag{2.23}$$

where we have substituted the balance laws (2.3) and (2.7), respectively in the first and second steps. Subsequently, (2.22) upon simplification in terms of substituting $\operatorname{div}(\dot{\mathbf{x}}\boldsymbol{\sigma}) = \dot{\mathbf{x}}\cdot\operatorname{div}(\boldsymbol{\sigma}) + \boldsymbol{\sigma}\colon\operatorname{grad}\dot{\mathbf{x}}$, (2.16) and (2.23), yields

$$\rho\dot{\varepsilon} = \rho r + [\boldsymbol{\sigma} - \mathbf{h}\otimes\mathbf{b} + (\mathbf{h}\cdot\mathbf{b})\mathbf{I}]\colon\mathbf{l} + \mathbf{h}\cdot\dot{\mathbf{b}} - \operatorname{div}\mathbf{q}, \tag{2.24}$$

where $\mathbf{I}$ is the second order identity tensor, $\mathbf{l} = \operatorname{grad}\dot{\mathbf{x}}$ is the deformation rate tensor and the rate $\operatorname{grad}\mathbf{b}\cdot\dot{\mathbf{x}}$ is replaced by the material time derivative $\dot{\mathbf{b}}$ since the time rate $\partial\mathbf{b}/\partial t$ vanishes identically in the MREs (Kankanala and Triantafyllidis, 2004).

2.1.7 Entropy imbalance

The entropy imbalance law dictates the rate of change of the entropy associated with an arbitrary volume $\mathcal{V}$ to be always positive. Thus, the entropy inequality in terms of the specific entropy η (per unit mass), absolute temperature ϑ, the heat generation r and the heat flux $\mathbf{q}$ is given by the classical Clausius-Duhem inequality

$$\frac{d}{dt}\left[\int_{\mathcal{V}} \rho\eta dv\right] \geqslant \int_{\mathcal{V}} \frac{\rho r}{\vartheta} dv - \int_{\partial\mathcal{V}} \mathbf{n}\cdot\frac{1}{\vartheta}\mathbf{q}\, da. \tag{2.25}$$

The localized Clausius-Duhem inequality hence reads

$$\rho\theta\dot{\eta} - \rho r + \vartheta\operatorname{div}(\vartheta^{-1}\mathbf{q}) \geqslant 0. \tag{2.26}$$

[2]The tensor inner product is defined via $\mathbf{A}\colon\mathbf{B} = A_{ij}B_{ij}$

Substituting the heat generation rate r from (2.24) into the last equation and simplifying we obtain

$$\rho_0\vartheta\dot{\eta} - \rho_0\dot{\varepsilon} + J[\boldsymbol{\sigma} - \mathbf{h}\otimes\mathbf{b} + (\mathbf{h}\cdot\mathbf{b})\mathbf{I}]\colon \mathbf{l} + J\mathbf{h}\cdot\dot{\mathbf{b}} + J\vartheta\mathbf{q}\cdot\operatorname{div}(\vartheta^{-1}) \geqslant 0. \tag{2.27}$$

For the quasi-static model the kinetic energy contribution to the specific energy ε is neglected. Therefore, ε becomes identical to the specific internal energy associated with the material, which we define to be comprised of i) the specific free energy density $w^b(\mathbf{F},\mathbf{b},\vartheta,\boldsymbol{\xi})/\rho_0$ and ii) specific thermal energy $\eta\vartheta$, such that

$$\varepsilon = \frac{1}{\rho_0}w^b(\mathbf{F},\mathbf{b},\vartheta,\boldsymbol{\xi}) + \eta\vartheta. \tag{2.28}$$

The general set $\boldsymbol{\xi}$ comprising of scalar, first and second order tensors in the definition of w^b represents a set of *thermodynamic internal variables*, which are, in turn, crucial in the modeling of history-dependent dissipative thermodynamic processes. It is noted that (2.28) is a constitutive choice for ε, which may have other energy density functions in terms of $\mathbf{h}$ or $\mathbf{m}$ as well (Kankanala and Triantafyllidis, 2004). This thesis considers the magneto-elastic models via considering the $\mathbf{F}-\mathbf{b}$ and $\mathbf{F}-\mathbf{h}$ to be the set of primary variables. Consequently, two different versions of the local Clausius-Duhem inequality (2.27) would surface.

$\mathbf{F}-\mathbf{b}$ *model* : Further specialization of (2.27) for the $\mathbf{F}-\mathbf{b}$ model can be obtained via substituting (2.28) into it. Thus, (2.27) reads upon simplification

$$J[\boldsymbol{\sigma} - \mathbf{h}\otimes\mathbf{b} + (\mathbf{h}\cdot\mathbf{b})\mathbf{I}]\colon \mathbf{l} + J\mathbf{h}\cdot\dot{\mathbf{b}} - \dot{w}^b - \rho_0\eta\dot{\vartheta} + J\vartheta\mathbf{q}\cdot\operatorname{div}(\vartheta^{-1}) \geqslant 0. \tag{2.29}$$

$\mathbf{F}-\mathbf{h}$ *model* : In order to specialize (2.27) for the $\mathbf{F}-\mathbf{h}$ model, we first rephrase (2.28) in terms of $w^h(\mathbf{F},\mathbf{h},\vartheta,\boldsymbol{\xi})$, which is the complimentary energy density to w^b, obtained via a partial Legendre-Fenchel transformation of it with respect to $\mathbf{b}$ such that (Bustamante et al., 2008; Danas, 2017)

$$w^h(\mathbf{F},\mathbf{h},\vartheta,\boldsymbol{\xi}) = w^b(\mathbf{F},\mathbf{b},\vartheta,\boldsymbol{\xi}) - J\mathbf{h}\cdot\mathbf{b}. \tag{2.30}$$

Furthermore, from the above relation, we rephrase (2.28) to be

$$\varepsilon = \frac{1}{\rho_0}w^h(\mathbf{F},\mathbf{h},\vartheta,\boldsymbol{\xi}) + \frac{J}{\rho_0}\mathbf{h}\cdot\mathbf{b} + \eta\vartheta. \tag{2.31}$$

Substitution of the last into (2.27) followed by simplification leads to the Clausius-Duhem inequality specialized for the $\mathbf{F}-\mathbf{h}$ formulation, given by

$$J[\boldsymbol{\sigma} - \mathbf{h}\otimes\mathbf{b}]\colon \mathbf{l} - J\mathbf{b}\cdot\dot{\mathbf{h}} - \dot{w}^h - \rho_0\eta\dot{\vartheta} + J\vartheta\mathbf{q}\cdot\operatorname{div}(\vartheta^{-1}) \geqslant 0. \tag{2.32}$$

To this end, the Clausius-Duhem inequality is specialized for the energy density functions defined in terms of $\mathbf{F}-\mathbf{b}$ and $\mathbf{F}-\mathbf{h}$, respectively. Specific form of the constitutive relations necessitates the definition of the internal variables and the functional forms of $w^b(\mathbf{F},\mathbf{b},\vartheta,\boldsymbol{\xi})$ or $w^h(\mathbf{F},\mathbf{h},\vartheta,\boldsymbol{\xi})$. No attempt is made in this chapter to set forth the specific constitutive relations emerging from (2.29) and (2.32). Rather, the specific constitutive relations will be provided while defining the specific material properties of the magneto-active solid in the subsequent sections.

Remark 2.2. Most of the existing models for the MREs consider a further decomposition of the energy densities w^b and w^h into the *specific Helmholtz free energy* ψ^b and ψ^h, respectively, and the

corresponding potential associated with the free space, so that (Kankanala and Triantafyllidis, 2004; Bustamante et al., 2008; Danas, 2017)

$$w^{b}(\mathbf{F},\mathbf{b},\vartheta,\boldsymbol{\xi}) = \rho_0\psi^{b}(\mathbf{F},\mathbf{b},\vartheta,\boldsymbol{\xi}) + \frac{J}{2\mu_0}\mathbf{b}\cdot\mathbf{b} \tag{2.33}$$

and

$$w^{h}(\mathbf{F},\mathbf{h},\vartheta,\boldsymbol{\xi}) = \rho_0\psi^{h}(\mathbf{F},\mathbf{h},\vartheta,\boldsymbol{\xi}) - \frac{J\mu_0}{2}\mathbf{h}\cdot\mathbf{h}. \tag{2.34}$$

Finally, substituting (2.33) and (2.34) into (2.29) and (2.32), respectively, we obtain the modified Clausius-Duhem inequalities in terms of the Helmholtz free energy ψ^{b} and ψ^{h}, so that

$$J\left[\boldsymbol{\sigma} - \mathbf{h}\otimes\mathbf{b} + \frac{\mu_0}{2}(|\mathbf{h}|^2 - |\mathbf{m}|^2)\mathbf{I}\right] : \mathbf{l} + J\mathbf{m}\cdot\dot{\mathbf{b}} - \rho_0\dot{\psi}^{b} - \rho_0\eta\dot{\vartheta} + J\vartheta\mathbf{q}\cdot\mathrm{div}(\vartheta^{-1}) \geqslant 0 \tag{2.35}$$

and

$$J\left[\boldsymbol{\sigma} - \mathbf{h}\otimes\mathbf{b} + \frac{\mu_0}{2}|\mathbf{h}|^2\mathbf{I}\right] : \mathbf{l} - J\mathbf{m}\cdot\dot{\mathbf{h}} - \rho_0\dot{\psi}^{h} - \rho_0\eta\dot{\vartheta} + J\vartheta\mathbf{q}\cdot\mathrm{div}(\vartheta^{-1}) \geqslant 0, \tag{2.36}$$

respectively, for the $\mathbf{F}-\mathbf{b}$ and $\mathbf{F}-\mathbf{h}$-based models. We note that (2.35) and (2.36) are identical to the Clausius-Duhem inequalities obtained by Kankanala and Triantafyllidis (2004).

2.1.8 Generalized standard materials framework

It is emphasized that the constitutive model for the dissipative MREs involve an additional potential, namely the *dissipation potential* apart from the energy density $w^{b}(\mathbf{F},\mathbf{b},\vartheta,\boldsymbol{\xi})$ or $w^{h}(\mathbf{F},\mathbf{h},\vartheta,\boldsymbol{\xi})$. In this context, the generalized standard materials (GSM) framework provides a constitutive relation connecting the dissipation ($\mathscr{D}^{b}(\mathbf{F},\mathbf{b},\vartheta,\boldsymbol{\xi},\dot{\boldsymbol{\xi}})$ and $\mathscr{D}^{h}(\mathbf{F},\mathbf{h},\vartheta,\boldsymbol{\xi},\dot{\boldsymbol{\xi}})$) and energetic ($w^{b}(\mathbf{F},\mathbf{b},\vartheta,\boldsymbol{\xi})$ or $w^{h}(\mathbf{F},\mathbf{h},\vartheta,\boldsymbol{\xi})$) potentials, such that (Halphen and Nguyen, 1975)

$$\frac{\partial w^{b}}{\partial\boldsymbol{\xi}} + \frac{\partial\mathscr{D}^{b}}{\partial\dot{\boldsymbol{\xi}}} = 0 \qquad \text{or} \qquad \frac{\partial w^{h}}{\partial\boldsymbol{\xi}} + \frac{\partial\mathscr{D}^{h}}{\partial\dot{\boldsymbol{\xi}}} = 0, \tag{2.37}$$

respectively. Notice that, the last relations holds for each individual element of $\boldsymbol{\xi}$. These relations are also referred to be the Biot's relation (Miehe et al., 2011; Rosato and Miehe, 2014). Finally, the ensemble of the Clausius-Duhem inequality (2.35) or (2.35) and the relation for generalized standard materials (2.37) upon the application of the standard Coleman-Noll-Gurtin (Coleman and Gurtin, 1967; Coleman and Noll, 1974) arguments lead to the constitutive relations along with the evolution equations for $\boldsymbol{\xi}$. Finally, the key balance laws, boundary/interface conditions, thermodynamic inequalities and the generalized standard material laws are summarized in Box 2.1

2.2 Reference configuration (Lagrangian) formulation

The reference configuration formulation considers the reference coordinate $\mathbf{X}$ to be the primary coordinate system and thus, the referential magnetic fields $\mathbf{B}(\mathbf{X})$ and $\mathbf{H}(\mathbf{X})$ to be the primary field variables. In this regard, both, the balance law-based direct formulation and the energy-based variational formulations are reported in the literature (Kankanala and Triantafyllidis, 2004; Dorfmann and Ogden, 2004; Bustamante et al., 2008). In this work we follow Steigmann (2004) in order to perform

transformation of each individual balance laws in Section 2.1 into the reference configuration. Consequently, the Lagrangian equivalent of the current magnetic and stress fields would be defined at relevant places.

Box 2.1: Balance laws and thermodynamic inequalities in the current configuration

Ampère's Law:	$\operatorname{curl}\mathbf{h}=\mathbf{0}$,	*boundary/interface condition*:	$\mathbf{n}\times[\![\mathbf{h}]\!]=\mathbf{0}$
Absence of magnetic monopole:	$\operatorname{div}\mathbf{b}=0$,	*boundary/interface condition*:	$\mathbf{n}\cdot[\![\mathbf{b}]\!]=0$
Linear momentum balance:	$\operatorname{div}\boldsymbol{\sigma}+\rho\mathbf{f}=\mathbf{0}$,	*boundary/interface condition*:	$[\![\boldsymbol{\sigma}]\!]\cdot\mathbf{n}+\mathbf{t}^{\text{mech}}=\mathbf{0}$
Angular momentum balance:	$\boldsymbol{\sigma}=\boldsymbol{\sigma}^{\mathsf{T}}$		

Clausius-Duhem inequality:

$\mathbf{F}-\mathbf{b}$ *model*: $\quad J\left[\boldsymbol{\sigma}-\mathbf{h}\otimes\mathbf{b}+\frac{\mu_0}{2}(|\mathbf{h}|^2-|\mathbf{m}|^2)\mathbf{I}\right]:\mathfrak{l}+J\mathbf{m}\cdot\dot{\mathbf{b}}-\rho_0\dot{\psi}^{\mathfrak{b}}-\rho_0\eta\dot{\vartheta}+J\vartheta\mathbf{q}\cdot\operatorname{div}(\vartheta^{-1})\geqslant 0$

$\mathbf{F}-\mathbf{h}$ *model*: $\quad J\left[\boldsymbol{\sigma}-\mathbf{h}\otimes\mathbf{b}+\frac{\mu_0}{2}|\mathbf{h}|^2\mathbf{I}\right]:\mathfrak{l}-J\mathbf{m}\cdot\dot{\mathbf{h}}-\rho_0\dot{\psi}^{\mathfrak{h}}-\rho_0\eta\dot{\vartheta}+J\vartheta\mathbf{q}\cdot\operatorname{div}(\vartheta^{-1})\geqslant 0$

Generalized standard material relation:

$\mathbf{F}-\mathbf{b}$ *model*: $\quad \dfrac{\partial w^{\mathfrak{b}}}{\partial\xi}+\dfrac{\partial\mathscr{D}^{\mathfrak{b}}}{\partial\dot{\xi}}=0$

$\mathbf{F}-\mathbf{h}$ *model*: $\quad \dfrac{\partial w^{\mathfrak{h}}}{\partial\xi}+\dfrac{\partial\mathscr{D}^{\mathfrak{h}}}{\partial\dot{\xi}}=0$

2.2.1 Ampère's law

The infinitesimal tangent vector $\mathbf{s}_0\mathrm{d}l$ along a closed path $\partial\mathcal{S}_0$ in the reference configuration is related to its current description via $\mathbf{F}\mathbf{s}_0\mathrm{d}l=\mathbf{s}\mathrm{d}\ell$. Thus, the Ampère's law (2.1) along a referential closed path $\partial\mathcal{S}_0$ is expressed to be

$$\int_{\partial\mathcal{S}_0}\mathbf{h}\cdot\mathbf{F}\mathbf{s}_0\mathrm{d}l=0\qquad\Rightarrow\qquad\int_{\mathcal{S}_0}\operatorname{Curl}(\mathbf{F}^{\mathsf{T}}\mathbf{h})\cdot\mathcal{N}\mathrm{d}A=0,\tag{2.38}$$

where "Curl" represents the curl operator with respect to the reference coordinate $\mathbf{X}$ and $\mathcal{N}$ is the unit normal on the infinitesimal reference surface $\mathrm{d}A$. The localization of $(2.38)_2$ leads to the point-wise form of the Ampère's law, so that

$$\operatorname{Curl}(\mathbf{F}^{\mathsf{T}}\mathbf{h})=\mathbf{0}.\tag{2.39}$$

The curl-free reference magnetic $\mathfrak{h}$-field $\mathbf{H}$ is thus defined to be

$$\boxed{\mathbf{H}=\mathbf{F}^{\mathsf{T}}\mathbf{h},}\tag{2.40}$$

which is, in turn, the "pull-back" of the current $\mathbf{h}$ to the reference configuration. Hence, the local Ampere's law in terms of the referential $\mathbf{H}$ reads

$$\operatorname{Curl}\mathbf{H}=\mathbf{0},\qquad\forall\,\mathbf{X}\in\mathbb{R}^3\tag{2.41}$$

Similarly, the Lagrangian counterpart of the jump condition (2.4) is given by

$$\mathcal{N}\times[\![\mathbf{H}]\!]=\mathbf{0}.\tag{2.42}$$

The last can be derived directly by applying (2.38) along a closed line element, that has its segments across the boundary surface. Again, no propagating surface discontinuity and no free surface charges are considered in this case.

2.2.2 Absence of magnetic monopole

The balance law associated with the preservation of magnetic dipoles in a closed surface $\partial\mathcal{V}_0$ in the reference configuration is obtained from its current form (2.7) via substituting the Nanson's formula $\mathbf{n}da = J\mathbf{F}^{-T}\mathcal{N}dA$, connecting the current and referential description of an area element. The balance of magnetic dipoles in a closed reference surface $\partial\mathcal{V}_0$ thus reads

$$\int_{\partial\mathcal{V}_0} \mathbf{b}\cdot J\mathbf{F}^{-T}\mathcal{N}dA = 0 \qquad \Rightarrow \qquad \int_{\mathcal{V}_0} \mathrm{Div}\big(J\mathbf{F}^{-1}\mathbf{b}\big)dV = 0, \tag{2.43}$$

where "Div" represents the divergence operator with respect to $\mathbf{X}$. The arbitrariness of the reference volume $\mathcal{V}_0$ leads to the local point-wise form of the last, such that

$$\mathrm{Div}\ \mathbf{B} = 0, \qquad \forall\, \mathbf{X} \in \mathbb{R}^3, \tag{2.44}$$

where the Lagrangian magnetic field $\mathbf{B}$ is defined via the pull-back transformation

$$\boxed{\mathbf{B} = J\mathbf{F}^{-1}\mathbf{b}.} \tag{2.45}$$

The Lagrangian version of the jump conditions can also be obtained via direct substitution of the Nanson's formula into (2.8), which upon simplification reads

$$\mathcal{N}\cdot[\![\mathbf{B}]\!] = 0. \tag{2.46}$$

We note that, the last can also be equivalently derived via applying $(2.43)_1$ in a "pill box", considered across the reference boundary surface.

One can, in principle, define a Lagrangian counterpart of $\mathbf{m}$ via postulating a definition of the Lagrangian magnetization per unit volume via a relation like (2.9). However, thorough investigations of Dorfmann and Ogden (2004, 2005) show that (2.9) does not lead exactly to the same relation between the Lagrangian $\mathbf{B}$, $\mathbf{H}$ and magnetization upon a pull-back transformation. Rather, some additional terms consisting $\mathbf{F}$ show up. Thus, in this work, we refrain from defining any Lagrangian definition of the magnetization. In turn, usage of the term "magnetization" henceforth would refer identically to the current magnetization $\mathbf{m}$.

2.2.3 Linear momentum balance

The condition for mass balance in the reference configuration simply reads $\dot{\rho}_0 = 0$. The linear momentum balance in a reference volume $\mathcal{V}_0$ is expressed from (2.14) via transforming the integrals therein via expressing the current volume element to be $dv = JdV$ and using the Nanson's formula, so that

$$\int_{\mathcal{V}_0} \rho_0\mathbf{f}\, dV + \int_{\partial\mathcal{V}_0} J\boldsymbol{\sigma}\cdot\mathbf{F}^{-T}\mathcal{N}dA = 0 \qquad \Rightarrow \qquad \int_{\mathcal{V}_0} (\rho_0\mathbf{f} + \mathrm{Div}\ \mathbf{S})dV = 0, \tag{2.47}$$

where $\mathbf{S}$ is the first Piola-Kirchhoff stress defined via

$$\boxed{\mathbf{S} = J\boldsymbol{\sigma}\mathbf{F}^{-T}.} \tag{2.48}$$

The arbitrariness of the elementary reference volume $\mathcal{V}_0$ eventually leads to the point-wise form of the linear momentum balance, such that

$$\rho_0\mathbf{f} + \text{Div } \mathbf{S} = 0, \qquad \forall\, \mathbf{X} \in \mathbb{R}^3. \tag{2.49}$$

A similar application of the Nanson's formula leads to the transformation of the jump condition (2.17) now reads

$$[\![\mathbf{S}]\!] \cdot \mathcal{N} + \mathbf{T}^{\text{mech}} = 0, \tag{2.50}$$

where $\mathbf{T}^{\text{mech}}$ is the total externally applied traction on the reference boundary $\partial\mathcal{V}_0$. It is important to note that $\mathbf{T}^{\text{mech}}$ is the total traction vector and it is impossible to apply traction that would be equilibriated via the purely mechanical or magnetic stress components (McMeeking and Landis, 2005; McMeeking et al., 2007). Nevertheless, a proper augmentation to the underlying variational principle may allow the application of "purely mechanical" external tractions (Danas, 2017). A thorough discussion on this will be provided in the subsequent chapters.

2.2.4 Angular momentum balance

The angular momentum balance law in the reference configuration can be expressed via simply taking moment of the linear momentum in $(2.47)_1$ with respect to the reference origin, such that

$$\int_{\mathcal{V}_0} \mathbf{y} \wedge \rho_0\mathbf{f}\, dV + \int_{\partial\mathcal{V}_0} \mathbf{y} \wedge \mathbf{S}\cdot\mathcal{N} dA = 0, \tag{2.51}$$

where $\mathbf{y}(\mathbf{X}, t)$ is the position of the volume element $\mathcal{V}_0$ with respect to the reference origin. Applying the divergence theorem and after thorough algebraic manipulations, we rephrase (2.51) to be

$$\int_{\mathcal{V}_0} (\mathbf{y} \wedge \rho_0\mathbf{f} + \mathbf{y} \wedge \text{Div } \mathbf{S} + \mathbf{S}\mathbf{F}^T - \mathbf{F}\mathbf{S}^T) dV = 0. \tag{2.52}$$

Localizing (2.52) after substituting (2.49) into it leads to the point-wise form of the angular momentum balance law in the reference configuration

$$\mathbf{S}\mathbf{F}^T = \mathbf{F}\mathbf{S}^T. \tag{2.53}$$

2.2.5 Energy balance

The Lagrangian description of the energy balance law is obtained via directly rephrasing (2.21) into the reference form, so that

$$\begin{aligned}\frac{d}{dt}\left[\int_{\mathcal{V}_0} \rho_0 \varepsilon dV\right] = &\left[\int_{\mathcal{V}_0} \dot{\mathbf{y}}\cdot\rho_0\mathbf{f}\, dV + \int_{\partial\mathcal{V}_0} \dot{\mathbf{y}}\cdot\boldsymbol{\sigma}\cdot J\mathbf{F}^{-T}\mathcal{N} dA\right] + \\ &\left[\int_{\mathcal{V}_0} \rho_0 r\, dV - \int_{\partial\mathcal{V}_0} J\mathbf{F}^{-T}\mathcal{N}\cdot\mathbf{q} dA\right] - \int_{\partial\mathcal{V}_0} \mathbf{p}\cdot J\mathbf{F}^{-T}\mathcal{N} dA.\end{aligned} \tag{2.54}$$

Application of the divergence theorem followed by localization of (2.54) leads to the point-wise energy balance equation given by

$$\rho_0 \dot{\varepsilon} = \rho_0 \mathbf{f} \cdot \dot{\mathbf{y}} + \rho_0 r + \mathrm{Div}\left[\dot{\mathbf{y}}\mathbf{S} - \mathcal{Q} - \mathbf{p}(J\mathbf{F}^{-T})\right], \tag{2.55}$$

where $\mathcal{Q} = J\mathbf{F}^{-1}\mathbf{q}$ is the reference heat flux across the surface $\partial\mathcal{V}_0$. Similar to the current energy balance, the term $\mathrm{Div}(\dot{\mathbf{y}}\mathbf{S})$ can further be expanded, such that $\mathrm{Div}(\dot{\mathbf{y}}\mathbf{S}) = \dot{\mathbf{y}} \cdot \mathrm{Div}\ \mathbf{S} + \mathbf{S} \colon \mathrm{Grad}\ \dot{\mathbf{y}} = \dot{\mathbf{y}} \cdot \mathrm{Div}\ \mathbf{S} + \mathbf{S} \colon \dot{\mathbf{F}}$. Moreover, it can be shown that the reference divergence of the referential Poynting flux $\mathrm{Div}[\mathbf{p}(J\mathbf{F}^{-T})]$ reduce identically to $-\mathbf{H} \cdot \dot{\mathbf{B}}$ (see Appendix 2.A for details). Finally, the substitution of (2.49) into (2.55) leads to a further simplification of (2.55), which now reads

$$\rho_0 \dot{\varepsilon} = \rho_0 r + \mathbf{S} \colon \dot{\mathbf{F}} + \mathbf{H} \cdot \dot{\mathbf{B}} - \mathrm{Div}\ \mathcal{Q}. \tag{2.56}$$

In fact, one recovers (2.56) directly from its Eulerian counterpart (2.22) by substituting the pull-back transformations (2.40), (2.45) and (2.48) of the current field variables into it followed by simplification.

2.2.6 Entropy imbalance

The second law of thermodynamics postulates that the rate of generation of the specific entropy η in an arbitrary reference volume $\mathcal{V}_0$ must always remain positive. Thus, the entropy imbalance equation in the reference configuration is given by the Clausius-Duhem inequality

$$\frac{d}{dt}\left[\int_{\mathcal{V}_0} \rho_0 \eta dV\right] \geqslant \int_{\mathcal{V}_0} \frac{\rho_0 r}{\vartheta} dV - \int_{\partial\mathcal{V}_0} \mathcal{N} \cdot \frac{1}{\vartheta} \mathcal{Q} dA, \tag{2.57}$$

where ϑ is the absolute temperature. The last equation, upon localization leads to

$$\rho_0 \dot{\eta}\vartheta - \rho_0 r + \mathrm{Div}\left[\vartheta^{-1}\mathcal{Q}\right] \geqslant 0. \tag{2.58}$$

We now rephrase (2.58) by substituting the heat rate $\rho_0 r$ from (2.56) into it, such that

$$\rho_0 \dot{\eta}\vartheta - \rho_0 \dot{\varepsilon} + \mathbf{S} \colon \dot{\mathbf{F}} + \mathbf{H} \cdot \dot{\mathbf{B}} + J\vartheta\mathcal{Q} \cdot \mathrm{Div}\left(\vartheta^{-1}\right) \geqslant 0. \tag{2.59}$$

It remains to specify the energy ε, which is, in turn, identical to the internal energy of the system in the present quasi-static case. As discussed in the context of current configuration formulation, a natural choice for ε is in terms of a energy density $W^B(\mathbf{F}, \mathbf{B}, \vartheta, \Xi)$ and the specific thermal energy $\eta\vartheta$, such that

$$\varepsilon = \frac{1}{\rho_0} W^B(\mathbf{F}, \mathbf{B}, \vartheta, \Xi) + \eta\vartheta, \tag{2.60}$$

where Ξ denotes a set of thermodynamic internal variables to be specified depending on the specific feature of any dissipative process under consideration. Nevertheless, one can find the complimentary energy density to $W^B(\mathbf{F}, \mathbf{B}, \vartheta, \Xi)$ via a partial Legendre-Fenchel transformation, such that (Bustamante et al., 2008)

$$W^H(\mathbf{F}, \mathbf{H}, \vartheta, \Xi) = W^B(\mathbf{F}, \mathbf{B}, \vartheta, \Xi) - \mathbf{H} \cdot \mathbf{B}, \tag{2.61}$$

which leads to an alternative expression for the specific energy ε given by

$$\varepsilon = \frac{1}{\rho_0} W^{H}(\mathbf{F}, \mathbf{H}, \vartheta, \boldsymbol{\Xi}) + \frac{1}{\rho_0} \mathbf{H} \cdot \mathbf{B} + \eta\vartheta. \tag{2.62}$$

Thus, the substitution of (2.60) or (2.62) into (2.59) yields two different Clausius-Duhem inequalities leading to, respectively, the $\mathbf{F}-\mathbf{B}$ or $\mathbf{F}-\mathbf{H}$-based constitutive models. These specific Clausius-Duhem inequalities for $\mathbf{F}-\mathbf{B}$ or $\mathbf{F}-\mathbf{H}$-based models reads

$$\mathbf{S} : \dot{\mathbf{F}} + \mathbf{H} \cdot \dot{\mathbf{B}} - \dot{W}^{B} - \rho_0 \eta \dot{\vartheta} + J\vartheta \boldsymbol{\mathcal{Q}} \cdot \mathrm{Div}\left(\vartheta^{-1}\right) \geqslant 0 \tag{2.63}$$

and

$$\mathbf{S} : \dot{\mathbf{F}} - \mathbf{B} \cdot \dot{\mathbf{H}} - \dot{W}^{H} - \rho_0 \eta \dot{\vartheta} + J\vartheta \boldsymbol{\mathcal{Q}} \cdot \mathrm{Div}\left(\vartheta^{-1}\right) \geqslant 0, \tag{2.64}$$

respectively. Again, specific constitutive relations would require the definition of the set of internal variables $\boldsymbol{\Xi}$. However, the specific choices for $\boldsymbol{\Xi}$ will be defined at relevant points in Chapter 4 and 6.

2.2.7 Generalized standard materials framework

The evolution equations for the individual elements of $\boldsymbol{\Xi}$ is obtained from the referential standard material relations which are given in terms of the energetic potentials $W^{B}(\mathbf{F}, \mathbf{B}, \vartheta, \boldsymbol{\Xi})$ and $W^{H}(\mathbf{F}, \mathbf{H}, \vartheta, \boldsymbol{\Xi})$ and the corresponding dissipation potentials, namely $D^{B}(\mathbf{F}, \mathbf{B}, \vartheta, \boldsymbol{\mathfrak{Z}}, \dot{\boldsymbol{\Xi}})$ and $D^{H}(\mathbf{F}, \mathbf{H}, \vartheta, \boldsymbol{\mathfrak{Z}}, \dot{\boldsymbol{\Xi}})$, which reads, respectively,

$$\frac{\partial W^{B}}{\partial \boldsymbol{\Xi}} + \frac{\partial D^{B}}{\partial \dot{\boldsymbol{\Xi}}} = 0 \qquad \text{and} \qquad \frac{\partial W^{H}}{\partial \boldsymbol{\Xi}} + \frac{\partial D^{H}}{\partial \dot{\boldsymbol{\Xi}}} = 0. \tag{2.65}$$

Thus, the set of referential constitutive relations are obtained from the Clausius-Duhem inequalities (2.63), (2.64) and the relation for generalized standard materials (2.65) via applying the classical Coleman-Noll-Gurtin method. Finally, Box 2.2 provides a summary of the balance laws and thermodynamic inequalities.

Box 2.2: Balance laws and thermodynamic inequalities in the reference configuration

Ampère's Law:	$\mathrm{Curl}\ \mathbf{H} = 0$,	*boundary/interface condition*:	$\mathcal{N} \times [\![\mathbf{H}]\!] = 0$
Absence of magnetic monopole:	$\mathrm{Div}\ \mathbf{B} = 0$,	*boundary/interface condition*:	$\mathcal{N} \cdot [\![\mathbf{B}]\!] = 0$
Linear momentum balance:	$\mathrm{Div}\ \mathbf{S} + \rho_0 \mathbf{f} = 0$,	*boundary/interface condition*:	$[\![\mathbf{S}]\!] \cdot \mathcal{N} + \mathbf{T}^{\mathrm{mech}} = 0$
Angular momentum balance:	$\mathbf{S}\mathbf{F}^{T} = \mathbf{F}\mathbf{S}^{T}$		
Clausius-Duhem inequality:			
$\mathbf{F}-\mathbf{B}$ *model*:	$\mathbf{S} : \dot{\mathbf{F}} + \mathbf{H} \cdot \dot{\mathbf{B}} - \dot{W}^{B} - \rho_0 \eta \dot{\vartheta} + J\vartheta \boldsymbol{\mathcal{Q}} \cdot \mathrm{Div}\left(\vartheta^{-1}\right) \geqslant 0$		
$\mathbf{F}-\mathbf{H}$ *model*:	$\mathbf{S} : \dot{\mathbf{F}} - \mathbf{B} \cdot \dot{\mathbf{H}} - \dot{W}^{H} - \rho_0 \eta \dot{\vartheta} + J\vartheta \boldsymbol{\mathcal{Q}} \cdot \mathrm{Div}\left(\vartheta^{-1}\right) \geqslant 0$		
Generalized standard material relation:			
$\mathbf{F}-\mathbf{B}$ *model*:	$\frac{\partial W^{B}}{\partial \boldsymbol{\Xi}} + \frac{\partial D^{B}}{\partial \dot{\boldsymbol{\Xi}}} = 0$		
$\mathbf{F}-\mathbf{H}$ *model*:	$\frac{\partial W^{H}}{\partial \boldsymbol{\Xi}} + \frac{\partial D^{H}}{\partial \dot{\boldsymbol{\Xi}}} = 0$		

Appendix 2.A. Divergence of the Poynting vector

This appendix provides a derivation for the relation $\mathrm{Div}[J\mathbf{F}^{-T}\mathbf{p}] = -\mathbf{H}\cdot\dot{\mathbf{B}}$, where $\mathbf{p} = (\dot{\mathbf{x}}\times\mathbf{b})\times\mathbf{h}$ is the Poynting vector. Firstly, $\mathrm{Div}[J\mathbf{F}^{-T}\mathbf{p}]$ is expanded, such that

$$\mathrm{Div}[J\mathbf{F}^{-T}\mathbf{p}] = \mathrm{Div}[J\mathbf{F}^{-T}]\cdot\mathbf{p} + J\mathbf{F}^{-T} : \mathrm{Grad}\ \mathbf{p}. \tag{2.A.1}$$

We notice that $\mathrm{Div}[J\mathbf{F}^{-T}] = 0$, whose proof is discussed in the following. Prior to the proof, we rephrase $J\mathbf{F}^{-T}$, so that

$$J\mathbf{F}^{-T} = \frac{\partial J}{\partial \mathbf{F}}. \tag{2.A.2}$$

Furthermore, the expression of J is given by the index notations, so that

$$J = \frac{1}{6}\epsilon_{ijk}\epsilon_{pqr}y_{i,p}y_{j,q}y_{k,r}, \tag{2.A.3}$$

where ϵ represents the permutation symbol and $y_{m,n} = \partial y_m/\partial X_n = F_{mn}$.

Divergence of $\partial J/\partial\mathbf{F}$: The tensor $\partial J/\partial\mathbf{F}$ is readily evaluated from (2.A.3), such that

$$\frac{\partial J}{\partial F_{mn}} = \frac{1}{2}\left[\epsilon_{mjk}\epsilon_{nqr}y_{j,q}y_{k,r}\right]. \tag{2.A.4}$$

In turn, $\mathrm{Div}(\partial J/\partial\mathbf{F})$ can be computed by taking the divergence on both sides of the above equation, such that

$$\left(\frac{\partial J}{\partial F_{mn}}\right)_{,n} = \frac{1}{2}\left[\epsilon_{mjk}\epsilon_{nqr}y_{j,qn}y_{k,r} + \epsilon_{mjk}\epsilon_{nqr}y_{j,q}y_{k,rn}\right].$$

By interchanging the dummy indices in the previous equation, one gets the desired divergence-free result

$$\left(\frac{\partial J}{\partial F_{mn}}\right)_{,n} = \frac{1}{2}\epsilon_{mjk}y_{j,q}\left[\epsilon_{nqr}y_{k,rn} - \epsilon_{nqr}y_{k,nr}\right] = 0. \tag{2.A.5}$$

Hence, substituting the last into (2.A.1) we obtain

$$\mathrm{Div}[J\mathbf{F}^{-T}\mathbf{p}] = J\mathbf{F}^{-T} : \mathrm{Grad}\ \mathbf{p} = J\mathbf{F}^{-T} : (\mathrm{grad}\ \mathbf{p})\mathbf{F} = J\mathrm{tr}(\mathrm{grad}\ \mathbf{p}) = J\mathrm{div}\ \mathbf{p}. \tag{2.A.6}$$

Notice that div $\mathbf{p}$ is given by (2.23), so that

$$\mathrm{Div}[J\mathbf{F}^{-T}\mathbf{p}] = [\mathbf{h}\otimes\mathbf{b} - (\mathbf{h}\cdot\mathbf{b})\mathbf{I}] : \mathbf{l} - \mathbf{h}\cdot\dot{\mathbf{b}}. \tag{2.A.7}$$

Finally, substituting (2.45) and (2.40) into the last and simplifying we obtain

$$\mathrm{Div}[J\mathbf{F}^{-T}\mathbf{p}] = -\mathbf{H}\cdot\dot{\mathbf{B}}. \tag{2.A.8}$$

Notably, (2.A.6) leads to an important relation between the divergence of the referential and current Poynting vectors taken with respect to $\mathbf{X}$ and $\mathbf{x}$, respectively.

Chapter

3 Ferromagnetic Hysteresis Model

Chapter summary: *We propose two equivalent, thermodynamically consistent, rate-independent, three dimensional models for ferromagnetic hysteresis in both* **h** *and* **b** *variable spaces. Constitutive choices for the independent internal variables are done via proposing additive decompositions of the primary* **h** *and* **b** *fields, each into energetic and remanent parts. In turn, the models are proposed in terms of energetic and dissipation potentials, those are the functions of primary and internal variables by using a relatively small number of model parameters that is capable of being implemented in a general incremental numerical setting. The dissipation process occurring during magnetization/demagnetization is described by a power-law potential, which leads to rate-independence at a certain limit of the rate-dependent exponent. Two limiting conditions, under which the hysteresis models yield non-dissipative magnetization responses are discussed thereafter. Finally, the proposed* **h** *and* **b***-based model parameters are computed via fitting the model response to the experimental data. The proposed models show very good agreements with the experiments for spark plasma sintered NdFeB magnets and also for commercially-available melt-spun NdFeB ribbons and powders.*

Chapter content

As discussed in the introduction, the $\mathfrak{h}$-MREs with NdFeB particles exhibit rate-independent hysteresis behavior, which is, in turn, a dissipative phenomena. Hence, this chapter is devoted towards developing an isotropic ferromagnetic hysteresis model in terms of the energetic $w^{\mathfrak{i}}$ and dissipation $\mathscr{D}^{\mathfrak{i}}$ ($\mathfrak{i} = \mathfrak{b}, \mathfrak{h}$) potentials. No effect of mechanical deformation is considered herein. We start from the Clausius-Duhem inequalities and the relations for generalized standard materials provided in Chapter 2 and propose specific energetic and dissipation potentials to obtain the desired model features. Both, **h** and **b**-based models are proposed hereby. We first propose a model by considering **h** to be the primary variable followed by a **b**-based model.

3.1 Hysteresis model based on h

Air and other magnetically inert media with no magnetization, are typically modeled by a linear constitutive relation $\mathbf{b} = \mu_0 \mathbf{h}$. The constitutive relation for magnetically soft iron with no significant hysteresis is typically given by an inverse sigmoid function like the inverse Langevin function or the inverse hyperbolic tangent function or any combination of them (Danas, 2017). In turn, the constitutive modeling of hard magnets that dissipate energy via hysteresis is not straightforward. The following discuss a step-by-step approach towards modeling the hysteresis response of hard magnets by considering $\mathbf{h}$ to be the primary variable.

3.1.1 Choice of the internal variable

The identification of the internal variable is carried out after an additive decomposition of the local $\mathbf{h}$ field into an energetic and a remanent part, such that (Linnemann et al., 2009; Miehe et al., 2011)

$$\mathbf{h} = \mathbf{h}^{e} + \mathbf{h}^{r}, \tag{3.1}$$

where the superscripts "e" and "r" represent the energetic and remanent components, respectively. It is emphasized that the choice of internal variable is constitutive and thus, one can, in principle, choose either the energetic or the remanent component from (3.1). Nonetheless, to be consistent with the dissipative continuum electro-magnetism literature (Huber and Fleck, 2001; Landis, 2002; Klinkel, 2006; Miehe et al., 2011), this work considers $\xi \equiv \mathbf{h}^{r}$ to be the internal variable while leaving $\mathbf{h}^{e}$ as a "derived" quantity to be determined from the primary variable $\mathbf{h}$ and the internal variable $\mathbf{h}^{r}$.

3.1.2 Constitutive relations

Given the energy density function $w^{h}(\mathbf{h}, \mathbf{h}^{r})$ and assuming further no mechanical deformation ($\mathbf{F} = \mathbf{I}$) and steady ($\dot{\vartheta} = 0$), isothermal magnetization process ($\mathbf{q} = 0$) the Clausius-Duhem inequality (2.32) can be rephrased, so that

$$-\mathbf{b} \cdot \dot{\mathbf{h}} - \dot{w}^{h} \geqslant 0. \tag{3.2}$$

Expanding $\dot{w}^{h}$ in terms of its arguments followed by rearrangements lead to

$$-\left[\mathbf{b} + \frac{\partial w^{h}}{\partial \mathbf{h}}\right] \cdot \dot{\mathbf{h}} - \frac{\partial w^{h}}{\partial \mathbf{h}^{r}} \cdot \dot{\mathbf{h}}^{r} \geqslant 0. \tag{3.3}$$

Since $\mathbf{h}$ is the primary variable then can vary arbitrarily, the standard arguments of the Coleman-Noll-Gurtin (Coleman and Noll, 1959; Coleman and Gurtin, 1967) approach suggest that, in order to hold the inequality (3.3) for all $\mathbf{h}$, the coefficient of $\dot{\mathbf{h}}$ must vanish, leading to the constitutive relation

$$\mathbf{b} = -\frac{\partial w^{h}}{\partial \mathbf{h}}. \tag{3.4}$$

The remaining term in (3.3) therefore reads

$$\mathbf{b}^{r} \cdot \dot{\mathbf{h}}^{r} \geqslant 0, \qquad \text{with} \qquad \mathbf{b}^{r} = -\frac{\partial w^{h}}{\partial \mathbf{h}^{r}}, \tag{3.5}$$

where the remanent b-field $\mathbf{b}^{\mathrm{r}}$ is the *energetic work conjugate* of $\mathbf{h}^{\mathrm{r}}$. In turn, the constitutive relation (2.37) for generalized standard materials with this specific choice of $\xi \equiv \mathbf{h}^{\mathrm{r}}$ reads

$$\frac{\partial w^{\mathrm{h}}}{\partial \mathbf{h}^{\mathrm{r}}} + \frac{\partial \mathscr{D}^{\mathrm{h}}}{\partial \dot{\mathbf{h}}^{\mathrm{r}}} = 0, \tag{3.6}$$

where $\mathscr{D}^{\mathrm{h}}(\mathbf{h}, \mathbf{h}^{\mathrm{r}}, \dot{\mathbf{h}}^{\mathrm{r}})$ is the specific choice for the dissipation potential for the present $\mathbf{h}$-based model. Furthermore, substituting $(3.5)_2$ into (3.6) leads to the familiar form of *dissipation inequality* in the context of standard material models, given by

$$\frac{\partial \mathscr{D}}{\partial \dot{\mathbf{h}}^{\mathrm{r}}} \cdot \dot{\mathbf{h}}^{\mathrm{r}} \geqslant 0, \qquad \text{with} \qquad \mathbf{b}^{\mathrm{r}} = \frac{\partial \mathscr{D}}{\partial \dot{\mathbf{h}}^{\mathrm{r}}}. \tag{3.7}$$

Evidently, $(3.7)_2$ imply that the remanent $\mathbf{b}^{\mathrm{r}}$ is also the *dissipation work conjugate* of $\dot{\mathbf{h}}^{\mathrm{r}}$, which is a crucial observation as will be referred back to in the subsequent sections. Moreover, in order to the dissipation inequality $(3.7)_1$ hold, $\mathscr{D}^{\mathrm{h}}(\mathbf{h}, \mathbf{h}^{\mathrm{r}}, \dot{\mathbf{h}}^{\mathrm{r}})$ must be a convex function of $\dot{\mathbf{h}}_{\mathrm{r}}$.

An additional desirable property of $w^{\mathrm{h}}(\mathbf{h}, \mathbf{h}^{\mathrm{r}})$ and $\mathscr{D}^{\mathrm{h}}(\mathbf{h}, \mathbf{h}^{\mathrm{r}}, \dot{\mathbf{h}}^{\mathrm{r}})$ in the context of modeling isotropic ferromagnets at negligibly small strains and rotations is, namely, an even magnetic response under the reversal of the loading direction. This property is ensured via satisfying the conditions (Kankanala and Triantafyllidis, 2004)

$$w^{\mathrm{h}}(-\mathbf{h}, -\mathbf{h}^{\mathrm{r}}) = w^{\mathrm{h}}(\mathbf{h}, \mathbf{h}^{\mathrm{r}}) \qquad \text{and} \qquad \mathscr{D}^{\mathrm{h}}(-\mathbf{h}, -\mathbf{h}^{\mathrm{r}}, -\dot{\mathbf{h}}^{\mathrm{r}}) = \mathscr{D}^{\mathrm{h}}(\mathbf{h}, \mathbf{h}^{\mathrm{r}}, \dot{\mathbf{h}}^{\mathrm{r}}). \tag{3.8}$$

Of course, additional constraints on these energy functions are further imposed during the proposition of a finite-strain coupled magneto-mechanical model (Kankanala and Triantafyllidis, 2004; Dorfmann and Ogden, 2004). A detailed account on such constraints/properties on/of w^{h} and $\mathscr{D}^{\mathrm{h}}$ will be provided in the subsequent chapters.

3.1.3 Choice of potentials

This section provides the specific functional forms for $w^{\mathrm{h}}(\mathbf{h}, \mathbf{h}^{\mathrm{r}})$ and $\mathscr{D}^{\mathrm{h}}(\mathbf{h}, \mathbf{h}^{\mathrm{r}}, \dot{\mathbf{h}}^{\mathrm{r}})$ that would essentially lead to a *rate-independent* ferromagnetic switching surface model. This particular model of hysteresis considers the magnetization to be separated in two distinct regimes, namely, the energetic and switching regimes, which, in turn, are determined by the switching criteria obtained from $\mathscr{D}^{\mathrm{h}}$. Specifically, the model considers a linear magnetization response while the state of local magnetic field is prior to switching, whereas a saturation magnetization response is considered when the switching criteria is satisfied.

Energy density w^{h} **:** The aforementioned considerations leads to a natural choice for the additive decomposition of the free energy density $w^{\mathrm{h}}(\mathbf{h}, \mathbf{h}^{\mathrm{r}})$ into an energetic and a remanent component, such that, (Klinkel, 2006; Linnemann et al., 2009)

$$w^{\mathrm{h}}(\mathbf{h}, \mathbf{h}^{\mathrm{r}}) = w_{\mathrm{e}}^{\mathrm{h}}(\mathbf{h} - \mathbf{h}^{\mathrm{r}}) + w_{\mathrm{r}}^{\mathrm{h}}(\mathbf{h}^{\mathrm{r}}). \tag{3.9}$$

Notice during the energetic response (i.e., for a non-evolving $\mathbf{h}^{\mathrm{r}}$), only $w_{\mathrm{e}}^{\mathrm{h}}$ evolves in (3.9), whereas, both $w_{\mathrm{e}}^{\mathrm{h}}$ and $w_{\mathrm{r}}^{\mathrm{h}}$ evolve during the switching regime.

Owing to the aforementioned observations along with satisfying $(3.8)_1$ as well, a natural choice

for w_e^h is quadratic in terms of $(\mathbf{h}-\mathbf{h}^r)$, such that (McMeeking and Landis, 2002; Landis, 2002; Klinkel, 2006; Linnemann et al., 2009)

$$w_e^h(\mathbf{h}-\mathbf{h}^r) = -\frac{\mu^e}{2}(\mathbf{h}-\mathbf{h}^r)\cdot(\mathbf{h}-\mathbf{h}^r) \qquad \text{with} \qquad \mu^e = \mu_0(1+\chi^e), \tag{3.10}$$

where μ^e and χ^e are, respectively, the *energetic permeability* and *energetic susceptibility* of the magnet. The choice of the remanent potential, by contrast, is not straightforward. A typical remanent potential for the switching surface model consists of a quadratic part in $\mathbf{h}_r$ along with an additional non-quadratic term in $\mathbf{h}_r$ such that (Klinkel, 2006; Linnemann et al., 2009)

$$w_r^h(\mathbf{h}^r) = \frac{\mu^e}{2}\mathbf{h}^r\cdot\mathbf{h}^r + \frac{\mu_0(m^s)^2}{\chi}f^h\left(\frac{|\mathbf{h}^r|}{m^s}\right), \tag{3.11}$$

where m^s and χ are the saturation magnetization and magnetic susceptibility of a permanent magnet, respectively. Inverse saturation-type functions are typically employed as f^h for the modeling the saturation-type magnetization response of hard magnets (Huber and Fleck, 2001; McMeeking and Landis, 2002; Landis, 2002; Klinkel, 2006; Linnemann et al., 2009; Miehe et al., 2011; Rosato and Miehe, 2014; Bottero and Idiart, 2016). In turn, f^h is defined to be a linear combination of three sufficiently smooth functions, so that

$$f^h\left(\frac{|\mathbf{h}^r|}{m^s}\right) = \sum_{\alpha=1}^{3}\kappa_h^{(\alpha)}f^{(\alpha)}\left(\frac{|\mathbf{h}^r|}{m^s}\right) \qquad \text{with} \qquad \sum_{\alpha=1}^{3}\kappa_h^{(\alpha)} = 1, \qquad \kappa_h^{(\alpha)} \geqslant 0, \tag{3.12}$$

where $\kappa_h^{(\alpha)}$ are the weight parameters that sum identically to 1. A set these three $f^{(\alpha)}(|\mathbf{h}^r|/m^s)$ along with their first derivatives with respect to their arguments is provided in Table 3.1.

Table 3.1: Different inverse saturation functions used in the remanent potential (3.11)

α	$f^{(\alpha)}(\lvert\mathbf{h}^r\rvert/m^s)$	$(f^{(\alpha)})'(\lvert\mathbf{h}^r\rvert/m^s)$
1	$-\left[\log\left\{1-\frac{\lvert\mathbf{h}^r\rvert}{m^s}\right\}+\frac{\lvert\mathbf{h}^r\rvert}{m^s}\right]$	$\frac{\lvert\mathbf{h}^r\rvert/m^s}{1-\lvert\mathbf{h}^r\rvert/m^s}$
2	$-\frac{4}{\pi^2}\log\left[\cos\left\{\frac{\pi}{2}\frac{\lvert\mathbf{h}^r\rvert}{m^s}\right\}\right]$	$\frac{2}{\pi}\tan\left\{\frac{\pi}{2}\frac{\lvert\mathbf{h}^r\rvert}{m^s}\right\}$
3	$-\left[\left(1-\frac{\lvert\mathbf{h}^r\rvert}{m^s}\right)\tanh^{-1}\left\{\frac{\lvert\mathbf{h}^r\rvert}{m^s}\right\}-\log\left\{\frac{\lvert\mathbf{h}^r\rvert}{m^s}+1\right\}\right]$	$\tanh^{-1}\left\{\frac{\lvert\mathbf{h}^r\rvert}{m^s}\right\}$

Notice that all the $f^{(\alpha)}$ in Table 3.1 reduce identically to $|\mathbf{h}^r|^2/2(m^s)^2$ in the limit of $|\mathbf{h}^r| \to 0$. Consequently, one obtains the identical initial slopes of $(f^{(\alpha)})'$ for all three functions in Table 3.1. Moreover, in the limit of $|\mathbf{h}^r|/m^s \to 1$, all these functions identically approach $+\infty$, although, at different rates. Finally, the local primary and remanent magnetic fields are obtained via substituting (3.9) into, (3.4) and (3.5), which yields, respectively,

$$\mathbf{b} = \mu^e(\mathbf{h}-\mathbf{h}^r) \qquad \text{and} \qquad \mathbf{b}^r = -\mu^e\mathbf{h} - \frac{\mu_0 m^s}{\chi}f^{h\prime}\left(\frac{|\mathbf{h}^r|}{m^s}\right)\frac{\mathbf{h}^r}{|\mathbf{h}|^r}. \tag{3.13}$$

The magnetization $\mathbf{m}$ can therefore be obtained via substituting (2.9) into (3.13), so that

$$\mathbf{m} = \chi^e \mathbf{h} - (\chi^e + 1)\mathbf{h}^r. \tag{3.14}$$

In turn, it is observed from (3.14) that $\mathbf{m}$ is given by $\mathbf{m} = -\mathbf{h}^r$ for "ideal" ferromagnets having $\chi^e = 0$. Nonetheless, most of the permanent magnets existing in nature exhibit a $\chi^e \leqslant 0.15$. Hence, the remanent field $\mathbf{h}^r$ may be considered to be a "magnetization-like" variable in the context of h-MREs.

Dissipation potential $\mathscr{D}^h$ **:** It remains to obtain the evolution equation for $\mathbf{h}^r$, which is, in turn, obtained via the generalized standard material relation (3.6). A convex dissipation potential that also satisfies $(3.8)_2$ is therefore defined in terms of a power law in $|\dot{\mathbf{h}}^r|$, such that (Danas et al., 2012a)

$$\mathscr{D}^h(\dot{\mathbf{h}}^r) = \frac{b^c \dot{h}^{r0}}{p+1}\left[\frac{|\dot{\mathbf{h}}^r|}{\dot{h}^{r0}}\right]^{p+1}, \tag{3.15}$$

where b^c is the coercive field of the magnet and $\dot{h}^{r0}$ is a reference rate of evolution of $\mathbf{h}^r$. The rate sensitivity exponent p in (3.15), for the specific value of $p = 1$ leads to a linear viscosity-type magnetization response, whereas, a dry friction-type rate-independent response is obtained for $p = 0$. The dissipation potential (3.15), by virtue of its convexity, admits to an explicit Legendre transform with respect to $\dot{\mathbf{h}}^r$, which in turn leads to its conjugate dissipation potential given by

$$\mathscr{D}^{h*}(\mathbf{b}^r) = \frac{b^c \dot{h}^{r0}}{q+1}\left[\frac{|\mathbf{b}^r|}{b^c}\right]^{q+1}, \tag{3.16}$$

where the rate sensitivity index $q = 1/p$. Thus, a rate-independent response is obtained from (3.16) for the special case of $q = +\infty$, which leads to the definition of a ferromagnetic switching surface given by (McMeeking and Landis, 2002; Landis, 2002; Klinkel, 2006; Linnemann et al., 2009; Miehe et al., 2011)

$$\phi^h := \mathbf{b}^r \cdot \mathbf{b}^r - (b^c)^2 = 0. \tag{3.17}$$

Finally, the evolution equation for $\dot{\mathbf{h}}^r$ is obtained via defining the associated switching rule

$$\dot{\mathbf{h}}^r = \dot{\lambda}^h \frac{\partial \phi^h}{\partial \mathbf{b}^r}, \tag{3.18}$$

where the switching multiplier is given by $\dot{\lambda}$. Thus, during a cyclic loading, the evolution of $\mathbf{h}^r$ is obtained via (3.18) along with the associated Kuhn-Tucker conditions, which read $\dot{\lambda} = 0$ if $\phi < 0$ and $\dot{\lambda} > 0$ if $\phi = 0$. To solve (3.18) incrementally, we employ an implicit radial return-based algorithm, which was originally proposed by Ortiz and Simo (1986) in the context of mechanical plasticity.

A number of representative $m - h$ hysteresis loops obtained from the proposed switching surface model is shown in Fig. 3.1. Specifically, Fig. 3.1a shows the "ideal" hysteresis loops with a vanishing χ^e for different choice of the inverse saturation function f^h, defined in terms of setting $\kappa_h^{(1)} = 1$, $\kappa_h^{(2)} = 1$ and $\kappa_h^{(3)} = 1$. Here we apply a fully reversed ramp-type cyclic loading along the $\mathbf{e}_1$ direction, so that $\mathbf{h} = h\mathbf{e}_1$ and consequently the resulting magnetization is obtained to be $\mathbf{m} = m\mathbf{e}_1$. Notice from Fig. 3.1a that during the initial loading m remains identically zero until the state of remanent $\mathbf{b}^r$ hits the switching surface at $h = b^c/\mu_0$. Furthermore, the initial switching susceptibility χ and the saturation magnetization m^s remain the same for any choice of $\kappa_h^{(\alpha)}$. In turn, the coefficients $\kappa_h^{(\alpha)}$

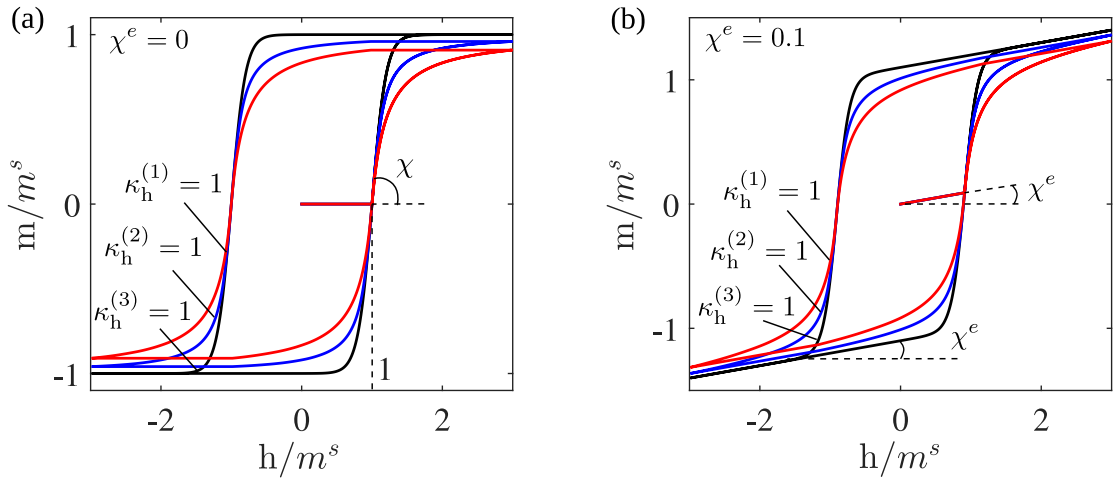

Figure 3.1: Hysteresis loops of (a) "ideal" magnets with $\chi^e = 0$ and (b) actual magnets having $\chi^e > 0$. Comparison of the hysteresis loops for $\chi = 5$, $b^c = \mu_0 m^s$ and three distinct choices of f^h defined by $\kappa_h^{(1)} = 1$, $\kappa_h^{(2)} = 1$ and $\kappa_h^{(3)} = 1$ are shown herein.

control the "rate" of magnetic saturation as a rapid saturation is observed in Fig. 3.1a for $\kappa_h^{(3)} = 1$, whereas, the saturation is more gradual for the choice $\kappa_h^{(1)} = 1$. Notice that the term "rate of saturation" indicates how fast the magnetization response saturates with increasing h and has no explicit relation with the time in the context of this rate-independent model.

Indeed, the natural rare-earth magnets exhibit slightly "inclined" hysteresis loops having $\chi^e > 0$ as shown in Fig. 3.1b. We note that all the features of Fig. 3.1b remain identical to Fig. 3.1a, except the initial energetic magnetization with a susceptibility χ^e, which, in turn, leads to an overall inclination in the resulting hysteresis loops. The hysteresis loops in Fig. 3.1 are depicted for the illustration of the model features and thus, computed for arbitrary model parameters χ^e, χ, b^c. Model parameter identification via fitting with experimental responses will be provided in the next section.

3.1.4 Limiting cases

The dissipative hysteresis model defined in terms of the potential energy (3.9) and the switching surface (3.17) leads to non-dissipative responses under a couple of limiting conditions, namely (i) $b^c \to +\infty$ and (ii) $b^c \to 0$.

(i) The limit of $b^c \to +\infty$ **:** Under this limit the switching surface radius becomes $+\infty$ resulting in $\phi < 0$ for all possible loading paths. Consequently, following the Kuhn-Tucker conditions, $\dot{\lambda}$ vanishes identically, leading to $\dot{\mathbf{h}}^r = \mathbf{0}$. Thus, the dissipation potential (3.15) vanishes in this limit, leading to a linear magnetization response in $\mathbf{h}$ having a slope χ^e (see Fig. 3.2a). Moreover, $\mathbf{m}$ vanishes identically in this limit for any non-magnetic media having $\chi^e = 0$. Hence, as shown in Fig. 3.2a, for $\chi^e = 0$, in the limit of $b^c \to +\infty$ one recovers the magnetic constitutive relation in any non-magnetic media, given by $\mathbf{b} = \mu_0 \mathbf{h}$.

(ii) The limit of $b^c \to 0$ **:** The limiting response of the hysteresis model under $b^c \to 0$ is rather involved. We observe that (3.15) also vanishes in the limit of $b^c \to 0$, thus, resulting an energetic response. Consequently, the switching surface (3.17) now leads to $\mathbf{b}^r = \mathbf{0}$. Therefore, the remanent field $\mathbf{h}^r$ no longer remains independent of $\mathbf{h}$, rather, is expressed explicitly in terms of $\mathbf{h}$, so that

$(3.13)_2$ now reads

$$(1+\chi^e)\chi\frac{\mathbf{h}}{m^s} = -f^{h\prime}\left(\frac{|\mathbf{h}^r|}{m^s}\right)\frac{\mathbf{h}^r}{|\mathbf{h}|^r}. \tag{3.19}$$

Notice that here the direction of $\mathbf{h}$ and $-\mathbf{h}^r$ becomes identical for the present choice of isotropic magnets. Inverting (3.19) we obtain the expression for $\mathbf{h}^r$, such that

$$\frac{\mathbf{h}^r}{m^s} = -(f^{h\prime})^{-1}\left\{(1+\chi^e)\chi\frac{|\mathbf{h}|}{m^s}\right\}\frac{\mathbf{h}}{|\mathbf{h}|}. \tag{3.20}$$

The potential energy (3.9) in this particular limit thus reads

$$w^h(\mathbf{h}) = -\mu^e\left[1+2\frac{m^s}{|\mathbf{h}|}(f^{h\prime})^{-1}\left\{(1+\chi^e)\chi\frac{|\mathbf{h}|}{m^s}\right\}\right]\mathbf{h}\cdot\mathbf{h} + \frac{\mu_0(m^s)^2}{\chi}f^h\left[(f^{h\prime})^{-1}\left\{(1+\chi^e)\chi\frac{|\mathbf{h}|}{m^s}\right\}\right]. \tag{3.21}$$

This potential energy, in turn, leads to a non-hysteretic saturation magnetization response. In this context, the experimental observations (Danas et al., 2012b; Bodelot et al., 2017) dictates that the saturation magnetic response of non-dissipative soft magnets exhibit no magnetic susceptibility after the saturation is achieved (see Fig. 1.2a). Thus, we set the energetic susceptibility $\chi^e = 0$ in this limiting case, which simplifies (3.21), so that

$$w^h(\mathbf{h}) = -\frac{\mu_0}{2}\mathbf{h}\cdot\mathbf{h} - \frac{\mu_0(m^s)^2}{\chi}g^h\left(\chi\frac{|\mathbf{h}|}{m^s}\right), \tag{3.22}$$

where the nonlinear energy function is now denoted by g, which is, in turn, a function of $\chi|\mathbf{h}|/m^s$, such that

$$g^h\left(\chi\frac{|\mathbf{h}|}{m^s}\right) = (f^{h\prime})^{-1}\left(\chi\frac{|\mathbf{h}|}{m^s}\right)\chi\frac{|\mathbf{h}|}{m^s} - f^h\left[(f^{h\prime})^{-1}\left(\chi\frac{|\mathbf{h}|}{m^s}\right)\right]. \tag{3.23}$$

Indeed, the function $f^{h\prime}$ computed from f^h given by (3.12) cannot be inverted in a closed form. Consequently, no simplified expression for g^h can be obtained for a general f^h. Nevertheless, evaluating $g^{h\prime}$ from (3.23) we obtain a straightforward relation between $g^{h\prime}$ and $f^{h\prime}$ given by

$$g^{h\prime}\left(\chi\frac{|\mathbf{h}|}{m^s}\right) = (f^{h\prime})^{-1}\left(\chi\frac{|\mathbf{h}|}{m^s}\right). \tag{3.24}$$

Thus, the magnetic b-field evaluated in this limit is obtained via substituting (3.22) into (3.4), so that

$$\mathbf{b} = \mu_0\left[\mathbf{h} + m^s(f^{h\prime})^{-1}\left(\chi\frac{|\mathbf{h}|}{m^s}\right)\right] \qquad \Rightarrow \qquad \mathbf{m} = m^s(f^{h\prime})^{-1}\left(\chi\frac{|\mathbf{h}|}{m^s}\right). \tag{3.25}$$

Hence, it is proved that a remanent potential that employ the inverse saturation-type potential characterized by f^h, in turn, leads to a saturating magnetization response ($|\mathbf{m}| \to m^s$) following $(f^{h\prime})^{-1}$ in the limiting case of $b^c = \chi^e = 0$. Moreover, three special choices for $\kappa_h^{(j)} = 1$ with $j = 1, 2$ or 3 leads to the three distinct and readily invertible f' functions, which are listed in the third column of Table 3.1. Thus, both g^h and $g^{h\prime}$ can be expressed explicitly in such special cases, which are listed in Table 3.2.

It is emphasized that such explicit form of the saturation-type potential energy (3.22) and the expressions for $\mathbf{b}$ and $\mathbf{m}$ in (3.25) cannot be obtained for any arbitrary choice of the remanent potential w_r^h. Rather, the *specific choice* in (3.11) eventually leads to the saturation-type energetic limiting

response. Moreover, some of the inverse-sigmoid functions (not listed in Table 3.1) are not invertible explicitly to a closed algebraic form. Thus, one should treat the functions in Table 3.2 to be the special cases of the general dissipative framework, that, in turn lead to the "familiar" saturation functions.

Table 3.2: Expressions for g^{h} and $g^{\mathrm{h}\prime}$

Choice of κ_{h}	$g^{\mathrm{h}}(\chi\lvert\mathbf{h}\rvert/m^{\mathrm{s}})$	$g^{\mathrm{h}\prime}(\chi\lvert\mathbf{h}\rvert/m^{\mathrm{s}})$
$\kappa_{\mathrm{h}}^{(1)}=1$	$-\left[\log\left\{1+\chi\frac{\lvert\mathbf{h}\rvert}{m^{\mathrm{s}}}\right\}-\chi\frac{\lvert\mathbf{h}\rvert}{m^{\mathrm{s}}}\right]$	$\frac{\chi\lvert\mathbf{h}\rvert/m^{\mathrm{s}}}{1+\chi\lvert\mathbf{h}\rvert/m^{\mathrm{s}}}$
$\kappa_{\mathrm{h}}^{(2)}=1$	$\tan^{-1}\left\{\chi\frac{\pi}{2}\frac{\lvert\mathbf{h}\rvert}{m^{\mathrm{s}}}\right\}\chi\frac{\lvert\mathbf{h}\rvert}{m^{\mathrm{s}}}-\frac{1}{2}\log\left[1+\chi^2\frac{\pi^2}{4}\left(\frac{\lvert\mathbf{h}\rvert}{m^{\mathrm{s}}}\right)^2\right]$	$\frac{2}{\pi}\tan^{-1}\left\{\chi\frac{\pi}{2}\frac{\lvert\mathbf{h}\rvert}{m^{\mathrm{s}}}\right\}$
$\kappa_{\mathrm{h}}^{(3)}=1$	$\log\left[\cosh\left\{\chi\frac{\lvert\mathbf{h}\rvert}{m^{\mathrm{s}}}\right\}\right]$	$\tanh\left\{\chi\frac{\lvert\mathbf{h}\rvert}{m^{\mathrm{s}}}\right\}$

A comparison of the full hysteresis model having $b^{\mathrm{c}}=0.1\mu_0 m^{\mathrm{s}}$ with the corresponding energetic approximations for $\kappa_{\mathrm{h}}^{(\mathrm{j})}=1$ with $\mathrm{j}=1,2$ or 3 is shown in Fig. 3.2b. Consequently, we infer from Fig. 3.1a and Fig. 3.2b that the "ideal" hysteretic $\mathrm{m}-\mathrm{h}$ response can be regarded as a "delayed magnetization", where the initiation of the magnetization/demagnetization is dictated by the coercive field b^{c} of the magnet. The ideal hysteretic response Fig. 3.1a eventually coincides with the non-dissipative saturation magnetization response in the limit of $b^{\mathrm{c}}\to 0$.

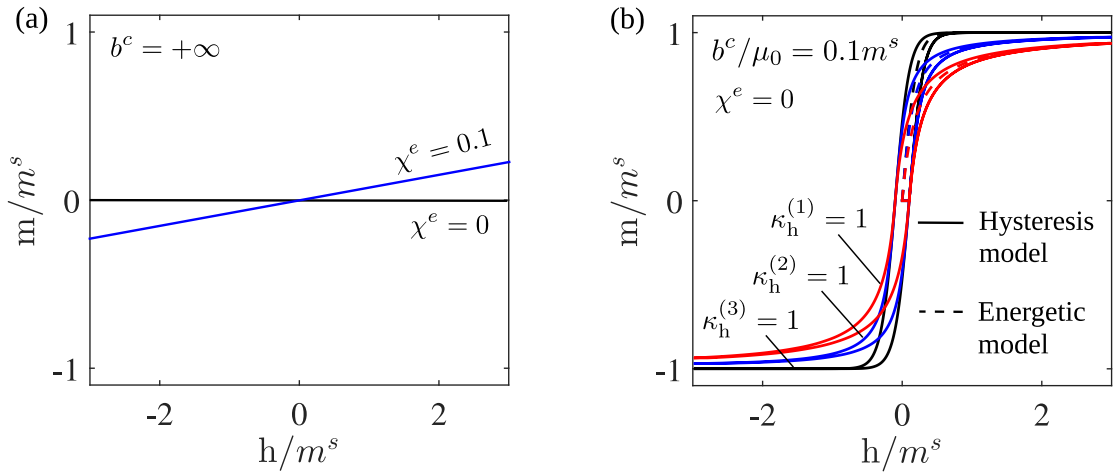

Figure 3.2: Model response in the two limiting cases (a) $b^{\mathrm{c}}=+\infty$ and (b) $b^{\mathrm{c}}\to 0$. (a) Model response for two representative χ^{e}, while the parameters χ and m^{s} remain inconsequential. (b) Saturation magnetization response for $\chi^{\mathrm{e}}=0$, $\chi=5$ and three distinct choices $\kappa_{\mathrm{h}}^{(1)}=1$, $\kappa_{\mathrm{h}}^{(2)}=1$ and $\kappa_{\mathrm{h}}^{(3)}=1$ and comparison with the corresponding energetic models given by (3.22) and Table 3.2.

Remark 3.1. A number of reported models for the s-MREs employ a potential $w^{\mathrm{h}}(\chi\lvert\mathbf{h}\rvert/m^{\mathrm{s}})$ that leads to the Langevin-type saturation magnetization response (Lefèvre et al., 2017; Danas, 2017; Psarra et al., 2019). The Langevin saturation function reads

$$\mathcal{L}\left(\chi\frac{\lvert\mathbf{h}\rvert}{m^{\mathrm{s}}}\right)=\coth\left(3\chi\frac{\lvert\mathbf{h}\rvert}{m^{\mathrm{s}}}\right)-\frac{1}{3\chi}\frac{m^{\mathrm{s}}}{\lvert\mathbf{h}\rvert}. \tag{3.26}$$

We observe that (3.26) is not invetible in a closed from. Thus, we refrain form defining a f, such that $f' \equiv \mathcal{L}^{-1}$ in Table 3.1. Nevertheless, as observed in the following model fitting section, (3.12) provides a sufficiently rich set of functions to model the major hysteresis loops of the NdFeB magnets.

3.2 Hysteresis model based on b

The equivalent **b**-based model is proposed herein. The "structure" of the constitutive modeling is allowed to remain the same, i.e, starting from choosing an internal variable, followed by obtaining the constitutive relation from the Clausius-Duhem inequality (2.29) via applying the Coleman-Noll-Gurtin method. This will be followed by the proposition of the specific forms of w^{b} and $\mathscr{D}^{\mathrm{b}}$. In this section we would use the same model parameters defined in the preceding section except one. Specific details if such difference will be provided at relevant places.

3.2.1 Constitutive relations

We first propose an additive decomposition to the primary **b** field into an energetic and a remanent part, so that

$$\mathbf{b} = \mathbf{b}^{e} + \mathbf{b}^{\mathrm{r}}. \tag{3.27}$$

It is emphasized that in this model $\mathbf{b}^{\mathrm{r}}$ is an independent internal variable and thus, should not be confused with same notation used in the previous section, where $\mathbf{b}^{\mathrm{r}}$ was used to denote the work conjugate of the remanent internal variable $\mathbf{h}^{\mathrm{r}}$. Hence, $\mathbf{b}^{\mathrm{r}}$ defined here is *not* an energy conjugate to $\mathbf{h}^{\mathrm{r}}$ defined in the previous section. Therefore, the internal variables should be treated independently in the **h** and **b**-based models. Subsequently, the Clausius-Duhem inequality for a non-deformable magnetic solid in isothermal, steady state is obtained via simplifying (2.29), so that

$$\mathbf{h} \cdot \dot{\mathbf{b}} - \dot{w}^{\mathrm{b}} \geqslant 0. \tag{3.28}$$

Expanding $\dot{w}^{\mathrm{b}}(\mathbf{b}, \mathbf{b}^{\mathrm{r}})$ in terms of its arguments followed by the rearrangements lead to

$$\left[\mathbf{h} - \frac{\partial w^{\mathrm{b}}}{\partial \mathbf{b}}\right] \cdot \dot{\mathbf{b}} - \frac{\partial w^{\mathrm{b}}}{\partial \mathbf{b}^{\mathrm{r}}} \cdot \dot{\mathbf{b}}^{\mathrm{r}} \geqslant 0. \tag{3.29}$$

Consequently, the standard arguments of the Coleman-Noll-Gurtin approach leads to the constitutive relation

$$\mathbf{h} = \frac{\partial w^{\mathrm{b}}}{\partial \mathbf{b}}. \tag{3.30}$$

Subsequently, the Clausius-Duhem inequality (3.29) reads

$$\mathbf{h}^{\mathrm{r}} \cdot \dot{\mathbf{b}}^{\mathrm{r}} \geqslant 0, \qquad \text{where} \qquad \mathbf{h}^{\mathrm{r}} = -\frac{\partial w^{\mathrm{b}}}{\partial \mathbf{b}^{\mathrm{r}}}. \tag{3.31}$$

is the *energetic work conjugate* of $\mathbf{b}^{\mathrm{r}}$. Again, the conjugate internal variable $\mathbf{h}^{\mathrm{r}}$ defined in (3.31) is *not* related to the $\mathbf{h}^{\mathrm{r}}$ of the **h**-based model. The dissipation inequality therefore yields from (3.31) via substituting the constitutive relation (2.37) for generalized standard materials (with $\xi \equiv \mathbf{b}^{\mathrm{r}}$), such

that

$$\frac{\partial \mathscr{D}^{\mathrm{b}}}{\partial \dot{\mathbf{b}}^{\mathrm{r}}} \cdot \dot{\mathbf{b}}^{\mathrm{r}} \geqslant 0, \qquad \mathbf{h}^{\mathrm{r}} = \frac{\partial \mathscr{D}^{\mathrm{b}}}{\partial \dot{\mathbf{b}}^{\mathrm{r}}}, \tag{3.32}$$

which, in turn, imposes the convexity condition on $\mathscr{D}^{\mathrm{b}}(\mathbf{b}, \mathbf{b}^{\mathrm{r}}, \dot{\mathbf{b}}^{\mathrm{r}})$ in terms of $\dot{\mathbf{b}}^{\mathrm{r}}$. Furthermore, the condition for even magnetization along the loading direction imposes further constraints on w^{b} and $\mathscr{D}^{\mathrm{b}}$, which read, respectively, (Kankanala and Triantafyllidis, 2004)

$$w^{\mathrm{b}}(-\mathbf{b}, -\mathbf{b}^{\mathrm{r}}) = w^{\mathrm{b}}(\mathbf{b}, \mathbf{b}^{\mathrm{r}}) \qquad \text{and} \qquad \mathscr{D}^{\mathrm{b}}(-\mathbf{b}, -\mathbf{b}^{\mathrm{r}}, -\dot{\mathbf{b}}^{\mathrm{r}}) = \mathscr{D}^{\mathrm{b}}(\mathbf{b}, \mathbf{b}^{\mathrm{r}}, \dot{\mathbf{b}}^{\mathrm{r}}). \tag{3.33}$$

Specific functional forms for the potentials $w^{\mathrm{b}}(\mathbf{b}, \mathbf{b}^{\mathrm{r}})$ and $\mathscr{D}^{\mathrm{b}}(\mathbf{b}, \mathbf{b}^{\mathrm{r}}, \dot{\mathbf{b}}^{\mathrm{r}})$ those satisfy the constraints (3.32) (specifically on $\mathscr{D}^{\mathrm{b}}$) and (3.33) are provided in the following.

3.2.2 Energy functions

The specific functional choices for $w^{\mathrm{b}}(\mathbf{b}, \mathbf{b}^{\mathrm{r}})$ and $\mathscr{D}^{\mathrm{b}}(\mathbf{b}, \mathbf{b}^{\mathrm{r}}, \dot{\mathbf{b}}^{\mathrm{r}})$ proposed here resemble closely to (3.9) and (3.15), respectively, except the arguments. In turn, the model parameters are kept identical to the **h**-based model except the inverse saturation function parameters $\kappa^{(\alpha)}$.

Energy density w^{b} **:** Following (3.9) the full energy density $w^{\mathrm{b}}(\mathbf{b}, \mathbf{b}^{\mathrm{r}})$ is decomposed into the energetic and remanent contributions, so that (McMeeking and Landis, 2002; Landis, 2002)

$$w^{\mathrm{b}}(\mathbf{b}, \mathbf{b}^{\mathrm{r}}) = w^{\mathrm{b}}_{\mathrm{e}}(\mathbf{b} - \mathbf{b}^{\mathrm{r}}) + w^{\mathrm{b}}_{\mathrm{r}}(\mathbf{b}^{\mathrm{r}}). \tag{3.34}$$

As observed in Section 3.1.3, in the energetic regime, with no evolution of the internal variable ($\mathbf{b}^{\mathrm{r}}$ in the present case), the magnetization response is linear in $\mathbf{h}$ defined by the linear slope χ^{e}. A complementary energy to the quadratic energy function $w^{\mathrm{h}}_{\mathrm{e}}(\mathbf{h} - \mathbf{h}^{\mathrm{r}})$ can therefore be obtained via the Legendre transform of (3.10) with respect to $\mathbf{h}^{e}$, such that

$$w^{\mathrm{b}}_{\mathrm{e}}(\mathbf{b} - \mathbf{b}^{\mathrm{r}}) = \frac{1}{2\mu^{e}} (\mathbf{b} - \mathbf{b}^{\mathrm{r}}) \cdot (\mathbf{b} - \mathbf{b}^{\mathrm{r}}). \tag{3.35}$$

In the switching regime, in contrast, the magnetization response is non-linear and dictated by the remanent potential. Thus, no attempt is made to transform the full energy (3.9) in the case of a switching response. Instead, $w^{\mathrm{b}}_{\mathrm{r}}(\mathbf{b}^{\mathrm{r}})$ is proposed to be

$$w^{\mathrm{b}}_{\mathrm{r}}(\mathbf{b}^{\mathrm{r}}) = -\frac{1}{2\mu^{e}} \mathbf{b}^{\mathrm{r}} \cdot \mathbf{b}^{\mathrm{r}} + \mu^{e} (m^{\mathrm{s}})^{2} \frac{(1+\chi)}{\chi} f^{\mathrm{b}}\left(\frac{|\mathbf{b}^{\mathrm{r}}|}{\mu^{e} m^{\mathrm{s}}} \right). \tag{3.36}$$

Notice that here we utilize the same modeling parameters μ^{e}, χ and m^{s} in (3.36). However, the inverse saturation function is now given by $f^{\mathrm{b}}(|\mathbf{b}^{\mathrm{r}}|/\mu^{e} m^{\mathrm{s}})$, which is defined to be

$$f^{\mathrm{b}}\left(\frac{|\mathbf{b}^{\mathrm{r}}|}{\mu^{e} m^{\mathrm{s}}} \right) = \sum_{\alpha=1}^{3} \kappa^{(\alpha)}_{\mathrm{b}} f^{(\alpha)}\left(\frac{|\mathbf{b}^{\mathrm{r}}|}{\mu^{e} m^{\mathrm{s}}} \right) \qquad \text{with} \qquad \sum_{\alpha=1}^{3} \kappa^{(\alpha)}_{\mathrm{b}} = 1, \qquad \kappa^{(\alpha)}_{\mathrm{b}} \geqslant 0, \tag{3.37}$$

where the set of $f^{(\alpha)}$ with $\alpha = 1-3$ is defined in Table 3.1 is employed here, of course, here with a different argument. Thus, the only set of new parameters introduced herein are $\kappa^{(\alpha)}_{\mathrm{b}}$ ($\alpha = 1-3$). Nevertheless, (3.36) ensures that the switching magnetization response has the same susceptibility of

χ and saturation magnetization m^s. However, the function f^b that dictates the rate of saturation of the $m-h$ response, is now different from the **h** model.

Eventually, the expressions for the full and remanent h-fields are obtained via substituting (3.34) into the constitutive relations (3.30) and $(3.31)_2$, respectively, such that

$$\mathbf{h} = \frac{1}{\mu^e}(\mathbf{b} - \mathbf{b}^r) \qquad \text{and} \qquad \mathbf{h}^r = \frac{1}{\mu^e}\mathbf{b} - m^s\frac{(1+\chi)}{\chi}f^{b\prime}\left(\frac{|\mathbf{b}^r|}{\mu^e m^s}\right)\frac{\mathbf{b}^r}{|\mathbf{b}^r|}. \tag{3.38}$$

The expression for **m** is obtained subsequently by substituting $(3.38)_1$ into (2.9), which leads to

$$\mathbf{m} = \frac{1}{\mu^e}(\chi^e\mathbf{b} + \mathbf{b}^r). \tag{3.39}$$

We note that for an "ideal" magnetic switching response (i.e., $\chi^e = 0$), the magnetization reads simply $\mathbf{m} = \mathbf{b}^r/\mu_0$. Hence, in analogy to the **h** model, here also the internal variable $\mathbf{b}^r$ can be regarded as the "magnetization like" variable.

Dissipation potential $\mathscr{D}^b$ **:** In analogy to the **h**-based model, the dissipation potential $\mathscr{D}^b$ is defined herein to be a power law in $|\dot{\mathbf{b}}^r|$ that satisfy the conditions $(3.32)_1$ and $(3.33)_2$, such that

$$\mathscr{D}^b(\dot{\mathbf{b}}^r) = \frac{b^c\dot{h}^{r0}}{p+1}\left[\frac{|\dot{\mathbf{b}}^r|}{\mu^e\dot{h}^{r0}}\right]^{p+1}, \tag{3.40}$$

which, in turn, leads to a linear viscosity-like switching response for $p = 1$ and to a rate-independent magnetic switching response for the limiting case of $p = 0$. The conjugate to the convex potential (3.40) can subsequently be obtained via a Legendre transform of (3.40) with respect to $\dot{\mathbf{b}}^r$. Straightforward algebraic manipulations thus lead to the conjugate potential to $\mathscr{D}^b$, which reads

$$\mathscr{D}^{b*}(\mathbf{h}^r) = \frac{b^c\dot{h}^{r0}}{q+1}\left[\frac{\mu^e|\mathbf{h}^r|}{b^c}\right]^{q+1}, \qquad \text{with} \qquad q = \frac{1}{p}. \tag{3.41}$$

Finally, is is noted that in the rate-independent limit, i.e., $q \to +\infty$, (3.41) eventually reduce to a ferromagnetic switching surface defined via (Landis, 2002; Klinkel, 2006)

$$\phi^b = (\mu^e)^2\mathbf{h}^r\cdot\mathbf{h}^r - (b^c)^2 = 0. \tag{3.42}$$

The rate-independent evolution equation for the remanent field $\mathbf{b}^r$ is hence proposed in terms of the associated switching rule that ensures maximum energy dissipation (Lubliner, 1986), so that

$$\dot{\mathbf{b}}^r = \dot{\lambda}^b\frac{\partial\phi^b}{\partial\mathbf{h}^r}, \tag{3.43}$$

where $\dot{\lambda}^b$ is the switching Lagrange multiplier that must satisfy the Kuhn-Tucker conditions given by i) $\dot{\lambda}^b = 0$ if $\phi^b < 0$ and ii) $\dot{\lambda}^b > 0$ while $\phi^b = 0$, i.e., during the magnetic switching response. Again, the incremental solution of (3.43) is carried out via employing the classical radial-return-type implicit backward Euler method. The solution algorithm will provided in the following chapter.

In turn, the features of the **b**-based model response remain identical to those shown in Fig. 3.1, except the rate of saturation, which becomes different for this model. Nonetheless, quantitative

estimates of the coefficients $\kappa_b^{(j)}$, with $j = 1, 2$ and 3 will be provided in the following section where the best fit to the experimental data would be investigated.

3.2.3 Limiting cases

The two limiting cases, namely, (i) $b^c \to +\infty$ and (ii) $b^c = 0$, as discussed in Section 3.1.4, lead to non-dissipative magnetization responses. The limiting case (i), in turn, leads to the linear constitutive law $\mathbf{h} = \mathbf{b}/\mu^e$, which is identical to the one obtained in Section 3.1.4. The second case, on the other hand, leads to a saturating magnetization response for $\chi^e = 0$. Carrying out a similar set of manipulations as presented in Section 3.1.4, we obtain the potential energy in the limiting case (ii) to be

$$w^b(\mathbf{b}) = \frac{1}{2\mu_0}\mathbf{b}\cdot\mathbf{b} - \mu_0(m^s)^2\frac{1+\chi}{\chi}g^b\left(\frac{\chi}{1+\chi}\frac{|\mathbf{b}|}{\mu_0 m^s}\right), \tag{3.44}$$

where the functional form of g^b remains identical to (3.23), so that

$$g^b\left(\frac{\chi}{1+\chi}\frac{|\mathbf{b}|}{\mu_0 m^s}\right) = (f^{b\,\prime})^{-1}\left(\frac{\chi}{1+\chi}\frac{|\mathbf{b}|}{\mu_0 m^s}\right)\frac{\chi}{1+\chi}\frac{|\mathbf{b}|}{\mu_0 m^s} - f^b\left[(f^{b\,\prime})^{-1}\left(\frac{\chi}{1+\chi}\frac{|\mathbf{b}|}{\mu_0 m^s}\right)\right]. \tag{3.45}$$

Again, the specific choices of $\kappa_b^{(\alpha)} = 1$, where $\alpha = 1, 2$ or 3 leads to a closed form representation of the functions g^b as provided in Table 3.2.

The limiting case (i) response matches identically to Fig. 3.2a, whereas a qualitative agreement to Fig. 3.2b is achieved for the limiting case (ii). Of course, by construction, the magnetic susceptibility and the saturation magnetization for case (ii) remains identical to the magnetization response in Fig. 3.2b. However, the rate of magnetic saturation becomes different in the present **b**-based model. Thus, the hysteresis loop shape parameters $\kappa_b^{(\alpha)}$ are expected to be different from its counterparts in the **h**-based model.

Remark 3.2. The **b**-based constitutive models of the s-MREs often employ a different magnetic susceptibility, defined via $\widehat{\chi} = \chi/(1+\chi)$ (Ponte Castañeda and Galipeau, 2011; Galipeau and Ponte Castañeda, 2013; Danas, 2017; Psarra et al., 2019). Nevertheless, in this text we refrain from defining two different susceptibility measures for clarity.

3.3 Model fitting with experiments

This section is devoted towards the model parameter identifications via fitting it to the experimentally-obtained $\mathtt{m}-\mathtt{h}$ hysteresis loops of NdFeB magnets. Till date, a handful of experimental data is available they report the major hysteresis loops of bulk and powdered NdFeB magnets (Périgo et al., 2012; Deng et al., 2015; Huang et al., 2016b). In particular, we estimate the model parameters by fitting the model response with the measured hysteresis loops for (a) isotropic NdFeB powders (Deng et al., 2015) and (b) spark plasma sintered, isotropic NdFeB bulk magnets (Huang et al., 2016b). As reported in these experiments, the magnetization/demagnetization responses remain rate-independent while loading at a low-to-moderate frequency (up to 1 kHz), which is, in turn, well above the working loading/unloading frequencies for the h-MREs (Linke et al., 2016; Kalina et al., 2017; Kim et al., 2018; Zhao et al., 2019; Sitti and Wiersma, 2020).

Table 3.3 provides the estimated model parameters, which are obtained via fitting the model predictions with the experiments of Deng et al. (2015) (Table 3.3.1) and Périgo et al. (2012) (Table 3.3.2). Notice that the general model parameters remain the same for the **h** and **b**-based models, while the fitted shape parameters $\kappa_{\mathrm{h}}^{(\alpha)}$ and $\kappa_{\mathrm{b}}^{(\alpha)}$ differ considerably.

Table 3.3: Model parameters for NdFeB magnets

3.3.1 NdFeB powder			**3.3.2** Sintered NdFeB		
Gen. parameters	**h** model	**b** model	Gen. parameters	**h** model	**b** model
$\chi^{\mathrm{e}} = 0.105$	$\kappa_{\mathrm{h}}^{(1)} = 1.0$	$\kappa_{\mathrm{b}}^{(1)} = 0.0$	$\chi^{\mathrm{e}} = 0.078$	$\kappa_{\mathrm{h}}^{(1)} = 0.5$	$\kappa_{\mathrm{b}}^{(1)} = 0.0$
$\chi = 8.0$	$\kappa_{\mathrm{h}}^{(2)} = 0.0$	$\kappa_{\mathrm{b}}^{(2)} = 0.1$	$\chi = 4.5$	$\kappa_{\mathrm{h}}^{(2)} = 0.5$	$\kappa_{\mathrm{b}}^{(2)} = 0.3$
$m^{\mathrm{s}} = 0.67$ MA/m	$\kappa_{\mathrm{h}}^{(3)} = 0.0$	$\kappa_{\mathrm{b}}^{(3)} = 0.9$	$m^{\mathrm{s}} = 0.68$ MA/m	$\kappa_{\mathrm{h}}^{(3)} = 0.0$	$\kappa_{\mathrm{b}}^{(3)} = 0.7$
$b^{\mathrm{c}} = 0.845\mu_0$ T			$b^{\mathrm{c}} = 1.30\mu_0$ T		

Here we employ a least square-based curve fitting algorithm `lsqcurvefit` of MATLAB (2017) , which – given a proper initial guess – is very efficient in estimating the optimal fitting parameters. The fitted **h** and **b** models with these experimental data are shown in Fig. 3.3, where we observe an

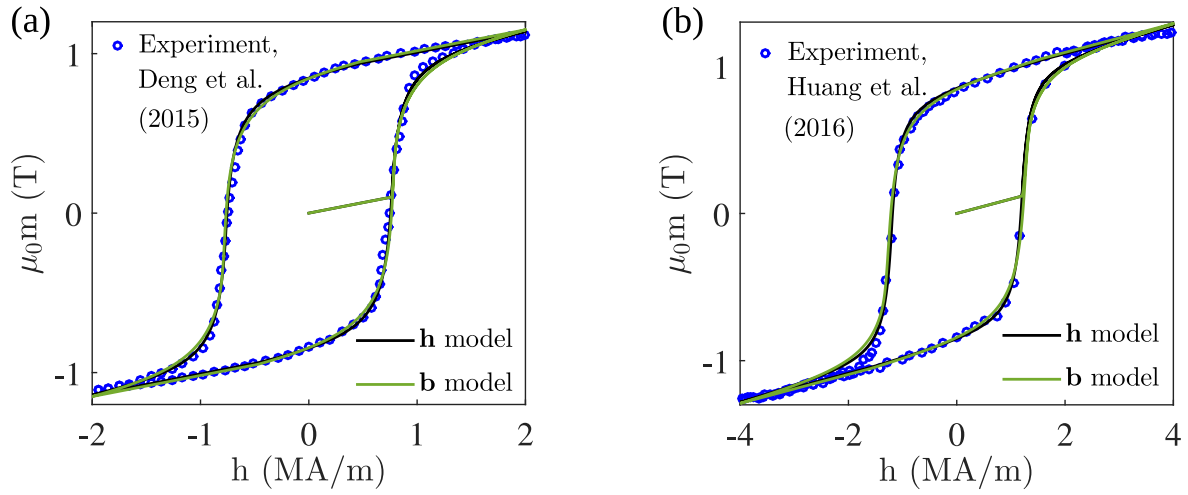

Figure 3.3: Experimental $\mathrm{m}-\mathrm{h}$ response of (a) NdFeB powder (Deng et al., 2015) and (b) spark plasma sintered NdFeB magnet (Huang et al., 2016b) along with the fitted rate-independent **h** and **b** models.

excellent agreement between these two. Moreover, as discussed in Section 3.2.2, the **b** model is proposed in such a way that it coincides with the **h** model in terms of the initial energetic and switching magnetization slopes, coercive field and saturation magnetization. However, the inverse saturation function emerging from the remanent potentials differ in these models terms of the difference in $\kappa_{\mathrm{h}}^{(\mathrm{j})}$ and $\kappa_{\mathrm{b}}^{(\mathrm{j})}$, whose fitted values (rounded-off after the first decimal place) are given in Table 3.3.

3.4 Concluding remarks

Two equivalent thermodynamically consistent, rate-independent ferromagnetic hysteresis models considering **h** and **b** to be the primary variables are proposed. Suitable choices for the remanent internal variable are made independently in both of them. The number of parameters in the model

has been kept relatively small, while making it rich enough to capture different rates of magnetic saturation. Both the models are shown to be leading to the non-hysteretic, saturation-type magnetization models in the limit of $b^c \to 0$. Finally, we find the model to capture considerably well the measured major hysteresis loops of NdFeB powders and sintered NdFeB magnets.

To this end, the developed ferromagnetic switching surface framework does not capture the initial magnetization response and minor hysteresis loops, which arise during a partially-reversed cyclic loading. Nevertheless, these effects can be incorporated in the present switching surface framework via proposing suitable phenomenological evolution laws for the coercive field b^c in terms a set of *history-dependent* parameters that take care of the whole loading/unloading history of the material. A proposal for such history-dependent phenomenological evolution laws of b^c for the **h**-based model and subsequently, the probe of the *evolving switching surface* model performance against the experimental data, are provided in Appendix A. Similar evolution equations can be proposed *mutatis mutandis* for the **b**-based model.

Chapter

4 Microscopic Model and Numerical Homogenization

Chapter summary: *An incremental numerical homogenization scheme for dissipative, hard-magnetic magneto-elastic composites is proposed herein. The microstrucutre of the two-phase composite is considered to be uniformly distributed spherical inclusions in a matrix, so that the statistical isotropy of the microstructure is ensured. An incremental variational principle is framed subsequently, that is employed to carry out the numerical homogenization computations. The variational principle is augmented thereafter in order to capture the magneto-mechanical coupling arising exclusively due to the particle rearrangements and particle rotations in the composite, without any macroscopic shape-effect. Besides the details of finite-element computations and local evolution algorithm for the internal variables, an account on the application of augmented potentials are also provided. Finally, the numerically computed effective magneto-mechanical responses along with the mesh convergence studies are presented.*

Chapter content

In this chapter we develop an incremental numerical homogenization framework for the isotropic ħ-MREs which is, in turn, a two phase composite having hard magnetic particles inside a soft elastomeric matrix. As discussed in Chapter 3, the soft magnetic response can be obtained as a limiting case of the dissipative hard magnetic models. Therefore, here we propose a numerical homogenization method for the ħ-MREs, whose limiting cases, those are relevant to the s-MREs, will also be provided therein. In this chapter, we follow Miehe et al. (2002), where an incremental numerical homogenization framework for the dissipative elasto-plastic composites is provided. We recast the same formalism for the dissipative magneto-hyperelastic two phase composites. The numerical realization of this incremental homogenization problem will be discussed thereafter. We start by defining the microstructure and properties of the individual phases therein.

4.1 Definition of the microstructure

We consider a macroscopic MRE sample[1] occupying a reference material volume $\mathcal{V}_0$ comprising numerous representative volume elements (RVEs) $\mathcal{V}_0^\#$, so that $\mathcal{V}_0^\# \ll \mathcal{V}_0$ (see Fig. 4.1). Thus, a complete

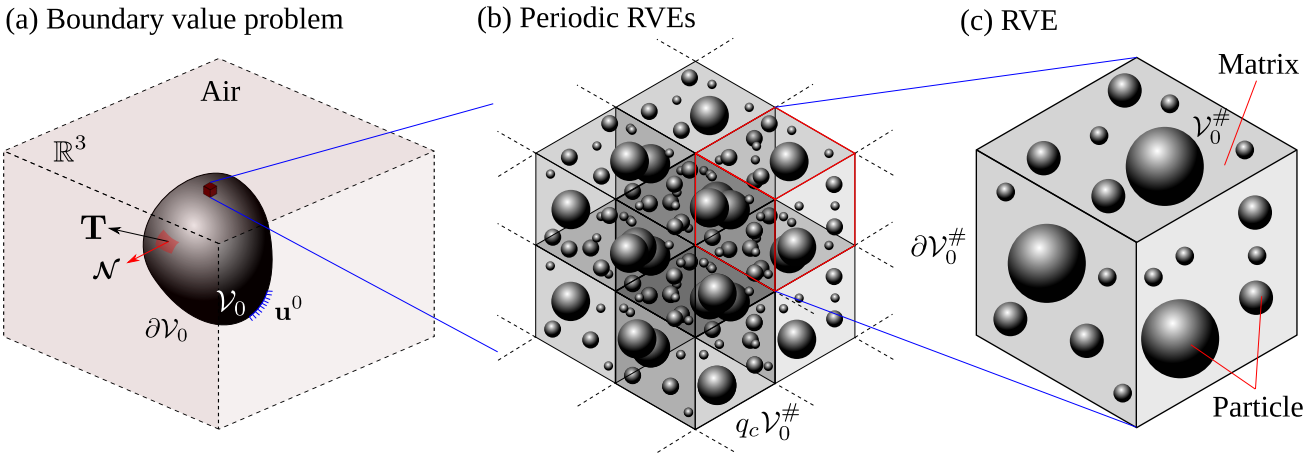

Figure 4.1: Schematic diagram of (a) macroscopic boundary value problem involving a MRE sample in air having a reference volume $\mathcal{V}_0$, (b) periodic arrangement of the statistically identical RVEs with polydisperse spherical inclusions and (c) a RVE occupying a reference volume $\mathcal{V}_0^\#$ and boundary $\partial\mathcal{V}_0^\#$.

separation in the length scales between $\mathcal{V}_0$ and $\mathcal{V}_0^\#$ is assumed in the case of MREs. Moreover, the RVEs are assumed to situate far from the macroscopic boundary $\partial\mathcal{V}_0$, on which, the macroscopic displacement and traction boundary conditions are applied (see Fig. 4.1a). Furthermore, a *slowly varying* microstructure is assumed, such that, as shown in Fig. 4.1b, the neighboring RVEs remain identical. It is emphasized that the RVEs must be rich enough to reflect the proper material proportions at the macroscale. Also, the distribution of the inclusion phases remains an important property of the RVE. Nevertheless, assuming a comprehensive representativity, the magnetic particles are considered to be occupying a reference volume $\mathcal{V}_{0\mathtt{p}}^\#$, whereas the elastomeric matrix phase occupies a volume of $\mathcal{V}_{0\mathtt{m}}^\#$,

[1] In a general discussion, we drop the prefixes s- and ħ- while referring to the MREs.

such that $\mathcal{V}_0^{\#} = \mathcal{V}_{0\mathtt{p}}^{\#} \cup \mathcal{V}_{0\mathtt{m}}^{\#}$ (see Fig. 4.1c). Consequently, the particle volume fraction $\mathtt{c}$ is defined via

$$\mathtt{c} = \frac{\mathcal{V}_{0\mathtt{p}}^{\#}}{\mathcal{V}_0^{\#}}. \tag{4.1}$$

We henceforth denote the quantities/properties associated with the particle and matrix phases by the subscripts "$\mathtt{p}$" and "$\mathtt{m}$", respectively. Motivated from the observed microstcuctures of the isotropic MREs in Fig. 1.1, the microstructure for RVE computations are defined to be a cubic volume having sides of length $\ell_0^{\#}$ (so that $\mathcal{V}_0^{\#} = (\ell_0^{\#})^3$) in the reference configuration, where the spherical inclusions are uniformly distributed in the matrix phase (see Fig. 4.1c). Moreover, these inclusions are considered to have several families, all of whose members are uniformly distributed in the cubic RVE, so that the *statistical isotropy* is ensured. Specific algorithms to generate such microstructures are discussed in Section 4.7.1.

In addition to the definition of the microstructure, it remains crucial to select a modeling framework, which must be straightforward to implement and also would lead to less expensive numerical computations. A complete account on the modeling framework selection and the specific energetic/dissipation energy functions associated with it are discussed in the following.

4.2 Local constitutive model

This section provides a microscopic constitutive model for the $\mathtt{h}$-MREs in terms of energetic and dissipation potentials. A specific choice for the microscopic modeling of the $\mathtt{s}$-MREs is provided thereafter. As discussed in Chapter 2, there exist several modeling frameworks, namely, the Lagrangian $\mathbf{F}-\mathbf{B}$, $\mathbf{F}-\mathbf{H}$, the Eulerian $\mathbf{F}-\mathbf{b}$, $\mathbf{F}-\mathbf{h}$ and the magnetization-based models (Kankanala and Triantafyllidis, 2004; Danas et al., 2012b; Lefèvre et al., 2017; Lefèvre et al., 2019; Keip and Rambausek, 2016, 2017; Kalina et al., 2016, 2020) for the MREs. In particular, we perform the present numerical homogenization investigations via considering the Lagrangian $\mathbf{F}-\mathbf{H}$ model. The advantage of this specific choice is two fold, namely, $\mathtt{i}$) evolution of the internal variables are easy to compute in a Lagrangian setting, where the variables are expressed in terms of the reference coordinate $\mathbf{X}$ and $\mathtt{ii}$) due to its curl-free nature (2.41), the local $\breve{\mathbf{H}}$[2] can be expressed in terms of the gradient of a scalar potential $\breve{\varphi}$, such that,

$$\breve{\mathbf{H}} = -\text{Grad}\ \breve{\varphi}, \tag{4.2}$$

which serve as local unknowns to be solved-for in a finite-element (FE) solution routine. In contrast, the divergence-free $\mathbf{B}$ field leads to a vector potential $\breve{\mathcal{A}}$, so that

$$\breve{\mathbf{B}} = \text{Curl}\ \breve{\mathcal{A}}, \tag{4.3}$$

which is then solved-for in a FE solver (Danas, 2017; Psarra et al., 2019). Moreover, in order to ensure the uniqueness of $\breve{\mathcal{A}}$, this vector potential-based formulation requires an additional constraint on it, namely, the Coulomb gage (Danas, 2017; Psarra et al., 2019). Thus, it is evident that, the scalar potential-based formulation results in substantially cheaper numerical computations by reducing the total degrees of freedom of the system, which is in the range of $1-15$ million for the present case

[2] All the microscopic fields are denoted by the ($\breve{\blacksquare}$) symbol in this text.

of scalar potential-based 3D RVE computations with polydisperse spherical inclusions. Thus, the following discussion is based entirely on the $\mathbf{F}-\mathbf{H}$ framework.

We propose the microscopic constitutive model by considering *nearly* incompressible matrix and particle phases, whereas, both pure and nearly incompressible models would be provided in the proposition of macroscopic models in the Chapters 5 and 6. Since the microstructure is *locally* heterogeneous, the referential representation of the local energetic ($\breve{W}^{\mathrm{H}}$) and dissipation ($\breve{D}^{\mathrm{H}}$) potentials depend on the reference coordinate $\mathbf{X}$, so that

$$\breve{W}^{\mathrm{H}}(\mathbf{X},\breve{\mathbb{C}},\breve{\mathbf{H}},\breve{\Xi}) = \Theta(\mathbf{X})\breve{W}^{\mathrm{H}}_{\mathtt{m}}(\breve{\mathbb{C}},\breve{\mathbf{H}},\breve{\Xi}) + (1-\Theta(\mathbf{X}))\breve{W}^{\mathrm{H}}_{\mathtt{p}}(\breve{\mathbb{C}},\breve{\mathbf{H}},\breve{\Xi}) \tag{4.4}$$

and

$$\breve{D}^{\mathrm{H}}(\mathbf{X},\breve{\mathbb{C}},\breve{\mathbf{H}},\breve{\Xi},\dot{\breve{\Xi}}) = \Theta(\mathbf{X})\breve{D}^{\mathrm{H}}_{\mathtt{m}}(\breve{\mathbb{C}},\breve{\mathbf{H}},\breve{\Xi},\dot{\breve{\Xi}}) + (1-\Theta(\mathbf{X}))\breve{D}^{\mathrm{H}}_{\mathtt{p}}(\breve{\mathbb{C}},\breve{\mathbf{H}},\breve{\Xi},\dot{\breve{\Xi}}), \tag{4.5}$$

respectively, where the $\breve{\mathbf{F}}$-dependence of $\breve{W}^{\mathrm{H}}$ is considered in terms of the right Cauchy-Green tensor $\breve{\mathbb{C}} = \breve{\mathbf{F}}^{\mathsf{T}}\breve{\mathbf{F}}$[3] that ensures objectivity (Coleman and Gurtin, 1967; Dorfmann and Ogden, 2004; Kankanala and Triantafyllidis, 2004), $\breve{\Xi}$ is a thermodynamic internal variable, ($\dot{\blacksquare}$) represents the material time derivative, and $\Theta(\mathbf{X})$ indicates the characteristics function taking the value $\Theta(\mathbf{X}) = 1$ if $\mathbf{X} \in \mathcal{V}^{\mathtt{m}}_0$ and $\Theta(\mathbf{X}) = 0$ if $\mathbf{X} \in \mathcal{V}^{\mathtt{p}}_0$ (Ponte Castañeda and Galipeau, 2011; Danas, 2017). Notice that the length scale of fluctuation of $\Theta(\mathbf{X})$ must be several order smaller than the macroscopic length scale, so that the hypothesis of separation of length scales holds.

Next, we propose a choice for the microscopic internal variable $\breve{\Xi}$ followed by setting forth the thermodynamic inequalities associated with this microscopic model. Afterwards, specific choices for the local potentials $\breve{W}^{\mathrm{H}}_{\mathtt{i}}$ and $\breve{D}^{\mathrm{H}}_{\mathtt{i}}$, $\mathtt{i} = \mathtt{m},\mathtt{p}$ will be provided.

4.2.1 Additive decomposition of the microscopic $\mathtt{h}$-field

The constitutive definition of a hard magnetic constitutive model first assumes an additive decomposition of the total $\mathtt{h}$-field into an "energetic" (denoted by the superscript $\mathtt{e}$) and a "remanent" (denoted by the superscript $\mathtt{r}$) part, which, in the reference and the current configurations read

$$\breve{\mathbf{H}} = \breve{\mathbf{H}}^{\mathtt{e}} + \breve{\mathbf{H}}^{\mathtt{r}} \qquad \equiv \qquad \breve{\mathbf{h}} = \breve{\mathbf{h}}^{\mathtt{e}} + \breve{\mathbf{h}}^{\mathtt{r}}, \tag{4.6}$$

respectively. Besides the reference $\breve{\mathbf{H}}$ is related to the current $\breve{\mathbf{h}}$ via (2.40), we define $\breve{\mathbf{h}}^{\mathtt{e}} = \breve{\mathbf{F}}^{-\mathsf{T}}\breve{\mathbf{H}}^{\mathtt{e}}$ and $\breve{\mathbf{h}}^{\mathtt{r}} = \breve{\mathbf{F}}^{-\mathsf{T}}\breve{\mathbf{H}}^{\mathtt{r}}$ to obtain (4.6). Of course, the latter two definitions are constitutive choices and may be altered if necessary. In addition to $\breve{\mathbf{F}}$ and $\breve{\mathbf{H}}$ to be the independent primary variables, we consider the reference $\breve{\mathbf{H}}^{\mathtt{r}}$ to be the internal variable that evolves with $\breve{\mathbf{F}}$ and $\breve{\mathbf{H}}$. Next, we derive the microscopic (local) constitutive relations from the localized entropy inequality.

4.2.2 Constitutive relations

Herein, we derive the microscopic Lagrangian constitutive equations from the Clausius-Duhem inequality. We assume the dissipative hard magneto-mechanical process to be isothermal and conse-

[3] We use the "blackboard bold" symbols for the right ($\mathbb{C}$) and the left Cauchy-Green ($\mathbb{B}$) tensors in order to distinguish them from the magnetic $\mathbf{B}$ field.

quently, no heat flux in/out is considered. Thus, (2.64) simplifies to

$$\breve{\mathbf{S}} : \dot{\breve{\mathbf{F}}} - \breve{\mathbf{B}} \cdot \dot{\breve{\mathbf{H}}} - \dot{\breve{W}}_i^H \geqslant 0, \qquad i = m,\ p, \tag{4.7}$$

with the equality holding exclusively for non-dissipative thermodynamic processes. Expressing the derivative $\dot{\breve{W}}_i^H$ in terms of the time derivatives of its arguments, followed by a rearrangement in the terms leads to

$$\left[\breve{\mathbf{S}} - 2\breve{\mathbf{F}}\frac{\partial \breve{W}_i^H}{\partial \breve{\mathbf{C}}}\right] : \dot{\breve{\mathbf{F}}} - \left[\breve{\mathbf{B}} + \frac{\partial \breve{W}_i^H}{\partial \breve{\mathbf{H}}}\right] \cdot \dot{\breve{\mathbf{H}}} - \frac{\partial \breve{W}_i^H}{\partial \breve{\mathbf{H}}^r} \cdot \dot{\breve{\mathbf{H}}}^r \geqslant 0. \tag{4.8}$$

Since the primary state variables $\breve{\mathbf{F}}$ and $\breve{\mathbf{H}}$ are independent, they can be varied in an arbitrary fashion. Hence, the standard arguments of the Coleman-Noll-Gurtin framework (Coleman and Noll (1959); Coleman and Gurtin (1967); see also the notes by Hütter (2017)) lead to the constitutive relations for the microscopic first Piola-Kirchhoff stress and the magnetic b-field are given by

$$\breve{\mathbf{S}} = 2\breve{\mathbf{F}}\frac{\partial \breve{W}_i^H}{\partial \breve{\mathbf{C}}} \qquad \text{and} \qquad \breve{\mathbf{B}} = -\frac{\partial \breve{W}_i^H}{\partial \breve{\mathbf{H}}}, \tag{4.9}$$

respectively. Subsequently, the microscopic Cauchy stress $\breve{\boldsymbol{\sigma}}$ is obtained via substituting $(4.9)_1$ into (2.48), so that

$$\breve{\boldsymbol{\sigma}} = \frac{2}{\breve{J}}\breve{\mathbf{F}}\frac{\partial \breve{W}_i^H}{\partial \breve{\mathbf{C}}}\breve{\mathbf{F}}^T, \tag{4.10}$$

which is, in turn, symmetric for any $\breve{W}_i^H$ and hence, satisfies the angular momentum balance law (2.20) (or, equivalently (2.53)). With these, the remaining part of the Clausius-Duhem inequality reads

$$\breve{\mathbf{B}}^r \cdot \dot{\breve{\mathbf{H}}}^r \geqslant 0, \qquad \text{with} \qquad \breve{\mathbf{B}}^r = -\frac{\partial \breve{W}_i^H}{\partial \breve{\mathbf{H}}^r}, \tag{4.11}$$

where the latter is the remanent Lagrangian b-field, which is, in turn, the energetic work conjugate of $\breve{\mathbf{H}}^r$. Moreover, the relation $(2.65)_2$ for generalized standard materials with this specific choice of the internal variable reads

$$\frac{\partial \breve{W}_i^H}{\partial \breve{\mathbf{H}}^r} + \frac{\partial \breve{D}_i^H}{\partial \dot{\breve{\mathbf{H}}}^r} = 0. \tag{4.12}$$

Finally, by combining (4.11) and (4.12), we obtain the dissipation inequality in terms of $\breve{D}_i^H$, such that

$$\frac{\partial \breve{D}_i^H}{\partial \dot{\breve{\mathbf{H}}}^r} \cdot \dot{\breve{\mathbf{H}}}^r \geqslant 0, \tag{4.13}$$

which imposes a thermodynamic constraint on $\breve{D}_i^H$ in terms of constraining it to be a convex function of $\dot{\breve{\mathbf{H}}}^r$. Thus, by proposing a convex $\breve{D}_i^H$ in terms of $\dot{\breve{\mathbf{H}}}^r$ a positive energy dissipation is ensured via (4.13) for *any* magneto-mechanical loading path.

It remains to propose specific forms for $\breve{W}_i^H$ and $\breve{D}_i^H$ given the thermodynamic restriction (4.13) is satisfied. Furthermore, it is noted that, in a finite strain setting, the choices for $\breve{W}_i^H$ and $\breve{D}_i^H$ are restricted further via the conditions of (i) even magneto-mechanical coupling, (ii) material frame indifference and (iii) material symmetry (Kankanala and Triantafyllidis, 2004; Dorfmann and Og-

den, 2004, 2005). In the following, we specify functional forms of $\breve{W}_i^H$ and $\breve{D}_i^H$ that satisfy the three aforementioned conditions.

4.2.3 Energy functions

Here we propose the specific functional forms of the local $\breve{W}_i^H(\breve{\mathbb{C}}, \breve{\mathbf{H}}, \breve{\mathbf{H}}^r)$ and $\breve{D}_i^H(\breve{\mathbb{C}}, \breve{\mathbf{H}}^r, \dot{\breve{\mathbf{H}}}^r)$ for the phase i. All phases are considered to be isotropic. To ensure the objectivity of the model, the two potentials must satisfy the material frame indifference and the material symmetry conditions. These conditions are in turn ensured via the proposition of $\breve{W}_i^H$ in terms of several mechanical and magneto-mechanical invariants listed in Table 4.1.

Table 4.1: Invariants associated with isotropic hard magneto-elastic phases

Mechanical			Magneto-mechanical		
Invariant	Lagrangian	Eulerian	Invariant	Lagrangian	Eulerian
$\breve{I}_1 =$	$\mathrm{tr}(\breve{\mathbb{C}})$	$\mathrm{tr}(\breve{\mathbb{B}})$	$\breve{I}_4^H =$	$\breve{\mathbf{H}}\cdot\breve{\mathbf{H}}$	$\breve{\mathbf{h}}\cdot\breve{\mathbb{B}}\breve{\mathbf{h}}$
$2\breve{I}_2 =$	$\mathrm{tr}(\breve{\mathbb{C}})^2 - \mathrm{tr}(\breve{\mathbb{C}}^2)$	$\mathrm{tr}(\breve{\mathbb{B}})^2 - \mathrm{tr}(\breve{\mathbb{B}}^2)$	$\breve{I}_4^{HHr} =$	$\breve{\mathbf{H}}\cdot\breve{\mathbf{H}}^r$	$\breve{\mathbf{h}}\cdot\breve{\mathbb{B}}\breve{\mathbf{h}}^r$
$\breve{I}_3 = \breve{J} =$	$\sqrt{\det\breve{\mathbb{C}}}$	$\sqrt{\det\breve{\mathbb{B}}}$	$\breve{I}_4^{Hr} =$	$\breve{\mathbf{H}}^r\cdot\breve{\mathbf{H}}^r$	$\breve{\mathbf{h}}^r\cdot\breve{\mathbb{B}}\breve{\mathbf{h}}^r$
Magneto-mechanical			Magneto-mechanical		
Invariant	Lagrangian	Eulerian	Invariant	Lagrangian	Eulerian
$\breve{I}_5^H =$	$\breve{\mathbf{H}}\cdot\breve{\mathbb{C}}^{-1}\breve{\mathbf{H}}$	$\breve{\mathbf{h}}\cdot\breve{\mathbf{h}}$	$\breve{I}_6^H =$	$\breve{\mathbf{H}}\cdot\breve{\mathbb{C}}^{-2}\breve{\mathbf{H}}$	$\breve{\mathbf{h}}\cdot\breve{\mathbb{C}}^{-1}\breve{\mathbf{h}}$
$\breve{I}_5^{HHr} =$	$\breve{\mathbf{H}}\cdot\breve{\mathbb{C}}^{-1}\breve{\mathbf{H}}^r$	$\breve{\mathbf{h}}\cdot\breve{\mathbf{h}}^r$	$\breve{I}_6^{HHr} =$	$\breve{\mathbf{H}}\cdot\breve{\mathbb{C}}^{-2}\breve{\mathbf{H}}^r$	$\breve{\mathbf{h}}\cdot\breve{\mathbb{C}}^{-1}\breve{\mathbf{h}}^r$
$\breve{I}_5^{Hr} =$	$\breve{\mathbf{H}}^r\cdot\breve{\mathbb{C}}^{-1}\breve{\mathbf{H}}^r$	$\breve{\mathbf{h}}^r\cdot\breve{\mathbf{h}}^r$	$\breve{I}_6^{Hr} =$	$\breve{\mathbf{H}}^r\cdot\breve{\mathbb{C}}^{-2}\breve{\mathbf{H}}^r$	$\breve{\mathbf{h}}^r\cdot\breve{\mathbb{C}}^{-1}\breve{\mathbf{h}}^r$

Notice in Table 4.1 that the mechanical invariants $\breve{I}_1 - \breve{I}_3$ and the magneto-mechanical invariant $\breve{I}_j^H$ with $j = 4-6$ are identical to those used in the modeling of s-MREs (Kankanala and Triantafyllidis, 2004; Lefèvre et al., 2017; Mukherjee et al., 2020). In addition, four new invariants, namely the "mixed" invariant $\breve{I}_j^{HHr}$ and the "remanent" invariant $\breve{I}_j^{Hr}$ ($j = 4-6$) are introduced. Since the internal variable $\breve{\mathbf{H}}^r$ is assumed to have the same push-forward transformation $\breve{\mathbf{h}}^r = \breve{\mathbf{F}}^{-T}\breve{\mathbf{H}}^r$ as the primary $\breve{\mathbf{H}}$, the mixed and remanent invariants can be readily shown to satisfy the material frame indifference and symmetry conditions.

Energy density **:** The energy density $\breve{W}_i^H$ is now proposed in terms of the Helmholtz free energy associated with the mechanical and magnetic parts, that read

$$\breve{W}_i^H(\breve{I}_1, \breve{J}, \breve{I}_4^{HHr}, \breve{I}_4^{Hr}, \breve{I}_5^H, \breve{I}_5^{HHr}) = \breve{\rho}_0\breve{\psi}_{\mathtt{mech},i}(\breve{I}_1, \breve{J}) + \breve{\rho}_0\breve{\psi}_{\mathtt{mag},i}^H(\breve{I}_4^{HHr}, \breve{I}_4^{Hr}, \breve{I}_5^H, \breve{I}_5^{HHr}) - \frac{\mu_0}{2}\breve{J}\breve{I}_5^H, \tag{4.14}$$

where the subscripts "mech" and "mag" indicate the mechanical and magnetic parts, respectively and the last term is the *magnetostatic energy* associated with any non-magnetic (ether) medium. Such assumption of a decoupled energy associated with the individual phases is sufficient to model the local microscopic behavior of the MREs, since its mechanically compliant matrix phase is magnetically inert, whereas the hard magnetic inclusions are mechanically stiff.

The mechanical free energy associated with the hard magnetic phases are typically expressed in terms of a Neo-Hookean energy, so that (Danas, 2017; Keip and Rambausek, 2017; Kalina et al., 2017; Lefèvre et al., 2017)

$$\breve{\rho}_0\breve{\psi}_{\mathtt{mech},i}(\breve{I}_1, \breve{J}) = \frac{G_i}{2}(\breve{I}_1 - 3 - 2\ln\breve{J}) + \frac{G_i'}{2}(\breve{J}-1)^2, \tag{4.15}$$

where G_i is the shear modulus and G_i' is the Lamé constant associated with the compressibility of each phase. This simple $\breve{I}_1$-based Neo-Hookean model is a constitutive choice. In fact, while proposing the phenomenological models in the following sections, we will use a homogenized version of the mechanical free energy $\breve{\psi}_{\mathtt{mech},i}$ that works for any $\breve{I}_1$-based hyperelastic model (Lopez-Pamies et al., 2013). Thus, the choice (4.15) remains open to be replaced with the other $\breve{I}_1$-based hyperelastic models (e.g., Gent model, Ogden model) without altering the other parts of (4.14).

The magnetic free energy is further decomposed into an energetic and a remanent part, which are, in turn, the functions of energetic invariants and the mixed and remanent invariants, respectively. Thus, $\breve{\psi}^{H}_{\mathtt{mag},i}$ reads

$$\breve{\rho}_0\breve{\psi}^{H}_{\mathtt{mag},i}(\breve{I}^{HHr}_4,\breve{I}^{Hr}_4,\breve{I}^{H}_5,\breve{I}^{HHr}_5)=\breve{\rho}_0\breve{\psi}^{H,en}_{\mathtt{mag},i}(\breve{I}^{H}_5)+\breve{\rho}_0\breve{\psi}^{H,rem}_{\mathtt{mag},i}(\breve{I}^{HHr}_4,\breve{I}^{Hr}_4,\breve{I}^{HHr}_5). \tag{4.16}$$

Specific choices for $\breve{\psi}^{\mathtt{mag}}_{\mathtt{en},i}$ and $\breve{\psi}^{\mathtt{mag}}_{\mathtt{rem},i}$ are given by

$$\breve{\rho}_0\breve{\psi}^{H,en}_{\mathtt{mag},i}(\breve{I}^{H}_5)=-\frac{\mu_0}{2}\chi^{e}_i\breve{I}^{H}_5 \tag{4.17}$$

and

$$\breve{\rho}_0\breve{\psi}^{H,rem}_{\mathtt{mag},i}(\breve{I}^{HHr}_4,\breve{I}^{Hr}_4,\breve{I}^{HHr}_5)=\frac{\mu_0}{2}(1+\chi^{e}_i)\left(\breve{I}^{HHr}_5+\breve{I}^{HHr}_4\right)+\frac{\mu_0}{\chi_i}(m^{s}_i)^2 f^{h}_i\left(\frac{\sqrt{\breve{I}^{Hr}_4}}{m^{s}_i}\right), \tag{4.18}$$

respectively. Note that the magnetic model parameters remain the same as in Chapter 3 in the present context of a finite-strain microscopic model. Of course, here the parameters are demarcated by an additional subscript "$\mathtt{i}$" that indicates the phase $\mathtt{i}=\mathtt{m}$ or $\mathtt{p}$, to which the magnetic property is associated with. The function f^{h}_i is defined via (3.12), where the coefficients are indicated via $\kappa^{(\alpha)}_{h,i}$, with $\alpha=1-3$ and the additional subscript $\mathtt{i}$ indicating the phase. Thus, we note that, in the limit of zero local strain, i.e., $\breve{\mathbf{C}}=\mathbf{I}$, (4.14) reduces identically to (3.9).

Dissipation potential **:** The dissipation potential in this finite strain setting is defined in terms of a power law in $|\dot{\breve{\mathbf{H}}}^{r}|$, so that

$$\breve{D}^{H}_i(|\dot{\breve{\mathbf{H}}}^{r}|)=\frac{b^{c}_i\dot{h}^{r0}_i}{p_i+1}\left[\frac{|\dot{\breve{\mathbf{H}}}^{r}|}{\dot{h}^{r0}_i}\right]^{p_i+1}, \tag{4.19}$$

where the parameters b^{c}_i, $\dot{h}^{r0}_i$ and p_i remain identical to those in (3.15). Similar to (3.15), a partial Legendre transform of (4.19) followed by taking the limiting case of rate-independence leads to the local microscopic ferromagnetic switching surface, which reads

$$\breve{\Phi}^{H}_i:=\breve{\mathbf{B}}^{r}\cdot\breve{\mathbf{B}}^{r}-(b^{c}_i)^2=0. \tag{4.20}$$

Consequently, the evolution equation for $\dot{\breve{\mathbf{H}}}^{r}$ is given the associated switching rule that ensures maximum energy dissipation, so that

$$\dot{\breve{\mathbf{H}}}^{r}=\dot{\lambda}^{H}_i\frac{\partial\breve{\Phi}^{H}_i}{\partial\breve{\mathbf{B}}^{r}},\qquad\text{with }\dot{\lambda}^{H}_i=0\text{ if }\breve{\Phi}^{H}_i<0\text{ and }\dot{\lambda}^{H}_i>0\text{ if }\breve{\Phi}^{H}_i=0, \tag{4.21}$$

indicating the Kuhn-Tucker conditions on the Lagrange multiplier $\dot{\lambda}^{H}_i$.

Potential for soft magnetic phases **:** As discussed in Chapter 3, the hysteresis model therein leads

to the non-hysteretic, saturation-type soft magnetic response in the limit of $b_i^c \to 0$. Thus, following (3.9) and (3.22), we recast (4.14) in terms of the purely energetic invariants of Table 4.1, such that

$$\breve{W}_i^H(\breve{I}_1, \breve{J}, \breve{I}_5^H) = \breve{\rho}_0 \breve{\psi}_{mech,i}(\breve{I}_1, \breve{J}) + \breve{\rho}_0 \breve{\psi}_{mag,i}^H(\breve{I}_5^H) - \frac{\mu_0}{2} \breve{J} \breve{I}_5^H, \tag{4.22}$$

where the mechanical free energy $\breve{\psi}_i^{mech}$ and the magnetostatic energy of the free space remain identical to (4.15). Nevertheless, the magnetic free energy, which is now expressed in terms of $\breve{I}_5^H$ is simply given in terms of the Langevin-type saturation energy function (3.26), so that (Lefèvre et al., 2017)

$$\breve{\rho}_0 \breve{\psi}_{mag,i}^H(\breve{I}_5^H) = -\frac{\mu_0 (m_i^s)^2}{3\chi_i} \left\{ \log\left[\sinh\left(\frac{3\chi_i}{m_i^s} \sqrt{\breve{I}_5^H} \right) \right] - \log\left[\frac{3\chi_i}{m_i^s} \sqrt{\breve{I}_5^H} \right] \right\}. \tag{4.23}$$

Instead, any saturation energy function listed in Table 3.2, or a linear combination of those can be used in equation (4.23). However, the saturation magnetization response of the commercially available carbonyl iron particles are observed to be modeled best by the Langevin-type saturation functions (Psarra et al., 2017; Bodelot et al., 2017). Furthermore, in this limiting case, the definition and evolution of the internal variables become inconsequential. Thus, the local constitutive relations are now given by (4.9).

Notably, the magnetic model parameters for the carbonyl iron particle-filled *s*-MREs reduce to two, namely, the susceptibility χ_i and the saturation magnetization m_i^s, since the coercive field b_i^c and energetic susceptibility χ_i^e vanish identically.

4.3 Incremental micro-potential

In general, the variation principle for the dissipative solids are expressed in terms of the local minimization of a set of internal variables during a finite time increment, namely $[t, t+\Delta t]$ (Carstensen et al., 2001; Miehe, 2002; Miehe et al., 2002, 2011; Rosato and Miehe, 2014). Hence, local incremental potential $\breve{\mathcal{W}}_i^H$ of the phase i at a *discrete* time $(t+\Delta t)$ for a coupled magneto-mechanical problem reads (Miehe, 2002; Miehe et al., 2002)

$$\breve{\mathcal{W}}_{i,t+\Delta t}^H(\breve{\mathbf{F}}, \breve{\mathbf{H}}) = \inf_{\breve{\mathbf{H}}^r} \left[\int_t^{t+\Delta t} (\dot{\breve{W}}_i^H + \breve{D}_i^H) dt \right], \qquad \text{with} \quad \breve{\mathbf{H}}^r(t) = \breve{\mathbf{H}}_t^r \tag{4.24}$$

is the given initial value of $\breve{\mathbf{H}}^r$ during this increment. In (4.24) the potentials $\breve{W}_i^H(\breve{\mathbb{C}}, \breve{\mathbf{H}}, \breve{\mathbf{H}}^r)$ and $\breve{D}_i^H(\breve{\mathbf{H}}^r, \dot{\breve{\mathbf{H}}}^r)$ represent the energetic and dissipation potentials, respectively. Moreover, the subscript $t+\Delta t$ of $\breve{\mathcal{W}}_i^H$ in (4.24) denotes its arguments $\breve{\mathbf{F}}$ and $\breve{\mathbf{H}}$ are evaluated at $t+\Delta t$.

The internal variable $\breve{\mathbf{H}}^r$ is *not* subjected to any differential or boundary constraints (Miehe, 2002; Miehe et al., 2011; Rosato and Miehe, 2014). In turn, the evolution of $\breve{\mathbf{H}}^r$ from its previous value $\breve{\mathbf{H}}_t^r$ is determined by the minimization problem $(4.24)_1$. Thus, we recast $(4.24)_1$ in the form

$$\breve{\mathcal{W}}_{i,t+\Delta t}^H(\breve{\mathbf{F}}, \breve{\mathbf{H}}) = \inf_{\breve{\mathbf{H}}^r} \left\{ [\breve{W}_i^H]_t^{t+\Delta t} + \int_t^{t+\Delta t} \breve{D}_i^H dt \right\}. \tag{4.25}$$

Taking the variation of $\breve{\mathcal{W}}_{i,t+\Delta t}^H$ while keeping $\breve{\mathbf{F}}$ and $\breve{\mathbf{H}}$ fixed leads to a stationarity condition that

reads

$$\left[\frac{\partial \breve{\mathcal{W}}_i^H}{\partial \breve{\mathbf{H}}^r}\cdot\delta\breve{\mathbf{H}}^r\right]_t^{t+\Delta t}+\int_t^{t+\Delta t}\left\{\frac{\partial \breve{\mathrm{D}}_i^H}{\partial \dot{\breve{\mathbf{H}}}^r}\cdot\delta\dot{\breve{\mathbf{H}}}^r+\frac{\partial \breve{\mathrm{D}}_i^H}{\partial \breve{\mathbf{H}}^r}\cdot\delta\breve{\mathbf{H}}^r\right\}dt=0. \tag{4.26}$$

Integrating by parts the first term under the integral of (4.26) and rearranging the terms we obtain (Miehe et al., 2002)

$$\left[\frac{\partial \breve{\mathcal{W}}_i^H}{\partial \breve{\mathbf{H}}^r}+\frac{\partial \breve{\mathrm{D}}_i^H}{\partial \dot{\breve{\mathbf{H}}}^r}\right]_{t+\Delta t}\cdot\delta\breve{\mathbf{H}}^r_{t+\Delta t}+\int_t^{t+\Delta t}\left\{-\frac{d}{dt}\frac{\partial \breve{\mathrm{D}}_i^H}{\partial \dot{\breve{\mathbf{H}}}^r}+\frac{\partial \breve{\mathrm{D}}_i^H}{\partial \breve{\mathbf{H}}^r}\right\}\cdot\delta\breve{\mathbf{H}}^r dt=0. \tag{4.27}$$

Note that $\delta\breve{\mathbf{H}}^r_t=0$ as it is a prescribed initial value given by $(4.24)_2$. Thus, the first bracketed term of (4.27) is at the right boundary of the time interval $[t,t+\Delta t]$, i.e., at the current time increment, whereas the second term is integrated over the time interval $[t,t+\Delta t]$. Hence, due to arbitrariness of the variation $\delta\breve{\mathbf{H}}^r$ during the increment from t to $t+\Delta t$, the integrand in the second term of (4.27) must vanish (Miehe et al., 2002). Consequently, (4.27) leads to the constitutive relation for generalized standard materials (GSMs) (Halphen and Nguyen, 1975)

$$\frac{\partial \breve{\mathcal{W}}_i^H}{\partial \breve{\mathbf{H}}^r}+\frac{\partial \breve{\mathrm{D}}_i^H}{\partial \dot{\breve{\mathbf{H}}}^r}=0,\qquad \forall\, t=t+\Delta t \tag{4.28}$$

which is the constitutive law that is used to update $\breve{\mathbf{H}}^r$ from $\breve{\mathbf{H}}^r_t$ to $\breve{\mathbf{H}}^r_{t+\Delta t}$. The updated $\breve{\mathbf{H}}^r_{t+\Delta t}$ is then substituted to (4.25), so that the optimal incremental potential $\breve{\mathcal{W}}^H_{i,t+\Delta t}$ can be obtained. The integrand of the second term of (4.27) leads to the Euler's equation governing the minimization path of $\breve{\mathbf{H}}^r$

$$-\frac{d}{dt}\left[\frac{\partial \breve{\mathrm{D}}_i^H}{\partial \dot{\breve{\mathbf{H}}}^r}\right]+\frac{\partial \breve{\mathrm{D}}_i^H}{\partial \breve{\mathbf{H}}^r}=0,\qquad \forall\, t\in[t,t+\Delta t]. \tag{4.29}$$

In practice, the minimization path of $\breve{\mathbf{H}}^r$ in the time interval $[t,t+\Delta t]$ carries no significance, as the local minimization of $\breve{\mathcal{W}}^H_{i,t+\Delta t}$ is carried out at each discrete time increment with a considerably small Δt (Miehe, 2002). Thus, (4.29) is dropped henceforth from the discussion.

The general form of the local incremental potential energy in a heterogeneous microstructure as in Fig. 4.1c can be expressed in a similar fashion to (4.4) to be a function of $\mathbf{X}$, so that

$$\breve{\mathcal{W}}^H_{t+\Delta t}(\mathbf{X},\breve{\mathbf{F}},\breve{\mathbf{H}})=\Theta(\mathbf{X})\breve{\mathcal{W}}^H_{m,t+\Delta t}(\breve{\mathbf{F}},\breve{\mathbf{H}})+\{1-\Theta(\mathbf{X})\}\breve{\mathcal{W}}^H_{p,t+\Delta t}(\breve{\mathbf{F}},\breve{\mathbf{H}}), \tag{4.30}$$

where the indicator function $\Theta(\mathbf{X})$ is defined in Section. 4.2. Once can, in turn, verify the last equation via substituting (4.4) and (4.5) into (4.24).

Finally, the local incremental constitutive relations are obtained via substituting (4.25) and (4.30) into (4.10), such that

$$\breve{\mathbf{S}}_{t+\Delta t}=\frac{\partial \breve{\mathcal{W}}^H_{t+\Delta t}}{\partial \breve{\mathbf{F}}_{t+\Delta t}},\qquad \breve{\mathbf{B}}_{t+\Delta t}=-\frac{\partial \breve{\mathcal{W}}^H_{t+\Delta t}}{\partial \breve{\mathbf{H}}_{t+\Delta t}}, \tag{4.31}$$

which leads to, respectively, the microscopic first Piola-Kirchhoff and magnetic b-field at a discrete time $t+\Delta t$. Thus, the incremental potential (4.25) (also referred as the "reduced potential" (Carstensen et al., 2001; Rosato and Miehe, 2014)) essentially provides a "quasi-energetic" approx-

imation of the dissipative model via computing *a-priori* the optimal internal variable $\breve{\mathbf{H}}^{\mathrm{r}}_{t+\Delta t}$ that minimizes the incremental energy (4.24) (Miehe et al., 2002). Thus, while computing the local constitutive response of such dissipative models for a given $\breve{\mathbf{F}}_{t+\Delta t}$ and $\breve{\mathbf{H}}_{t+\Delta t}$, we first update $\breve{\mathbf{H}}^{\mathrm{r}}_{t}$ to $\breve{\mathbf{H}}^{\mathrm{r}}_{t+\Delta t}$ from (4.28), which is followed by computing the local $\breve{\mathbf{S}}_{t+\Delta t}$ and $\breve{\mathbf{B}}_{t+\Delta t}$ from (4.31) (Rosato and Miehe, 2014). In turn, by computing these local $\breve{\mathbf{S}}_{t+\Delta t}$ and $\breve{\mathbf{B}}_{t+\Delta t}$ and subsequently, the tangent tensors, one constructs the element force and stiffness matrices in a FE numerical solution routine (Rosato and Miehe, 2014). Further details on the FE computations are provided in Section 4.6. Next, an incremental homogenization framework is proposed in terms of obtaining the *effective incremental potential* from the local incremental potential (4.25).

4.4 Incremental homogenization framework

Since h-MREs are dissipative in nature, the microscopic primary constitutive relations in terms of a quasi-energetic constitutive laws (4.31) depend on the specific time increment under consideration. We henceforth denote the current time $t + \Delta t$ by $\tau \equiv t + \Delta t$ for brevity.

The macroscopic deformation gradient $\mathbf{F}$ and the Lagrangian h-field $\mathbf{H}$ at a discrete time τ are now expressed in terms of the volume averages of the corresponding microscopic quantities, so that (Miehe et al., 2002; Ponte Castañeda and Galipeau, 2011; Danas, 2017; Lefèvre et al., 2017)[4]

$$\mathbf{F}_\tau = \frac{1}{\mathcal{V}_0^\#}\int_{\mathcal{V}_0^\#} \breve{\mathbf{F}}_\tau(\mathbf{X})\,\mathrm{dV}, \qquad \mathbf{H}_\tau = \frac{1}{\mathcal{V}_0^\#}\int_{\mathcal{V}_0^\#} \breve{\mathbf{H}}_\tau(\mathbf{X})\,\mathrm{dV}, \tag{4.32}$$

respectively. The periodicity of the RVE $\mathcal{V}_0^\#$ leads to the representation of the local displacement $\breve{\mathbf{u}}_\tau(\mathbf{X})$ and scalar potential $\breve{\varphi}_\tau(\mathbf{X})$ can be decomposed into "average" and "fluctuation" fields. The average $\mathbf{u}_\tau(\mathbf{X})$ and $\varphi_\tau(\mathbf{X})$ are related to the average (macroscopic) $\mathbf{F}_\tau$ and $\mathbf{H}_\tau$ via $\mathbf{u}_\tau(\mathbf{X}) = (\mathbf{F}_\tau - \mathbf{I})\cdot\mathbf{X}$ and $\varphi_\tau(\mathbf{X}) = -\mathbf{H}_\tau\cdot\mathbf{X}$, respectively. Thus, the local $\breve{\mathbf{u}}_\tau(\mathbf{X})$ and $\breve{\varphi}_\tau(\mathbf{X})$ admit to the decomposition

$$\breve{\mathbf{u}}_\tau(\mathbf{X}) = (\mathbf{F}_\tau - \mathbf{I})\cdot\mathbf{X} + \widetilde{\mathbf{u}}_\tau(\mathbf{X}) \qquad \text{and} \qquad \breve{\varphi}_\tau(\mathbf{X}) = -\mathbf{H}_\tau\cdot\mathbf{X} + \widetilde{\varphi}_\tau(\mathbf{X}), \qquad \forall\, \mathbf{X}\in\mathcal{V}_0^\#, \tag{4.33}$$

respectively, where $\widetilde{\mathbf{u}}_\tau(\mathbf{X})$ and $\widetilde{\varphi}_\tau(\mathbf{X})$ are the fluctuation fields, whose average in $\mathcal{V}_0^\#$ are identically zero. Thus, (4.32) can be verified via substituting (4.33) into it. Moreover, the average Eulerian $\mathbf{h}_\tau$ can be related to its Lagrangian counterpart via (Ponte Castañeda and Galipeau, 2011; Chatzigeorgiou et al., 2012; Javili et al., 2013)

$$\mathbf{h}_\tau = \frac{1}{\mathcal{V}_\tau^\#}\int_{\mathcal{V}_\tau^\#} \breve{\mathbf{h}}_\tau(\mathbf{x}_\tau)\,\mathrm{d}v_\tau = \mathbf{F}_\tau^{-\mathsf{T}}\mathbf{H}_\tau. \tag{4.34}$$

The derivation of the last relation is provided in Appendix 4.A, where the divergence-free property (2.A.5) of $\breve{J}_\tau\breve{\mathbf{F}}_\tau^{-\mathsf{T}}$ along with the periodic boundary condition on $\widetilde{\varphi}_\tau$ are exploited.

Having defined the RVE and the periodic boundary conditions (4.33), the incremental homogenization problem is now defined as the optimization problem give by (Ponte Castañeda and Galipeau,

[4] Miehe et al. (2002) considers such volume averages at a specific increment in the context of mechanical plasticity. The other references, which deal with magneto-mechanical homogenization of non-dissipative soft MREs, do not mention specific time increments in these average estimates.

2011; Danas, 2017; Lefèvre et al., 2017)

$$\mathcal{W}_\tau^{\mathrm{H}}(\mathbf{F},\mathbf{H}) = \inf_{\breve{\mathbf{u}}_\tau\in\mathcal{K}(\mathbf{F}_\tau)} \sup_{\breve{\varphi}_\tau\in\mathcal{G}(\mathbf{H}_\tau)} \left[\frac{1}{\mathcal{V}_0^{\#}}\int_{\mathcal{V}_0^{\#}} \breve{\mathcal{W}}_\tau^{\mathrm{H}}(\mathbf{X},\breve{\mathbf{F}},\breve{\mathbf{H}})\,\mathrm{dV}\right], \tag{4.35}$$

where $\breve{\mathcal{W}}_\tau^{\mathrm{H}}(\mathbf{X},\breve{\mathbf{F}},\breve{\mathbf{H}})$ is defined in (4.30), $\mathcal{K}$ and $\mathcal{G}$ represent the sets of admissible microscopic $\breve{\mathbf{u}}_\tau$ and $\breve{\varphi}_\tau$ fields, such that

$$\begin{aligned}\mathcal{K}(\mathbf{F}_\tau) = \big\{\breve{\mathbf{F}}_\tau : \exists\ \mathbf{x}_\tau = \mathbf{y}_\tau(\mathbf{X}) \text{ with } \breve{\mathbf{F}}_\tau = \mathbf{I} + \mathrm{Grad}\ \breve{\mathbf{u}}_\tau,\ \breve{J}_\tau > 0,\\ \breve{\mathbf{u}}_\tau = (\mathbf{F}_\tau - \mathbf{I})\cdot\mathbf{X} + \widetilde{\mathbf{u}}_\tau,\ \widetilde{\mathbf{u}}_\tau \text{ periodic in } \mathcal{V}_0^{\#}\big\}\end{aligned} \tag{4.36}$$

and

$$\mathcal{G}(\mathbf{H}_\tau) = \big\{\breve{\mathbf{H}}_\tau : \exists\ \mathbf{x}_\tau = \mathbf{y}_\tau(\mathbf{X}) \text{ with } \breve{\mathbf{H}}_\tau = -\mathrm{Grad}\ \breve{\varphi}_\tau,\ \breve{\varphi}_\tau = -\mathbf{H}_\tau\cdot\mathbf{X} + \widetilde{\varphi}_\tau,\ \widetilde{\varphi}_\tau \text{ periodic in } \mathcal{V}_0^{\#}\big\}. \tag{4.37}$$

The Hill-Mandel lemma along with the incremental constitutive relations (4.31) leads to the macroscopic constitutive relations at the time increment τ, such that (Miehe et al., 2002)

$$\mathbf{S}_\tau = \frac{\partial \mathcal{W}_\tau^{\mathrm{H}}}{\partial \mathbf{F}_\tau}, \qquad \mathbf{B}_\tau = -\frac{\partial \mathcal{W}_\tau^{\mathrm{H}}}{\partial \mathbf{H}_\tau}. \tag{4.38}$$

Again, notice that the incremental homogenization framework, that is proposed following (Miehe et al., 2002), essentially considers a quasi-energetic material model in terms of the potential (4.24), which, contains a history-dependent remanent field term. Thus, the standard, non-dissipative magneto-mechanical homogenization framework (Ponte Castañeda and Galipeau, 2011; Javili et al., 2013; Danas, 2017; Lefèvre et al., 2017) is employed here, except by using a history-dependent (in terms of the microscopic internal variables) incremental potential.

The microscopic remanent field $\breve{\mathbf{H}}^{\mathrm{r}}$ is not subjected to any differential/boundary constraint. Thus, unlike the primary variables in (4.33), no direct correlation can be defined between the microscopic $\breve{\mathbf{H}}^{\mathrm{r}}$ and its macroscopic counterpart. Of course, due the dissipative nature of the hard magnetic particle phase, the macroscopic response will be dissipative. However, no homogenized constitutive law for the macroscopic internal variable can be obtained from this incremental homogenization setting. Nevertheless, while defining the macroscopic model in Chapter 6, we will define independent macroscopic internal variables and their evolution laws from the macroscopic Clausius-Duhem inequalities.

Remark 4.1. For the special case of *s*-MREs (i.e., $b_{\mathrm{p}}^{\mathrm{c}} = 0$ and $\chi_{\mathrm{p}}^{e} = 0$), the microscopic dissipation potential $\breve{\mathrm{D}}_{\mathrm{i}}^{\mathrm{H}}$ vanishes identically and thus, the relation (4.28) for generalized standard materials yields an explicit expression for $\breve{\mathbf{H}}_\tau^{\mathrm{r}}$ in terms of $\breve{\mathbf{H}}_\tau$. Hence, the homogenization problem (4.35) reads for the *s*-MREs

$$\mathcal{W}_\tau^{\mathrm{H}}(\mathbf{F},\mathbf{H}) = \inf_{\breve{\mathbf{u}}_\tau\in\mathcal{K}(\mathbf{F}_\tau)} \sup_{\breve{\varphi}_\tau\in\mathcal{G}(\mathbf{H}_\tau)} \left[\frac{1}{\mathcal{V}_0^{\#}}\int_{\mathcal{V}_0^{\#}} \breve{\mathcal{W}}_\tau^{\mathrm{H}}(\mathbf{X},\breve{\mathbf{F}},\breve{\mathbf{H}})\,\mathrm{dV}\right], \tag{4.39}$$

which, in turn, can be rephrased to be (Lefèvre et al., 2017)

$$W^{\mathrm{H}}(\mathbf{F},\mathbf{H}) = \inf_{\breve{\mathbf{u}}\in\mathcal{K}(\mathbf{F})} \sup_{\breve{\varphi}\in\mathcal{G}(\mathbf{H})} \left[\frac{1}{\mathcal{V}_0^{\#}}\int_{\mathcal{V}_0^{\#}} \breve{W}^{\mathrm{H}}(\mathbf{X},\breve{\mathbf{F}},\breve{\mathbf{H}})\,\mathrm{dV}\right], \tag{4.40}$$

where the effective potential $W^{\mathrm{H}}(\mathbf{F},\mathbf{H})$ is no longer history-dependent, since the remanent field $\breve{\mathbf{H}}^{\mathrm{r}}$ becomes inconsequential. Consequently, the macroscopic constitutive relations read

$$\mathbf{S} = \frac{\partial W^{\mathrm{H}}}{\partial \mathbf{F}}, \qquad \mathbf{B} = -\frac{\partial W^{\mathrm{H}}}{\partial \mathbf{H}}. \tag{4.41}$$

Of course, the resulting $\mathbf{S}$ and $\mathbf{B}$ are path-independent and thus, given uniquely for a given $\mathbf{F}$ and $\mathbf{H}$. Analytical estimates to the energetic homogenization problem (4.40) have been provided by Ponte Castañeda and Galipeau (2011) and Lefèvre et al. (2017). However, both of these estimates are implicit and thus, require solving additional algebraic equations along with (4.41). A brief outline of the analytical homogenization estimates of Lefèvre et al. (2017) is provided in Section 5.1.

4.5 Augmented variational principle

In order to numerically compute the effective RVE response, one must exploit the incremental variational principle (4.35) so that the optimal microscopic $\breve{\mathbf{u}}_\tau$ and $\breve{\varphi}_\tau$ belonging to the sets $\mathcal{K}(\mathbf{F}_\tau)$ and $\mathcal{G}(\mathbf{H}_\tau)$, respectively, can be computed. The effective responses are thence computed from (4.32) and (4.38). Nevertheless, the numerical homogenization of the MREs should be carried out under suitably applied macroscopic boundary conditions across the RVE. As pointed out by Danas (2017), we note that a macroscopic MRE sample is subjected to an external magnetic field that is applied far from its boundary, which is schematically shown by Fig. 4.2a. Moreover, the externally applied magnetic field does *not* follow the deformation of the magnet. Rather, the applied field stays as a uniformly-applied

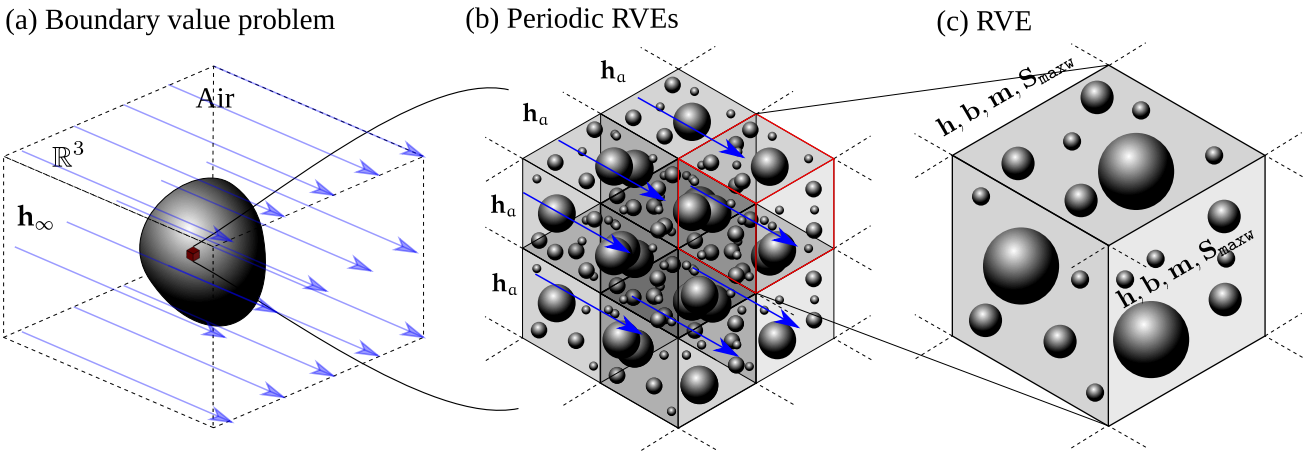

Figure 4.2: Schematic diagram of (a) macroscopic boundary value problem involving a MRE sample in air having a reference volume $\mathcal{V}_0$, (b) periodic arrangement of the statistically identical RVEs with polydisperse spherical inclusions and (c) a RVE occupying a reference volume $\mathcal{V}_0^{\#}$ and boundary $\partial\mathcal{V}_0^{\#}$.

background magnetic field (shown by the blue arrows in Fig. 4.2a), which is, in turn, perturbed by the MRE sample (see Fig. 4.2b). Naturally, the applied magnetic field that is controlled remains Eulerian. Hence, the macroscopic boundary conditions that are applied across the RVE in a numerical computation must include the effects of (i) fixed magnetic poles situated far away and (ii) applied magnetic load that does not follow the deformation.

These two boundary terms allow us to analyze the microstructurally induced magneto-mechanical coupling in the RVE remaining free from any geometry/shape effects. The application of such

boundary conditions in the homogenization problem (4.35) is a non-trivial operation. Such operation necessitates the evaluation of $\mathbf{F}$, $\mathbf{S}$, $\mathbf{h}$, $\mathbf{b}$ and $\mathbf{m}$ from (4.35) followed by the application of the macroscopic boundary conditions. Instead, an augmented variational principal (Danas, 2017), that is capable of applying both the conditions (i) and (ii) directly to the homogenization problem, is employed.

Specifically, in order to ensure the continuity of the energetic Maxwell stress $\mathbf{S}^{\text{en}}_{\text{maxw}}$ across the neighboring RVEs (see Fig. 4.2c), one needs to deduct the average Maxwell energy, $W^{\text{H}}_{\text{maxw},\tau}$, of the RVE from the homogenized energy (4.35). The former is defined as

$$W^{\text{H}}_{\text{maxw},\tau}(\mathbf{F},\mathbf{H}) = -\frac{\mu_0}{2} J_\tau \mathbf{F}_\tau^{-\text{T}}\mathbf{H}_\tau \cdot \mathbf{F}_\tau^{-\text{T}}\mathbf{H}_\tau, \tag{4.42}$$

and alone gives rise to a deformation gradient $\mathbf{F}$ under the application of $\mathbf{H}$ across the RVE. Thus, if it is not deducted from (4.35), one obtains a fictitious $\mathbf{F}$ in the RVE, even when non-magnetic phases (such as a simple polymer) are analyzed (Danas, 2017). In other words, the deduction of $W^{\text{H}}_{\text{maxw},\tau}$ from $\mathcal{W}^{\text{H}}_\tau$ upholds the practical condition (i) of having fixed, far-away magnets from the sample by not allowing the poles to move towards each other under an applied $\mathfrak{h}$-field $\mathbf{H}$; see Fig. 4.2a. The energy $\mathcal{W}^{\text{H}}_\tau$ in its original form (4.35) represents the electro-active homogenization problem, where the electrodes are attached directly on the sample.

As noted earlier, the magnetic poles create a uniform background magnetic field, which is indeed perturbed by the presence of the MRE sample by creating a self field around itself. Thus, a material point in the MRE sees an Eulerian $\mathfrak{h}$-field and not a Lagrangian field, which is the case observed in the electro-active problems. The application of such an average Eulerian field as the loading in our homogenization problem can be achieved in various manners. The simplest and more practical way we follow in this work consists in constraining the product $\mathbf{F}^{-\text{T}}\mathbf{H} = \mathbf{h}$ to be equal to an *applied* average $\mathfrak{h}$-field across the RVE, denoted as $\mathbf{h}_a$ (see Fig. 4.2b).

The deduction of the average Maxwell energy, $W^{\text{H}}_{\text{maxw},\tau}$, defined in (4.42) together with the last constraint $\mathbf{F}^{-\text{T}}\mathbf{H} = \mathbf{h}_a$ are employed by the augmented, incremental variational principle, whose total incremental potential reads (Danas, 2017)

$$\mathscr{P}^{\text{H}}_\tau(\mathbf{F},\mathbf{H}) = \mathcal{W}^{\text{H}}_\tau(\mathbf{F},\mathbf{H}) + \frac{\mu_0}{2} J_\tau \mathbf{F}_\tau^{-\text{T}}\mathbf{H}_\tau \cdot \mathbf{F}_\tau^{-\text{T}}\mathbf{H}_\tau + \frac{\mu_0}{2\zeta}|\mathbf{F}_\tau^{-\text{T}}\mathbf{H}_\tau - \mathbf{h}_{a,\tau}|^2 - \mathbf{S}^{\text{mech}}_{a,\tau} : (\mathbf{F}_\tau - \mathbf{I}). \tag{4.43}$$

Here, $\mathcal{W}^{\text{H}}_\tau(\mathbf{F},\mathbf{H})$ is given by (4.35), ζ is a non-dimensional penalty factor serving to enforce the application of a Eulerian background $\mathfrak{h}-$field and $\mathbf{S}^{\text{mech}}_a$ is the applied macroscopic stress on the RVE. Notice that $\mathbf{S}^{\text{mech}}_a$ is different from the mechanical first Piola-Kirchhoff stress $\mathbf{S}_{\text{mech}}$, which is a part of the total $\mathbf{S}$, computed from the constitutive relations. In practice, it suffices to set ζ equal to a very small number left to be defined in Section 4.7. Also note that the last term in (4.43) should be dropped unless a non-zero average mechanical traction is applied.

The augmented variational principle (4.43) leads to a traction boundary condition that is free from the effect of the energetic Maxwell stress, which is uniformly present in the neighboring RVEs as well. This observation can be demonstrated directly from (4.43) via taking the variation of it, so that

$$\delta\mathscr{P}^{\text{H}}_\tau(\mathbf{F},\mathbf{H}) = \frac{\partial \mathscr{P}^{\text{H}}_\tau}{\partial \mathbf{F}_\tau} : \delta\mathbf{F}_\tau + \frac{\partial \mathscr{P}^{\text{H}}_\tau}{\partial \mathbf{H}_\tau} \cdot \delta\mathbf{H}_\tau = 0. \tag{4.44}$$

Consequently, the arbitrariness of the independent variations $\delta\mathbf{F}_\tau$ and $\delta\mathbf{H}_\tau$ in (4.44) leads to their

coefficients vanish independently. First, the vanishing coefficient of $\delta\mathbf{H}_\tau$ yields the condition

$$\frac{\partial \mathscr{P}_\tau^{\mathrm{H}}}{\partial \mathbf{H}_\tau} = \frac{\partial \mathcal{W}_\tau^{\mathrm{H}}}{\partial \mathbf{H}_\tau} + \mu_0 J_\tau \mathbf{F}_\tau^{-1}\mathbf{F}_\tau^{-\mathrm{T}}\mathbf{H}_\tau + \frac{\mu_0}{\zeta}\mathbf{F}_\tau^{-1}(\mathbf{F}_\tau^{-\mathrm{T}}\mathbf{H}_\tau - \mathbf{h}_{a,\tau}) = 0. \tag{4.45}$$

Substituting the constitutive relation $(4.38)_2$ and employing the push-forward transformations (2.40), (2.45), the last equation can be recast in the form

$$\mathbf{b}_\tau = \mu_0\mathbf{h}_\tau + \frac{\mu_0}{J_\tau\zeta}(\mathbf{h}_\tau - \mathbf{h}_{a,\tau}) = \mu_0(\mathbf{h}_\tau + \mathbf{m}_\tau), \qquad \text{with} \qquad \mathbf{m}_\tau = \frac{1}{J_\tau\zeta}(\mathbf{h}_\tau - \mathbf{h}_{a,\tau}). \tag{4.46}$$

Notice that, the difference $|\mathbf{h}_\tau - \mathbf{h}_{a,\tau}|$ remains in the order of the penalty parameter ζ. Hence, the ratio $|\mathbf{h}_\tau - \mathbf{h}_{a,\tau}|/\zeta$ remains in the O(1), which is proportional to the effective magnetization $\mathbf{m}_\tau$. Finally, the variation of $\mathscr{P}_\tau^{\mathrm{H}}(\mathbf{F},\mathbf{H})$ with respect to $\mathbf{F}_\tau$ yields the equation

$$\frac{\partial \mathscr{P}_\tau^{\mathrm{H}}}{\partial \mathbf{F}_\tau} = \mathbf{S}_\tau - J_\tau\left(\mathbf{h}_\tau \otimes \mathbf{b}_\tau - \frac{\mu_0}{2}|\mathbf{h}_\tau|^2\mathbf{I}\right)\mathbf{F}_\tau^{-\mathrm{T}} - \mathbf{S}_{a,\tau}^{\mathrm{mech}} = \mathbf{S}_\tau - \mathbf{S}_{\mathrm{maxw},\tau}^{\mathrm{en}} - \mathbf{S}_{a,\tau}^{\mathrm{mech}} = 0, \tag{4.47}$$

where the first Piola-Kirchhoff Maxwell stress $\mathbf{S}_{\mathrm{maxw},\tau}$ is related to the familiar energetic form of the Cauchy Maxwell stress $\boldsymbol{\sigma}_{\mathrm{maxw},\tau}^{\mathrm{en}}$ via $\mathbf{S}_{\mathrm{maxw},\tau}^{\mathrm{en}} = J_\tau\boldsymbol{\sigma}_{\mathrm{maxw},\tau}^{\mathrm{en}}\mathbf{F}_\tau^{-\mathrm{T}}$. In turn, $\boldsymbol{\sigma}_{\mathrm{maxw},\tau}^{\mathrm{en}}$ is given by (Kankanala and Triantafyllidis, 2004)

$$\boldsymbol{\sigma}_{\mathrm{maxw},\tau}^{\mathrm{en}} = \mathbf{h}_\tau \otimes \mathbf{b}_\tau - \frac{\mu_0}{2}|\mathbf{h}_\tau|^2\mathbf{I}. \tag{4.48}$$

Therefore, by employing the augmented variational principle (4.43), we practically ensure that the incremental traction boundary condition across the RVE in the numerical computations is given by

$$\mathbf{T}_\tau = \left[\mathbf{S}_\tau - \mathbf{S}_{\mathrm{maxw},\tau}^{\mathrm{en}} - \mathbf{S}_{a,\tau}^{\mathrm{mech}}\right]\cdot\mathcal{N} = 0, \qquad \forall\, \mathbf{X} \in \partial\mathcal{V}_0^{\#} \tag{4.49}$$

Thus, in absence of any externally applied mechanical stress $\mathbf{S}_{a,\tau}^{\mathrm{mech}}$, the strain in the RVE is now ensured to be resulting from the particle rearrangements and particle rotations, but *not* from the Maxwell stress, which is uniform in the RVE and its neighbors. We conclude this section by two remarks.

Remark 4.2. For a s-MRE with no memory of prior loading/unloading, the total $\boldsymbol{\sigma}$ is given by a simple decomposition into $\boldsymbol{\sigma} = \boldsymbol{\sigma}_{\mathrm{mech}} + \boldsymbol{\sigma}_{\mathrm{maxw}}^{\mathrm{en}}$. Here, we suppress the subscript τ since no memory dependence is present in these MREs. Thus, by applying the traction (4.49) it is ensured that the resulting strain is due to *purely mechanical* rearrangements of the particles, which experience mutual attraction/repulsion forces due to magnetization (Danas, 2017). On the other hand, in addition to the particle-to-particle attraction/repulsion, the hard magnetic particles in the h-MREs may also experience *magnetic torques* due to a misalignment in the local $\mathbf{h}$ and $\mathbf{m}$ fields, which is commonly observed during the non-proportional loading of a h-MRE sample (Kim et al., 2018; Zhao et al., 2019). Thus, even if the effect of the background energetic Maxwell stress is removed by applying (4.49), in contrast to the s-MREs, the resulting strains in the h-MREs *may not* be only due to mechanical rearrangements of the permanently magnetized particles. Rather, the magnetic torques in these particles may induce their rotations, which may eventually cause mechanical strains.

Remark 4.3. The *mathematical* incremental homogenization problem (4.35) is well-posed and the additional terms in (4.43) are employed after solving for $\mathcal{W}_\tau^{\mathrm{H}}$ in (4.35). This is because the analytical

estimates for energetic W^{H} are independent of the boundary conditions (Ponte Castañeda and Galipeau, 2011; Lefèvre et al., 2017). However, the practical boundary conditions (i) and (ii) are crucial for the proper interpretation of the effective $\mathbf{F}_\tau$, $\mathbf{S}_\tau$, $\mathbf{h}_\tau$, $\mathbf{b}_\tau$ and $\mathbf{m}_\tau$ fields for a given RVE. For this reason, in the case of analytical homogenization or phenomenological modeling of an MRE, the function $\mathcal{W}^{\mathrm{H}}_\tau$ is obtained explicitly or implicitly first, while the subtraction of $W^{\mathrm{H}}_{\mathsf{maxw},\tau}$ together with the application of the constraint $\mathbf{F}_\tau^{-\mathsf{T}}\mathbf{H}_\tau = \mathbf{h}_{\mathrm{a},\tau}$ is carried out *a posteriori* to extract the relevant estimates for $\mathbf{F}_\tau$, $\mathbf{S}_\tau$, $\mathbf{h}_\tau$, $\mathbf{b}_\tau$ and $\mathbf{m}_\tau$ during the current time increment τ. However, in a numerical simulation of an RVE, that would require extremely long computation times since one has to obtain numerically the incremental effective energy $\mathcal{W}^{\mathrm{H}}_\tau(\mathbf{F},\mathbf{H})$ and its derivatives. The augmented potential energy (4.43) offers a direct alternative allowing the direct evaluation of the desired estimates for $\mathbf{F}_\tau$, $\mathbf{S}_\tau$, $\mathbf{h}_\tau$, $\mathbf{b}_\tau$ and $\mathbf{m}_\tau$ under given loading conditions $\mathbf{h}_{\mathrm{a},\tau}$ and $\mathbf{S}^{\mathsf{mech}}_{\mathrm{a},\tau}$.

4.6 Finite-element computations

The finite-element computations of the effective response is associated with three distinct parts, namely, (i) discretization of the microscopic boundary value problem and construction of element force and stiffness matrices, (ii) application of the periodic boundary conditions across the opposite facing boundaries of $\mathcal{V}_0^{\#}$ and (iii) application of the macroscopic boundary conditions in terms of employing the macroscopic variational principle (4.43). Here we employ a "total Lagrangian" finite-element method by expressing all the field variables in terms of the fixed reference coordinate $\mathbf{X}$.

4.6.1 Discretization of the microscopic boundary value problem

The spatial discretization of the microscopic boundary value problem (BVP) is obtained via proposing a microscopic variational principle that reads

$$\breve{\mathscr{P}}^{\mathrm{H}}_\tau(\breve{\mathbf{u}}_\tau,\breve{\varphi}_\tau) = \inf_{\breve{\mathbf{u}}_\tau\in\mathcal{K}(\mathbf{F}_\tau)}\sup_{\breve{\varphi}_\tau\in\mathcal{G}(\mathbf{H}_\tau)}\left[\int_{\mathcal{V}_0^{\#}}\breve{\mathcal{W}}^{\mathrm{H}}_\tau(\mathbf{X},\breve{\mathbf{F}},\breve{\mathbf{H}})\,\mathrm{dV}\right], \tag{4.50}$$

where the admissible sets $\mathcal{K}(\mathbf{F}_\tau)$ and $\mathcal{G}(\mathbf{H}_\tau)$ are defined via (4.36) and (4.37), respectively. Notice that no microscopic body force or boundary traction is considered in the microscopic variational principle. Nonetheless, the boundary displacements are controlled via the periodic boundary conditions and the macroscopic traction boundary condition (4.49) is applied in terms of employing the macroscopic variational principle (4.43).

The primary field variables in $\mathcal{V}_0^{\#}$ at any discrete time τ are represented via a single vector $\breve{\mathbf{q}}_\tau \equiv \{\breve{\mathbf{u}}_\tau,\breve{\varphi}_\tau\}$, which results in easy-to-follow notations of the finite-element discretization. Moreover, $\breve{\mathbf{q}}_\tau$ admits to the form within each element given by

$$[\breve{\mathbf{q}}_\tau(\breve{\boldsymbol{\xi}})] = [\breve{\mathbf{N}}^e(\breve{\boldsymbol{\xi}})][\breve{\mathbf{q}}^e_\tau], \qquad \text{with} \qquad [\mathbf{X}(\breve{\boldsymbol{\xi}})] = [\breve{\mathbf{N}}^e(\breve{\boldsymbol{\xi}})][\mathbf{X}^e], \tag{4.51}$$

where $[\breve{\mathbf{N}}^e(\breve{\boldsymbol{\xi}})]$ is the matrix containing nodal interpolation functions and $[\breve{\mathbf{q}}^e_\tau]$ is the element degrees of freedom vector (consisting of four dofs, namely, $(\breve{u}_\tau)_1,(\breve{u}_\tau)_2,(\breve{u}_\tau)_3,\breve{\varphi}_\tau$ per node) in the element e, $\breve{\boldsymbol{\xi}}$ and $\mathbf{X}$ are the local and reference coordinates, respectively and $\mathbf{X}^e$ are the nodal coordinates with respect to the reference frame. In turn, the finite-element discretization leads to a set of nonlinear

algebraic equations emerging from the variational principle (4.50), so that

$$\delta\breve{\mathscr{P}}^{\mathrm{H}}_{\tau} = \frac{\partial\breve{\mathscr{P}}^{\mathrm{H}}_{\tau}}{\partial\breve{\mathbf{q}}_{\tau}} \cdot \delta\breve{\mathbf{q}}_{\tau} \equiv [\delta\breve{\mathbf{q}}_{\tau}]^{\mathrm{T}}[\breve{\mathcal{F}}(\breve{\mathbf{q}}_{\tau})] = 0, \tag{4.52}$$

where $[\breve{\mathcal{F}}(\breve{\mathbf{q}}_{\tau})]$ is the global force vector associated with the discretized system. Consequently, owing to the arbitrariness of $\delta\breve{\mathbf{q}}_{\tau}$, the resulting set of nonlinear algebraic equations read $[\breve{\mathcal{F}}(\breve{\mathbf{q}}_{\tau})] = 0$, which is solved via the Newton-Raphson method. The incremental solution of the global system of equations necessitates the following linearization of $[\breve{\mathcal{F}}(\breve{\mathbf{q}}_{\tau})]$.

$$[\breve{\mathcal{F}}(\breve{\mathbf{q}}_{\tau} + \Delta\breve{\mathbf{q}}_{\tau})] = [\breve{\mathcal{F}}(\breve{\mathbf{q}}_{\tau})] + [\breve{\mathcal{K}}(\breve{\mathbf{q}}_{\tau})][\Delta\breve{\mathbf{q}}_{\tau}] = 0, \tag{4.53}$$

where $[\breve{\mathcal{K}}(\breve{\mathbf{q}}_{\tau})]$ is the global stiffness matrix, that can be obtained from the second variation of $\breve{\mathscr{P}}^{\mathrm{H}}_{\tau}$, which follows readily from (4.52), so that

$$\Delta\delta\breve{\mathscr{P}}^{\mathrm{H}}_{\tau} = \delta\breve{\mathbf{q}}_{\tau} \cdot \frac{\partial^2\breve{\mathscr{P}}^{\mathrm{H}}_{\tau}}{\partial\breve{\mathbf{q}}_{\tau}\partial\breve{\mathbf{q}}_{\tau}} \cdot \Delta\breve{\mathbf{q}}_{\tau} \equiv [\delta\breve{\mathbf{q}}_{\tau}]^{\mathrm{T}}[\breve{\mathcal{K}}(\breve{\mathbf{q}}_{\tau})][\Delta\breve{\mathbf{q}}_{\tau}]. \tag{4.54}$$

It is noted that the solution for the unknown primary field $\breve{\mathbf{q}}_{\tau}$ in $\mathcal{V}^{\#}_{0}$ is not trivial. Therefore, $\breve{\mathbf{q}}_{\tau}$ is described in terms of the unknown nodal variables $\breve{\mathbf{q}}^{e}_{\tau}$ and a set of prescribed interpolation functions $\breve{\mathbf{N}}^{e}(\breve{\xi})$ in a finite volume element e. Since in the microscopic model of the MREs, the potential $\breve{\mathscr{P}}^{\mathrm{H}}_{\tau}$ is expressed in terms of Grad $\breve{\mathbf{q}}_{\tau}$ (i.e., Grad $\breve{\mathbf{u}}_{\tau}$ and Grad $\breve{\varphi}_{\tau}$), only a C^0 continuity of $\breve{\mathbf{u}}_{\tau}$ and $\breve{\varphi}_{\tau}$ is required at the element boundaries, which must be ensured by the $\breve{\mathbf{N}}^{e}(\breve{\xi})$ functions. Consequently, the global force and stiffness matrices can be expressed in terms of an ensemble of element force and stiffness matrices, which are provided in the following.

Element force and stiffness matrix **:** In order to obtain the element force and stiffness matrices, we first consider the RVE volume $\mathcal{V}^{\#}_{0}$ to be consisting of a number of finite volume elements, so that

$$\mathcal{V}^{\#}_{0} = \sum_{j=1}^{\mathtt{nelem}} \mathcal{V}^{\#(j)}_{0e}, \tag{4.55}$$

where $\mathcal{V}^{\#(j)}_{0e}$ is the reference volume of the j^{th} element and `nelem` represents the total number of elements. Consequently, the variational principle (4.50) can be rephrased, such that

$$\breve{\mathscr{P}}^{\mathrm{H}}_{\tau}(\breve{\mathbf{u}}_{\tau}, \breve{\varphi}_{\tau}) = \inf_{\breve{\mathbf{u}}_{\tau}\in\mathcal{K}(\mathbf{F}_{\tau})} \sup_{\breve{\varphi}_{\tau}\in\mathcal{G}(\mathbf{H}_{\tau})} \left[\sum_{j=1}^{\mathtt{nelem}} \int_{\mathcal{V}^{\#(j)}_{0e}} \breve{\mathcal{W}}^{\mathrm{H}}_{\tau}(\mathbf{X}, \breve{\mathbf{F}}, \breve{\mathbf{H}})\, \mathrm{dV} \right]. \tag{4.56}$$

The first variation of the total potential $\breve{\mathscr{P}}^{\mathrm{H}}_{\tau}$ therefore reads

$$\begin{aligned}
\delta\breve{\mathscr{P}}^{\mathrm{H}}_{\tau}(\breve{\mathbf{u}}_{\tau}, \breve{\varphi}_{\tau}) &= \sum_{j=1}^{\mathtt{nelem}} \int_{\mathcal{V}^{\#(j)}_{0e}} \left[\frac{\partial\breve{\mathcal{W}}^{\mathrm{H}}_{\tau}}{\partial\breve{\mathbf{F}}_{\tau}} : \delta\breve{\mathbf{F}}_{\tau} + \frac{\partial\breve{\mathcal{W}}^{\mathrm{H}}_{\tau}}{\partial\breve{\mathbf{H}}_{\tau}} \cdot \delta\breve{\mathbf{H}}_{\tau} \right] \mathrm{dV} \\
&= \sum_{j=1}^{\mathtt{nelem}} \int_{\mathcal{V}^{\#(j)}_{0e}} \left[\frac{\partial\breve{\mathcal{W}}^{\mathrm{H}}_{\tau}}{\partial\breve{\mathbf{F}}_{\tau}} : \mathrm{Grad}\ \delta\breve{\mathbf{u}}_{\tau} - \frac{\partial\breve{\mathcal{W}}^{\mathrm{H}}_{\tau}}{\partial\breve{\mathbf{H}}_{\tau}} \cdot \mathrm{Grad}\ \delta\breve{\varphi}_{\tau} \right] \mathrm{dV}.
\end{aligned} \tag{4.57}$$

Notice that the incremental micro-potential $\breve{\mathcal{W}}_\tau^{\mathrm{H}}$ does contain the contribution from the history-dependent microscopic $\breve{\mathbf{H}}_\tau^{\mathrm{r}}$ field. Nevertheless, by the definition of $\breve{\mathcal{W}}_\tau^{\mathrm{H}}$ in (4.24), it is minimized *a priori* with respect to $\breve{\mathbf{H}}_\tau^{\mathrm{r}}$, which is ensured by the evolution of $\breve{\mathbf{H}}_\tau^{\mathrm{r}}$ from $\breve{\mathbf{H}}_t^{\mathrm{r}}$ via the relation (4.28) for generalized standard materials. Thus, the derivative of $\breve{\mathcal{W}}_\tau^{\mathrm{H}}$ with respect to $\breve{\mathbf{H}}_\tau^{\mathrm{r}}$ vanishes identically, leading to the first variation $\delta\breve{\mathcal{W}}_\tau^{\mathrm{H}}$ given by (4.57). Furthermore, the field variables $\breve{\mathbf{u}}_\tau$ and $\breve{\varphi}_\tau$ can be expressed in terms of the nodal unknowns in the element (j), such that

$$[\breve{\mathbf{u}}_\tau(\boldsymbol{\xi})] = [\breve{\mathbf{N}}_{\mathbf{u}}^{\mathrm{e}}(\breve{\boldsymbol{\xi}})][\breve{\mathbf{q}}_\tau^{\mathrm{e}}], \qquad [\breve{\varphi}_\tau(\boldsymbol{\xi})] = [\breve{\mathbf{N}}_{\varphi}^{\mathrm{e}}(\breve{\boldsymbol{\xi}})][\breve{\mathbf{q}}_\tau^{\mathrm{e}}]. \tag{4.58}$$

Substituting (4.52) and (4.58) into (4.57) we rephrase it to be

$$[\delta\breve{\mathbf{q}}_\tau]^{\mathsf{T}}[\breve{\mathcal{F}}(\breve{\mathbf{q}}_\tau)] = \sum_{\mathrm{j}=1}^{\mathtt{nelem}} [\delta\breve{\mathbf{q}}_\tau^{\mathrm{e}}]^{\mathsf{T}} \int_{\mathcal{V}_{0\mathrm{e}}^{\#(\mathrm{j})}} \begin{bmatrix} (\breve{\mathbf{G}}_{\mathbf{u}}^{\mathrm{e}})^{\mathsf{T}} & -(\breve{\mathbf{G}}_{\varphi}^{\mathrm{e}})^{\mathsf{T}} \end{bmatrix} \begin{bmatrix} \dfrac{\partial\breve{\mathcal{W}}_\tau^{\mathrm{H}}}{\partial\breve{\mathbf{F}}_\tau} \\ \dfrac{\partial\breve{\mathcal{W}}_\tau^{\mathrm{H}}}{\partial\breve{\mathbf{H}}_\tau} \end{bmatrix} \mathrm{d}V \equiv \sum_{\mathrm{j}=1}^{\mathtt{nelem}} [\delta\breve{\mathbf{q}}_\tau^{\mathrm{e}}]^{\mathsf{T}}[\breve{\mathbf{f}}^{\mathrm{e}}(\breve{\mathbf{q}}_\tau^{\mathrm{e}})], \tag{4.59}$$

where the element force vector is denoted by $[\breve{\mathbf{f}}^{\mathrm{e}}(\breve{\mathbf{q}}_\tau^{\mathrm{e}})]$, $[\breve{\mathbf{G}}_{\mathbf{u}}^{\mathrm{e}}] = \mathrm{Grad}[\breve{\mathbf{N}}_{\mathbf{u}}^{\mathrm{e}}]$ and $[\breve{\mathbf{G}}_{\varphi}^{\mathrm{e}}] = \mathrm{Grad}[\breve{\mathbf{N}}_{\varphi}^{\mathrm{e}}]$ (see Appendix 4.B for details).

The second variation of $\breve{\mathscr{P}}_\tau^{\mathrm{H}}(\breve{\mathbf{u}}_\tau, \breve{\varphi}_\tau)$ is expressed similarly in terms of an ensemble of element stiffness matrices. To obtain this, a further variation of (4.57) is taken, which reads

$$\begin{aligned}
\Delta\delta\breve{\mathscr{P}}_\tau^{\mathrm{H}}(\breve{\mathbf{u}}_\tau, \breve{\varphi}_\tau) = \sum_{\mathrm{j}=1}^{\mathtt{nelem}} \int_{\mathcal{V}_{0\mathrm{e}}^{\#(\mathrm{j})}} \Bigg[& \Delta\breve{\mathbf{F}}_\tau : \frac{\partial^2\breve{\mathcal{W}}_\tau^{\mathrm{H}}}{\partial\breve{\mathbf{F}}_\tau\partial\breve{\mathbf{F}}_\tau} : \delta\breve{\mathbf{F}}_\tau + \Delta\breve{\mathbf{H}}_\tau \cdot \frac{\partial^2\breve{\mathcal{W}}_\tau^{\mathrm{H}}}{\partial\breve{\mathbf{H}}_\tau\partial\breve{\mathbf{F}}_\tau} : \delta\breve{\mathbf{F}}_\tau + \Delta\breve{\mathbf{H}}_\tau^{\mathrm{r}} \cdot \frac{\partial^2\breve{\mathcal{W}}_\tau^{\mathrm{H}}}{\partial\breve{\mathbf{H}}_\tau^{\mathrm{r}}\partial\breve{\mathbf{F}}_\tau} : \delta\breve{\mathbf{F}}_\tau \\
& + \Delta\breve{\mathbf{F}}_\tau : \frac{\partial^2\breve{\mathcal{W}}_\tau^{\mathrm{H}}}{\partial\breve{\mathbf{F}}_\tau\partial\breve{\mathbf{H}}_\tau} \cdot \delta\breve{\mathbf{H}}_\tau + \Delta\breve{\mathbf{H}}_\tau \cdot \frac{\partial^2\breve{\mathcal{W}}_\tau^{\mathrm{H}}}{\partial\breve{\mathbf{H}}_\tau\partial\breve{\mathbf{H}}_\tau} \cdot \delta\breve{\mathbf{H}}_\tau + \Delta\breve{\mathbf{H}}_\tau^{\mathrm{r}} \cdot \frac{\partial^2\breve{\mathcal{W}}_\tau^{\mathrm{H}}}{\partial\breve{\mathbf{H}}_\tau^{\mathrm{r}}\partial\breve{\mathbf{H}}_\tau} \cdot \delta\breve{\mathbf{H}}_\tau \Bigg] \, \mathrm{d}V \\
\equiv \sum_{\mathrm{j}=1}^{\mathtt{nelem}} \int_{\mathcal{V}_{0\mathrm{e}}^{\#(\mathrm{j})}} \Big[& \Delta\breve{\mathbf{F}}_\tau : \breve{\mathcal{L}}_\tau^{\mathbf{FF}} : \delta\breve{\mathbf{F}}_\tau + \Delta\breve{\mathbf{H}}_\tau \cdot \breve{\mathcal{L}}_\tau^{\mathbf{HF}} : \delta\breve{\mathbf{F}}_\tau + \Delta\breve{\mathbf{H}}_\tau^{\mathrm{r}} \cdot \breve{\mathcal{L}}_\tau^{\mathbf{H}^{\mathrm{r}}\mathbf{F}} \cdot \delta\breve{\mathbf{F}}_\tau \\
& + \Delta\breve{\mathbf{F}}_\tau : \breve{\mathcal{L}}_\tau^{\mathbf{FH}} \cdot \delta\breve{\mathbf{H}}_\tau + \Delta\breve{\mathbf{H}}_\tau \cdot \breve{\mathcal{L}}_\tau^{\mathbf{HH}} \cdot \delta\breve{\mathbf{H}}_\tau + \Delta\breve{\mathbf{H}}_\tau^{\mathrm{r}} \cdot \breve{\mathcal{L}}_\tau^{\mathbf{H}^{\mathrm{r}}\mathbf{H}} \cdot \delta\breve{\mathbf{H}}_\tau \Big] \, \mathrm{d}V,
\end{aligned} \tag{4.60}$$

where we introduce the $\breve{\mathcal{L}}_\tau^{(\cdot)(\cdot)}$ notations for preciseness. In general, $\breve{\mathcal{L}}_\tau^{(\cdot)(\cdot)}$ can be second, third or fourth order tensor depending on its superscript. Notice that here we retain the derivatives of $\partial\breve{\mathcal{W}}_\tau^{\mathrm{H}}/\partial\breve{\mathbf{F}}_\tau$ and $\partial\breve{\mathcal{W}}_\tau^{\mathrm{H}}/\partial\breve{\mathbf{H}}_\tau$ with respect to $\mathbf{H}_\tau^{\mathrm{r}}$, so that an *algorithmically consistent* global stiffness matrix can be obtained (Klinkel, 2006; Linnemann et al., 2009). Furthermore, the variation $\Delta\breve{\mathbf{H}}_\tau^{\mathrm{r}}$ of the remanent field can be expressed in terms of $\Delta\breve{\mathbf{H}}_\tau$ by exploiting the consistency condition of the microscopic switching surface (4.20). The consistency of the switching surface $\breve{\Phi}_\tau^{\mathrm{H}}$ thus reads (Lubliner, 2008, p. 145-150)

$$\Delta\breve{\Phi}_\tau^{\mathrm{H}} = 0 \qquad \Rightarrow \qquad \Delta\breve{\mathbf{B}}_\tau^{\mathrm{r}} = \mathbf{0}. \tag{4.61}$$

The variation $\Delta\breve{\mathbf{B}}^{\mathrm{r}}_{\tau}$ is subsequently obtained from its definition (4.11) to be

$$\begin{aligned}\Delta\breve{\mathbf{B}}^{\mathrm{r}}_{\tau} &= -\frac{\partial^2\breve{W}^{\mathrm{H}}_{\tau}}{\partial\breve{\mathbf{F}}_{\tau}\partial\breve{\mathbf{H}}^{\mathrm{r}}_{\tau}} : \Delta\breve{\mathbf{F}}_{\tau} - \frac{\partial^2\breve{W}^{\mathrm{H}}_{\tau}}{\partial\breve{\mathbf{H}}_{\tau}\partial\breve{\mathbf{H}}^{\mathrm{r}}_{\tau}} \cdot \Delta\breve{\mathbf{H}}_{\tau} - \frac{\partial^2\breve{W}^{\mathrm{H}}_{\tau}}{\partial\breve{\mathbf{H}}^{\mathrm{r}}_{\tau}\partial\breve{\mathbf{H}}^{\mathrm{r}}_{\tau}} \cdot \Delta\breve{\mathbf{H}}^{\mathrm{r}}_{\tau} \\ &\equiv -\breve{\mathcal{J}}^{\mathbf{FH}^{\mathrm{r}}}_{\tau} : \Delta\breve{\mathbf{F}}_{\tau} - \breve{\mathcal{J}}^{\mathbf{HH}^{\mathrm{r}}}_{\tau} \cdot \Delta\breve{\mathbf{H}}_{\tau} - \breve{\mathcal{J}}^{\mathbf{H}^{\mathrm{r}}\mathbf{H}^{\mathrm{r}}}_{\tau} \cdot \Delta\breve{\mathbf{H}}^{\mathrm{r}}_{\tau} = 0,\end{aligned} \tag{4.62}$$

where the third $\breve{\mathcal{J}}^{\mathbf{FH}^{\mathrm{r}}}_{\tau}$ and second-order tensor notations $\breve{\mathcal{J}}^{\mathbf{HH}^{\mathrm{r}}}_{\tau}$ and $\breve{\mathcal{J}}^{\mathbf{H}^{\mathrm{r}}\mathbf{H}^{\mathrm{r}}}_{\tau}$ are introduced for brevity. Consequently, equation (4.62) yields the relation between $\Delta\breve{\mathbf{H}}_{\tau}$ and $\Delta\breve{\mathbf{H}}^{\mathrm{r}}_{\tau}$, that is

$$\Delta\breve{\mathbf{H}}^{\mathrm{r}}_{\tau} = \widetilde{\mathcal{M}}^{\mathbf{H}^{\mathrm{r}}\mathbf{F}}_{\tau} : \Delta\breve{\mathbf{F}}_{\tau} + \widetilde{\mathcal{M}}^{\mathbf{H}^{\mathrm{r}}\mathbf{H}}_{\tau} \cdot \Delta\breve{\mathbf{H}}_{\tau}, \tag{4.63}$$

with

$$\widetilde{\mathcal{M}}^{\mathbf{H}^{\mathrm{r}}\mathbf{F}}_{\tau} = -\big(\breve{\mathcal{J}}^{\mathbf{H}^{\mathrm{r}}\mathbf{H}^{\mathrm{r}}}_{\tau}\big)^{-1}\breve{\mathcal{J}}^{\mathbf{FH}^{\mathrm{r}}}_{\tau} \qquad \text{and} \qquad \widetilde{\mathcal{M}}^{\mathbf{H}^{\mathrm{r}}\mathbf{H}}_{\tau} = -\big(\breve{\mathcal{J}}^{\mathbf{H}^{\mathrm{r}}\mathbf{H}^{\mathrm{r}}}_{\tau}\big)^{-1}\breve{\mathcal{J}}^{\mathbf{HH}^{\mathrm{r}}}_{\tau}. \tag{4.64}$$

Thus, substituting (4.63) into (4.60), we obtain the consistent second variation $\Delta\delta\breve{\mathscr{P}}^{\mathrm{H}}_{\tau}$ given by

$$\begin{aligned}\Delta\delta\breve{\mathscr{P}}^{\mathrm{H}}_{\tau}(\breve{\mathbf{u}}_{\tau}, \breve{\varphi}_{\tau}) = \sum_{\mathrm{j}=1}^{\mathtt{nelem}} \int_{\mathcal{V}^{\#(\mathrm{j})}_{0e}} \Big[&\Delta\breve{\mathbf{F}}_{\tau} : \breve{\mathcal{L}}^{\mathbf{FF}}_{\mathtt{Algo},\tau} : \delta\breve{\mathbf{F}}_{\tau} + \Delta\breve{\mathbf{H}}_{\tau} \cdot \breve{\mathcal{L}}^{\mathbf{HF}}_{\mathtt{Algo},\tau} : \delta\breve{\mathbf{F}}_{\tau} + \\ &\Delta\breve{\mathbf{F}}_{\tau} : \breve{\mathcal{L}}^{\mathbf{FH}}_{\mathtt{Algo},\tau} \cdot \delta\breve{\mathbf{H}}_{\tau} + \Delta\breve{\mathbf{H}}_{\tau} \cdot \breve{\mathcal{L}}^{\mathbf{HH}}_{\mathtt{Algo},\tau} \cdot \delta\breve{\mathbf{H}}_{\tau}\Big]\, \mathrm{dV},\end{aligned} \tag{4.65}$$

where $\breve{\mathcal{L}}^{(\cdot)(\cdot)}_{\mathtt{Algo},\tau}$ represents the *consistent algorithmic tangent* tensors, which are given by

$$\breve{\mathcal{L}}^{\mathbf{FF}}_{\mathtt{Algo},\tau} = \breve{\mathcal{L}}^{\mathbf{FF}}_{\tau} + \big(\widetilde{\mathcal{M}}^{\mathbf{H}^{\mathrm{r}}\mathbf{F}}_{\tau}\big)^{\mathsf{T}}\breve{\mathcal{L}}^{\mathbf{H}^{\mathrm{r}}\mathbf{F}}_{\tau}, \qquad \breve{\mathcal{L}}^{\mathbf{HF}}_{\mathtt{Algo},\tau} = \breve{\mathcal{L}}^{\mathbf{HF}}_{\tau} + \big(\widetilde{\mathcal{M}}^{\mathbf{H}^{\mathrm{r}}\mathbf{H}}_{\tau}\big)^{\mathsf{T}}\breve{\mathcal{L}}^{\mathbf{H}^{\mathrm{r}}\mathbf{F}}_{\tau},$$

$$\breve{\mathcal{L}}^{\mathbf{FH}}_{\mathtt{Algo},\tau} = \breve{\mathcal{L}}^{\mathbf{FH}}_{\tau} + \big(\widetilde{\mathcal{M}}^{\mathbf{H}^{\mathrm{r}}\mathbf{F}}_{\tau}\big)^{\mathsf{T}}\breve{\mathcal{L}}^{\mathbf{H}^{\mathrm{r}}\mathbf{H}}_{\tau}, \qquad \breve{\mathcal{L}}^{\mathbf{HH}}_{\mathtt{Algo},\tau} = \breve{\mathcal{L}}^{\mathbf{HH}}_{\tau} + \big(\widetilde{\mathcal{M}}^{\mathbf{H}^{\mathrm{r}}\mathbf{H}}_{\tau}\big)^{\mathsf{T}}\breve{\mathcal{L}}^{\mathbf{H}^{\mathrm{r}}\mathbf{H}}_{\tau}.$$

Finally, the consistent element stiffness matrix is obtained via substituting (4.51) and (4.54) into (4.65), such that

$$\begin{aligned}[\delta\breve{\mathbf{q}}_{\tau}]^{\mathsf{T}}[\breve{\mathcal{K}}(\breve{\mathbf{q}}_{\tau})][\Delta\breve{\mathbf{q}}_{\tau}] &= \sum_{\mathrm{j}=1}^{\mathtt{nelem}} [\delta\breve{\mathbf{q}}^{e}_{\tau}]^{\mathsf{T}} \int_{\mathcal{V}^{\#(\mathrm{j})}_{0e}} \begin{bmatrix}(\breve{\mathbf{G}}^{e}_{\mathbf{u}})^{\mathsf{T}} & -(\breve{\mathbf{G}}^{e}_{\varphi})^{\mathsf{T}}\end{bmatrix} \begin{bmatrix}\breve{\mathcal{L}}^{\mathbf{FF}}_{\mathtt{Algo},\tau} & \breve{\mathcal{L}}^{\mathbf{FH}}_{\mathtt{Algo},\tau} \\ \breve{\mathcal{L}}^{\mathbf{HF}}_{\mathtt{Algo},\tau} & \breve{\mathcal{L}}^{\mathbf{HH}}_{\mathtt{Algo},\tau}\end{bmatrix} \begin{bmatrix}\breve{\mathbf{G}}^{e}_{\mathbf{u}} \\ -\breve{\mathbf{G}}^{e}_{\varphi}\end{bmatrix} \mathrm{dV}\, [\Delta\breve{\mathbf{q}}^{e}_{\tau}] \\ &\equiv \sum_{\mathrm{j}=1}^{\mathtt{nelem}} [\delta\breve{\mathbf{q}}^{e}_{\tau}]^{\mathsf{T}}[\breve{\mathbf{k}}^{e}(\breve{\mathbf{q}}^{e}_{\tau})][\Delta\breve{\mathbf{q}}^{e}_{\tau}].\end{aligned} \tag{4.66}$$

It is noted that the algorithmic global stiffness matrix $[\breve{\mathcal{K}}(\breve{\mathbf{q}}_{\tau})]$ is constructed to ensure a better rate of numerical convergence of the nonlinear FE solver. The algorithmic tangent stiffness matrix in the FE computations for rate-independent mechanical elasto-plasticity is commonly utilized in order to ensure a quadratic rate of asymptotic convergence (Lubliner, 2008). Nonetheless, no effect on the algorithmic tangent stiffness on the rate of convergence is investigated in the present study.

The volume integrations of (4.59) and (4.66) in the element $\mathcal{V}^{\#(\mathrm{j})}_{0e}$ are evaluated via using a reduced Gaussian quadrature. The reduced integration ensures a better rate of convergence and helps to

avoid the shear locking. Notably, the Gauss quadrature integration requires to evaluate the $[\breve{\mathbf{f}}^e(\breve{\mathbf{q}}^e_\tau)]$ and $[\breve{\mathbf{k}}^e(\breve{\mathbf{q}}^e_\tau)]$ matrices only at the integration (Gauss) points. In this regard, the matrices involving $\breve{\mathbf{G}}^e_{\mathbf{u}}$ and $\breve{\mathbf{G}}^e_{\varphi}$ in (4.59) and (4.66) are evaluated at the individual integration points from the definition of the element interpolation functions $\breve{\mathbf{N}}^e_{\mathbf{u}}$ and $\breve{\mathbf{N}}^e_{\varphi}$, respectively (see Appendix 4.B for details). Moreover, given the nodal values $\breve{\mathbf{q}}^e_\tau$ from the previous iteration of the Newton-Raphson solver at time τ, one can evaluate $\breve{\mathbf{F}}_\tau$ and $\breve{\mathbf{H}}_\tau$ at each integration point through the interpolation functions $\breve{\mathbf{N}}^e$. Nonetheless, the evaluations of $\breve{\mathbf{F}}_\tau$ and $\breve{\mathbf{H}}_\tau$ do *not* complete the local definitions of $[\breve{\mathbf{f}}^e(\breve{\mathbf{q}}^e_\tau)]$ and $[\breve{\mathbf{k}}^e(\breve{\mathbf{q}}^e_\tau)]$. In addition, the remanent $\breve{\mathbf{H}}^r$ field must be updated from its last converged state $\breve{\mathbf{H}}^r_t$ to $\breve{\mathbf{H}}^r_\tau$ from the "inner" minimization condition of (4.24) at each integration point. Notice that the inner minimization condition of the incremental energy $\breve{\mathcal{W}}^H_\tau$ is the constitutive relation (4.28) for generalized standard materials, which is further specialized for the present rate-independent model to be the associated switching rule (4.21). The numerical update routine for $\breve{\mathbf{H}}^r_\tau$ is discussed in the following.

Evaluating the local $\breve{\mathbf{H}}^r_\tau$ **:** We employ a radial-return-type implicit backward Euler scheme to numerically solve the associated switching equation (4.21) locally at each integration point (Ortiz and Simo, 1986). The radial-return algorithm in the context of ferromagnetic switching relies on the energetic predictor/remanent corrector scheme. Firstly, the energetic predictor is estimated via computing the switching function $\breve{\Phi}^H_i(\breve{\mathbf{H}}_\tau, \breve{\mathbf{H}}^r_t)$, where we use the local $\breve{\mathbf{H}}_\tau$ at the current Newton-Raphson iteration and the remanent internal variable $\breve{\mathbf{H}}^r_t$ from the previous converged state. If $\breve{\Phi}^H_i(\breve{\mathbf{H}}_\tau, \breve{\mathbf{H}}^r_t) < 0$, then the energetic prediction is considered to be correct. Consequently, the local remanent field remains unchanged, so that

$$\breve{\mathbf{H}}^r_\tau = \breve{\mathbf{H}}^r_t \qquad \text{if} \qquad \breve{\Phi}^H_i(\breve{\mathbf{H}}_\tau, \breve{\mathbf{H}}^r_t) < 0. \tag{4.67}$$

Notice from (4.21) that the Kuhn-Tucker condition for $\breve{\Phi}^H_i(\breve{\mathbf{H}}_\tau, \breve{\mathbf{H}}^r_t) < 0$ is $\dot{\breve{\lambda}}^H_i = 0$, such that $\dot{\breve{\mathbf{H}}}^r = \mathbf{0}$, which results in (4.67).

On the other hand, if the switching criteria is satisfied, such that $\breve{\Phi}^H_i(\breve{\mathbf{H}}_\tau, \breve{\mathbf{H}}^r_t) \geqslant 0$, the energetic predictor remains no longer correct. Rather, a correction to the remanent field $\breve{\mathbf{H}}^r_t$ is required. The corrected $\breve{\mathbf{H}}^r_\tau$ is computed via solving a set of nonlinear algebraic equations obtained via the temporal discretization of (4.21), so that

$$\breve{\mathbf{H}}^r_\tau = \breve{\mathbf{H}}^r_t + 2\breve{\gamma}^H_i \breve{\mathbf{B}}^r_\tau(\breve{\mathbf{H}}_\tau, \breve{\mathbf{H}}^r_\tau) \qquad \text{and} \qquad \breve{\mathbf{B}}^r_\tau(\breve{\mathbf{H}}_\tau, \breve{\mathbf{H}}^r_\tau) \cdot \breve{\mathbf{B}}^r_\tau(\breve{\mathbf{H}}_\tau, \breve{\mathbf{H}}^r_\tau) - (b^c_i)^2 = 0, \tag{4.68}$$

where $\breve{\gamma}^H_i = \breve{\lambda}^H_{i,\tau} - \breve{\lambda}^H_{i,t}$ is the increment of Lagrange multiplier $\breve{\lambda}^H_i$. The preceding set of four nonlinear algebraic equations are solved using the classical Newton-Raphson method. In this regard, we introduce a *trial remanent field* $\breve{\mathbf{H}}^{r,\mathtt{trial}}_\tau = \breve{\mathbf{H}}^r_t$ at the beginning of the Newton iterations, which are essentially involved with minimizing the residues

$$\breve{\mathcal{R}}^{\breve{\mathbf{H}}^r} = \breve{\mathbf{H}}^{r,\mathtt{trial}}_\tau - \breve{\mathbf{H}}^r_t - 2\breve{\gamma}^{H,\mathtt{trial}}_i \breve{\mathbf{B}}^r_\tau(\breve{\mathbf{H}}_\tau, \breve{\mathbf{H}}^{r,\mathtt{trial}}_\tau) \tag{4.69}$$

and

$$\breve{\mathcal{R}}^{\breve{\Phi}^r} = \breve{\mathbf{B}}^r_\tau(\breve{\mathbf{H}}_\tau, \breve{\mathbf{H}}^{r,\mathtt{trial}}_\tau) \cdot \breve{\mathbf{B}}^r_\tau(\breve{\mathbf{H}}_\tau, \breve{\mathbf{H}}^{r,\mathtt{trial}}_\tau) - (b^c_i)^2. \tag{4.70}$$

Consequently, the increments in the trial field and the Lagrange multiplier are computed from the

following linear algebraic equations obtained via linearizing (4.69) and (4.70) with respect to the trial fields themselves, such that

$$\begin{bmatrix} \partial\breve{\mathfrak{R}}^{\breve{\mathbf{H}}^{r}}/\partial\breve{\mathbf{H}}_{\tau}^{r,\mathrm{trial}} & \partial\breve{\mathfrak{R}}^{\breve{\mathbf{H}}^{r}}/\partial\breve{\gamma}_{i}^{H,\mathrm{trial}} \\ \partial\breve{\mathfrak{R}}^{\breve{\Phi}^{r}}/\partial\breve{\mathbf{H}}_{\tau}^{r,\mathrm{trial}} & \partial\breve{\mathfrak{R}}^{\breve{\Phi}^{r}}/\partial\breve{\gamma}_{i}^{H,\mathrm{trial}} \end{bmatrix} \begin{Bmatrix} \Delta\breve{\mathbf{H}}_{\tau}^{r,\mathrm{trial}} \\ \Delta\breve{\gamma}_{i}^{H,\mathrm{trial}} \end{Bmatrix} = - \begin{Bmatrix} \breve{\mathfrak{R}}^{\breve{\mathbf{H}}^{r}} \\ \breve{\mathfrak{R}}^{\breve{\Phi}^{r}} \end{Bmatrix}. \tag{4.71}$$

Appendix 4.C provides the specific form of (4.71) for the local constitutive model defined in Section 4.2. The trial remanent field and Lagrange multiplier increment are subsequently updated to be

$$\breve{\mathbf{H}}_{\tau}^{r,\mathrm{trial}} = \breve{\mathbf{H}}_{\tau}^{r,\mathrm{trial}} + \Delta\breve{\mathbf{H}}_{\tau}^{r,\mathrm{trial}}, \qquad \text{and} \qquad \breve{\gamma}_{i}^{H,\mathrm{trial}} = \breve{\gamma}_{i}^{H,\mathrm{trial}} + \Delta\breve{\gamma}_{i}^{H,\mathrm{trial}}, \tag{4.72}$$

respectively. Finally, the updated residue vector $\breve{\mathfrak{R}} = \{(\breve{\mathfrak{R}}^{\breve{\mathbf{H}}^{r}})^{T}, \breve{\mathfrak{R}}^{\breve{\Phi}^{r}}\}$ is computed using the updated trial fields (4.72). At this point, if the Eulerian norm of the updated residue $|\breve{\mathfrak{R}}|$ becomes less than a prescribed tolerance, the local Newton iterations are considered to be converged. Consequently, the updated variables at the current time increment τ are given by

$$\breve{\mathbf{H}}_{\tau}^{r} = \breve{\mathbf{H}}_{\tau}^{r,\mathrm{trial}} \qquad \text{and} \qquad \breve{\gamma}_{i}^{H} = \breve{\gamma}_{i}^{H,\mathrm{trial}}. \tag{4.73}$$

With these *locally updated* $\breve{\mathbf{H}}_{\tau}^{r}$ at each integration point, the element force and algorithmic stiffness matrix are computed, respectively, from (4.59) and (4.66), which are then assembled into a global force and algorithmic tangent stiffness for the global Newton iterations. Notice that the locally updated $\breve{\mathbf{H}}_{\tau}^{r}$ are stored as "state-dependent variables" at the integration points *only after* the convergence of the global Newton-Raphson solver is achieved. The preceding update algorithm is summarized in Algorithm 4.1. It should be noted in the numerical computations that $\breve{\gamma}_{i}^{H}$ must remain positive under all loading conditions, so that the Kuhn-Tucker condition in (4.21) is satisfied.

Remark 4.4. One can choose two distinct strategies to compute the effective response of the s-MREs having non-hysteretic carbonyl iron particles. Firstly, one can implement the microscopic FE computations as discussed herein, but with the particle coercivity $b_{p}^{c} \ll 1$ and the energetic susceptibility $\chi_{p}^{e} = 0$. As noted earlier, these two conditions would essentially lead to a soft magnetic response and the same finite-element solver as developed for the h-MREs can be implemented readily. Nonetheless, one can avoid the expensive local storage of the remanent $\breve{\mathbf{H}}^{r}$ fields and the implementation Algorithm 4.1 at each integration points during each increment for the s-MREs via considering directly the variational homogenization problem (4.40). In turn, the local potential energy associated with this soft magnetic composite is given by (4.22), whereas the dissipation potential vanishes identically. Since in this second approach the local radial return-based update algorithm is no longer employed, one can readily replace $\breve{\mathcal{L}}_{\mathtt{Algo},\tau}^{(\cdot)(\cdot)}$ in (4.66) via $\breve{\mathcal{L}}_{\tau}^{(\cdot)(\cdot)}$. Here we employ the second method in order to reduce the computational expense.

Remark 4.5. The reduced integration is considered further for integrating the mechanical energy evolving the bulk modulus term. A high bulk modulus is used in these computations, in order to achieve a nearly incompressible material response. However, such high bulk modulus leads to volumetric locking of the finite elements in terms of hindering its deformations that are volume preserving. In order to avoid this problem, we employ a single point Gauss integration scheme for

Algorithm 4.1: Local update algorithm for $\breve{\mathbf{H}}_\tau^{\mathrm{r}}$

Set tolerance $\mathtt{tol} = 10^{-6}$
Input $\breve{\mathbf{H}}_\tau$, $\breve{\mathbf{H}}_t^{\mathrm{r}}$
Initialization $\breve{\mathbf{H}}_\tau^{\mathrm{r,trial}} \leftarrow \breve{\mathbf{H}}_t^{\mathrm{r}}$, $\breve{\gamma}_i^{\mathrm{H,trial}} \leftarrow 0$
Compute $\breve{\Phi}_i^{\mathrm{H}}\big(\breve{\mathbf{H}}_\tau, \breve{\mathbf{H}}_\tau^{\mathrm{r,trial}}\big)$
if $\breve{\Phi}_i^{\mathrm{H}} < 0$ **then**
  $\breve{\mathbf{H}}_\tau^{\mathrm{r}} \leftarrow \breve{\mathbf{H}}_\tau^{\mathrm{r,trial}}$ *% energetic predictor is correct*
else
  Compute $\breve{\mathfrak{R}}^{\breve{\mathbf{H}}^{\mathrm{r}}}$, $\breve{\mathfrak{R}}^{\breve{\Phi}^{\mathrm{r}}}$
  $\breve{\mathfrak{R}} \leftarrow \big\{\big(\breve{\mathfrak{R}}^{\breve{\mathbf{H}}^{\mathrm{r}}}\big)^{\mathsf{T}}, \breve{\mathfrak{R}}^{\breve{\Phi}^{\mathrm{r}}}\big\}$ *% construct the residue vector*
  while $|\breve{\mathfrak{R}}| > \mathtt{tol}$ **do**
    Compute $\Delta\breve{\mathbf{H}}_\tau^{\mathrm{r,trial}}$, $\Delta\breve{\gamma}_i^{\mathrm{H,trial}}$ *% compute from (4.71)*
    $\breve{\mathbf{H}}_\tau^{\mathrm{r,trial}} \leftarrow \breve{\mathbf{H}}_\tau^{\mathrm{r,trial}} + \Delta\breve{\mathbf{H}}_\tau^{\mathrm{r,trial}}$
    $\breve{\gamma}_i^{\mathrm{H,trial}} \leftarrow \breve{\gamma}_i^{\mathrm{H,trial}} + \Delta\breve{\gamma}_i^{\mathrm{H,trial}}$
    Compute $\breve{\mathfrak{R}}^{\breve{\mathbf{H}}^{\mathrm{r}}}$, $\breve{\mathfrak{R}}^{\breve{\Phi}^{\mathrm{r}}}$
    $\breve{\mathfrak{R}} \leftarrow \big\{\big(\breve{\mathfrak{R}}^{\breve{\mathbf{H}}^{\mathrm{r}}}\big)^{\mathsf{T}}, \breve{\mathfrak{R}}^{\breve{\Phi}^{\mathrm{r}}}\big\}$ *% construct the updated residue vector*
  end
  $\breve{\mathbf{H}}_\tau^{\mathrm{r}} \leftarrow \breve{\mathbf{H}}_\tau^{\mathrm{r,trial}}$ *% remanent corrector added to energetic predictor*
end

the local stress part that is arising from the bulk energy associated with the MREs. Such reduced integration is used for both the hard and soft MREs.

4.6.2 Application of the periodic boundary conditions

Next, the periodic boundary conditions (PBCs) on the microscopic displacement $\breve{\mathbf{u}}_\tau$ and potential $\breve{\varphi}_\tau$ are specified. In order to prescribe the PBCs, we further divide the surface boundaries $\partial\mathcal{V}_0^\#$ of the RVE into the set (see Fig. 4.3)

$$\partial\mathcal{V}_0^\# = \partial\mathcal{V}_0^{\#,\mathtt{RIGHT}} \cup \partial\mathcal{V}_0^{\#,\mathtt{LEFT}} \cup \partial\mathcal{V}_0^{\#,\mathtt{TOP}} \cup \partial\mathcal{V}_0^{\#,\mathtt{BOTTOM}} \cup \partial\mathcal{V}_0^{\#,\mathtt{FRONT}} \cup \partial\mathcal{V}_0^{\#,\mathtt{BACK}}, \tag{4.74}$$

on which $\breve{\mathbf{u}}_\tau$ and $\breve{\varphi}_\tau$ are represented by the respective superscripts (e.g., $\breve{\mathbf{u}}_\tau^{\mathtt{RIGHT}}$ and $\breve{\varphi}_\tau^{\mathtt{RIGHT}}$, $\breve{\mathbf{u}}_\tau^{\mathtt{TOP}}$ and $\breve{\varphi}_\tau^{\mathtt{TOP}}$, etc.). Moreover, four corner nodes of the RVE in the present finite-element setting are denoted via `P0`, `P1`, `P2` and `P3`. We set both the microscopic and average displacements and potentials at `P0` to be zero, in order to prevent any rigid body motion of the RVE, so that

$$\breve{\mathbf{u}}_\tau^{\mathtt{P0}} = \widetilde{\mathbf{u}}_\tau^{\mathtt{P0}} = \mathbf{u}_\tau^{\mathtt{P0}} = 0 \qquad \text{and} \qquad \breve{\varphi}_\tau^{\mathtt{P0}} = \widetilde{\varphi}_\tau^{\mathtt{P0}} = \varphi_\tau^{\mathtt{P0}} = 0. \tag{4.75}$$

In fact, the periodicity of the fluctuation fields $\widetilde{\mathbf{u}}_\tau$ and $\widetilde{\varphi}_\tau$ in $\mathcal{V}_0^\#$ defined by, respectively, (4.36) and (4.37) can be interpreted in this FE setting to be setting $\widetilde{\mathbf{u}}_\tau$ and $\widetilde{\varphi}_\tau$ at the opposite nodes on $\partial\mathcal{V}_0^\#$ to be equal.

Since the reference coordinate system is defined as in Fig. 4.3, we further exploit the periodicity conditions of $\widetilde{\mathbf{u}}_\tau$ and $\widetilde{\varphi}_\tau$ along with (4.36) and (4.37) to obtain the relations of the microscopic

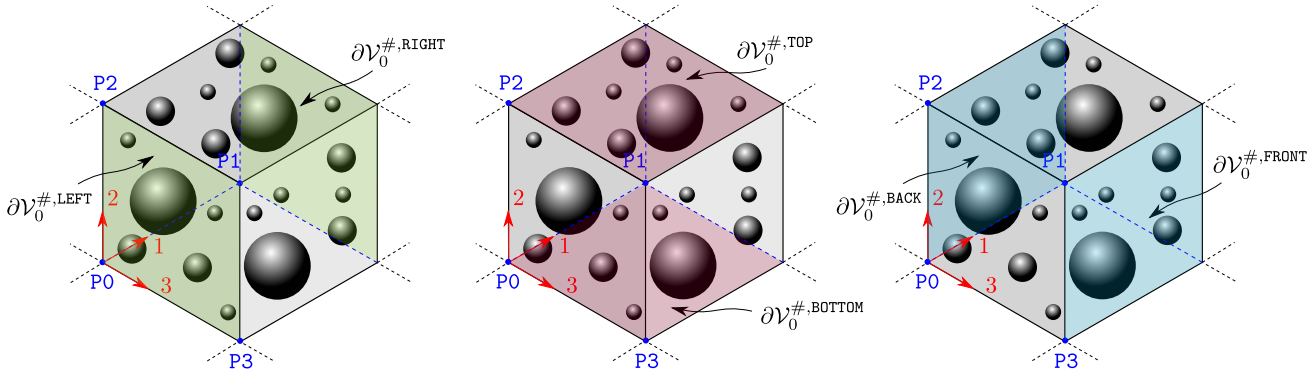

Figure 4.3: Opposite facing boundaries of the RVE of volume $\mathcal{V}_0^{\#}$ along with the reference coordinate system and four key corner nodes P0, P1, P2 and P3.

displacements (scalar potentials) at P1, P2 and P3 to the effective deformation gradient $\mathbf{F}_\tau$ (effective h-field $\mathbf{H}_\tau$), so that

$$(\breve{u}_\tau^{P1})_i = (u_\tau^{P1})_i = \{(F_\tau)_{i1} - \delta_{i1}\}\ell_0^{\#}, \qquad \breve{\varphi}_\tau^{P1} = \varphi_\tau^{P1} = -(H_\tau)_1\ell_0^{\#}, \tag{4.76}$$

$$(\breve{u}_\tau^{P2})_i = (u_\tau^{P2})_i = \{(F_\tau)_{i2} - \delta_{i2}\}\ell_0^{\#}, \qquad \breve{\varphi}_\tau^{P2} = \varphi_\tau^{P2} = -(H_\tau)_2\ell_0^{\#}, \tag{4.77}$$

$$(\breve{u}_\tau^{P3})_i = (u_\tau^{P3})_i = \{(F_\tau)_{i3} - \delta_{i3}\}\ell_0^{\#}, \qquad \breve{\varphi}_\tau^{P3} = \varphi_\tau^{P3} = -(H_\tau)_3\ell_0^{\#}, \tag{4.78}$$

where $\ell_0^{\#}$ is the length of the sides of the cubic RVE. The last set of equations reveal that the microscopic displacement and potential fields at P1, P2 and P3 are related directly to the effective $\mathbf{F}_\tau$ and $\mathbf{H}_\tau$. Thus, one can apply a macroscopic $\mathbf{F}_\tau$ or $\mathbf{H}_\tau$ across the RVE via specifying directly the displacement and potentials at these three (P1, P2 and P3) nodes. Nevertheless, application of the traction boundary condition (4.49) on $\partial\mathcal{V}_0^{\#}$ requires the exploitation of the augmented variational principle in the present FE setting, which will be discussed in the following. Prior to that, the PBCs on the boundary displacements/potentials are discussed.

Again, from the periodicity of the fluctuation fields in $\mathcal{V}_0^{\#}$, we can set them to be equal at the opposite faces of $\partial\mathcal{V}_0^{\#}$. Thus, the opposite face microscopic displacements and potentials are related via

$$\breve{\mathbf{u}}_\tau^{RIGHT} - \breve{\mathbf{u}}_\tau^{LEFT} = \mathbf{u}_\tau^{RIGHT} - \mathbf{u}_\tau^{LEFT} = \mathbf{u}_\tau^{P1}, \qquad \breve{\varphi}_\tau^{RIGHT} - \breve{\varphi}_\tau^{LEFT} = \varphi_\tau^{RIGHT} - \varphi_\tau^{LEFT} = \varphi_\tau^{P1}, \tag{4.79}$$

$$\breve{\mathbf{u}}_\tau^{TOP} - \breve{\mathbf{u}}_\tau^{BOTTOM} = \mathbf{u}_\tau^{TOP} - \mathbf{u}_\tau^{BOTTOM} = \mathbf{u}_\tau^{P2}, \qquad \breve{\varphi}_\tau^{TOP} - \breve{\varphi}_\tau^{BOTTOM} = \varphi_\tau^{TOP} - \varphi_\tau^{BOTTOM} = \varphi_\tau^{P2}, \tag{4.80}$$

$$\breve{\mathbf{u}}_\tau^{FRONT} - \breve{\mathbf{u}}_\tau^{BACK} = \mathbf{u}_\tau^{FRONT} - \mathbf{u}_\tau^{BACK} = \mathbf{u}_\tau^{P3}, \qquad \breve{\varphi}_\tau^{FRONT} - \breve{\varphi}_\tau^{BACK} = \varphi_\tau^{FRONT} - \varphi_\tau^{BACK} = \varphi_\tau^{P3}. \tag{4.81}$$

In practice, these conditions are applied via constraining the opposite nodal displacements and scalar potentials on $\partial\mathcal{V}_0^{\#}$ in terms of applying the multi-point constraints (MPCs) in ABAQUS (2018).

4.6.3 Application of the macroscopic boundary conditions

As discussed in Section 4.5, the macroscopic boundary conditions and the magnetic loading are applied in terms of proposing augmentations to the variational homogenization problem (4.35). Notice that, in the present periodic homogenization setting, the effective $\mathbf{F}_\tau$ and $\mathbf{H}_\tau$ fields can be expressed in terms of the microscopic displacement and the scalar potential at the three corner nodes P1, P2 and P3.

Specifically, the set $\breve{\mathbf{q}}_\tau^{\mathsf{P}} = \left\{(\breve{u}_\tau^{\mathsf{P1}})_1, (\breve{u}_\tau^{\mathsf{P1}})_2, (\breve{u}_\tau^{\mathsf{P1}})_3, \breve{\varphi}_\tau^{\mathsf{P1}}, (\breve{u}_\tau^{\mathsf{P2}})_1, (\breve{u}_\tau^{\mathsf{P2}})_2, (\breve{u}_\tau^{\mathsf{P2}})_3, \breve{\varphi}_\tau^{\mathsf{P2}}, (\breve{u}_\tau^{\mathsf{P3}})_1, (\breve{u}_\tau^{\mathsf{P3}})_2, (\breve{u}_\tau^{\mathsf{P3}})_3, \breve{\varphi}_\tau^{\mathsf{P3}}\right\}^{\mathsf{T}}$ can be utilized in (4.43) replacing the effective $\mathbf{F}_\tau$ and $\mathbf{H}_\tau$. Then, the first variation of (4.43) with respect to $\breve{\mathbf{q}}_\tau^{\mathsf{P}}$ is now expressed to be

$$\delta\breve{\mathscr{P}}_\tau^{\mathsf{H}}(\breve{\mathbf{q}}_\tau^{\mathsf{P}}) = [\delta\breve{\mathbf{q}}_\tau^{\mathsf{P}}]^{\mathsf{T}}[\breve{\mathbf{f}}_\tau^{\mathsf{P}}(\breve{\mathbf{q}}_\tau^{\mathsf{P}})] + [\delta\breve{\mathbf{q}}_\tau^{\mathsf{P}}]^{\mathsf{T}}[\breve{\mathbf{f}}_\tau^{\mathsf{Augm}}(\breve{\mathbf{q}}_\tau^{\mathsf{P}})], \tag{4.82}$$

Notice that the first term on the left hand side of (4.82) is obtained from the FE discretization of the microscopic BVP (4.52) and the second term is obtained from the variation of the augmented potentials, namely, the Maxwell energy, the penalty potential and the energy due to applied mechanical stress $\mathbf{S}_{a,\tau}^{\mathsf{mech}}$. In practice, one can simply add the augmented force vector $[\breve{\mathbf{f}}_\tau^{\mathsf{Augm}}(\breve{\mathbf{q}}_\tau^{\mathsf{P}})]$ to the global microscopic force vector $[\breve{\mathcal{F}}(\breve{\mathbf{q}}_\tau)]$ in order to apply the traction boundary condition (4.49) and the Eulerian $\hbar$-field $\mathbf{h}_{a,\tau}$ across the RVE.

Nonetheless, the convergence the implicit global FE solver is ensured via augmenting further the global tangent stiffness matrix $[\breve{\mathcal{K}}(\breve{\mathbf{q}}_\tau)]$ with $[\breve{\mathbf{k}}_\tau^{\mathsf{Augm}}(\breve{\mathbf{q}}_\tau^{\mathsf{P}})]$, which is obtained from a further variation of (4.82) with respect to $\breve{\mathbf{q}}_\tau^{\mathsf{P}}$, such that

$$\Delta\delta\breve{\mathscr{P}}_\tau^{\mathsf{H}}(\breve{\mathbf{q}}_\tau^{\mathsf{P}}) = [\delta\breve{\mathbf{q}}_\tau^{\mathsf{P}}]^{\mathsf{T}}[\breve{\mathbf{k}}_\tau^{\mathsf{P}}(\breve{\mathbf{q}}_\tau^{\mathsf{P}})][\Delta\breve{\mathbf{q}}_\tau^{\mathsf{P}}] + [\delta\breve{\mathbf{q}}_\tau^{\mathsf{P}}]^{\mathsf{T}}[\breve{\mathbf{k}}_\tau^{\mathsf{Augm}}(\breve{\mathbf{q}}_\tau^{\mathsf{P}})][\Delta\breve{\mathbf{q}}_\tau^{\mathsf{P}}]. \tag{4.83}$$

Of course, the contribution from the tangent stiffness $[\breve{\mathbf{k}}_\tau^{\mathsf{P}}(\breve{\mathbf{q}}_\tau^{\mathsf{P}})]$ is already present in $[\breve{\mathcal{K}}(\breve{\mathbf{q}}_\tau)]$ due to the discretization of the microscopic BVP (4.66). In addition, the stiffness $[\breve{\mathbf{k}}_\tau^{\mathsf{Augm}}(\breve{\mathbf{q}}_\tau^{\mathsf{P}})]$ must be augmented to $[\breve{\mathcal{K}}(\breve{\mathbf{q}}_\tau)]$ so that the convergence of the implicit global FE solver is ensured. Indeed, the matrices $[\breve{\mathbf{f}}_\tau^{\mathsf{Augm}}(\breve{\mathbf{q}}_\tau^{\mathsf{P}})]$ and $[\breve{\mathbf{k}}_\tau^{\mathsf{Augm}}(\breve{\mathbf{q}}_\tau^{\mathsf{P}})]$ can be computed directly from (4.43) via straightforward algebraic manipulations, which are not shown explicitly in this text for brevity.

4.7 Results

This section provides a set of the numerical finite-element (FE) computations for the effective response of s- and $\hbar$-MREs. The results are provided here in three parts. First, in Section 4.7.1, we define the RVE microsctucture in terms of specifying crucial microstructural parameters, namely, particle volume fraction c, number of families of the spherical particles, equivalent number of monodisperse spheres and particle size ratio. Upon this definition, in Section 4.7.2, we provide the magnetization and magnetostriction responses of the s-MREs, having different particle volume fractions, under no applied mechanical stress $\mathbf{S}_{a,\tau}^{\mathsf{mech}}$. Rigorous particle and mesh convergence studies for the computed response are also provided. Finally, in Section 4.7.3, we provide the dissipative magnetization and magnetostriction responses of the $\hbar$-MREs under proportional cyclic loading. Also, a mesh convergence study is presented. In addition, some crucial observation on the effect of mechanical stretch and shear on the remanent magnetization is discussed by the end of this section.

4.7.1 Microstructure generation and meshing

In the numerical FE computations, we consider polydisperse spherical particles comprising three different size families with a size ratio of $1 : 7/9 : 4/9$ and whose relative proportions with respect to the total particle volume are taken to be 0.6, 0.3 and 0.1, respectively (Lopez-Pamies et al., 2013; Anoukou et al., 2018). We consider three distinct particle volume fractions, $c = 0.1$, 0.2 and 0.3.

In order to define the maximum particle radius, we consider a reference number of monodisperse particles, denoted with $N_{mono} = 60$. Then, the radius of the maximum particle size family is simply $R_{max}/L = (3c/4\pi N_{mono})^{1/3}$. This readily leads to $R_{max}/L = 0.074, 0.093, 0.106$ and a total number of particles $N_{tot} \sim 130$, 280 and 290 for $c = 0.1$, 0.2 and 0.3, respectively. In Fig. 4.4, we show three such representative microstructures and their corresponding meshes, which use standard 10-node tetrahedral quadratic elements (TET-10). Conformal meshes with TET-10 finite elements are generated in

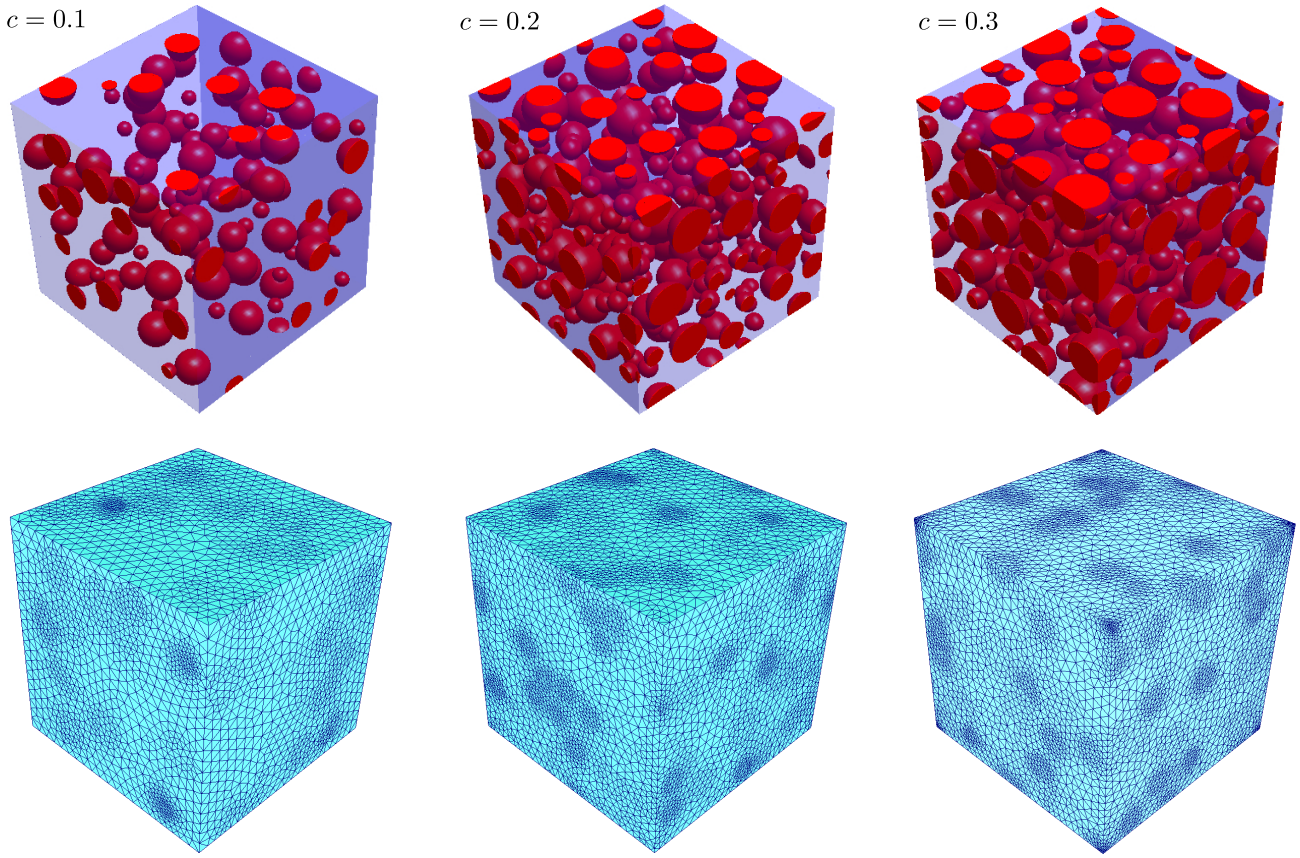

Figure 4.4: (top) Three representative polydisperse microstructures for $c = 0.1$, 0.2 and 0.3 having approximate number of polydisperse particles $N_{tot} \sim 130$, 280 and 290, respectively. (bottom) The corresponding unstructured meshes with quadratic ten-node tetrahedral elements leading to 1.55×10^6, 1.62×10^6 and 1.50×10^6 degrees of freedom, respectively, for $c = 0.1$, 0.2 and 0.3.

these RVEs via employing a Python-based open source meshing software NETGEN. In particular, the 3D mesh generated with NETGEN ensures the periodicity of the RVE and also provides the multi-point constraint (MPC) equations associated with the degrees of freedom of the boundary nodes (4.79)-(4.81).

The same set of RVEs are used to compute the effective responses of both s- and h-MREs. Nevertheless, it is noted that, even if the total nodal degrees of freedom remain the same in these two cases, the numerical computations with the h-MREs are way more expensive due to (i) storage of the high number of internal variables and (ii) local update of the internal variable following Algorithm 4.1 at each integration (Gauss) point.

4.7.2 Effective response of s-MREs

In the numerical computations for s-MREs, we choose to work with a matrix that resembles a moderately soft silicone and thus exhibits a shear modulus in the order of 0.3MPa. The particles are made of carbonyl iron and exhibit a shear modulus in the order of ~ 200GPa. On the other hand, the silicone matrix is magnetically inert having zero magnetic susceptibility, whereas the iron particles exhibit a Langevin saturating m–h response. Following the recent work of Psarra et al. (2017), the initial susceptibility and saturation magnetization of the iron particles is reported in Table 4.2. In the following, we have chosen the material parameters as indicated in Table 4.2. It is noted here that use of lower shear moduli for the matrix phase leads to very large local strains, especially between two closely adjacent particles. This, in turn, leads to an extreme distortion of the mesh in those regions rendering the numerical simulations extremely difficult.

Table 4.2: Material parameters for the silicone matrix and the carbonyl-iron particles

	G_i (MPa)	G'_i/G_i	χ_i	$\mu_0 m_i^s$ (T)	μ_0 (μN·A^2)
Matrix ($i = m$)	0.3	500	0.0	–	$4\pi 10^{-1}$
Particle ($i = p$)	300	500	30.0	2.5	$4\pi 10^{-1}$

Due to the large actual contrast between the matrix and the particles, it is sufficient to consider $G_p = 1000 G_m$ to ensure numerical convergence as well as a sufficiently rigid response of the particles (see work of Lopez-Pamies et al. (2013)). The bulk modulus of the matrix and the particle phase are chosen to be 500 times their respective shear modulus. Such a choice for G' ensures a nearly incompressible material response leading to $\breve{J} \approx 1$. In order to avoid volumetric locking, the volumetric term, i.e., the term involving the $(\breve{J}-1)^2$ term in (4.15), is under-integrated by using a single Gauss point at the center of the element. The remaining of the terms in (4.22) are integrated using a standard 4-point Gauss quadrature for the tetrahedral elements. Finally, as discussed in Section 4.6.3, the effects of the two augmented terms in (4.43) are taken care of by introducing a fictitious element connecting the master nodes. The FE computations are carried out by developing a user-element (UEL) subroutine, which is then coupled with the commercially available finite element package ABAQUS (2018). The developed code is rigorously benchmarked with analytical uniaxial loading solutions under both mechanical and magnetic loading. Moreover, the computed responses are probed against the analytical homogenization model of Lefèvre et al. (2017).

Subsequently, we prescribe a loading path where the normal components of the average mechanical traction are equal to zero. In addition, the shear components of the deformation gradient are also blocked to ensure a uniaxial magnetostriction response. The Eulerian h-field $\mathbf{h}_a$ is applied in direction 1, while the response in the other directions is on average the same due to isotropy of the RVE. These boundary and loading conditions imply

$$S^{mech}_{a,11} = S^{mech}_{a,22} = S^{mech}_{a,33} = 0, \qquad F_{ij} = 0,\ \forall\, i \neq j, \qquad \mathbf{h} = \mathbf{h}_a = h\mathbf{e}_1. \tag{4.84}$$

The last condition is applied by constraining $|\mathbf{h}_a - \mathbf{F}^{-T}\mathbf{H}|$ to be zero via the penalty term in (4.43). In all the computations, the penalty parameter ζ is taken to be 10^{-3}.

First, we study the evolution of the effective magnetization and magnetostriction of a numerical RVE with the applied h for volume fractions $c = 0.1, 0.2$ and 0.3. As discussed by Danas (2017) in the context of 2D RVEs, a converged magnetostriction response (i.e. in terms of scatter of the response

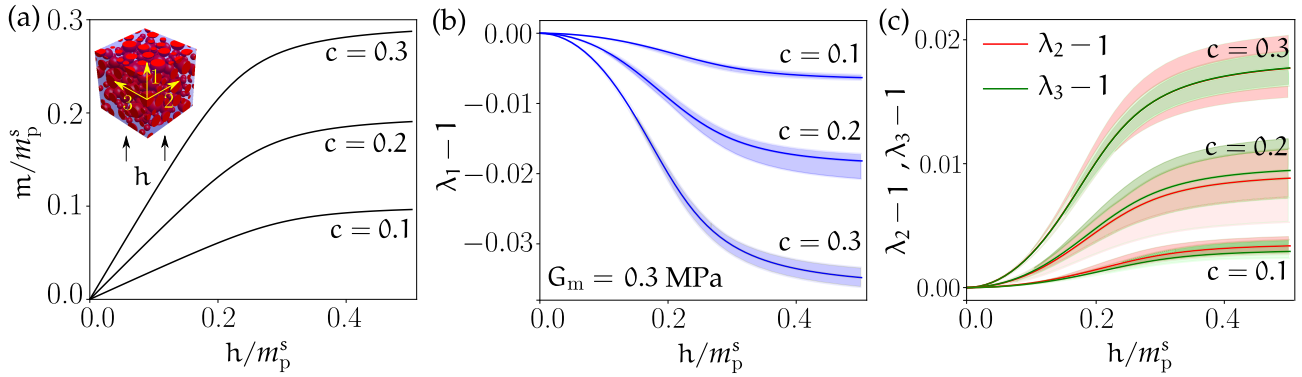

Figure 4.5: Numerically computed effective response of cubic RVEs comprising of random polydisperse spherical magnetizable inclusions, coming from three distinct families. The composite is subjected to an Eulerian h-field along the X_1 direction and zero overall mechanical traction. The overall Eulerian h-field is applied from 0 to $0.5 m_p^s$ with a maximum increment of $0.01 m_p^s$. (a) The effective magnetization for different particle volume fractions. Average of the (b) parallel and (c) transverse magnetostrictions (solid lines) obtained from 10 different realizations of the RVEs with $c = 0.1, 0.2$ and 0.3, along with the 95% trust regions (light patches) associated with each estimates.

for different realizations) necessitates a substantially large number of particles in the unit cell. The present 3D computations also show a highly fluctuating magnetostriction response in both parallel (see Fig. 4.5b) and transverse (see Fig. 4.5c) directions of the applied h-field. Evidently, in 3D, the computations become extremely costly by further increase of the number of particles beyond $N_{mono} > 60$. Therefore, we follow a second approach to obtain a converged average response. This consists in computing the effective response of the unit-cells for a sufficiently large number of realizations but a smaller number of particles (e.g., $N_{mono} = 60$, which leads to a total number of polydisperse particles $N_{tot} \sim 130$, 280 and 290 for $c = 0.1$, 0.2 and 0.3, respectively). Subsequently, by considering the average magnetostriction out of all the realizations, we assume that the response is representative in terms of a volume element. While this approach does not constitute a rigorous method to estimate the response of the RVE in a highly nonlinear setting, it still provides a useful assessment tool for the analytical solutions, even though any differences found between the numerical and the analytical homogenization model should be rationalized with extreme caution.

In this regard, we employ 10 different realizations for each volume fraction and show the average effective magnetization, parallel and transverse magnetostrictions in Fig 4.5a, b and c, respectively. In accord with previous studies by Danas (2017), the fluctuations in the effective magnetization m_1 are negligible and thus are not shown in Fig. 4.5a. Therein, the effective saturation magnetization m^s of the composite is observed to be directly proportional to the particle volume fraction, i.e., $m^s = c\, m_p^s$. In turn, the fluctuations in the parallel magnetostriction are not negligible. The continuous lines in Fig. 4.5b indicate the average magnetostriction extracted from 10 realizations, whereas the light blue patches indicate the 95% trust region of the random RVE response. The trust regions of the transverse magnetostriction components are even larger (see Fig. 4.5c) as compared to the parallel magnetostriction one. Moreover, the transverse stretch components λ_2 and λ_3 of a unit cell may differ considerably. However, the average transverse magnetostriction components are very close indicating an acceptable convergence to isotropy (see Fig. 4.5c). Note that the scatter of the results observed in the average magnetostriction response is substantially larger than the one observed for

the average magnetization response as well as the average purely mechanical response (not shown here but can be found in Lopez-Pamies et al. (2013)). Nonetheless, the scatter in the parallel and transverse components of the magnetostriction tend to vanish with the increase of N_{tot}.

We attempt to rationalize further the previous results by showing in Fig. 4.6 representative contour plots for the three volume fractions $c = 0.1$, 0.2 and 0.3 at an overall applied macroscopic field $h/m_p^s = 0.5$. The Figs. 4.6a-f, show the normalized local component $\check{b}_1/\mu_0 m_p^s$, whereas Figs. 4.6g-l, show the local nominal mechanical strain $\check{\lambda}_1 - 1$. A first observation in the context of Figs. 4.6a-f is that the particle interactions exhibit a long range, which can be larger than 4 radii of the largest particle along the direction of the applied field. This interaction is stronger at higher volume fractions (see for instance Fig. 4.6f), while it reveals that extreme caution needs to be taken when such material systems are analyzed with simpler dipole-dipole models. Also, the concentration of the $\check{b}_1$ field, which can reach rather high values, is strongly dependent on local particle distributions, thus explaining partially the difficulty in obtaining a converged isotropic response under such loading conditions and magneto-mechanical loads. In other words, by slightly changing the positions of the particles, one can change substantially the corresponding interactions. Figs. 4.6g-l, reveal the strong concentration of strains in-between particles. Due to particle rearrangement, we also observe significant tensile strains at various points in the unit-cell. It is further noted that these strains can exceed the value of 1 when the matrix is softer, as was recently discussed by Danas (2017). Such high strains can lead to debonding and final loss of efficiency in the magneto-mechanical coupling, unless specific fabrication steps are taken (for a more detailed discussion, see Bodelot et al. (2017)). Unfortunately, in the present 3D study, we were not able to carry out such computations for softer matrices (e.g., $G_m < 0.1$MPa) due to computational convergence problems.

Convergence of the number of particles **:** In addition to a set of 10 realizations of the polydisperse RVEs having $N_{mono} = 60$ ($N_{tot} \sim 290$) considered in Fig. 4.5, we analyze here two additional sets of 10 RVEs each. As defined in Section 4.7.1, in the first set of RVEs, we use the same three different families having the same size ratio (i.e. $(1, 7/9, 4/9)$) and relative volume proportion $(0.6, 0.3, 0.1)c$, respectively. Furthermore, it comprises polydisperse spherical particles obtained by setting $N_{mono} = 100$, which leads to a $R_{max}/L = 0.0895$ (with $L = 1$ denoting the size of the cubic unit cell) and a total number of actual particles $N_{tot} \sim 450$. The last set has 10 RVE realizations with polydisperse spherical particles from four different families of size ratio 1.0, 0.778, 0.556, and 0.333, whose relative proportion in the total particle volume are 0.6, 0.3, 0.2 and 0.1, respectively. This last set is obtained by considering $N_{mono} = 120$, which leads to a maximum sphere radius $R_{max}/L = 0.0842$ and a total number of particles $N_{tot} \sim 750$. The average value of the total degrees of freedom for each set of RVEs is 1.5×10^6, 2.7×10^6 and 8.5×10^5 for $N_{tot} \sim 290$, 450 and 750, respectively. Notice that, the N_{tot} in these polydisperse RVEs is not a primary variable. Rather, it is a derived quantity. The primary variables that define a polydisperse RVE is given by the particle volume fraction c, the equivalent number of monodisperse particles N_{mono}, the size ratio of different families and their relative volume proportions. For a detailed discussion of these RVE constructions the reader is referred to the recent works of Anoukou et al. (2018), Zerhouni et al. (2019) and Tarantino et al. (2019).

The average of the computed magnetostriction responses for the three aforementioned sets of RVEs are shown in Fig 4.7a. Here we observe that, with increasing number of particles, the average parallel ($\lambda_1 - 1$) and transverse ($\lambda_2 - 1$, $\lambda_3 - 1$) magnetostrictions converge to that reported in Fig 4.5b and c, respectively. Furthermore, the scatter of the computed magnetostrictions are observed to

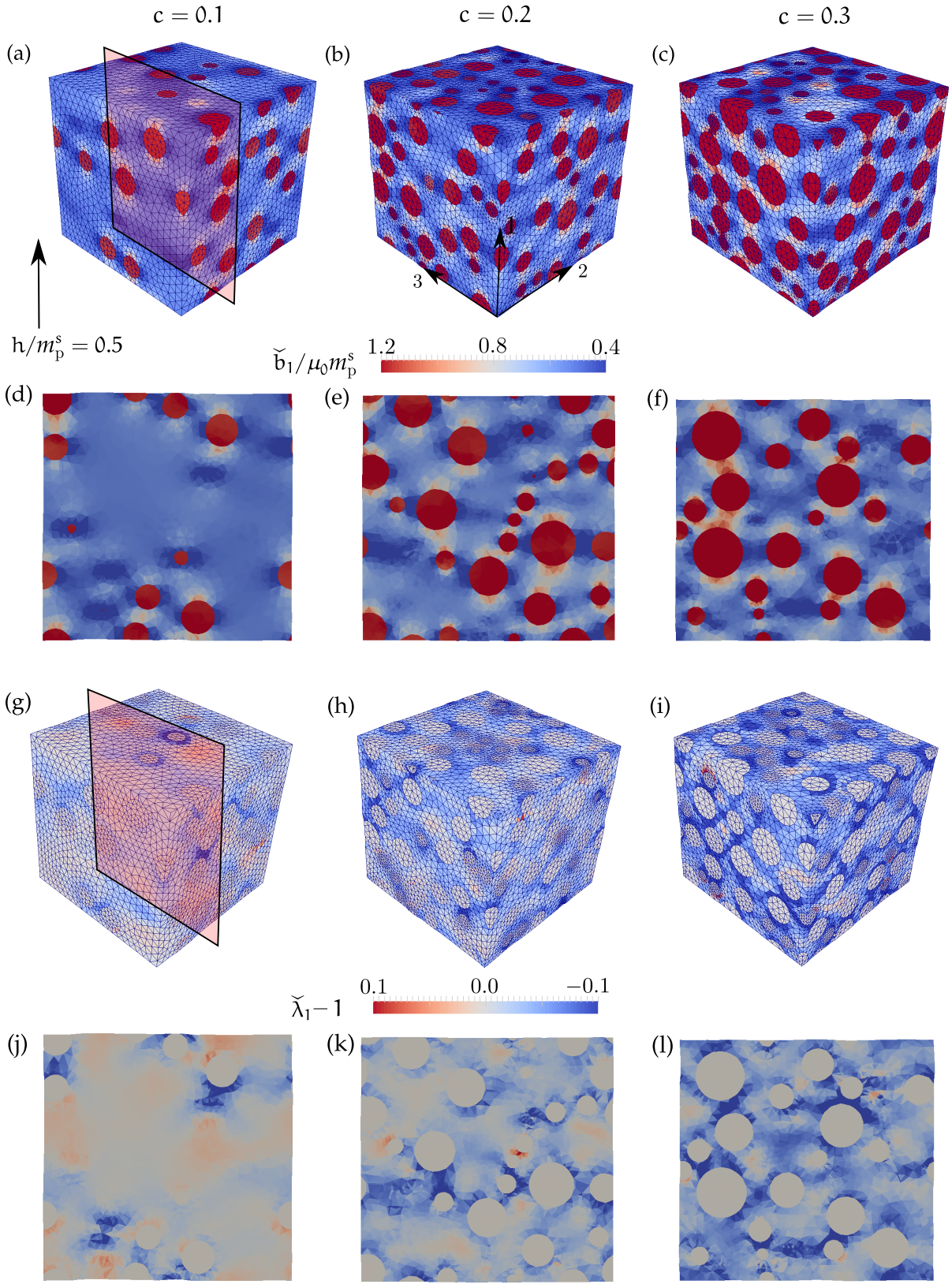

Figure 4.6: Numerically computed (a-c) normalized local magnetic field $\breve{b}_1/\mu_0 m_p^s$ and (g-i) local nominal mechanical strain $\breve{\lambda}_1 - 1$ for three particle volume fractions $c = 0.1$, 0.2 and 0.3 at an overall applied macroscopic field $h/m_p^s = 0.5$. (d-f) and (j-l) correspond to a given cross-section of the unit-cell as depicted in (a).

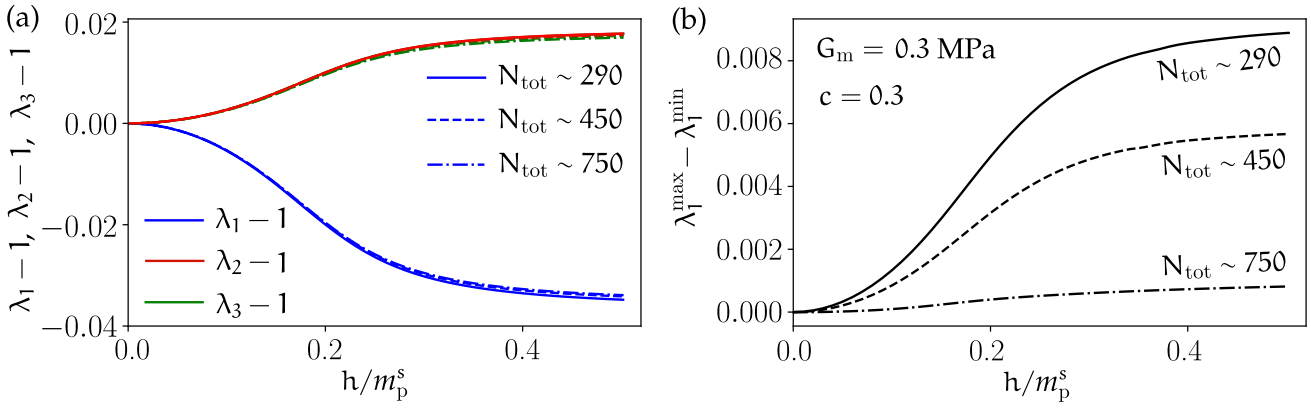

Figure 4.7: (a) Average effective parallel and transverse magnetostriction stretches, (b) scatter in the parallel magnetostrictions as obtained from the numerical homogenization for the particle volume fraction of $c = 0.3$ and the total number of particles $N_{tot} \sim 290$ (firm lines), $N_{tot} \sim 450$ (dashed lines) and $N_{tot} \sim 750$ (chain-dotted lines). Eulerian h-field is applied at a local point in the MRE, which is free from mechanical tractions.

decrease considerably (see Fig. 4.7b) with the increase of the number of particles.

It should be noted here that the convergence of the computed magnetostriction in Fig. 4.7a and b is valid for the present use of energy functions (e.g. Neo-Hookean mechanical response defined in (4.15)). A different hyperelastic law with more pronounced nonlinearities (such as Gent hyperelasticity) for the matrix phase may need additional convergence studies and perhaps even larger number of particles.

Mesh convergence **:** Next, we investigate the mesh convergence of the computed effective magnetization and magnetostriction for a specific RVE given by Fig. 4.5 for $c = 0.3$. In addition to the given mesh in Fig. 4.5, we perform the computations for three additional meshes; one with a coarser mesh with total number of degrees of freedom equal to 0.8×10^6 and two with finer meshes having 3.4×10^6 and 5.1×10^6 degrees of freedom. As shown in Fig. 4.8a, the effective magnetization is converging rapidly for all meshes, whereas, the parallel and transverse magnetostrictions in Fig. 4.8b and c are seen to be slightly underestimated when the coarse mesh with 0.8×10^6 degrees of

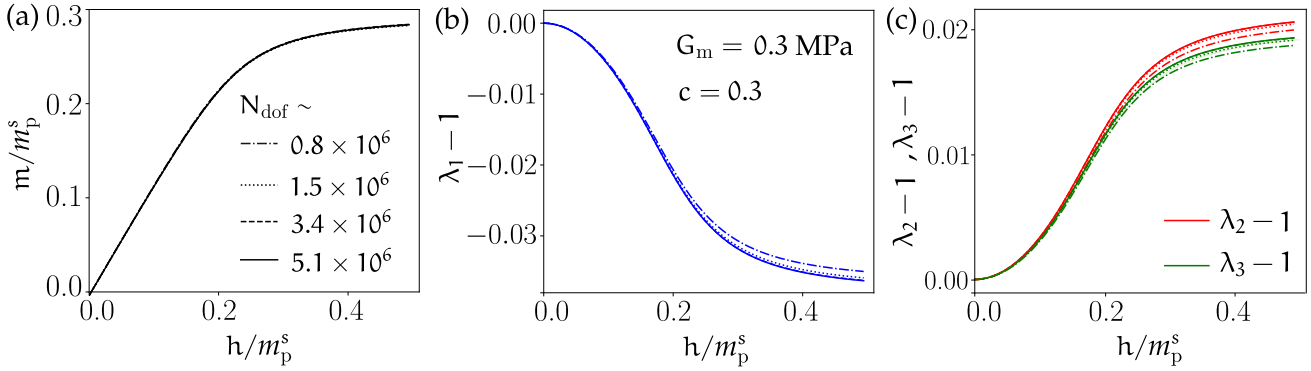

Figure 4.8: Computed (a) effective magnetization and (b-c) effective parallel and transverse magnetostrictions for a RVE with $c = 0.3$ and $N_{tot} \sim 290$ having four different meshes with total degrees of freedom 0.8×10^6 (dashed-dotted lines), 1.5×10^6 (dotted lines), 3.4×10^6 (dashed lines) and 5.1×10^6 (solid lines).

freedom is used. Nevertheless, the magnetostriction response is observed to converge rapidly with the subsequent mesh refinements. Notice that in the reported results in Fig. 4.5, we use the RVEs

with approximately 1.5×10^6 degrees of freedom, which leads to fully-converged magnetization and magnetostriction responses as observed in Fig. 4.8.

4.7.3 Effective response of h-MREs

Next, we present the numerically computed effective response of the h-MREs under proportional cyclic loading paths. Subsequently, we investigate a couple of cases, which consider first a magnetic, followed by a mechanical loading, in order to probe the effect of mechanical stresses on a pre-magnetized h-MRE. The latter is crucial in the context of determining the dependence of residual magnetization (i.e., $\mathbf{m}^0$ at $\mathbf{h}_a = \mathbf{0}$) on $\mathbf{F}$, which is, in turn, a key information required in the macroscopic modeling of the h-MREs and would be utilized in Chapter 6.

Proportional cyclic loading **:** The schematic diagram of the proportional loading direction and its temporal variation are shown by Fig. 4.9a and b, respectively. Notice that here the time scale is irrelevant since both the matrix and particles are defined to exhibit rate-independent constitutive responses. The proportional cyclic loading path is consider to be a simple ramp-type load-

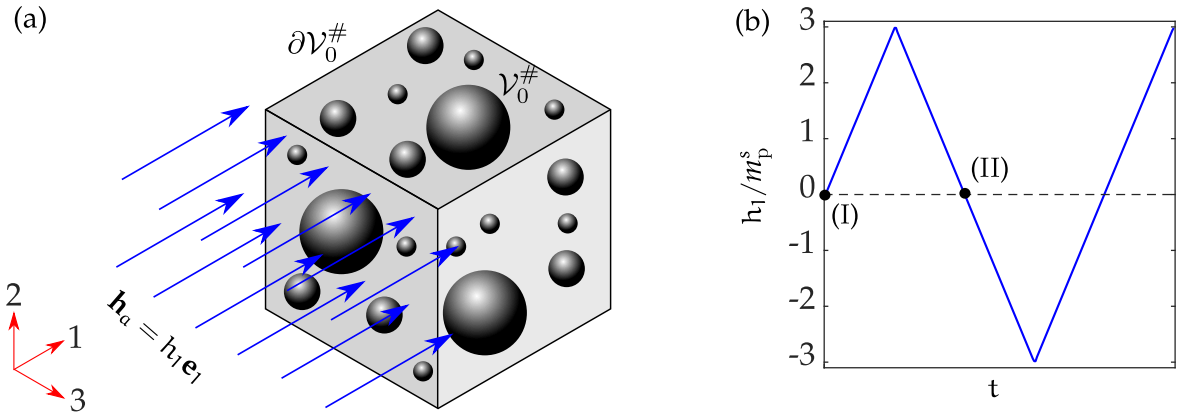

Figure 4.9: (a) Schematic diagram of the applied $\mathbf{h}_a$ on the RVE along $\mathbf{e}_1$. (b) Loading evolution with time. The time scale is irrelevant for the present rate-independent model.

ing/unloading. The macroscopic stress and displacement boundary conditions are considered to be identical to (4.84).

Here we perform computations for three set of polydisperse RVEs having $c = 0.1$, 0.2 and 0.3, all having $N_{mono} = 60$. In fact, we use the same FE meshes shown in Fig. 4.4 for the FE computations herein. The shear modulus of the matrix is now considered to be $G_m = 0.5$ MPa, which resembles closely to the moderately-soft PDMS (Park et al., 2018; Wang et al., 2019). The shear moduli of the particles are considered to be $G_p = G_m = 500$ MPa, that is sufficient in order to ensure a vanishingly small deformation in the particles. Furthermore, the matrix and particle bulk moduli are selected to be $G_i' = 500G_i$, with $i = m, p$, which are found to be sufficient to ensure a *nearly incompressible* effective response. The magnetic properties of the hard particle phase are taken to be those of the NdFeB powder, which are identified in Table 3.3.1. The magnetically inert matrix, on the other hand, is modeled simply by setting $b_m^c = 10^6 b_p^c$ and $\chi_m^e = 0$, such that the local constitutive response $\breve{\mathbf{b}} = \mu_0\breve{\mathbf{h}}$ is ensured (see Fig. 3.2a).

Since the hard magnets require a greater $\mathbf{h}_a$ to saturate (c.f. Fig. 1.2a and b), here the loading is performed up to $h_1/m_p^s = 3.0$, in order to ensure a saturated magnetic hysteresis loop. Consequently,

a greater number of load increments are required at each step of the FE computations for the h-MREs. Thus, the numerical computations for the h-MREs under fully-reversed, cyclic loading conditions, as shown in Fig. 4.9b, are $16-20$ times more expensive than the s-MRE computations shown in Fig 4.5. Moreover, the storage of the local remanent $\breve{\mathbf{H}}^{\mathrm{r}}$ at each integration point and the computations for their local evolution also add up to the storage and computation costs.

Similar to the s-MREs (see Fig. 4.5b and c), we note that, for different RVE realizations, the effective magnetostriction responses of the h-MREs also fluctuate around an average. Hence, we need several realizations of each RVE in order to estimate the average magnetostriction response, that is independent of the effect of local field fluctuations. However, the numerical computations of the h-MRE responses under a fully reversed cyclic loading is extremely expensive. Thus, in order to reduce the computation time, we first consider the loading path to be the initial half cycle from (I) to (II), as indicated in Fig. 4.9b and compute the effective responses for five different realizations of the polydisperse RVEs for particle volume fractions $c = 0.1$, 0.2 and 0.3. Nevertheless, the numerical computations remain $5-6$ times more expensive than their counterparts for the s-MREs.

The average magnetization and the parallel and transverse magnetostrictions computed for $c = 0.1$, 0.2 and 0.3 are shown in Fig 4.10, where we show the average of the five RVE computations along with the relative scatter in the computed results with the light-colored patches around the respective averages. Similar to the s-MREs, the scatter of the magnetization responses are observed

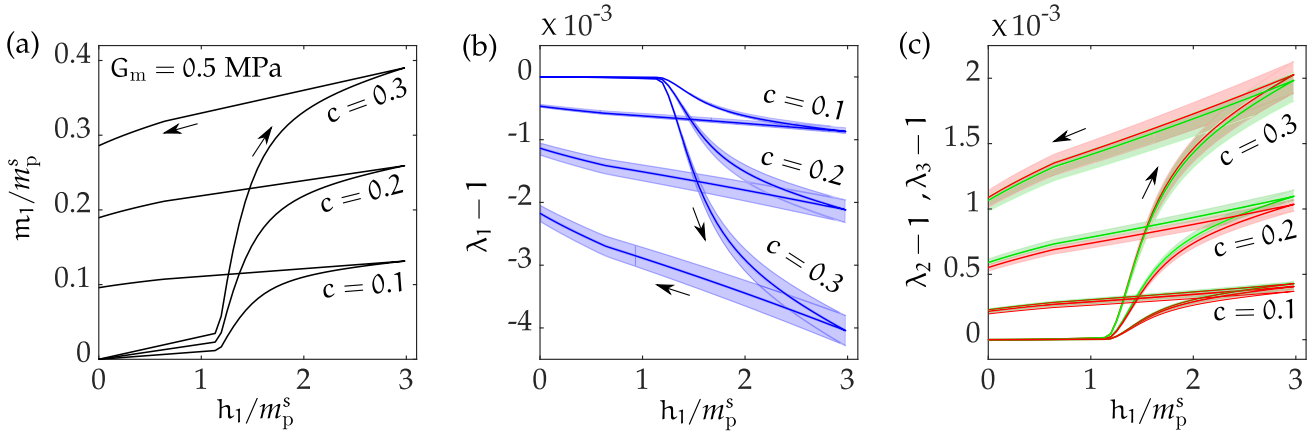

Figure 4.10: Numerically computed effective (a) magnetization, (b) parallel and (c) transverse magnetostrictions the h-MRE RVEs, subjected to uniaxial Eulerian $\mathbf{h}_a = h_1 \mathbf{e}_1$ loading from (I) to (II) as shown in Fig. 4.9b. The average effective responses (solid lines) along with the range of their fluctuations (light patches) for different realizations of the respective RVEs are indicated. The RVEs of different volume fractions are comprised of random polydisperse spherical hard-magnetic inclusions, coming from three distinct families.

to be negligibly small, whereas, those of the parallel and transverse magnetostrictions are finite. Notice from Fig. 4.10 that, unlike the s-MRE responses, neither the effective magnetization, nor the magnetostrictions saturates at higher h-fields. Rather, they maintain a slope with the applied h_1. This can be attributed to the inherent non-saturating magnetization response of the NdFeB particles, as observed in Fig. 1.2b. Moreover, notice that the magnitude of the magnetostrictions are considerably less in the h-MREs as compared to those of the s-MREs, c.f. Fig. 4.10b and Fig. 4.5b. This effect can be attributed to the weaker magnetization of the NdFeB particles than the iron particles at higher applied h-fields (see Fig. 1.2c), which, results in less particle-to-particle interaction forces in the h-MREs and eventually lead to less particle rearrangements.

The magnetization and magnetostriction responses under a fully reversed proportional loading are then computed for $c = 0.1$, 0.2 and 0.3 by considering one RVE of each volume fraction. The

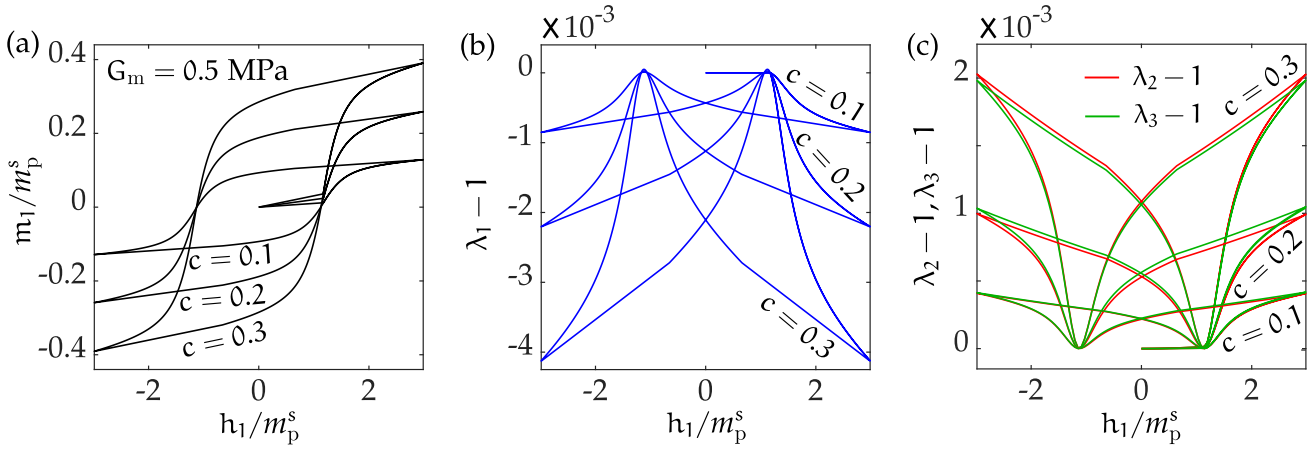

Figure 4.11: Computed hysteresis loops of effective (a) magnetization, (b) parallel and (c) transverse magnetostrictions of h-MRE RVEs having particle volume fractions $c = 0.1$, 0.2 and 0.3. The RVEs are subjected to a fully reversed, proportional loading shown in Fig. 4.9. The average of the effective responses computed from five realizations of a RVE are shown without the fluctuation patches for the magnetostrictions.

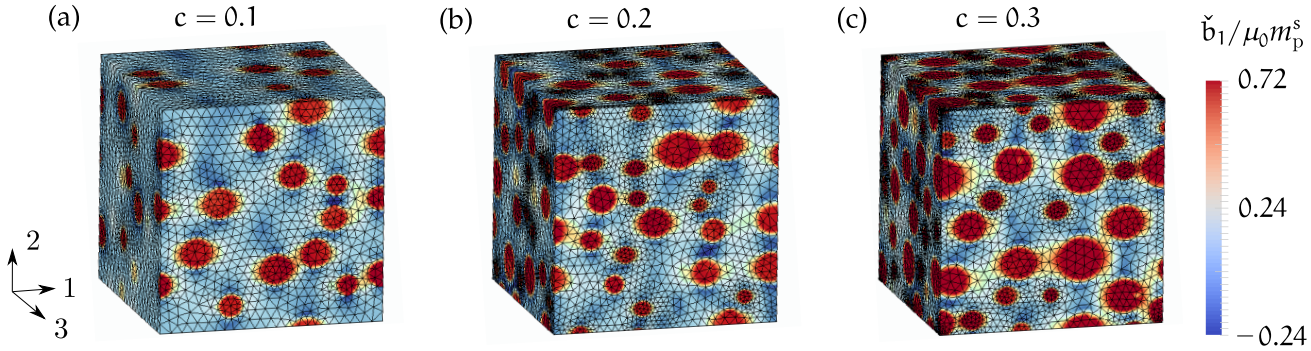

Figure 4.12: Contours of the numerically computed, normalized microscopic $\breve{b}_1$ in the RVEs after the first half cycle, i.e., at loading point (II) indicated on Fig. 4.9b. Three different, RVEs having (a) $c = 0.1$, (b) 0.2 and (c) 0.3 are shown.

RVEs are selected to be those, whose responses are the closest ones to the respective averages for each volume fractions. The resulting magnetization and magnetostriction hysteresis loops are shown in Fig. 4.11. Notice that the effective magnetic hysteresis loops look qualitatively the same to that of the NdFeB particles, whereas the butterfly-shaped hysteresis loops are obtained for both parallel and transverse magnetostriction components.

Finally, we show the contours of the microscopic $\breve{b}_1/\mu_0 m_p^s$ fields after the initial half-cycle (i.e., loading up to (II)) in the deformed RVEs for three particle volume fractions in Fig. 4.12. In accordance with the computed effective magnetostrictions in Fig. 4.10b and c, we observe very small overall deformation of the RVEs, although the local (microscopic) strain fields may be considerably high, as observed in Fig. 4.6 and also in (Danas, 2017) for the *s*-MREs.

Mesh convergence **:** For completeness, we perform a mesh convergence study for one of the representative effective response. The loading path is considered to be the same as shown in Fig. 4.9b

and the mechanical boundary conditions are considered to be (4.84). Subsequently, we consider three increasingly refined meshes of a RVE having $c = 0.3$ and $N_{mono} = 60$ having approximate number of degrees-of-freedom $N_{dof} = 0.8 \times 10^6$, 1.5×10^6 and 3.4×10^6. The resulting magnetization and magnetostriction responses during the first half-cycle is plotted in Fig. 4.13. In accordance to the

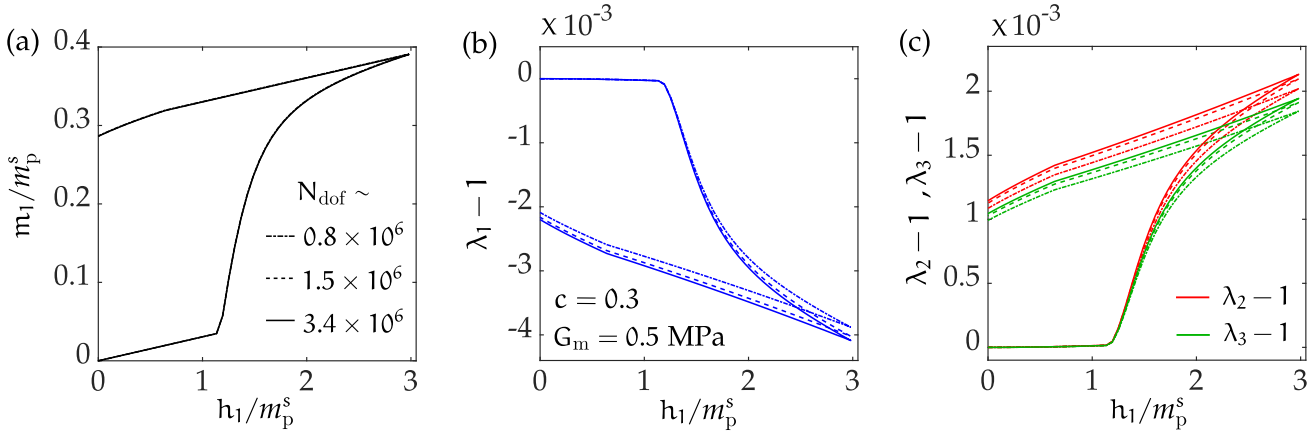

Figure 4.13: Computed (a) effective magnetization and (b-c) effective parallel and transverse magnetostrictions for a RVE with $c = 0.3$ and $N_{tot} \sim 290$ having four different meshes with total degrees-of-freedom 0.8×10^6 (dashed-dotted lines), 1.5×10^6 (dashed lines), 3.4×10^6 (solid lines).

mesh convergence study for the s-MREs in Fig. 4.8, we observe from Fig. 4.13a that, the effective magnetization responses remain identical with the increasingly refined meshes. Furthermore, the parallel (Fig. 4.13b) and transverse (Fig. 4.13c) magnetostriction components are also observed to be converging with the increasing refinement of the meshes.

Effect of mechanical tension and shear **:** Next, we investigate the effect of mechanical tension and shear stresses on a pre-magnetized h-MRE. To accomplish this, we consider the mechanical stress and displacement boundary conditions to be

$$S^{mech}_{a,11} = S^{mech}_{a,33} = S^{mech}_{a,32} = S^{mech}_{a,13} = 0, \quad S^{mech}_{a,22} \neq 0, \quad S^{mech}_{a,12} \neq 0 \quad \text{and} \quad F_{21} = F_{23} = F_{31} = 0, \tag{4.85}$$

where the specific forms of $S^{mech}_{a,22}$ and $S^{mech}_{a,12}$ will be provided at relevant places and lastly, the three displacement conditions in therms of F are imposed to ensure no rigid-body rotations under applied $S^{mech}_{a,22}$ or $S^{mech}_{a,12}$.

Notice that, the first half cycle (I) — (II) leads to a permanently magnetized h-MRE upon the complete removal of the applied h_1 at (II). The mechanical stresses are applied subsequently in terms of applied (i) $S^{mech}_{a,22} = S^{mech}_{22}$, $S^{mech}_{a,12} = 0$ and (ii) $S^{mech}_{a,22} = 0$, $S^{mech}_{a,12} = S^{mech}_{12}$, while all other independent mechanical stress components are given by $(4.85)_1$. We note that, unlike the magnetostriction responses, the mechanical loading responses of a pre-magnetized h-MRE do not fluctuate with the RVE realizations under applied S^{mech}_{22} or S^{mech}_{12}. This is simply because the applied mechanical stresses induce considerably high amount of strains in the material, as compared to the magnetostriction responses under proportional loading, which has a maximum magnitude of 5×10^{-3} (see Fig. 4.10b). Moreover, Fig. 4.10b shows that, the maximum magnitude of fluctuations in the effective strains ae not more than 5×10^{-4}. Although such fluctuations significantly modify the magnetostriction responses, their effects on the coupled magneto-mechanical responses, having strains in the range of $0.2 - 1.0$, are negligible. Also, notice from Fig. 4.13b and c that, a relatively coarse mesh *do not* alter the resulting

magnetostriction responses substantially.

Consequently, in order to reduce the computation cost, we consider a monodisperse RVE, with $N_{mono} = 60$, having a particle volume fraction $c = 0.2$. Instead, the effect of matrix shear modulus is investigated here for three distinct G_m, namely, $G_m = 1.0$, 0.5 and 0.3 MPa. The corresponding shear moduli of the particle phases are considered to be $G_p = 100G_m$, which is a sufficient contrast to ensure negligibly small strain components in the particle phases. All other material parameters are considered to remain the same as defined in the previous proportional loading case.

Figure 4.14b and c shows that the current remanent magnetization remain unaffected by the mechanical stretch, shown in Fig. 4.14a, that is induced by the applied S_{22}^{mech}/G_m. Moreover, the effec-

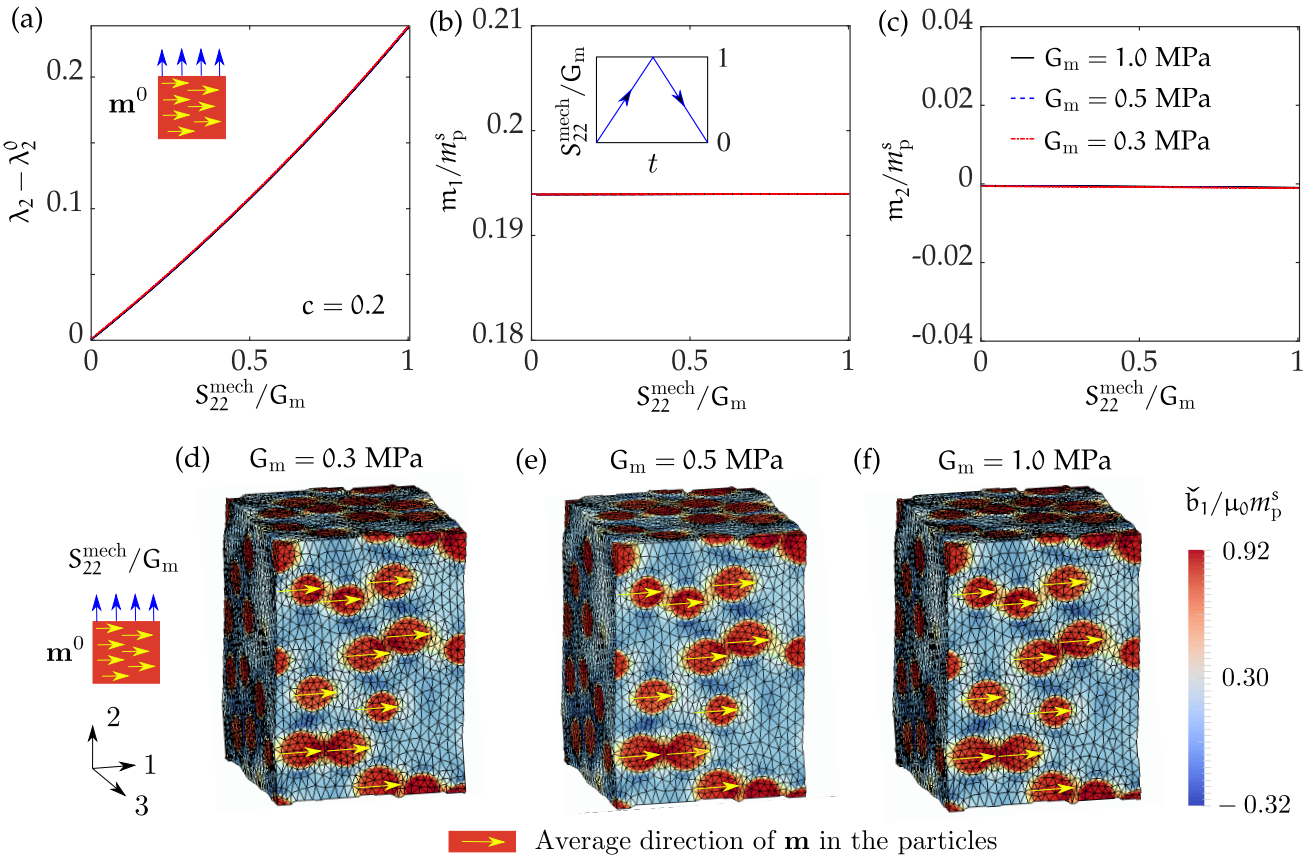

Figure 4.14: Deformation of a magnetized RVE having $c = 0.2$ and monodisperse spherical inclusions with $N_{mono} = 60$, under applied uniaxial tensile stress $S_{\alpha,22}^{mech} = S_{22}^{mech}$, whose temporal variation is shown in the inset of (b). Numerically computed effective (a) parallel stretch $\lambda_2 - \lambda_2^0$ under the applied S_{22}^{mech} and variation of (b) m_1 and (c) m_2 under the same are shown for the matrix shear moduli $G_m = 1.0$, 0.5 and 0.3 MPa. Contours of the normalized microscopic $\breve{b}_1$ in the deformed RVEs having (d) $G_m = 1.0$, (e) 0.5 and (f) 0.3 MPa, under applied $S_{22}^{mech}/G_m = 1$. Directions of the microscopic $\breve{\mathbf{m}}$ in some of the particles are shown by yellow arrows.

tive magneto-mechanical responses due to the applied normalized stress S_{22}^{mech}/G_m remain unaffected by the matrix shear modulus G_m. The $\breve{b}_1/\mu_0 m_p^s$ contour plots in the deformed configuration under $S_{22}^{mech}/G_m = 1$ in Fig. 4.14d-f show that the permanently magnetized particles only get rearranged by the applied uniaxial tension, without being rotated. For visual illustration purpose, we indicate the average directions of the local magnetization $\breve{\mathbf{m}}$ in the individual particles by yellow-colored arrows, as shown in Fig. 4.14d-f. Notice that all these arrows remain aligned to the 1 direction, i.e., in the

direction of their pre-magnetization, under applied S_{22}^{mech}. Thus, since the local $\breve{\mathbf{m}}$ is finite *only* in the particle phases, effectively, the average $\mathbf{m}$ remain independent of mechanical stretch.

To elaborate further on the effect of mechanical stretch on the average magnetic $\mathbf{B}$ and $\mathbf{H}^r$ fields, and their Eulerian counterparts $\mathbf{b}$ and $\mathbf{h}^r$, we numerically compute the ensemble average of these quantities over the volume $\mathcal{V}_0^{\#}$ (or equivalently $\mathcal{V}^{\#}$ for the Eulerian fields) and plot them with respect to S_{22}^{mech}/G_m in Fig. 4.15. Subsequently, we note that, even though the mechanical stretch affects

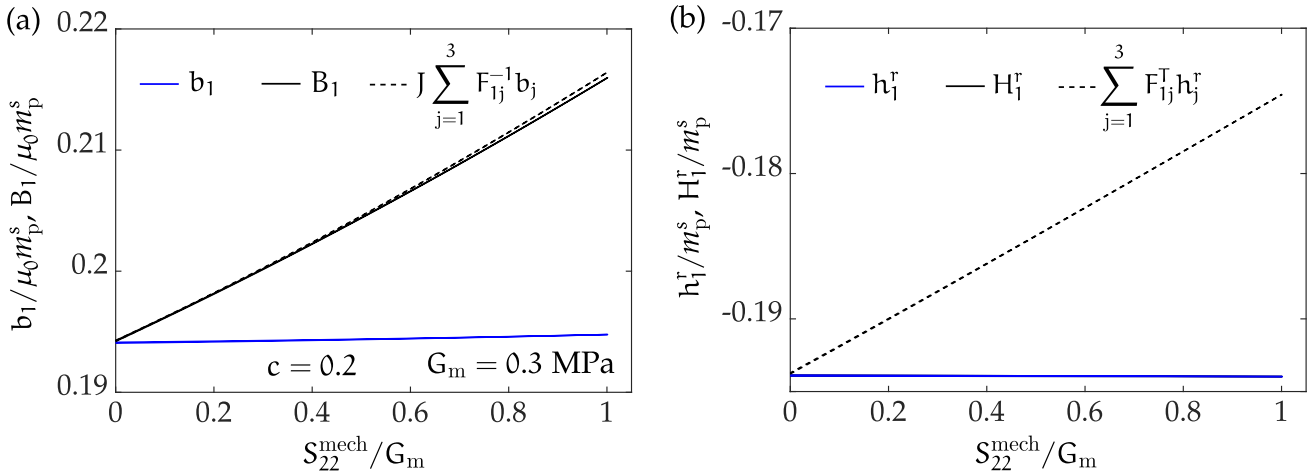

Figure 4.15: Numerically computed (a) b_1, B_1 and the $\mathbf{e}_1$ component $J\mathbf{F}^{-1}\mathbf{b}$ and (b) average remanent fields h_1^r, H_1^r, the $\mathbf{e}_1$ components of $\mathbf{F}^T\mathbf{h}^r$, where $\mathbf{F}$ and $\mathbf{b}$ are obtained from the numerical computations under applied S_{22}^{mech}/G_m, whose time evolution is shown in the inset of Fig. 4.14b.

the resulting Lagrangian $\mathbf{B}$, the computed effective $\mathbf{H}^r$ remains independent of S_{22}^{mech}/G_m. In turn, Fig. 4.15a validate the fact that the pull-back transformation of $\mathbf{b}$ is given by $\mathbf{B} = J\mathbf{F}^{-1}\mathbf{b}$, since the solid and dotted black lines coincide. In contrast, Fig. 4.15b shows that the Eulerian $\mathbf{h}^r$ and its Lagrangian counterpart $\mathbf{H}^r$ *do not* confirm to the pull-back transformation $\mathbf{H}^r = \mathbf{F}^T\mathbf{h}^r$. Instead, $\mathbf{H}^r$ and $\mathbf{h}^r$ are observed remain the same under applied S_{22}^{mech}/G_m. This is a crucial observation, which we will recall in Chapter 6, while proposing a macroscopic constitutive model for the h-MREs.

Next, the effect of applied shear stress S_{12}^{mech}/G_m on the effective $\mathbf{m}$ is shown in Fig. 4.16. The applied S_{12}^{mech}/G_m leads to a shear strain γ_{12}, whose evolution with S_{12}^{mech}/G_m is shown in Fig. 4.16a. Moreover, it is observed that the effect of G_m on these results remain negligibly small. We subsequently notice from Fig. 4.16b and c along with the inset of Fig. 4.16b that $\mathbf{m}$ undergoes rotation under the applied S_{12}^{mech}/G_m, resulting in non-constant m_1 and m_2 values, even though $|\mathbf{m}|$ remains constant. Hence, the change in m_1 and m_2 can be clearly attributed to the particle rotations. In this regard, Fig. 4.16d-f show the contour plots of $\breve{b}_1/m_p^s$ in the deformed configuration, which clearly show the particle rotations in the RVE, as indicated by yellow arrows. We also notice that the average particle rotation is approximately equal to the macroscopic rotation $\mathbf{R}$, which can be computed from the polar decomposition of $\mathbf{F}$.

The effect of applied shear on the magnetic induction $\mathbf{b}$ and its Lagrangian counterpart $\mathbf{B}$ and the remanent field $\mathbf{h}^r$ and $\mathbf{H}^r$ are investigated subsequently by plotting their evolution under applied S_{12}^{mech}/G_m in Fig. 4.17. The comparison of the 1 and 2 components of $\mathbf{b}$, $\mathbf{B}$ and the computed $J\mathbf{F}^{-1}\mathbf{b}$ in Fig. 4.17a and Fig. 4.17b, respectively, ascertain that the current $\mathbf{b}$ transforms to the Lagrangian configuration via the pull-back transformation $\mathbf{B} = J\mathbf{F}^{-1}\mathbf{b}$. Furthermore, Fig. 4.17c and Fig. 4.17d confirm

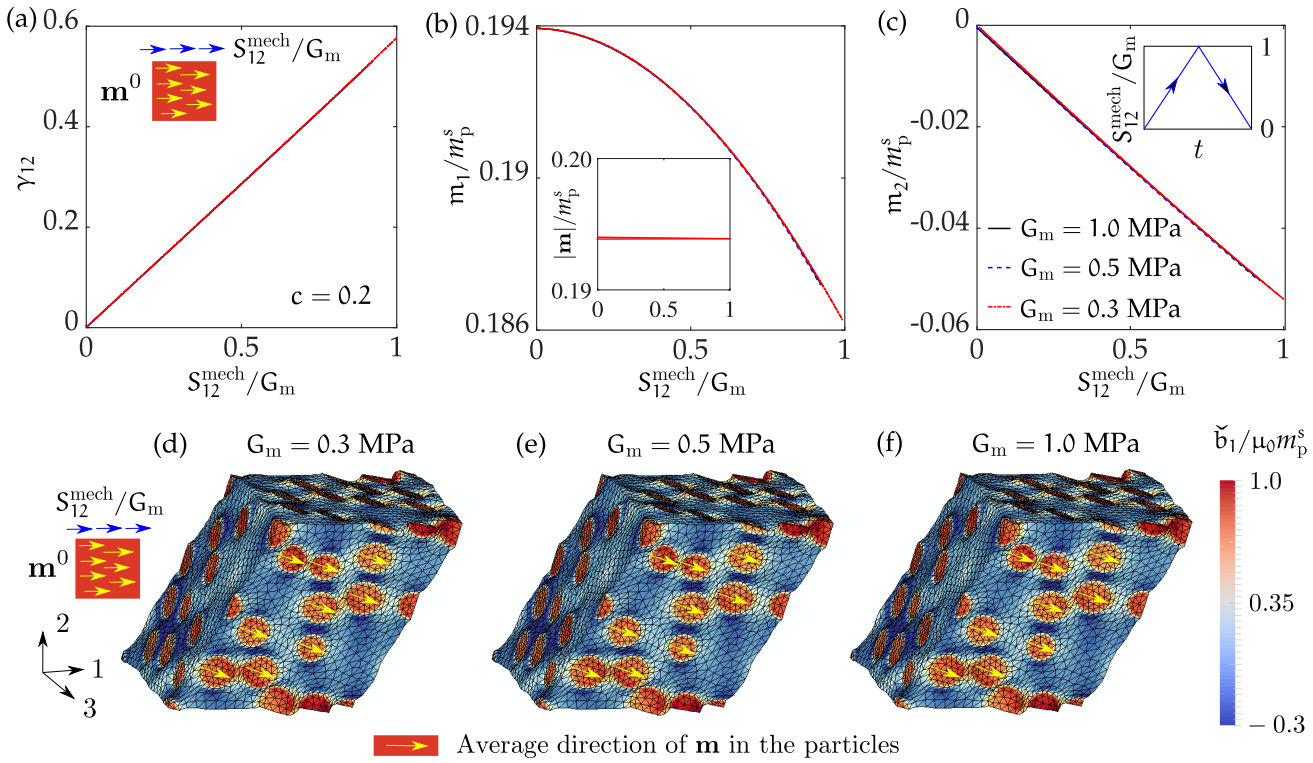

Figure 4.16: Deformation of a magnetized RVE having $c = 0.2$ and monodisperse spherical inclusions with $N_{mono} = 60$, under applied shear stress $S_{\alpha,12}^{mech} = S_{12}^{mech}$, whose temporal variation is shown in the inset of (c) (time scale is irrelevant for the rate-independent models). Numerically computed effective (a) shear strain γ_{12} by the applied S_{12}^{mech} and the variations of (b) m_1, (c) m_2 and (b)(inset) $|\mathbf{m}|$ under the same are shown for the matrix shear moduli $G_m = 1.0$, 0.5 and 0.3 MPa. Contours of the normalized microscopic $\breve{b}_1$ in the deformed RVEs having (d) $G_m = 1.0$, (e) 0.5 and (f) 0.3 MPa, under applied $S_{12}^{mech}/G_m = 1$. Directions of the microscopic $\breve{\mathbf{m}}$ in some of the particles are shown by yellow arrows.

that, the pull-back transformation of $\mathbf{h}^r$ is given by the relation $\mathbf{h}^r = \mathbf{R}^T\mathbf{H}^r$ and not by $\mathbf{h}^r = \mathbf{F}^T\mathbf{H}^r$. In this regard, we notice that the macroscopic primary $\mathbf{h}$ and its conjugate $\mathbf{b}$ have their Lagrangian counterparts are defined via (4.34) and $(4.38)_2$ to be $\mathbf{H} = \mathbf{F}^T\mathbf{h}$ and $\mathbf{B} = J\mathbf{F}^{-1}\mathbf{b}$, respectively (see also (Ponte Castañeda and Galipeau, 2011; Javili et al., 2013)). In contrast, the remanent internal variable $\mathbf{h}^r$ has no such rigorous definition of its pull-back transformation. Nonetheless, the observations from Fig. 4.17c and Fig. 4.17d along with the uniaxial stretch results in Fig. 4.16b suggest that the Lagrangian counterpart of the current $\mathbf{h}^r$ may be defined to be in a *stretch-free intermediate configuration* and, consequently, the mapping between $\mathbf{h}^r$ and $\mathbf{H}^r$ may be defined via an *overall particle rotation tensor* $\mathbf{R}_p$.

This rotation $\mathbf{R}_p$ is found to be identical to the macroscopic rotation tensor $\mathbf{R}$ *under the specific mechanical shear* loading S_{12}^{mech}. This pull-back transformation may not necessarily hold for other coupled magneto-mechanical loading paths, where the particle rotations may not be identical to $\mathbf{R}$. This point will be elaborated further in Chapter 6. In this context, we recall that there is no rigorous analytical estimate for the microstructural particle rotations under applied magneto-mechanical loads. Thus, to this end, one can only estimate such *effective* particle rotation tensor $\mathbf{R}_p$ via the full-field numerical computations under a prescribed loading path.

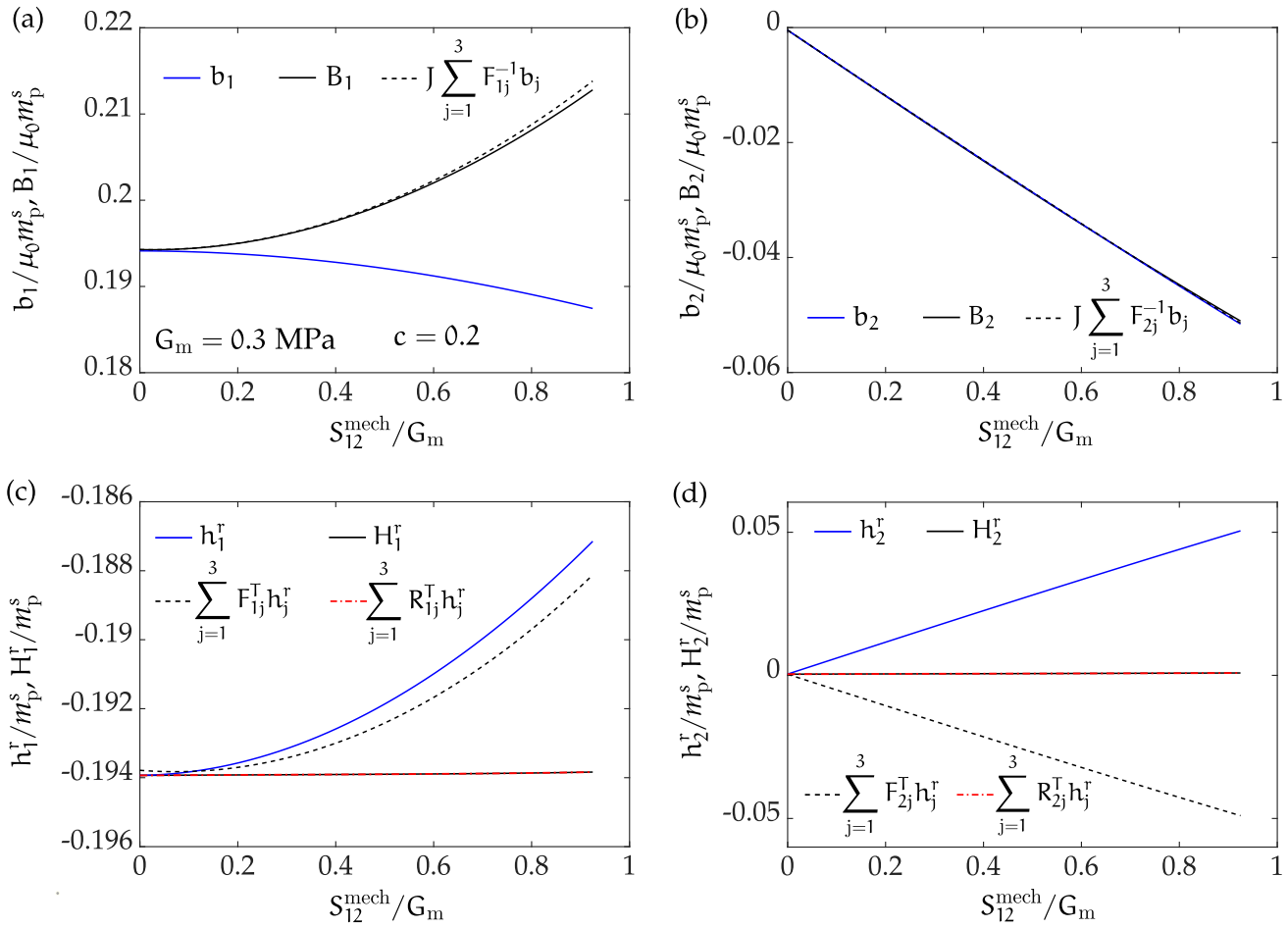

Figure 4.17: Numerically computed (a) b_1, B_1 and the $\mathbf{e}_1$ component $J\mathbf{F}^{-1}\mathbf{b}$, (b) b_2, B_2 and the $\mathbf{e}_2$ component of $J\mathbf{F}^{-1}\mathbf{b}$, (c) average remanent fields h_1^r, H_1^r, the $\mathbf{e}_1$ components of $\mathbf{F}^T\mathbf{h}^r$ and $\mathbf{R}^T\mathbf{h}^r$ and (d) h_2^r, H_2^r, the $\mathbf{e}_2$ components $\mathbf{F}^T\mathbf{h}^r$ and $\mathbf{R}^T\mathbf{h}^r$, where $\mathbf{F}$, $\mathbf{R}$ and $\mathbf{b}$ are obtained from the numerical computations under applied S_{12}^{mech}/G_m, whose temporal profile is shown in the inset of Fig. 4.16c.

4.8 Concluding remarks

In summary, this chapter presents a general framework for the incremental numerical homogenization of dissipative magneto-mechanical composites in a fully Lagrangian setting via defining an augmented variational principle. Specific local (microscopic) constitutive relations for the iron/NdFeB particles and the Neo-Hookean matrix are also provided along with the specific forms of element force and stiffness matrices, which are utilized in the FE computations. Furthermore, the local update algorithm for the microscopic internal variable $\breve{\mathbf{H}}^r$ is provided explicitly. The key advantages of the presented incremental homogenization framework is listed in the following.

1. The presented incremental potential-based homogenization framework is the exact equivalent of that developed in the context of mechanical elasto-plasticity (Miehe, 2002; Miehe et al., 2002). This framework first defines an incremental potential energy (also referred to be the reduced potential (Carstensen et al., 2001; Miehe et al., 2011; Rosato and Miehe, 2014)) as a function of the energetic and dissipation potentials. This incremental potential is then treated as a *quasi*

energetic equivalent of the dissipative system, specifically at the current time increment $t = \tau$. Subsequently, the associated homogenization problem is defined via the standard energetic homogenization problem (Ponte Castañeda and Galipeau, 2011; Galipeau and Ponte Castañeda, 2013; Javili et al., 2013; Danas, 2017; Lefèvre et al., 2017) for magneto-active composites, but here at the current increment $t = \tau$. Notice that the fully energetic homogenization problem is independent of the time increment, whereas the proposed incremental framework for h-MREs is not.

2. Fully objective and thermodynamically consistent constitutive models for the two phase hard magnetic composite are proposed for the matrix and particle phases in Section 4.2. A *nearly incompressible* response is ensured by setting the bulk modulus $G_i' = 500G_i$ for both $i = m, p$. Furthermore, the specific form of the non-dissipative, soft magnetic model is provided therein after taking the limit of $b_p^c \to 0$. In fact, as pointed out in Remark 4.1, one can retrieve the energetic homogenization framework of Lefèvre et al. (2017), from the proposed $\mathbf{F}-\mathbf{H}$ incremental homogenization setting directly via substituting $b_i^c = 0$ to (4.19). Hence, one can treat the homogenization problem for s-MREs to be a special case of that proposed in the context of h-MREs in this chapter.

3. Suitable augmentation to the incremental homogenization variational principle is provided in Section 4.5. This augmented variational principle, in turn, enables the numerical homogenization to yield a coupled magneto-mechanical response, that is free from the boundary and shape effects.

4. As detailed in Section 4.6, a fully Lagrangian $\mathbf{F}-\mathbf{H}$-based microscopic model is considered here for the finite-element computations. Since the $\mathbf{F}-\mathbf{H}$ can be treated in a numerical setting to be in terms of the mechanical displacement field $\breve{\mathbf{u}}$ and a scalar magnetic potential $\breve{\varphi}$, it reduces the nodal degrees-of-freedom as compared to the vector potential-based $\mathbf{F}-\mathbf{B}$ model (Danas, 2017).

The resulting effective responses are shown first for the s-MREs via defining the RVEs to be comprised of a random polydisperse spherical inclusions, coming from three distinct families. Later, the same RVEs are used to compute the effective response of the h-MREs under proportional magnetic loading. The qualitative effective responses of the s- and h-MREs are observed to be the same, exhibiting realization-dependent fluctuations in the magnetostriction responses, while no fluctuation in the effective magnetization is observed. Finally, the effect of mechanical tension and shear in the pre-magnetized h-MRE RVEs are investigated. Crucial insights on the stretch-independence of $\mathbf{h}^r$ is obtained therein, which will be recalled in Chapter 6 while proposing a macroscopic constitutive model for the h-MREs.

Appendix 4.A. Pull-back transformation of effective Eulerian field h

In this appendix we drop the subscript τ from the fields for brevity. Nevertheless, the relation derived herein holds for any discrete time τ during the entire loading/unloading path. We express (4.34) in

terms of the index notation as

$$h_i = \frac{1}{J\mathcal{V}_0^{\#}} \int_{\mathcal{V}_0^{\#}} \frac{\partial \breve{J}}{\partial \breve{F}_{ij}} \breve{H}_j \, dV = -\frac{1}{J\mathcal{V}_0^{\#}} \int_{\mathcal{V}_0^{\#}} \frac{\partial \breve{J}}{\partial \breve{F}_{ij}} \breve{\varphi}_{,j} \, dV. \tag{4.A.1}$$

Here, the curl-free condition on $\breve{\mathbf{H}}$ allows to write the latter in terms of a scalar potential $\breve{\varphi}$ such that $\breve{\mathbf{H}} = -\text{Grad}\ \breve{\varphi}$ (or equivalently, $\breve{H}_i = -\breve{\varphi}_{,i}$). From the divergence theorem and the divergence-free property of $\partial \breve{J}/\partial \breve{\mathbf{F}}$, we recast (4.A.1) to read

$$h_i = -\frac{1}{J\mathcal{V}_0^{\#}} \int_{\partial \mathcal{V}_0^{\#}} \frac{\partial \breve{J}}{\partial \breve{F}_{ij}} \breve{\varphi} N_j \, dS, \tag{4.A.2}$$

where N_j is the unit normal on the reference boundary $\partial \mathcal{V}_0^{\#}$. Notice that, in $\mathcal{V}_0^{\#}$, the scalar potential $\breve{\varphi}$ is defined by $(4.33)_2$ to be $\breve{\varphi} = -H_k X_k + \widetilde{\varphi}$ with $\widetilde{\varphi}$ periodic (i.e. takes identical values in opposite faces of the periodic boundary). Next, substituting this last expression in (4.A.2), we obtain

$$h_i = \frac{1}{J\mathcal{V}_0^{\#}} \left\{ \int_{\partial \mathcal{V}_0^{\#}} \frac{\partial \breve{J}}{\partial \breve{F}_{ij}} H_k X_k N_j \, dS - \int_{\partial \mathcal{V}_0^{\#}} \widetilde{\varphi} \frac{\partial \breve{J}}{\partial \breve{F}_{ij}} N_j \, dS \right\}, \tag{4.A.3}$$

where we recall that the effective H_k is constant. The second term in (4.A.3) is identically zero since $\widetilde{\varphi}$ is periodic and the term $N_j \partial \breve{J}/\partial \breve{F}_{ij}$ is anti-periodic (by simple use of the divergence-free property of $\partial \breve{J}/\partial \breve{F}_{ij}$). By employing the divergence theorem in the first term of (4.A.3) together with the divergence-free property of $\partial \breve{J}/\partial \breve{F}_{ij}$, we obtain

$$h_i = \frac{1}{J\mathcal{V}_0^{\#}} \int_{\mathcal{V}_0^{\#}} \frac{\partial \breve{J}}{\partial \breve{F}_{ij}} H_k \delta_{kj} \, dV = \frac{1}{J} \left[\frac{1}{\mathcal{V}_0^{\#}} \int_{\mathcal{V}_0^{\#}} \frac{\partial \breve{J}}{\partial \breve{F}_{ij}} \, dV \right] H_j. \tag{4.A.4}$$

Again, using the divergence-free property of $\partial \breve{J}/\partial \breve{F}_{ij}$, the last term in the square brackets is simply equal to the average $\partial J/\partial F_{ij}$, such that

$$h_i = \frac{1}{J} \frac{\partial J}{\partial F_{ij}} H_j = F_{ji}^{-1} H_j, \qquad \text{or} \qquad \mathbf{h} = \mathbf{F}^{-T} \mathbf{H}. \tag{4.A.5}$$

Appendix 4.B. Element force and stiffness matrices for TET-10 elements

This appendix provides the specific forms of the gradient matrices $[\breve{\mathbf{G}}^e_{\mathbf{u}}]$ and $[\breve{\mathbf{G}}^e_{\varphi}]$ and finally the element force and algorithmic tangent stiffness matrices for a 10-node tetrahedral (TET-10) element. The position of the nodes and the local coordinate system $\breve{\boldsymbol{\xi}} \equiv (\breve{\xi}_1, \breve{\xi}_2, \breve{\xi}_3)$ adhered to a TET-10 element are shown in Fig. 4.18. Furthermore, given the nodal reference coordinates $\mathbf{X}^{(n)}$, with $n = 1 - 10$, the global reference coordinate system $\mathbf{X}$ can be expressed in terms of $\breve{\boldsymbol{\xi}}$ so that $(4.51)_2$

$$\mathbf{X} = \sum_{n=1}^{10} \breve{N}^{(n)}(\breve{\boldsymbol{\xi}}) \mathbf{X}^{(n)}, \tag{4.B.1}$$

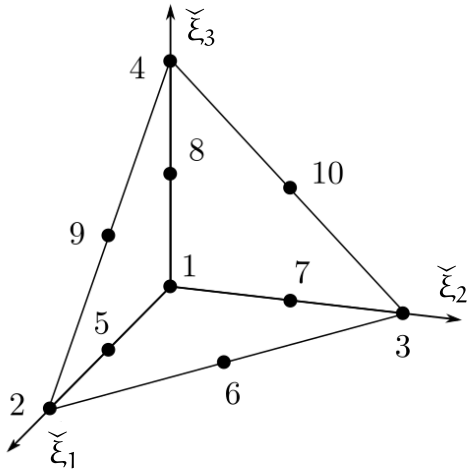

Figure 4.18: Local coordinate system along with the position of nodes in a 10-node tetrahedral (TET-10) element.

where $N^{(n)}(\xi)$ are scalar-valued element shape functions associated with the TET-10 elements. Consequently, the Jacobian matrix associated with the the last transformation is given by

$$\breve{\mathbb{J}} = \frac{\partial \mathbf{X}}{\partial \breve{\xi}} = \sum_{n=1}^{10} \frac{\partial \breve{N}^{(n)}}{\partial \breve{\xi}} \otimes \mathbf{X}^{(n)} \qquad \text{or,} \qquad \breve{\mathbb{J}}_{ij} = \sum_{n=1}^{10} \frac{\partial \breve{N}^{(n)}}{\partial \breve{\xi}_i} X_j^{(n)}. \tag{4.B.2}$$

Now, the unknown variables in the element e can be expressed in terms of the element dofs $[\breve{\mathbf{q}}_\tau^e]$, which is a column vector having the dimension 40×1. The element primary variables vector, namely, $\{\breve{u}_{1,\tau}(\breve{\xi}), \breve{u}_{2,\tau}(\breve{\xi}), \breve{u}_{3,\tau}(\breve{\xi}), \breve{\varphi}_\tau(\breve{\xi})\}^T$ is expressed in terms of $\breve{N}^{(n)}$ and $[\breve{\mathbf{q}}_\tau^e]$, such that

$$\begin{Bmatrix} \breve{u}_{1,\tau}(\breve{\xi}) \\ \breve{u}_{2,\tau}(\breve{\xi}) \\ \breve{u}_{3,\tau}(\breve{\xi}) \\ \breve{\varphi}_\tau(\breve{\xi}) \end{Bmatrix} = \begin{bmatrix} \breve{N}^{(1)}(\breve{\xi}) & 0 & 0 & 0 & \dots & \breve{N}^{(10)}(\breve{\xi}) & 0 & 0 & 0 \\ 0 & \breve{N}^{(1)}(\breve{\xi}) & 0 & 0 & \dots & 0 & \breve{N}^{(10)}(\breve{\xi}) & 0 & 0 \\ 0 & 0 & \breve{N}^{(1)}(\breve{\xi}) & 0 & \dots & 0 & 0 & \breve{N}^{(10)}(\breve{\xi}) & 0 \\ 0 & 0 & 0 & \breve{N}^{(1)}(\breve{\xi}) & \dots & 0 & 0 & 0 & \breve{N}^{(10)}(\breve{\xi}) \end{bmatrix} \begin{Bmatrix} \breve{u}_{1,\tau}^{(1)} \\ \breve{u}_{2,\tau}^{(1)} \\ \breve{u}_{3,\tau}^{(1)} \\ \breve{\varphi}_\tau^{(1)} \\ \vdots \\ \vdots \\ \breve{u}_{1,\tau}^{(10)} \\ \breve{u}_{2,\tau}^{(10)} \\ \breve{u}_{3,\tau}^{(10)} \\ \breve{\varphi}_\tau^{(10)} \end{Bmatrix},$$

which is equivalent to $(4.51)_1$. The derivatives of the primary variables with respect to the local

coordinate system is obtained from the last equation to be

$$\begin{Bmatrix} \partial\breve{u}_{1,\tau}/\partial\breve{\xi}_1 \\ \partial\breve{u}_{1,\tau}/\partial\breve{\xi}_2 \\ \partial\breve{u}_{1,\tau}/\partial\breve{\xi}_3 \\ \partial\breve{u}_{2,\tau}/\partial\breve{\xi}_1 \\ \partial\breve{u}_{2,\tau}/\partial\breve{\xi}_2 \\ \partial\breve{u}_{2,\tau}/\partial\breve{\xi}_3 \\ \partial\breve{u}_{3,\tau}/\partial\breve{\xi}_1 \\ \partial\breve{u}_{3,\tau}/\partial\breve{\xi}_2 \\ \partial\breve{u}_{3,\tau}/\partial\breve{\xi}_3 \\ \partial\breve{\varphi}_\tau/\partial\breve{\xi}_1 \\ \partial\breve{\varphi}_\tau/\partial\breve{\xi}_2 \\ \partial\breve{\varphi}_\tau/\partial\breve{\xi}_3 \end{Bmatrix} = \begin{bmatrix} \breve{\mathscr{G}}_1^{(1)} & 0 & 0 & 0 & \dots & \breve{\mathscr{G}}_1^{(10)} & 0 & 0 & 0 \\ \breve{\mathscr{G}}_2^{(1)} & 0 & 0 & 0 & \dots & \breve{\mathscr{G}}_2^{(10)} & 0 & 0 & 0 \\ \breve{\mathscr{G}}_3^{(1)} & 0 & 0 & 0 & \dots & \breve{\mathscr{G}}_3^{(10)} & 0 & 0 & 0 \\ 0 & \breve{\mathscr{G}}_1^{(1)} & 0 & 0 & \dots & 0 & \breve{\mathscr{G}}_1^{(10)} & 0 & 0 \\ 0 & \breve{\mathscr{G}}_2^{(1)} & 0 & 0 & \dots & 0 & \breve{\mathscr{G}}_2^{(10)} & 0 & 0 \\ 0 & \breve{\mathscr{G}}_3^{(1)} & 0 & 0 & \dots & 0 & \breve{\mathscr{G}}_3^{(10)} & 0 & 0 \\ 0 & 0 & \breve{\mathscr{G}}_1^{(1)} & 0 & \dots & 0 & 0 & \breve{\mathscr{G}}_1^{(10)} & 0 \\ 0 & 0 & \breve{\mathscr{G}}_2^{(1)} & 0 & \dots & 0 & 0 & \breve{\mathscr{G}}_2^{(10)} & 0 \\ 0 & 0 & \breve{\mathscr{G}}_3^{(1)} & 0 & \dots & 0 & 0 & \breve{\mathscr{G}}_3^{(10)} & 0 \\ 0 & 0 & 0 & \breve{\mathscr{G}}_1^{(1)} & \dots & 0 & 0 & 0 & \breve{\mathscr{G}}_1^{(10)} \\ 0 & 0 & 0 & \breve{\mathscr{G}}_2^{(1)} & \dots & 0 & 0 & 0 & \breve{\mathscr{G}}_2^{(10)} \\ 0 & 0 & 0 & \breve{\mathscr{G}}_3^{(1)} & \dots & 0 & 0 & 0 & \breve{\mathscr{G}}_3^{(10)} \end{bmatrix} \begin{Bmatrix} \breve{u}_{1,\tau}^{(1)} \\ \breve{u}_{2,\tau}^{(1)} \\ \breve{u}_{3,\tau}^{(1)} \\ \breve{\varphi}_\tau^{(1)} \\ \vdots \\ \vdots \\ \breve{u}_{1,\tau}^{(10)} \\ \breve{u}_{2,\tau}^{(10)} \\ \breve{u}_{3,\tau}^{(10)} \\ \breve{\varphi}_\tau^{(10)} \end{Bmatrix},$$

which we express in terms of compact notation, that is $[\partial\breve{\mathbf{q}}_\tau/\partial\breve{\boldsymbol{\xi}}] = [\breve{\mathscr{G}}][\breve{\mathbf{q}}_\tau^e]$ with $[\breve{\mathscr{G}}]$ given by a 12×40 matrix for the present case of 3D element having 40 dofs. Notice that, the notation $\breve{\mathscr{G}}_i^{(n)}$, used in the matrix $[\breve{\mathscr{G}}]$, essentially represents the derivative of $\breve{N}^{(n)}(\breve{\boldsymbol{\xi}})$ with respect to $\breve{\xi}_i$, so that $\breve{\mathscr{G}}_i^{(n)} = \partial\breve{N}^{(n)}/\partial\breve{\xi}_i$. Furthermore, we notice from (4.59) and (4.66) that the gradient of $\breve{\mathbf{q}}_\tau$ is taken with respect to the reference coordinate $\mathbf{X}$. Nevertheless, $[\partial\breve{\mathbf{q}}_\tau/\partial\mathbf{X}]$ can be expressed in terms of $[\partial\breve{\mathbf{q}}_\tau/\partial\breve{\boldsymbol{\xi}}]$ in terms of utilizing the Jacobian matrix, such that

$$\begin{Bmatrix} \partial\breve{u}_{1,\tau}/\partial X_1 \\ \partial\breve{u}_{1,\tau}/\partial X_2 \\ \partial\breve{u}_{1,\tau}/\partial X_3 \\ \partial\breve{u}_{2,\tau}/\partial X_1 \\ \partial\breve{u}_{2,\tau}/\partial X_2 \\ \partial\breve{u}_{2,\tau}/\partial X_3 \\ \partial\breve{u}_{3,\tau}/\partial X_1 \\ \partial\breve{u}_{3,\tau}/\partial X_2 \\ \partial\breve{u}_{3,\tau}/\partial X_3 \\ -\partial\breve{\varphi}_\tau/\partial X_1 \\ -\partial\breve{\varphi}_\tau/\partial X_2 \\ -\partial\breve{\varphi}_\tau/\partial X_3 \end{Bmatrix} = \begin{bmatrix} \breve{\mathbb{J}}_{11}^{-1} & \breve{\mathbb{J}}_{12}^{-1} & \breve{\mathbb{J}}_{13}^{-1} & 0 & 0 & 0 & 0 & 0 & 0 & 0 & 0 & 0 \\ \breve{\mathbb{J}}_{21}^{-1} & \breve{\mathbb{J}}_{22}^{-1} & \breve{\mathbb{J}}_{23}^{-1} & 0 & 0 & 0 & 0 & 0 & 0 & 0 & 0 & 0 \\ \breve{\mathbb{J}}_{31}^{-1} & \breve{\mathbb{J}}_{32}^{-1} & \breve{\mathbb{J}}_{33}^{-1} & 0 & 0 & 0 & 0 & 0 & 0 & 0 & 0 & 0 \\ 0 & 0 & 0 & \breve{\mathbb{J}}_{11}^{-1} & \breve{\mathbb{J}}_{12}^{-1} & \breve{\mathbb{J}}_{13}^{-1} & 0 & 0 & 0 & 0 & 0 & 0 \\ 0 & 0 & 0 & \breve{\mathbb{J}}_{21}^{-1} & \breve{\mathbb{J}}_{22}^{-1} & \breve{\mathbb{J}}_{23}^{-1} & 0 & 0 & 0 & 0 & 0 & 0 \\ 0 & 0 & 0 & \breve{\mathbb{J}}_{31}^{-1} & \breve{\mathbb{J}}_{32}^{-1} & \breve{\mathbb{J}}_{33}^{-1} & 0 & 0 & 0 & 0 & 0 & 0 \\ 0 & 0 & 0 & 0 & 0 & 0 & \breve{\mathbb{J}}_{11}^{-1} & \breve{\mathbb{J}}_{12}^{-1} & \breve{\mathbb{J}}_{13}^{-1} & 0 & 0 & 0 \\ 0 & 0 & 0 & 0 & 0 & 0 & \breve{\mathbb{J}}_{21}^{-1} & \breve{\mathbb{J}}_{22}^{-1} & \breve{\mathbb{J}}_{23}^{-1} & 0 & 0 & 0 \\ 0 & 0 & 0 & 0 & 0 & 0 & \breve{\mathbb{J}}_{31}^{-1} & \breve{\mathbb{J}}_{32}^{-1} & \breve{\mathbb{J}}_{33}^{-1} & 0 & 0 & 0 \\ 0 & 0 & 0 & 0 & 0 & 0 & 0 & 0 & 0 & -\breve{\mathbb{J}}_{11}^{-1} & -\breve{\mathbb{J}}_{12}^{-1} & -\breve{\mathbb{J}}_{13}^{-1} \\ 0 & 0 & 0 & 0 & 0 & 0 & 0 & 0 & 0 & -\breve{\mathbb{J}}_{11}^{-1} & -\breve{\mathbb{J}}_{12}^{-1} & -\breve{\mathbb{J}}_{13}^{-1} \\ 0 & 0 & 0 & 0 & 0 & 0 & 0 & 0 & 0 & -\breve{\mathbb{J}}_{11}^{-1} & -\breve{\mathbb{J}}_{12}^{-1} & -\breve{\mathbb{J}}_{13}^{-1} \end{bmatrix} \begin{Bmatrix} \partial\breve{u}_{1,\tau}/\partial\breve{\xi}_1 \\ \partial\breve{u}_{1,\tau}/\partial\breve{\xi}_2 \\ \partial\breve{u}_{1,\tau}/\partial\breve{\xi}_3 \\ \partial\breve{u}_{2,\tau}/\partial\breve{\xi}_1 \\ \partial\breve{u}_{2,\tau}/\partial\breve{\xi}_2 \\ \partial\breve{u}_{2,\tau}/\partial\breve{\xi}_3 \\ \partial\breve{u}_{3,\tau}/\partial\breve{\xi}_1 \\ \partial\breve{u}_{3,\tau}/\partial\breve{\xi}_2 \\ \partial\breve{u}_{3,\tau}/\partial\breve{\xi}_3 \\ \partial\breve{\varphi}_\tau/\partial\breve{\xi}_1 \\ \partial\breve{\varphi}_\tau/\partial\breve{\xi}_2 \\ \partial\breve{\varphi}_\tau/\partial\breve{\xi}_3 \end{Bmatrix}.$$

Again, the last can be expressed in compact form to be $[\partial\breve{\mathbf{q}}_\tau/\partial\mathbf{X}] = [\widetilde{\mathscr{J}}][\partial\breve{\mathbf{q}}_\tau/\partial\breve{\boldsymbol{\xi}}]$, where $[\widetilde{\mathscr{J}}]$ is a 12×12 matrix in terms of the inverse of $\breve{\mathbb{J}}$. The negative sign associated with the negative gradient of $\breve{\varphi}_\tau$ is taken care herein with the definition of $[\widetilde{\mathscr{J}}]$. Finally, the matrix $[\breve{\mathbf{G}}] = [\breve{\mathbf{G}}_{\mathbf{u}} \quad -\breve{\mathbf{G}}_\varphi]^T$ is given by,

$$[\breve{\mathbf{G}}] = [\widetilde{\mathscr{J}}][\breve{\mathscr{G}}], \tag{4.B.3}$$

which relates the $[\partial\breve{\mathbf{q}}_\tau/\partial\mathbf{X}]$ with the nodal dofs, so that

$$[\partial\breve{\mathbf{q}}_\tau/\partial\mathbf{X}] = [\breve{\mathbf{G}}][\breve{\mathbf{q}}_\tau^e] \tag{4.B.4}$$

Notably, here $[\breve{\mathbf{G}}]$ is a 12×40 matrix and $[\breve{\mathbf{q}}^e_\tau]$ is a 40×1 column of nodal dofs. The set of 10 shape functions in terms of the local coordinate $\breve{\xi}$ for the TET-10 elements read

$$\breve{N}^{(1)} = (1-\widehat{\xi})(1-2\widehat{\xi}),\quad \breve{N}^{(2)} = \breve{\xi}_1(2\breve{\xi}_1-1),\quad \breve{N}^{(3)} = \breve{\xi}_2(2\breve{\xi}_2-1),\quad \breve{N}^{(4)} = \breve{\xi}_3(2\breve{\xi}_3-1),\quad \breve{N}^{(5)} = 4\breve{\xi}_1(1-\widehat{\xi})$$
$$\breve{N}^{(6)} = 4\breve{\xi}_1\breve{\xi}_2,\qquad \breve{N}^{(7)} = 4\breve{\xi}_2(1-\widehat{\xi}),\quad \breve{N}^{(8)} = 4\breve{\xi}_3(1-\widehat{\xi}),\quad \breve{N}^{(9)} = 4\breve{\xi}_1\breve{\xi}_3,\qquad \breve{N}^{(10)} = 4\breve{\xi}_2\breve{\xi}_3,$$

where $\widehat{\xi} = \breve{\xi}_1 + \breve{\xi}_2 + \breve{\xi}_3$. The elements of the $[\breve{\mathscr{G}}]$ matrix can then be obtained via computing the derivatives of these shape functions with respect to $\breve{\xi}_i$.

Consequently, the element force vector $[\breve{\mathbf{f}}^e(\breve{\mathbf{q}}^e_\tau)]$ and algorithmic tangent stiffness matrix $[\breve{\mathbf{k}}^e(\breve{\mathbf{q}}^e_\tau)]$ for the choice of TET-10 elements follow from their definitions in (4.59) and (4.66), such that

$$\left[\breve{\mathbf{f}}^e(\breve{\mathbf{q}}^e_\tau)\right] = \sum_{\jmath=1}^{\mathtt{ngp}} \breve{\omega}^{(\jmath)} \det\left[\breve{\mathbb{J}}(\breve{\xi}^{(\jmath)})\right]\left[\breve{\mathbf{G}}(\breve{\xi}^{(\jmath)})\right]^{\mathsf{T}}\left[\partial\breve{\mathcal{W}}_\tau/\partial\breve{\mathbf{q}}_\tau(\breve{\xi}^{(\jmath)},\breve{\mathbf{q}}^e_\tau)\right] \tag{4.B.5}$$

and

$$\left[\breve{\mathbf{k}}^e(\breve{\mathbf{q}}^e_\tau)\right] = \sum_{\jmath=1}^{\mathtt{ngp}} \breve{\omega}^{(\jmath)} \det\left[\breve{\mathbb{J}}(\breve{\xi}^{(\jmath)})\right]\left[\breve{\mathbf{G}}(\breve{\xi}^{(\jmath)})\right]^{\mathsf{T}}\left[\breve{\mathcal{L}}_{\mathtt{Algo},\tau}(\breve{\xi}^{(\jmath)},\breve{\mathbf{q}}^e_\tau)\right]\left[\breve{\mathbf{G}}(\breve{\xi}^{(\jmath)})\right], \tag{4.B.6}$$

respectively. Here the matrices $[\breve{\mathbb{J}}(\breve{\xi}^{(\jmath)})]$ and $[\breve{\mathbf{G}}(\breve{\xi}^{(\jmath)})]$ are the Jacobian and gradient matrix, respectively, evaluated at $\breve{\xi} = \breve{\xi}^{(\jmath)}$ and $\mathtt{ngp}$ is the number of Gauss points and $\breve{\omega}^{(\jmath)}$ and $\breve{\xi}^{(\jmath)}$ are the weighting factor and local coordinate, associated with the $\jmath^{\text{th}}$ Gauss point. As discussed by Zienkiewicz and Taylor (2000, p. 223-224), a four-point Gauss quadrature is adequate to ensure convergence of the implicit FE solver. Thus, we choose $\mathtt{ngp} = 4$ and the corresponding $\breve{\omega}^{(\jmath)}$ and $\breve{\xi}^{(\jmath)}$ from the Table 9.3 of (Zienkiewicz and Taylor, 2000). Exceptionally, we employ a 1-point Gauss quadrature scheme to integrate the force and stiffness contributions from the volumetric potential involving the bulk modulus G_i'. This is done to ensure the numerical results remain free from the *volumetric locking*, which arises due to the high bulk modulus $\mathsf{G}_i' \gg \mathsf{G}_i$ if integrated with the 4-point Gauss quadrature. Notably, the 1-point quadrature rule can also be found in the Table 9.3 of (Zienkiewicz and Taylor, 2000).

It remains to provide the explicit forms of $\left[\partial\breve{\mathcal{W}}^{\mathrm{H}}_\tau/\partial\breve{\mathbf{q}}_\tau(\breve{\xi}^{(\jmath)},\breve{\mathbf{q}}^e_\tau)\right]$ and $\left[\breve{\mathcal{L}}_{\mathtt{Algo},\tau}(\breve{\xi}^{(\jmath)},\breve{\mathbf{q}}^e_\tau)\right]$. Notice from (4.59) and (4.66) that these matrices are expressed in terms of $\breve{\mathbf{F}}_\tau$, $\breve{\mathbf{H}}_\tau$ and $\breve{\mathbf{H}}^{\mathrm{r}}_\tau$. At the $\jmath^{\text{th}}$ Gauss point, $\breve{\mathbf{F}}^{(\jmath)}_\tau$ and $\breve{\mathbf{H}}^{(\jmath)}_\tau$ are computed in terms of, respectively, the nodal $\breve{\mathbf{u}}^{(\mathfrak{n})}_\tau$ and $\breve{\varphi}^{(\mathfrak{n})}_\tau$ along with the Gauss point locations $\breve{\xi}^{(\jmath)}$ via (4.B.4). Specifically, $\breve{\mathbf{F}}^{(\jmath)}_\tau$ is expressed in terms of $[\partial\breve{\mathfrak{u}}_{\mathfrak{m},\tau}/\partial X_{\mathfrak{n}}]_{\breve{\xi}=\breve{\xi}^{(\jmath)}}$, such that

$$\breve{\mathrm{F}}^{(\jmath)}_{\mathrm{ij},\tau} = \delta_{\mathrm{ij}} + \left[\frac{\partial\breve{\mathfrak{u}}_{\mathrm{i},\tau}}{\partial X_{\mathrm{j}}}\right]_{\breve{\xi}=\breve{\xi}^{(\jmath)}}. \tag{4.B.7}$$

Similarly, $\breve{\mathbf{H}}^{(\jmath)}_\tau$ is expressed in terms of $[\partial\breve{\varphi}_\tau/\partial X_{\mathfrak{n}}]_{\breve{\xi}=\breve{\xi}^{(\jmath)}}$, obtained from the left-hand-side column vector of (4.B.4), so that

$$\breve{\mathrm{H}}^{(\jmath)}_{\mathrm{i},\tau} = -\left[\frac{\partial\breve{\varphi}_\tau}{\partial X_{\mathrm{i}}}\right]_{\breve{\xi}=\breve{\xi}^{(\jmath)}}. \tag{4.B.8}$$

Finally, provided $\breve{\mathbf{H}}^{(\jmath)}_\tau$, the *local update* in the remanent field is computed via Algorithm 4.1, which takes $\breve{\mathbf{H}}^{(\jmath)}_\tau$ and $\breve{\mathbf{H}}^{\mathrm{r},(\jmath)}_{\mathrm{t}}$ as the input parameters to yield $\breve{\mathbf{H}}^{\mathrm{r},(\jmath)}_\tau$. Notice that, $\breve{\mathbf{H}}^{\mathrm{r},(\jmath)}_\tau$ is stored at each Gauss point after each converged global Newton iteration, which is then used as $\breve{\mathbf{H}}^{\mathrm{r},(\jmath)}_{\mathrm{t}}$ during the subsequent iteration. In practice, $\breve{\mathbf{H}}^{\mathrm{r},(\jmath)}_\tau$ is stored by defining 12 state-dependet variables (`SVARS`) per

element in the user-element (UEL), that is developed to solve implicitly the global FE equation (4.53) in ABAQUS (2018).

Thus, $\left[\partial\breve{\mathcal{W}}_\tau^{\mathrm{H}}/\partial\breve{\mathbf{q}}_\tau(\breve{\boldsymbol{\xi}}^{(\jmath)},\breve{\mathbf{q}}_\tau^{e})\right]$ and $\left[\breve{\mathcal{L}}_{\mathtt{Algo},\tau}(\breve{\boldsymbol{\xi}}^{(\jmath)},\breve{\mathbf{q}}_\tau^{e})\right]$ are computed in terms of $\breve{\mathbf{F}}_\tau^{(\jmath)}$, $\breve{\mathbf{H}}_\tau^{(\jmath)}$ and $\breve{\mathbf{H}}_\tau^{\mathrm{r},(\jmath)}$, such that

$$\begin{aligned}\left[\partial\breve{\mathcal{W}}_\tau^{\mathrm{H}}/\partial\breve{\mathbf{q}}_\tau(\breve{\boldsymbol{\xi}}^{(\jmath)},\breve{\mathbf{q}}_\tau^{e})\right] \equiv \Bigg\{&\frac{\partial\breve{\mathcal{W}}_\tau^{\mathrm{H}}}{\partial\breve{\mathrm{F}}_{\tau,11}},\frac{\partial\breve{\mathcal{W}}_\tau^{\mathrm{H}}}{\partial\breve{\mathrm{F}}_{\tau,12}},\frac{\partial\breve{\mathcal{W}}_\tau^{\mathrm{H}}}{\partial\breve{\mathrm{F}}_{\tau,13}},\frac{\partial\breve{\mathcal{W}}_\tau^{\mathrm{H}}}{\partial\breve{\mathrm{F}}_{\tau,21}},\frac{\partial\breve{\mathcal{W}}_\tau^{\mathrm{H}}}{\partial\breve{\mathrm{F}}_{\tau,22}},\frac{\partial\breve{\mathcal{W}}_\tau^{\mathrm{H}}}{\partial\breve{\mathrm{F}}_{\tau,23}},\\ &\frac{\partial\breve{\mathcal{W}}_\tau^{\mathrm{H}}}{\partial\breve{\mathrm{F}}_{\tau,31}},\frac{\partial\breve{\mathcal{W}}_\tau^{\mathrm{H}}}{\partial\breve{\mathrm{F}}_{\tau,32}},\frac{\partial\breve{\mathcal{W}}_\tau^{\mathrm{H}}}{\partial\breve{\mathrm{F}}_{\tau,33}},\frac{\partial\breve{\mathcal{W}}_\tau^{\mathrm{H}}}{\partial\breve{\mathrm{H}}_{\tau,1}},\frac{\partial\breve{\mathcal{W}}_\tau^{\mathrm{H}}}{\partial\breve{\mathrm{H}}_{\tau,2}},\frac{\partial\breve{\mathcal{W}}_\tau^{\mathrm{H}}}{\partial\breve{\mathrm{H}}_{\tau,3}}\Bigg\}^{\mathrm{T}}\Bigg|_{\breve{\boldsymbol{\xi}}=\breve{\boldsymbol{\xi}}^{(\jmath)}},\end{aligned} \tag{4.B.9}$$

which is a 12×1 vector evaluated at the Gauss points. Consequently, element force vector of dimension 40×1 is obtained via substituting the last and (4.B.3) into (4.B.5). Similarly, the matrix $\left[\breve{\mathcal{L}}_{\mathtt{Algo},\tau}(\breve{\boldsymbol{\xi}}^{(\jmath)},\breve{\mathbf{q}}_\tau^{e})\right]$ having dimension 12×12 is given by

$$\left[\breve{\mathcal{L}}_{\mathtt{Algo},\tau}(\breve{\boldsymbol{\xi}}^{(\jmath)},\breve{\mathbf{q}}_\tau^{e})\right] \equiv \begin{bmatrix} (\breve{\mathcal{L}}^{\mathbf{FF}}_{\mathtt{Algo},\tau})_{1111} & (\breve{\mathcal{L}}^{\mathbf{FF}}_{\mathtt{Algo},\tau})_{1112} & \cdots & (\breve{\mathcal{L}}^{\mathbf{FH}}_{\mathtt{Algo},\tau})_{112} & (\breve{\mathcal{L}}^{\mathbf{FH}}_{\mathtt{Algo},\tau})_{113}\\ (\breve{\mathcal{L}}^{\mathbf{FF}}_{\mathtt{Algo},\tau})_{1211} & (\breve{\mathcal{L}}^{\mathbf{FF}}_{\mathtt{Algo},\tau})_{1212} & \cdots & (\breve{\mathcal{L}}^{\mathbf{FH}}_{\mathtt{Algo},\tau})_{122} & (\breve{\mathcal{L}}^{\mathbf{FH}}_{\mathtt{Algo},\tau})_{123}\\ \vdots & \vdots & \ddots & \vdots & \vdots\\ (\breve{\mathcal{L}}^{\mathbf{HF}}_{\mathtt{Algo},\tau})_{211} & (\breve{\mathcal{L}}^{\mathbf{HF}}_{\mathtt{Algo},\tau})_{212} & \cdots & (\breve{\mathcal{L}}^{\mathbf{HH}}_{\mathtt{Algo},\tau})_{22} & (\breve{\mathcal{L}}^{\mathbf{HH}}_{\mathtt{Algo},\tau})_{23}\\ (\breve{\mathcal{L}}^{\mathbf{HF}}_{\mathtt{Algo},\tau})_{311} & (\breve{\mathcal{L}}^{\mathbf{HF}}_{\mathtt{Algo},\tau})_{312} & \cdots & (\breve{\mathcal{L}}^{\mathbf{HH}}_{\mathtt{Algo},\tau})_{32} & (\breve{\mathcal{L}}^{\mathbf{HH}}_{\mathtt{Algo},\tau})_{33}\end{bmatrix}_{\breve{\boldsymbol{\xi}}=\breve{\boldsymbol{\xi}}^{(\jmath)}}. \tag{4.B.10}$$

Notice that $\left[\breve{\mathcal{L}}_{\mathtt{Algo},\tau}(\breve{\boldsymbol{\xi}}^{(\jmath)},\breve{\mathbf{q}}_\tau^{e})\right]$ is not symmetric in its general form. Nevertheless, we observe from (4.60) that, for purely energetic s-MREs $\left[\breve{\mathcal{L}}_{\mathtt{Algo},\tau}(\breve{\boldsymbol{\xi}}^{(\jmath)},\breve{\mathbf{q}}_\tau^{e})\right]$ becomes symmetric. Also, some specific choice of the microscopic potential energy $\breve{\mathcal{W}}_{\mathrm{i}}^{\mathrm{H}}$ are found to yield a symmetric $\left[\breve{\mathcal{L}}_{\mathtt{Algo},\tau}(\breve{\boldsymbol{\xi}}^{(\jmath)},\breve{\mathbf{q}}_\tau^{e})\right]$ for the general dissipative case. However, this is not a general observation.

***Derivatives in* (4.B.9) *and* (4.B.10):** Notice that the computations of (4.B.9) and (4.B.10) require the first and second derivatives of the incremental energy $\breve{\mathcal{W}}_\tau^{\mathrm{H}}$ with respect to $\breve{\mathbf{F}}_\tau$ and $\breve{\mathbf{H}}_\tau$. The first derivative is given in terms of the index notation by (for clarity in the notations we henceforth suppress the subscript τ)

$$\frac{\partial\breve{\mathcal{W}}^{\mathrm{H}}}{\partial\breve{\mathrm{F}}_{\mathrm{ij}}}=\frac{\partial\breve{\mathcal{W}}^{\mathrm{H}}}{\partial\breve{\mathrm{F}}_{\mathrm{ij}}}=\sum_{\mathrm{p}=1}^{3}\frac{\partial\breve{\mathcal{W}}^{\mathrm{H}}}{\partial\breve{\mathrm{I}}_{\mathrm{p}}}\frac{\partial\breve{\mathrm{I}}_{\mathrm{p}}}{\partial\breve{\mathrm{F}}_{\mathrm{ij}}}+\left\{\frac{\partial\breve{\mathcal{W}}^{\mathrm{H}}}{\partial\breve{\mathrm{I}}_5^{\mathrm{H}}}\frac{\partial\breve{\mathrm{I}}_5^{\mathrm{H}}}{\partial\breve{\mathrm{F}}_{\mathrm{ij}}}+\frac{\partial\breve{\mathcal{W}}^{\mathrm{H}}}{\partial\breve{\mathrm{I}}_5^{\mathrm{HHr}}}\frac{\partial\breve{\mathrm{I}}_5^{\mathrm{HHr}}}{\partial\breve{\mathrm{F}}_{\mathrm{ij}}}+\frac{\partial\breve{\mathcal{W}}^{\mathrm{H}}}{\partial\breve{\mathrm{I}}_5^{\mathrm{Hr}}}\frac{\partial\breve{\mathrm{I}}_5^{\mathrm{Hr}}}{\partial\breve{\mathrm{F}}_{\mathrm{ij}}}\right\} \tag{4.B.11}$$

and

$$\frac{\partial\breve{\mathcal{W}}^{\mathrm{H}}}{\partial\breve{\mathrm{H}}_{\mathrm{i}}}=\frac{\partial\breve{\mathcal{W}}^{\mathrm{H}}}{\partial\breve{\mathrm{H}}_{\mathrm{i}}}=\sum_{\mathrm{q}=4}^{5}\left\{\frac{\partial\breve{\mathcal{W}}^{\mathrm{H}}}{\partial\breve{\mathrm{I}}_{\mathrm{q}}^{\mathrm{H}}}\frac{\partial\breve{\mathrm{I}}_{\mathrm{q}}^{\mathrm{H}}}{\partial\breve{\mathrm{H}}_{\mathrm{i}}}+\frac{\partial\breve{\mathcal{W}}^{\mathrm{H}}}{\partial\breve{\mathrm{I}}_{\mathrm{q}}^{\mathrm{HHr}}}\frac{\partial\breve{\mathrm{I}}_{\mathrm{q}}^{\mathrm{HHr}}}{\partial\breve{\mathrm{H}}_{\mathrm{i}}}+\frac{\partial\breve{\mathcal{W}}^{\mathrm{H}}}{\partial\breve{\mathrm{I}}_{\mathrm{q}}^{\mathrm{Hr}}}\frac{\partial\breve{\mathrm{I}}_{\mathrm{q}}^{\mathrm{Hr}}}{\partial\breve{\mathrm{H}}_{\mathrm{i}}}\right\}, \tag{4.B.12}$$

where we drop the $\breve{\mathrm{I}}_4^{\mathrm{H}}$, $\breve{\mathrm{I}}_4^{\mathrm{HHr}}$ and $\breve{\mathrm{I}}_4^{\mathrm{Hr}}$ terms from the former and the mechanical invariant dependence from the latter since they are independent of $\breve{\mathbf{F}}_\tau$ and $\breve{\mathbf{H}}_\tau$, respectively. The second derivatives can then be computed leading to the expressions in terms of index notations

$$\begin{aligned}\breve{\mathcal{L}}^{\mathbf{FF}}_{\mathrm{ijkl}}=\frac{\partial^2\breve{\mathcal{W}}^{\mathrm{H}}}{\partial\breve{\mathrm{F}}_{\mathrm{ij}}\partial\breve{\mathrm{F}}_{\mathrm{kl}}}=&\sum_{\mathrm{p}=1}^{3}\left\{\frac{\partial\breve{\mathcal{W}}^{\mathrm{H}}}{\partial\breve{\mathrm{I}}_{\mathrm{p}}}\frac{\partial^2\breve{\mathrm{I}}_{\mathrm{p}}}{\partial\breve{\mathrm{F}}_{\mathrm{ij}}\partial\breve{\mathrm{F}}_{\mathrm{kl}}}\right\}+\sum_{\mathrm{p}=1}^{3}\sum_{\mathrm{q}=1}^{3}\left\{\frac{\partial^2\breve{\mathcal{W}}^{\mathrm{H}}}{\partial\breve{\mathrm{I}}_{\mathrm{p}}\partial\breve{\mathrm{I}}_{\mathrm{q}}}\frac{\partial\breve{\mathrm{I}}_{\mathrm{p}}}{\partial\breve{\mathrm{F}}_{\mathrm{ij}}}\frac{\partial\breve{\mathrm{I}}_{\mathrm{q}}}{\partial\breve{\mathrm{F}}_{\mathrm{kl}}}\right\}+\left\{\frac{\partial\breve{\mathcal{W}}^{\mathrm{H}}}{\partial\breve{\mathrm{I}}_5^{\mathrm{H}}}\frac{\partial^2\breve{\mathrm{I}}_5^{\mathrm{H}}}{\partial\breve{\mathrm{F}}_{\mathrm{ij}}\partial\breve{\mathrm{F}}_{\mathrm{kl}}}+\frac{\partial\breve{\mathcal{W}}^{\mathrm{H}}}{\partial\breve{\mathrm{I}}_5^{\mathrm{HHr}}}\right.\\ &\left.\frac{\partial^2\breve{\mathrm{I}}_5^{\mathrm{HHr}}}{\partial\breve{\mathrm{F}}_{\mathrm{ij}}\partial\breve{\mathrm{F}}_{\mathrm{kl}}}+\frac{\partial\breve{\mathcal{W}}^{\mathrm{H}}}{\partial\breve{\mathrm{I}}_5^{\mathrm{Hr}}}\frac{\partial^2\breve{\mathrm{I}}_5^{\mathrm{Hr}}}{\partial\breve{\mathrm{F}}_{\mathrm{ij}}\partial\breve{\mathrm{F}}_{\mathrm{kl}}}+\frac{\partial^2\breve{\mathcal{W}}^{\mathrm{H}}}{\partial(\breve{\mathrm{I}}_5^{\mathrm{H}})^2}\frac{\partial\breve{\mathrm{I}}_5^{\mathrm{H}}}{\partial\breve{\mathrm{F}}_{\mathrm{ij}}}\frac{\partial\breve{\mathrm{I}}_5^{\mathrm{H}}}{\partial\breve{\mathrm{F}}_{\mathrm{kl}}}+\frac{\partial^2\breve{\mathcal{W}}^{\mathrm{H}}}{\partial(\breve{\mathrm{I}}_5^{\mathrm{HHr}})^2}\frac{\partial\breve{\mathrm{I}}_5^{\mathrm{HHr}}}{\partial\breve{\mathrm{F}}_{\mathrm{ij}}}\frac{\partial\breve{\mathrm{I}}_5^{\mathrm{HHr}}}{\partial\breve{\mathrm{F}}_{\mathrm{kl}}}+\frac{\partial^2\breve{\mathcal{W}}^{\mathrm{H}}}{\partial(\breve{\mathrm{I}}_5^{\mathrm{Hr}})^2}\frac{\partial\breve{\mathrm{I}}_5^{\mathrm{Hr}}}{\partial\breve{\mathrm{F}}_{\mathrm{ij}}}\frac{\partial\breve{\mathrm{I}}_5^{\mathrm{Hr}}}{\partial\breve{\mathrm{F}}_{\mathrm{kl}}}\right\},\end{aligned} \tag{4.B.13}$$

$$\breve{\mathcal{L}}^{\mathbf{FH}}_{ijk} = \frac{\partial^2 \breve{W}^{H}}{\partial \breve{F}_{ij} \partial \breve{H}_k} = \Big\{ \frac{\partial \breve{W}^{H}}{\partial \breve{I}^{H}_5} \frac{\partial^2 \breve{I}^{H}_5}{\partial \breve{F}_{ij} \partial \breve{H}_k} + \frac{\partial \breve{W}^{H}}{\partial \breve{I}^{HHr}_5} \frac{\partial^2 \breve{I}^{HHr}_5}{\partial \breve{F}_{ij} \partial \breve{H}_k} + \frac{\partial \breve{W}^{H}}{\partial \breve{I}^{Hr}_5} \frac{\partial^2 \breve{I}^{Hr}_5}{\partial \breve{F}_{ij} \partial \breve{H}_k} + \frac{\partial^2 \breve{W}^{H}}{\partial (\breve{I}^{H}_5)^2} \frac{\partial \breve{I}^{H}_5}{\partial \breve{F}_{ij}} \frac{\partial \breve{I}^{H}_5}{\partial \breve{H}_k} + \frac{\partial^2 \breve{W}^{H}}{\partial (\breve{I}^{HHr}_5)^2} \frac{\partial \breve{I}^{HHr}_5}{\partial \breve{F}_{ij}} \frac{\partial \breve{I}^{HHr}_5}{\partial \breve{H}_k} + \frac{\partial^2 \breve{W}^{H}}{\partial (\breve{I}^{Hr}_5)^2} \frac{\partial \breve{I}^{Hr}_5}{\partial \breve{F}_{ij}} \frac{\partial \breve{I}^{Hr}_5}{\partial \breve{H}_k} \Big\}, \tag{4.B.14}$$

$$\breve{\mathcal{L}}^{\mathbf{HH}}_{ij} = \frac{\partial^2 \breve{W}^{H}}{\partial \breve{H}_i \partial \breve{H}_j} = \sum_{q=4}^{5} \Big\{ \frac{\partial \breve{W}^{H}}{\partial \breve{I}^{H}_q} \frac{\partial^2 \breve{I}^{H}_q}{\partial \breve{H}_i \partial \breve{H}_j} + \frac{\partial \breve{W}^{H}}{\partial \breve{I}^{HHr}_q} \frac{\partial^2 \breve{I}^{HHr}_q}{\partial \breve{H}_i \partial \breve{H}_j} + \frac{\partial \breve{W}^{H}}{\partial \breve{I}^{Hr}_q} \frac{\partial^2 \breve{I}^{Hr}_q}{\partial \breve{H}_i \partial \breve{H}_j} + \frac{\partial^2 \breve{W}^{H}}{\partial (\breve{I}^{H}_q)^2} \frac{\partial \breve{I}^{H}_q}{\partial \breve{H}_i} \frac{\partial \breve{I}^{H}_q}{\partial \breve{H}_j} + \frac{\partial^2 \breve{W}^{H}}{\partial (\breve{I}^{HHr}_q)^2} \frac{\partial \breve{I}^{HHr}_q}{\partial \breve{H}_i} \frac{\partial \breve{I}^{HHr}_q}{\partial \breve{H}_j} + \frac{\partial^2 \breve{W}^{H}}{\partial (\breve{I}^{Hr}_q)^2} \frac{\partial \breve{I}^{Hr}_q}{\partial \breve{H}_i} \frac{\partial \breve{I}^{Hr}_q}{\partial \breve{H}_j} \Big\}. \tag{4.B.15}$$

Notice that, we only show the second-order tangent derivatives those are relevant to the proposed constitutive model given by equation (4.14). Thus, all the second-order derivatives of $\breve{W}^{H}$ with respect to two different $\breve{I}^{(\cdot)}_5$ and $\breve{I}^{(\cdot)}_4$ are dropped henceforth. Also, note that the second-order derivative of $\breve{W}^{H}$ with respect to $\breve{I}_3$ and $\breve{I}^{H}_5$ is dropped from (4.B.13), since it vanish identically, given the form of $\breve{W}^{H}$ in (4.14).

Since the partial derivatives commute, one can set $\breve{\mathcal{L}}^{\mathbf{HF}}_{ijk} = \breve{\mathcal{L}}^{\mathbf{FH}}_{ijk}$. However, we note from (4.65) that the algorithmic $(\breve{\mathcal{L}}^{\mathbf{HF}}_{\mathtt{Algo}})_{ijk} \neq (\breve{\mathcal{L}}^{\mathbf{FH}}_{\mathtt{Algo}})_{ijk}$. The algorithmic consistent linearization (4.60) leads to two additional tensors of second derivatives given by

$$\breve{\mathcal{L}}^{\mathbf{H^r F}}_{ijk} = \frac{\partial^2 \breve{W}^{H}}{\partial \breve{F}_{ij} \partial \breve{H}^{r}_k} = \Big\{ \frac{\partial \breve{W}^{H}}{\partial \breve{I}^{H}_5} \frac{\partial^2 \breve{I}^{H}_5}{\partial \breve{F}_{ij} \partial \breve{H}^{r}_k} + \frac{\partial \breve{W}^{H}}{\partial \breve{I}^{HHr}_5} \frac{\partial^2 \breve{I}^{HHr}_5}{\partial \breve{F}_{ij} \partial \breve{H}^{r}_k} + \frac{\partial \breve{W}^{H}}{\partial \breve{I}^{Hr}_5} \frac{\partial^2 \breve{I}^{Hr}_5}{\partial \breve{F}_{ij} \partial \breve{H}^{r}_k} + \frac{\partial^2 \breve{W}^{H}}{\partial (\breve{I}^{H}_5)^2} \frac{\partial \breve{I}^{H}_5}{\partial \breve{F}_{ij}} \frac{\partial \breve{I}^{H}_5}{\partial \breve{H}^{r}_k} + \frac{\partial^2 \breve{W}^{H}}{\partial (\breve{I}^{HHr}_5)^2} \frac{\partial \breve{I}^{HHr}_5}{\partial \breve{F}_{ij}} \frac{\partial \breve{I}^{HHr}_5}{\partial \breve{H}^{r}_k} + \frac{\partial^2 \breve{W}^{H}}{\partial (\breve{I}^{Hr}_5)^2} \frac{\partial \breve{I}^{Hr}_5}{\partial \breve{F}_{ij}} \frac{\partial \breve{I}^{Hr}_5}{\partial \breve{H}^{r}_k} \Big\}, \tag{4.B.16}$$

$$\breve{\mathcal{L}}^{\mathbf{H^r H}}_{ij} = \frac{\partial^2 \breve{W}^{H}}{\partial \breve{H}_i \partial \breve{H}^{r}_j} = \sum_{q=4}^{5} \Big\{ \frac{\partial \breve{W}^{H}}{\partial \breve{I}^{H}_q} \frac{\partial^2 \breve{I}^{H}_q}{\partial \breve{H}_i \partial \breve{H}^{r}_j} + \frac{\partial \breve{W}^{H}}{\partial \breve{I}^{HHr}_q} \frac{\partial^2 \breve{I}^{HHr}_q}{\partial \breve{H}_i \partial \breve{H}^{r}_j} + \frac{\partial \breve{W}^{H}}{\partial \breve{I}^{Hr}_q} \frac{\partial^2 \breve{I}^{Hr}_q}{\partial \breve{H}_i \partial \breve{H}^{r}_j} + \frac{\partial^2 \breve{W}^{H}}{\partial (\breve{I}^{H}_q)^2} \frac{\partial \breve{I}^{H}_q}{\partial \breve{H}_i} \frac{\partial \breve{I}^{H}_q}{\partial \breve{H}^{r}_j} + \frac{\partial^2 \breve{W}^{H}}{\partial (\breve{I}^{HHr}_q)^2} \frac{\partial \breve{I}^{HHr}_q}{\partial \breve{H}_i} \frac{\partial \breve{I}^{HHr}_q}{\partial \breve{H}^{r}_j} + \frac{\partial^2 \breve{W}^{H}}{\partial (\breve{I}^{Hr}_q)^2} \frac{\partial \breve{I}^{Hr}_q}{\partial \breve{H}_i} \frac{\partial \breve{I}^{Hr}_q}{\partial \breve{H}^{r}_j} \Big\}. \tag{4.B.17}$$

Since the dissipation potential (4.19) is defined only in terms of the material rate of $\breve{\mathbf{H}}^{r}_{\tau}$, we observe no $\breve{D}^{H}$ to appear in (4.B.11) – (4.B.17). Also, the evaluation of $\breve{\mathcal{L}}^{(\cdot)(\cdot)}_{\mathtt{Algo}}$ necessitates the evaluation of the local remanent b-field $\breve{\mathbf{B}}^{r}$ and its first variation thereafter. The former is given by (4.11), which now reads

$$\breve{B}^{r}_i = -\frac{\partial \breve{W}^{H}}{\partial \breve{H}^{r}_i} = -\sum_{q=4}^{5} \Big\{ \frac{\partial \breve{W}^{H}}{\partial \breve{I}^{H}_q} \frac{\partial \breve{I}^{H}_q}{\partial \breve{H}^{r}_i} + \frac{\partial \breve{W}^{H}}{\partial \breve{I}^{HHr}_q} \frac{\partial \breve{I}^{HHr}_q}{\partial \breve{H}^{r}_i} + \frac{\partial \breve{W}^{H}}{\partial \breve{I}^{Hr}_q} \frac{\partial \breve{I}^{Hr}_q}{\partial \breve{H}^{r}_i} \Big\}. \tag{4.B.18}$$

A variation in $\breve{\mathbf{B}}^{r}$ is then given by (4.62), such that

$$\Delta \breve{B}^{r}_i = -\breve{\mathcal{L}}^{\mathbf{H^r F}}_{ijk} \Delta \breve{F}_{jk} - \breve{\mathcal{L}}^{\mathbf{H^r H}}_{ij} \Delta \breve{H}_j - \breve{\mathcal{L}}^{\mathbf{H^r H^r}}_{ij} \Delta \breve{H}^{r}_j, \tag{4.B.19}$$

where we use the commutative property of the subsequent partial derivatives and $\breve{\mathcal{L}}_{ij}^{\mathbf{H}^r\mathbf{H}^r}$ is given by

$$\breve{\mathcal{L}}_{ij}^{\mathbf{H}^r\mathbf{H}^r} = \frac{\partial^2 \breve{W}^H}{\partial \breve{H}_i^r \partial \breve{H}_j^r} = \sum_{q=4}^{5} \left\{ \frac{\partial \breve{W}^H}{\partial \breve{I}_q^H} \frac{\partial^2 \breve{I}_q^H}{\partial \breve{H}_i^r \partial \breve{H}_j^r} + \frac{\partial \breve{W}^H}{\partial \breve{I}_q^{HHr}} \frac{\partial^2 \breve{I}_q^{HHr}}{\partial \breve{H}_i^r \partial \breve{H}_j^r} + \frac{\partial \breve{W}^H}{\partial \breve{I}_q^{Hr}} \frac{\partial^2 \breve{I}_q^{Hr}}{\partial \breve{H}_i^r \partial \breve{H}_j^r} + \right.$$
$$\left. \frac{\partial^2 \breve{W}^H}{\partial (\breve{I}_q^H)^2} \frac{\partial \breve{I}_q^H}{\partial \breve{H}_i^r} \frac{\partial \breve{I}_q^H}{\partial \breve{H}_j^r} + \frac{\partial^2 \breve{W}^H}{\partial (\breve{I}_q^{HHr})^2} \frac{\partial \breve{I}_q^{HHr}}{\partial \breve{H}_i^r} \frac{\partial \breve{I}_q^{HHr}}{\partial \breve{H}_j^r} + \frac{\partial^2 \breve{W}^H}{\partial (\breve{I}_q^{Hr})^2} \frac{\partial \breve{I}_q^{Hr}}{\partial \breve{H}_i^r} \frac{\partial \breve{I}_q^{Hr}}{\partial \breve{H}_j^r} \right\}. \tag{4.B.20}$$

The tensors (4.B.11) – (4.B.20) are evaluated at each individual Gauss points and subsequently used in (4.B.5) and (4.B.6) to finally compute the element force vector and algorithmic tangent stiffness. We write the expressions (4.B.11) – (4.B.20) explicitly in the ABAQUS UEL routine. The algorithmic tangent stiffness tensors are then numerically computed via substituting (4.B.13) – (4.B.17) and (4.B.20) into (4.65). The scalar derivatives of $\breve{W}^H$ with respect to the invariants in (4.B.11) – (4.B.20) are straightforward to evaluate. On the other hand, the expressions for the first and second derivatives of the invariants in Table 4.1 with respect to $\breve{\mathbf{F}}$, $\breve{\mathbf{H}}$ and $\breve{\mathbf{H}}^r$ are rather involved. These derivatives are provided in the following.

Derivatives of the invariants with respect to $\breve{\mathbf{F}}$, $\breve{\mathbf{H}}$ and $\breve{\mathbf{H}}^r$: For ease in the numerical implementations, we provide the derivatives in terms of the index notations. First, the derivative of the purely mechanical invariants with respect to $\breve{F}_{ij}$ are given by

$$\frac{\partial \breve{I}_1}{\partial \breve{F}_{ij}} = 2\breve{F}_{ij}, \qquad \frac{\partial \breve{I}_2}{\partial \breve{F}_{ij}} = 2(\breve{I}_1 \breve{F}_{ij} - \breve{F}_{ia}\breve{F}_{ab}\breve{F}_{bj}), \qquad \frac{\partial \breve{I}_3}{\partial \breve{F}_{ij}} = \frac{\partial \breve{J}}{\partial \breve{F}_{ij}} = \breve{J}\breve{F}^{-1}_{ji}.$$

Evidently, the derivatives of the mechanical invariants with respect to $\breve{H}_i$ and $\breve{H}_i^r$ vanish identically and hence, are not provided explicitly. The derivatives of the magneto-mechanical invariants are now given by

$$\frac{\partial \breve{I}_4^H}{\partial \breve{F}_{ij}} = 0, \qquad \frac{\partial \breve{I}_4^{HHr}}{\partial \breve{F}_{ij}} = 0, \qquad \frac{\partial \breve{I}_4^{Hr}}{\partial \breve{F}_{ij}} = 0,$$

$$\frac{\partial \breve{I}_4^H}{\partial \breve{H}_i} = 2\breve{H}_i, \qquad \frac{\partial \breve{I}_4^{HHr}}{\partial \breve{H}_i} = \breve{H}_i^r, \qquad \frac{\partial \breve{I}_4^{Hr}}{\partial \breve{H}_i} = 0, \qquad \frac{\partial \breve{I}_4^H}{\partial \breve{H}_i^r} = 0, \qquad \frac{\partial \breve{I}_4^{HHr}}{\partial \breve{H}_i^r} = \breve{H}_i, \qquad \frac{\partial \breve{I}_4^{Hr}}{\partial \breve{H}_i^r} = 2\breve{H}_i^r,$$

$$\frac{\partial \breve{I}_5^H}{\partial \breve{F}_{ij}} = -2\breve{F}^{-T}_{ia}\breve{H}_a\breve{F}^{-1}_{jb}\breve{F}^{-T}_{bc}\breve{H}_c, \quad \frac{\partial \breve{I}_5^{HHr}}{\partial \breve{F}_{ij}} = -\breve{F}^{-T}_{ia}\breve{H}_a\breve{F}^{-1}_{jb}\breve{F}^{-T}_{bc}\breve{H}^r_c - \breve{F}^{-T}_{ia}\breve{H}^r_a\breve{F}^{-1}_{jb}\breve{F}^{-T}_{bc}\breve{H}_c, \quad \frac{\partial \breve{I}_5^{Hr}}{\partial \breve{F}_{ij}} = -2\breve{F}^{-T}_{ia}\breve{H}^r_a\breve{F}^{-1}_{jb}\breve{F}^{-T}_{bc}\breve{H}^r_c,$$

$$\frac{\partial \breve{I}_5^H}{\partial \breve{H}_i} = 2\breve{F}^{-1}_{ia}\breve{F}^{-T}_{ab}\breve{H}_b, \quad \frac{\partial \breve{I}_5^{HHr}}{\partial \breve{H}_i} = \breve{F}^{-1}_{ia}\breve{F}^{-T}_{ab}\breve{H}^r_b, \quad \frac{\partial \breve{I}_5^{Hr}}{\partial \breve{H}_i} = 0, \quad \frac{\partial \breve{I}_5^H}{\partial \breve{H}_i^r} = 0, \quad \frac{\partial \breve{I}_5^{HHr}}{\partial \breve{H}_i^r} = \breve{F}^{-1}_{ia}\breve{F}^{-T}_{ab}\breve{H}_b, \quad \frac{\partial \breve{I}_5^{Hr}}{\partial \breve{H}_i^r} = 2\breve{F}^{-1}_{ia}\breve{F}^{-T}_{ab}\breve{H}^r_b.$$

Subsequently, the second derivative of the mechanical invariants with respect to $\breve{F}_{ij}$ are given by

$$\frac{\partial^2 \breve{I}_1}{\partial \breve{F}_{ij}\partial \breve{F}_{kl}} = 2\delta_{ik}\delta_{jl}, \qquad \frac{\partial^2 \breve{J}}{\partial \breve{F}_{ij}\partial \breve{F}_{kl}} = \breve{J}(\breve{F}^{-1}_{ji}\breve{F}^{-1}_{lk} - \breve{F}^{-1}_{jk}\breve{F}^{-1}_{li}),$$
$$\frac{\partial^2 \breve{I}_2}{\partial \breve{F}_{ij}\partial \breve{F}_{kl}} = 2(2\breve{F}_{ij}\breve{F}_{kl} + \breve{I}_1\delta_{ik}\delta_{jl} - \breve{F}_{il}\breve{F}_{kj} - \delta_{ik}\breve{F}_{aj}\breve{F}_{al} - \delta_{jl}\breve{F}_{ib}\breve{F}_{kb}).$$

Notice that all the second order derivatives of all $\breve{I}_4^H$, $\breve{I}_4^{HHr}$ and $\breve{I}_4^{Hr}$ with respect to $\breve{F}_{ij}$ vanish identically.

Next, the second order derivatives of the $\breve{I}_5^{H}, \breve{I}_5^{HHr}$ and $\breve{I}_5^{Hr}$ invariants are given by

$$\frac{\partial^2 \breve{I}_5^{H}}{\partial \breve{F}_{ij} \partial \breve{F}_{kl}} = 2\Big\{ \breve{F}_{il}^{-T} \big(\breve{F}_{ja}^{-1} \breve{F}_{ab}^{-T} \breve{H}_b\big) \big(\breve{F}_{kc}^{-T} \breve{H}_c\big) + \big(\breve{F}_{ia}^{-T} \breve{H}_a\big) \big(\breve{F}_{lb}^{-1} \breve{F}_{bc}^{-T} \breve{H}_c\big) \breve{F}_{jk}^{-1} + \big(\breve{F}_{ia}^{-T} \breve{H}_a\big) \big(\breve{F}_{kb}^{-T} \breve{H}_b\big) \big(\breve{F}_{jc}^{-1} \breve{F}_{cl}^{-T}\big) \Big\},$$

$$\begin{aligned}\frac{\partial^2 \breve{I}_5^{HHr}}{\partial \breve{F}_{ij} \partial \breve{F}_{kl}} = {} & \breve{F}_{il}^{-T} \big(\breve{F}_{ja}^{-1} \breve{F}_{ab}^{-T} \breve{H}_b\big) \big(\breve{F}_{kc}^{-T} \breve{H}_c^r\big) + \big(\breve{F}_{ia}^{-T} \breve{H}_a\big) \big(\breve{F}_{lb}^{-1} \breve{F}_{bc}^{-T} \breve{H}_c^r\big) \breve{F}_{jk}^{-1} + \big(\breve{F}_{ia}^{-T} \breve{H}_a\big) \big(\breve{F}_{kb}^{-T} \breve{H}_b^r\big) \big(\breve{F}_{jc}^{-1} \breve{F}_{cl}^{-T}\big) + \\ & \breve{F}_{il}^{-T} \big(\breve{F}_{ja}^{-1} \breve{F}_{ab}^{-T} \breve{H}_b^r\big) \big(\breve{F}_{kc}^{-T} \breve{H}_c\big) + \big(\breve{F}_{ia}^{-T} \breve{H}_a^r\big) \big(\breve{F}_{lb}^{-1} \breve{F}_{bc}^{-T} \breve{H}_c\big) \breve{F}_{jk}^{-1} + \big(\breve{F}_{ia}^{-T} \breve{H}_a^r\big) \big(\breve{F}_{kb}^{-T} \breve{H}_b\big) \big(\breve{F}_{jc}^{-1} \breve{F}_{cl}^{-T}\big),\end{aligned}$$

$$\frac{\partial^2 \breve{I}_5^{Hr}}{\partial \breve{F}_{ij} \partial \breve{F}_{kl}} = 2\Big\{ \breve{F}_{il}^{-T} \big(\breve{F}_{ja}^{-1} \breve{F}_{ab}^{-T} \breve{H}_b^r\big) \big(\breve{F}_{kc}^{-T} \breve{H}_c^r\big) + \big(\breve{F}_{ia}^{-T} \breve{H}_a^r\big) \big(\breve{F}_{lb}^{-1} \breve{F}_{bc}^{-T} \breve{H}_c^r\big) \breve{F}_{jk}^{-1} + \big(\breve{F}_{ia}^{-T} \breve{H}_a^r\big) \big(\breve{F}_{kb}^{-T} \breve{H}_b^r\big) \big(\breve{F}_{jc}^{-1} \breve{F}_{cl}^{-T}\big) \Big\},$$

$$\frac{\partial^2 \breve{I}_5^{H}}{\partial \breve{F}_{ij} \partial \breve{H}_k} = -2\Big\{ \breve{F}_{ik}^{-T} \big(\breve{F}_{jb}^{-1} \breve{F}_{bc}^{-T} \breve{H}_c\big) + \big(\breve{F}_{ia}^{-T} \breve{H}_a\big) \big(\breve{F}_{jb}^{-1} \breve{F}_{bk}^{-T}\big) \Big\}, \qquad \frac{\partial^2 \breve{I}_5^{H}}{\partial \breve{F}_{ij} \partial \breve{H}_k^r} = 0,$$

$$\frac{\partial^2 \breve{I}_5^{HHr}}{\partial \breve{F}_{ij} \partial \breve{H}_k} = -\Big\{ \breve{F}_{ik}^{-T} \big(\breve{F}_{jb}^{-1} \breve{F}_{bc}^{-T} \breve{H}_c^r\big) + \big(\breve{F}_{ia}^{-T} \breve{H}_a^r\big) \big(\breve{F}_{jb}^{-1} \breve{F}_{bk}^{-T}\big) \Big\},$$

$$\frac{\partial^2 \breve{I}_5^{HHr}}{\partial \breve{F}_{ij} \partial \breve{H}_k^r} = -\Big\{ \breve{F}_{ik}^{-T} \big(\breve{F}_{jb}^{-1} \breve{F}_{bc}^{-T} \breve{H}_c\big) + \big(\breve{F}_{ia}^{-T} \breve{H}_a\big) \big(\breve{F}_{jb}^{-1} \breve{F}_{bk}^{-T}\big) \Big\},$$

$$\frac{\partial^2 \breve{I}_5^{Hr}}{\partial \breve{F}_{ij} \partial \breve{H}_k} = 0, \qquad \frac{\partial^2 \breve{I}_5^{Hr}}{\partial \breve{F}_{ij} \partial \breve{H}_k^r} = -2\Big\{ \breve{F}_{ik}^{-T} \big(\breve{F}_{jb}^{-1} \breve{F}_{bc}^{-T} \breve{H}_c^r\big) + \big(\breve{F}_{ia}^{-T} \breve{H}_a^r\big) \big(\breve{F}_{jb}^{-1} \breve{F}_{bk}^{-T}\big) \Big\}.$$

Finally, the second-order derivatives of $\breve{I}_4^{H}, \breve{I}_4^{HHr}, \breve{I}_4^{Hr}$ and $\breve{I}_5^{H}, \breve{I}_5^{HHr}, \breve{I}_5^{Hr}$ invariants with respect to $\breve{H}_j$ and $\breve{H}_j^r$ read

$$\begin{aligned}
&\frac{\partial^2 \breve{I}_4^{H}}{\partial \breve{H}_i \partial \breve{H}_j} = 2\delta_{ij}, && \frac{\partial^2 \breve{I}_4^{HHr}}{\partial \breve{H}_i \partial \breve{H}_j} = 0, && \frac{\partial^2 \breve{I}_4^{Hr}}{\partial \breve{H}_i \partial \breve{H}_j} = 0, \\
&\frac{\partial^2 \breve{I}_4^{H}}{\partial \breve{H}_i^r \partial \breve{H}_j} = 0, && \frac{\partial^2 \breve{I}_4^{HHr}}{\partial \breve{H}_i^r \partial \breve{H}_j} = \delta_{ij}, && \frac{\partial^2 \breve{I}_4^{Hr}}{\partial \breve{H}_i^r \partial \breve{H}_j} = 0, \\
&\frac{\partial^2 \breve{I}_4^{H}}{\partial \breve{H}_i^r \partial \breve{H}_j^r} = 0, && \frac{\partial^2 \breve{I}_4^{HHr}}{\partial \breve{H}_i^r \partial \breve{H}_j^r} = 0, && \frac{\partial^2 \breve{I}_4^{Hr}}{\partial \breve{H}_i^r \partial \breve{H}_j^r} = 2\delta_{ij}, \\
&\frac{\partial^2 \breve{I}_5^{H}}{\partial \breve{H}_i \partial \breve{H}_j} = 2\breve{F}_{ia}^{-1} \breve{F}_{aj}^{-T}, && \frac{\partial^2 \breve{I}_5^{HHr}}{\partial \breve{H}_i \partial \breve{H}_j} = 0, && \frac{\partial^2 \breve{I}_5^{Hr}}{\partial \breve{H}_i \partial \breve{H}_j} = 0, \\
&\frac{\partial^2 \breve{I}_5^{H}}{\partial \breve{H}_i^r \partial \breve{H}_j} = 0, && \frac{\partial^2 \breve{I}_5^{HHr}}{\partial \breve{H}_i^r \partial \breve{H}_j} = \breve{F}_{ia}^{-1} \breve{F}_{aj}^{-T}, && \frac{\partial^2 \breve{I}_5^{Hr}}{\partial \breve{H}_i^r \partial \breve{H}_j} = 0, \\
&\frac{\partial^2 \breve{I}_5^{H}}{\partial \breve{H}_i^r \partial \breve{H}_j^r} = 0, && \frac{\partial^2 \breve{I}_5^{HHr}}{\partial \breve{H}_i^r \partial \breve{H}_j^r} = 0, && \frac{\partial^2 \breve{I}_5^{Hr}}{\partial \breve{H}_i^r \partial \breve{H}_j^r} = 2\breve{F}_{ia}^{-1} \breve{F}_{aj}^{-T}.
\end{aligned}$$

Appendix 4.C. Residue and derivatives in local Newton iterations

This appendix provides the expressions for the vector ($\breve{\mathfrak{R}}^{\breve{\mathbf{H}}^{\mathrm{r}}}$) and scalar ($\breve{\mathfrak{R}}^{\breve{\Phi}^{\mathrm{r}}}$) residues associated with the computation of local increment in $\breve{\mathbf{H}}^{\mathrm{r}}$ via Algorithm 4.1. Notice from (4.69) and (4.70) that both $\breve{\mathfrak{R}}^{\breve{\mathbf{H}}^{\mathrm{r}}}$ and $\breve{\mathfrak{R}}^{\breve{\Phi}^{\mathrm{r}}}$ require the expression of $\breve{\mathbf{B}}^{\mathrm{r}}_{\tau}$ in terms of $\breve{\mathbf{H}}_{\tau}$ and $\breve{\mathbf{H}}^{\mathrm{r,trial}}_{\tau}$. The expression for $\breve{\mathbf{B}}^{\mathrm{r}}_{\tau}$ is obtained via substituting (4.14) into (4.B.18) along with the relevant derivatives of the invariants given in Appendix 4.B, such that

$$\breve{\mathbf{B}}^{\mathrm{r}}_{\tau}(\breve{\mathbf{H}}_{\tau},\breve{\mathbf{H}}^{\mathrm{r,trial}}_{\tau}) = -\frac{\mu^{e}_{\mathrm{p}}}{2}\big(\mathbf{I}+\mathbb{C}^{-1}_{\tau}\big)\breve{\mathbf{H}}_{\tau} - \frac{\mu_0 m^{s}_{\mathrm{p}}}{\chi_{\mathrm{p}}}(f^{\mathrm{h}}_{\mathrm{p}})'\left(\frac{|\breve{\mathbf{H}}^{\mathrm{r,trial}}_{\tau}|}{m^{s}_{\mathrm{p}}}\right)\frac{\breve{\mathbf{H}}^{\mathrm{r,trial}}_{\tau}}{|\breve{\mathbf{H}}^{\mathrm{r,trial}}_{\tau}|}. \tag{4.C.1}$$

Since the evolution of $\breve{\mathbf{H}}^{\mathrm{r}}$ is only relevant in the particle phase, the material properties of the hard magnetic particles are used in (4.C.1). Consequently, the residues are computed via (4.69) and (4.70). In turn, the local Newton iterative solver (4.71) requires computing the derivatives of $\breve{\mathfrak{R}}^{\breve{\mathbf{H}}^{\mathrm{r}}}$ and $\breve{\mathfrak{R}}^{\breve{\Phi}^{\mathrm{r}}}$ with respect to $\breve{\mathbf{H}}^{\mathrm{r,trial}}_{\tau}$ and $\breve{\gamma}^{\mathrm{H,trial}}_{\mathrm{i}}$, so that

$$\breve{\mathfrak{K}}^{\breve{\mathbf{H}}^{\mathrm{r}}\breve{\mathbf{H}}^{\mathrm{r}}} \equiv \frac{\partial\breve{\mathfrak{R}}^{\breve{\mathbf{H}}^{\mathrm{r}}}}{\partial\breve{\mathbf{H}}^{\mathrm{r,trial}}_{\tau}} = \mathbf{I} - 2\breve{\gamma}^{\mathrm{H,trial}}_{\mathrm{i}}\frac{\partial\breve{\mathbf{B}}^{\mathrm{r}}_{\tau}}{\partial\breve{\mathbf{H}}^{\mathrm{r,trial}}_{\tau}}, \qquad \breve{\mathfrak{K}}^{\breve{\mathbf{H}}^{\mathrm{r}}\breve{\Phi}^{\mathrm{r}}} \equiv \frac{\partial\breve{\mathfrak{R}}_{\breve{\mathbf{H}}^{\mathrm{r}}}}{\partial\breve{\gamma}^{\mathrm{H,trial}}_{\mathrm{i}}} = -2\breve{\mathbf{B}}^{\mathrm{r}}_{\tau},$$
$$\breve{\mathfrak{K}}^{\breve{\Phi}^{\mathrm{r}}\breve{\mathbf{H}}^{\mathrm{r}}} \equiv \frac{\partial\breve{\mathfrak{R}}_{\breve{\Phi}^{\mathrm{r}}}}{\partial\breve{\mathbf{H}}^{\mathrm{r,trial}}_{\tau}} = 2\frac{\partial\breve{\mathbf{B}}^{\mathrm{r}}_{\tau}}{\partial\breve{\mathbf{H}}^{\mathrm{r,trial}}_{\tau}}\cdot\breve{\mathbf{B}}^{\mathrm{r}}_{\tau}, \qquad \breve{\mathfrak{K}}^{\breve{\Phi}^{\mathrm{r}}\breve{\Phi}^{\mathrm{r}}} \equiv \frac{\partial\breve{\mathfrak{R}}_{\breve{\Phi}^{\mathrm{r}}}}{\partial\breve{\gamma}^{\mathrm{H,trial}}_{\mathrm{i}}} = 0.$$

Note that the last set of derivatives require the evaluation of the derivative of $\breve{\mathbf{B}}^{\mathrm{r}}_{\tau}$ with respect to $\breve{\mathbf{H}}^{\mathrm{r,trial}}_{\tau}$, which from (4.C.1) reads

$$\frac{\partial\breve{\mathbf{B}}^{\mathrm{r}}_{\tau}}{\partial\breve{\mathbf{H}}^{\mathrm{r,trial}}_{\tau}} = -\frac{\mu_0}{\chi_{\mathrm{p}}}\left\{(f^{\mathrm{h}}_{\mathrm{p}})''\left(\frac{|\breve{\mathbf{H}}^{\mathrm{r,trial}}_{\tau}|}{m^{s}_{\mathrm{p}}}\right) - \frac{m^{s}_{\mathrm{p}}}{|\breve{\mathbf{H}}^{\mathrm{r,trial}}_{\tau}|}(f^{\mathrm{h}}_{\mathrm{p}})'\left(\frac{|\breve{\mathbf{H}}^{\mathrm{r,trial}}_{\tau}|}{m^{s}_{\mathrm{p}}}\right)\right\}\left\{\frac{\breve{\mathbf{H}}^{\mathrm{r,trial}}_{\tau}}{|\breve{\mathbf{H}}^{\mathrm{r,trial}}_{\tau}|}\otimes\frac{\breve{\mathbf{H}}^{\mathrm{r,trial}}_{\tau}}{|\breve{\mathbf{H}}^{\mathrm{r,trial}}_{\tau}|}\right\}. \tag{4.C.2}$$

Finally, the linear set of equations to compute the increments $\Delta\breve{\mathbf{H}}^{\mathrm{r,trial}}_{\tau}$ and $\breve{\gamma}^{\mathrm{H,trial}}_{\mathrm{i}}$ reads from (4.71) to be

$$\begin{bmatrix}\breve{\mathfrak{K}}^{\breve{\mathbf{H}}^{\mathrm{r}}\breve{\mathbf{H}}^{\mathrm{r}}}_{11} & \breve{\mathfrak{K}}^{\breve{\mathbf{H}}^{\mathrm{r}}\breve{\mathbf{H}}^{\mathrm{r}}}_{12} & \breve{\mathfrak{K}}^{\breve{\mathbf{H}}^{\mathrm{r}}\breve{\mathbf{H}}^{\mathrm{r}}}_{13} & \breve{\mathfrak{K}}^{\breve{\mathbf{H}}^{\mathrm{r}}\breve{\Phi}^{\mathrm{r}}}_{1}\\ \breve{\mathfrak{K}}^{\breve{\mathbf{H}}^{\mathrm{r}}\breve{\mathbf{H}}^{\mathrm{r}}}_{21} & \breve{\mathfrak{K}}^{\breve{\mathbf{H}}^{\mathrm{r}}\breve{\mathbf{H}}^{\mathrm{r}}}_{22} & \breve{\mathfrak{K}}^{\breve{\mathbf{H}}^{\mathrm{r}}\breve{\mathbf{H}}^{\mathrm{r}}}_{23} & \breve{\mathfrak{K}}^{\breve{\mathbf{H}}^{\mathrm{r}}\breve{\Phi}^{\mathrm{r}}}_{2}\\ \breve{\mathfrak{K}}^{\breve{\mathbf{H}}^{\mathrm{r}}\breve{\mathbf{H}}^{\mathrm{r}}}_{31} & \breve{\mathfrak{K}}^{\breve{\mathbf{H}}^{\mathrm{r}}\breve{\mathbf{H}}^{\mathrm{r}}}_{32} & \breve{\mathfrak{K}}^{\breve{\mathbf{H}}^{\mathrm{r}}\breve{\mathbf{H}}^{\mathrm{r}}}_{33} & \breve{\mathfrak{K}}^{\breve{\mathbf{H}}^{\mathrm{r}}\breve{\Phi}^{\mathrm{r}}}_{3}\\ \breve{\mathfrak{K}}^{\breve{\Phi}^{\mathrm{r}}\breve{\mathbf{H}}^{\mathrm{r}}}_{1} & \breve{\mathfrak{K}}^{\breve{\Phi}^{\mathrm{r}}\breve{\mathbf{H}}^{\mathrm{r}}}_{2} & \breve{\mathfrak{K}}^{\breve{\Phi}^{\mathrm{r}}\breve{\mathbf{H}}^{\mathrm{r}}}_{3} & \breve{\mathfrak{K}}^{\breve{\Phi}^{\mathrm{r}}\breve{\Phi}^{\mathrm{r}}}\end{bmatrix}\begin{Bmatrix}\Delta(\breve{\mathbf{H}}^{\mathrm{r,trial}}_{\tau})_1\\ \Delta(\breve{\mathbf{H}}^{\mathrm{r,trial}}_{\tau})_2\\ \Delta(\breve{\mathbf{H}}^{\mathrm{r,trial}}_{\tau})_3\\ \Delta\breve{\gamma}^{\mathrm{H,trial}}_{\mathrm{i}}\end{Bmatrix} = -\begin{Bmatrix}\breve{\mathfrak{R}}^{\breve{\mathbf{H}}^{\mathrm{r}}}_{1}\\ \breve{\mathfrak{R}}^{\breve{\mathbf{H}}^{\mathrm{r}}}_{2}\\ \breve{\mathfrak{R}}^{\breve{\mathbf{H}}^{\mathrm{r}}}_{3}\\ \breve{\mathfrak{R}}^{\breve{\Phi}^{\mathrm{r}}}\end{Bmatrix}. \tag{4.C.3}$$

The last is solved in the UEL at each Gauss point in order to implement the Algorithm 4.1.

Chapter

5 Microstructurally-guided Continuum models for s-MREs

Chapter summary: *Explicit, phenomenological models for the s-MREs are proposed here in both* $\mathbf{F}-\mathbf{H}$ *and* $\mathbf{F}-\mathbf{B}$ *(or equivalently,* $\mathbf{F}-\mathbf{h}$ *and* $\mathbf{F}-\mathbf{b}$*) variable spaces. These models are constructed so that they recover the same purely mechanical, initial and saturation magnetization and initial magnetostriction response of the analytical homogenization model of Lefèvre et al. (2017) for all sets of material parameters, such as the particle volume fraction and the material properties of the constituents (e.g., the matrix shear modulus, the magnetic susceptibility and magnetization saturation of the particles). The functional forms of the proposed phenomenological models are based on simple energy functions with small number of calibration parameters thus allowing for the description of magnetoelastic solids in a more general setting. This, in turn, makes them suitable to probe a large set of experimental or numerical results. The models of the present study show that in isotropic MREs, the entire magnetization response is insensitive to the shear modulus of the matrix material even when the latter ranges between 0.003-0.3MPa, while the magnetostriction response is extremely sensitive to the mechanical properties of the matrix material.*

Chapter content

In this chapter, we present two distinct families of theoretical models; an "implicit" one obtained by a rigorous homogenization analysis (Lefèvre and Lopez-Pamies, 2016; Lefèvre et al., 2017) and "explicit" homogenization-guided phenomenological models, which are calibrated to recover the implicit homogenization estimates for a very large range of material parameters. In particular, motivated by microscopic images of standard MREs (Semisalova et al., 2013), we consider in this study

only the case of spherical mechanically stiff but magnetically soft inclusions that are isotropically and uniformly distributed in a non-magnetic matrix phase. Nevertheless, the same ideas may apply to other composites such as polymers comprising ferrofluid inclusions (Lefèvre et al., 2017). Notice that the macroscopic constitutive relations for the s-MREs are given by (4.41). Nonetheless, the macroscopic constitutive relations in the Lagrangian (Eulerian) setting can equivalently be obtained from the macroscopic Clausius-Duhem inequalities (2.64) and (2.63) ((2.36) and (2.35)) (Kankanala and Triantafyllidis, 2004). Since similar to the microscopic model (4.22), the potential energy functions are defined in terms of the invariants, it can be equivalently expressed in terms of both, the Lagrangian ($\mathbf{H}$ or $\mathbf{B}$) and Eulerian ($\mathbf{h}$ or $\mathbf{b}$) magnetic fields.

In the original work of Lefèvre et al. (2017), the variational homogenization-based models for both $W^{\mathrm{H}}(\mathbf{F},\mathbf{H})$ and $W^{\mathrm{B}}(\mathbf{F},\mathbf{B})$ were proposed. In the first case, an explicit estimate has been proposed for linear magnetic particles (i.e. linear local magnetic response of the particles) and an implicit one for nonlinearly saturating ones. However, only an explicit model for linear magnetic particles has been proposed for $W^{\mathrm{B}}(\mathbf{F},\mathbf{B})$, which resulted by a partial Legendre-Fenchel transform of the corresponding $W^{\mathrm{H}}(\mathbf{F},\mathbf{H})$ model.

To fill this gap and simplify possible numerical implementations of such models in general purpose finite element codes, we propose simple explicit energy densities $W^{\mathrm{H}}(\mathbf{F},\mathbf{H})$ and $W^{\mathrm{B}}(\mathbf{F},\mathbf{B})$ for nonlinearly saturating magnetic particles that are calibrated by using the analytical explicit and implicit homogenization models. Note, however, that the free parameters in the phenomenological models can be calibrated independently by available experiments or other numerical calculations, thus offering a well-designed yet simple energy description for MREs.

Specifically, the analytical solutions of Lefèvre et al. (2017) consider an incompressible I_1-dependent matrix phase and mechanically rigid but magnetically soft particles without magnetic hysteresis. Thus, for the incompressible matrix phase, which is also magnetically inert (i.e., $\chi_{\mathrm{m}}=0$), (4.22) along with (4.15) and (4.23) reduce to (Lefèvre et al., 2017)

$$\breve{W}_{\mathrm{m}}(\breve{\mathbf{F}},\breve{\mathbf{H}})=\begin{cases}\breve{\rho}_0\breve{\psi}_{\mathrm{mech,m}}(\breve{\mathrm{I}}_1)-\dfrac{\mu_0}{2}\breve{\mathrm{I}}_5^{\mathrm{H}} & \text{if}\quad \breve{\mathrm{J}}=1,\\ +\infty & \text{otherwise.}\end{cases}\tag{5.1}$$

In the special case of an incompressible Neo-Hookean material, $\breve{\rho}_0\breve{\psi}_{\mathrm{mech,m}}(\breve{\mathrm{I}}_1)=\mathrm{G}_{\mathrm{m}}(\breve{\mathrm{I}}_1-3)/2$, with G_{m} denoting the shear modulus of the matrix. Here, the energy associated with the magneto-active mechanically rigid particles (i.e., with shear modulus $\mathrm{G}_{\mathrm{p}}=+\infty$) is given by

$$\breve{W}_{\mathrm{p}}^{\mathrm{H}}(\breve{\mathbf{F}},\breve{\mathbf{H}})=\begin{cases}-\mathcal{S}_{\mathrm{p}}(\breve{\mathrm{I}}_5^{\mathrm{H}}) & \text{if}\quad \breve{\mathrm{J}}=1,\\ +\infty & \text{otherwise.}\end{cases}\tag{5.2}$$

where $\breve{\mathrm{I}}_5^{\mathrm{H}}$ is the local invariant and has been defined in Table 4.1, while the function $\mathcal{S}(\breve{\mathrm{I}}_5^{\mathrm{H}})$ is any nonlinear saturation function. In the present study, we report results for the Langevin-type saturation function defined in (4.23) for $\breve{\mathrm{J}}=1$, such that

$$\mathcal{S}_{\mathrm{p}}(\breve{\mathrm{I}}_5^{\mathrm{H}})=\frac{\mu_0}{2}\breve{\mathrm{I}}_5^{\mathrm{H}}+\frac{\mu_0(m_{\mathrm{p}}^{\mathrm{s}})^2}{3\chi_{\mathrm{p}}}\left\{\ln\left[\sinh\left(\frac{3\chi_{\mathrm{p}}}{m_{\mathrm{p}}^{\mathrm{s}}}\sqrt{\breve{\mathrm{I}}_5^{\mathrm{H}}}\right)\right]-\ln\left[\frac{3\chi_{\mathrm{p}}}{m_{\mathrm{p}}^{\mathrm{s}}}\sqrt{\breve{\mathrm{I}}_5^{\mathrm{H}}}\right]\right\}.\tag{5.3}$$

Here, χ_{p} and $m_{\mathrm{p}}^{\mathrm{s}}$ are the magnetic susceptibility and magnetization saturation of the particles, respec-

tively. While the analytical homogenization model of Lefèvre et al. (2017) only provides $W^{H}(\mathbf{F},\mathbf{H})$ and $W^{B}(\mathbf{F},\mathbf{B})$ for an incompressible material, the proposed phenomenological models also provide the compressible versions of $W^{H}(\mathbf{F},\mathbf{H})$ and $W^{B}(\mathbf{F},\mathbf{B})$, which, in turn, ease the FE computations considerably.

5.1 Analytical homogenization solutions

Given the above-described local energies for the matrix and the particle phase by (5.1) and (5.2), respectively, the homogenized energy reads (Lefèvre et al., 2017)

$$W^{H}(\mathbf{F},\mathbf{H}) = \begin{cases} \rho_0\psi_{mech}(\mathbf{F}) - c\,\mathcal{S}_p(\mathcal{I}_5^H) + \dfrac{c\,\xi}{2}\mathcal{I}_5^H + \dfrac{1}{2}\left(\nu(\xi) - z(\xi)\right) I_4^H - \dfrac{\nu(\xi)}{2} I_5^H & \text{if} \quad J = 1 \\ +\infty & \text{otherwise.} \end{cases} \tag{5.4}$$

In this expression, the purely mechanical effective energy is given by (Lopez-Pamies et al., 2013)

$$\psi_{mech}(\mathbf{F}) = (1-c)\breve{\psi}_{mech,m}(\mathcal{I}_1), \tag{5.5}$$

where $\breve{\psi}_{mech,m}$ is defined in (4.15) for a Neo-Hookean material, c denotes the particle volume fraction,

$$I_1 = \mathrm{tr}(\mathbf{F}^T\mathbf{F}), \qquad I_4^H = \mathbf{H}\cdot\mathbf{H} = \mathbf{F}^T\mathbf{h}\cdot\mathbf{F}^T\mathbf{h}, \qquad I_5^H = \mathbf{F}^{-T}\mathbf{H}\cdot\mathbf{F}^{-T}\mathbf{H} = \mathbf{h}\cdot\mathbf{h} \tag{5.6}$$

are the macroscopic invariants and

$$\mathcal{I}_1 = \frac{I_1 - 3}{(1-c)^{7/2}} + 3, \quad \mathcal{I}_5^H = -\frac{54c(1-c)(\xi-\mu_0)\mu_0^2}{5[(2+c)\mu_0 + (1-c)\xi]^3} I_4^H + \frac{9[(10-c+6c^2)\mu_0 + (5+c-6c^2)\xi]\mu_0^2}{5[(2+c)\mu_0+(1-c)\xi]^3} I_5^H. \tag{5.7}$$

The effective coefficients $\nu(\xi)$ and $z(\xi)$ are given by

$$\nu(\xi) = \mu_0 + \frac{3c(10+2c+3c^2)(\xi-\mu_0)\mu_0^2}{5[(2+c)\mu_0+(1-c)\xi]^2} + \frac{3c(1-c)(5+3c)(\xi-\mu_0)\mu_0\xi}{5[(2+c)\mu_0+(1-c)\xi]^2} \tag{5.8}$$

and

$$z(\xi) = \mu_0 + \frac{3c\mu_0(\xi-\mu_0)}{[(2+c)\mu_0+(1-c)\xi]}, \tag{5.9}$$

respectively. The variables ν and z depend also on c and implicitly via ξ on $\mathbf{F}$ and $\mathbf{H}$ but for the sake of clarity in the notation, we have omitted this dependence in the last two equations.

Then, the variable ξ is defined implicitly as solution of the nonlinear algebraic equation

$$2\mathcal{S}_p'(\mathcal{I}_5^H) - \xi = 0. \tag{5.10}$$

This last equation cannot be solved analytically for any standard nonlinear saturation function. It implies that the term ξ has *no* explicit expression in terms of the model parameters, rather, it has an implicit dependence on the $\mathbf{F}$ and $\mathbf{H}$ fields as well as on the volume fraction c and the magnetic constants χ_p and m_p^s. Therefore, W^H in (5.4) is an implicit function of $\mathbf{F}$ and $\mathbf{H}$.

For practical purposes, we recall the expressions used to evaluate the total stress $\mathbf{S}$ and Lagrangian

magnetic field $\mathbf{B}$, i.e.,

$$\mathbf{S} = 2\rho_0(1-c)^{-5/2}(\breve{\psi}_m^{\text{mech}})'(\mathcal{I}_1)\mathbf{F} + \nu(\xi)\mathbf{F}^{-T}\mathbf{H}\otimes\mathbf{F}^{-1}\mathbf{F}^{-T}\mathbf{H} - p\mathbf{F}^{-T}, \tag{5.11}$$

with p indicating an arbitrary hydrostatic pressure arising from the incompressibility constraint $J = 1$ and

$$\mathbf{B} = (z(\xi) - \nu(\xi))\mathbf{H} + \nu(\xi)\mathbf{F}^{-1}\mathbf{F}^{-T}\mathbf{H}. \tag{5.12}$$

Those expressions can be used appropriately to impose a Eulerian field $\mathbf{h}_a$ together with a purely mechanical traction as described in equation (4.49) (see the discussion under Remark 4.2). In the following, it is necessary to remark two important limiting cases for equation (5.10).

Remark 5.1. In the limit of small h-fields and deformation gradients, i.e., $\bar{I}_4^H \to \bar{I}_5^H$ and $\bar{I}_5^H \to 0$ or equivalently $|\mathbf{H}| \to 0$ and $|\mathbf{FH}| \to 0$, $\mathcal{S}(\mathcal{I}_5^H)$ becomes linear in $\mathcal{I}_5^H$, which now reads $\mathcal{S}(\mathcal{I}_5^H) = \mu_p \mathcal{I}_5^H/2$, with $\mu_p = \mu_0(1+\chi_p)$ or equivalently $\xi = \mu_p$. This linearization of $\mathcal{S}$, together with (5.10), lead to the effective magnetic permeability μ of the MRE at small magnetic fields, which reads

$$\mu = z(\mu_p) = \mu_0 + \frac{3\,c\,\mu_0(\mu_p - \mu_0)}{[(2+c)\mu_0 + (1-c)\mu_p]} \equiv (1+\chi)\mu_0, \tag{5.13}$$

while

$$\nu = \nu(\mu_p) = \mu_0 + \frac{3c(10+2c+3c^2)(\mu_p-\mu_0)\mu_0^2}{5[(2+c)\mu_0+(1-c)\mu_p]^2} + \frac{3c(1-c)(5+3c)(\mu_p-\mu_0)\mu_0\mu_p}{5[(2+c)\mu_0+(1-c)\mu_p]^2}. \tag{5.14}$$

Both μ and ν[1] are of course independent of $\mathbf{F}$ and $\mathbf{H}$. In this last expression, and for later use, we have also defined the effective susceptibility $\chi = \mu/\mu_0 - 1$ of the MRE. It is also noted that (5.13) corresponds to the well-known Maxwell-Garnett (or equivalently Hashin-Shtrikman) estimate for purely magnetic composites (Psarra et al., 2017). As a consequence, (5.4) may be expressed explicitly as

$$W_0^H(\mathbf{F},\mathbf{H}) = \begin{cases} \rho_0\psi_{\text{mech}}(\mathbf{F}) + \dfrac{\nu-\mu}{2}I_4^H - \dfrac{\nu}{2}I_5^H & \text{if} \quad J = 1 \\ +\infty & \text{otherwise.} \end{cases} \tag{5.15}$$

Here, the superscript 0 is used to denote the limiting case of $|\mathbf{H}| \to 0$, while the coefficient $\nu(\mu_p)$ is given by (5.14).

Remark 5.2. In the limit of very large magnetic fields, i.e., $|\mathbf{H}| \to \infty$, $\mathcal{S}(\mathcal{I}_5^H) = \mu_0\mathcal{I}_5^H/2$ and hence $z = \xi = \mu_0$. In that same limit, the effective magnetization may be found to be simply

$$\mathbf{m} = m^s\frac{\mathbf{h}}{|\mathbf{h}|}, \qquad m^s = c\,m_p^s, \tag{5.16}$$

which readily defines the effective saturation magnetization m^s of the MRE. This result has also been confirmed numerically by Danas (2017) in the context of MREs, where the magnetization saturation of the MRE was shown to be independent of the microstructure itself but only function of the volume fraction of the particles.

[1] Henceforth, it is implied $\nu = \nu(\mu_p)$.

These last two remarks are extremely important for proposing simple and consistent phenomenological models in the following sections.

5.1.1 Explicit homogenization estimates for linear magnetic particles: F-B version

Owing to the linearity of W_0^{H} defined in (5.15) in the magneto-mechanical invariants I_4^{H} and I_5^{H}, one can obtain the corresponding complimentary energy density $W_0^{\mathrm{B}}(\mathbf{F},\mathbf{B})$ by application of the partial Legendre-Fenchel transform with respect to $\mathbf{H}$ (Bustamante and Ogden, 2012)

$$W^{\mathrm{B}}(\mathbf{F},\mathbf{B}) = \sup_{\mathbf{H}} \left[\mathbf{B}\cdot\mathbf{H} + W^{\mathrm{H}}(\mathbf{F},\mathbf{H})\right], \tag{5.17}$$

such that (Lefèvre et al., 2017)

$$W_0^{\mathrm{B}}(\mathbf{F},\mathbf{B}) = \begin{cases} \rho_0\psi_{\mathtt{mech}}(\mathbf{F}) + \dfrac{1}{2\nu}\left[\dfrac{I_5^{\mathrm{B}} + \eta^2 I_4^{\mathrm{B}} + \eta(I_1 I_5^{\mathrm{B}} - I_6^{\mathrm{B}})}{1+\eta^3+\eta^2 I_2 + \eta I_1}\right] & \text{if} \quad J = 1 \\ +\infty & \text{otherwise,} \end{cases} \tag{5.18}$$

where the coefficient $\eta = (\mu-\nu)/\nu$ is introduced for convenience in the notation. The invariants I_4^{B}, I_5^{B} and I_6^{B} are the standard magneto-mechanical ones defined in terms of $\mathbf{B}$ and, in the incompressible limit $J = 1$[2], they are given by

$$I_4^{\mathrm{B}} = \mathbf{B}\cdot\mathbf{B} = \mathbf{F}^{-1}\mathbf{b}\cdot\mathbf{F}^{-1}\mathbf{b}, \qquad I_5^{\mathrm{B}} = \mathbf{F}\mathbf{B}\cdot\mathbf{F}\mathbf{B} = \mathbf{b}\cdot\mathbf{b} \qquad I_6^{\mathrm{B}} = \mathbf{F}^{\mathrm{T}}\mathbf{F}\mathbf{B}\cdot\mathbf{F}^{\mathrm{T}}\mathbf{F}\mathbf{B} = \mathbf{F}\mathbf{b}\cdot\mathbf{F}\mathbf{b}, \tag{5.19}$$

respectively.

As it is evident from relation (5.18), W_0^{B} exhibits a non-trivial coupling between purely mechanical and magneto-mechanical invariants. Nevertheless, by a closer inspection of the expression (5.18), we

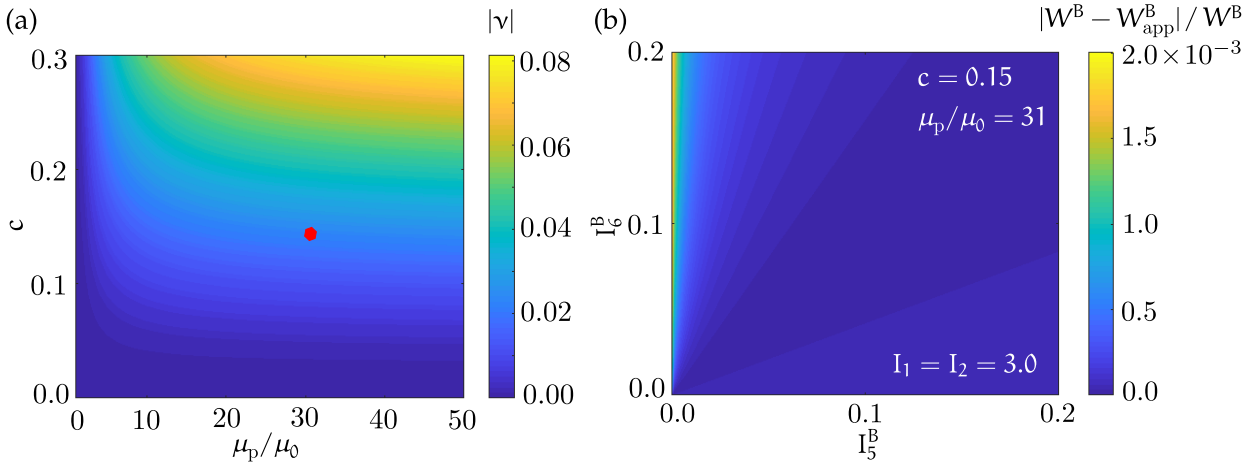

Figure 5.1: (a) Contour plot of the coefficient η as a function of the particle volume fraction c and the normalized magnetic permeability of the particles μ_p/μ_0. (b) Difference between the exact and approximate homogenization energy functions for a representative case of $c = 0.15$ and $\mu_p/\mu_0 = 31$ indicated by a red point in part (a).

[2]The invariants I_4^{B}, I_5^{B} and I_6^{B} are all multiplied with J^2 in the case of compressible materials.

observe that the parameter η is proportional to $\mu - \nu$, which is shown in Fig. 5.1a to be significantly smaller than unity for volume fractions $c \leqslant 0.3$ and magnetic permeabilities of particles $\mu_p/\mu_0 < 50$. This observation allows us to approximate W_0^B even further, an operation that will prove very useful in the next section where we propose explicit phenomenological models.

Thus, by neglecting higher order terms in $O(\eta^2)$ in (5.18), and keeping only the zero order term in $I_1 = 3 + O(|\mathbf{F}-\mathbf{I}|^2)$, we obtain the approximate energy density

$$W_0^B\big|_{|\eta|\ll 1}(\mathbf{F},\mathbf{B}) = \begin{cases} \rho_0\psi_{mech}(\mathbf{F}) + \dfrac{1}{2\nu}\left[\dfrac{\tau\, I_5^B + \eta(3I_5^B - I_6^B)}{1+3\eta}\right] & \text{if} \quad J = 1 \\ +\infty & \text{otherwise.} \end{cases} \tag{5.20}$$

Here, the coefficient τ is introduced to ensure that the second term of (5.20) consistently leads to $I_5^B/2\mu$ in the limiting case of $|\mathbf{b}| \to 0$ and is consequently evaluated to be

$$\tau = \frac{5\nu\mu - 2\nu^2 - 2\mu^2}{\nu\mu} \tag{5.21}$$

after considering the limit $|\mathbf{b}| \to 0$ in (5.20). Finally, substitution of (5.21) into (5.20) leads to

$$W_{app}^B(\mathbf{F},\mathbf{B}) = \begin{cases} \rho_0\psi_{mech}(\mathbf{F}) + \dfrac{(\nu-\mu)}{2\nu(2\nu-3\mu)}(I_5^B - I_6^B) + \dfrac{1}{2\mu}I_5^B & \text{if} \quad J = 1 \\ +\infty & \text{otherwise,} \end{cases} \tag{5.22}$$

The approximate linearized energy (5.22) is compared with the original homogenized energy (5.18) in Fig. 5.1b. As is easily observed, the difference between those two estimates is very small and thus allows us to use expression (5.22) to obtain the initial response of the subsequent phenomenological model in the $\mathbf{F}-\mathbf{B}$ space in a straightforward manner. It is finally noted that all energies discussed in this section comprise the same purely mechanical part, which is explicit and has been originally proposed in the work of Lopez-Pamies et al. (2013).

5.2 Microstructurally-guided explicit phenomenological models

In this section, we propose fully explicit, homogenization-guided phenomenological models for the MRE using both $\mathbf{F}-\mathbf{H}$ and $\mathbf{F}-\mathbf{B}$ variables. The phenomenological models are proposed in terms of two additional modeling parameters, which are subsequently obtained via consistent linearization and fitting with the homogenized models. First, we propose models for incompressible MREs and then extend in an ad-hoc manner those models for nearly incompressible ones. This extension serves only practical purposes since it allows for a simpler numerical implementation. For consistency, we impose on the phenomenological model certain important properties, which are:

1. the phenomenological models shall have the same purely mechanical part than the homogenized models, i.e., $\psi_{mech}(\mathbf{F}) = (1-c)\breve{\psi}_{mech,m}(\mathcal{I}_1)$ with $\mathcal{I}_1$ given by (5.7).

2. for $\mathbf{H} = \mathbf{0}$ and arbitrary $\mathbf{F}$, both phenomenological models shall recover exactly the analytical homogenization solutions (5.15) and (5.22) for the $\mathbf{F}-\mathbf{H}$ and $\mathbf{F}-\mathbf{B}$ versions, respectively. This condition implies first that the phenomenological and homogenized models shall deliver the

same initial magnetization response or equivalently give the same slope in the $\mathbf{b}-\mathbf{h}$ space, i.e., μ as defined from relation (5.13). Secondly it implies that they both result in the same magnetostrictive response as $\mathbf{H}\to\mathbf{0}$ or whenever the magnetic particles are modeled as linear magnetic materials without saturation.

3. for $|\mathbf{H}|\to\infty$, both phenomenological and homogenized models shall lead to the same saturation magnetization response, i.e., $|\mathbf{m}|=m^s$ obtained in (5.16).

5.2.1 Explicit F-H phenomenological model

Given the above requirements, we propose a phenomenological energy function for incompressible MREs in terms of three distinct energy contributions, namely, a fully decoupled mechanical and magnetic energy and an additional coupling energy, which reads

$$W^{\mathrm{H}}(\mathbf{F},\mathbf{H})=\begin{cases}\rho_0\psi_{\mathtt{mech}}(\mathbf{F})+\rho_0\psi^{\mathrm{H}}_{\mathtt{mag}}(I^{\mathrm{H}}_5)+\rho_0\psi^{\mathrm{H}}_{\mathtt{couple}}(I^{\mathrm{H}}_4,I^{\mathrm{H}}_5)-\dfrac{\mu_0}{2}I^{\mathrm{H}}_5 & \text{if}\quad J=1\\ +\infty & \text{otherwise,}\end{cases} \tag{5.23}$$

where the effective mechanical free energy $\rho_0\psi_{\mathtt{mech}}$ is given by (5.5), and I^{H}_4 and I^{H}_5 by (5.6). Instead, the *purely* magnetic part $\rho_0\psi^{\mathrm{H}}_{\mathtt{mag}}$ is given in terms of a Gaussian Hypergeometric function, denoted by ${}_2\mathcal{F}_1$, as

$$\begin{aligned}\rho_0\psi^{\mathrm{H}}_{\mathtt{mag}}(I^{\mathrm{H}}_5)&=-\frac{\mu_0}{2}\chi I^{\mathrm{H}}_5\,{}_2\mathcal{F}_1\left[\frac{1}{k^{\mathrm{H}}},\frac{2}{k^{\mathrm{H}}},1+\frac{2}{k^{\mathrm{H}}},-\left(\frac{\chi\sqrt{I^{\mathrm{H}}_5}}{m^s}\right)^{k^{\mathrm{H}}}\right],\\ &=-\frac{\mu_0}{2}\chi|\mathbf{h}|^2\,{}_2\mathcal{F}_1\left[\frac{1}{k^{\mathrm{H}}},\frac{2}{k^{\mathrm{H}}},1+\frac{2}{k^{\mathrm{H}}},-\left(\frac{\chi|\mathbf{h}|}{m^s}\right)^{k^{\mathrm{H}}}\right]=\rho_0\psi^{\mathrm{h}}_{\mathtt{mag}}(\mathbf{h}).\end{aligned} \tag{5.24}$$

In this expression, k^{H} is a positive integer, $m^s=c\,m^s_{\mathrm{p}}$ denotes the effective saturation magnetization and $\chi=(\mu/\mu_0-1)$ is the effective magnetic susceptibility, which is given by (5.13). The function ${}_2\mathcal{F}_1$ is typically expressed in terms of a series given by,

$${}_2\mathcal{F}_1[a,b,c;z]=\sum_{n=0}^{\infty}\frac{(a)_n(b)_n}{(c)_n}\frac{z^n}{n!}, \tag{5.25}$$

with

$$(x)_0=1\qquad\text{and}\qquad(x)_n=x(x+1)\cdots(x+n-1).$$

It can be shown via rigorous convergence tests that the infinite series in (5.25) converge for all $z<0$ and non-negative a, b and c (Abramowitz and Stegun, 1972, p. 81-86). Hence, (5.25) can be evaluated numerically in a straightforward manner (Perger et al., 1993; Hankin, 2015). Of interest, however, are the first and second derivatives of $\rho_0\psi^{\mathrm{h}}_{\mathtt{mag}}(\mathbf{h})$ with respect to $\mathbf{h}$, which, as shown in the following, take very simple algebraic forms.

Subsequently, motivated by the corresponding homogenized model in equation (5.4), we express the coupled magneto-mechanical energy as a function of the two invariants I^{H}_4 and I^{H}_5, thus taking

the form

$$\rho_0\psi^H_{couple}(I^H_4, I^H_5) = \rho_0\psi^H_4(I^H_4) - \rho_0\psi^H_5(I^H_5), \tag{5.26}$$

with

$$\rho_0\psi^H_i(I^H_i) = \beta^H_1 \frac{\mu_0(m^s)^2}{2\chi} \ln\left[1 + \sum_{q=1}^{4} \frac{1}{c}\left(\frac{4}{5}\chi\right)^{q+1}\left(\frac{c}{\beta^H_2}\right)^q\left(\frac{\sqrt{I^H_i}}{m^s}\right)^{2q}\right], \qquad i = 4, 5. \tag{5.27}$$

In the above expressions, we have introduced three free parameters, namely, k^H, β^H_1 and β^H_2. The evaluation and selection of these parameters using the analytical homogenization model in (5.4) is described in detail in the following.

The selection of the parameter k^H **:** We start by noting that the derivative of the Gaussian Hypergeometric function ${}_2\mathcal{F}_1$ with respect to its argument has a very simple form, which reads

$$\mathbf{m} = -\frac{\rho_0}{\mu_0}\frac{\partial\psi^H_{mag}}{\partial\mathbf{h}} = \frac{\chi\mathbf{h}}{\left[1 + (\chi)^{k^H}\left(|\mathbf{h}|/m^s\right)^{k^H}\right]^{1/k^H}}. \tag{5.28}$$

Here, the initial susceptibility is always χ irrespective of the value of k^H thus leading to the correct (in the sense of homogenization) initial effective magnetization response of the MRE. The same is true for the saturation response, which gives $|\mathbf{m}| = m^s$ as required by the homogenization process. On the other hand, the rate of magnetization depends on the power coefficient k^H, which may be calibrated to follow closely the homogenized response. Specifically, by direct calibration, we find in Section 5.3 that a value

$$k^H = 4 \tag{5.29}$$

leads to a good fit for the magnetization response for all volume fractions $c \in [0, 0.3]$ and matrix

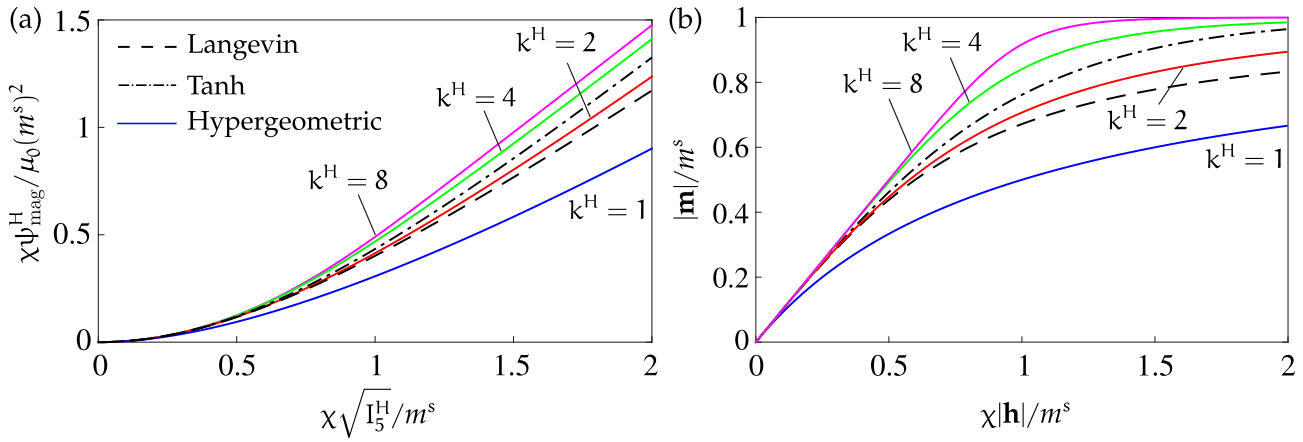

Figure 5.2: Comparison of (a) the magnetic energy functions and of (b) their derivatives obtained from and hypergeometric ψ^H_{mag} saturation function given in equation (5.28) for various exponents k^H, the Langevin function (based on definition (4.23)) and the hyperbolic tangent function (see equations (2.12) and (2.14) in Danas (2017)).

shear moduli analyzed in the present study. Of course, given any experimental data, a different value for k^H may be used. For illustration purposes, we show in Fig. 5.2 representative curves of the hypergeometric function and its derivative, which gives the $\mathbf{m} - \mathbf{h}$ response as evaluated from equation (5.28). For comparison, magnetization curves obtained by the Langevin (based on definition

(3.26)) and the hyperbolic tangent functions (see equations (2.12) and (2.14) in Danas (2017)) are also shown. The use of a hypergeometric function is done in order to allow for flexibility in the calibration process since the homogenized response of an MRE comprising magnetic particles with Langevin-type magnetization saturation response does not lead to an effective magnetization response of a Langevin-type, as is discussed in Section 5.3. Before proceeding to the coupled energy part, we note further that the decoupled mechanical and magnetic energies are expressed in terms of the homogenized material parameters, which can be evaluated directly in terms of the constituents' properties and the particle volume fraction c.

The evaluation of the parameter β_1^H **:** To facilitate the relevant discussion, we show in Fig. 5.3 the response of $\rho_0\psi_i^H$ as a function of the invariant I_i^H. First, we observe that $\rho_0\psi_i^H$ is non-convex with respect to $\sqrt{I_i^H}$ since its derivative increases rapidly from zero to a maximum and then gradually decreases to zero (see Fig. 5.3b). As we will see in the following, such a function allows to obtain

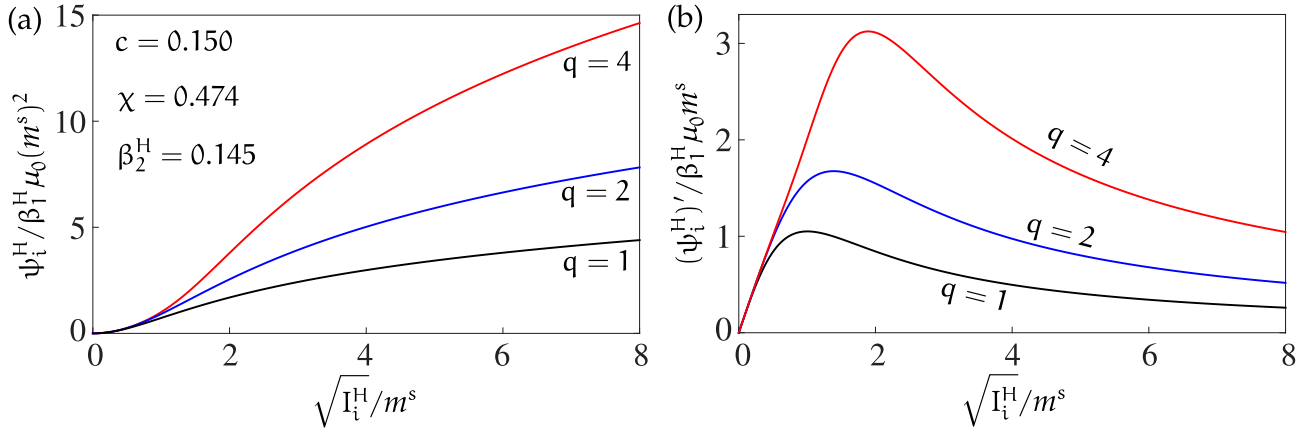

Figure 5.3: Representative plots of (a) the function $\rho_0\psi_i^H$ (with $i = 4, 5$) and (b) of its derivative with respect to $\sqrt{I_i^H}$ for $q = 1, 2, 4$.

a material magnetostriction response that is initially quadratic, subsequently increases in a non-quadratic manner until finally reaching a saturating state.

Another important comment is related to the specific form of $\rho_0\psi_{\text{couple}}^H$, i.e., the subtraction term $\rho_0\psi_4^H(I_4^H) - \rho_0\psi_5^H(I_5^H)$. This is done for two reasons. First, the derivation of $\rho_0\psi_{\text{couple}}^H$ with respect to $\mathbf{h}$ leaves the magnetization response completely unaffected at small and very large applied magnetic fields $\mathbf{h}_a$, thus allowing the hypergeometric function in equation (5.24) to completely control the $\mathbf{m} - \mathbf{h}$ response at the initial regime and the saturation regime. The second reason is that only the $I_4^H = \mathbf{F}^T\mathbf{h}\cdot\mathbf{F}^T\mathbf{h}$ part of the function contributes to the magnetostriction whenever a Eulerian field $\mathbf{h}_a$ is applied, while the corresponding $I_5^H = \mathbf{h}\cdot\mathbf{h}$ part induces no magnetostriction.

In view of the above observations, the evaluation of β_1^H is readily obtained by enforcing an exact equivalence between the phenomenological model (5.23) and the linearized homogenized model (5.4) in the limit of $|\mathbf{h}| \to 0$. To achieve that, we expand W^H in equation (5.23) around $I_4^H = I_5^H = 0$, to obtain

$$W_0^H(\mathbf{F},\mathbf{H}) = \begin{cases} \rho_0\psi_{\text{mech}}(\mathcal{J}_1) + 16\dfrac{(\mu-\mu_0)}{50}\dfrac{\beta_1^H}{\beta_2^H}(I_4^H - I_5^H) - \dfrac{\mu}{2}I_5^H & \text{if} \quad J = 1 \\ +\infty & \text{otherwise.} \end{cases} \tag{5.30}$$

By direct matching of the individual coefficients of I_4^H and I_5^H in (5.30) with those in (5.15), one gets

$$\beta_1^H = \frac{25}{16}\frac{(\nu-\mu)}{(\mu-\mu_0)}\beta_2^H. \tag{5.31}$$

The above definition of β_1^H ensures that the initial (quadratic) magnetostriction obtained from the homogenization model (5.4) and the phenomenological model (5.23) is exactly the same. Evidently, (5.30) becomes independent of β_2^H after substitution of (5.31) for β_1^H.

The selection of the parameter β_2^H **:** The parameter β_2^H affects the magnetostriction response at larger h-fields as a result of the nonlinearity of the coupled function $\rho_0\psi^H_{\texttt{couple}}$ in (5.26) but not the initial magnetostriction. Therefore, the parameter β_2^H needs to be calibrated numerically by fitting the magnetostriction response of the phenomenological model with that of the homogenized model (5.4) at large $\mathbf{h}$. It is worth noting here that the numerical fitting process is carried out by considering a zero applied mechanical traction (see equation (4.49)) and a Eulerian applied h-field $\mathbf{h}_a$, as discussed in Section 4.6.3. To achieve that, we employ the least square-based curve fitting algorithm `lsqcurvefit` of MATLAB (2017).

More specifically, the coupling coefficient β_2^H essentially depends on four material parameters: the shear modulus G_m of the matrix, the initial susceptibility χ_p, the saturation magnetization m_p^s of the particles and the particle volume fraction c. In practice, most of the MREs are fabricated by curing the commercially available carbonyl iron particles along with various elastomers in different proportions (Danas et al., 2012b; Psarra et al., 2017; Bodelot et al., 2017; Psarra et al., 2019). Therefore, G_m and c are the two key parameters[3] that vary for different MRE samples, while we set $\chi_p = 30$ and $\mu_0 m_p^s = 2.5$T, as obtained experimentally in Psarra et al. (2017).

First, we observe that β_2^H becomes almost independent of G_m and c for $G_m > 1$MPa. Hence, we introduce a non-dimensional shear modulus, $G_m^* = G_m/G_m^{\texttt{Ref}}$, where $G_m^{\texttt{Ref}} = 1$MPa. The fitting process then involves scanning for the optimum β_2^H in the $0.001 \leqslant G_m^* \leqslant 1.5$ and $0 < c \leqslant 0.3$ range, as shown in Fig. 5.4a. The fitting of the contour in that figure gives

$$\beta_2^H(G_m^*, c) = \alpha_1^H(G_m^*) - \alpha_2^H(G_m^*)\mathcal{L}\left[c\,\alpha_3^H(G_m^*)\right], \tag{5.32}$$

with

$$\begin{aligned}
\alpha_1^H(G_m^*) &= \exp\left[-0.29\tanh\left\{0.27(\ln G_m^* + 7)\right\} - 1.575\right],\\
\alpha_2^H(G_m^*) &= \exp\left[4.4\mathcal{L}(-0.78\ln G_m^*) - 5.2\right],\\
\alpha_3^H(G_m^*) &= \frac{0.1}{G_m^* + 0.0007} - 5.4G_m^* + 6.75.
\end{aligned}$$

Here, $\mathcal{L}(.)$ is the Langevin function given by (3.26). Specifically, the evolution of β_2^H with respect to G_m^* is mainly controlled by the coefficients α_1^H and α_2^H. The third coefficient α_3^H is used to model the variation of β_2^H with respect to c for a given G_m^*. The dependence of the functions α_1^H and α_2^H on G_m^* is shown in Fig. 5.4b, where we observe that $\alpha_2^H \approx 0$ for $G_m^* > 1$, i.e., for all $G_m > G_m^*$. Hence, beyond $G_m^* > 1$ a constant $\beta_2^H \approx 0.155$ is sufficient. On the other hand, for very soft, gel-like MREs, i.e., in

[3]Different values of χ_p and m_p^s are expected to change the functions obtained below but only weakly, whereas one can always find the optimal coefficient β_2^H by simply fitting the homogenized model for the given set of material properties of interest.

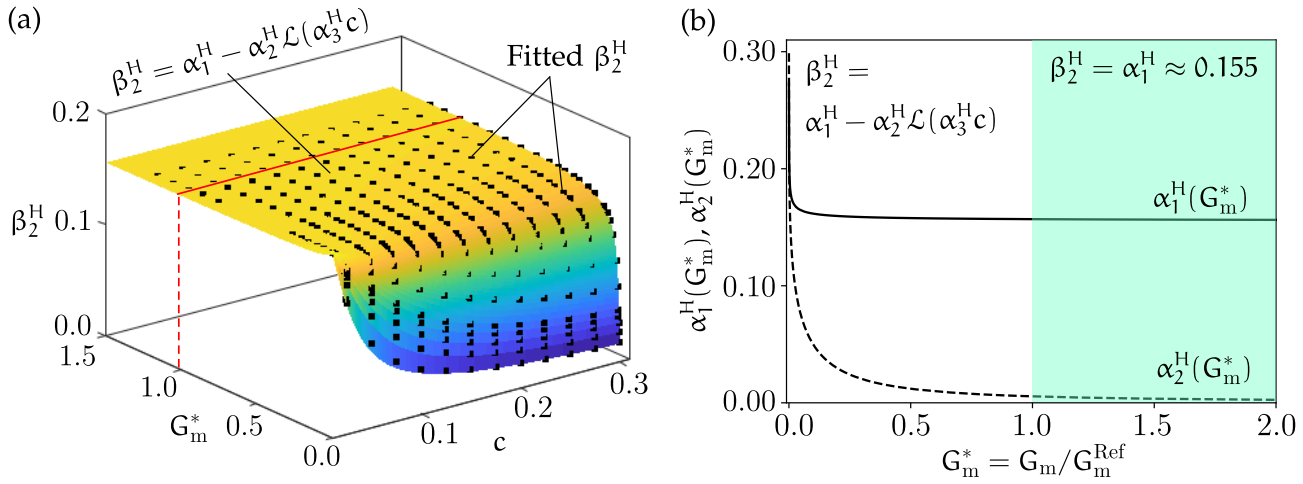

Figure 5.4: (a) Calibrated $\beta_2^H(G_m^*, c)$ in the $G_m^* - c$ space with the smooth surface showing the profile of the function (5.32) for $\beta_2^H(G_m^*, c)$ and the black dots representing the optimized β_2^H as obtained via fitting the magnetostriction response with the analytical homogenization model. (b) Evolution of the functions $\alpha_1^H(G_m^*)$ and $\alpha_2^H(G_m^*)$ in (5.32) with G_m^*.

the range of $0.01 \leqslant G_m^* \leqslant 0.001$, the coupling coefficient β_2^H becomes highly sensitive to G_m^* and c, resulting in a significant variation of β_2^H in this particular range (see Fig.5.4a).

Remark 5.3. In spite of the fact that the assumption of an incompressible matrix and rigid particles leads to very efficient analytical estimates of the effective response, compressible models for the MREs are employed in most of the computational investigations due to their simplicity to incorporate them in a finite-element solver. Unfortunately, carrying out the homogenization problem for a compressible matrix is extremely difficult and no rigorous model is available up to date neither for the purely mechanical part nor for the magneto-mechanical part. In this regard, we propose an ad-hoc extension of the incompressible phenomenological model (5.23) that essentially relaxes the assumption of incompressibility without affecting the aforementioned key features of the model at least in the case of high bulk modulus (i.e. nearly incompressible materials). The proposed compressible model reads

$$W_{comp}^H(\mathbf{F}, \mathbf{H}) = \rho_0 \psi_{mech}^{comp}(\mathcal{I}_1, J) + \rho_0 \psi_{mag}^H(I_5^H) + \rho_0 \psi_{couple}^H(I_4^H, I_5^H) - \frac{J \mu_0}{2} I_5^H, \tag{5.33}$$

where

$$\rho_0 \psi_{mech}^{comp}(\mathcal{I}_1, J) = \rho_0 \psi_{mech}(\mathcal{I}_1) - \frac{G_m}{(1-c)^{5/2}} \ln J + \frac{G_m'}{2(1-c)^6}(J-1)^2. \tag{5.34}$$

where $\rho_0 \psi_{mech}$ and $\mathcal{I}_1$ have been defined in (5.5) and (5.7), respectively, whereas G_m' is the Lamé constant associated with the compressibility modulus of the matrix. A nearly incompressible response is obtained for values $G_m' \geqslant 100 G_m$, which is the key assumption in most of the numerical computations associated with MREs. In that range, we observe no visible difference between the incompressible and the nearly incompressible versions for both the magnetostriction and the magnetization response. Nevertheless, as noted in Appendix 4.B, special care must be taken while computing the element force and stiffness matrices for such *nearly incompressible* materials, which are prone to volumetric locking if a standard 4-point Gauss quadrature rule is applied.

5.2.2 Explicit F-B phenomenological model

In principle, one can obtain an equivalent F-B model via the partial Legendre-Fenchel transformation (5.17) of (5.23) with respect to $\mathbf{H}$. However, due to the severe nonlinearity of the functions associated with the proposed F-H model (5.23), one can not obtain its complementary energy in an explicit form. Instead, a complementary energy W^{B}, which has the exact same form as that of W^{H} in (5.23), is proposed directly as

$$W^{B}(\mathbf{F},\mathbf{B}) = \begin{cases} \rho_0\psi_{\text{mech}}(\mathbf{F}) + \rho_0\psi^{B}_{\text{mag}}(I^{B}_5) + \rho_0\psi^{B}_{\text{couple}}(I^{B}_5, I^{B}_6) + \dfrac{1}{2\mu_0} I^{B}_5 & \text{if} \quad J = 1 \\ +\infty & \text{otherwise,} \end{cases} \tag{5.35}$$

where the magneto-mechanical invariants I^{B}_5 and I^{B}_6 have been defined in (5.19). Evidently, the first term of (5.35) that represents the purely mechanical component of W^{B} is identical to that in (5.4) and (5.23), and is given by (5.5). Also, the last term of (5.35) represents the F-B version of the magnetostatic energy of free space (Dorfmann and Ogden, 2004).

It remains then to prescribe the two free energies, namely, the magnetic and the coupled free energy. Due to their intrinsic properties, $\rho_0\psi^{B}_{\text{mag}}$ and $\rho_0\psi^{B}_{\text{couple}}$ retain the same functional form to their F-H counterparts (5.24) and (5.26), respectively. Note that, as shown in Figs. 5.2 and 5.3, the hypergeometric ${}_2\mathcal{F}_1$ and the $\rho_0\psi^{H}_i$ functions are rich enough to model a wide variety of constitutive responses.

In this regard, the purely magnetic part $\rho_0\psi^{B}_{\text{mag}}$ is chosen as

$$\begin{aligned} \rho_0\psi^{B}_{\text{mag}}(I^{B}_5) &= -\frac{\chi}{2\mu_0(1+\chi)} I^{B}_5 \, {}_2\mathcal{F}_1\left[\frac{1}{k^{B}}, \frac{2}{k^{B}}, 1+\frac{2}{k^{B}}, -\left(\frac{\chi\sqrt{I^{B}_5}}{(1+\chi)\mu_0 m^{s}}\right)^{k^{B}}\right] \\ &= -\frac{\chi}{2\mu_0(1+\chi)} |\mathbf{b}|^2 \, {}_2\mathcal{F}_1\left[\frac{1}{k^{B}}, \frac{2}{k^{B}}, 1+\frac{2}{k^{B}}, -\left(\frac{\chi|\mathbf{b}|}{(1+\chi)\mu_0 m^{s}}\right)^{k^{B}}\right] = \rho_0\psi^{b}_{\text{mag}}(\mathbf{b}), \end{aligned} \tag{5.36}$$

while, the coupling free energy is defined by

$$\rho_0\psi^{B}_{\text{couple}}(I^{B}_5, I^{B}_6) = \rho_0\psi^{B}_6(I^{B}_6) - \rho_0\psi^{B}_5(I^{B}_5), \tag{5.37}$$

with

$$\rho_0\psi^{B}_i(I^{B}_i) = \beta^{B}_1 \frac{(1+\chi)\mu_0(m^{s})^2}{2\chi} \ln\left[1 + \sum_{q=1}^{4} \frac{1}{c}\left(\frac{5}{4}\frac{\chi}{1+\chi}\right)^{q+1}\left(\frac{c}{\beta^{B}_2}\right)^{q}\left(\frac{\sqrt{I^{B}_i}}{\mu_0 m^{s}}\right)^{2q}\right], \tag{5.38}$$

where $i = 5, 6$ and again $m^{s} = c\, m^{s}_{p}$. Notice that (5.36) admits to a similar form as in (3.44) with a different g^{b} in this context of s-MREs having CI particles.

Remark 5.4. As stated earlier, (5.37) retains an identical functional form as its F-H counterpart in (5.26) except that the magneto-mechanical coupling is now modeled in terms of the invariant I^{B}_6. This choice of the coupling invariant is not arbitrary. Rather, it is directly equivalent to the F-H model. The invariant I^{H}_4 in the F-H model can be expressed in terms of the Eulerian $\mathbf{h}$ as $I^{H}_4 = \mathbf{F}^{T}\mathbf{h}\cdot\mathbf{F}^{T}\mathbf{h}$. The Legendre-Fenchel transform of that invariant leads to the invariant $I^{B}_6 = \mathbf{F}^{T}\mathbf{b}\cdot\mathbf{F}^{T}\mathbf{b}$. In addition, and perhaps more importantly, we have shown that, in the linearized regime, the corresponding

homogenized model (5.18) can be approximated accurately by the model in (5.22), which in turn depends on I_5^B and I_6^B.

In expressions (5.36) and (5.37), we have introduced three free parameters, namely, k^B, β_1^B and β_2^B. The evaluation and selection of these parameters using the analytical homogenization model defined in (5.4) as well as the approximate linearized one in (5.22) is described in detail in the following.

The selection of the parameter k^B **:** Similar to the F-H version, a single exponent

$$k^B = 6 \tag{5.39}$$

provides a good fit to the magnetization response for all particle volume fractions and matrix shear moduli considered in this study. Note that the purely magnetic energy (5.36) in the F-B model is *not* an exact Legendre transform of the corresponding magnetic energy (5.24) of the F-H model. Thus, no direct correlation can be drawn between the model parameters k^B and k^H and their calibration values. Nevertheless, this observation of having a relatively stiffer saturation function for the $\mathbf{F}-\mathbf{B}$ model as compared to its $\mathbf{F}-\mathbf{H}$ counterpart also features in the hysteretic magnetization response, which is detailed in Chapter 3.

The evaluation of the parameter β_1^B **:** The evaluation of the coefficient β_1^B is carried out in a similar fashion (i.e., via consistent linearization and fitting with the homogenized response) to the F-B homogenization model. In the limit of small $|\mathbf{b}| \to 0$, (5.35) can be expanded in terms of the invariants around $I_i^B = 0$ (with $i = 5, 6$). Thus, retaining only the leading order terms in I_i^B, one can express (5.35) as

$$W_0^B(\mathbf{F},\mathbf{B}) = \begin{cases} \rho_0\psi_{\text{mech}}(\mathbf{F}) + \dfrac{25}{32}\dfrac{\beta_1^B}{\beta_2^B}\dfrac{(\mu-\mu_0)}{\mu\mu_0}(I_6^B - I_5^B) + \dfrac{1}{2\mu}I_5^B & \text{if} \quad J = 1 \\ +\infty & \text{otherwise.} \end{cases} \tag{5.40}$$

By direct matching of this last free energy function with the approximate linearized one defined in equation (5.22), we obtain

$$\beta_1^B = \frac{16}{25}\frac{\mu_0\mu(\nu-\mu)}{\nu(\mu-\mu_0)(3\mu-2\nu)}\beta_2^B. \tag{5.41}$$

The above relation for β_1^B ensures that the initial (quadratic) magnetostriction obtained from the homogenization model (5.22) and the phenomenological model (5.35) is exactly the same. Evidently, (5.40) becomes independent of β_2^B after substitution of (5.41) for β_1^B.

The selection of the parameter β_2^B **:** The parameter β_2^B affects the magnetostriction response at larger h-fields as a result of the nonlinearity of the coupled function ψ_{couple}^B in (5.37). Thus, the F-B phenomenological model is also reduced to a single modeling parameter, β_2^B. This parameter is then obtained by fitting the material magnetostriction obtained from the phenomenological model (5.35) with that from the homogenization model (5.4). The optimal β_2^B for a given G_m^* and c is shown by black squares in Fig. 5.5, which is qualitatively similar to Fig. 5.4a. For convenience in the notation, here we use the same non-dimensional shear modulus G_m^* as defined in Section 5.2.1. Specifically, we use two piecewise continuous functions of G_m^* and c to model the variation of β_2^B in the $G_m^* - c$ space,

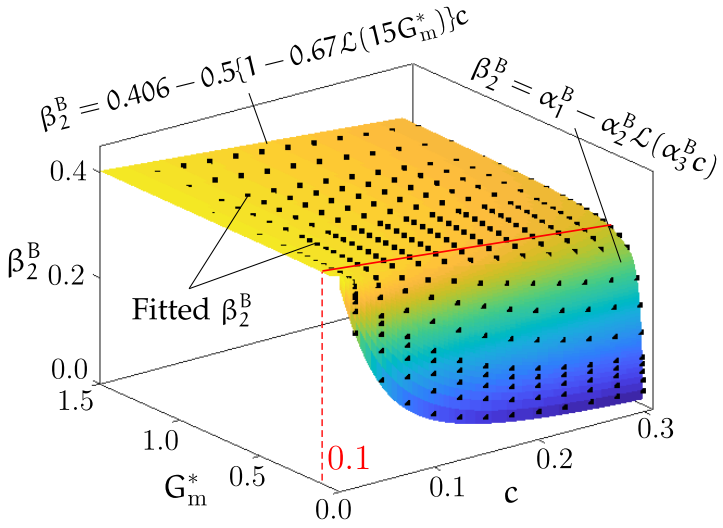

Figure 5.5: Calibrated $\beta_2^B(G_m^*, c)$ in the $G_m^* - c$ space with the smooth surface showing the profile of the function (5.42) for $\beta_2^B(G_m^*, c)$ and the black dots representing the optimized β_2^B as obtained via fitting the magnetostriction response with the analytical homogenization model.

which reads

$$\beta_2^B(G_m^*, c) = \begin{cases} \alpha_1^B(G_m^*) - \alpha_2^B(G_m^*)\mathcal{L}\left[c\,\alpha_3^B(G_m^*)\right], & \text{if} \quad G_m^* \leqslant 0.1 \\ 0.4055 - 0.5\,c\,\left[1 - 0.67\mathcal{L}(15G_m^*)\right] & \text{otherwise} \end{cases} \tag{5.42}$$

with

$$\begin{aligned} \alpha_1^B(G_m^*) &= \exp\left[-0.029\ln G_m^* - 0.982\right], \\ \alpha_2^B(G_m^*) &= \exp\left[1.78\mathcal{L}(-0.32\ln G_m^*) - 1.78\right], \\ \alpha_3^B(G_m^*) &= \exp\left[0.14 - 0.54\ln G_m^*\right]. \end{aligned}$$

Here, $\mathcal{L}(.)$ is again the Langevin function defined in (3.26). The first function is similar to β_2^H with three coefficients α_1^B, α_2^B and α_3^B, which are functions of G_m^*, whereas, the second function, which models β_2^B for all $G_m^* > 0.1$, is rather a simple function of G_m^* and c. We observe in Fig. 5.5 that the two fitting functions for β_2^B have approximately the same magnitude near $G_m^* = 0.1$. Thus, the particular choice of piecewise continuous β_2^B ensures a constant transition from the Langevin decay to the linear decrease regime. Again, it is emphasized that the calibration (5.42) is valid for the Neo-Hookean hyperelastic matrices. Any other model (e.g. Gent model) for the soft matrix material may necessitate re-calibration of β_2^B.

Remark 5.5. A compressible version of (5.35) is given by

$$W_{\text{comp}}^B(\mathbf{F}, \mathbf{B}) = \rho_0\psi_{\text{mech}}^{\text{comp}}(\mathcal{I}_1, J) + \rho_0\psi_{\text{mag}}^B\left(\frac{I_5^B}{J^2}\right) + \rho_0\psi_{\text{couple}}^B\left(\frac{I_5^B}{J^2}, \frac{I_6^B}{J^4}\right) + \frac{1}{2\mu_0 J}I_5^B, \tag{5.43}$$

where $\rho_0\psi_{\text{mech}}^{\text{comp}}$ is given by (5.34). Unlike the compressible $\mathbf{F} - \mathbf{H}$ model (5.33), the argument of the magnetic energy in the $\mathbf{F} - \mathbf{B}$ is not a function of the I_5^B invariant alone. Rather, I_5^B/J^2 is used in (5.43)

as the argument of $\rho_0\psi^{B}_{mag}$, which thus ensures a nearly incompressible material response (see also (Danas, 2017)). In turn, the I^{B}_{6}-based argument of the coupled free energy $\rho_0\psi^{B}_{couple}$ is defined to be in terms of I^{B}_{6}/J^4 in this compressible version of the $\mathbf{F}-\mathbf{B}$ model. Again, special care must be taken while numerically integrating such nearly incompressible constitutive models while constructing the element force and stiffness matrices. In particular, it is recommended to use the 1-point Gauss quadrature while integrating the volumetric energy term of $\rho_0\psi^{comp}_{mech}$.

5.3 Results: assessment of the theoretical models

The assessments of the analytical homogenization and the phenomenological models are carried out via first, probing the analytical model with the RVE computations. The responses of proposed $\mathbf{F}-\mathbf{H}$ and $\mathbf{F}-\mathbf{B}$ phenomenological models are then compared with the analytical homogenization responses under no mechanical pre-loads, i.e., in the loading path, which is considered to calibrate β^{H}_{2} and β^{B}_{2}. Finally, the model response is also compared to the analytical homogenization estimates under applied mechanical pre-loads, namely, pre-uniaxial and equibiaxial tension/compression and pre-shear.

5.3.1 Comparison between analytical homogenization and numerical computations

First, we compare the average FE magnetization and magnetostriction response of Fig. 4.5 with those obtained from the analytical F-H homogenization model, defined in (5.4). Note that the homogenization model is incompressible. Thus, we consider $\mathbf{F} = \lambda_1\mathbf{e}_1\otimes\mathbf{e}_1 + 1/\sqrt{\lambda_1}\mathbf{e}_2\otimes\mathbf{e}_2 + 1/\sqrt{\lambda_1}\mathbf{e}_3\otimes\mathbf{e}_3$ and subsequently, for a given $\mathbf{h}$, we compute λ_1 and the arbitrary pressure p by solving the first two equations given by the traction conditions $(4.84)_1$. The magnetization and the magnetostriction response

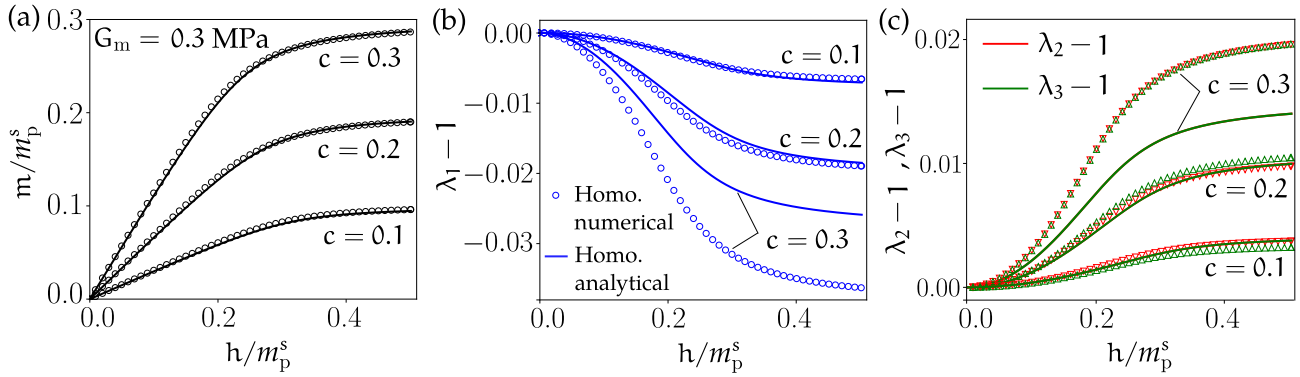

Figure 5.6: (a) Effective magnetization and effective (b) parallel and (c) transverse magnetostrictions as obtained from the numerical homogenization (discrete points), analytical homogenization (firm lines) for the particle volume fractions $c = 0.1, 0.2$ and 0.3. Eulerian h-field is applied at a local point in the MRE, which is free from mechanical tractions.

from the analytical homogenization model and the FE simulations are compared in Fig. 5.6. In this figure, for volume fractions $c = 0.1$ and 0.2, we observe an excellent agreement between the analytical and FE homogenization models for both the magnetization and the magnetostriction. For the higher particle volume fractions, $c = 0.3$, the analytical homogenization estimates for λ_i $(i = 1, 2, 3)$ are significantly lower in absolute value than that obtained from the FE calculations, as shown in Figs. 5.6b

and c. Instead, the agreement in the magnetization response is excellent even for $c = 0.3$.

In this regard, given the fact that the analytical homogenization estimates are very accurate at volume fractions of practical interest (i.e. $c \leqslant 0.2$), we choose them in the following to calibrate our phenomenological models even for larger volume fractions but, more importantly, for much lower matrix shear moduli, where FE calculations do not converge. Note, however, that the phenomenological models may be calibrated using available experimental results or directly numerical FE computations.

5.3.2 Comparison between the phenomenological and homogenization estimates without mechanical pre-load

This section assesses the $\mathbf{F}-\mathbf{H}$ (see equation (5.23)) and $\mathbf{F}-\mathbf{B}$ (see equation (5.35)) incompressible phenomenological models for a large range of matrix shear moduli, spanning a range of $0.003 < G_m < 0.3$ MPa (or equivalently $0.003 < G_m^* < 0.3$). In particular, we choose for illustration purposes, three shear moduli $G_m = 0.003, 0.03, 0.3$MPa. We set the magnetic properties of the iron particles, i.e., χ_p and m_p^s unaltered (see Table 4.2). Finally, we apply the boundary/loading conditions described in (4.84).

The effective magnetization and magnetostriction for $G_m^* = 0.3, 0.03$ and 0.003 and four different volume fractions $c = 0.05, 0.1, 0.2$ and 0.3 are shown as a function of the applied Eulerian h–field h/m_p^s in Figs. 5.7a,d,g and Figs. 5.7b,e,h, respectively. The transverse magnetostriction components, λ_2 and λ_3, are equal to $1/\sqrt{\lambda_1}$ since we consider the MRE to be incompressible in both the analytical homogenization and the phenomenological models. We find an excellent agreement between the analytical homogenization estimates and the proposed phenomenological ones, both in terms of m_1 and λ_1 for all c considered here.

In Figs. 5.7c,f,i, we show the magnetostriction $\lambda_1 - 1$ at various values of the applied Eulerian field h/m_p^s. At $h = 0.2m_p^s$, the phenomenological estimates are slightly different from the corresponding homogenization estimates for particle volume fractions $c > 0.25$. At higher h-fields, such as $h = 0.5m_p^s$ or $h = 1.5m_p^s$, the phenomenological models are in very close agreement with the homogenization estimates, even for higher particle volume fractions such as $c = 0.35$. Hence, the slight mismatch between the phenomenological and the homogenization estimates at moderate fields and large volume fraction can be directly attributed to the specific functional form of the coupling free energy (5.26) and (5.37). We note that the calibrated coupling coefficients β_2^H and β_2^B manage to model very accurately the saturation magnetostriction, even for $c > 0.25$, as indicated by the almost perfect overlap of the λ_1 curves in Figs. 5.7c,f,i at higher applied h-fields. Thus, the overall performance of the phenomenological models is found to be excellent up to $c = 0.25$ and even sufficiently accurate for particle volume fraction of $c = 0.35$. We recall, here, that the homogenization estimates were found to underestimate the magnetostriction by comparison to FE results for volume fraction $c = 0.3$. Hence, the use of the proposed phenomenological models for volume fractions $c > 0.2$ should be done with caution.

Finally, an important observation in the context of Fig. 5.7 is that the computed magnetization response is fairly independent of the matrix shear modulus G_m^*, as easily observed by comparing parts (a), (d) and (g). Instead, the magnetostriction response is a very strong function of G_m^*.

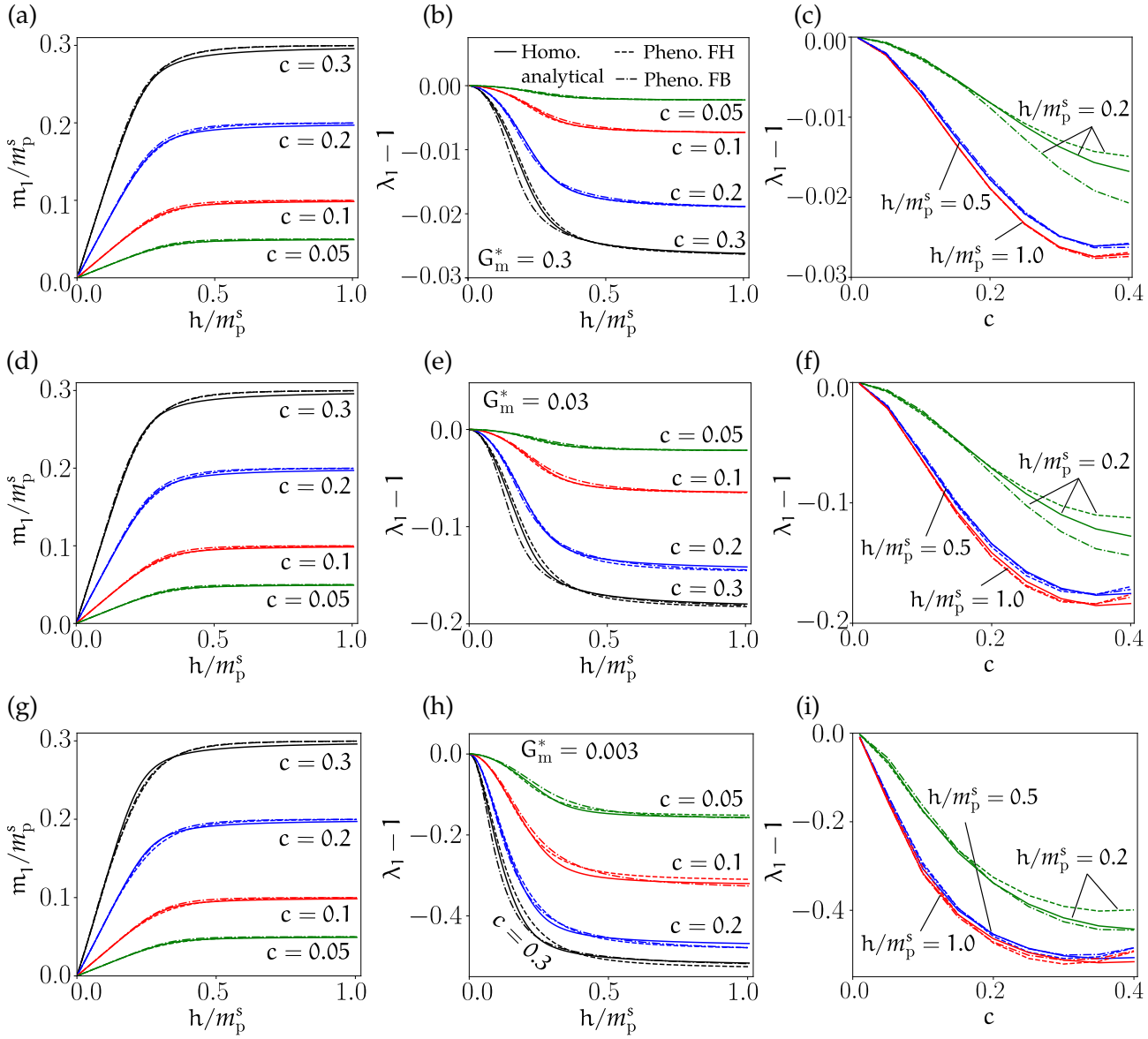

Figure 5.7: Effective (a,d,g) magnetization and (b,e,h) magnetostriction as a function of the applied normalized Eulerian field h/m_p^s obtained by the analytical $\mathbf{F}-\mathbf{H}$ homogenization model (5.4) (solid lines), the phenomenological $\mathbf{F}-\mathbf{H}$ model (5.23) (dashed lines) and the phenomenological $\mathbf{F}-\mathbf{B}$ model (5.35) (dashed-dot lines) for particle volume fractions $c = 0.05, 0.1, 0.2$ and 0.3 for matrix shear moduli of $G_m = 0.3, 0.03$ and 0.003MPa. Zero average axial mechanical pres-stress is applied. (c,f,i) Effect of particle volume fractions c on the magnetostrictions at various values of h/m_p^s.

5.3.3 Comparison between the phenomenological and homogenization estimates with mechanical pre-load

The final step in the assessment of the proposed phenomenological models is to probe the model for mechanical pre-loads that lie outside the previous calibration range. We thus consider three different mechanical pre-loads, namely, the uniaxial pre-stress, the equibiaxial pre-stress and the pre-shear stress. In this regard, Fig. 5.8, 5.9 and 5.10 show the effective magnetization and pure

magnetostriction (i.e. $\lambda_1 - \lambda_1^0$ with λ_1^0 denoting the initial pre-stretching due to the applied pre-stress) for $G_m = 0.003$ and 0.03MPa at a volume fraction $c = 0.2$ as a function of the applied Eulerian h–field h/m_p^s. In all subsequent cases, the direction of magnetic loading is prescribed along $\mathbf{e}_1$, while the direction of applied pre-stresses are varied. The magnitude of the applied pre-stresses is selected in accord with experimentally-relevant pre-stress conditions (see Danas et al. (2012b)). The corresponding pre-stretches λ_i^0 $(i = 1,2,3)$ can be easily computed numerically or analytically for Neo-Hookean solids and are not presented explicitly here (see e.g., Danas and Triantafyllidis (2014)).

Uniaxial pre-stress load **:** The uniaxial pre-stresses are applied along the direction 1 or 2, i.e., $S_{11}^{mech}/G_m \neq 0$ or $S_{22}^{mech}/G_m \neq 0$, respectively, retaining the rest of the boundary conditions the same as those described in (4.84). As discussed before and in agreement with the earlier results of Danas et al.

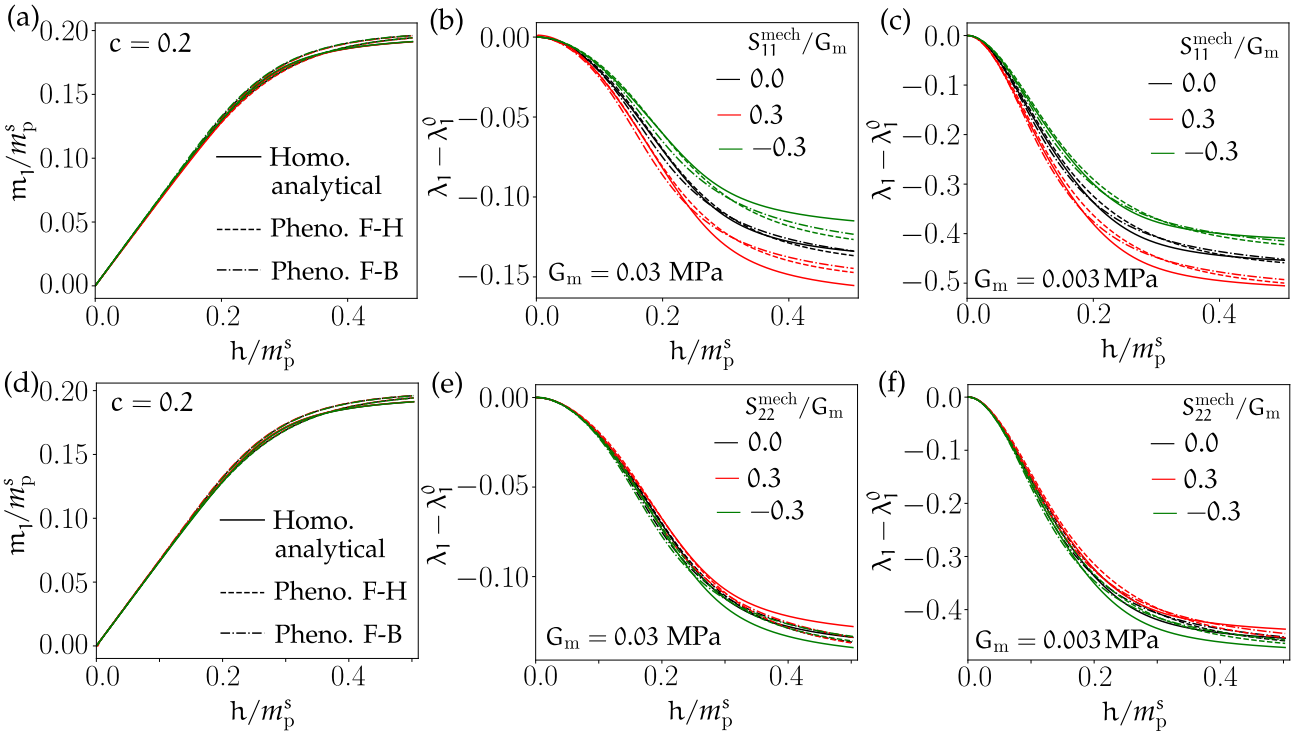

Figure 5.8: Effective (a,d) magnetization and (b,c,e,f) magnetostriction as a function of the applied normalized Eulerian field h/m_p^s obtained by the analytical $\mathbf{F}-\mathbf{H}$ homogenization model (5.4) (solid lines), the phenomenological $\mathbf{F}-\mathbf{H}$ model (5.23) (dashed lines) and the phenomenological $\mathbf{F}-\mathbf{B}$ model (5.35) (dashed-dot lines) for particle volume fraction $c = 0.2$ and for matrix shear moduli of $G_m = 0.03$ and 0.003MPa. (a-c) and (d-f): Two sets of average uniaxial mechanical pres-stress are applied as $S_{11}^{mech}/G_m = -0.3, 0, 0.3$ and $S_{22}^{mech}/G_m = -0.3, 0, 0.3$, respectively.

(2012b), the magnetization response in Fig. 5.8a and d are independent of the matrix shear modulus G_m and the pre-stress (not labeled in the figure for clarity). All models are in excellent agreement in this case of magnetization response.

In Fig. 5.8b, c, e and f, the magnetostriction response depends on the pre-stress as expected. We observe that application of a tensile pre-stress S_{11}^{mech}/G_m along the direction of the magnetic loading leads to an enhancement of compression, while application of a compressive pre-stress moves the magnetostriction curve upwards, i.e. to less compression. These results are in qualitative agreement with the reported experimental results in Danas et al. (2012b). On the other hand, applied transverse

tensile and compressive pre-stresses S_{22}^{mech}/G_m leads to a reduction and an enhancement in the magnetostriction, respectively (see Fig. 5.8e and f). Moreover, the variability of the magnetostriction due to the transverse pre-stress S_{22}^{mech} is found to be weaker than the axial one, S_{11}^{mech}.

In all these magnetostriction responses we observe that the phenomenological model, while remaining in very good agreement with the homogenization model for small to moderate values of h, tends to underestimate (in absolute value) the saturating magnetostriction at higher fields. The differences between the phenomenological and homogenization estimates are larger for the higher matrix shear modulus $G_m = 0.03$MPa, while they become much smaller for the lower one $G_m = 0.003$MPa. Nevertheless, the phenomenological model retains the correct characteristics even at large pre-stresses.

Equibiaxial pre-stress load **:** Equibiaxial mechanical loading together with a transverse applied magnetic field along the third direction is often encountered in layered MRE structures (Danas and Triantafyllidis, 2014; Psarra et al., 2017, 2019). Thus, motivated from such practical loading situations, we probe, next, the phenomenological model under applied equi-biaxial pre-stress along directions 2 and 3, such that $S_{22}^{mech}/G_m = S_{33}^{mech}/G_m \equiv S_{Bi}^{mech}/G_m \neq 0$, while the remaining boundary conditions are given by (4.84). Similar to the uniaxial pre-loading, no significant change in the magnetization is observed in Fig. 5.9a. The magnetotsriction obtained from the homogenization model is found

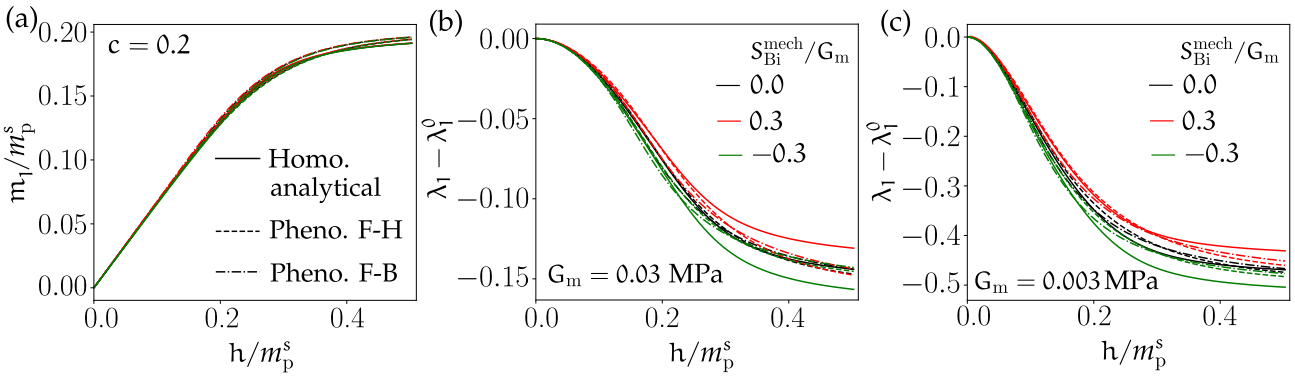

Figure 5.9: Effective (a) magnetization and (b,c) magnetostriction as a function of the applied normalized Eulerian field h/m_p^s obtained by the analytical $\mathbf{F}-\mathbf{H}$ homogenization model (5.4) (solid lines), the phenomenological $\mathbf{F}-\mathbf{H}$ model (5.23) (dashed lines) and the phenomenological $\mathbf{F}-\mathbf{B}$ model (5.35) (dashed-dot lines) for particle volume fraction $c = 0.2$ and for matrix shear moduli of $G_m = 0.03$ and 0.003MPa. (a-c) Three average equibiaxial mechanical pres-stress are applied, so that $S_{22}^{mech}/G_m = S_{33}^{mech}/G_m = S_{Bi}^{mech}/G_m = -0.3, 0, 0.3$.

to change in Fig. 5.9b and c depending on the direction of S_{Bi}^{mech}/G_m. A very weak change is observed in the phenomenolgical magnetostriction response. We note that an equibiaxial pre-tension (pre-compression) along directions 2-3 leads to a pre-compression (pre-tension) along 1, which is the direction of magnetic loading. Hence, the magnetostriction is observed to decrease (increase) for $S_{Bi}^{mech}/G_m > 0$ ($S_{Bi}^{mech}/G_m < 0$), which is in agreement with the previous observations in the context of uniaxial pre-stresses. Again the phenomenological model is in better agreement with the homogenization model for softer matrices.

Shear pre-stress load *:* The magneto-mechanical measurements in (Danas, 2017) also consider mechanical loading paths where a shear pre-stress is applied transverse to the applied magnetic field. Thus, a shear pre-loading is considered in this section by applying $S_{21}^{mech}/G_m > 0$, while keeping the rest of the boundary conditions identical to (4.84). In agreement with the previous observations, the

magnetization remains unaffected by the applied S_{12}^{mech} (see Fig. 5.10a). In Figs. 5.10b and c, the mag-

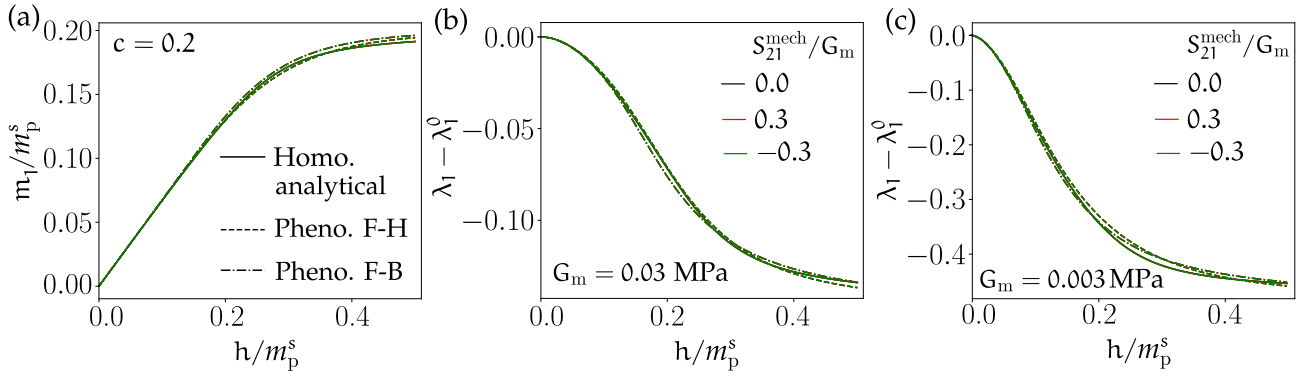

Figure 5.10: Effective (a) magnetization and (b,c) magnetostriction as a function of the applied normalized Eulerian field h/m_p^s obtained by the analytical $\mathbf{F}-\mathbf{H}$ homogenization model (5.4) (solid lines), the phenomenological $\mathbf{F}-\mathbf{H}$ model (5.23) (dashed lines) and the phenomenological $\mathbf{F}-\mathbf{B}$ model (5.35) (dashed-dot lines) for particle volume fraction $c = 0.2$ and for matrix shear moduli of $G_m = 0.03$ and 0.003MPa. (a-c) Three overall pre-shear stresses are applied: $S_{21}^{mech}/G_m = 0, 0.3, 0.5$.

netostriction estimates obtained by both models are *completely* independent of S_{21}^{mech}. Furthermore, the application of S_{21}^{mech} leads to a shear stain and a transverse magnetization along $\mathbf{e}_2$. The resulting shear strain is interestingly found by both models to be completely independent of the applied magnetic field and thus is not included in Figs. 5.10b and c. Similarly, the transverse magnetization remains considerably lower ($\sim 10^{-3} m_p^s$) than the parallel magnetization and thus is not included in Fig. 5.10a. We note in passing that very similar results are also obtained by both models for a shear pre-stress $S_{12}^{mech}/G_m \neq 0$ and thus is not included here for brevity.

In summary, the above results are in qualitative agreement with those in Danas et al. (2012b) and suggest that MRE devices that are based on a shearing mechanical load exhibit very weak coupling along that direction and thus negligible magnetorheological stiffening. This is one of the substantial differences between MR elastomers and MR fluids, since the latter can mainly operate in shearing conditions. Instead, the MR solids can mainly operate under uniaxial and multi-axial ones.

5.4 Concluding remarks

In this chapter, we present explicit phenomenological models both in the $\mathbf{F}-\mathbf{H}$ and the $\mathbf{F}-\mathbf{B}$ space, which are based on a rigorous homogenization solution and lie in the space of the deformation gradient, $\mathbf{F}$, and Lagrangian h–field, $\mathbf{H}$. We analyze the magnetization and magnetostriction problem using an augmented variational principle in an effort to retrieve the pure microscopic "material" magneto-mechanical coupling in magnetorheological elastomers (MREs). We then use this framework to study numerically and analytically the homogenized response of isotropic MREs comprising I_1–based hyperelastic matrix and mechanically rigid iron particles that exhibit negligible magnetic hysteresis (i.e. magnetically soft). The most important part of this study consists in proposing simple explicit homogenization-guided phenomenological models in both $\mathbf{F}-\mathbf{H}$ and $\mathbf{F}-\mathbf{B}$ variable space. Those phenomenological models are proposed both in the context of incompressible and nearly incompressible setting, making them highly versatile and easy-to-implement in finite element user material subroutines.

Specifically, we show by comparison with full-field FE RVE calculations that the analytical homogenization model of Lefèvre et al. (2017) is sufficiently accurate for small to moderate particle volume fractions (i.e., $0 < c \leqslant 0.2$). While this model is general since it is based on a rigorous homogenization procedure, it is implicit for the case of magnetically saturating particles and thus requires the solution of an additional nonlinear algebraic equation for the complete description of the MRE response. Also it is only proposed in the $\mathbf{F}-\mathbf{H}$ variable space since a Legendre-Fenchel transform is not analytically feasible in the general nonlinear magnetic saturation context. Nonetheless, it offers an extremely valuable base to investigate the response of isotropic MREs and to help calibrate phenomenological models.

In this regard, in the present study, we propose explicit phenomenological models that are based on the homogenization model. In particular, the proposed energy functions recover three main features of the Lefèvre et al. (2017) homogenization model: (i) they recover the exact (in the sense of homogenization) effective magnetization response at small and very large (i.e. at magnetization saturation) magnetic fields, (ii) they predict the exact magnetostriction response at small-to-moderate magnetic fields for any mechanical pre-loads and (iii) their purely mechanical response is exactly that of the homogenization model, which has been originally obtained in Lopez-Pamies et al. (2013). In order to maintain the simplicity of the models, we choose not to recover exactly the magnetostriction response at very large saturating magnetic fields (but see along these directions the recent work in the $\mathbf{F}-\mathbf{H}$ space of Lefèvre et al. (2019)). In particular, in a number of applications where the geometry plays a predominant role (see for instance Psarra et al. (2019)) or the coupling is weak (i.e., at fairly large shear moduli of the matrix phase, e.g. larger than 0.3MPa for instance), the coupled part of the energy can be easily dropped while maintaining the dependence on the volume fraction of the particles in the mechanical and magnetic energy. This last modeling approach is straightforward and fairly accurate for such applications and requires a minimum set of calibration such as the mechanical and purely magnetic constitutive parameters of the MRE.

Specifically, in order to obtain the nontrivial behavior of the magnetostrictive response as a function of the applied Eulerian magnetic field (i.e., is initially quadratic, subsequently increases in a slower non-quadratic manner reaching a saturating value), we propose a coupling energy that is a nonconvex function of its argument. It is noted, however, that the coefficient multiplying this coupling part is rather small thus leading to an overall convex magneto-elastic energy function. However, it is evident from that observation that for more complex MREs (i.e. with non-spherical particles or particle-chain distributions) such nonconvexities could lead to instabilities and loss of ellipticity (see for instance (Danas and Triantafyllidis, 2014) and (Psarra et al., 2017, 2019)). Such an analysis is beyond the scope of the present manuscript and is left for a future study.

Furthermore, the proposed phenomenological model comprises very few calibration parameters, which in the present study are reduced to a single one, i.e., $\beta_2^{H,B}$. This parameter is then calibrated numerically by comparison with the analytical homogenization model of Lefèvre et al. (2017). Nevertheless, the form of the phenomenological energy functions is more universal and can be used more generally in fitting any experimental or numerical estimates that may be available. As also shown, extrapolation of the phenomenological estimates in a regime that lies rather far from the calibration process (e.g. significant applied pre-stresses) gives very satisfactory and accurate results at small and moderate applied magnetic fields and even large fields particularly for softer matrices.

By using the simple explicit energy functions together with the variational framework of Danas

(2017) that allows to study the pure material magneto-mechanical coupling, we have obtained several interesting results. Specifically, all presented models show that in the context of isotropic MREs, the magnetization response is insensitive to the shear modulus of the matrix material even when the latter ranges from values between 0.003-0.3MPa (this observation is also valid for the larger range 0.001-1MPa not explicitly shown here). On the other hand, the magnetostriction response is highly dependent of the shear modulus of the matrix G_m, as intuitively expected. A second observation, which is consistent with the recent work of Danas (2017), is that the microscopic deformation of isotropic MREs leads to compressive magnetostriction for zero overall mechanical tractions in the RVE. Hence, the observed overall extensive response of MRE specimens in experiments (see for instance Bodelot et al. (2017)) is a result of the specimen shape and the entire set of boundary conditions and geometry of the experimental setup. This has been discussed in detail in Lefèvre et al. (2017), who showed that in zones of (almost) zero mechanical tractions, the MRE exhibits compressive strains. Finally, application of pre-stresses results in the phenomenological models becoming less accurate especially at larger magnetic fields, even though their predictions become increasingly better for softer matrices. Finally, we find that the effect of a mechanical pre-load is maximum for uniaxial pre-stressing and negligible for shearing ones.

Chapter

6 Microstructurally-guided continuum models for ħ-MREs

Chapter summary: *Microstructurally-guided, explicit continuum models for the isotropic ħ-MREs are proposed in the* $\mathbf{F}-\mathbf{H}$, $\mathbf{F}-\mathbf{h}$, $\mathbf{F}-\mathbf{B}$ *and* $\mathbf{F}-\mathbf{b}$ *variable spaces. While the* $\mathbf{F}-\mathbf{H}$ *and* $\mathbf{F}-\mathbf{B}$ *models are proposed in terms of the reference variables, the* $\mathbf{F}-\mathbf{h}$ *and* $\mathbf{F}-\mathbf{b}$ *models consider the current* $\mathbf{h}$ *and* $\mathbf{b}$ *to be the primary variables, respectively. Specific choices for the remanent internal variables at the macroscale are proposed via carefully observing the microstructure behaviour obtained from the numerical computations, under different magneto-mechanical loading paths. Fully objective energetic and dissipation potentials are proposed thereafter in terms of the microstructural model properties, the particle volume fraction and a phenomenological coupling constant, which is the only model parameter that is computed subsequently by fitting the model response with the numerically computed ones under a proportional cyclic loading. Rigorous probe of the proposed models are carried out against the numerically computed effective response under several non-trivial magneto-mechanical loading paths. Excellent agreement of all the model predictions are obtained with the numerical homogenization results for the moderately soft to (mechanically) hard elastomeric matrices, having the shear modulus of* 0.3 *to* 1.0 *MPa.*

Chapter content

In this chapter, we propose a set of internal variable-based constitutive frameworks for the macroscopic modeling of isotropic h-MREs in both Lagrangian and Eulerian settings. Specifically, we propose four independent versions of the model, namely the $\mathbf{F}-\mathbf{H}$, $\mathbf{F}-\mathbf{h}$, $\mathbf{F}-\mathbf{B}$ and $\mathbf{F}-\mathbf{b}$ model. The choice of the independent internal variables in these models play a pivotal role in the mictostructurally-guided phenomenological modeling of the effective response. Since the internal variables do *not* admit any differential or boundary constraints in $\mathcal{V}_0$ (or $\mathcal{V}$), unlike the primary variables, no constitutive relation are obtained for them from the incremental homogenization framework presented in Chapter 4. Therefore, the macroscopic models presented herein rely on independently-proposed thermodynamic internal variables, whose evolution laws are then obtained from the macroscopic Clausius-Duhem inequalities and generalized standard material relations.

First, we derive the constitutive relations for $\mathbf{F}-\mathbf{H}$ and $\mathbf{F}-\mathbf{h}$ formulations from the Clausius-Duhem inequality. This will be followed by the proposal of specific energetic and dissipation potentials in terms of the independent primary and internal variables. The evolution equations for the internal variables in the $\mathbf{F}-\mathbf{H}$ and $\mathbf{F}-\mathbf{h}$ settings are proposed thereafter. Moreover, a comprehensive discussion on the material objectivity and material symmetry for such models are provided. Subsequently, the $\mathbf{F}-\mathbf{B}$ and $\mathbf{F}-\mathbf{b}$-based models are proposed and a similar type of model features regarding the material objectivity and symmetry are highlighted. In analogy to the microstructurally-guided models for the s-MREs, the purely decoupled models are proposed here only in terms of the microstructure material (e.g. $G_m, \chi_p^e, \chi_p, m_p^s$, etc.) and geometric (e.g. c) properties. The magneto-mechanical coupling energy is proposed thereafter by introducing an additional model parameter, which is estimated by fitting the model response to the numerical homogenization results or to the experimental data. In addition, all the proposed models must satisfy the following conditions.

1. The models must lead to symmetric Cauchy stress measures and thus, satisfy the angular momentum balance condition (2.20).

2. In absence of any magnetic field, the models should reduce to the effective hyperelastic mechanical model, which is given in terms of the free energy (5.5).

3. In the limit of $b_p^c \to 0$, the h-MRE model responses should be identical to that of the analytical homogenization model of Lefèvre et al. (2017), for the specific choice of $\chi_p^e = 0$.

4. Under the special case having $\chi_p^e = 0$, the slope of initial magnetization response after switching shall be given by χ, which the Maxwell-Garnett lower bound for the effective susceptibility. Also, for $|\mathbf{H}| \to \infty$, the magnetization should saturate at $|\mathbf{m}| = m^s = c\, m_p^s$.

5. In the limit of $c \to 1$, the proposed models must recover the classical continuum model of Robinson (1975) for metallic permanent magnets.

Finally, the responses from the proposed model are probed against those from the numerical homogenization estimates, under both proportional and non-proportional magneto-mechanical loads.

Prior to the definition of specific constitutive models, we highlight a key assumption related to the modeling that follows. We assume *affine particle rotations* in the development of these constitutive models. Under this assumption, the schematic representation of the effect of tensile and shear loading on a pre-magnetized RVE is shown in Fig. 6.1. Specifically, it is assumed that a pure stretch of the magnetized ħ-MRE leads to particle displacements, while keeping their effective (average) rotations unaltered (see Fig. 6.1b). On the other hand, the particles do rotate under applied macroscopic shear,

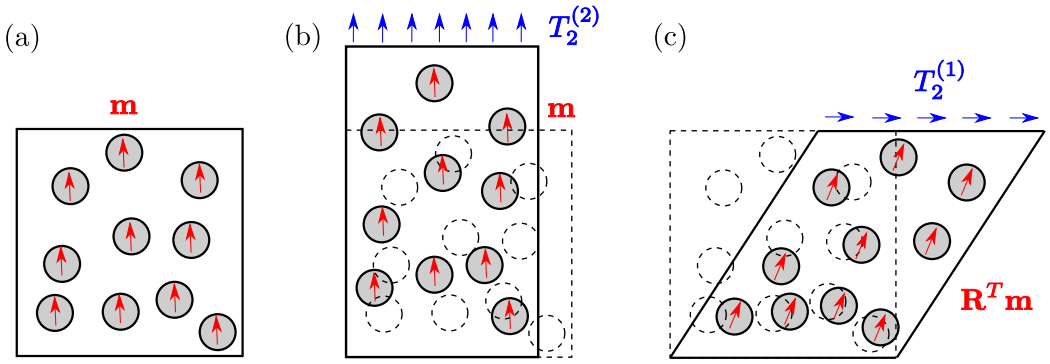

Figure 6.1: Schematic diagram of affine rotation of magnetic particles in a RVE. (a) Magnetized RVE with effective magnetization $\mathbf{m}$. (b) Deformed RVE under applied traction $\mathrm{T}_2^{(2)} = \mathrm{S}_{22}^{\mathrm{mech}}\mathcal{N}_2$ with displaced particles. (c) Sheared RVE under applied traction $\mathrm{T}_2^{(1)} = \mathrm{S}_{12}^{\mathrm{mech}}\mathcal{N}_2$ with affine particle rotation by $\mathbf{R}$.

as shown in Fig. 6.1c, thus rotating the effective magnetization vector $\mathbf{m}$. The present model assumes *affine rotation* of the magnetized particles with the imposed macroscopic rotation $\mathbf{R}$ of the ħ-MRE under all possible magneto-mechanical loading paths.

It is emphasized that such fully affine rotation of hard magnetic particles is a constitutive assumption. Moreover, there is no rigorous analytical estimate for the average particle rotations under applied macroscopic shear or non-proportional magnetic fields. Nonetheless, the affine rotation assumption serves as a first approximation towards modeling the rather complicated macroscopic behavior of the ħ-MREs. Rigorous probe of the model against the numerically computed effective responses under proportional and non-proportional magneto-mechanical loading paths will be provided in Section 6.4.

In this regard, we note the works of McMeeking and Landis (2005) and McMeeking et al. (2007) where the notion of a "rotation preserving" electric polarization has been introduced. The preset model is cornered around the same idea, albeit considering *only* a rotation preserving remanent ħ-field. The following elaborates on the step-by-step modeling approach towards a finite-strain dissipative magneto-elasticity framework.

Remark 6.1. We will use the following identities regarding the derivative of a sufficiently smooth scalar-valued tensor function $(\blacksquare)$ with respect to the strain-like variables $\mathbf{F}$, $\mathbb{C}$ and $\mathbb{B}$, where $\mathbb{C} = \mathbf{F}^{\mathsf{T}}\mathbf{F}$ and $\mathbb{B} = \mathbf{F}\mathbf{F}^{\mathsf{T}}$. These identities read (Steigmann, 2010)

$$\frac{\partial(\blacksquare)}{\partial\mathbf{F}} = 2\mathbf{F}\frac{\partial(\blacksquare)}{\partial\mathbb{C}}, \qquad \text{and} \qquad \frac{\partial(\blacksquare)}{\partial\mathbf{F}} = 2\frac{\partial(\blacksquare)}{\partial\mathbb{B}}\mathbf{F}^{\mathsf{T}}. \tag{6.1}$$

Notice that the derivatives $\partial(\blacksquare)/\partial\mathbb{C}$ and $\partial(\blacksquare)/\partial\mathbb{B}$ yield symmetric tensors due to the symmetry of $\mathbb{C}$ and $\mathbb{B}$, respectively.

6.1 $\mathbf{F}-\mathbf{H}$ and $\mathbf{F}-\mathbf{h}$ constitutive models

While defining the constitutive models in the $\mathbf{F}-\mathbf{H}$ and $\mathbf{F}-\mathbf{h}$ space, we first select the independent internal variables. This will be followed by the derivation of constitutive relations in the Lagrangian ($\mathbf{F}-\mathbf{H}$) and Eulerian ($\mathbf{F}-\mathbf{h}$) settings. Finally, the specific choice for the macroscopic energetic and dissipation potentials are provided, followed by the specific evolution laws for the Lagrangian and Eulerian internal variables.

6.1.1 Additive decomposition of H and h

In this section, we propose an additive decomposition of the effective (macroscopic) $\mathbf{H}$ into an energetic and a remanent parts. In contrast to the ferromagnetic model of mechanically stiff microparticles (4.14), we observe in Fig. 6.1 that the remanent magnetization (in absence of $\mathbf{h}$) remains unaffected by the mechanical stretch $\mathbf{U}$, but changes its orientation under a mechanical rotation $\mathbf{R}$. The macroscopic stretch $\mathbf{U}$ and rotation $\mathbf{R}$ tensors are obtained via the polar decomposition of the macroscopic deformation gradient $\mathbf{F} = \mathbf{RU}$. Notably, we observe from (3.14) that, in absence of any applied $\mathbf{h}$, the remanent field $\mathbf{h}^r$ is directly proportional to the current magnetization $\mathbf{m}$. We therefore propose the referential counterpart of $\mathbf{h}^r$ in the stretch-free intermediate configuration $\mathcal{V}_i$ (see Fig. 6.2). This definition leads to the intermediate remanent field $\mathcal{H}^r$ that is independent of the

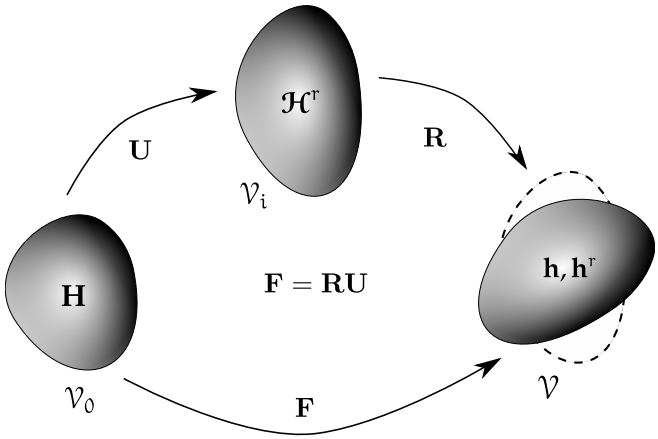

Figure 6.2: Definition of the independent internal variable $\mathcal{H}^r$ at the intermediate configuration $\mathcal{V}_i$.

mechanical stretch $\mathbf{U}$. Thus, the additive decomposition of $\mathbf{H}$ reads

$$\mathbf{H} = \mathbf{H}^e + \mathbf{U}\mathcal{H}^r, \tag{6.2}$$

where $\mathbf{H}^e$ is the referential energetic h-field. The push-forward transformation via (2.40) of (6.2) to the current configuration $\mathcal{V}$ reads

$$\mathbf{F}^{-T}\mathbf{H} = \mathbf{F}^{-T}\mathbf{H}^e + \mathbf{F}^{-T}\mathbf{U}\mathcal{H}^r \implies \mathbf{h} = \mathbf{h}^e + \mathbf{R}\mathcal{H}^r \equiv \mathbf{h}^e + \mathbf{h}^r. \tag{6.3}$$

Hence, it follows from the last decomposition that $\mathbf{h}^r = \mathbf{R}\mathcal{H}^r$, i.e., the reference description of $\mathbf{h}^r$ is independent of $\mathbf{U}$ (see Fig. 6.2). In this context, we note that the independent internal variables in the remanent polarization problems are typically defined in an intermediate configuration (McMeeking

and Landis, 2005; McMeeking et al., 2007; Rosato and Miehe, 2014).

6.1.2 Thermodynamic inequalities and constitutive relations

In the following, we derive the constitutive relations for the ħ-MREs in the reference and current configurations. The local Clausius-Duhem inequality, which is derived from the "global" entropy imbalance (see Chapter 2 for details), leads to the thermodynamically consistent constitutive frameworks for the dissipative ferro-electric/magnetic materials (McMeeking and Landis, 2002; Landis, 2002; Klinkel, 2006; Rosato and Miehe, 2014). The following referential and current constitutive frameworks for the ħ-MREs are henceforth developed from the Clausius-Duhem inequalities (2.64) and (2.36), respectively. Here we consider isothermal thermodynamic processes that involve zero heat flux and local variation in the temperature.

Constitutive relations in the reference configuration **:** The local form of the Clausius-Duhem inequality for a magnetoelastic solid in the reference configuration is obtained via simplifying further (2.64), so that

$$\mathbf{S} : \dot{\mathbf{F}} - \mathbf{B} \cdot \dot{\mathbf{H}} - \dot{W}^{\mathrm{H}} \geqslant 0, \tag{6.4}$$

where $\mathbf{S}$ is the first Piola-Kirchhoff stress and $\dot{(\,)}$ represents the material time derivative. The macroscopic potential energy $W^{\mathrm{H}} = W^{\mathrm{H}}(\mathbb{C}, \mathbf{H}, \mathcal{H}^{\mathrm{r}})$ is expressed in terms of the right Cauchy-Green tensor $\mathbb{C} = \mathbf{F}^{\mathsf{T}}\mathbf{F}$, referential $\mathbf{H}$ and the internal variable $\mathcal{H}^{\mathrm{r}}$. Such definition of W^{H} in terms of $\mathbb{C}$ ensures the material objectivity and thus is typical in the formulation of s- and ħ-MREs (Kankanala and Triantafyllidis, 2004; Rosato and Miehe, 2014; Keip and Rambausek, 2016, 2017). Expanding subsequently $\dot{W}$ in terms of its arguments, we rephrase (6.4) to be

$$\left[\mathbf{S} - 2\mathbf{F}\frac{\partial W^{\mathrm{H}}}{\partial \mathbb{C}}\right] : \dot{\mathbf{F}} - \left[\mathbf{B} + \frac{\partial W^{\mathrm{H}}}{\partial \mathbf{H}}\right] \cdot \dot{\mathbf{H}} - \frac{\partial W^{\mathrm{H}}}{\partial \mathcal{H}^{\mathrm{r}}} \cdot \dot{\mathcal{H}}^{\mathrm{r}} \geqslant 0, \tag{6.5}$$

Given the arbitrariness of the rates $\dot{\mathbf{F}}$ and $\dot{\mathbf{H}}$, the standard Coleman-Noll-Gurtin arguments leads to the constitutive relations in the reference configuration, given by (Keip and Rambausek, 2016, 2017; Lefèvre et al., 2017)

$$\mathbf{S} = 2\mathbf{F}\frac{\partial W^{\mathrm{H}}}{\partial \mathbb{C}}, \qquad \mathbf{B} = -\frac{\partial W^{\mathrm{H}}}{\partial \mathbf{H}}. \tag{6.6}$$

Since the derivative of a scalar-valued tensor function with respect to a symmetric tensor is symmetric, the Cauchy stress $\boldsymbol{\sigma} = (1/J)\mathbf{S}\mathbf{F}^{\mathsf{T}}$ computed from $(6.6)_1$ remains identically symmetric, thus satisfying the angular momentum balance (Kankanala and Triantafyllidis, 2004; Suo et al., 2008; Rosato and Miehe, 2014). Notice that it is difficult to express $\mathbf{S}$ explicitly in terms of the mechanical and the magnetic stress contributions, unless the referential $\mathbf{H}$ and $\mathcal{H}^{\mathrm{r}}$ are expressed in terms of their current ($\mathbf{h} = \mathbf{h}(\mathbf{F}, \mathbf{H})$, $\mathbf{h}^{\mathrm{r}} = \mathbf{h}^{\mathrm{r}}(\mathbf{R}, \mathcal{H}^{\mathrm{r}})$) counterparts (Danas, 2017). Thus, by rephrasing W^{H} in terms of the current variables, so that $W^{\mathrm{H}}(\mathbb{C}, \mathbf{H}, \mathcal{H}^{\mathrm{r}}) \equiv w^{\mathrm{h}}(\mathbb{B}, \mathbf{h}, \mathbf{h}^{\mathrm{r}}; \mathbf{F}, \mathbf{H}, \mathcal{H}^{\mathrm{r}})$[1], one can rephrase $\mathbf{S}$ (or equivalently $\boldsymbol{\sigma}$) explicitly in terms of the mechanical and magnetic contributions. Notice that the independent magnetic primary and internal variables in w^{h} still remain $\mathbf{H}$ and $\mathcal{H}^{\mathrm{r}}$. However, w^{h} is expressed in terms of the variables $\mathbb{B}$, $\mathbf{h}$ and $\mathbf{h}^{\mathrm{r}}$ with the latter two being explicit functions of $\mathbf{F}$, $\mathbf{H}$ and $\mathcal{H}^{\mathrm{r}}$. Consequently, the equivalent representation of $\boldsymbol{\sigma}$ in terms of w^{h} is obtained via applying the chain

[1]Since $w(\mathbb{B}, \mathbf{h}, \mathbf{h}^{\mathrm{r}})$ is the free energy in terms current variables $\mathbf{h}$ and $\mathbf{h}^{\mathrm{r}}$, it is typically expressed in terms of the left Cauchy-Green tensor $\mathbb{B}$ to satisfy the objectivity conditions (Kankanala and Triantafyllidis, 2004).

rules (6.1), such that

$$\begin{aligned}\boldsymbol{\sigma} &= \frac{2}{J}\mathbf{F}\frac{\partial W^{H}}{\partial \mathbb{C}}\mathbf{F}^{T} = \frac{1}{J}\frac{\partial w^{h}}{\partial \mathbf{F}}\mathbf{F}^{T} = \frac{2}{J}\left[\frac{\partial w^{h}}{\partial \mathbb{B}}\right]_{\mathbf{h},\mathbf{h}^{r}}\mathbb{B} + \frac{1}{J}\left(\left[\frac{\partial w^{h}}{\partial \mathbf{h}}\right]_{\mathbf{F},\mathbf{h}^{r}}\cdot\frac{\partial \mathbf{h}}{\partial \mathbf{F}}\right)\mathbf{F}^{T} + \frac{1}{J}\left(\left[\frac{\partial w^{h}}{\partial \mathbf{h}^{r}}\right]_{\mathbf{F},\mathbf{h}}\cdot\frac{\partial \mathbf{h}^{r}}{\partial \mathbf{F}}\right)\mathbf{F}^{T} \\ &= \underbrace{\frac{2\rho_{0}}{J}\left[\frac{\partial \psi^{h}}{\partial \mathbb{B}}\right]_{\mathbf{h},\mathbf{h}^{r}}\mathbb{B}}_{\boldsymbol{\sigma}_{\text{mech}}} + \underbrace{\left(\mathbf{h}\otimes\mathbf{b} - \frac{\mu_{0}}{2}|\mathbf{h}|^{2}\mathbf{I}\right)}_{\boldsymbol{\sigma}^{\text{en}}_{\text{maxw}}} + \underbrace{\frac{\rho_{0}}{J}\left\{\left(\left[\frac{\partial \psi^{h}}{\partial \mathbf{h}^{r}}\right]_{\mathbf{F},\mathbf{h}}\otimes\mathbf{R}^{T}\mathbf{h}^{r}\right)\colon\frac{\partial \mathbf{R}}{\partial \mathbf{F}}\right\}\mathbf{F}^{T}}_{\boldsymbol{\sigma}^{\text{rem}}_{\text{maxw}}},\end{aligned} \tag{6.7}$$

where we decompose the potential $w^{h}(\mathbb{B},\mathbf{h},\mathbf{h}^{r})$, so that $w^{h}(\mathbb{B},\mathbf{h},\mathbf{h}^{r}) = \rho_{0}\psi^{h}(\mathbb{B},\mathbf{h},\mathbf{h}^{r}) - (\mu_{0}/2)J\mathbf{h}\cdot\mathbf{h}$, where ψ^{h} is the Helmholtz free energy associated with the h-MRE. The first two terms in (6.7) are identical to the stress associated with the non-remanent, soft MREs (Kankanala and Triantafyllidis, 2004; Lefèvre et al., 2017), whereas the remanent Maxwell stress contribution $\boldsymbol{\sigma}^{\text{rem}}_{\text{maxw}}$ is an additional stress that is not observed in the non-remanent magnetization problems. Again, the symmetry of the "total" Cauchy stress $\boldsymbol{\sigma}$ is guaranteed via defining the potential energy in terms of $W^{H}(\mathbb{C},\mathbf{H},\mathcal{H}^{r}) = w^{h}(\mathbb{B},\mathbf{h},\mathbf{h}^{r};\mathbf{F},\mathbf{H},\mathcal{H}^{r})$, whereas its individual components $\boldsymbol{\sigma}_{\text{mech}}$, $\boldsymbol{\sigma}^{\text{en}}_{\text{maxw}}$ and $\boldsymbol{\sigma}^{\text{rem}}_{\text{maxw}}$ are not, in general, symmetric. This is an important observation, to which we will refer back while developing an Eulerian equivalent to the proposed Lagrangian framework.

Finally, the remaining terms in (6.5) leads to the dissipation inequality, which reads

$$\mathcal{B}^{r}\cdot\dot{\mathcal{H}}^{r} \geqslant 0, \qquad \text{with} \qquad \mathcal{B}^{r} = -\frac{\partial W^{H}}{\partial \mathcal{H}^{r}}. \tag{6.8}$$

Of course, the remanent field $\mathcal{B}^{r}$ is an intermediate quantity. Hence, unlike the primary constitutive relations (6.6), the generalized standard material relation is expressed in the intermediate configuration such that (Halphen and Nguyen, 1975)

$$\frac{\partial W^{H}}{\partial \mathcal{H}^{r}} + \frac{\partial D^{H}}{\partial \dot{\mathcal{H}}^{r}} = 0 \qquad \Longrightarrow \qquad \mathcal{B}^{r} = \frac{\partial D^{H}}{\partial \dot{\mathcal{H}}^{r}}, \tag{6.9}$$

where $D^{H}(\mathbb{C},\mathbf{H},\mathcal{H}^{r},\dot{\mathcal{H}}^{r})$ is the dissipation potential. We note that, this hybrid reference-intermediate formulation leads to the primary constitutive relations (6.6) in the reference configuration, whereas the remanent constitutive relations $(6.8)_{2}$ and (6.9) are defined in the intermediate configuration. One can develop the full constitutive framework in the intermediate configuration (see e.g., (Rosato and Miehe, 2014)), however, the reference primary variables lead to *familiar* stress measures like $\mathbf{S}$ and also facilitate the numerical computations (Kankanala and Triantafyllidis, 2004; Dorfmann and Ogden, 2004, 2005; Danas, 2017; Lefèvre et al., 2017). Thus, in practice, the hybrid constitutive framework (6.6) and (6.9) leads to an efficient but easy model.

Constitutive relations in the current configuration **:** The equivalent constitutive framework in the current configuration is expressed now by considering the $\mathbf{h}$ and $\mathbf{h}^{r}$ to be the independent primary and internal variables, respectively. Notice that, unlike the Lagrangian formulation, here both the primary and the internal variables are defined in the current configuration $\mathcal{V}$ (see Fig. 6.2). Again, we start by considering the localized Clausius-Duhem inequality in the current configuration (2.36), such that (Kankanala and Triantafyllidis, 2004)

$$J\left(\boldsymbol{\sigma} - \mathbf{h}\otimes\mathbf{b} + \frac{\mu_{0}}{2}|\mathbf{h}|^{2}\mathbf{I}\right)\colon\mathbf{l} - \mu_{0}J\mathbf{m}\cdot\dot{\mathbf{h}} - \rho_{0}\dot{\psi}^{h} \geqslant 0, \tag{6.10}$$

where $\mathbf{l} = \dot{\mathbf{F}}\mathbf{F}^{-1}$ is the mechanical deformation rate. Chapter 2 shows that (6.10) is equivalent to the Clausius-Duhem inequality in the reference configuration given by (6.4). Expanding subsequently the material rate of the Helmholtz free energy $\dot{\psi}^{\mathrm{h}}(\mathbb{B}, \mathbf{h}, \mathbf{h}^{\mathrm{r}})$ of (6.10) in terms of its arguments, we obtain

$$J\left(\boldsymbol{\sigma} - \mathbf{h}\otimes\mathbf{b} + \frac{\mu_0}{2}|\mathbf{h}|^2\mathbf{I}\right) : \mathbf{l} - \mu_0 J\mathbf{m}\cdot\dot{\mathbf{h}} - \rho_0\frac{\partial\psi^{\mathrm{h}}}{\partial\mathbb{B}} : \dot{\mathbb{B}} - \rho_0\frac{\partial\psi^{\mathrm{h}}}{\partial\mathbf{h}}\cdot\dot{\mathbf{h}} - \rho_0\frac{\partial\psi^{\mathrm{h}}}{\partial\mathbf{h}^{\mathrm{r}}}\cdot\dot{\mathbf{h}}^{\mathrm{r}} \geqslant 0, \tag{6.11}$$

which upon rearrangement finally reads

$$\begin{aligned} &J\left[\boldsymbol{\sigma} - \frac{2\rho_0}{J}\frac{\partial\psi^{\mathrm{h}}}{\partial\mathbb{B}}\mathbb{B} - \left(\mathbf{h}\otimes\mathbf{b} - \frac{\mu_0}{2}|\mathbf{h}|^2\mathbf{I}\right) - \frac{\rho_0}{J}\left\{\left(\frac{\partial\psi^{\mathrm{h}}}{\partial\mathbf{h}^{\mathrm{r}}}\otimes\mathbf{R}^{\mathsf{T}}\mathbf{h}^{\mathrm{r}}\right) : \frac{\partial\mathbf{R}}{\partial\mathbf{F}}\right\}\mathbf{F}^{\mathsf{T}}\right] : \mathbf{l} \\ &-J\left[\mathbf{m} + \frac{\rho_0}{J}\frac{\partial\psi^{\mathrm{h}}}{\partial\mathbf{h}}\right]\cdot\dot{\mathbf{h}} - \rho_0\frac{\partial\psi^{\mathrm{h}}}{\partial\mathbf{h}^{\mathrm{r}}}\cdot\overset{\vartriangle}{\mathbf{h}}^{\mathrm{r}} \geqslant 0, \end{aligned} \tag{6.12}$$

where $\overset{\vartriangle}{\mathbf{h}}^{\mathrm{r}} = \dot{\mathbf{h}}^{\mathrm{r}} - \boldsymbol{\Omega}\mathbf{h}^{\mathrm{r}}$ is the objective Green-Naghdi rate of the remanent h-field with $\boldsymbol{\Omega} = \dot{\mathbf{R}}\mathbf{R}^{\mathsf{T}}$ is the mechanical spin tensor (Green and Naghdi, 1965)[2]. Notably, the Green-Nagdi rate of the internal variable in (6.12) ensures the energy dissipation to remain independent of the mechanical spin $\boldsymbol{\Omega}$. In other words, the Green-Nagdi rate of $\mathbf{h}^{\mathrm{r}}$ ensures that, in the absence of external magnetic fields, a rigid rotation of a permanently magnetized h-MRE does not add to any energy dissipation.

We now show that, besides the symmetry of $\boldsymbol{\sigma}$ in (6.12), the sum of the remaining three terms inside the first square bracket of (6.12) is also symmetric. This symmetry can be readily proved via rephrasing w^{h} in terms of $\mathbb{C}$, $\mathbf{H}$ and $\mathcal{H}^{\mathrm{r}}$, so that $w^{\mathrm{h}}(\mathbb{B}, \mathbf{h}, \mathbf{h}^{\mathrm{r}}) = W^{\mathrm{H}}(\mathbb{C}, \mathbf{H}, \mathcal{H}^{\mathrm{r}}; \mathbf{F}, \mathbf{h}, \mathbf{h}^{\mathrm{r}})$ and then, by exploiting the chain rules (6.1) and the Lagrangian constitutive relations $(6.6)_2$ and $(6.8)_2$. The aforementioned algebraic operations, in a conjugate sense to (6.7), finally leads to the relation

$$\frac{2\rho_0}{J}\frac{\partial\psi^{\mathrm{h}}}{\partial\mathbb{B}}\mathbb{B} + \left(\mathbf{h}\otimes\mathbf{b} - \frac{\mu_0}{2}|\mathbf{h}|^2\mathbf{I}\right) + \frac{\rho_0}{J}\left\{\left(\frac{\partial\psi^{\mathrm{h}}}{\partial\mathbf{h}^{\mathrm{r}}}\otimes\mathbf{R}^{\mathsf{T}}\mathbf{h}^{\mathrm{r}}\right) : \frac{\partial\mathbf{R}}{\partial\mathbf{F}}\right\}\mathbf{F}^{\mathsf{T}} = \frac{2}{J}\mathbf{F}\left[\frac{\partial W^{\mathrm{H}}}{\partial\mathbb{C}}\right]_{\mathbf{H},\mathcal{H}^{\mathrm{r}}}\mathbf{F}^{\mathsf{T}}. \tag{6.13}$$

The right-hand-side of the last equation proves that the sum in the first square bracket of (6.12) is symmetric. Hence, we rephrase (6.12) to be

$$\begin{aligned} &J\left[\boldsymbol{\sigma} - \frac{2\rho_0}{J}\frac{\partial\psi^{\mathrm{h}}}{\partial\mathbb{B}}\mathbb{B} - \left(\mathbf{h}\otimes\mathbf{b} - \frac{\mu_0}{2}|\mathbf{h}|^2\mathbf{I}\right) - \frac{\rho_0}{J}\left\{\left(\frac{\partial\psi^{\mathrm{h}}}{\partial\mathbf{h}^{\mathrm{r}}}\otimes\mathbf{R}^{\mathsf{T}}\mathbf{h}^{\mathrm{r}}\right) : \frac{\partial\mathbf{R}}{\partial\mathbf{F}}\right\}\mathbf{F}^{\mathsf{T}}\right] : \mathbf{d} \\ &-J\left[\mathbf{m} + \frac{\rho_0}{J}\frac{\partial\psi^{\mathrm{h}}}{\partial\mathbf{h}}\right]\cdot\dot{\mathbf{h}} - \rho_0\frac{\partial\psi^{\mathrm{h}}}{\partial\mathbf{h}^{\mathrm{r}}}\cdot\overset{\vartriangle}{\mathbf{h}}^{\mathrm{r}} \geqslant 0, \end{aligned} \tag{6.14}$$

where $\mathbf{d} = \mathrm{sym}[\mathbf{l}]$ is the symmetric part of the mechanical deformation rate. It is now observed that $\mathbf{d}$ and $\dot{\mathbf{h}}$ are independent and thus, can be increased arbitrarily[3]. Therefore, owing to the arbitrariness of $\mathbf{d}$ and $\dot{\mathbf{h}}$, the standard arguments of the Coleman-Noll-Gurtin framework leads to the constitutive relations for the total Cauchy stress and the current b-field, such that

$$\boldsymbol{\sigma} = \frac{2\rho_0}{J}\frac{\partial\psi^{\mathrm{h}}}{\partial\mathbb{B}}\mathbb{B} + \left(\mathbf{h}\otimes\mathbf{b} - \frac{\mu_0}{2}|\mathbf{h}|^2\mathbf{I}\right) + \frac{\rho_0}{J}\left\{\left(\frac{\partial\psi^{\mathrm{h}}}{\partial\mathbf{h}^{\mathrm{r}}}\otimes\mathbf{R}^{\mathsf{T}}\mathbf{h}^{\mathrm{r}}\right) : \frac{\partial\mathbf{R}}{\partial\mathbf{F}}\right\}\mathbf{F}^{\mathsf{T}} \tag{6.15}$$

[2]The original work of Green and Naghdi (1965) propose objective rates in the context of mechanics. Nonetheless, the vectorial representation of the Green-Nagdi rate is referred in this paper.

[3]The current stretch rate $\mathbf{d}$ is independent of the spin $\boldsymbol{\Omega} = \dot{\mathbf{R}}\mathbf{R}^{\mathsf{T}}$. Hence, the Green-Nagdi rate $\overset{\vartriangle}{\mathbf{h}}^{\mathrm{r}}$, which is a function of the spin tensor, remains independent of $\mathbf{d}$.

and

$$\mathbf{m} = -\frac{\rho_0}{J}\frac{\partial \psi^h}{\partial \mathbf{h}} \qquad \Rightarrow \qquad \mathbf{b} = -\frac{1}{J}\frac{\partial w^h}{\partial \mathbf{h}}, \tag{6.16}$$

respectively, where the latter is obtained via the relation $w^h(\mathbb{B},\mathbf{h},\mathbf{h}^r) = \rho_0\psi^h(\mathbb{B},\mathbf{h},\mathbf{h}^r) - (\mu_0/2)J\mathbf{h}\cdot\mathbf{h}$. Of course, the expression of total $\boldsymbol{\sigma}$ in terms of the mechanical, Maxwell and remanent parts remains identical to (6.7). Subsequently, the dissipation inequality at the current configuration reads

$$\mathbf{b}^r \cdot \overset{\vartriangle}{\mathbf{h}}^r \geqslant 0, \qquad \text{with} \qquad \mathbf{b}^r = -\rho_0\frac{\partial \psi^h}{\partial \mathbf{h}^r} = -\frac{\partial w^h}{\partial \mathbf{h}^r}, \tag{6.17}$$

where $\mathbf{b}^r$ is the remanent b-field that is the energetic work conjugate of $\mathbf{h}^r$. Furthermore, standard material relation in the current configuration is given in terms of $w^h(\mathbb{B},\mathbf{h},\mathbf{h}^r)$ and $\mathscr{D}^h(\mathbb{B},\mathbf{h},\mathbf{h}^r,\overset{\vartriangle}{\mathbf{h}}^r)$, such that (Halphen and Nguyen, 1975)

$$\frac{\partial w^h}{\partial \mathbf{h}^r} + \frac{\partial \mathscr{D}^h}{\partial \dot{\mathbf{h}}^r} = 0. \tag{6.18}$$

Since the dissipation potential $\mathscr{D}^h(\mathbb{B},\mathbf{h},\mathbf{h}^r,\overset{\vartriangle}{\mathbf{h}}^r)$ is defined in terms of the objective Green-Nagdi rate, we can suitably rephrase the derivative of $\mathscr{D}^h$ with respect to $\dot{\mathbf{h}}^r$ in the last equation in terms of its derivative with respect to $\overset{\vartriangle}{\mathbf{h}}^r$ by applying the chain rule, such that

$$\frac{\partial w^h}{\partial \mathbf{h}^r} + \frac{\partial \mathscr{D}^h}{\partial \overset{\vartriangle}{\mathbf{h}}^r} = 0 \qquad \Longrightarrow \qquad \mathbf{b}^r = \frac{\partial \mathscr{D}^h}{\partial \overset{\vartriangle}{\mathbf{h}}^r}. \tag{6.19}$$

Thus, the dissipative work conjugate of $\overset{\vartriangle}{\mathbf{h}}^r$ is obtained to be $\mathbf{b}^r$. This property of $\mathscr{D}^h$ will be used in the following section while defining the current form of the *rate-independent* evolution equation for $\mathbf{h}^r$.

To this end, the reference and current constitutive relations, (6.6) and (6.16) along with the generalized standard material laws (6.9) and (6.18), respectively, are derived from the Clausius-Duhem inequality. Even though the primary and internal variable arguments of the energetic ($W^H(\mathbb{C},\mathbf{H},\mathcal{H}^r)$ and $w^h(\mathbb{B},\mathbf{h},\mathbf{h}^r)$) and dissipation ($D^H(\mathbb{C},\mathbf{H},\mathcal{H}^r,\dot{\mathcal{H}}^r)$ and $\mathscr{D}^h(\mathbb{B},\mathbf{h},\mathbf{h}^r,\overset{\vartriangle}{\mathbf{h}}^r)$) potentials are specified herein, the aforementioned potentials *cannot* assume any arbitrary functional form in terms their arguments. Instead, these choices are further constrained by a number of physically-motivated conditions and the material properties. Next, we set forth all these constraints on the choice of these potentials, which will be followed by the choice of specific energy functions.

6.1.3 Properties of the potentials W^H, D^H, w^h and $\mathscr{D}^h$

Herein, we detail the constraints on the energetic and dissipation potentials in order to ensure (a) an even magneto-mechanical coupling and (b) material frame indifference. In addition, in order to ensure an isotropic material response, further material symmetry restrictions are imposed on these potentials. Furthermore, in order to ensure a positive dissipation, the potentials D^H and $\mathscr{D}^h$ are subjected to the thermodynamic constraints $(6.8)_1$ and $(6.17)_1$, respectively. It is noted that the material objectivity and symmetry conditions are well known for the soft MREs with iron particles (Kankanala and Triantafyllidis, 2004; Dorfmann and Ogden, 2004). However, as shown in Fig. 6.2,

the proposed model for ħ-MREs introduces the remanent internal variables that are insensitive to the stretch $\mathbf{U}$, which lead to non-familiar magneto-mechanical invariants and rates. Hence, this section is devoted towards stating explicitly all the aforementioned constraints in the context of isotropic ħ-MREs.

Even magnetomechanical coupling **:** The magnetomechanical potential energy W^{H} and w^{h} must be exactly the same when the magnetic loading is performed in the reverse direction (Kankanala and Triantafyllidis, 2004). The even magnetomechanical coupling conditions for the Lagrangian and the Eulerian energetic and dissipation potentials thus read

$$W^{\mathrm{H}}(\mathbb{C},-\mathbf{H},-\mathcal{H}^{\mathrm{r}})=W^{\mathrm{H}}(\mathbb{C},\mathbf{H},\mathcal{H}^{\mathrm{r}}),\qquad \mathrm{D}^{\mathrm{H}}(\mathbb{C},-\mathbf{H},-\mathcal{H}^{\mathrm{r}},-\dot{\mathcal{H}}^{\mathrm{r}})=\mathrm{D}^{\mathrm{H}}(\mathbb{C},\mathbf{H},\mathcal{H}^{\mathrm{r}},\dot{\mathcal{H}}^{\mathrm{r}}) \tag{6.20}$$

and

$$w^{\mathrm{h}}(\mathbb{B},-\mathbf{h},-\mathbf{h}^{\mathrm{r}})=w^{\mathrm{h}}(\mathbb{B},\mathbf{h},\mathbf{h}^{\mathrm{r}}),\qquad \mathscr{D}^{\mathrm{h}}(\mathbb{B},-\mathbf{h},-\mathbf{h}^{\mathrm{r}},-\overset{\vartriangle}{\mathbf{h}}^{\mathrm{r}})=\mathscr{D}^{\mathrm{h}}(\mathbb{B},\mathbf{h},\mathbf{h}^{\mathrm{r}},\overset{\vartriangle}{\mathbf{h}}^{\mathrm{r}}), \tag{6.21}$$

respectively, for arbitrary $\mathbb{C},\ \mathbb{B},\ \mathbf{H},\ \mathcal{H}^{\mathrm{r}},\ \mathbf{h}$ and $\mathbf{h}^{\mathrm{r}}$.

Material frame indifference **:** This criteria imposes the condition that the energetic W^{H}, w^{h} and the dissipation D^{H}, $\mathscr{D}^{\mathrm{h}}$ potentials must remain invariant under the change of observer. A change in the observer leads to the new current position vector $\mathbf{x}^{*}=\mathbf{c}+\mathbf{Q}\mathbf{x}$, where $\mathbf{c}$ is a rigid displacement field and $\mathbf{Q}$ is a rotation tensor (Gurtin, 1982, p. 139-142). Standard calculations show that the invariance of the energetic and dissipation potentials under a transformation $\mathbf{x}\to\mathbf{x}^{*}$ leads to the constraints on W^{H}, D^{H}, w^{h} and $\mathscr{D}^{\mathrm{h}}$, which read (Gurtin, 1982; Kankanala and Triantafyllidis, 2004)

$$W^{\mathrm{H}}(\mathbb{C},\mathbf{H},\mathcal{H}^{\mathrm{r}})=W^{\mathrm{H}}(\mathbb{C},\mathbf{H},\mathcal{H}^{\mathrm{r}}),\qquad \mathrm{D}^{\mathrm{H}}(\mathbb{C},\mathbf{H},\mathcal{H}^{\mathrm{r}},\dot{\mathcal{H}}^{\mathrm{r}})=\mathrm{D}^{\mathrm{H}}(\mathbb{C},\mathbf{H},\mathcal{H}^{\mathrm{r}},\dot{\mathcal{H}}^{\mathrm{r}}) \tag{6.22}$$

and

$$w^{\mathrm{h}}(\mathbf{Q}\mathbb{B}\mathbf{Q}^{\mathsf{T}},\mathbf{Q}\mathbf{h},\mathbf{Q}\mathbf{h}^{\mathrm{r}})=w^{\mathrm{h}}(\mathbb{B},\mathbf{h},\mathbf{h}^{\mathrm{r}}), \tag{6.23}$$

$$\mathscr{D}^{\mathrm{h}}(\mathbf{Q}\mathbb{B}\mathbf{Q}^{\mathsf{T}},\mathbf{Q}\mathbf{h},\mathbf{Q}\mathbf{h}^{\mathrm{r}},\overline{\overset{\vartriangle}{\mathbf{Q}\mathbf{h}^{\mathrm{r}}}})=\mathscr{D}^{\mathrm{h}}(\mathbf{Q}\mathbb{B}\mathbf{Q}^{\mathsf{T}},\mathbf{Q}\mathbf{h},\mathbf{Q}\mathbf{h}^{\mathrm{r}},\mathbf{Q}\overset{\vartriangle}{\mathbf{h}}^{\mathrm{r}})=\mathscr{D}^{\mathrm{h}}(\mathbb{B},\mathbf{h},\mathbf{h}^{\mathrm{r}},\overset{\vartriangle}{\mathbf{h}}^{\mathrm{r}}), \tag{6.24}$$

respectively. Notice that the material frame indifference condition imposes no further restrictions on the Lagrangian potentials W^{H} and D^{H}. This is because the right Cauchy-Green tensor $\mathbb{C}$ and the reference $\mathbf{H}$ remain invariant under the operation $\mathbf{x}\to\mathbf{x}^{*}$. Nevertheless, it is also noted that the intermediate vector $\mathcal{H}^{\mathrm{r}}$ and its rate also remain unaltered under the same operation. This observation is in agreement with the objectivity conditions used in mechanical visco-plasticity, where the intermediate strain-like variables remain unaffected by a change in the observer (Dashner, 1993; Kumar and Lopez-Pamies, 2016). Finally, the relation $\overline{\overset{\vartriangle}{\mathbf{Q}\mathbf{h}^{\mathrm{r}}}}=\mathbf{Q}\overset{\vartriangle}{\mathbf{h}}^{\mathrm{r}}$ for the Green-Nagdi rate in $(6.24)_2$ is obtained via expressing $\overset{\vartriangle}{\mathbf{h}}^{\mathrm{r}}=\mathbf{R}\overline{\dot{\mathbf{R}^{\mathsf{T}}\mathbf{h}^{\mathrm{r}}}}$ and then performing the transformations $\mathbf{R}\to\mathbf{Q}\mathbf{R}$ and $\mathbf{h}^{\mathrm{r}}\to\mathbf{Q}\mathbf{h}^{\mathrm{r}}$.

Material symmetry **:** For the isotropic MREs with material symmetry group $\mathcal{S}\mathrm{ymm}\in\mathcal{O}\mathrm{rth}^{+}$, the energetic and dissipation potentials must remain invariant under a change in the reference configuration via the tensor $\mathbf{K}\in\mathcal{S}\mathrm{ymm}$. The material symmetry conditions on the potentials thus read

$$W^{\mathrm{H}}(\mathbf{K}^{\mathsf{T}}\mathbb{C}\mathbf{K},\mathbf{K}^{\mathsf{T}}\mathbf{H},\mathbf{K}^{\mathsf{T}}\mathcal{H}^{\mathrm{r}})=W^{\mathrm{H}}(\mathbb{C},\mathbf{H},\mathcal{H}^{\mathrm{r}}), \tag{6.25}$$

$$D^{H}(\mathbf{K}^{T}\mathbb{C}\mathbf{K}, \mathbf{K}^{T}\mathbf{H}, \mathbf{K}^{T}\mathcal{H}^{r}, \mathbf{K}^{T}\dot{\mathcal{H}}^{r}) = D^{H}(\mathbb{C}, \mathbf{H}, \mathcal{H}^{r}, \dot{\mathcal{H}}^{r}) \tag{6.26}$$

and

$$w^{h}(\mathbb{B}, \mathbf{h}, \mathbf{h}^{r}) = w^{h}(\mathbb{B}, \mathbf{h}, \mathbf{h}^{r}), \qquad \mathscr{D}^{h}(\mathbb{B}, \mathbf{h}, \mathbf{h}^{r}, \overset{\vartriangle}{\mathbf{h}}^{r}) = \mathscr{D}^{h}(\mathbb{B}, \mathbf{h}, \mathbf{h}^{r}, \overset{\vartriangle}{\mathbf{h}}^{r}). \tag{6.27}$$

Again, the material symmetry conditions do *not* impose any additional constraint on the Eulerian description (6.27) of the potentials. Note from $(6.26)_1$ that the intermediate $\mathcal{H}^{r}$ transforms via $\mathcal{H}^{r} \to \mathbf{K}^{T}\mathcal{H}^{r}$, which follows from the additive decomposition (6.2) of the Lagrangian $\mathbf{H}$ and the transformation of $\mathbf{U} \to \mathbf{K}^{T}\mathbf{U}\mathbf{K}$ under a change in the reference configuration. It is also noted that in mechanical visco-plasticity the change in the reference configuration also modifies the intermediate plastic internal variables (Dashner, 1993; Bennett et al., 2016). Moreover, since the symmetry transformation tensor $\mathbf{K}$ is, by definition, constant in time (Malvern, 1969, p. 415-421), the material symmetry conditions on the dissipation potentials D^{H} and $\mathscr{D}^{h}$ take the form given by (6.26) and $(6.27)_2$, respectively.

Entropy imbalance **:** The dissipation inequalities $(6.8)_1$ and $(6.17)_1$ impose additional constraints on $D^{H}(\mathbb{C}, \mathbf{H}, \mathcal{H}^{r}, \dot{\mathcal{H}}^{r})$ and $\mathscr{D}^{h}(\mathbb{B}, \mathbf{h}, \mathbf{h}^{r}, \overset{\vartriangle}{\mathbf{h}}^{r})$, respectively, so that the entropy production remains always positive, thus ensuring a positive dissipation for any loading paths. These constraints on $D^{H}(\mathbb{C}, \mathbf{H}, \mathcal{H}^{r}, \dot{\mathcal{H}}^{r})$ and $\mathscr{D}^{h}(\mathbb{B}, \mathbf{h}, \mathbf{h}^{r}, \overset{\vartriangle}{\mathbf{h}}^{r})$ read

$$\frac{\partial D^{H}}{\partial \dot{\mathcal{H}}^{r}}(\mathbb{C}, \mathbf{H}, \mathcal{H}^{r}, \dot{\mathcal{H}}^{r}) \cdot \dot{\mathcal{H}}^{r} \geqslant 0 \qquad \text{and} \qquad \frac{\partial \mathscr{D}^{h}}{\partial \overset{\vartriangle}{\mathbf{h}}^{r}}(\mathbb{B}, \mathbf{h}, \mathbf{h}^{r}, \overset{\vartriangle}{\mathbf{h}}^{r}) \cdot \overset{\vartriangle}{\mathbf{h}}^{r} \geqslant 0, \tag{6.28}$$

respectively. Thus, in order to satisfy (6.28), $D^{H}(\mathbb{C}, \mathbf{H}, \mathcal{H}^{r}, \dot{\mathcal{H}}^{r})$ and $\mathscr{D}^{h}(\mathbb{B}, \mathbf{h}, \mathbf{h}^{r}, \overset{\vartriangle}{\mathbf{h}}^{r})$ must be convex functions of $\dot{\mathcal{H}}^{r}$ and $\overset{\vartriangle}{\mathbf{h}}^{r}$, respectively.

Definition of invariants **:** Finally, in order to satisfy the material frame indifference and the material symmetry conditions, the energy functions are typically expressed in terms of frame invariant quantities, which leads to identical functional forms of W^{H} and w^{h} in terms of these invariants. We provide a set of invariants that are relevant to the modeling of isotropic h-MREs in Table 6.1,

Table 6.1: Invariants associated with isotropic hard magneto-elastic solids

Invariant	Lagrangian	Eulerian	Invariant	Lagrangian	Eulerian
$I_4^{H} =$	$\mathbf{H}\cdot\mathbf{H}$	$\mathbf{h}\cdot\mathbb{B}\mathbf{h}$	$I_5^{H} =$	$\mathbf{H}\cdot\mathbb{C}^{-1}\mathbf{H}$	$\mathbf{h}\cdot\mathbf{h}$
$I_4^{HHr} =$	$\mathbf{H}\cdot\mathbb{C}^{1/2}\mathcal{H}^{r}$	$\mathbf{h}\cdot\mathbb{B}\mathbf{h}^{r}$	$I_5^{HHr} =$	$\mathbf{H}\cdot\mathbb{C}^{-1/2}\mathcal{H}^{r}$	$\mathbf{h}\cdot\mathbf{h}^{r}$
$I_4^{Hr} =$	$\mathcal{H}^{r}\cdot\mathbb{C}\mathcal{H}^{r}$	$\mathbf{h}^{r}\cdot\mathbb{B}\mathbf{h}^{r}$	$I_5^{Hr} =$	$\mathcal{H}^{r}\cdot\mathcal{H}^{r}$	$\mathbf{h}^{r}\cdot\mathbf{h}^{r}$

where all the mechanical and the I_4^{H} and I_5^{H} magneto-mechanical invariants are the standard ones that are employed in non-dissipative magnetoelasticity (Keip and Rambausek, 2016, 2017; Lefèvre et al., 2017; Lefèvre et al., 2019). Nevertheless, the finite strain framework for h-MREs necessitates a set of additional invariants associated with the remanent fields. In this regard, Table 6.1 shows four additional magneto-mechanical invariants, among which I_4^{HHr} and I_5^{HHr} are the dot products of the full h-field with the remanent h in the Lagrangian and Eulerian settings, respectively. Again, we note from (6.2) that the Lagrangian remanent field is given by $\mathbf{U}\mathcal{H}^{r}$, which leads to such non-trivial expressions of I_4^{HHr} and I_5^{HHr} in Table 6.1 (note that $\mathbf{U} = \mathbb{C}^{1/2}$)[4]. However, the purely remanent

[4]Since $\mathbb{C}^{1/2}$ and $\mathbb{C}^{-1/2}$ are symmetric, the invariants I_4^{HHr} and I_5^{HHr} can be equivalently defined via $I_4^{HHr} =$

invariants I_4^{Hr} and I_5^{Hr} are straightforward to obtain in terms of their Lagrangian and Eulerian dot products, respectively.

It is straightforward to verify that the mechanical (I_1, I_2, J), energetic and remanent magneto-mechanical invariants (I_i^H, I_i^{Hr} with $i = 4, 5$) satisfy the frame indifference and symmetry conditions. The invariance of the "mixed" invariants I_i^{HHr} under the change of the reference configuration can also be proved via employing the identities $(\mathbf{K}^T\mathbb{C}\mathbf{K})^{1/2} = \mathbf{K}^T\mathbb{C}^{1/2}\mathbf{K}$ and $(\mathbf{K}^T\mathbb{C}\mathbf{K})^{-1/2} = \mathbf{K}^T\mathbb{C}^{-1/2}\mathbf{K}$ (Gurtin, 1982, p. 169). Of course, one can propose a number of additional magneto-mechanical invariants involving higher powers of $\mathbb{C}$ (or $\mathbb{B}$). Nonetheless, in the present model we limit out choice of invariants to those given by Table 6.1.

Finally, we propose an additional scalar invariant in terms of the referential ($\dot{\mathcal{H}}^r$) and current ($\overset{\triangle}{\mathbf{h}}^r$) rates of the internal variables. These two rates are related via $|\dot{\mathcal{H}}^r| = |\overset{\triangle}{\mathbf{h}}^r|$. Moreover, we note that both $|\dot{\mathcal{H}}^r|$ and $|\overset{\triangle}{\mathbf{h}}^r|$ satisfy the conditions of even magneto-mechanical coupling, material frame indifference and symmetry. Thus, a dissipation potential that is defined in terms of the invariants in Table 6.1 and $|\dot{\mathcal{H}}^r|$ or $|\overset{\triangle}{\mathbf{h}}^r|$ remains fully objective and material symmetric. In the following, we define the specific functional forms of W^H and D^H (or equivalently, w^h and $\mathscr{D}^h$).

6.1.4 Choice of energy functions : decoupled model

Here we propose fully decoupled energetic and dissipation potentials associated with an incompressible ħ-MRE. In particular, the decoupled model ensures no mechanical deformation under applied proportional Eulerian magnetic loading cycles (Danas, 2017). Notably, for the soft MREs, a decoupled model ensures no mechanical deformations under any Eulerian magnetic loading path. However, as observed in (4.43), the imposition of Eulerian ħ-fields does not cancel the effect of magnetic body torques. Hence, the decoupled response in the ħ-MREs are obtained *only* under a proportional cyclic Eulerian ħ-field, which ensures, on an average sense, no misalignment between the current magnetization $\mathbf{m}$ and the applied ħ-field, thus leading to a vanishing remanent stress.

Energetic potential **:** Earlier investigations with the soft MREs (Danas, 2017; Lefèvre et al., 2017; Lefèvre et al., 2019) show that an the I_5^H-based magnetic energy leads to a decoupled magneto-mechanical response. Thus, the incompressible potential energy reads

$$W^H(I_1, I_5^H, I_5^{HHr}, I_5^{Hr}) = w^h(I_1, I_5^H, I_5^{HHr}, I_5^{Hr}) = \begin{cases} \rho_0\psi_{mech}(I_1) + \rho_0\psi_{mag}^H(I_5^{Hr}, I_5^{HHr}, I_5^{Hr}) & \\ \qquad\qquad -\dfrac{\mu_0}{2} I_5^H & \text{if } J = 1 \\ +\infty & \text{otherwise,} \end{cases} \tag{6.29}$$

where ψ_{mech} and ψ_{mag}^H represent the mechanical and the magnetic parts of the Helmholtz free energy, respectively. The effective mechanical energy is given by (5.5), which is the analytical homogenization estimate, provided by Lopez-Pamies et al. (2013) for I_1-based incompressible two phase composites having rigid particulate inclusions.

The magnetic free energy is further decomposed into an energetic and a remanent part, so that

$$\rho_0\psi_{mag}^H(I_5^H, I_5^{HHr}, I_5^{Hr}) = \rho_0\psi_{mag}^{H,en}(I_5^H) + \rho_0\psi_{mag}^{H,rem}(I_5^{HHr}, I_5^{Hr}). \tag{6.30}$$

$\mathbb{C}^{1/2}$: $\mathrm{sym}(\mathbf{H}\otimes\mathcal{H}^r)$ and $I_5^{HHr} = \mathbb{C}^{-1/2}$: $\mathrm{sym}(\mathbf{H}\otimes\mathcal{H}^r)$, respectively.

To this end, no explicit analytical homogenization model is available for remanent magnetization response. Nevertheless, we propose an effective model that satisfies exactly two limiting conditions, under which the analytical homogenization estimates are available. Firstly, in the limit of $b_p^c \to \infty$, the constant homogenized slope of the linear magnetic response is given by the classical Maxwell-Garnett (M-G) lower bound (Ponte Castañeda and Galipeau, 2011; Lefèvre et al., 2017). Therefore, the effective energetic magnetic free energy $\psi_{mag}^{H,en}$ reads

$$\rho_0 \psi_{mag}^{H,en}(I_5^H) = -\frac{\mu_0}{2}\chi^e I_5^H \qquad \text{with} \qquad \chi^e = \frac{3c\chi_p^e}{3+(1-c)\chi_p^e}, \tag{6.31}$$

where χ^e is the effective energetic susceptibility. Consequently, the effective energetic permeability is obtained via $\mu^e = \mu_0(1+\chi^e)$. Secondly, we note from Chapter 3 that, in the limit of $b_p^c \to 0$ and $\chi_p^e = 0$, we recover the reversible saturation magnetic response. Hence, we propose a remanent potential given by

$$\rho_0 \psi_{mag}^{H,rem}(I_5^{HHr}, I_5^{Hr}) = \mu_0(1+\chi^e)I_5^{HHr} + \frac{\mu_0}{2}\left(\frac{1-c}{3c}\right)I_5^{Hr} + \frac{\mu_0}{c}\frac{(m^s)^2}{\chi_p} f_p^h\left(\frac{\sqrt{I_5^{Hr}}}{m^s}\right), \tag{6.32}$$

that leads to an excellent approximation of the analytical homogenization estimates of Ponte Castañeda and Galipeau (2011) and Lefèvre et al. (2017) in the limit of $b_p^c \to 0$ and $\chi_p^e = 0$. The effective saturation magnetization m^s in (6.32) is given by $m^s = c\, m_p^s(\mu^e/\mu_p^e)$, which leads to the "standard" effective saturation magnetization $m^s = c\, m_p^s$ for "ideal" hard magnets with $\chi_p^e = 0$, so that $\mu^e = \mu_p^e = \mu_0$. Finally, the function f_p^h remains identical to its definition in (3.12) and Table 3.1, of course, here with a different argument in the macroscopic model. Moreover, in the limiting case of $|\mathbf{h}^r| \to 0$, the nonlinear remanent potential (6.32) becomes linear in I_5^{Hr}, so that

$$\rho_0 \psi_{mag,|\mathbf{h}^r|\to 0}^{H,rem}(I_5^{HHr}, I_5^{Hr}) = \mu_0(1+\chi^e)I_5^{HHr} + \frac{\mu_0}{2\chi} I_5^{Hr} \qquad \text{with} \qquad \chi = \frac{3c\chi_p}{3+(1-c)\chi_p}, \tag{6.33}$$

that is the Maxwell-Garnett lower bound of the initial susceptibility of the composite. Hence, the effective initial slope of the saturation magnetization response also remains identical to the analytical estimate. Nevertheless, the probe of the full model against numerically computed effective response will be provided in Section 6.4.

Dissipation potential **:** It remains to define the evolution law for the internal variables $\mathcal{H}^r$ and $\mathbf{h}^r$, which is obtained via defining a convex magnetic dissipation potential in terms of a power law in $|\dot{\mathcal{H}}^r|$ (or equivalently, in $|\overset{\Delta}{\mathbf{h}}{}^r|$), which reads

$$D^H(|\dot{\mathcal{H}}^r|) = \frac{b^c \dot{h}^{r0}}{(p+1)}\left[\frac{|\dot{\mathcal{H}}^r|}{\dot{h}^{r0}}\right]^{p+1} = \frac{b^c \dot{h}^{r0}}{(p+1)}\left[\frac{|\overset{\Delta}{\mathbf{h}}{}^r|}{\dot{h}^{r0}}\right]^{p+1} = \mathscr{D}^h(|\overset{\Delta}{\mathbf{h}}{}^r|), \qquad \text{with} \qquad b^c = b_p^c\left(\frac{\mu^e}{\mu_p^e}\right)^{4/5} \tag{6.34}$$

denoting the effective coercive field of the composite and with p is the rate exponent that leads to a linear visco-switching response for $p = 1$ and a rate-independent hysteretic response for $p = 0$ (Danas et al., 2012a; Rosato and Miehe, 2014). Notice that $\dot{h}^{r0}$ in (6.34) is a reference rate parameter. The numerical homogenization estimates (will be shown in Section 5.3) and experiments (Huber et al., 2017; Kim et al., 2018) show that the effective coercivity b^c remains *nearly* equal to the coercivity of the hard magnetic inclusions b_p^c. Nevertheless, in order to incorporate the effect of non-zero χ^e, the

factor $(\mu^e/\mu_p^e)^{4/5}$ is multiplied in $(6.34)_2$, which leads to a weak dependence of b^c on c depending on the magnitude of χ^e.

Notice that the dissipation potentials in (6.34) are independent of the mechanical deformations. This is because the definition of $\mathcal{H}^r$ in a stretch-free intermediate configuration and consequently, the dissipation in terms of the Green-Naghdi rate of the current $\mathbf{h}^r$. Therefore, it is observed that the relation $|\dot{\mathcal{H}}^r| = |\overset{\triangle}{\mathbf{h}}^r|$ is valid for any loading path. Hence, (6.34) is fully objective and remains independent of both mechanical stretch $\mathbf{U}$ and the rotation $\mathbf{R}$.

The relation $(6.9)_1$ yields that the intermediate remanent field $\mathcal{B}^r$ is the work conjugate of $\dot{\mathcal{H}}^r$. Thus, a Legendre transform $D^H(|\dot{\mathcal{H}}^r|)$ with respect to $\dot{\mathcal{H}}^r$ leads to its complimentary dissipation potential $D^{H*}(|\mathcal{B}^r|)$, which is also a power law with an exponent $(n+1)/n$ on $|\mathcal{B}^r|$. Subsequently, in the limit of rate-independence (i.e., $n \to 0$), the dissipation potentials $D^H(|\dot{\mathcal{H}}^r|)$ and $\mathscr{D}^h(\overset{\triangle}{\mathbf{h}}^r)$ lead to the switching surface in terms of $\mathcal{B}^r$ and $\mathbf{b}^r$, respectively, which reads

$$\Phi^H := \mathcal{B}^r \cdot \mathcal{B}^r - (b^c)^2 = 0, \qquad \phi^h := \mathbf{b}^r \cdot \mathbf{b}^r - (b^c)^2 = 0. \tag{6.35}$$

Finally, the evolution equations for $\mathcal{H}^r$ and $\mathbf{h}^r$ are obtained from the principal of maximum remanent dissipation, that leads to the associated switching rules in the intermediate and current configurations, given by (Landis, 2002; Klinkel, 2006; Linnemann et al., 2009)

$$\dot{\mathcal{H}}^r = \dot{\lambda}^H \frac{\partial \Phi^H}{\partial \mathcal{B}^r} \qquad \text{and} \qquad \overset{\triangle}{\mathbf{h}}^r = \dot{\lambda}^h \frac{\partial \phi^h}{\partial \mathbf{b}^r}, \tag{6.36}$$

respectively, where $\dot{\lambda}^H$ and $\dot{\lambda}^h$ are the Lagrange multipliers that satisfy the Kuhn-Tucker conditions given by

$$\begin{cases} \dot{\lambda}^H = 0 & \text{if } \Phi^H < 0 \\ \dot{\lambda}^H > 0 & \text{if } \Phi^H = 0 \end{cases} \quad \text{and} \quad \begin{cases} \dot{\lambda}^h = 0 & \text{if } \phi^h < 0 \\ \dot{\lambda}^h > 0 & \text{if } \phi^h = 0. \end{cases} \tag{6.37}$$

Constitutive equations in Lagrangian and Eulerian settings **:** Two equivalent decoupled formulations in the reference and current configurations are proposed for the h-MREs. The reference formulation utilizes the constitutive laws (6.6) along with the intermediate switching surface $(6.35)_1$ and the corresponding associated switching rule $(6.36)_1$, whereas, the current constitutive laws, switching surface and switching rule are given by (6.16), $(6.35)_2$ and $(6.36)_2$, respectively. The set of constitutive relations for the incompressible h-MREs are thereby listed in Table 6.2. Notice that an arbitrary hydrostatic pressure contribution is added to the stresses in order to apply the incompressibility constraint. We conclude this part by making two remarks. Moreover, the expression (6.15) for $\boldsymbol{\sigma}$ is simplified further after substituting (6.17) into it (see Appendix 6.A for details).

Symmetry of $\boldsymbol{\sigma}$ **:** Given the choice of $w^H(I_1, I_5^H, I_5^{HHr}, I_5^{Hr})$ for the decoupled model, we note that all the arguments of $\rho_0\psi^H$ are independent of $\mathbb{B}$ except the mechanical invariant I_1. Hence, the mechanical Cauchy stress $\boldsymbol{\sigma}_{\text{mech}}$ is symmetric for this incompressible model (Ogden, 1997). Moreover, the constitutive choice (6.29) leads to the current $\mathbf{b}$ and $\mathbf{b}^r$ given by

$$\mathbf{b} = \mu_0(1+\chi^e)(\mathbf{h}-\mathbf{h}^r) \quad \text{and} \quad \mathbf{b}^r = -\mu_0(1+\chi^e)\mathbf{h} - \mu_0\left(\frac{1-c}{3c}\right)\mathbf{h}^r - \frac{\mu_0}{c}\frac{m^s}{\chi_p}(f_p^h)'\left(\frac{\sqrt{I_5^{Hr}}}{m^s}\right)\frac{\mathbf{h}^r}{|\mathbf{h}^r|}, \tag{6.38}$$

Table 6.2: Constitutive relations and associated switching rules for incompressibe h-MREs in the Lagrangian and Eulerian frameworks

Lagrangian	Eulerian
$\mathbf{S} = 2\mathbf{F}\dfrac{\partial W^{\mathrm{H}}}{\partial \mathbb{C}} - p\mathbf{F}^{-\mathsf{T}}$	$\boldsymbol{\sigma} = 2\rho_0 \dfrac{\partial \psi^{\mathrm{h}}}{\partial \mathbb{B}}\mathbb{B} + \left(\mathbf{h}\otimes\mathbf{b} - \dfrac{\mu_0}{2}\lvert\mathbf{h}\rvert^2\mathbf{I}\right) + \dfrac{2}{\det\mathbf{Z}}\mathbf{Z}\,\mathrm{skw}\left(\mathbf{h}^{\mathrm{r}}\otimes\mathbf{b}^{\mathrm{r}}\right)\mathbf{V}\mathbf{Z} - p\mathbf{I}$
$\mathbf{B} = -\dfrac{\partial W^{\mathrm{H}}}{\partial \mathbf{H}}$	$\mathbf{b} = -\dfrac{\partial w^{\mathrm{h}}}{\partial \mathbf{h}}$
$\mathcal{B}^{\mathrm{r}} = -\dfrac{\partial W^{\mathrm{H}}}{\partial \mathcal{H}^{\mathrm{r}}}$	$\mathbf{b}^{\mathrm{r}} = -\dfrac{\partial w^{\mathrm{h}}}{\partial \mathbf{h}^{\mathrm{r}}}$
$\Phi^{\mathrm{H}} := \mathcal{B}^{\mathrm{r}}\cdot\mathcal{B}^{\mathrm{r}} - (b^{\mathrm{c}})^2 = 0$	$\phi^{\mathrm{h}} := \mathbf{b}^{\mathrm{r}}\cdot\mathbf{b}^{\mathrm{r}} - (b^{\mathrm{c}})^2 = 0$
$\dot{\mathcal{H}}^{\mathrm{r}} = \dot{\lambda}^{\mathrm{H}}\dfrac{\partial \Phi^{\mathrm{H}}}{\partial \mathcal{B}^{\mathrm{r}}}$	$\overset{\triangle}{\mathbf{h}}^{\mathrm{r}} = \dot{\lambda}^{\mathrm{h}}\dfrac{\partial \phi^{\mathrm{h}}}{\partial \mathbf{b}^{\mathrm{r}}}$

respectively. Substitution of (6.38) into $(6.16)_1$ followed by some algebraic manipulations leads to the expression for the remanent stress given by (see Appendix 6.A for details)

$$\boldsymbol{\sigma}^{\mathrm{rem}}_{\mathtt{maxw}} = -\frac{2\mu_0}{\det\mathbf{Z}}\mathbf{Z}\,\mathrm{skw}\left(\mathbf{h}\otimes\mathbf{m}\right)\mathbf{V}\mathbf{Z}, \tag{6.39}$$

where $\mathbf{V} = \mathbb{B}^{1/2}$ is the left stretch tensor and $\mathbf{Z} = \mathrm{tr}(\mathbf{V})\mathbf{I} - \mathbf{V}$. Notice that, unlike the "classical" definition (Pao and Hutter, 1975; Robinson, 1975) of the magnetic body torques, $\boldsymbol{\sigma}^{\mathrm{rem}}_{\mathtt{maxw}}$ is *not* skew-symmetric for the h-MREs. Nevertheless, in addition to the demonstrations in Section 6.1.2, Appendix 6.A also shows that the total $\boldsymbol{\sigma}$ is symmetric from its explicit expression, derived therein.

6.1.5 Coupled potential

In order to introduce a coupling potential, we follow (Mukherjee et al., 2020) and augment a coupled free energy $\psi^{\mathrm{H}}_{\mathtt{couple}}$ to the fully decoupled model (6.29). The full expression for W^{H} thus reads

$$W^{\mathrm{H}}(I_1, I_4^{\mathrm{Hr}}, I_4^{\mathrm{HHr}}, I_5^{\mathrm{H}}, I_5^{\mathrm{Hr}}, I_5^{\mathrm{HHr}}) = \begin{cases} \rho_0\psi_{\mathtt{mech}}(I_1) + \rho_0\psi^{\mathrm{H}}_{\mathtt{mag}}(I_5^{\mathrm{H}}, I_5^{\mathrm{Hr}}, I_5^{\mathrm{HHr}}) + \\ \qquad \rho_0\psi^{\mathrm{H}}_{\mathtt{couple}}(I_4^{\mathrm{Hr}}, I_4^{\mathrm{HHr}}, I_5^{\mathrm{Hr}}, I_5^{\mathrm{HHr}}) - \dfrac{\mu_0}{2}I_5^{\mathrm{H}} & \text{if } J = 1 \\ +\infty & \text{otherwise.} \end{cases} \tag{6.40}$$

In the absence of any energetic magnetization (equivalent to the ferroelectric hysteresis response) , i.e., $\chi^e = 0$, the coupled energy is observed to be directly proportional to the square of the remanent field $\mathcal{H}^{\mathrm{r}}$. Thus, the purely remanent $\psi^{\mathrm{H}}_{\mathtt{couple}}$ reads

$$\rho_0\psi^{\mathrm{H}}_{\mathtt{couple}}(I_4^{\mathrm{Hr}}, I_5^{\mathrm{Hr}}) = c\beta^{\mathrm{Hr}}\mu_0\left(I_4^{\mathrm{Hr}} - I_5^{\mathrm{Hr}}\right), \tag{6.41}$$

[4] In the Lagrangian setting, the remanent fields and the associated switching rules are expressed in the intermediate configuration.

where β^{Hr} is a real material parameter, namely the remanent coupling coefficient. Nonetheless, the finite energetic magnetization for $\chi^e \neq 0$ necessitates the definition of an additional coupling energy. The full ψ^H_{couple} is hence defined via

$$\rho_0\psi^H_{couple}(I_4^{Hr}, I_4^{HHr}, I_5^{Hr}, I_5^{HHr}) = c\beta^{Hr}\mu_0\Big\{\big(I_4^{Hr} - I_5^{Hr}\big) - 2\chi^e\big(I_4^{HHr} - I_5^{HHr}\big)\Big\}. \tag{6.42}$$

Notice that in (6.42) we introduce two $I_4^{(\bullet)}$-type invariants, namely I_4^{Hr} and I_4^{HHr}. Moreover, the $(I_4^{(\bullet)} - I_5^{(\bullet)})$ form in (6.42) ensures a negligibly small effect of the coupled energy on the effective magnetization $\mathbf{m}$.

Since the potential W^H is augmented without altering its arguments, it follows from (6.7) that $\boldsymbol{\sigma}$ is symmetric. Nonetheless, the full expression of $\boldsymbol{\sigma}$ obtained from the proposed fully-coupled model (6.40) and the symmetry of $\boldsymbol{\sigma}$ is discussed extensively in Appendix 6.A. Furthermore, we notice from Table 6.1 and 6.2 that in the Lagrangian formulation, it is necessary to estimate the derivatives of $\mathbb{C}^{1/2}$ and $\mathbb{C}^{-1/2}$ with respect to $\mathbb{C}$, which is a non-trivial operation. Thus, complete expressions for the derivatives of I_i^{HHr}, $(i = 4, 5)$ with respect to $\mathbb{C}$ are provided thereafter in Appendix 6.B.

It is noted that the magneto-mechanical coupling energy contribution is relatively smaller than the decoupled energy contributions (Danas et al., 2012b). In fact, several structural problems involving soft and hard MREs are observed to predict perfectly the magneto-mechanical structural response while ignoring completely the coupling energy contribution (Psarra et al., 2017, 2019; Zhao et al., 2019). Nevertheless, in order to obtain a magnetostrictive response of the ħ-MREs, the coupled potential (6.40) is employed. Finally, no additional coupling is introduced in the dissipation potential, which is still given by (6.34) in this coupled model.

Remark 6.2. We note that the *nearly incompressible* models of the ħ-MREs are often useful while carrying out the numerical computations for a boundary value problem. Thus, we provide an equivalent compressible model for the ħ-MREs, which is a simple extension of the proposed fully-coupled model (6.40). The compressible counterpart of (6.40) thus reads

$$W^{H,comp}(I_1, J, I_4^{Hr}, I_4^{HHr}, I_5^{H}, I_5^{Hr}, I_5^{HHr}) = \rho_0\psi^{H,comp}_{mech}(I_1, J) + \rho_0\psi^{H}_{mag}(I_5^{H}, I_5^{Hr}, I_5^{HHr}) + \rho_0\psi^{H}_{couple}(I_4^{Hr}, I_4^{HHr}, I_5^{Hr}, I_5^{HHr}) - \frac{\mu_0}{2}JI_5^{H}, \tag{6.43}$$

where $\rho_0\psi^{comp}_{mech}(I_1, J)$ is given by (5.34). The Lame constant G_m' is associated with the matrix phase as defined in the microscopic model (4.15). Notably, in a *nearly* incompressible model, the Lame constant is typically set to be $G_m' \geqslant 100G_m$, which imposes a penalty on J to constraint it to $J \approx 1$.

6.2 F − B and F − b constitutive models

The proposition of constitutive models in the $\mathbf{F}-\mathbf{B}$ and $\mathbf{F}-\mathbf{b}$ spaces follow a similar path to the preceding $\mathbf{F}-\mathbf{H}$ and $\mathbf{F}-\mathbf{h}$-based modeling. Notice from Chapter 2 that the choice of the primary variables are crucial and they changes the local pointwise Clausius-Duhem inequalities. Specifically, we utilize the inequalities (2.63) and (2.35), while deriving the constitutive models in the Lagrangian and Eulerian settings, respectively, by following the standard Coleman-Noll-Gurtin (Coleman and Noll, 1959; Coleman and Gurtin, 1967) method. Again, in a similar note to the $\mathbf{F}-\mathbf{H}$ and $\mathbf{F}-\mathbf{h}$

models, we start by proposing an additive decomposition of the primary magnetic field variable, which is $\mathbf{B}$ or $\mathbf{b}$ in the present case.

6.2.1 Additive decomposition of B and b

As discussed in Section 6.1.1, the additive decomposition of the primary magnetic variables must respect the stretch independence of the current magnetization $\mathbf{m}$, under no externally applied magnetic field. Such condition can be obtained in the present dissipation framework via defining the independent Lagrangian remanent $\mathfrak{b}$-field in a stretch-free intermediate configuration $\mathcal{V}_\mathfrak{i}$ (see Fig. 6.3). Thus, the additive decomposition of the total $\mathbf{B}$ reads

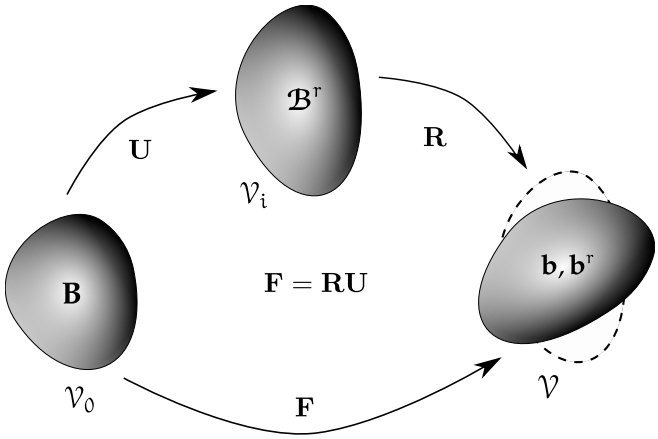

Figure 6.3: Definition of the independent internal variable $\mathcal{B}^\mathfrak{r}$ at the intermediate configuration $\mathcal{V}_\mathfrak{i}$.

$$\mathbf{B}=\mathbf{B}^e+\mathfrak{J}\mathbf{U}^{-1}\mathcal{B}^\mathfrak{r}, \tag{6.44}$$

where $\mathbf{B}^e$ is the energetic and $\mathcal{B}^\mathfrak{r}$ is the intermediate remanent part of $\mathbf{B}$. In turn, (6.44) can be pushed forward via the transformation (2.45), so that

$$\mathbf{b}=\frac{1}{\mathfrak{J}}\mathbf{F}\mathbf{B}^e+\mathbf{F}\mathbf{U}^{-1}\mathcal{B}^\mathfrak{r}=\mathbf{b}^e+\mathbf{R}\mathcal{B}^\mathfrak{r}\equiv\mathbf{b}^e+\mathbf{b}^\mathfrak{r}, \tag{6.45}$$

where $\mathbf{b}^\mathfrak{r}=\mathbf{R}\mathcal{B}^\mathfrak{r}$. The latter ensures a stretch-free independent description of the remanent $\mathfrak{b}$-field in the Lagrangian setting. Again, it is emphasized that the additive decompositions (6.44) and (6.45) are the direct consequences of the "affine rotation" assumption. Thus, (6.44) and (6.45) remain open for the suitable modifications considering more complicated kinematics of the rotating and rearranging particles inside a $\mathfrak{h}$-MRE. Next, we derive the constitutive relations in the Lagrangian and Eulerian settings from the respective point-wise Clausius-Duhem inequalities via considering $\mathcal{B}^\mathfrak{r}$ and $\mathbf{b}^\mathfrak{r}$ to be the independent internal variables, respectively.

6.2.2 Thermodynamic inequalities and constitutive relations

Here we derive the constitutive relations from the two equivalent point-wise Clausius-Duhem inequalities (2.63) and (2.35) in the Lagrangian (reference) and Eulerian (current) settings, respectively.

Constitutive relations in the reference configuration **:** The Lagrangian formulation of the constitutive framework considers $\mathbf{F}$ and $\mathbf{B}$ to be the primary variables, along with the intermediate $\mathcal{B}^{\mathrm{r}}$ to be the independent internal variable. Under isothermal magneto-mechanical loading conditions with no heat flux, the referential Clausius-Duhem inequality (2.63) reads (McMeeking and Landis, 2002; Landis, 2002; Klinkel, 2006)

$$\mathbf{S}:\dot{\mathbf{F}}+\mathbf{H}\cdot\dot{\mathbf{B}}-\dot{W}^{\mathrm{B}}\geqslant 0, \tag{6.46}$$

where the potential energy $W^{\mathrm{B}}=W^{\mathrm{B}}(\mathbb{C},\mathbf{B},\mathcal{B}^{\mathrm{r}})$ is considered to be a function of $\mathbb{C}$, $\mathbf{B}$ and the intermediate $\mathcal{B}^{\mathrm{r}}$. Such definition of W^{B} ensures the material objectivity conditions (Kankanala and Triantafyllidis, 2004; Dorfmann and Ogden, 2004, 2005). Expanding further $\dot{W}^{\mathrm{B}}$ in terms of its arguments and substituting the result into (6.46) leads to

$$\left[\mathbf{S}-2\mathbf{F}\frac{\partial W^{\mathrm{B}}}{\partial\mathbb{C}}\right]:\dot{\mathbf{F}}+\left[\mathbf{H}-\frac{\partial W^{\mathrm{B}}}{\partial\mathbf{B}}\right]\cdot\dot{\mathbf{B}}-\frac{\partial W^{\mathrm{B}}}{\partial\mathcal{B}^{\mathrm{r}}}\cdot\dot{\mathcal{B}}^{\mathrm{r}}\geqslant 0. \tag{6.47}$$

Again, due to the arbitrariness in the variations of the primary field variables $\mathbf{F}$ and $\mathbf{B}$, the standard arguments of the Coleman-Noll-Gurtin method leads to the local constitutive relations

$$\mathbf{S}=2\mathbf{F}\frac{\partial W^{\mathrm{B}}}{\partial\mathbb{C}},\qquad\qquad \mathbf{H}=\frac{\partial W^{\mathrm{B}}}{\partial\mathbf{B}}. \tag{6.48}$$

Similar to the $\mathbf{F}-\mathbf{H}$ model, $W^{\mathrm{B}}(\mathbb{C},\mathbf{B},\mathcal{B}^{\mathrm{r}})$ can be equivalently expressed in terms of $W^{\mathrm{B}}(\mathbf{F},\mathbf{B},\mathcal{B}^{\mathrm{r}})\equiv w^{\mathrm{b}}(\mathbb{B},\mathbf{b},\mathbf{b}^{\mathrm{r}};\mathbf{F},\mathbf{B},\mathcal{B}^{\mathrm{r}})$, where $\mathbf{b}=(1/\mathrm{J})\mathbf{F}\mathbf{B}$ and $\mathbf{b}^{\mathrm{r}}=\mathbf{R}\mathcal{B}^{\mathrm{r}}$ are the two derived variables, depending explicitly on $\mathbf{F},\mathbf{B}$ and $\mathcal{B}^{\mathrm{r}}$. With this representation, the total Cauchy stress $\boldsymbol{\sigma}$ is expressed from $(6.48)_1$, so that

$$\begin{aligned}\boldsymbol{\sigma}&=\frac{2}{\mathrm{J}}\mathbf{F}\frac{\partial W^{\mathrm{B}}}{\partial\mathbb{C}}\mathbf{F}^{\mathrm{T}}=\frac{1}{\mathrm{J}}\frac{\partial w^{\mathrm{b}}}{\partial\mathbf{F}}\mathbf{F}^{\mathrm{T}}=\frac{1}{\mathrm{J}}\left[\frac{\partial w^{\mathrm{b}}}{\partial\mathbf{F}}\right]_{\mathbf{b},\mathbf{b}^{\mathrm{r}}}\mathbf{F}^{\mathrm{T}}+\frac{1}{\mathrm{J}}\left(\left[\frac{\partial w^{\mathrm{b}}}{\partial\mathbf{b}}\right]_{\mathbf{F},\mathbf{b}^{\mathrm{r}}}\cdot\frac{\partial\mathbf{b}}{\partial\mathbf{F}}\right)\mathbf{F}^{\mathrm{T}}+\frac{1}{\mathrm{J}}\left(\left[\frac{\partial w^{\mathrm{b}}}{\partial\mathbf{b}^{\mathrm{r}}}\right]_{\mathbf{F},\mathbf{b}}\cdot\frac{\partial\mathbf{b}^{\mathrm{r}}}{\partial\mathbf{F}}\right)\mathbf{F}^{\mathrm{T}}\\&=\underbrace{\frac{\rho_0}{\mathrm{J}}\left[\frac{\partial\psi^{\mathrm{b}}}{\partial\mathbb{B}}\right]_{\mathbf{b},\mathbf{b}^{\mathrm{r}}}\mathbb{B}}_{\boldsymbol{\sigma}_{\mathtt{mech}}}+\underbrace{\left\{\mathbf{h}\otimes\mathbf{b}-\frac{\mu_0}{2}\left(|\mathbf{h}|^2+|\mathbf{m}|^2\right)\mathbf{I}\right\}}_{\boldsymbol{\sigma}^{\mathtt{en}}_{\mathtt{maxw}}}+\underbrace{\frac{\rho_0}{\mathrm{J}}\left\{\left(\left[\frac{\partial\psi^{\mathrm{b}}}{\partial\mathbf{b}^{\mathrm{r}}}\right]_{\mathbf{F},\mathbf{b}}\otimes\mathbf{R}^{\mathrm{T}}\mathbf{b}^{\mathrm{r}}\right):\frac{\partial\mathbf{R}}{\partial\mathbf{F}}\right\}\mathbf{F}^{\mathrm{T}}}_{\boldsymbol{\sigma}^{\mathtt{rem}}_{\mathtt{maxw}}},\end{aligned} \tag{6.49}$$

where we substitute (2.33) to further express $w^{\mathrm{b}}(\mathbb{B},\mathbf{b},\mathbf{b}^{\mathrm{r}};\mathbf{F},\mathbf{B},\mathcal{B}^{\mathrm{r}})=\rho_0\psi^{\mathrm{b}}(\mathbb{B},\mathbf{b},\mathbf{b}^{\mathrm{r}};\mathbf{F},\mathbf{B},\mathcal{B}^{\mathrm{r}})+(\mathrm{J}/2\mu_0)\mathbf{b}\cdot\mathbf{b}$, with ψ^{b} is the specific Helmholtz free energy. Notice that, unlike W^{B}, w^{b} is not a function that depends explicitly on $\mathbb{C}$. Rather, the latter is a function of $\mathbf{F}$, $\mathbf{B}$ and $\mathcal{B}^{\mathrm{r}}$ (note that $\mathbf{R}$ is also a function of $\mathbf{F}$). Hence, we apply first the identity $(6.1)_1$ in (6.49) to express the $\mathbb{C}$ derivative in terms of the derivative with respect to $\mathbf{F}$. The identity $(6.1)_2$ is subsequently applied while expressing the $\mathbf{F}$ derivative in $\boldsymbol{\sigma}_{\mathtt{mech}}$ in terms of $\mathbb{B}$. Furthermore, the constitutive relation $(6.48)_2$ is also used in the algebraic manipulations while obtaining the final expression in (6.49).

Similar to the $\mathbf{F}-\mathbf{H}$ model, the total $\boldsymbol{\sigma}$ is thus obtained as a sum of three distinct stress contributions, namely the mechanical, energetic Maxwell and the remanent Maxwell stresses, so that $\boldsymbol{\sigma}=\boldsymbol{\sigma}_{\mathtt{mech}}+\boldsymbol{\sigma}^{\mathtt{en}}_{\mathtt{maxw}}+\boldsymbol{\sigma}^{\mathtt{rem}}_{\mathtt{maxw}}$. Notably, Danas (2017) provides a similar decomposition of the total $\boldsymbol{\sigma}$, derived from the Lagrangian $\mathbf{F}-\mathbf{B}$ model in the context of s-MREs, so that $\boldsymbol{\sigma}=\boldsymbol{\sigma}_{\mathtt{mech}}+\boldsymbol{\sigma}^{\mathtt{en}}_{\mathtt{maxw}}$. Eventually, the remanent magnetization in the ħ-MREs leads to the additional stress component $\boldsymbol{\sigma}^{\mathtt{rem}}_{\mathtt{maxw}}$, which is given in (6.49) for the $\mathbf{F}-\mathbf{B}$ model.

The referential angular momentum balance (2.53) is ensured via the definition of $W^{\mathrm{B}}=W^{\mathrm{B}}(\mathbb{C},\mathbf{B},\mathcal{B}^{\mathrm{r}})$

(Coleman and Gurtin, 1967; Suo et al., 2008). This specialization leads to an expression for the total $\boldsymbol{\sigma}$ given by (6.49), such that

$$\boldsymbol{\sigma} = \frac{2}{J}\mathbf{F}\frac{\partial W^{B}}{\partial \mathbb{C}}\mathbf{F}^{T}. \tag{6.50}$$

Owing to the symmetry of $\mathbb{C}$, the symmetry of $\boldsymbol{\sigma}$ can be observed readily from the last equation. Thus, as a direct consequence of the relations $W^{B}(\mathbf{F},\mathbf{B},\mathcal{B}^{r}) \equiv w^{b}(\mathbb{B},\mathbf{b},\mathbf{b}^{r};\mathbf{F},\mathbf{B},\mathcal{B}^{r})$ and (6.1), we note that the sum $\boldsymbol{\sigma}_{\mathtt{mech}} + \boldsymbol{\sigma}^{\mathtt{en}}_{\mathtt{maxw}} + \boldsymbol{\sigma}^{\mathtt{rem}}_{\mathtt{maxw}}$ in (6.49) remains symmetric, while the symmetry of the individual stress components are not ensured.

With the constitutive relations (6.48), the thermodynamic Clausius-Duhem inequality (6.47) now reads

$$\mathcal{H}^{r}\cdot\dot{\mathcal{B}}^{r} \geqslant 0, \qquad \text{with} \qquad \mathcal{H}^{r} = -\frac{\partial W^{B}}{\partial \mathcal{B}^{r}}, \tag{6.51}$$

where $\mathcal{H}^{r}$ is the energetic work conjugate of $\mathcal{B}^{r}$. Again, similar to the $\mathbf{F}-\mathbf{H}$ model, the constitutive relation for the internal variable (6.51) in the Lagrangian formulation is given in the stretch-free intermediate configuration, while the primary constitutive relations (6.48) are proposed in the reference configuration. Finally, the evolution equation for $\mathcal{B}^{r}$ is obtained from the intermediate generalized standard material relation, which reads

$$\frac{\partial W^{B}}{\partial \mathcal{B}^{r}} + \frac{\partial D^{B}}{\partial \dot{\mathcal{B}}^{r}} = 0, \tag{6.52}$$

where $D^{B}(\mathbb{C},\mathbf{B},\mathcal{B}^{r},\dot{\mathcal{B}}^{r})$ is the dissipation potential. Substituting the last equation into (6.51) we obtain the dissipation inequality, that is

$$\frac{\partial D^{B}}{\partial \dot{\mathcal{B}}^{r}}\cdot\dot{\mathcal{B}}^{r} \geqslant 0, \tag{6.53}$$

which is satisfied for any choice of D^{B} that is convex in $\dot{\mathcal{B}}^{r}$. Specific choice for D^{B} in the context of $\mathbf{F}-\mathbf{B}$-based model for the $\hbar$-MREs is provided in the following. Prior to that, we set forth the constitutive relation in the current configuration, i.e., in the Eulerian setting.

Constitutive relations in the current configuration **:** The equivalent constitutive framework in the current configuration considers the Eulerian magnetic field $\mathbf{b}$ and internal variable $\mathbf{b}^{r}$ to be the independent variables. Consequently, the Clausius-Duhem inequality for this $\mathbf{F}-\mathbf{b}$ modeling framework is given by (2.35), which for the present case of the isothermal magneto-mechanical modeling reads (Kankanala and Triantafyllidis, 2004)

$$J\left[\boldsymbol{\sigma} - \mathbf{h}\otimes\mathbf{b} + \frac{\mu_0}{2}(|\mathbf{h}|^2 - |\mathbf{m}|^2)\mathbf{I}\right] : \mathbf{l} + J\mathbf{m}\cdot\dot{\mathbf{b}} - \rho_0\dot{\psi}^{b} \geqslant 0. \tag{6.54}$$

Expanding further the material derivative of $\psi^{b}(\mathbb{B},\mathbf{b},\mathbf{b}^{r})$ in terms of its arguments, we rephrase (6.54) to be

$$J\left[\boldsymbol{\sigma} - \mathbf{h}\otimes\mathbf{b} + \frac{\mu_0}{2}(|\mathbf{h}|^2 - |\mathbf{m}|^2)\mathbf{I}\right] : \mathbf{l} + J\mathbf{m}\cdot\dot{\mathbf{b}} - \rho_0\frac{\partial\psi^{b}}{\partial\mathbb{B}} : \dot{\mathbb{B}} - \rho_0\frac{\partial\psi^{b}}{\partial\mathbf{b}}\cdot\dot{\mathbf{b}} - \rho_0\frac{\partial\psi^{b}}{\partial\mathbf{b}^{r}}\cdot\dot{\mathbf{b}}^{r} \geqslant 0, \tag{6.55}$$

which reads upon rearrangements

$$J\left[\boldsymbol{\sigma}-\frac{2\rho_0}{J}\frac{\partial\psi^b}{\partial\mathbb{B}}\mathbb{B}-\mathbf{h}\otimes\mathbf{b}+\frac{\mu_0}{2}(|\mathbf{h}|^2-|\mathbf{m}|^2)\mathbf{I}-\frac{\rho_0}{J}\left\{\left(\frac{\partial\psi^b}{\partial\mathbf{b}^r}\otimes\mathbf{R}^T\mathbf{b}^r\right)\colon\frac{\partial\mathbf{R}}{\partial\mathbf{F}}\right\}\mathbf{F}^T\right]:\mathfrak{l}$$
$$+J\left(\mathbf{m}-\frac{\rho_0}{J}\frac{\partial\psi^b}{\partial\mathbf{b}}\right)\cdot\dot{\mathbf{b}}-\rho_0\frac{\partial\psi^b}{\partial\mathbf{b}^r}\cdot\overset{\triangle}{\mathbf{b}}^r\geqslant 0, \tag{6.56}$$

where $\overset{\triangle}{\mathbf{b}}^r=\dot{\mathbf{b}}^r-\boldsymbol{\Omega}\mathbf{b}^r$ is the Green-Naghdi rate of the current remanent field $\mathbf{b}^r$ with $\boldsymbol{\Omega}$ the spin rate as defined in Section 6.1.2. In order to prove the symmetry of the terms in contraction with $\mathfrak{l}$ in (6.56), except $\boldsymbol{\sigma}$, we frame an equivalent expression for $w^b(\mathbb{B},\mathbf{b},\mathbf{b}^r)\equiv W^B(\mathbb{C},\mathbf{B},\mathcal{B}^r;\mathbf{F},\mathbf{b},\mathbf{b}^r)$ in terms of the Lagrangian $\mathbf{B}=J\mathbf{F}^{-1}\mathbf{b}$ and the intermediate $\mathcal{B}^r=\mathbf{R}^T\mathbf{b}^r$. Notice that, here the primary magnetic and internal variables are still given by $\mathbf{b}$ and $\mathbf{b}^r$, respectively. Nonetheless, in a complimentary sense to (6.49), the expression of $w^b(\mathbb{B},\mathbf{b},\mathbf{b}^r)$ in terms of $W^B(\mathbb{C},\mathbf{B},\mathcal{B}^r;\mathbf{F},\mathbf{b},\mathbf{b}^r)$ leads to the relation

$$\frac{2\rho_0}{J}\frac{\partial\psi^b}{\partial\mathbb{B}}\mathbb{B}+\mathbf{h}\otimes\mathbf{b}-\frac{\mu_0}{2}(|\mathbf{h}|^2-|\mathbf{m}|^2)\mathbf{I}+\frac{\rho_0}{J}\left\{\left(\frac{\partial\psi^b}{\partial\mathbf{b}^r}\otimes\mathbf{R}^T\mathbf{b}^r\right)\colon\frac{\partial\mathbf{R}}{\partial\mathbf{F}}\right\}\mathbf{F}^T=\frac{2}{J}\mathbf{F}\left[\frac{\partial W^B}{\partial\mathbb{C}}\right]_{\mathbf{B},\mathcal{B}^r}\mathbf{F}^T, \tag{6.57}$$

which ensures the symmetry of the sum on the left hand side of the last. Thus, the symmetry of $\boldsymbol{\sigma}$ from (2.20) and the symmetry of the ensemble of the additional terms contracted with $\mathfrak{l}$ in (6.56) allow us to replace $\mathfrak{l}$ by the current stretch rate $\mathbf{d}=\mathrm{sym}[\mathfrak{l}]$, so that

$$J\left[\boldsymbol{\sigma}-\frac{2\rho_0}{J}\frac{\partial\psi^b}{\partial\mathbb{B}}\mathbb{B}-\mathbf{h}\otimes\mathbf{b}+\frac{\mu_0}{2}(|\mathbf{h}|^2-|\mathbf{m}|^2)\mathbf{I}-\frac{\rho_0}{J}\left\{\left(\frac{\partial\psi^b}{\partial\mathbf{b}^r}\otimes\mathbf{R}^T\mathbf{b}^r\right)\colon\frac{\partial\mathbf{R}}{\partial\mathbf{F}}\right\}\mathbf{F}^T\right]:\mathbf{d}$$
$$+J\left(\mathbf{m}-\frac{\rho_0}{J}\frac{\partial\psi^b}{\partial\mathbf{b}}\right)\cdot\dot{\mathbf{b}}-\rho_0\frac{\partial\psi^b}{\partial\mathbf{b}^r}\cdot\overset{\triangle}{\mathbf{b}}^r\geqslant 0. \tag{6.58}$$

Since $\mathbf{d}$ and $\dot{\mathbf{b}}$ are arbitrary and $\overset{\triangle}{\mathbf{b}}^r$ is independent of the former two, the standard arguments of the Coleman-Noll-Gurtin method (Coleman and Noll, 1959; Coleman and Gurtin, 1967; Hütter, 2017) leads to the constitutive relations

$$\boldsymbol{\sigma}=\frac{2\rho_0}{J}\frac{\partial\psi^b}{\partial\mathbb{B}}\mathbb{B}+\mathbf{h}\otimes\mathbf{b}-\frac{\mu_0}{2}(|\mathbf{h}|^2-|\mathbf{m}|^2)\mathbf{I}+\frac{\rho_0}{J}\left\{\left(\frac{\partial\psi^b}{\partial\mathbf{b}^r}\otimes\mathbf{R}^T\mathbf{b}^r\right)\colon\frac{\partial\mathbf{R}}{\partial\mathbf{F}}\right\}\mathbf{F}^T \tag{6.59}$$

and

$$\mathbf{m}=\frac{\rho_0}{J}\frac{\partial\psi^b}{\partial\mathbf{b}}\qquad\Longrightarrow\qquad\mathbf{h}=\frac{1}{J}\frac{\partial w^b}{\partial\mathbf{b}}. \tag{6.60}$$

Taking the relation (2.33) between w^b and ψ^b and the constitutive relations (6.59) and (6.60) into account, (6.58) now reads

$$\mathbf{h}^r\cdot\overset{\triangle}{\mathbf{b}}^r\geqslant 0,\qquad\text{with}\qquad\mathbf{h}^r=-\frac{\partial w^b}{\partial\mathbf{b}^r}, \tag{6.61}$$

where the remanent $\mathbf{h}^r$ is defined to be the work conjugate of the current $\mathbf{b}^r$. Finally, the evolution equation for the $\mathbf{b}^r$ is obtained from the constitutive relation for generalized standard materials in the current configuration, which in the context of the present $\mathbf{F}-\mathbf{b}$ model reads

$$\frac{\partial w^b}{\partial\mathbf{b}^r}+\frac{\partial\mathscr{D}^b}{\partial\dot{\mathbf{b}}^r}=0, \tag{6.62}$$

where $\mathscr{D}^{\mathrm{b}} = \mathscr{D}^{\mathrm{b}}(\mathbf{B}, \mathbf{b}, \mathbf{b}^{\mathrm{r}}, \overset{\vartriangle}{\mathbf{b}}^{\mathrm{r}})$ is the dissipation potential, expressed in terms of current variables. Notice that we define the explicit dependence of $\mathscr{D}^{\mathrm{b}}$ on the Green-Naghdi rate $\overset{\vartriangle}{\mathbf{b}}^{\mathrm{r}}$. Furthermore, we rephrase (6.62) by exploiting the relation $\overset{\vartriangle}{\mathbf{b}}^{\mathrm{r}} = \dot{\mathbf{b}}^{\mathrm{r}} - \boldsymbol{\Omega}\mathbf{b}^{\mathrm{r}}$, such that

$$\frac{\partial w^{\mathrm{b}}}{\partial \mathbf{b}^{\mathrm{r}}} + \frac{\partial \mathscr{D}^{\mathrm{b}}}{\partial \overset{\vartriangle}{\mathbf{b}}^{\mathrm{r}}} = 0. \tag{6.63}$$

Consequently, (6.61) along with (6.63) leads to the dissipation inequality, given by

$$\frac{\partial \mathscr{D}^{\mathrm{b}}}{\partial \overset{\vartriangle}{\mathbf{b}}^{\mathrm{r}}} \cdot \overset{\vartriangle}{\mathbf{b}}^{\mathrm{r}} \geqslant 0, \tag{6.64}$$

which constraints $\mathscr{D}^{\mathrm{b}}$ to be a convex function of $\overset{\vartriangle}{\mathbf{b}}^{\mathrm{r}}$, thus ensuring a positive dissipation under any loading path. Of course, the choice for W^{B}, D^{B}, w^{b} and $\mathscr{D}^{\mathrm{b}}$ are restricted further by the conditions discussed in Section 6.1.3. These conditions eventually lead to the definitions of invariants, which we now define in terms of $\mathbb{C}$, $\mathbf{B}$ and $\mathcal{B}^{\mathrm{r}}$ (or equivalently, $\mathbb{B}$, $\mathbf{b}$ and $\mathbf{b}^{\mathrm{r}}$) in the following.

Remark 6.3. As discussed in Chapter 2, the potential energy W^{H} (w^{h}) can be obtained from W^{B} (w^{b}) via a partial Legendre transform of W^{B} (w^{b}) with respect to $\mathbf{B}$ ($\mathbf{b}$), or vice-versa. However, (2.61) and (2.30) suggest that the independent internal variables in the $\mathbf{F}-\mathbf{B}$ ($\mathbf{F}-\mathbf{b}$) model can be kept identical to that in the $\mathbf{F}-\mathbf{H}$ ($\mathbf{F}-\mathbf{h}$) model. Nonetheless, here we consider different notations for the independent internal variable in the $\mathbf{F}-\mathbf{H}$ and $\mathbf{F}-\mathbf{B}$ (or equivalently, the $\mathbf{F}-\mathbf{h}$ and $\mathbf{F}-\mathbf{b}$) models. This is done in order to remain consistent with the remanent magnetization/polarization literature that considers the independent additive decompositions $\mathbf{H} = \mathbf{H}^{\mathrm{e}} + \mathbf{H}^{\mathrm{r}}$ and $\mathbf{B} = \mathbf{B}^{\mathrm{e}} + \mathbf{B}^{\mathrm{r}}$ in the context of $\mathbf{F}-\mathbf{H}$ and $\mathbf{F}-\mathbf{B}$-based models, respectively (McMeeking and Landis, 2002; Landis, 2002; Klinkel, 2006; Linnemann et al., 2009; Miehe et al., 2011; Kalina et al., 2017). It is emphasized that no explicit relation must be drawn between the independent and conjugate $\mathcal{H}^{\mathrm{r}}$ and $\mathcal{B}^{\mathrm{r}}$ in the context of the $\mathbf{F}-\mathbf{H}$ model with those defined in the context of $\mathbf{F}-\mathbf{B}$ model. The same is applicable for the $\mathbf{F}-\mathbf{h}$ and $\mathbf{F}-\mathbf{b}$-based models as well. Thus, one should treat the $\mathbf{F}-\mathbf{H}$, $\mathbf{F}-\mathbf{h}$ and $\mathbf{F}-\mathbf{B}$, $\mathbf{F}-\mathbf{b}$-based models independently.

6.2.3 Properties of the potentials W^{B}, D^{B}, w^{b} and $\mathscr{D}^{\mathrm{b}}$

The energetic and dissipation potentials must satisfy the conditions of (a) even magneto-mechanical coupling, (b) material frame indifference, as discussed in Section 6.1.3 in the context of $\mathbf{F}-\mathbf{H}$ model. In addition, these potentials must satisfy the material symmetry conditions for the isotropic MREs and the entropy imbalance conditions on D^{B} and $\mathscr{D}^{\mathrm{b}}$. Section 6.1.3 provides a detail on each of these conditions. Thus, here we set forth directly the aforementioned conditions for the present context of $\mathbf{F}-\mathbf{B}$ and $\mathbf{F}-\mathbf{b}$ models.

Even magneto-mechanical coupling **:** The even magneto-mechanical coupling is ensured if the energetic and dissipation potential satisfy the conditions

$$W^{\mathrm{B}}(\mathbb{C}, -\mathbf{B}, -\mathcal{B}^{\mathrm{r}}) = W^{\mathrm{B}}(\mathbb{C}, \mathbf{B}, \mathcal{B}^{\mathrm{r}}), \qquad \mathrm{D}^{\mathrm{B}}(\mathbb{C}, -\mathbf{B}, -\mathcal{B}^{\mathrm{r}}, -\dot{\mathcal{B}}^{\mathrm{r}}) = \mathrm{D}(\mathbb{C}, \mathbf{B}, \mathcal{B}^{\mathrm{r}}, \dot{\mathcal{B}}^{\mathrm{r}}) \tag{6.65}$$

and

$$w^{\mathrm{b}}(\mathbb{B}, -\mathbf{b}, -\mathbf{b}^{\mathrm{r}}) = w^{\mathrm{b}}(\mathbb{B}, \mathbf{b}, \mathbf{b}^{\mathrm{r}}), \qquad \mathscr{D}^{\mathrm{b}}(\mathbb{B}, -\mathbf{b}, -\mathbf{b}^{\mathrm{r}}, -\overset{\vartriangle}{\mathbf{b}}^{\mathrm{r}}) = \mathscr{D}^{\mathrm{b}}(\mathbb{B}, \mathbf{b}, \mathbf{b}^{\mathrm{r}}, \overset{\vartriangle}{\mathbf{b}}^{\mathrm{r}}), \tag{6.66}$$

respectively, for arbitrary $\mathbb{C}$, $\mathbb{B}$, $\mathbf{B}$, $\mathcal{B}^r$, $\dot{\mathcal{B}}^r$, $\mathbf{b}$, $\mathbf{b}^r$ and $\overset{\vartriangle}{\mathbf{b}}{}^r$.

Material frame indifference **:** The material frame indifference conditions on the W^B, D^B, w^b and $\mathscr{D}^b$ essentially ensures that these potentials remain invariant under an arbitrary change in the observer, whose rotation is given by $\mathbf{Q}$, so that

$$W^B(\mathbb{C},\mathbf{B},\mathcal{B}^r) = W^B(\mathbb{C},\mathbf{B},\mathcal{B}^r), \qquad D^B(\mathbb{C},\mathbf{B},\mathcal{B}^r,\dot{\mathcal{B}}^r) = D^B(\mathbb{C},\mathbf{B},\mathcal{B}^r,\dot{\mathcal{B}}^r) \tag{6.67}$$

and

$$w^b(\mathbf{Q}\mathbb{B}\mathbf{Q}^T,\mathbf{Q}\mathbf{b},\mathbf{Q}\mathbf{b}^r) = w^b(\mathbb{B},\mathbf{b},\mathbf{b}^r), \tag{6.68}$$

$$\mathscr{D}^b(\mathbf{Q}\mathbb{B}\mathbf{Q}^T,\mathbf{Q}\mathbf{b},\mathbf{Q}\mathbf{b}^r,\overline{\mathbf{Q}\overset{\vartriangle}{\mathbf{b}}{}^r}) = \mathscr{D}^b(\mathbf{Q}\mathbb{B}\mathbf{Q}^T,\mathbf{Q}\mathbf{b},\mathbf{Q}\mathbf{b}^r,\mathbf{Q}\overset{\vartriangle}{\mathbf{b}}{}^r) = \mathscr{D}^b(\mathbb{B},\mathbf{b},\mathbf{b}^r,\overset{\vartriangle}{\mathbf{b}}{}^r). \tag{6.69}$$

In analogy to Section 6.1.3, here the Green-Naghdi rate $\overline{\mathbf{Q}\overset{\vartriangle}{\mathbf{b}}{}^r}$ of the transformed $\mathbf{b}^r$ can be shown to yield the relation $\overline{\mathbf{Q}\overset{\vartriangle}{\mathbf{b}}{}^r} = \mathbf{Q}\overset{\vartriangle}{\mathbf{b}}{}^r$, thus ensuring its objectivity.

Material symmetry **:** In order to satisfy the material symmetry conditions for the isotropic ħ-MREs, the potentials must remain invariant under a transformation of the reference configuration by an arbitrary orthogonal tensor $\mathbf{K}$, so that

$$W^B(\mathbf{K}^T\mathbb{C}\mathbf{K},\mathbf{K}^T\mathbf{B},\mathbf{K}^T\mathcal{B}^r) = W^B(\mathbb{C},\mathbf{B},\mathcal{B}^r), \quad D^B(\mathbf{K}^T\mathbb{C}\mathbf{K},\mathbf{K}^T\mathbf{B},\mathbf{K}^T\mathcal{B}^r,\mathbf{K}^T\dot{\mathcal{B}}^r) = D^B(\mathbb{C},\mathbf{B},\mathcal{B}^r,\dot{\mathcal{B}}^r) \tag{6.70}$$

and

$$w^b(\mathbb{B},\mathbf{b},\mathbf{b}^r) = w^b(\mathbb{B},\mathbf{b},\mathbf{b}^r), \qquad \mathscr{D}^b(\mathbb{B},\mathbf{b},\mathbf{b}^r,\overset{\vartriangle}{\mathbf{b}}{}^r) = \mathscr{D}^b(\mathbb{B},\mathbf{b},\mathbf{b}^r,\overset{\vartriangle}{\mathbf{b}}{}^r). \tag{6.71}$$

Entropy imbalance **:** In addition, the dissipation potentials $D^B(\mathbb{C},\mathbf{B},\mathcal{B}^r,\dot{\mathcal{B}}^r)$ and $\mathscr{D}^b(\mathbb{B},\mathbf{b},\mathbf{b}^r,\overset{\vartriangle}{\mathbf{b}}{}^r)$ must be convex functions of $\dot{\mathcal{B}}^r$ and $\overset{\vartriangle}{\mathbf{b}}{}^r$, respectively, in order to satisfy the intermediate and Eulerian dissipation inequalities given by (6.53) and (6.64).

Definition of invariants **:** It is customary to express the potentials W^B, D^B, w^b and $\mathscr{D}^b$ in terms of a set of purely mechanical and magneto-mechanical invariants, that satisfy the conditions of even magneto-mechanical coupling, material frame indifference and material symmetry. The relevant mechanical invariants are defined via the standard $I_1 = \mathrm{tr}(\mathbb{C})$ and $I_3 = J = (\det\mathbb{C})^{1/2}$, while the relevant magneto-mechanical invariants are listed in Table 6.3. Here we only prescribe the I_5 and I_6-type invariants since they are the only ones which would be used while defining the energy functions. Notice from Table 6.3 that, along with the commonly-used I_5^B and I_6^B invariants (Dorfmann and Ogden, 2004, 2005; Ponte Castañeda and Galipeau, 2011; Danas, 2017), we define an additional set of "mixed" and "remanent" invariants indicated by the superscripts "BBr" and "Br", respectively. It is straightforward to verify that all these invariants satisfy the set of aforementioned conditions regarding the even magneto-mechanical coupling, material frame indifference and material symmetry.

Table 6.3: Invariants associated with the $\mathbf{F}-\mathbf{B}$ and $\mathbf{F}-\mathbf{b}$ models of isotropic ħ-MREs

Invariant	Lagrangian	Eulerian	Invariant	Lagrangian	Eulerian
$I_5^B =$	$\mathbf{B}\cdot\mathbb{C}\mathbf{B}$	$J^2\mathbf{b}\cdot\mathbf{b}$	$I_6^B =$	$\mathbf{B}\cdot\mathbb{C}^2\mathbf{B}$	$J^2\mathbf{b}\cdot\mathbb{B}\mathbf{b}$
$I_5^{BBr} =$	$J\mathbf{B}\cdot\mathbb{C}^{1/2}\mathcal{B}^r$	$J^2\mathbf{b}\cdot\mathbf{b}^r$	$I_6^{BBr} =$	$J\mathbb{C}\mathbf{B}\cdot\mathbb{C}^{1/2}\mathcal{B}^r$	$J^2\mathbf{b}\cdot\mathbb{B}\mathbf{b}^r$
$I_5^{Br} =$	$J^2\mathcal{B}^r\cdot\mathcal{B}^r$	$J^2\mathbf{b}^r\cdot\mathbf{b}^r$	$I_6^{Br} =$	$J^2\mathcal{B}^r\cdot\mathbb{C}\mathcal{B}^r$	$J^2\mathbf{b}^r\cdot\mathbb{B}\mathbf{b}^r$

It remains to prescribe the invariant rate. Similar to Section 6.1.3, it is observed here that the norms $|\dot{\mathcal{B}}^{r}|$ and $|\overset{\Delta}{\mathbf{b}}^{r}|$ are equal to each other and are objective as well. Thus, the dissipation potential that is proposed in terms of the invariants of Table 6.3 and $|\dot{\mathcal{B}}^{r}|$ or $|\overset{\Delta}{\mathbf{b}}^{r}|$ remains fully objective and isotropic. In addition, the dissipation potentials must satisfy (6.53) or (6.64) in order to ensure a positive dissipation. The proposition of the specific functional forms for D^{B} and $\mathscr{D}^{b}$ are given in the following.

6.2.4 Choice of energy functions: decoupled model

In a similar note to the s-MRE models in Chapter 4 and the proposed $\mathbf{F}-\mathbf{H}$ and $\mathbf{F}-\mathbf{h}$ model for the h-MREs in Section 6.1, here we propose first a decoupled model for the effective response of incompressible h-MREs. Again, the decoupled model ensures no mechanical strains under proportional magnetic loading cycles. The magnetostriction, arising due to the particle rearrangements under proportional loading paths, will be modeled afterwards in terms of proposing the coupling potentials. Also, we emphasize that the "decoupled" model for the h-MREs ensure a decoupled magneto-mechanical response *only under proportional magnetic loading cycles*. A non-proportional magnetic loading or a coupled magneto-mechanical loading path may induce mechanical strains and the change in current $\mathbf{m}$ obtained from the decoupled model. This is due to the existence of the history-dependent remanent magnetization in the h-MREs that makes the effective response path-dependent and consequently, a fully decoupled magneto-mechanical response is not, in general, ensured.

Energetic potential **:** The I_1 and I_5^{B}-based decoupled energetic potential for the incompressible h-MREs is defined to be

$$W^{B}(I_1, I_5^{B}, I_5^{BBr}, I_5^{Br}) = w^{b}(I_1, I_5^{B}, I_5^{BBr}, I_5^{Br}) = \begin{cases} \rho_0\psi_{mech}(I_1) + \rho_0\psi_{mag}^{B}(I_5^{B}, I_5^{BBr}, I_5^{Br}) & \\ \qquad\qquad + \dfrac{1}{2\mu_0} I_5^{B} & \text{if } J = 1 \\ +\infty & \text{otherwise,} \end{cases} \tag{6.72}$$

where the purely mechanical effective energy $\psi_{mech}(I_1)$ is given by (5.5). Furthermore, the I_5^{B}-based magnetic potential is proposed herein to be comprising of energetic and remanent contributions, such that

$$\rho_0\psi_{mag}^{B}(I_5^{B}, I_5^{BBr}, I_5^{Br}) = \rho_0\psi_{mag}^{B,en}(I_5^{B}) + \rho_0\psi_{mag}^{B,rem}(I_5^{BBr}, I_5^{Br}). \tag{6.73}$$

The $\mathbf{F}-\mathbf{B}$ model is also designed vis-a-vis the $\mathbf{F}-\mathbf{H}$ model, that match the analytical estimates for the effective energetic and remanent susceptibilities. As detailed in Chapter 3, $\psi_{mag}^{B,en}$ is associated with the linear energetic response of the magnet outside the switching regime. Thus, the effective linear response for this composite is given by

$$\rho_0\psi_{mag}^{B,en}(I_5^{B}) = \frac{1}{2}\left(\frac{1}{\mu^{e}} - \frac{1}{\mu_0}\right) I_5^{B}, \tag{6.74}$$

where $\mu^{e} = \mu_0(1+\chi^{e})$ with χ^{e} for the composite is given by $(6.31)_2$, which is the M-G lower bound

for the effective energetic susceptibility. Subsequently, the remanent free energy is given by

$$\rho_0\psi^{B,rem}_{mag}(I_5^{BBr}, I_5^{Br}) = -\frac{1}{\mu^e} I_5^{BBr} - \frac{1}{3\mu^e}\left(\frac{1-c}{c}\right) I_5^{Br} + \frac{\mu^e}{c}\frac{(1+\chi_p)}{\chi_p}(m^s)^2 f_p^b\left(\frac{\sqrt{I_5^{Br}}}{\mu^e m^s}\right), \tag{6.75}$$

which, in the limit of $c \to 1$, leads to the remanent free energy (3.36) associated with the metallic magnets. Here f_p^b is the inverse saturation function defined by (3.37) for the particle phase, whereas m^s is the effective saturation magnetization, defined to be $m^s = c\, m_p^s(\mu^e/\mu_p^e)^{0.8}$. Thus, in a similar note to the decoupled $\mathbf{F}-\mathbf{H}$ model in Section 6.1.4, here the decoupled $\mathbf{F}-\mathbf{B}$ model is defined fully in terms of the material and microstructural properties of the underlying microstructure, without introducing any additional model parameters.

As discussed in the context of the effective $\mathbf{F}-\mathbf{H}$ model, at the onset of switching, i.e., in the limit of $|\mathbf{b}^r| \to 0$, one can linearize the nonlinear inverse saturation function f_p^b. Consequently, (6.75) becomes linear in I_5^{BBr} and I_5^{Br}, such that

$$\rho_0\psi^{B,rem}_{mag,|\mathbf{b}^r|\to 0}(I_5^{BBr}, I_5^{Br}) = -\frac{1}{\mu^e} I_5^{BBr} + \frac{1}{\mu^e}\left(\frac{1+\chi}{\chi}\right) I_5^{Br}, \tag{6.76}$$

where χ is the effective susceptibility given by $(6.33)_2$. It is noted here that the "effective susceptibility" for the $\mathbf{F}-\mathbf{B}$ model is given by $\chi/(1+\chi)$, which is identical to that provided by Ponte Castañeda and Galipeau (2011) in the context of s-MREs. Even though Ponte Castañeda and Galipeau (2011) provide the estimate of effective susceptibility in terms of $\widehat{\chi}_p$, that is related to χ_p via $\widehat{\chi}_p = \chi_p/(1+\chi_p)$, one recovers the effective susceptibility in (6.76) via straightforward algebraic manipulations.

Dissipation potential **:** The definition of the effective dissipation potential takes a similar form to that in (6.34), except the arguments are now given in terms of $|\dot{\mathcal{B}}^r|$ and $|\overset{\triangle}{\mathbf{b}}^r|$, so that

$$D^B(|\dot{\mathcal{B}}^r|) = \frac{b^c \dot{h}^{r0}}{(p+1)}\left[\frac{|\dot{\mathcal{B}}^r|}{\mu^e \dot{h}^{r0}}\right]^{p+1} = \frac{b^c \dot{h}^{r0}}{(p+1)}\left[\frac{|\overset{\triangle}{\mathbf{b}}^r|}{\mu^e \dot{h}^{r0}}\right]^{p+1} = \mathscr{D}^b(|\overset{\triangle}{\mathbf{b}}^r|), \tag{6.77}$$

where the effective coercive field b^c is defined via $(6.34)_2$. Notice that both $D^B(|\dot{\mathcal{B}}^r|)$ and $\mathscr{D}^b(|\overset{\triangle}{\mathbf{b}}^r|)$ are objective and are convex in terms of $\dot{\mathcal{B}}^r$ and $\overset{\triangle}{\mathbf{b}}^r$, respectively. Hence, the entropy inequalities (6.53) and (6.64) are satisfied for all $b^c \geqslant 0$ and $\mu^e > 0$. Since a rate-independent response is sought-for in such quasi-static h-MRE responses, we obtain the ferromagnetic switching surfaces from (6.77) in the limit of $p \to 0$, which are given in the reference and current configurations by

$$\Phi^B := (\mu^e)^2 \mathcal{H}^r \cdot \mathcal{H}^r - (b^c)^2 = 0 \qquad \text{and} \qquad \phi^b := (\mu^e)^2 \mathbf{h}^r \cdot \mathbf{h}^r - (b^c)^2 = 0, \tag{6.78}$$

respectively. Notice that $\mathcal{H}^r$ and $\mathbf{h}^r$ in the former and the latter are defined via the constitutive relations (6.51) and (6.61), respectively. Thus, both $\mathcal{H}^r$ and $\mathbf{h}^r$ can now be computed explicitly from the potential energy (6.72). Subsequently, the evolution equations for $\mathcal{B}^r$ and $\mathbf{b}^r$ is given by the associated switching rules, so that

$$\dot{\mathcal{B}}^r = \dot{\lambda}^B \frac{\partial \Phi^B}{\partial \mathcal{H}^r} \qquad \text{and} \qquad \overset{\triangle}{\mathbf{b}}^r = \dot{\lambda}^b \frac{\partial \phi^b}{\partial \mathbf{h}^r}, \tag{6.79}$$

where $\dot{\lambda}^{B}$ and $\dot{\lambda}^{b}$ are the Lagrange multipliers in the context of $\mathbf{F}-\mathbf{B}$ and $\mathbf{F}-\mathbf{b}$ models, respectively. Notably, both $\dot{\lambda}^{B}$ and $\dot{\lambda}^{b}$ must satisfy the Kuhn-Tucker conditions, given by

$$\begin{cases} \dot{\lambda}^{B} = 0 & \text{if } \Phi^{B} < 0 \\ \dot{\lambda}^{B} > 0 & \text{if } \Phi^{B} = 0 \end{cases} \quad \text{and} \quad \begin{cases} \dot{\lambda}^{b} = 0 & \text{if } \phi^{b} < 0 \\ \dot{\lambda}^{b} > 0 & \text{if } \phi^{b} = 0, \end{cases} \tag{6.80}$$

respectively. Next, we provide a summary of the constitutive relations those are relevant to the $\mathbf{F}-\mathbf{B}$ and $\mathbf{F}-\mathbf{b}$ models.

Remark 6.4. Experimental investigations with $\mathfrak{h}$-MREs typically report the effective coercivity in terms of defining a coercive field in terms of h^{c}, which is considered to be the $\mathfrak{h}$-field where the $\mathfrak{m}-\mathfrak{h}$ hysteresis loop crosses the $\mathfrak{h}$ axis (Kalina et al., 2017; Kim et al., 2018). Thus, one can replace b^{c} by $\mu^{e}h^{c}$ in (6.78), so that the switching criteria can be set in terms of specifying h^{c}. Nevertheless, in this work we only specify b_{p}^{c} as a measure of the particle coercivity and all the effective coercivity measures are expressed in terms of b_{p}^{c}, μ^{e} and c.

Constitutive equations in Lagrangian and Eulerian settings **:** Here we summarize the constitutive relations in the Lagrangian and Eulerian settings. In particular, the $\mathbf{F}-\mathbf{B}$-based model is associated with the constitutive relations given by (6.48), $(6.51)_2$ and the local evolution equation for the remanent $\mathcal{B}^{r}$ is given by $(6.78)_1$, $(6.79)_1$. The $\mathbf{F}-\mathbf{b}$-based constitutive relations in the current configuration is given by (6.59), (6.60) and $(6.61)_1$. Finally, the local evolution equation for $\mathbf{b}^{r}$ is given in terms of its Green-Naghdi rate $(6.79)_2$. These constitutive relations in the Lagrangian and Eulerian settings are summarized in Table 6.4.

Table 6.4: Constitutive relations and associated switching rules for the incompressibe $\mathfrak{b}$-field-based models of $\mathfrak{h}$-MREs in the Lagrangian and Eulerian settings

Lagrangian	Eulerian
$\mathbf{S} = 2\mathbf{F}\dfrac{\partial W^{B}}{\partial \mathbb{C}} - p\mathbf{F}^{-T}$	$\boldsymbol{\sigma} = 2\rho_0 \dfrac{\partial \psi^{b}}{\partial \mathbb{B}}\mathbb{B} + \left[\mathbf{h}\otimes\mathbf{b} - \dfrac{\mu_0}{2}\left(\lvert\mathbf{h}\rvert^2 - \lvert\mathbf{m}\rvert^2\right)\mathbf{I}\right] + \dfrac{2}{\det \mathbf{Z}}\mathbf{Z}\,\mathrm{skw}\left(\mathbf{b}^{r}\otimes\mathbf{h}^{r}\right)\mathbf{V}\mathbf{Z} - p\mathbf{I}$
$\mathbf{H} = \dfrac{\partial W^{B}}{\partial \mathbf{B}}$	$\mathbf{h} = \dfrac{\partial w^{b}}{\partial \mathbf{b}}$
$\mathcal{H}^{r} = -\dfrac{\partial W^{B}}{\partial \mathcal{B}^{r}}$	$\mathbf{h}^{r} = -\dfrac{\partial w^{b}}{\partial \mathbf{b}^{r}}$
$\Phi^{B} := (\mu^{e})^2\mathcal{H}^{r}\cdot\mathcal{H}^{r} - (b^{c})^2 = 0$	$\phi^{b} := (\mu^{e})^2\mathbf{h}^{r}\cdot\mathbf{h}^{r} - (b^{c})^2 = 0$
$\dot{\mathcal{B}}^{r} = \dot{\lambda}^{B}\dfrac{\partial \Phi^{B}}{\partial \mathcal{H}^{r}}$	$\overset{\triangle}{\mathbf{b}}^{r} = \dot{\lambda}^{b}\dfrac{\partial \phi^{b}}{\partial \mathbf{h}^{r}}$

Again, the constitutive relations presented here are provided for the specific case of an incompressible model. Consideration of the material compressibility leads to a little alteration of the constitutive relations for $\mathbf{S}$, $\boldsymbol{\sigma}$ and $\mathbf{h}$. However, the constitutive relations for $\mathcal{H}^{r}$ and $\mathbf{h}^{r}$ and finally, the evolution equations for $\mathcal{B}^{r}$ and $\mathbf{b}^{r}$ remain identical to those in Table 6.4. This observation can be attributed directly to the stretch-insensitivity of $\mathbf{b}^{r}$ that is defined via the definition of its Lagrangian counterpart in the stretch-free intermediate configuration $\mathcal{V}_{i}$.

***Symmetry of* $\boldsymbol{\sigma}$:** Even though the symmetry of $\boldsymbol{\sigma}$ is confirmed via (6.57) in the developed constitutive framework, one can prove the symmetry of $\boldsymbol{\sigma}$ provided in Table 6.4 explicitly via expanding it in terms of the invariants provided by Table 6.3. The algebraic procedure to prove its symmetry follows the exact path as in Appendix 6.A and thus, is not shown explicitly in this text.

One can further simplify the expression for $\boldsymbol{\sigma}$, given in Table 6.4 via considering the specific forms of $\mathbf{h}$ and $\mathbf{h}^{\mathrm{r}}$ for the proposed decoupled potential (6.72). Specifically, the remanent stress part of $\boldsymbol{\sigma}$ is now simplified via considering the expressions for $\mathbf{h}$ and $\mathbf{h}^{\mathrm{r}}$ in terms of $\mathbf{b}$ and $\mathbf{b}^{\mathrm{r}}$, such that

$$\mathbf{h}=\frac{1}{\mu^{e}}(\mathbf{b}-\mathbf{b}^{\mathrm{r}})\qquad\text{and}\qquad\mathbf{h}^{\mathrm{r}}=\frac{1}{\mu^{e}}\mathbf{b}+\frac{2}{3\mu^{e}}\left(\frac{1-c}{c}\right)\mathbf{b}^{\mathrm{r}}-\frac{m^{s}}{c}\frac{(1+\chi_{p})}{\chi_{p}}(f_{p}^{b})'\left(\frac{\sqrt{I_{5}^{\mathrm{Br}}}}{\mu^{e}m^{s}}\right)\frac{\mathbf{b}^{\mathrm{r}}}{|\mathbf{b}^{\mathrm{r}}|}.\tag{6.81}$$

Substituting the last two into the expression for $\boldsymbol{\sigma}$ in Table 6.4, one eventually obtains the same expression for $\boldsymbol{\sigma}^{\mathtt{rem}}_{\mathtt{maxw}}$ as given by (6.39). Thus, *for the specific decoupled* $\mathbf{F}-\mathbf{h}$ *and* $\mathbf{F}-\mathbf{b}$ *models proposed in this chapter*, the expressions for $\boldsymbol{\sigma}^{\mathtt{rem}}_{\mathtt{maxw}}$ becomes identical.

6.2.5 Coupled potential

In order to propose the coupling potential for the $\mathbf{F}-\mathbf{B}$ (or equivalently, $\mathbf{F}-\mathbf{b}$) model, we follow an identical approach as in Section 5.2.2 in the context of s-MREs. Thus, we augment the total potential W^{B} (or w^{b}) with a coupling energy that is a function of both I_5 and I_6-based mixed and remanent invariants, so that

$$W^{\mathrm{B}}(I_1,I_5^{\mathrm{B}},I_5^{\mathrm{BBr}},I_5^{\mathrm{Br}},I_6^{\mathrm{BBr}},I_6^{\mathrm{Br}})=\begin{cases}\rho_0\psi_{\mathtt{mech}}(I_1)+\rho_0\psi^{\mathrm{B}}_{\mathtt{mag}}(I_5^{\mathrm{B}},I_5^{\mathrm{BBr}},I_5^{\mathrm{Br}})\\ \qquad\qquad+\rho_0\psi^{\mathrm{B}}_{\mathtt{couple}}(I_5^{\mathrm{BBr}},I_5^{\mathrm{Br}},I_6^{\mathrm{BBr}},I_6^{\mathrm{Br}})+\dfrac{1}{2\mu_0}I_5^{\mathrm{B}} & \text{if } J=1\\ +\infty & \text{otherwise,}\end{cases}\tag{6.82}$$

where all the relevant invariants are listed in Table 6.3. We consider no coupling in terms of the dissipation potential since the energy dissipation remains purely due to the magnetic switching, whereas the other possible sources of dissipation are ignored in the micro and macroscopic models.

Specifically, the coupling potential for this model is proposed to be

$$\rho_0\psi^{\mathrm{B}}_{\mathtt{couple}}(I_5^{\mathrm{BBr}},I_5^{\mathrm{Br}},I_6^{\mathrm{BBr}},I_6^{\mathrm{Br}})=\frac{c}{\mu_0}\beta^{\mathrm{Br}}\left\{(I_6^{\mathrm{Br}}-I_5^{\mathrm{Br}})+2\frac{\chi^{e}}{1+\chi^{e}}(I_6^{\mathrm{BBr}}-I_5^{\mathrm{BBr}})\right\},\tag{6.83}$$

where β^{Br} is the coupling coefficient for the $\mathbf{F}-\mathbf{B}$ model. This coefficient will be identified via fitting the model magnetostriction response to that estimated from the numerical computations. It is emphasized that (6.83) provides *one possible* phenomenological energy function that models the magnetostriction response of the ħ-MREs. Nevertheless, one can introduce more modeling parameters in (6.83) whenever necessary.

We observe that explicit expression for $\mathbf{S}$ in case of the Lagrangian model necessitates the computations of the derivatives of I_5^{B} and I_6^{B} with respect to $\mathbb{C}$. While the $\mathbb{C}$ derivatives of the energetic I_5^{B}, I_6^{B} and remanent I_5^{Br}, I_6^{Br} are straightforward to compute, that of I_5^{BBr}, I_6^{BBr} are not trivial. Thus, explicit expressions for the derivatives of I_5^{BBr}, I_6^{BBr} with respect to $\mathbb{C}$ is provided in Appendix 6.B.

Remark 6.5. In view of practical implementation of the proposed $\mathbf{F}-\mathbf{B}$ constitutive model in an

incremental FE solver, we provide a compressible version of the incompressible potential energy (6.82), such that

$$W^{\mathrm{B}}(I_1, J, I_5^{\mathrm{B}}, I_5^{\mathrm{BBr}}, I_5^{\mathrm{Br}}, I_6^{\mathrm{BBr}}, I_6^{\mathrm{Br}}) = \rho_0 \psi^{\mathtt{comp}}_{\mathtt{mech}}(I_1, J) + \rho_0 \psi^{\mathrm{B}}_{\mathtt{mag}}\left(\frac{I_5^{\mathrm{B}}}{J^2}, \frac{I_5^{\mathrm{BBr}}}{J^2}, \frac{I_5^{\mathrm{Br}}}{J^2}\right) + \rho_0 \psi^{\mathrm{B}}_{\mathtt{couple}}\left(\frac{I_5^{\mathrm{BBr}}}{J^2}, \frac{I_5^{\mathrm{Br}}}{J^2}, \frac{I_6^{\mathrm{BBr}}}{J^4}, \frac{I_6^{\mathrm{Br}}}{J^4}\right) + \frac{1}{2\mu_0 J} I_5^{\mathrm{B}}. \tag{6.84}$$

The compressible mechanical free energy $\psi^{\mathtt{comp}}_{\mathtt{mech}}$ in (6.84) is given by (5.34), which leads to a *nearly incompressible* effective model in the limit of $G_m' \gg G_m$, where G_m' is the bulk modulus of the matrix phase. In a similar note to (5.43), the compressible versions of $\psi^{\mathrm{B}}_{\mathtt{mag}}$ and $\psi^{\mathrm{B}}_{\mathtt{couple}}$ consider their arguments in terms of I_5/J^2 and I_6/J^4 invariants. Notice that, no modification in the definition of the effective switching surface (6.78) and the associated switching rule (6.79) is carried out in the present case of a nearly incompressible modeling.

6.3 Limiting conditions

The proposed incompressible constitutive relations in the $\mathbf{F}-\mathbf{h}$ and $\mathbf{F}-\mathbf{b}$ spaces, which are summarized in Table 6.2 and 6.4, respectively, can be simplified under a number of limiting conditions. Moreover, such limiting cases also show the proposed models' capability to reproduce exactly the previously-known models for metallic hard magnets (Robinson, 1975) and *s*-MREs (Kankanala and Triantafyllidis, 2004; Dorfmann and Ogden, 2004, 2005; Steigmann, 2004). In particular, we discuss a couple of limits, namely, `(i)` the limit of $c \to 1$, where the effective models approach the magneto-mechanical model of metallic permanent magnets and `(ii)` the limit of $b_p^c \to 0$, which leads to a soft magnetic response.

`(i)` ***The limit of*** $c \to 1$ **:** In the limit of $c \to 1$, the effective shear modulus in (5.5) approach $+\infty$, thus, constraining the effective strain to become infinitesimally small. Consequently, by substituting $\mathbf{V} = \mathbf{I}$ (since Grad $\mathbf{u} \ll \mathbf{I}$, we ignore the sym(Grad $\mathbf{u}$) and the higher-order terms in Grad $\mathbf{u}$ in the expression of $\mathbf{V}$) in the expressions of $\boldsymbol{\sigma}$ in Table 6.2 and 6.4, we obtain the classical expression of the total $\boldsymbol{\sigma}$ for the permanent metallic magnets, which reads (Robinson, 1975)

$$\boldsymbol{\sigma} = \begin{cases} \boldsymbol{\sigma}_{\mathtt{mech}} + \left(\mathbf{h}\otimes\mathbf{b} - \dfrac{\mu_0}{2}|\mathbf{h}|^2\mathbf{I}\right) + \mathrm{skw}\left(\mu_0 \mathbf{m}\otimes\mathbf{h}\right) - p\mathbf{I} & \text{for } \mathbf{F}-\mathbf{h} \text{ model,} \\ \boldsymbol{\sigma}_{\mathtt{mech}} + \left[\mathbf{h}\otimes\mathbf{b} - \dfrac{\mu_0}{2}\left(|\mathbf{h}|^2 - |\mathbf{m}|^2\right)\mathbf{I}\right] + \mathrm{skw}\left(\mu_0 \mathbf{m}\otimes\mathbf{h}\right) - p\mathbf{I} & \text{for } \mathbf{F}-\mathbf{b} \text{ model,} \end{cases} \tag{6.85}$$

where $\boldsymbol{\sigma}_{\mathtt{mech}}$ can be expressed in terms of the infinitesimal strain sym(Grad $\mathbf{u}$) and the effective shear modulus G (see e.g., (Kumar and Lopez-Pamies, 2016)). Thus, in the limit of small strains, the Cauchy stress measures in the proposed $\mathbf{F}-\mathbf{h}$ and $\mathbf{F}-\mathbf{b}$ frameworks lead identically to the classical small strain theory of Robinson (1975) for the metallic permanent magnets. Notice from (6.85) that the expressions of $\boldsymbol{\sigma}$ remain the same for the $\mathbf{F}-\mathbf{h}$ and $\mathbf{F}-\mathbf{b}$ models except the added hydrostatic stress contribution with $|\mathbf{m}|^2$ that appears additionally in the $\mathbf{F}-\mathbf{b}$ modeling framework.

Moreover, in this limit the Green-Naghdi rate $\overset{\vartriangle}{\mathbf{h}}^{\mathrm{r}}$ ($\overset{\vartriangle}{\mathbf{b}}^{\mathrm{r}}$) of the current $\mathbf{h}^{\mathrm{r}}$ ($\mathbf{b}^{\mathrm{r}}$) tends to the objective Truesdell rate defined via $\overset{\circ}{\mathbf{h}}^{\mathrm{r}} = \dot{\mathbf{h}}^{\mathrm{r}} - \mathbf{l}\mathbf{h}^{\mathrm{r}}$ ($\overset{\circ}{\mathbf{b}}^{\mathrm{r}} = \dot{\mathbf{b}}^{\mathrm{r}} - \mathbf{l}\mathbf{b}^{\mathrm{r}}$), which is also referred to be the Lie rate of $\mathbf{h}^{\mathrm{r}}$

($\mathbf{b}^r$) with respect to the reference configuration (Pinsky et al., 1983; Szabó and Balla, 1989). Thus the models of metallic magnets at the current configuration typically define the dissipation potential in terms of $\overset{\circ}{\mathbf{h}}{}^r$ (or equivalently, $\overset{\circ}{\mathbf{b}}{}^r$) (see e.g., (Keip and Sridhar, 2018)).

(ii) ***The limit of*** $b_p^c \to 0$ **:** As discussed in Chapter 3, the pure magnetic hysteresis model in the limit of $b_p^c \to 0$ leads to a non-dissipative saturation magnetization model. Consequently, a modification in the expression of $\boldsymbol{\sigma}$ is also obtained. Notice that, setting $b_p^c = 0$ leads to the switching conditions given by $\mathbf{b}^r \cdot \mathbf{b}^r = 0$ and $\mathbf{h}^r \cdot \mathbf{h}^r = 0$ for the $\mathbf{F}-\mathbf{h}$ and $\mathbf{F}-\mathbf{b}$ models, respectively. Thus, substituting these two switching constraints, namely, $\mathbf{b}^r = \mathbf{0}$ and $\mathbf{h}^r = \mathbf{0}$ into the expressions of $\boldsymbol{\sigma}$ in Table 6.2 and 6.4, respectively, we obtain the resulting expressions for $\boldsymbol{\sigma}$ under the aforementioned limit, so that

$$\boldsymbol{\sigma} = \begin{cases} 2\rho_0 \dfrac{\partial \psi^h}{\partial \mathbb{B}} \mathbb{B} + \left[\mathbf{h} \otimes \mathbf{b} - \dfrac{\mu_0}{2} |\mathbf{h}|^2 \mathbf{I} \right] - p\mathbf{I} & \text{for } \mathbf{F}-\mathbf{h} \text{ model,} \\ 2\rho_0 \dfrac{\partial \psi^b}{\partial \mathbb{B}} \mathbb{B} + \left[\mathbf{h} \otimes \mathbf{b} - \dfrac{\mu_0}{2} \left(|\mathbf{h}|^2 - |\mathbf{m}|^2 \right) \mathbf{I} \right] - p\mathbf{I} & \text{for } \mathbf{F}-\mathbf{b} \text{ model.} \end{cases} \tag{6.86}$$

Notice that (6.86) provides the constitutive relations for $\boldsymbol{\sigma}$ identical to those provided by Kankanala and Triantafyllidis (2004), who provide the current constitutive frameworks for s-MREs.

As noted in Chapter 3, the condition $b_p^c = 0$ leads to the explicit expressions of the internal variables $\mathbf{h}^r$ and $\mathbf{b}^r$ in terms of $\mathbf{h}$ and $\mathbf{b}$, respectively. In contrast, in the effective $\mathbf{F}-\mathbf{h}$ and $\mathbf{F}-\mathbf{b}$ models proposed in this chapter, one cannot express $\mathbf{h}^r$ and $\mathbf{b}^r$ explicitly in terms of $\mathbf{h}$ and $\mathbf{b}$, respectively, from $(6.38)_2$ and $(6.81)_2$ by setting $\mathbf{b}^r = \mathbf{0}$ and $\mathbf{h}^r = \mathbf{0}$, respectively. Thus, an effective soft magnetic model cannot be put forth explicitly from the proposed hysteretic effective models. That's why the homogenization-based effective model of Lefèvre et al. (2017) is associated with the solving a nonlinear transcendental equation (5.10), which takes an identical form to $(6.38)_2$, once we substitute $\mathbf{b}^r = \mathbf{0}$ into it.

6.4 Results: assessment of the macroscopic models

The proposed $\mathbf{F}-\mathbf{H}$, $\mathbf{F}-\mathbf{h}$, $\mathbf{F}-\mathbf{B}$ and $\mathbf{F}-\mathbf{b}$-based macroscopic models are now probed against the numerically computed effective responses. The macroscopic model responses are computed following a similar two step numerical computation procedure for the dissipative constitutive response. First, we update the intermediate internal variables $\mathcal{H}^r$ and $\mathcal{B}^r$ by employing directly the fully-implicit radial-return-type scheme given in Algorithm 4.1. In contrast, we employ an *incrementally objective* radial-return algorithm (Hughes and Winget, 1980) in order to update the Eulerian internal variables $\mathbf{h}^r$ and $\mathbf{b}^r$, whose evolution equations are given in terms of their Green-Naghdi rates. Subsequently, the macroscopic stress and primary magnetic fields are computed from the constitutive relations provided in Table 6.2 and 6.4. The resulting magnetostriction components are then computed from the macroscopic stress boundary conditions (4.84) or (4.85), depending on the loading path. Notice from (4.84) and (4.85) that, some of the shear components are blocked in order to prevent any rigid body rotations during the loading/unloading.

As observed in Chapter 5 and in the development of the models, we notice that the effective magnetization response require no further fitting of the model parameters. Rather, the coupling coefficients β^{Hr} and β^{Br} for the $\mathbf{F}-\mathbf{H}$ (or, equivalently $\mathbf{F}-\mathbf{h}$) and $\mathbf{F}-\mathbf{B}$ (or, equivalently $\mathbf{F}-\mathbf{b}$) models

are estimated via fitting the resulting magnetostriction response to the numerically computed average response as shown in Fig. 4.11. Next, the fitted model is assessed against the computed effective responses under a number of non-proportional magneto-mechanical loading paths.

In the following, we represent all the FE computed responses by discrete points, whereas the $\mathbf{F}-\mathbf{H}$ and $\mathbf{F}-\mathbf{B}$ model responses are shown by continuous solid and dashed lines, respectively. Notice that the equivalent $\mathbf{F}-\mathbf{h}$ and $\mathbf{F}-\mathbf{b}$ models yield identical results to their Lagrangian counterparts and hence, are not shown explicitly in the following plots for brevity. Moreover, the model responses are shown only for the purely incompressible cases.

6.4.1 Proportional cyclic magnetic loading

The fitting is performed via considering a proportional cyclic loading path as shown in Fig. 4.9b. Here neglect any shear component and assume a form of $\mathbf{F}$ so that $\mathbf{F} = \sum_{i=1}^{3} \lambda_i \mathbf{e}_i \otimes \mathbf{e}_i$, i.e., only in terms of the principal stretch components, where $\mathbf{e}_i$ are the unit vectors associated to the reference coordinates system $\mathbf{X}$.

The coupling parameters β^{Hr} and β^{Br} are estimated subsequently, by fitting the macroscopic parallel effective magnetostriction $\lambda_1 - 1$ to that computed via the FE simulations. We employ the `lsqcurvefit` algorithm of MATLAB (2017) to find the optimal coupling parameters β^{Hr} and β^{Br}, which are estimated for three particle volume fractions, namely, $c = 0.1$, 0.2 and 0.3, and a matrix shear modulus $G_m = 0.5$ MPa. We subsequently fit smooth quadratic polynomials that provides the parameters β^{Hr} and β^{Br} as a polynomial in c, such that

$$\beta^{Hr} = 18.5c^2 - 10.2c + 1.67 \qquad \text{and} \qquad \beta^{Br} = 18.0c^2 - 9.8c + 1.58, \tag{6.87}$$

respectively. Notice that the last expressions for β^{Hr} and β^{Br} are valid for $G_m = 0.5$ MPa and may be modified for the other G_m values. Nonetheless, a variation in these coupling parameters does not alter the qualitative nature of the magnetostriction responses.

Figure 6.4 shows a set of fitted model responses along with the numerical homogenization estimates for $c = 0.1$ (a-c), 0.2 (d-f) and 0.3 (g-i). We note that the effective hysteretic magnetization responses, which remain insensitive to the parameters β^{Hr} and β^{Br}, at least under the proportional loading path, are predicted sufficiently well by both the $\mathbf{F}-\mathbf{H}$ and $\mathbf{F}-\mathbf{B}$ models for all three c values (see Fig. 6.4a, d and g). As shown in Fig. 6.4b, e and h, the modeled effective parallel magnetostriction $\lambda_1 - 1$ fits perfectly to the corresponding numerical homogenization results. Moreover, the Fig. 6.4c, f and i show that the transverse magnetostriction components $\lambda_2 - 1$ and $\lambda_3 - 1$ are modeled perfectly by the proposed macroscopic framework. Notice that, due to the perfectly incompressible constituents, the transverse magnetostriction components obtained from the proposed macroscopic models are equal, given by $\lambda_2 = \lambda_3 = 1/\sqrt{\lambda_1}$. Nonetheless, the numerically computed transverse magnetostriction components exhibit minor differences between $\lambda_2 - 1$ and $\lambda_3 - 1$, which can be attributed directly to the compressible (near incompressibility is imposed only by setting $G_m' = 100 G_m$) constitutive models in the numerical computations.

The effect of c on the effective responses are depicted in Fig. 6.5. Here we show only the $\mathbf{F}-\mathbf{H}$ and $\mathbf{F}-\mathbf{B}$ model responses and drop the computed effective responses for brevity. Notice that, in spite of being dissipative and path-dependent, the c-dependence of the effective responses resemble closely to the non-dissipative effective responses of s-MREs. In particular, the effective maximum

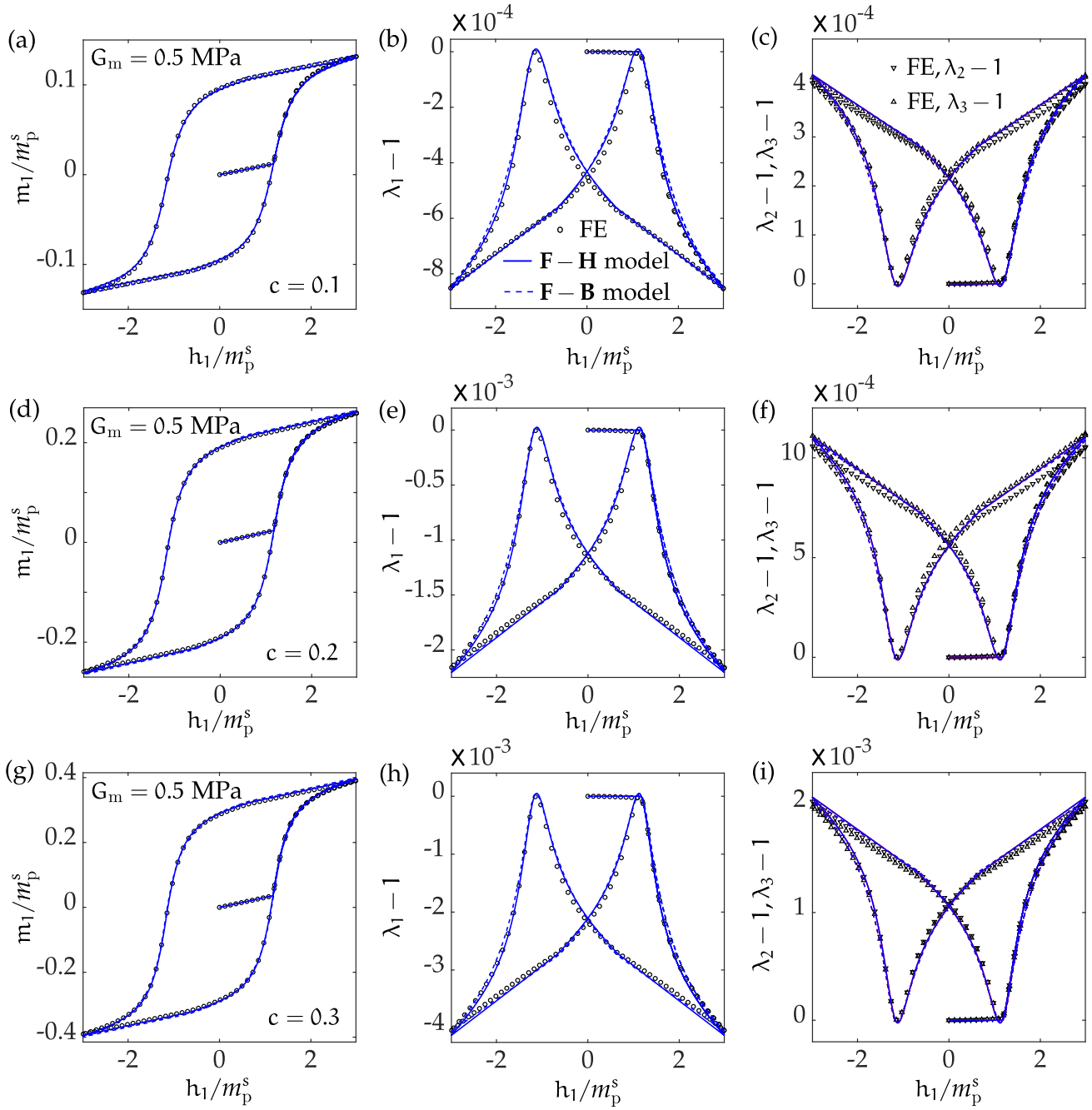

Figure 6.4: Comparison of the fitted $\mathbf{F}-\mathbf{H}$ (solid lines) and $\mathbf{F}-\mathbf{B}$ (dashed lines) model responses under proportional cyclic loading along $\mathbf{e}_1$ with the corresponding numerical homogenization response (discrete points). The effective magnetization (a,d,g), parallel (b,e,h) and transverse (c,f,i) magnetostrictions are compared for three different particle volume fractions $c = 0.1$ (a-c), 0.2 (d-f) and 0.3 (g-i).

magnetization is observed to be approximately proportional to c (see Fig. 6.5a), whereas a nonlinear c-dependence of the maximum magnetostriction at $|h_1|/m_p^s = 3.0$ is observed in Fig. 6.5b and c. Since the local magnetization never saturates, but rather maintains a constant slope of χ_p^e in the hard-magnetic particle phases, the effective magnetization and magnetostriction responses in Fig 6.5 do *not* exhibit any saturation. Nevertheless, one can compare the magnetization and magnetostrictions

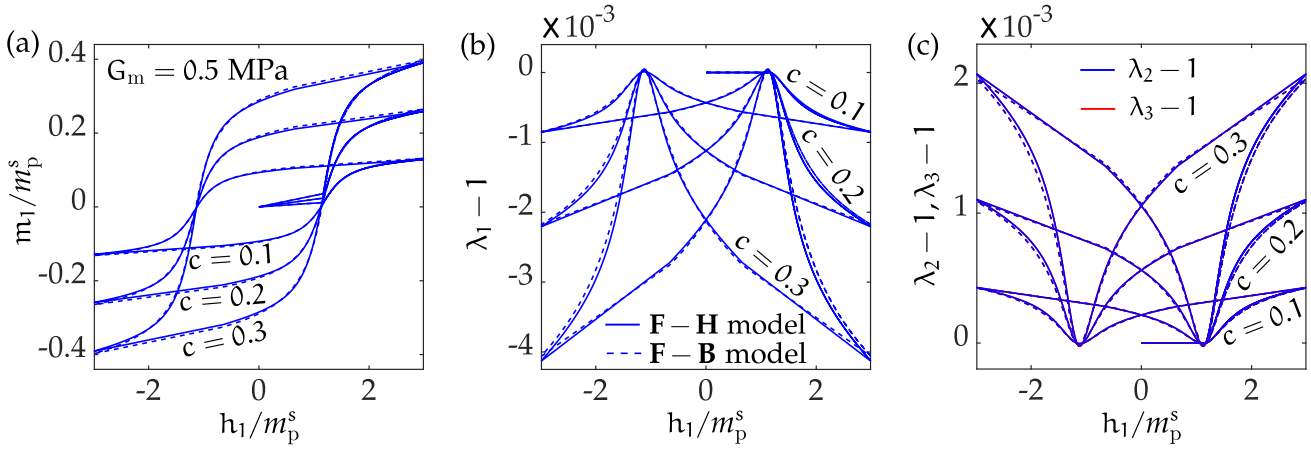

Figure 6.5: $\mathbf{F}-\mathbf{H}$ (solid lines) and $\mathbf{F}-\mathbf{B}$ (dashed lines) model (a) magnetization and (b) parallel and (c) transverse magnetostriction responses under proportional cyclic loading along $\mathbf{e}_1$ for three different particle volume fractions $c = 0.1$, 0.2 and 0.3.

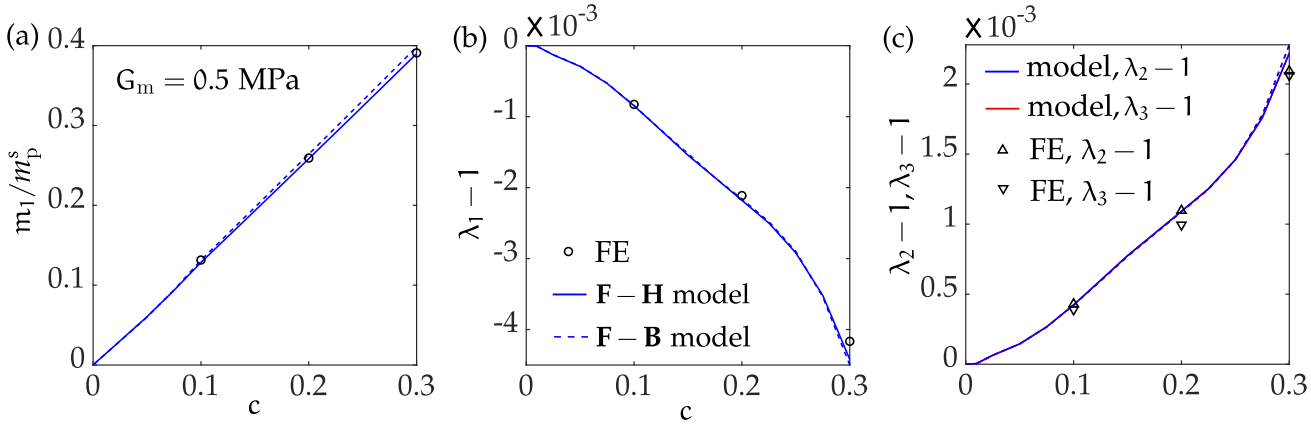

Figure 6.6: Variation of the maximum (a) magnetization, (b) parallel and (c) transverse magnetostrictions with c ($0.0 < c \leqslant 0.3$) under a proportional loading cycle having amplitude $|h_1|/m_p^s = 3.0$. Numerical homogenization estimates (discrete points) along with the $\mathbf{F}-\mathbf{H}$ (solid lines) and $\mathbf{F}-\mathbf{B}$ (dashed lines) model predictions.

under the applied maximum $|h_1|/m_p^s = 3.0$ to have a notion of their dependence on c.

The variation of the effective m_1 and the magnetostriction components with c are shown in Fig. 6.6, where the effective fields are computed at an applied $h_1/m_p^s = 3.0$ during the first loading cycle from 0 to 3. We note from Fig. 6.6a that, unlike the s-MREs, m_1/m_p^s is not equal to c and is directly proportional to c with a certain constant of proportionality, which is > 1. This observation is a direct consequence of the non-saturating effective magnetization response, while a perfectly saturating effective magnetization maintains a constant of proportionality to 1. The maximum parallel and transverse magnetostriction components, on the other hand, exhibit a nearly quadratic variation with an increasing c up to a particle volume fraction $c = 0.3$. We observe from the numerical homogenization estimates for s-MREs that the effective magnetostrictions start decreasing for $c > 0.35$ (Danas, 2017). However, this range of volume fractions with $c > 0.3$ is not investigated explicitly in the present study. Thus, it is emphasized to regard the fitting parameters in (6.87) *only* for the range of $0 < c \leqslant 0.3$. Re-calibration of the coupling parameters are recommended for the h-MREs having $c > 0.3$. Nonetheless, most of the h-MREs in practice have a particle volume fraction in the range of

$0.05 \leqslant c \leqslant 0.3$ (Kim et al., 2018; Zhao et al., 2019), which is investigated in this study.

6.4.2 Non-proportional magneto-mechanical loading of h-MREs with $c = 0.2$

Next, we probe the proposed $\mathbf{F}-\mathbf{H}$ and $\mathbf{F}-\mathbf{B}$ model predictions against the numerical homogenization computations under non-proportional magneto-mechanical loading paths. The boundary conditions are kept identical to that in the RVE computations, given by (4.85). The specific form of $\mathbf{F}$ is now chosen to be $\mathbf{F} = \sum_{i=1}^{3} \lambda_i \mathbf{e}_i \otimes \mathbf{e}_i + \gamma_{12} \mathbf{e}_1 \otimes \mathbf{e}_2$.

We note from several experiments that the magneto-mechanical responses of a pre-magnetized h-MRE sample are particularly of interest in most of the applications (Kim et al., 2018; Zhao et al., 2019). Thus, here we choose to probe the performance of the proposed models when a pre-magnetized h-MRE is subjected to various mechanical, magnetic and magneto-mechanical loadings. The pre-magnetization process remains identical in all the results herein. We pre-magnetize the RVE from the initial state of zero magnetization up to its saturation by applying the magnetic field $\mathbf{h}_a = h_1 \mathbf{e}_1$ having magnitude $|h_1|/m_p^s = 3.0$. This applied field is subsequently removed steadily at the same rate of its application, thus leading to a remanent magnetization in the h-MREs. The magnetization and magnetostriction responses under this initial magnetization loading step looks identical to the first quadrants of (6.6)a-c.

Specifically, here we choose to work with a h-MRE having particle volume fraction $c = 0.2$ and three distinct matrix shear moduli, namely $G_m = 1.0$, 0.5 and 0.3 MPa. The material parameters related to the magnetic particle phase "p" remains identical to that in Table 3.3a, whereas the coupling coefficients β^{Hr} and β^{Br} are considered to be defined by (6.87). Note that the optimal β^{Hr} and β^{Br} may vary for the matrix shear moduli $G_m = 1.0$ and 0.3 MPa. Nonetheless, such variations are not expected to be drastic in these two cases. Hence, we choose to work with the same β^{Hr} and β^{Br} as in (6.87) for all three matrix shear moduli. Moreover, it would be observed in the subsequent investigations that these coupling constants play minimal roles in altering the model responses under such non-proportional loading conditions.

First, we investigate the effects of mechanical tension and simple shear on the pre-magnetized h-MRE and also probe the model performance under these loading conditions. The effect of non-proportional magnetic loading perpendicular to the pre-magnetization direction will be investigated subsequently. Finally, we will investigate the effect of the simultaneous magneto-mechanical loading paths on the response of the h-MREs.

Effect of mechanical tension **:** A mechanical tension is applied on the pre-magnetized h-MRE along the $\mathbf{e}_2$ direction, such that $S^{mech}_{a,22} = S^{mech}_{22}$, with a maximum magnitude of G_m, while setting $S^{mech}_{a,12} = 0$ and all the other mechanical stress and displacement boundary conditions are considered to be given by $(4.85)_1$ and $(4.85)_4$, respectively. As shown in the inset of Fig. 6.7a, the loading and unloading path is considered to be a simple linear increase of S^{mech}_{22} from 0 to G_m and its subsequent linear decrease to 0. The resulting model and homogenization responses in terms of the mechanical stretch λ_2 and the magnetizations along the $\mathbf{e}_1$ and $\mathbf{e}_2$ directions are shown in Fig. 6.7a, b and c, respectively. Notice that, for this specific case, the numerical results for the effective responses are already shown in Fig. 4.14a-c, while the deformed RVEs under S^{mech}_{22} are depicted in Fig. 4.14d-f.

We observe excellent agreement between the numerical homogenization computations and the proposed $\mathbf{F}-\mathbf{H}$ and $\mathbf{F}-\mathbf{B}$ models in all the responses, shown in Fig. 6.7. The model predictions for the transverse stretches λ_2 and λ_3 also match perfectly the numerically computed responses. These

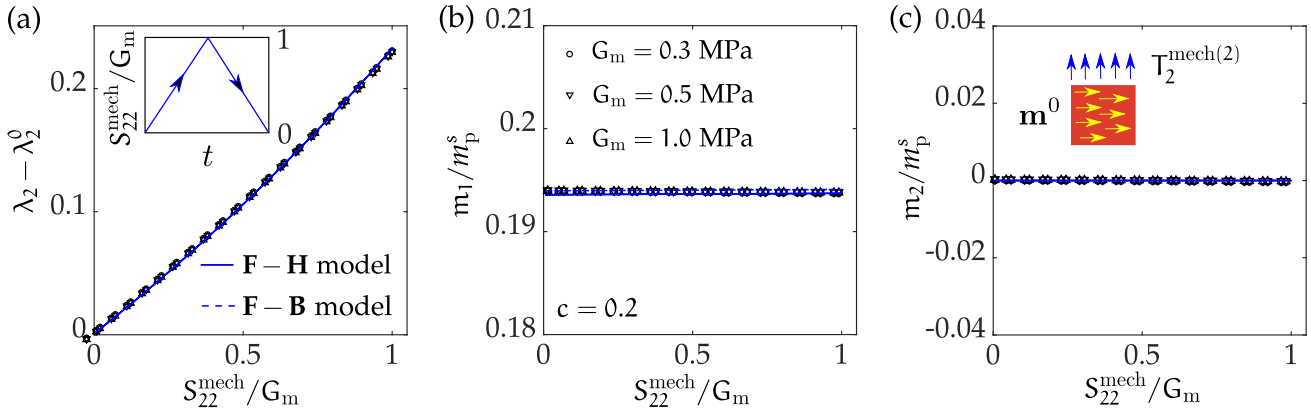

Figure 6.7: Evolutions of (a) mechanical stretch λ_2 and magnetizations along (b) $\mathbf{e}_1$ and (c) $\mathbf{e}_2$ under applied uniaxial tensile stress S_{22}^{mech}, whose loading path is shown in the inset of (a). The inset of (c) shown a schematic of the h-MRE with the direction of pre-magnetization $\mathbf{m}^0$ and the applied uniaxial tension.

comparisons are not shown explicitly for brevity. Note that the stretch-independence of the current remanent magnetization $\mathbf{m}^0$ is captured perfectly by the proposed models. Again, this feature is a direct consequence of the defining Lagrangian independent remanent variables in a stretch-free intermediate configuration, as shown in Fig. 6.2 and 6.3.

Effect of simple shear **:** We now apply a simple shear stress $S_{a,12}^{mech} = S_{12}^{mech}$ along the direction $\mathbf{e}_1$ on the surface having an unit normal along $\mathbf{e}_2$, while considering $S_{a,22}^{mech} = 0$ and all other mechanical boundary conditions given by $(4.85)_1$ and $(4.85)_4$. The loading path is shown in the inset of Fig. 6.8a, which is identical to the uniaxial tension case, but now in a different direction on the surface having

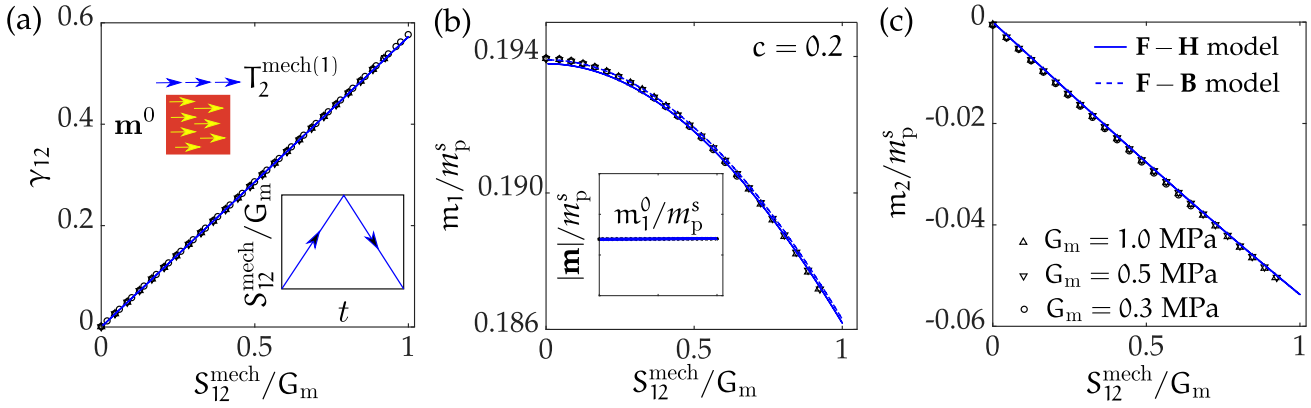

Figure 6.8: Evolutions of (a) shear strain γ_{12} and magnetizations along (b) $\mathbf{e}_1$ and (c) $\mathbf{e}_2$ under applied simple shear stress S_{12}^{mech}, whose loading path is shown in the inset of (a), which also show a schematic of the h-MRE with the direction of pre-magnetization $\mathbf{m}^0$ and the applied shear.

unit reference normal along $\mathbf{e}_2$.

We observe excellent agreements in Fig. 6.8a, b and c, between the model predictions and the numerical homogenization computations for the effective shear strain γ_{12}, effective magnetizations along $\mathbf{e}_1$ and $\mathbf{e}_2$, respectively, which are previously shown in Fig. 4.16. Also, the inset of Fig. 6.8a ascertains the fact that the applied simple shear stress rotates the current magnetization.

Non-proportional magnetic loading along $\mathbf{e}_2$ **:** Next, the effect of applied non-proportional mag-

netic loading, perpendicular to the direction of the pre-magnetization is investigated. As shown in the inset of Fig. 6.9a, the loading/unloading path remain a simple ramp-type linear increase/decrease

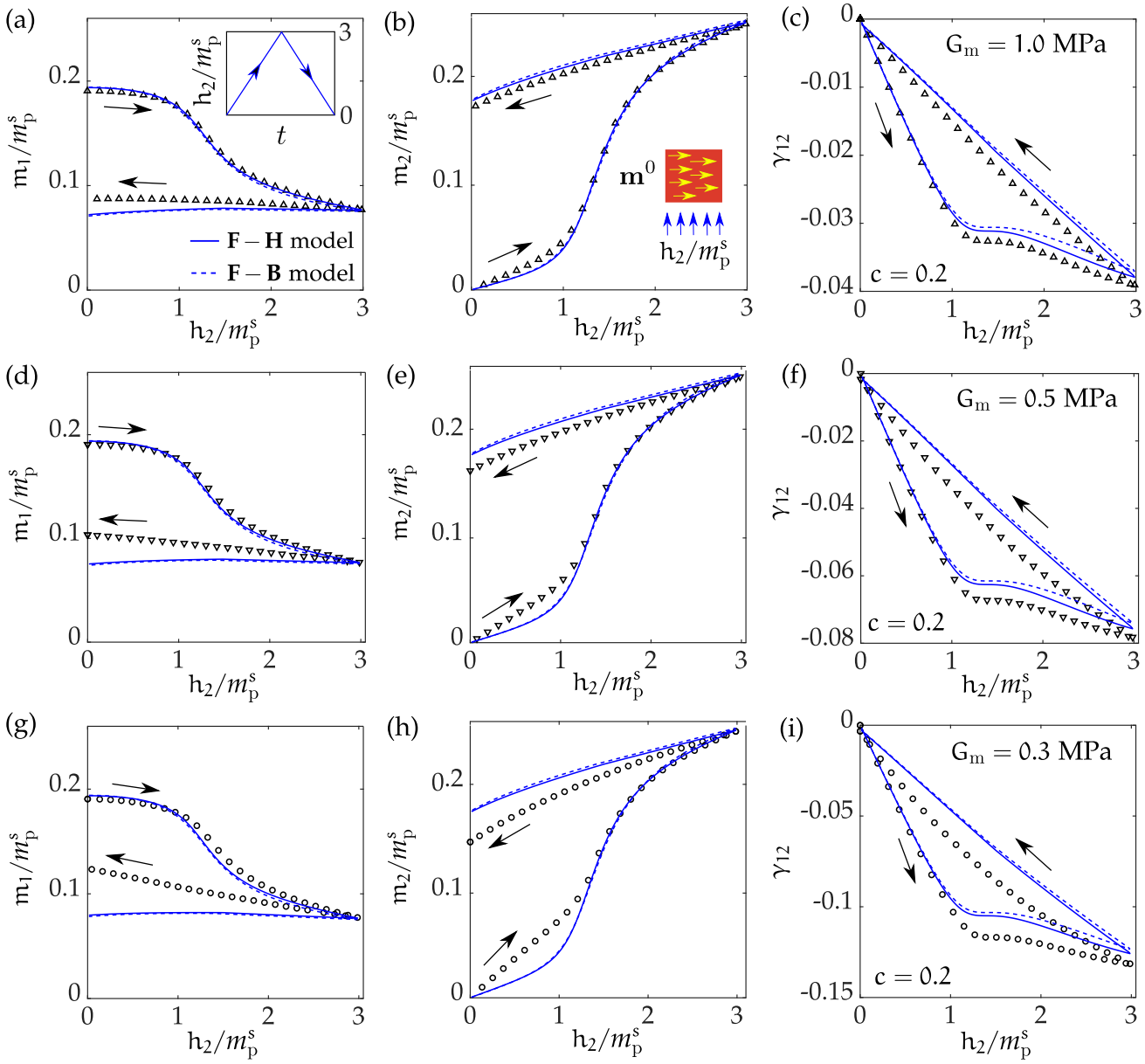

Figure 6.9: Evolution of the magnetization components along $\mathbf{e}_1$ (a,d,g) and $\mathbf{e}_2$ (b,e,h) and the induced shear strain γ_{12} (c,f,i) under applied non-proportional magnetic loading (inset of b) of a pre-magnetized h-MRE along $\mathbf{e}_1$ (inset of c). Effect of three distinct G_m, namely, $G_m = 1.0$ (a-c), 0.5 (d-f) and 0.3 (g-i) MPa on the effective magnetization components and induced shear strain.

from a zero applied field to $h_2 = 3m_p^s$ and vice-versa. In a similar note to the previous two cases, h-MREs with a particle volume fraction $c = 0.2$ and three different matrix shear moduli, $G_m = 1.0$, 0.5 and 0.3 are considered herein. For this particular case, the applied mechanical stress $S^{mech}_{a,22}$ and $S^{mech}_{a,12}$ considered to be zero, while the other mechanical stress and displacement conditions remain identical to the preceding two cases of applied tension and shear.

Since all the shear degrees of freedom on the surface with reference unit normal along $\mathbf{e}_2$ are left

free, the applied non-proportional loading readily induces an average shear strain along direction 1, namely γ_{12}, in the RVE due to the rotation of the microscopic hard magnetic particles. The evolution of the magnetization components along $\mathbf{e}_1$ and $\mathbf{e}_2$ along with that of the induced shear under applied h_1 are shown in Fig. 6.9. Unlike the preceding two results involving mechanical tension and shear of a pre-magnetized h-MRE, here we observe a strong dependence of the resulting magneto-mechanical responses on G_m. First, we notice from Fig. 6.9c, f and i that the induced shear strain increases with the decreasing shear modulus of the matrix. Furthermore, the magnitude of the induced shear strains are one to two orders higher than those of the magnetostrictions under a proportional loading, as observed in Fig. 6.4. The last observation suggests that the effect of particle rotations under non-proportional magnetic loading induces way more magneto-mechanical coupling than the simple particle rearrangements under the proportional loading paths. That is why most of the soft robotic applications of h-MREs exploit its large deflections under non-proportional magnetic loadings (Kim et al., 2018; Zhao et al., 2019). We also note from the numerical homogenization computations that, under this non-proportional loading condition, the scale of variations in the magnetostriction stretch components λ_i $(i = 1-3)$ remain less than 10^{-2}. Being significantly smaller, such variations do not play significant roles in the macroscopic response of the h-MREs under the non-proportional loading paths. These variations in λ_i are not shown in this text for brevity.

Both the $\mathbf{F}-\mathbf{H}$ and $\mathbf{F}-\mathbf{B}$ model predictions agrees very well with the computed effective responses, specially for the more stiff h-MREs having $G_m \geqslant 0.5$ MPa. The predicted effective magnetization and shear responses, however, start differing from the numerical computations for the relatively softer h-MRE with $G_m = 0.3$ MPa. To further investigate on this disparity, we plot the relative error in the magnitude of the predicted magnetization and the predicted direction of the magnetization with respect to the numerical homogenization estimates in Fig. 6.10 b and c. In particular, we observe from

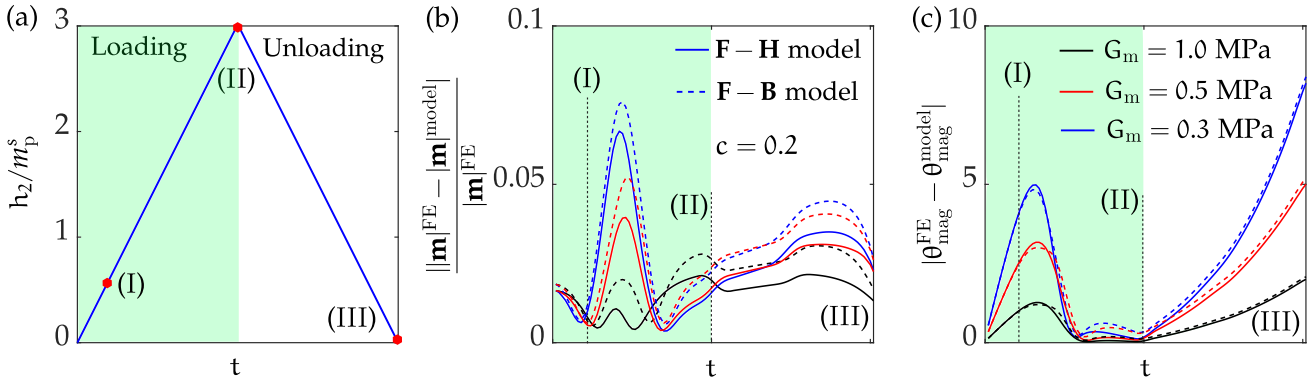

Figure 6.10: (a) Non-proportional loading path, (b) relative difference between the computed and model predicted magnitudes of m and (c) angle (in an absolute sense) between the computed and the model-predicted effective magnetizations.

Fig. 6.10b that, the relative error in the predicted magnitude of $\mathbf{m}$ remains below 3% during most of the loading/unloading. On the other hand, Fig. 6.10c shows that the absolute difference between θ^{FE}_{mag} and θ^{model}_{mag} becomes significant at the initiation of the non-proportional loading and during the unloading. Here the angles θ_{mag} are considered simply to be the angle with the reference X_1 axis and therefore, are computed simply via $\theta_{mag} = \tan^{-1}(m_2/m_1)$.

Such increasing difference between the predicted and computed directions of the effective $\mathbf{m}$, while their magnitudes match significantly well, is therefore solely due to the *non-affine* particle

rotations in the microstructure. Evidently, the extent of these non-affine rotations increase with the decreasing G_m, thus, leading to more disparity between the model predictions and the numerical homogenization estimates. Nonetheless, the predicted induced shear strain responses for $G_m = 0.3$ MPa in Fig. 6.9i have a qualitative agreement in terms of their similar evolution patterns.

Figure 6.11 shows a number of representative contour plots of the local $\breve{b}_2$ fields in the composite at various loading instants, indicated by (I), (II) and (III) on Fig. 6.10a. Evidently, the deformed

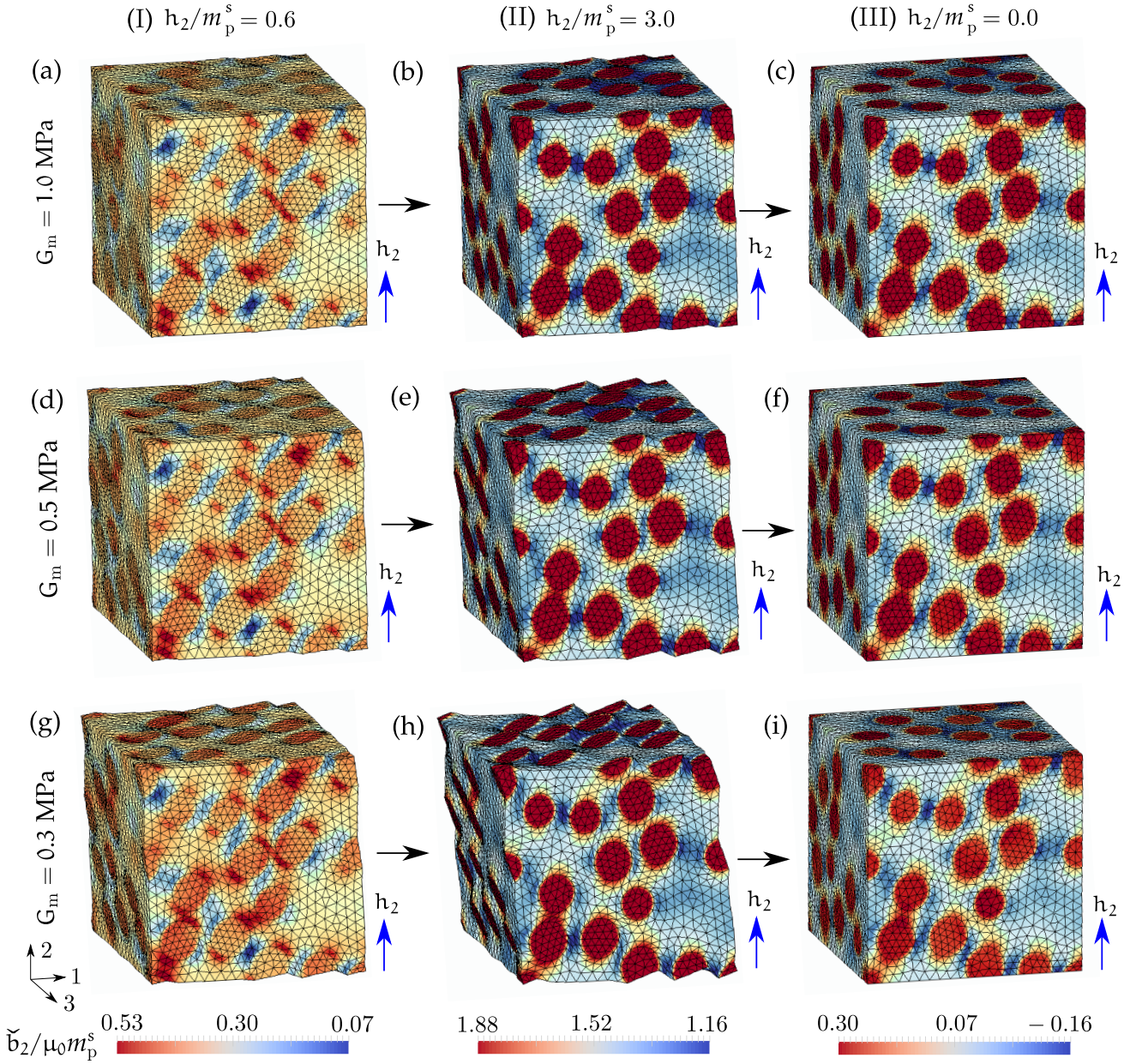

Figure 6.11: Contours of the numerically computed local $\breve{b}_2$ fields in a deformed mesh at the loading/unloading instances (I) (a,d,g), (II) (b,e,h) and (III) (c,f,i) as indicated in Fig. 6.10a. Contours are shown for three different matrix shear modulus, namely, $G_m = 1.0$ MPa (a-c), 0.5 MPa (d-f) and 0.3 (g-i).

configurations in Fig. 6.11 show a greater extent of induced shear in the RVEs with softer matrix (cf., Fig. 6.11b and h), which are in accordance with the effective responses in Fig. 6.9. Furthermore, visual

inspections of the individual particles in Fig. 6.11b, e and h clearly show an increasing tendency of non-proportional particle rotations. Even if the deformed configurations in state (III), i.e., Fig. 6.11c, f and i look identical, the directions of the local magnetization in the particles differ considerably. This is due to the higher extents of non-affine particle rotations in the softer matrix ($G_m = 0.3$ MPa) during the initial non-proportional loading cycle, as shown by the initial bump in the non-affine rotations in Fig. 6.10c.

In other words, the magnetization of h-MREs along the direction of non-proportional magnetic loading is results from two competing mechanisms: first, the particle rotations in the soft elastomer matrix and second, the magnetic switching in the particles. As shown in Fig 6.10c, during the initial non-proportional loading, the particles are more susceptible to undergo rotations in order to align themselves with the applied h-field, thus, inducing an overall shear strain γ_{12} in the RVE. Moreover, the tendency of the particles to undergo additional non-affine rotations increases with the decreasing G_m. Nevertheless, both affine and non-affine particle rotations are hindered by the elastic restoring torques, exerted by the matrix. Such hindrance to the (affine and non-affine) particle rotations increase with the increasing G_m, leading to smaller induced γ_{12} and also lesser non-affine rotations (see Fig. 6.10c). Eventually, the magnetic switching mechanism wins over the particle rotations at higher applied fields and consequently, the induced shear start saturating or having a more subtle rate of increasing (see Fig. 6.9c, f and i). Also, we observe negligibly small non-affine particle rotations in Fig. 6.10c during the later part of the loading half cycle, when the magnetic switching mechanism dominates in the process of rotating the average $\mathbf{m}$.

During the unloading, on the other hand, no magnetic switching takes place. Nonetheless, because of the elastic restoring torques, the rotated particles start coming back to their initial position while the applied magnetic field h_2 is removed gradually. Consequently, the induced γ_{12} vanishes upon the removal of the applied h_2 (see Fig. 6.9c, f, i and Fig. 6.11c, f and i). In addition, the particles also undergo non-affine rotations while restoring back to their initial positions, in order to compensate for their non-affine rotations during the initial part of the loading half cycle. Consequently, this leads to the disparity between numerical homogenization and the affine rotation-based $\mathbf{F}-\mathbf{H}$ and $\mathbf{F}-\mathbf{B}$ model predictions, specifically significant in Fig. 6.9g and h.

Simultaneous mechanical shear and non-proportional magnetic loading **:** We now investigate the effect of applied mechanical shear simultaneously with the non-proportional magnetic loading, whose loading path is considered to be the same as in Fig. 6.9a (inset). The mechanical shear loading path is considered to be identical to Fig. 6.8a (inset). Here we use the same RVE as shown in Fig. 6.11 for the FE computations, now with an applied shear stress $S^{mech}_{a,12} = S^{mech}_{12}$. In addition, we set $S^{mech}_{a,22} = 0$ and all the other macroscopic stress and displacement conditions are considered to be given by $(4.85)_1$ and $(4.85)_4$, respectively.

The resulting coupled magneto-mechanical responses for $c = 0.2$ and $G_m = 1.0$, 0.5 and 0.3 MPa are compared with the corresponding FE computations in Fig. 6.12. In particular, Fig. 6.12a, b, d, e, g and h show the same feature observed in the previous case of non-proportional magnetic loading, that is, the affine rotation models predict the m_1 and m_2 components better for relatively stiff matrices, even though, the magnetization responses are not identical to those in Fig. 6.9 due to the simultaneously applied shear stress S^{mech}_{12}.

The resulting shear strain γ_{12} evolves, however, in a different way in this case again due to the applied shear stress S^{mech}_{12}. As shown in Fig. 6.12c, f and i, the resulting γ_{12} increases with the applied

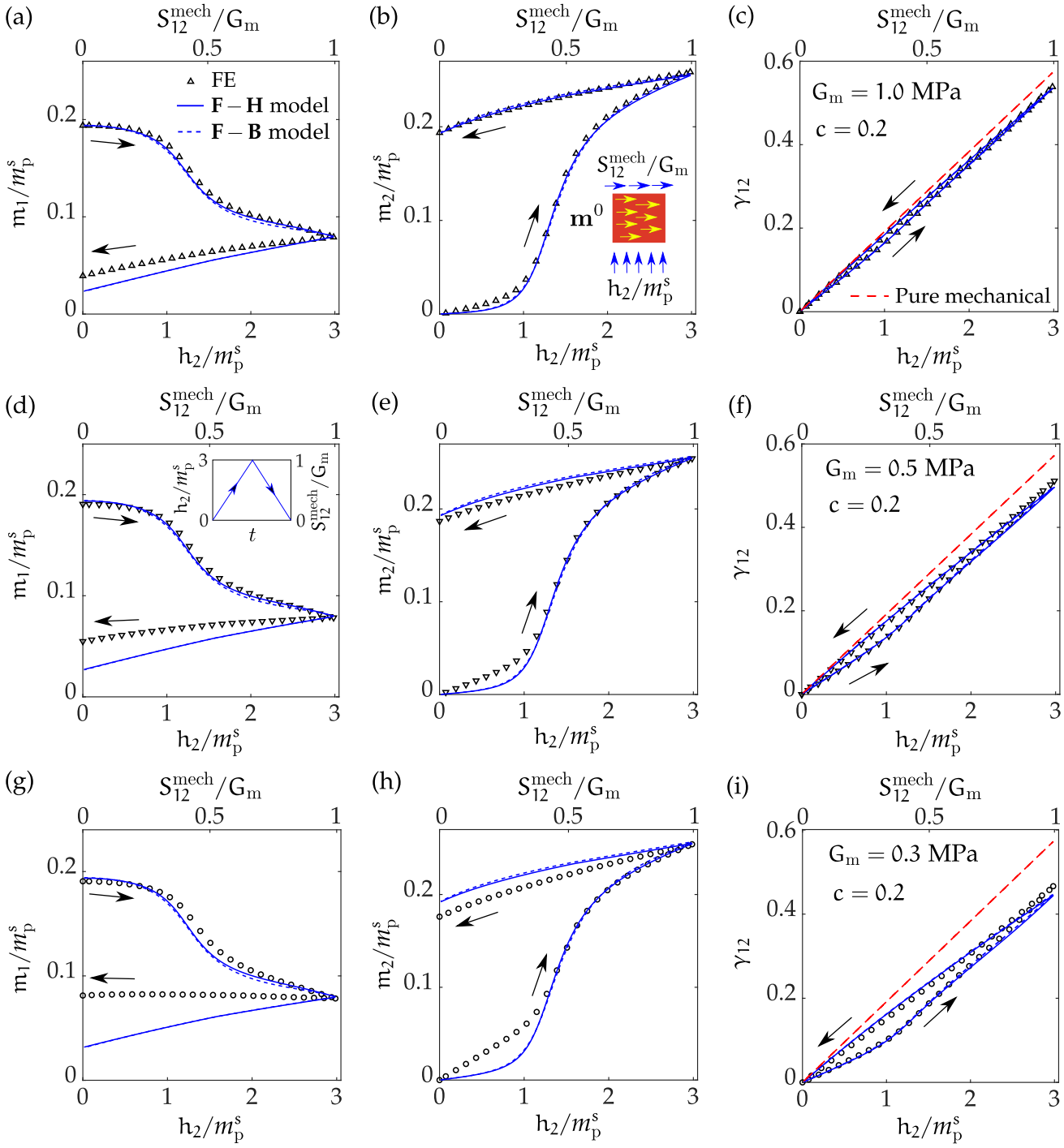

Figure 6.12: Evolution of the magnetization components along $\mathbf{e}_1$ (a,d,g) and $\mathbf{e}_2$ (b,e,h) and the induced shear strain γ_{12} (c,f,i) under applied non-proportional magnetic loading (inset of b) of a pre-magnetized ħ-MRE along $\mathbf{e}_1$ (inset of c). Effect of three distinct G_m, namely, $G_m = 1.0$ (a-c), 0.5 (d-f) and 0.3 (g-i) MPa on the effective magnetization components and induced shear strain.

S_{12}^{mech}/G_m and h_2/m_p^s in an irreversible path, such that the unloading path becomes different from the loading path. Notice that such irreversibility increases with the increasing softness of the matrix, i.e., for a decreasing G_m, while for all three G_m values under consideration, the model predictions

for γ_{12} match perfectly with the FE computations. For comparison, the purely mechanical shear loading/unloading response is shown in Fig. 6.12c, f and i by the red dashed line. We observe that the shear resistance of the material along the direction $\mathbf{e}_1$ increase substantially under the applied magnetic load h_1/m_p^s, specially for $G_m = 0.3$ MPa. Such increase in the shear resistance, however, becomes less significant for the stiffer h-MREs, as observed in Fig. 6.12c and f. This effect can be attributed directly to the extent of induced shear, shown in Fig. 6.9c, f and i for different G_m values, where we observe that the effect of induced shear increases with the decreasing G_m. Thus, the path-dependent induced shear imposes the path-dependence in the present case as well. Hence, since the amount of induced shear is greater for $G_m = 0.3$ MPa, we observe a greater shift of the computed γ_{12} from the pure mechanical shear response in Fig. 6.12i. In this regard, we show the $\breve{b}_2$ contours in the deformed RVE in Fig. 6.13, where the results for all three G_m are shown. Evidently, we see a

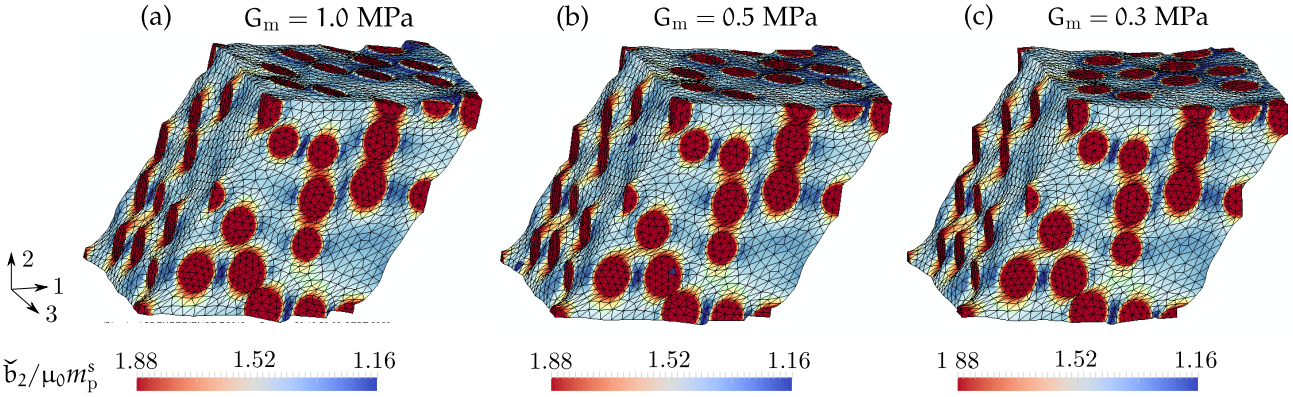

Figure 6.13: Contours of the numerically computed local $\breve{b}_2$ fields in a deformed mesh at the loading instance $h_2/m_p^s = 3.0$ and S_{12}^{mech}

relatively less amount of overall shear for $G_m = 0.3$ MPa in Fig. 6.13c, as compared to Fig. 6.13a, i.e., for $G_m = 1.0$ MPa.

Again, the difference between the computed and model-predicted m_1 and m_2 components in Fig. 6.12a, b, d, e, g and h can be attributed directly to the non-affine particle rotations in the matrix. Thus, we plot the relative error in the computed and predicted magnitudes $|\mathbf{m}|$ and the angle between computed and predicted $\mathbf{m}$ vectors in Fig. 6.14b and Fig. 6.14c, respectively, while the loading path for h_2 and S_{12} are shown in Fig. 6.14a. We note that the qualitative nature of the relative error in $|\mathbf{m}|$ and the angle between the $\mathbf{m}$ vectors remain identical to those shown in Fig. 6.10b and c, respectively. Notice from Fig. 6.14b that the relative error in the predicted $|\mathbf{m}|$ remains less than 5% during most of the loading/unloading path. Moreover, the magnitude of $|\theta_{mag}^{FE} - \theta_{mag}^{model}|$ remains nearly the same as in the pure non-proportional magnetic loading case (c.f., Fig. 6.10c and Fig. 6.14c). Thus, it can be inferred that the superimposed mechanical shear S_{12}^{mech} *do not affect substantially* the extent of non-affine particle rotations in the matrix. This observation may play a crucial role in quantifying the non-affine rotations of hard-magnetic particles in a matrix under applied magneto-mechanical loadings.

6.4.3 Non-proportional magnetic loading of h-MREs having other volume fractions

Finally, we probe the non-proportional magnetic loading responses of the proposed $\mathbf{F}-\mathbf{H}$ and $\mathbf{F}-$

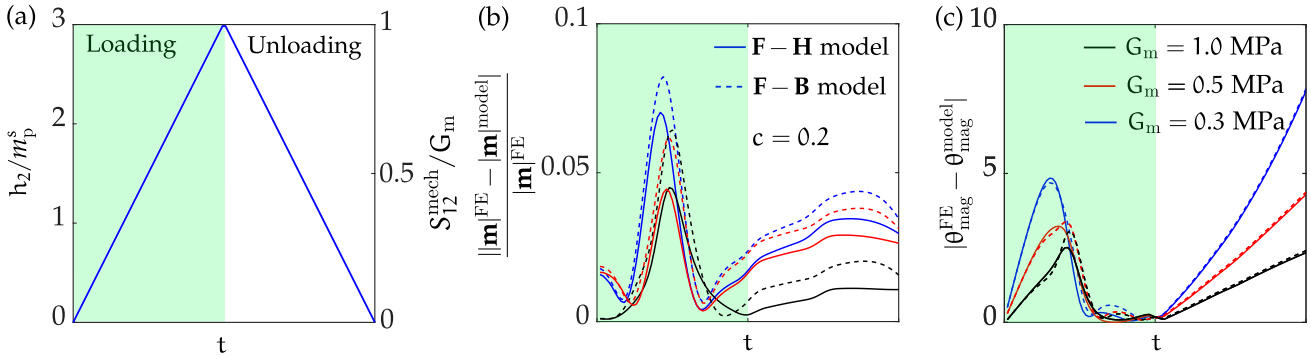

Figure 6.14: (a) Non-proportional loading path, (b) relative difference between the computed and model predicted magnitudes of m and (c) angle (in an absolute sense) between the computed and the model-predicted effective magnetizations.

B models for two other volume fractions, namely $c = 0.1$ and $c = 0.3$ under the same boundary conditions as defined for $c = 0.2$. The results are shown in Fig. 6.15 and 6.16, respectively, for $c = 0.1$ and 0.3, where three distinct matrix shear moduli, namely, $G_m = 1.0$, 0.5 and 0.3 MPa are considered. Both, Fig. 6.15 and 6.16 exhibit qualitatively similar features to those observed in Fig. 6.9 for $c = 0.2$. Thus, the proposed models are found to predict the material behavior considerably well for all volume fractions $c \leqslant 0.3$ and the matrix shear moduli $G_m \geqslant 0.3$ MPa.

Of interest is to investigate the effect of particle volume fractions on the overall non-affine rotation of the particles, which is shown in Fig. 6.17. Here we plot the absolute value of the angle between the computed and predicted **m** for three volume fractions $c = 0.1$, 0.2 and 0.3 for the matrix shear moduli $G_m = 1.0$, 0.5 and 0.3, in Fig. 6.17a, b and c respectively. We notice from Fig. 6.17 that the extent of non-affine particle rotation decreases with the increasing c, irrespective of the matrix shear modulus G_m. Such an observation is quite intuitive since a higher c indicates more closely packed particles in the matrix (see Fig. 4.4), which hinders the tendency of the particles to rotate in a non-affine way, that is different from the macroscopic RVE rotation **R**. Moreover, notice that the amount of maximum γ_{12} for $c = 0.3$ and $G_m = 0.3$ MPa in Fig. 6.16i is *nearly* the same as that obtained for $c = 0.2$ in Fig. 6.9i, although, the maximum γ_{12} is considerably less for $c = 0.1$ and $G_m = 0.3$, as shown in Fig. 6.15i. However, the extent of non-affine particle rotation is less for $c = 0.3$ as compared to $c = 0.2$ (see Fig. 6.17c). Consequently, we observe a better agreement of the computed results with the proposed affine rotation-based models for $c = 0.3$ and this agreement becomes less with the decreasing c.

6.5 Concluding remarks

In this chapter, we propose a set of $\mathbf{F}-\mathbf{H}$ and $\mathbf{F}-\mathbf{B}$-based constitutive models for the h-MREs in both Lagrangian and Eulerian settings by assuming affine particle rotations in the underlying microstructure. The key advantages of the proposed models are the following.

1. Thermodynamic consistency of the models are ensured by deriving the constitutive relations from the localized Clausius-Duhem inequalities and employing further the generalized standard materials framework, which yields the evolution laws for the remanent internal variables.

2. The objectivity and material symmetry properties of the isotropic h-MREs are ensured by

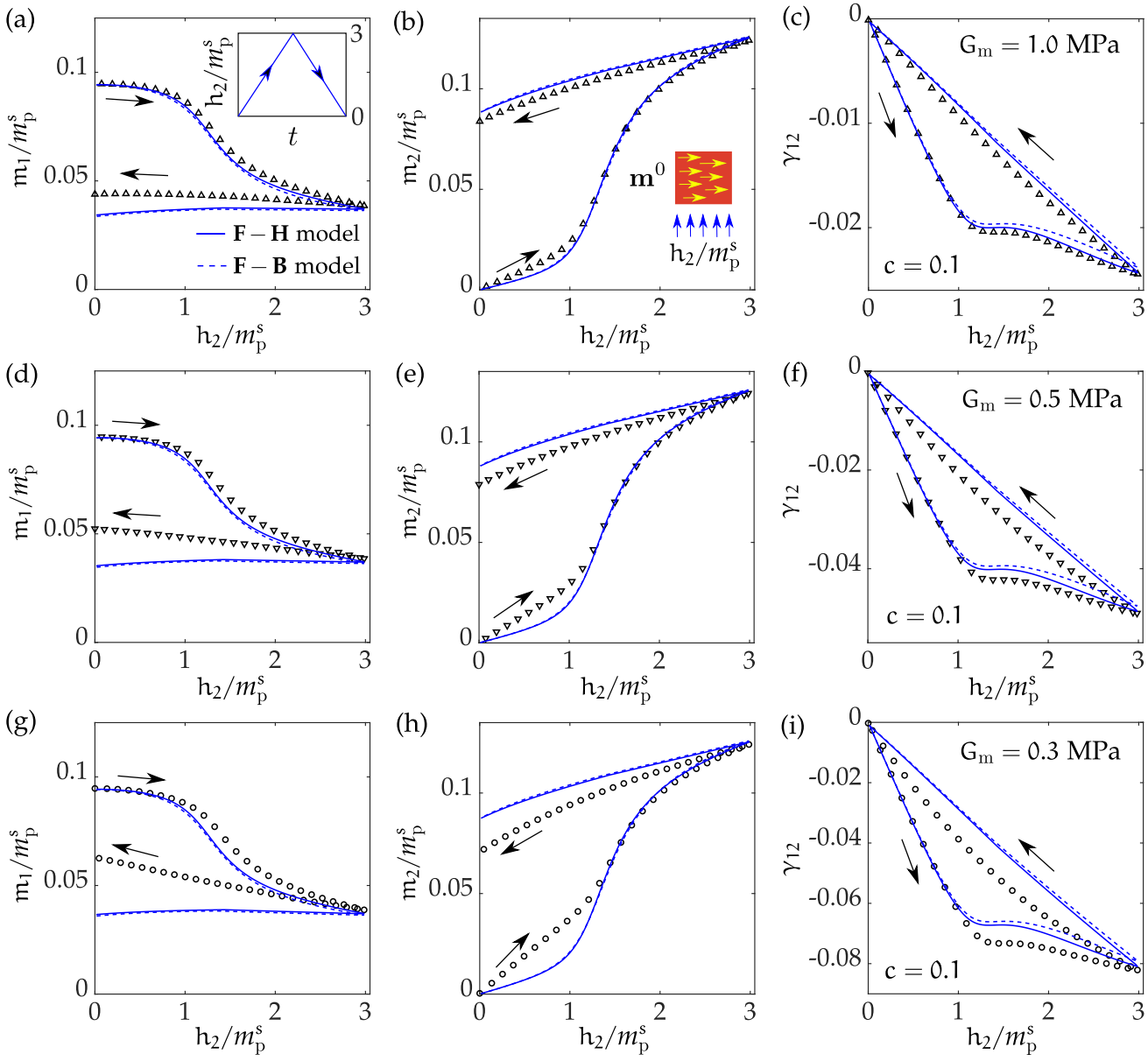

Figure 6.15: Evolution of the magnetization components along $\mathbf{e}_1$ (a,d,g) and $\mathbf{e}_2$ (b,e,h) and the induced shear strain γ_{12} (c,f,i) under applied non-proportional magnetic loading (inset of b) of a pre-magnetized $\mathfrak{h}$-MRE along $\mathbf{e}_1$ (inset of c). Effect of three distinct G_m, namely, $G_m = 1.0$ (a-c), 0.5 (d-f) and 0.3 (g-i) MPa on the effective magnetization components and induced shear strain.

proposing the energetic and dissipation potentials in terms of the suitable invariants. Specially, the current dissipation potentials are proposed in terms of the objective Green-Naghdi rate of the internal variables. This rate is a direct consequence of the definition of the Lagrangian counterparts of these internal variables in a stretch-free intermediate configuration.

3. The proposed modeling framework inherently takes care of the magnetic body force and body torque-like terms in a magneto-active solid by incorporating their effects in the total Cauchy stress $\boldsymbol{\sigma}$. Thus, no additional body force/torque like terms are required to be incorporated in

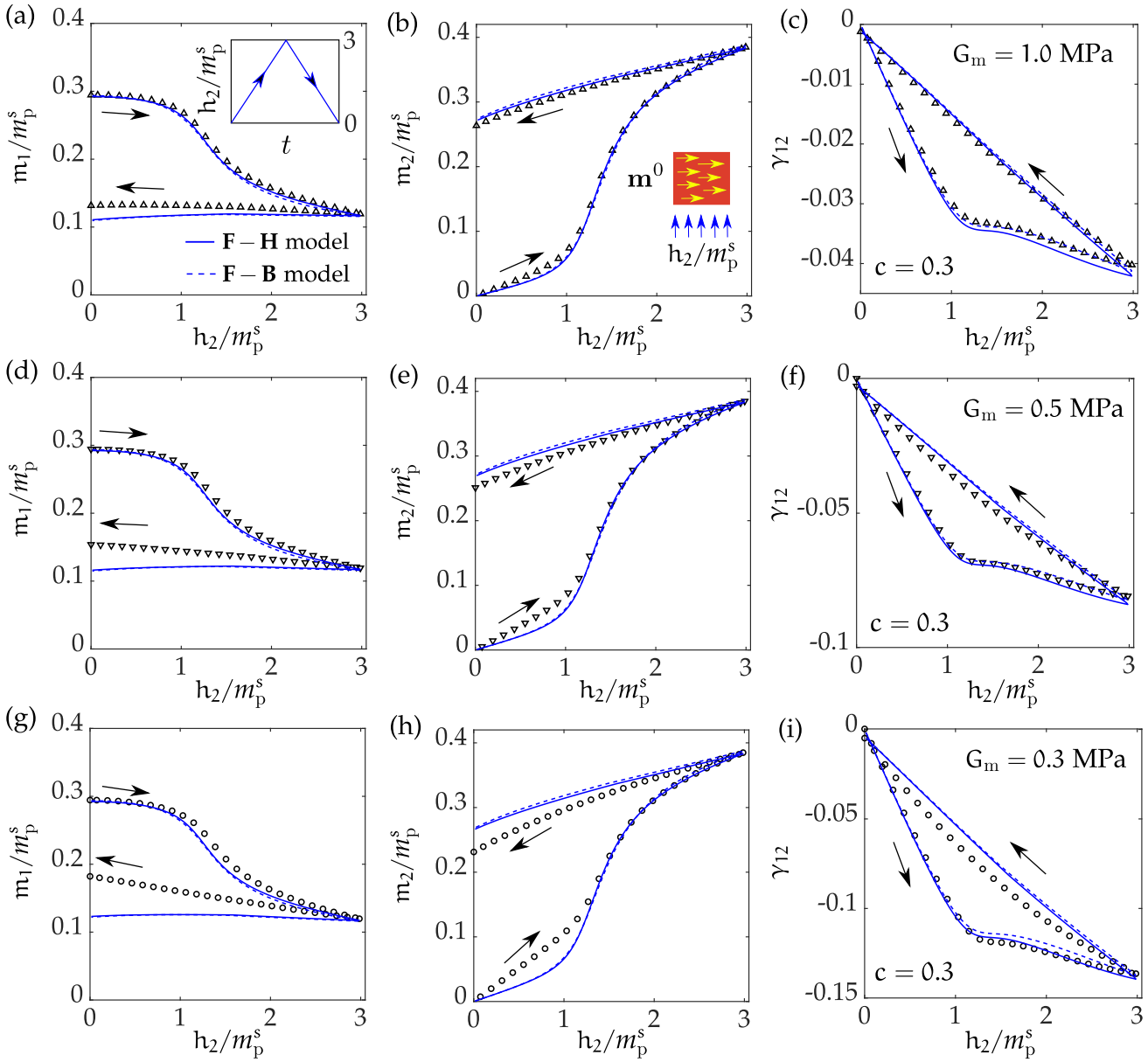

Figure 6.16: Evolution of the magnetization components along $\mathbf{e}_1$ (a,d,g) and $\mathbf{e}_2$ (b,e,h) and the induced shear strain γ_{12} (c,f,i) under applied non-proportional magnetic loading (inset of b) of a pre-magnetized ħ-MRE along $\mathbf{e}_1$ (inset of c). Effect of three distinct G_m, namely, $G_m = 1.0$ (a-c), 0.5 (d-f) and 0.3 (g-i) MPa on the effective magnetization components and induced shear strain.

the local linear/angular momentum balance equations. The total $\boldsymbol{\sigma}$ remains symmetric in the proposed modeling framework.

4. The Helmholtz free energy associated with the proposed macroscopic models of the ħ-MREs are considered to be an addition of three distinct contributions, namely the mechanical, magnetic and coupling free energies. Among these, the mechanical and magnetic free energies are proposed entirely in terms of the properties of the underlying constituents and the particle volume fraction c. Only one additional modeling parameter is introduced in the coupling energy term,

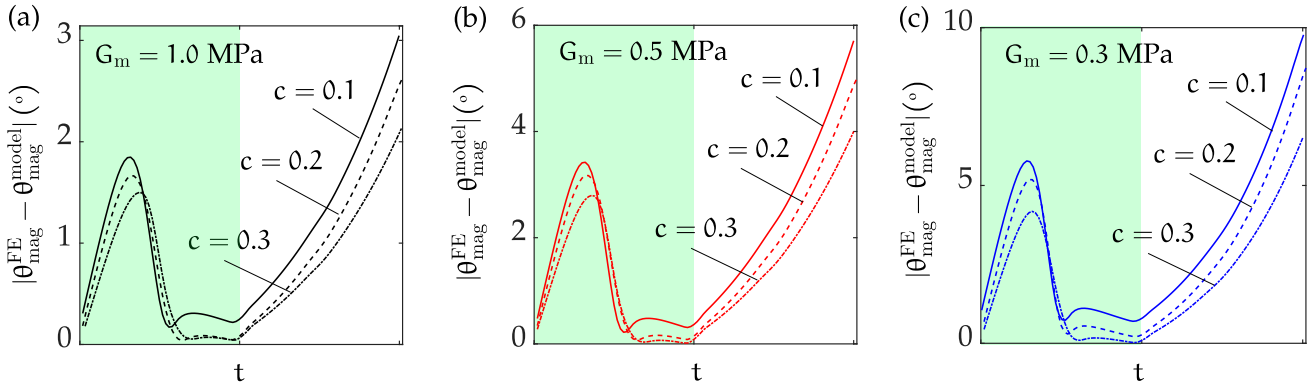

Figure 6.17: Comparison of the non-affine overall particle rotations $|\theta^{FE}_{mag} - \theta^{model}_{mag}|$ under non-proportional magnetic loading along $\mathbf{e}_2$, as defined in Fig. 6.10, for three distinct particle volume fractions $c = 0.1$, 0.2 and 0.3 and three matrix shear moduli (a) $G_m = 1.0$, (b) 0.5 and (c) 0.3 MPa. Time scale is irrelevant for the present case of rate-independent constitutive models.

which is then estimated via fitting the model predictions with the numerical homogenization responses.

5. The proposition of equivalent $\mathbf{F}-\mathbf{H}$ and $\mathbf{F}-\mathbf{B}$ models along with their Eulerian counterparts gives us the flexibility in terms of framing the macroscopic boundary value problems with the h-MREs. In this regard, it is noted that both Lagrangian $\mathbf{F}-\mathbf{H}$ (Keip and Rambausek, 2016, 2017; Lefèvre et al., 2017) and $\mathbf{F}-\mathbf{B}$ (Danas, 2017; Psarra et al., 2017, 2019) models and also the Eulerian $\mathbf{F}-\mathbf{b}$ model (Zhao et al., 2019) are employed in solving the macroscopic magneto-mechanical BVPs associated with the MREs.

6. The proposed models admit a number of limiting conditions and lead to the stress measures as reported in the literature. Specifically, in the limit of soft magnetic response, i.e., $b^c_p \to 0$, the stress measures lead to those defined by Kankanala and Triantafyllidis (2004) and the resulting effective model response reproduce exactly the response from the analytical homogenization model of Lefèvre et al. (2017). Secondly, in the limit of $c \to 1$, the proposed $\boldsymbol{\sigma}$ yields the classical definition of the total $\boldsymbol{\sigma}$ by Robinson (1975) in the context of metallic permanent magnets.

The model responses both under proportional and non-proportional loading paths show comprehensive agreements with the full-field numerical homogenization estimates. Specifically, the model responses under the proportional magnetic loading and under the mechanical loadings of a pre-magnetized h-MRE are in excellent agreement with the numerical homogenization results. The non-proportional magnetic loading, however, leads to non-affine particle rotations in the mechanically softer h-MREs. This effect leads to the disparity between the numerically computed and model predicted results, specifically for $G_m < 0.5$ MPa. Nevertheless, the qualitative nature of the evolution of the resulting mechanical and magnetic fields are predicted very well by the proposed models. The model predictions become better with increasing c under non-proportional loading. In this context, we observe that the extent of non-affine particle rotations become less for a denser composite, while the overall induced shear in the RVE remains of the same order.

In this regard, it is noted that the non-affine particle rotations control the magnetization/ demagnetization responses of the softer, gel-like h-MREs having $G_m \sim 0.01 - 0.1$ MPa (Linke et al.,

2016; Kalina et al., 2017). Of course, the proposed affine rotation model cannot be applied readily to model such highly compliant composites. Indeed, further augmentations to the proposed framework are needed in order to take care of the high non-affine particle rotations. Nonetheless, it is noted that most of the practical applications of the ħ-MREs consider a relatively stiffer PDMS matrix having $G_m \sim 0.25 - 1.5$ MPa. Moreover, such ħ-MREs, once permanently magnetized, are typically subjected to high mechanical but no or very low magnetic fields (Kim et al., 2018; Zhao et al., 2019; Sitti and Wiersma, 2020). Contextually, in the aforementioned loading regime, the proposed affine rotation model is observed to predict the microstructure response sufficiently well. Hence, it can be employed readily to solve any magneto-mechanical boundary value problems.

Appendix 6.A. Expressions for σ

This appendix provides explicit expressions for $\boldsymbol{\sigma}$ arising from the proposed $\mathbf{F}-\mathbf{h}$ and $\mathbf{F}-\mathbf{b}$ models, in terms of the corresponding current magnetic and remanent variables along with the left Cauchy-Green tensor $\mathbb{B}$. In this context, Dorfmann and Ogden (2003, 2004) have shown that the total $\boldsymbol{\sigma}$ is symmetric for the soft MREs via expressing it in terms of the current $\mathbf{b}$ and the right Cauchy-Green tensor $\mathbb{B}$. This appendix takes a similar route in order to establish the symmetry of $\boldsymbol{\sigma}$ as defined by (6.15) for the ħ-MREs. Notice that, the total $\boldsymbol{\sigma}$ is symmetric due to the definition of the equivalent potential energy functions to be $W^{\mathrm{H}}(\mathbb{C},\mathbf{H},\mathcal{H}^{\mathrm{r}}) \equiv w^{\mathrm{h}}(\mathbb{B},\mathbf{h},\mathbf{h}^{\mathrm{r}})$ and $W^{\mathrm{B}}(\mathbb{C},\mathbf{B},\mathcal{B}^{\mathrm{r}}) \equiv w^{\mathrm{b}}(\mathbb{B},\mathbf{b},\mathbf{b}^{\mathrm{r}})$. Here we show the the explicit expressions for $\boldsymbol{\sigma}$ can also be shown to be symmetric in its closed form.

$\mathbf{F}-\mathbf{h}$ *model* : First, we derive the expression for $\boldsymbol{\sigma}$ from the proposed $\mathbf{F}-\mathbf{h}$ model. Prior to expressing explicitly the full $\boldsymbol{\sigma}$, we further simplify the remanent Maxwell stress $\boldsymbol{\sigma}^{\mathrm{rem}}_{\mathrm{maxw}}$ via expanding the derivative $\partial\mathbf{R}/\partial\mathbf{F}$. The fourth order tensor $\partial\mathbf{R}/\partial\mathbf{F}$ is given in terms of index notations via (Chen and Wheeler, 1993)

$$\frac{\partial R_{ij}}{\partial F_{mn}} = \frac{1}{\det \mathbf{Y}} R_{ip}\Big[Y_{pq}R_{mq}Y_{nj} - Y_{pn}R_{mq}Y_{qj}\Big], \qquad \text{with} \qquad \mathbf{Y} = \mathrm{tr}(\mathbf{U})\mathbf{I} - \mathbf{U}. \tag{6.A.1}$$

Substituting $(6.A.1)_1$ into $(6.16)_1$ we obtain the expression for $\boldsymbol{\sigma}^{\mathrm{rem}}_{\mathrm{maxw}}$ that reads

$$\begin{aligned}\boldsymbol{\sigma}^{\mathrm{rem}}_{\mathrm{maxw}} &= -\frac{1}{J\det\mathbf{Y}}\mathbf{R}\big(\mathbf{Y}\mathbf{R}^{\mathsf{T}}\mathbf{b}^{\mathrm{r}}\otimes\mathbf{Y}\mathbf{R}^{\mathsf{T}}\mathbf{h}^{\mathrm{r}} - \mathbf{Y}\mathbf{R}^{\mathsf{T}}\mathbf{h}^{\mathrm{r}}\otimes\mathbf{Y}\mathbf{R}^{\mathsf{T}}\mathbf{b}^{\mathrm{r}}\big)\mathbf{F}^{\mathsf{T}}\\ &= -\frac{2}{J\det\mathbf{Y}}\mathbf{R}\mathbf{Y}\mathbf{R}^{\mathsf{T}}\mathrm{skw}\big(\mathbf{b}^{\mathrm{r}}\otimes\mathbf{h}^{\mathrm{r}}\big)\mathbf{R}\boldsymbol{\Upsilon}\mathbf{R}^{\mathsf{T}},\end{aligned}$$

where $\boldsymbol{\Upsilon} = \mathbf{Y}\mathbf{U} = \mathbf{U}\mathbf{Y}$ is a symmetric tensor (follows from the definition of $\mathbf{Y}$ in $(6.A.1)_2$) and skw(■) is the skew symmetric part of (■). The tensor $\mathbf{R}\boldsymbol{\Upsilon}\mathbf{R}^{\mathsf{T}}$ in the last equation can further be decomposed in the following form.

$$\mathbf{R}\boldsymbol{\Upsilon}\mathbf{R}^{\mathsf{T}} = \mathbf{R}\mathbf{U}\mathbf{Y}\mathbf{R}^{\mathsf{T}} = (\mathbf{R}\mathbf{U}\mathbf{R}^{\mathsf{T}})(\mathbf{R}\mathbf{Y}\mathbf{R}^{\mathsf{T}}) = \mathbf{V}\mathbf{Z}, \tag{6.A.2}$$

where $\mathbf{V} = \mathbf{R}\mathbf{U}\mathbf{R}^{\mathsf{T}}$ is the right stretch tensor and $\mathbf{Z} = \mathbf{R}\mathbf{Y}\mathbf{R}^{\mathsf{T}}$. It can be easily verified that $\mathbf{Z}$ can be expressed in terms of $\mathbf{V}$ via (Chen and Wheeler, 1993)

$$\mathbf{Z} = \mathrm{tr}(\mathbf{V})\mathbf{I} - \mathbf{V}. \tag{6.A.3}$$

Thus, the expression for $\boldsymbol{\sigma}^{\text{rem}}_{\text{maxw}}$ now reads

$$\boldsymbol{\sigma}^{\text{rem}}_{\text{maxw}} = -\frac{2}{J\det\mathbf{Z}}\mathbf{Z}\,\text{skw}\big(\mathbf{b}^{\text{r}}\otimes\mathbf{h}^{\text{r}}\big)\mathbf{V}\mathbf{Z}. \tag{6.A.4}$$

Subsequently, the expression for the total $\boldsymbol{\sigma}$ in terms of the current magnetic and internal variables is given via the constitutive relation $(6.16)_1$, so that

$$\boldsymbol{\sigma} = \frac{2\rho_0}{J}\frac{\partial\psi^{\text{H}}}{\partial\mathbb{B}}\mathbb{B} + \Big(\mathbf{h}\otimes\mathbf{b} - \frac{\mu_0}{2}|\mathbf{h}|^2\mathbf{I}\Big) - \frac{2}{J\det\mathbf{Z}}\mathbf{Z}\,\text{skw}\big(\mathbf{b}^{\text{r}}\otimes\mathbf{h}^{\text{r}}\big)\mathbf{V}\mathbf{Z} \tag{6.A.5}$$

Here we assume no specific function for the free energy ψ^{H}, albeit its arguments are given in terms of the invariants defined in Table 6.1. Thus, the expressions for $\mathbf{b}$ and $\mathbf{b}^{\text{r}}$, obtained, respectively, from the constitutive relations $(6.16)_2$ and $(6.17)_2$, such that

$$\mathbf{b} = \mu_0\mathbf{h} - \frac{\rho_0}{J}\Big(2\frac{\partial\psi^{\text{H}}}{\partial I_4^{\text{H}}}\mathbb{B}\mathbf{h} + \frac{\partial\psi^{\text{H}}}{\partial I_4^{\text{HHr}}}\mathbb{B}\mathbf{h}^{\text{r}} + 2\frac{\partial\psi^{\text{H}}}{\partial I_5^{\text{H}}}\mathbf{h} + \frac{\partial\psi^{\text{H}}}{\partial I_5^{\text{HHr}}}\mathbf{h}^{\text{r}}\Big) \tag{6.A.6}$$

and

$$\mathbf{b}^{\text{r}} = -\rho_0\Big(\frac{\partial\psi^{\text{H}}}{\partial I_4^{\text{HHr}}}\mathbb{B}\mathbf{h} + 2\frac{\partial\psi^{\text{H}}}{\partial I_4^{\text{Hr}}}\mathbb{B}\mathbf{h}^{\text{r}} + \frac{\partial\psi^{\text{H}}}{\partial I_5^{\text{HHr}}}\mathbf{h} + 2\frac{\partial\psi^{\text{H}}}{\partial I_5^{\text{Hr}}}\mathbf{h}^{\text{r}}\Big). \tag{6.A.7}$$

Subsequently, substituting (6.A.6) and (6.A.7) into (6.A.5) and simplifying we obtain

$$\begin{aligned}\boldsymbol{\sigma} =& \frac{2\rho_0}{J}\Big[\frac{\partial\psi^{\text{H}}}{\partial I_1}\mathbb{B} + J\frac{\partial\psi^{\text{H}}}{\partial J}\mathbf{I} + \frac{\partial\psi^{\text{H}}}{\partial I_4^{\text{H}}}(\mathbf{h}\otimes\mathbf{h})\mathbb{B} + \frac{\partial\psi^{\text{H}}}{\partial I_4^{\text{HHr}}}\,\text{sym}(\mathbf{h}\otimes\mathbf{h}^{\text{r}})\mathbb{B} + \frac{\partial\psi^{\text{H}}}{\partial I_4^{\text{Hr}}}(\mathbf{h}^{\text{r}}\otimes\mathbf{h}^{\text{r}})\mathbb{B}\Big]\\ &- \frac{\rho_0}{J}\Big[\mathbf{h}\otimes\Big(2\frac{\partial\psi^{\text{H}}}{\partial I_4^{\text{H}}}\mathbb{B}\mathbf{h} + \frac{\partial\psi^{\text{H}}}{\partial I_4^{\text{HHr}}}\mathbb{B}\mathbf{h}^{\text{r}} + 2\frac{\partial\psi^{\text{H}}}{\partial I_5^{\text{H}}}\mathbf{h} + \frac{\partial\psi^{\text{H}}}{\partial I_5^{\text{HHr}}}\mathbf{h}^{\text{r}}\Big)\Big] + \mu_0\mathbf{h}\otimes\mathbf{h} - \frac{\mu_0}{2}|\mathbf{h}|^2\mathbf{I}\\ &+ \frac{\rho_0}{J}\frac{2}{\det\mathbf{Z}}\mathbf{Z}\,\text{skw}\Big[\Big(\frac{\partial\psi^{\text{H}}}{\partial I_4^{\text{HHr}}}\mathbb{B}\mathbf{h} + 2\frac{\partial\psi^{\text{H}}}{\partial I_4^{\text{Hr}}}\mathbb{B}\mathbf{h}^{\text{r}} + \frac{\partial\psi^{\text{H}}}{\partial I_5^{\text{HHr}}}\mathbf{h} + 2\frac{\partial\psi^{\text{H}}}{\partial I_5^{\text{Hr}}}\mathbf{h}^{\text{r}}\Big)\otimes\mathbf{h}^{\text{r}}\Big]\mathbf{V}\mathbf{Z},\end{aligned} \tag{6.A.8}$$

where we suppress the I_2 dependence of ψ^{H} for simplicity. Further simplification of (6.A.8) leads to

$$\begin{aligned}\boldsymbol{\sigma} =& \frac{\rho_0}{J}\Big[2\frac{\partial\psi^{\text{H}}}{\partial I_1}\mathbb{B} + 2J\frac{\partial\psi^{\text{H}}}{\partial J}\mathbf{I} + \frac{\partial\psi^{\text{H}}}{\partial I_4^{\text{HHr}}}\mathbb{B}(\mathbf{h}^{\text{r}}\otimes\mathbf{h}) + 2\frac{\partial\psi^{\text{H}}}{\partial I_4^{\text{Hr}}}(\mathbf{h}^{\text{r}}\otimes\mathbf{h}^{\text{r}})\mathbb{B}\Big] - \frac{\rho_0}{J}\Big[\mathbf{h}\otimes\Big(2\frac{\partial\psi^{\text{H}}}{\partial I_5^{\text{H}}}\mathbf{h} + \frac{\partial\psi^{\text{H}}}{\partial I_5^{\text{HHr}}}\mathbf{h}^{\text{r}}\Big)\Big]\\ &+ \mu_0\mathbf{h}\otimes\mathbf{h} - \frac{\mu_0}{2}|\mathbf{h}|^2\mathbf{I} + \frac{\rho_0}{J}\frac{2}{\det\mathbf{Z}}\mathbf{Z}\,\text{skw}\Big[\Big(\frac{\partial\psi^{\text{H}}}{\partial I_4^{\text{HHr}}}\mathbb{B}\mathbf{h} + 2\frac{\partial\psi^{\text{H}}}{\partial I_4^{\text{Hr}}}\mathbb{B}\mathbf{h}^{\text{r}} + \frac{\partial\psi^{\text{H}}}{\partial I_5^{\text{HHr}}}\mathbf{h}\Big)\otimes\mathbf{h}^{\text{r}}\Big]\mathbf{V}\mathbf{Z},\end{aligned} \tag{6.A.9}$$

Finally, the expression for $\boldsymbol{\sigma}$ in the incompressible decoupled model (6.29) can then be obtained from (6.A.9), so that

$$\begin{aligned}\boldsymbol{\sigma} =& \frac{G_m}{(1-c)^{5/2}}\mathbb{B} + \Big[\mu_0(1+\chi^{\text{e}})\mathbf{h}\otimes(\mathbf{h}-\mathbf{h}^{\text{r}}) - \frac{\mu_0}{2}|\mathbf{h}|^2\mathbf{I}\Big] - \frac{2}{\det\mathbf{Z}}\mathbf{Z}\,\text{skw}\big[-\mu_0(1+\chi^{\text{e}})(\mathbf{h}\otimes\mathbf{h}^{\text{r}})\big]\mathbf{V}\mathbf{Z} - p\mathbf{I}\\ \equiv& \frac{G_m}{(1-c)^{5/2}}\mathbb{B} + \Big[\mathbf{h}\otimes\mathbf{b} - \frac{\mu_0}{2}|\mathbf{h}|^2\mathbf{I}\Big] + \frac{2}{\det\mathbf{Z}}\mathbf{Z}\,\text{skw}\big(\mu_0\mathbf{m}\otimes\mathbf{h}\big)\mathbf{V}\mathbf{Z} - p\mathbf{I}.\end{aligned} \tag{6.A.10}$$

To this end, the explicit expression for $\boldsymbol{\sigma}$ is given by (6.A.9). However, the symmetry of $\boldsymbol{\sigma}$ is not straightforward to follow from (6.A.9). In order to prove the symmetry of $\boldsymbol{\sigma}$, we simply perform the skw(■) operation on both sides of (6.A.9). Furthermore, during the computation of skw($\boldsymbol{\sigma}$), we

employ the following lemma.

Lemma 6.A.1. *Assuming* Lin *to be the set of all linear transformations (tensors) on* $\mathbb{R}^3$*, for any tensor* $\mathbf{A} \in \text{Lin}$ *defined via*

$$\mathbf{A} = \frac{2}{\det \mathbf{Z}} \mathbf{Z}\mathbf{W}\mathbf{V}\mathbf{Z}, \tag{6.A.11}$$

where $\mathbf{W} \in \text{Skw}$, $\mathbf{V} \in \text{Sym}$ *and* $\mathbf{Z} = \text{tr}(\mathbf{V})\mathbf{I} - \mathbf{V}$*, the skew-symmetric part of* $\mathbf{A}$ *is given by* $\text{skw}(\mathbf{A}) = \mathbf{W}$.

Proof: The skew symmetric part of $\mathbf{A}$ is obtained from (6.A.11), so that

$$\text{skw}(\mathbf{A}) = \frac{2}{\det \mathbf{Z}} \text{skw}(\mathbf{Z}\mathbf{W}\mathbf{V}\mathbf{Z}) = \frac{1}{\det \mathbf{Z}} \big(\mathbf{Z}\mathbf{W}\mathbf{V}\mathbf{Z} - \mathbf{Z}^T\mathbf{V}^T\mathbf{W}^T\mathbf{Z}^T\big) = \frac{1}{\det \mathbf{Z}} \mathbf{Z}\big(\mathbf{W}\mathbf{V} + \mathbf{V}\mathbf{W}\big)\mathbf{Z}, \tag{6.A.12}$$

where we utilize the symmetry of $\mathbf{V}$ and $\mathbf{Z}$ and the skew-symmetry of $\mathbf{W}$. Next, we express $\mathbf{V}$ and $\mathbf{W}$ in the eigenbasis $\mathbf{e}_k$ of $\mathbf{V}$, such that (Chen and Wheeler, 1993)

$$\mathbf{V} = \sum_{k=1}^{3} v_k \mathbf{e}_k \otimes \mathbf{e}_k \qquad \text{and} \qquad \mathbf{W} = \sum_{p=1}^{3} \sum_{q=1, p\neq q}^{3} w_{pq} \mathbf{e}_p \otimes \mathbf{e}_q \tag{6.A.13}$$

Consequently, $\mathbf{Z}$ is expressed in terms of the spectral basis $\mathbf{e}_j$ via

$$\mathbf{Z} = \sum_{j=1}^{3} \Big(\sum_{i=1}^{3} v_i - v_j \Big) \mathbf{e}_j \otimes \mathbf{e}_j \tag{6.A.14}$$

Substituting (6.A.13) and (6.A.14) into (6.A.12) and simplifying we obtain

$$\begin{aligned}
\text{skw}(\mathbf{A}) &= \frac{1}{\prod_{p=1}^{3} \Big(\sum_{i=1}^{3} v_i - v_p \Big)} \sum_{j=1}^{3} \sum_{k=1, k\neq j}^{3} \Big(\sum_{i=1}^{3} v_i - v_j \Big) \Big(\sum_{i=1}^{3} v_i - v_k \Big) (v_j + v_k) w_{jk} \mathbf{e}_j \otimes \mathbf{e}_k \\
&= \sum_{j=1}^{3} \sum_{k=1, k\neq j}^{3} \frac{1}{\Big(\sum_{i=1}^{3} v_i - v_j \Big) \Big(\sum_{i=1}^{3} v_i - v_k \Big) (v_j + v_k)} \Big(\sum_{i=1}^{3} v_i - v_j \Big) \Big(\sum_{i=1}^{3} v_i - v_k \Big) (v_j + v_k) w_{jk} \mathbf{e}_j \otimes \mathbf{e}_k \\
&= \sum_{j=1}^{3} \sum_{k=1, k\neq j}^{3} w_{jk} \mathbf{e}_j \otimes \mathbf{e}_k = \mathbf{W}.
\end{aligned} \tag{6.A.15}$$

Hence, we note that Lemma 6.A.1 is a direct consequence of the Lemma 1 of Chen and Wheeler (1993), which reads $\mathbf{Z}\big(\mathbf{W}\mathbf{V} + \mathbf{V}\mathbf{W}\big)\mathbf{Z} = (\det \mathbf{Z})\mathbf{W}$ for all $\mathbf{V}$, $\mathbf{W}$ and $\mathbf{Z}$ as defined in the statement of Lemma 6.A.1.

Thus, taking skw(■) on the both sides of (6.A.9) and employing Lemma 6.A.1 we obtain upon simplification

$$\begin{aligned}
\text{skw}(\boldsymbol{\sigma}) = &\frac{\rho_0}{J} \text{skw}\left[\frac{\partial \psi^H}{\partial I_4^{HHr}} \mathbb{B}(\mathbf{h}^r \otimes \mathbf{h}) + 2 \frac{\partial \psi^H}{\partial I_4^{Hr}} (\mathbf{h}^r \otimes \mathbf{h}^r) \mathbb{B} \right] - \frac{\rho_0}{J} \text{skw}\left[\frac{\partial \psi^H}{\partial I_5^{HHr}} (\mathbf{h} \otimes \mathbf{h}^r) \right] \\
&+ \frac{\rho_0}{J} \text{skw}\left[\left(\frac{\partial \psi^H}{\partial I_4^{HHr}} \mathbb{B}\mathbf{h} + 2 \frac{\partial \psi^H}{\partial I_4^{Hr}} \mathbb{B}\mathbf{h}^r + \frac{\partial \psi^H}{\partial I_5^{HHr}} \mathbf{h} \right) \otimes \mathbf{h}^r \right] = \mathbf{0}.
\end{aligned} \tag{6.A.16}$$

Hence, it is proved that, any choice of ψ^{H} in terms of the isotropic invariants given in Table 6.1 leads to a symmetric $\boldsymbol{\sigma}$. Nevertheless, as shown in (6.7), the very definition of the current energy function $w^{h}(\mathbb{B},\mathbf{h},\mathbf{h}^{r})$ leads to a symmetric $\boldsymbol{\sigma}$ due to its equivalence with the reference potential energy $W^{H}(\mathbb{C},\mathbf{H},\mathcal{H}^{r})$. However, the symmetry of $\boldsymbol{\sigma}$ is not straightforward to observe from its definition $(6.16)_1$. Thus, this appendix shows explicitly the symmetry of $\boldsymbol{\sigma}$ for a fairly general choice of ψ^{H}.

$\mathbf{F}-\mathbf{b}$ *model* : Similarly, the expression for $\boldsymbol{\sigma}$ from the proposed $\mathbf{F}-\mathbf{b}$ model can be obtained. In particular, we consider the specific Helmholtz free energy ψ^{B} to be an explicit function of the invariants defined in Table 6.3. Consequently, the expression for $\boldsymbol{\sigma}$ is obtained via substituting (6.A.1) into (6.59), such that

$$\boldsymbol{\sigma}=\frac{2\rho_0}{J}\frac{\partial\psi^{B}}{\partial\mathbb{B}}\mathbb{B}+\mathbf{h}\otimes\mathbf{b}-\frac{\mu_0}{2}(|\mathbf{h}|^2-|\mathbf{m}|^2)\mathbf{I}+\frac{2}{J\det\mathbf{Z}}\mathbf{Z}\text{skw}\left(\mathbf{b}^{r}\otimes\mathbf{h}^{r}\right)\mathbf{V}\mathbf{Z}, \tag{6.A.17}$$

where the primary $\mathbf{h}$ and remanent $\mathbf{h}^{r}$ are given by the constitutive relations $(6.60)_2$ and $(6.61)_2$, respectively. Explicit expressions of these two fields reads

$$\mathbf{h}=\frac{1}{\mu_0}\mathbf{b}+\rho_0 J\left[2\frac{\partial\psi^{B}}{\partial I_5^{B}}\mathbf{b}+\frac{\partial\psi^{B}}{\partial I_5^{BBr}}\mathbf{b}^{r}+2\frac{\partial\psi^{B}}{\partial I_6^{B}}\mathbb{B}\mathbf{b}+\frac{\partial\psi^{B}}{\partial I_6^{BBr}}\mathbb{B}\mathbf{b}^{r}\right] \tag{6.A.18}$$

and

$$\mathbf{h}^{r}=-\rho_0 J^2\left[\frac{\partial\psi^{B}}{\partial I_5^{BBr}}\mathbf{b}+2\frac{\partial\psi^{B}}{\partial I_5^{Br}}\mathbf{b}^{r}+\frac{\partial\psi^{B}}{\partial I_6^{BBr}}\mathbb{B}\mathbf{b}+2\frac{\partial\psi^{B}}{\partial I_6^{Br}}\mathbb{B}\mathbf{b}^{r}\right], \tag{6.A.19}$$

respectively. Substituting (6.A.18) and (6.A.19) into (6.A.17) we obtain the expression for $\boldsymbol{\sigma}$ explicitly in terms of various tensors involved, so that

$$\begin{aligned}\boldsymbol{\sigma}=&\frac{2\rho_0}{J}\left[\frac{\partial\psi^{B}}{\partial I_1}\mathbb{B}+J\frac{\partial\psi^{B}}{\partial J}\mathbf{I}+2J^2\frac{\partial\psi^{B}}{\partial I_6^{B}}\text{sym}\Big\{(\mathbf{b}\otimes\mathbf{b})\mathbb{B}\Big\}+J^2\frac{\partial\psi^{B}}{\partial I_6^{BBr}}\text{sym}\Big\{(\mathbf{b}\otimes\mathbf{b}^{r})\mathbb{B}\Big\}+\frac{J^2}{2}\frac{\partial\psi^{B}}{\partial I_6^{BBr}}(\mathbf{b}^{r}\otimes\mathbf{b}\mathbb{B})\right.\\&\left.+J^2\frac{\partial\psi^{B}}{\partial I_6^{Br}}(\mathbf{b}^{r}\otimes\mathbb{B}\mathbf{b}^{r})\right]+\frac{1}{\mu_0}\mathbf{b}\otimes\mathbf{b}-\frac{\mu_0}{2}\Big(|\mathbf{h}|^2-|\mathbf{m}|^2\Big)\mathbf{I}+\rho_0 J\left[2\frac{\partial\psi^{B}}{\partial I_5^{B}}\mathbf{b}\otimes\mathbf{b}+\frac{\partial\psi^{B}}{\partial I_5^{BBr}}\mathbf{b}^{r}\otimes\mathbf{b}\right]\\&-\frac{2}{J\det\mathbf{Z}}\mathbf{Z}\,\text{skw}\left[\frac{\partial\psi^{B}}{\partial I_5^{BBr}}\mathbf{b}^{r}\otimes\mathbf{b}+\frac{\partial\psi^{B}}{\partial I_6^{BBr}}\mathbf{b}^{r}\otimes\mathbb{B}\mathbf{b}+2\frac{\partial\psi^{B}}{\partial I_6^{Br}}\mathbf{b}^{r}\otimes\mathbb{B}\mathbf{b}^{r}\right]\mathbf{V}\mathbf{Z}.\end{aligned} \tag{6.A.20}$$

One can eventually show that the skew part of the expression for $\boldsymbol{\sigma}$ in (6.A.20) vanish identically.

Appendix 6.B. Derivatives of I_4^{HHr}, I_5^{HHr}, I_5^{BBr} and I_6^{BBr} with respect to $\mathbb{C}$

Computation of the first Piola-Kirchhoff stress in a Lagrangian setting from the constitutive relation $(6.6)_1$ is performed via finding the derivative of (6.40) with respect to $\mathbb{C}$. Similar to (6.A.8), the computation of $\mathbf{S}$ is involved with computing the derivatives of the invariants in Table 6.1 with respect to $\mathbb{C}$. In this regard, it is noted from Table 6.1 and 6.3 that the derivatives of all the invariants therein with respect to $\mathbb{C}$ are straightforward except the mixed invariants I_4^{HHr}, I_5^{HHr}, I_5^{BBr} and I_6^{BBr}, which are the functions of $\mathbb{C}^{1/2}$ and $\mathbb{C}^{-1/2}$, respectively. This appendix is, therefore, devoted towards providing the $\mathbb{C}$ derivatives of I_4^{HHr}, I_5^{HHr}, I_5^{BBr} and I_6^{BBr}.

In this context Hoger and Carlson (1984) provide explicit expressions for $\mathrm{d}\mathbb{C}^{1/2}/\mathrm{d}\mathbb{C}$, which is derived from the solution of the tensor equation having a general form $\mathbb{A}\mathbb{X}+\mathbb{X}\mathbb{A}=\mathbb{Q}$. Thus, the

derivative of $\mathrm{I}_4^{\mathrm{HHr}}$ with respect to $\mathbb{C}$ is computed via first considering the scalar equation

$$\mathbb{C}^{1/2}\mathbb{C}^{1/2} : \operatorname{sym}(\mathbf{H}\otimes\mathcal{H}^{\mathrm{r}}) = \mathbb{C} : \operatorname{sym}(\mathbf{H}\otimes\mathcal{H}^{\mathrm{r}}). \tag{6.B.1}$$

Differentiating both sides of the last equation with respect to $\mathbb{C}$ yields

$$\mathbb{C}^{1/2}\frac{\partial}{\partial\mathbb{C}}[\mathbb{C}^{1/2} : \operatorname{sym}(\mathbf{H}\otimes\mathcal{H}^{\mathrm{r}})] + \frac{\partial}{\partial\mathbb{C}}[\mathbb{C}^{1/2} : \operatorname{sym}(\mathbf{H}\otimes\mathcal{H}^{\mathrm{r}})]\mathbb{C}^{1/2} = \operatorname{sym}(\mathbf{H}\otimes\mathcal{H}^{\mathrm{r}}), \tag{6.B.2}$$

which can be rephrased such that

$$\mathbb{C}^{1/2}\frac{\partial \mathrm{I}_4^{\mathrm{HHr}}}{\partial\mathbb{C}} + \frac{\partial \mathrm{I}_4^{\mathrm{HHr}}}{\partial\mathbb{C}}\mathbb{C}^{1/2} = \operatorname{sym}(\mathbf{H}\otimes\mathcal{H}^{\mathrm{r}}), \tag{6.B.3}$$

having the same general form of $\mathbb{A}\mathbb{X}+\mathbb{X}\mathbb{A}=\mathbb{Q}$. The solution to (6.B.3) is thus given by (Hoger and Carlson, 1984)

$$\begin{aligned}\frac{\partial \mathrm{I}_4^{\mathrm{HHr}}}{\partial\mathbb{C}} =& \frac{4}{\Delta}\Big[I_1\mathbb{C}\operatorname{sym}(\mathbf{H}\otimes\mathcal{H}^{\mathrm{r}})\mathbb{C} - I_1^2\Big\{\mathbb{C}\operatorname{sym}(\mathbf{H}\otimes\mathcal{H}^{\mathrm{r}})\mathbb{C}^{1/2} + \mathbb{C}^{1/2}\operatorname{sym}(\mathbf{H}\otimes\mathcal{H}^{\mathrm{r}})\mathbb{C}\Big\} + \\ & (I_1I_2-I_3)\Big\{\mathbb{C}\operatorname{sym}(\mathbf{H}\otimes\mathcal{H}^{\mathrm{r}}) + \operatorname{sym}(\mathbf{H}\otimes\mathcal{H}^{\mathrm{r}})\mathbb{C}\Big\} + (I_1^3+I_3)\mathbb{C}^{1/2}\operatorname{sym}(\mathbf{H}\otimes\mathcal{H}^{\mathrm{r}})\mathbb{C}^{1/2} - \\ & I_1^2I_2\Big\{\mathbb{C}^{1/2}\operatorname{sym}(\mathbf{H}\otimes\mathcal{H}^{\mathrm{r}}) + \operatorname{sym}(\mathbf{H}\otimes\mathcal{H}^{\mathrm{r}})\mathbb{C}^{1/2}\Big\} + \Big\{I_1^2I_3 + (I_1I_2-I_3)I_2\Big\}\operatorname{sym}(\mathbf{H}\otimes\mathcal{H}^{\mathrm{r}})\Big],\end{aligned} \tag{6.B.4}$$

where I_1, I_2 and I_3 are three principal invariants of $\mathbb{C}^{1/2}$ and $\Delta = 8(I_1I_2-I_3)I_3$. Notice that $\partial \mathrm{I}_4^{\mathrm{HHr}}/\partial\mathbb{C}$ is symmetric.

Next, the derivative $\partial \mathrm{I}_5^{\mathrm{HHr}}/\partial\mathbb{C}$ is computed via considering the scalar equation

$$\mathbb{C}^{-1/2}\mathbb{C}^{-1/2} : \operatorname{sym}(\mathbf{H}\otimes\mathcal{H}^{\mathrm{r}}) = \mathbb{C}^{-1} : \operatorname{sym}(\mathbf{H}\otimes\mathcal{H}^{\mathrm{r}}). \tag{6.B.5}$$

Differentiating both sides of the last equation with respect to $\mathbb{C}$ yields

$$\mathbb{C}^{-1/2}\frac{\partial}{\partial\mathbb{C}}[\mathbb{C}^{-1/2} : \operatorname{sym}(\mathbf{H}\otimes\mathcal{H}^{\mathrm{r}})] + \frac{\partial}{\partial\mathbb{C}}[\mathbb{C}^{-1/2} : \operatorname{sym}(\mathbf{H}\otimes\mathcal{H}^{\mathrm{r}})]\mathbb{C}^{-1/2} = \operatorname{sym}(\mathbf{H}\otimes\mathcal{H}^{\mathrm{r}}), \tag{6.B.6}$$

which can be rephrased such that

$$\mathbb{C}^{-1/2}\frac{\partial \mathrm{I}_5^{\mathrm{HHr}}}{\partial\mathbb{C}} + \frac{\partial \mathrm{I}_5^{\mathrm{HHr}}}{\partial\mathbb{C}}\mathbb{C}^{-1/2} = -\mathbb{C}^{-1}\operatorname{sym}(\mathbf{H}\otimes\mathcal{H}^{\mathrm{r}})\mathbb{C}^{-1}, \tag{6.B.7}$$

having the same general form of $\mathbb{A}\mathbb{X}+\mathbb{X}\mathbb{A}=\mathbb{Q}$. The solution to (6.B.7) is thus given by (Hoger and Carlson, 1984)

$$\begin{aligned}\frac{\partial \mathrm{I}_5^{\mathrm{HHr}}}{\partial\mathbb{C}} =& -\frac{4}{\Delta^*}\Big[I_1^*\mathbb{C}^{-2}\operatorname{sym}(\mathbf{H}\otimes\mathcal{H}^{\mathrm{r}})\mathbb{C}^{-2} - (I_1^*)^2\Big\{\mathbb{C}^{-2}\operatorname{sym}(\mathbf{H}\otimes\mathcal{H}^{\mathrm{r}})\mathbb{C}^{-3/2} + \mathbb{C}^{-3/2}\operatorname{sym}(\mathbf{H}\otimes\mathcal{H}^{\mathrm{r}})\mathbb{C}^{-2}\Big\} + \\ & (I_1^*I_2^*-I_3^*)\Big\{\mathbb{C}^{-2}\operatorname{sym}(\mathbf{H}\otimes\mathcal{H}^{\mathrm{r}})\mathbb{C}^{-1} + \mathbb{C}^{-1}\operatorname{sym}(\mathbf{H}\otimes\mathcal{H}^{\mathrm{r}})\mathbb{C}^{-2}\Big\} + \{(I_1^*)^3 + I_3^*\}\mathbb{C}^{-3/2} \\ & \operatorname{sym}(\mathbf{H}\otimes\mathcal{H}^{\mathrm{r}})\mathbb{C}^{-3/2} - (I_1^*)^2I_2^*\Big\{\mathbb{C}^{-3/2}\operatorname{sym}(\mathbf{H}\otimes\mathcal{H}^{\mathrm{r}})\mathbb{C}^{-1} + \mathbb{C}^{-1}\operatorname{sym}(\mathbf{H}\otimes\mathcal{H}^{\mathrm{r}})\mathbb{C}^{-3/2}\Big\} + \\ & \Big\{(I_1^*)^2I_3^* + (I_1^*I_2^*-I_3^*)I_2^*\Big\}\mathbb{C}^{-1}\operatorname{sym}(\mathbf{H}\otimes\mathcal{H}^{\mathrm{r}})\mathbb{C}^{-1}\Big],\end{aligned} \tag{6.B.8}$$

where I_1^*, I_2^* and I_3^* are three principal invariants of $\mathbb{C}^{-1/2}$ and $\Delta^* = 8(I_1^* I_2^* - I_3^*)I_3^*$. Notice that $\partial I_5^{HHr}/\partial \mathbb{C}$ is also symmetric.

Similarly, the expressions for $\partial I_5^{BBr}/\partial \mathbb{C}$ and $\partial I_6^{BBr}/\mathbb{C}$ are given by

$$\begin{aligned}\frac{\partial I_5^{BBr}}{\partial \mathbb{C}} =& \frac{1}{2}\mathbf{B}\cdot\mathbb{C}^{-1/2}\mathcal{B}^r + \frac{4J}{\Delta}\Big[I_1\mathbb{C}\ \mathrm{sym}(\mathbf{B}\otimes\mathcal{B}^r)\mathbb{C} - I_1^2\Big\{\mathbb{C}\ \mathrm{sym}(\mathbf{B}\otimes\mathcal{B}^r)\mathbb{C}^{1/2} + \mathbb{C}^{1/2}\mathrm{sym}(\mathbf{B}\otimes\mathcal{B}^r)\mathbb{C}\Big\} + \\ & (I_1I_2 - I_3)\Big\{\mathbb{C}\ \mathrm{sym}(\mathbf{B}\otimes\mathcal{B}^r) + \mathrm{sym}(\mathbf{B}\otimes\mathcal{B}^r)\mathbb{C}\Big\} + (I_1^3 + I_3)\mathbb{C}^{1/2}\mathrm{sym}(\mathbf{B}\otimes\mathcal{B}^r)\mathbb{C}^{1/2} - \\ & I_1^2I_2\Big\{\mathbb{C}^{1/2}\mathrm{sym}(\mathbf{B}\otimes\mathcal{B}^r) + \mathrm{sym}(\mathbf{B}\otimes\mathcal{B}^r)\mathbb{C}^{1/2}\Big\} + \Big\{I_1^2I_3 + (I_1I_2 - I_3)I_2\Big\}\mathrm{sym}(\mathbf{B}\otimes\mathcal{B}^r)\Big] \end{aligned} \tag{6.B.9}$$

and

$$\begin{aligned}\frac{\partial I_6^{BBr}}{\partial \mathbb{C}} =& \frac{1}{2}\mathbf{B}\cdot\mathbb{C}^{-1/2}\mathcal{B}^r + J\mathbf{B}\cdot\mathbb{C}^{1/2}\mathcal{B}^r + \frac{4J}{\Delta}\mathbb{C}\Big[I_1\mathbb{C}\ \mathrm{sym}(\mathbf{B}\otimes\mathcal{B}^r)\mathbb{C} - I_1^2\Big\{\mathbb{C}\ \mathrm{sym}(\mathbf{B}\otimes\mathcal{B}^r)\mathbb{C}^{1/2} \\ & + \mathbb{C}^{1/2}\mathrm{sym}(\mathbf{B}\otimes\mathcal{B}^r)\mathbb{C}\Big\} + (I_1I_2 - I_3)\Big\{\mathbb{C}\ \mathrm{sym}(\mathbf{B}\otimes\mathcal{B}^r) + \mathrm{sym}(\mathbf{B}\otimes\mathcal{B}^r)\mathbb{C}\Big\} \\ & + (I_1^3 + I_3)\mathbb{C}^{1/2}\mathrm{sym}(\mathbf{B}\otimes\mathcal{B}^r)\mathbb{C}^{1/2} - I_1^2I_2\Big\{\mathbb{C}^{1/2}\mathrm{sym}(\mathbf{B}\otimes\mathcal{B}^r) + \mathrm{sym}(\mathbf{B}\otimes\mathcal{B}^r)\mathbb{C}^{1/2}\Big\} \\ & + \Big\{I_1^2I_3 + (I_1I_2 - I_3)I_2\Big\}\mathrm{sym}(\mathbf{B}\otimes\mathcal{B}^r)\Big], \end{aligned} \tag{6.B.10}$$

respectively, where the invariants I_1, I_2, I_3 and Δ are the same as defined in the context of equation (6.B.4). Again, we verify that both $\partial I_5^{BBr}/\partial \mathbb{C}$ and $\partial I_6^{BBr}/\mathbb{C}$ are symmetric.

Chapter

7 Conclusion

In this chapter, we first summarize the key outcomes of the thesis, and specifically, the important features of the proposed microstructurally-guided constitutive models. This will be followed by a potential definition of the future avenues that can be initiated from the outcomes of the presented work.

7.1 Concluding remarks

With the increasing number of applications of the s- and h-MREs in soft robotic devices (Kim et al., 2018; Sitti and Wiersma, 2020), sensors (Kaidarova et al., 2018) and actuators (Zhao et al., 2019), the need for efficient yet straightforward macroscopic constitutive models becomes paramount. In this context, this work provides explicit macroscopic constitutive models for the s- and h-MREs in the $\mathbf{F}-\mathbf{H}$, $\mathbf{F}-\mathbf{h}$, $\mathbf{F}-\mathbf{B}$ and $\mathbf{F}-\mathbf{b}$ variable spaces, which can be readily implemented in a general incremental finite-element setting.

The well-known balance laws for the total Cauchy stress $\boldsymbol{\sigma}$ and the Eulerian $\mathbf{h}$ and $\mathbf{b}$ fields (Kankanala and Triantafyllidis, 2004) and the total first Piola-Kirchhoff stress $\mathbf{S}$ and the Lagrangian magnetic fields $\mathbf{H}$ and $\mathbf{B}$ (Dorfmann and Ogden, 2004; Steigmann, 2004) are derived in Chapter 2, along with the localized Clausius-Duhem inequalities for the $\mathbf{F}-\mathbf{H}$, $\mathbf{F}-\mathbf{h}$, $\mathbf{F}-\mathbf{B}$ and $\mathbf{F}-\mathbf{b}$-based constitutive models. We note that the localized Clausius-Duhem inequality reads differently depending on the definition of the independent primary variable ($\mathbf{H}/\mathbf{B}$) and the configuration (reference/current). We avoid defining the macroscopic stress and magnetic field balance laws in the intermediate configurations. This is because such definition may lead to non-familiar stress measures. Thus, in contrast to Rosato and Miehe (2014), we do not work with the intermediate constitutive laws for the work conjugates (i.e., stress) of the primary variables (i.e., displacement). Rather, the constitutive laws for the stresses and the conjugate magnetic fields are derived in either the reference or the current configuration from the respective Clausius-Duhem inequalities by employing the Coleman-Noll-Gurtin (Coleman and Noll, 1959; Coleman and Gurtin, 1967) method.

Even though the non-dissipative, saturation-type constitutive models for the iron particles are employed widely in the literature in both $\mathbf{F}-\mathbf{H}$ (Keip and Rambausek, 2016, 2017; Lefèvre et al., 2017) and $\mathbf{F}-\mathbf{B}$ (Danas, 2017; Psarra et al., 2017, 2019) models, the dissipative constitutive models for the hysteretic magnetic response of the NdFeB particles are not so well-known. Thus, in Chapter 3, we propose two equivalent, rate-independent constitutive models in terms of considering both $\mathbf{h}$ and $\mathbf{b}$ to be the primary variables. These models resemble closely to the "switching surface" models, which are mostly employed in the context of ferroelectric switching (Huber et al., 1999; Huber and Fleck, 2001; McMeeking and Landis, 2002; Landis, 2002; Klinkel, 2006; Linnemann et al., 2009; Miehe

et al., 2011; Rosato and Miehe, 2014). Moreover, the non-dissipative saturation-type response is shown therein to be a special case of the proposed hysteresis models. This observation becomes crucial in inferring the limiting responses of the h-MRE models in the later sections. The constitutive model for the matrix phase, on the other hand, is considered to be a simple I_1-based Neo-Hookean model, which is typically employed in the modeling of MREs (Ponte Castañeda and Galipeau, 2011; Galipeau and Ponte Castañeda, 2013; Danas et al., 2012b; Danas, 2017; Lefèvre et al., 2017; Psarra et al., 2017, 2019).

Given the constitutive models for the particle and matrix phases, the proposition of an incremental numerical homogenization framework in Chapter 4 is developed following the earlier works on the numerical homogenization of mechanical elasto-plastic composites by Miehe (2002) and Miehe et al. (2002). The aforementioned articles first propose an incremental potential energy for its constituents and then homogenize them to obtain an effective incremental energy at a given time increment $t + \Delta t$. It is noted that, unlike the non-dissipative composites, both the local and effective incremental potentials are history-dependent in terms of their explicit dependence on the microscopic internal variables. Furthermore, the numerical homogenization for the coupled magneto-mechanical composites require additional augmentation in the macroscopic (global) variational principle, so that the macroscopic boundary and shape effects are not taken into account (Danas, 2017). A detailed account on the fully Lagrangian, $\mathbf{F}-\mathbf{H}$ model-based finite-element implementation of the incremental homogenization framework is provided in Chapter 4. This framework can also be utilized in a general macroscopic boundary value problem, of course, after certain modifications.

The non-dissipative homogenization problem for the iron particle-filled s-MREs are shown in Chapter 4 to be a special case of the general incremental homogenization problem. In fact, for the limiting case of zero particle coercivity, i.e., $b_p^c = 0$, we recover exactly the definition of the non-dissipative homogenization problem for s-MREs given by Lefèvre et al. (2017) in the Lagrangian $\mathbf{F}-\mathbf{H}$ setting. Hence, our work generalizes the numerical homogenization problem for the MREs in a broader area of hard-magnetic constituent phases, whose limiting cases, in turn, yield the well-known definition of the homogenization problem for the s-MREs.

Even though the analytical homogenization model of Lefèvre et al. (2017) for the isotropic s-MREs yields comprehensively good macroscopic responses as compared to the numerical computations, it is implicit, i.e., requires additional algebraic equations to be solved during the numerical computations of the macroscopic response. A set of alternative, fully-explicit, $\mathbf{F}-\mathbf{H}$ and $\mathbf{F}-\mathbf{B}$-based constitutive models are therefore proposed for the s-MREs in Chapter 5. These models are designed to become exact to their respective analytical homogenization estimates, given by Lefèvre et al. (2017), specifically at small magnetic fields, i.e., in the limit of $|\mathbf{H}|, |\mathbf{B}| \to 0$. Moreover, in the limit of $|\mathbf{H}| \to \pm\infty$, the magnetization and magnetostriction are considered to be saturating at a constant magnitude. These considerations help us to reduce the phenomenological model parameters to one coupling parameter, which is further estimated by fitting the model magnetostriction response to that of the analytical homogenization model. Thus, the proposed phenomenological model becomes rich enough to take care of different particle volume fractions and matrix shear moduli, yet having only one parameter to estimate. This approach is advantageous over the other microstructurally-guided phenomenological modeling approaches (Kalina et al., 2020), where the estimates for a considerably higher number of model parameters are sought for.

Till date, no macroscopic model for the NdFeB particle-filled h-MREs is available, where the

effect of the stretch-independence of the current and reference remanent fields are considered. The macroscopic model proposed by Zhao et al. (2019) considers a very specific loading path around the remanent magnetization response and thus, the effect of magnetic switching is not taken care of. The proposed models in Chapter 6, on the other hand, are applicable under any magneto-mechanical loading condition. In this context, we also refer to the constitutive model of Rosato and Miehe (2014) for the ferroelectric hysteresis at finite strains, who consider a fully-reversed and proportional loading path. However, none of the aforementioned models consider both the reference and current remanent fields to be independent of mechanical stretch, which is a key observation in our work, yielding directly from the numerical homogenization estimates for the h-MREs. Therefore, the Lagrangian counterparts of the current remanent fields $\mathbf{h}^r$ and $\mathbf{b}^r$ are defined in the proposed models to be in a stretch-free intermediate configuration $\mathcal{V}_i$ (see Fig. 6.2 and Fig. 6.3). Furthermore, we observe from the full-field RVE computations that the mapping between the current $\mathbf{h}^r$ ($\mathbf{b}^r$) and the intermediate $\mathcal{H}^r$ ($\mathcal{B}^r$) fields is given by the average particle rotations $\mathbf{R}_p$, such that $\mathcal{H}^r = \mathbf{R}_p^T \mathbf{h}^r$ ($\mathcal{B}^r = \mathbf{R}_p^T \mathbf{b}^r$).

We note that the explicit analytical or phenomenological estimates for $\mathbf{R}_p = \mathbf{R}_p(\mathbf{F}, \mathbf{H}, \mathcal{H}^r)$ under arbitrary magneto-mechanical loading paths are extremely difficult to obtain. Nevertheless, we observe from the numerical computations for purely mechanical loading/unloading of a pre-magnetized h-MREs (see Fig. 4.15 and Fig. 4.17) that $\mathbf{R}_p \approx \mathbf{R}$ under *these specific* loading conditions, where $\mathbf{R} = \mathbf{F}\mathbf{U}^{-1}$ is the macroscopic rotation. Motivated by such observations, we assume *affine particle rotations*, i.e., $\mathbf{R}_p = \mathbf{R}$ under all possible loading paths and propose the pull-back mapping for the remanent field to be $\mathcal{H}^r = \mathbf{R}^T \mathbf{h}^r$ ($\mathcal{B}^r = \mathbf{R}^T \mathbf{b}^r$). Under this assumption, we subsequently propose fully objective, equivalent constitutive models in the $\mathbf{F}-\mathbf{H}$, $\mathbf{F}-\mathbf{h}$, $\mathbf{F}-\mathbf{B}$ and $\mathbf{F}-\mathbf{b}$ variable spaces and probe the model responses under various magneto, mechanical and combined magneto-mechanical loading paths against the numerical homogenization estimates. The Coleman-Noll-Gurtin method is applied while deriving the constitutive laws in the reference and current configurations. Specifically, this method applied to the current configuration formulation leads to the expression for the symmetric total Cauchy stress $\boldsymbol{\sigma}$, which is comprised of the contributions from the mechanical stress, energetic and remanent Maxwell stresses. Eventually, the remanent Maxwell stress vanishes for the special case of the vanishing coercivity $b_p^c \to 0$ leading to the well-known constitutive relations for the s-MREs (Kankanala and Triantafyllidis, 2004; Dorfmann and Ogden, 2003, 2004). Moreover, the Coleman-Noll-Gurtin method leads to the dissipation inequality that is defined in terms of the objective Green-Naghdi rate of $\mathbf{h}^r$ ($\mathbf{b}^r$). Subsequently, we define the dissipation potential in terms of this Green-Naghdi rate of $\mathbf{h}^r$ ($\mathbf{b}^r$), which, in the limit of rate-independent response, leads to the current switching surface and the associated switching rule.

In a similar note to the s-MRE models, the choice of the energetic and dissipation potentials are carried out in a way, such that the models reproduce exactly the initial slopes of magnetization and magnetostriction responses. Consequently, there remains only one model parameter, namely the coupling constant β^{Hr} (or, equivalently β^{Br}), to be identified by fitting the model magnetostriction response with the numerical homogenization estimates. Both $\mathbf{F}-\mathbf{H}$ and $\mathbf{F}-\mathbf{B}$-based models with the identified β^{Hr} and β^{Br} are then probed against other coupled magneto-mechanical loading conditions. Excellent agreement of both these model responses with the numerical homogenization estimates are achieved for particle volume fractions in the range $c \leqslant 0.3$ and for matrix shear moduli $G_m \geqslant 0.3$ MPa.

Of course, further improvement of the model is required in order to model softer h-MRE composites having $G_p \sim 0.1$ MPa. Such modeling would require the non-affine particle rotations to be taken into account. Again, $\mathbf{R}_p$ is not known explicitly for the h-MRE composites. Nevertheless, one can find a better approximations for $\mathbf{R}_p$, those maybe valid only for certain loading paths, instead of simply the macroscopic rotation $\mathbf{R}$. In turn, the constitutive relations and the evolution equations for the internal variables for the modified non-affine rotation model can be derived *mutatis mutandis* as carried out in Chapter 6.

Finally, it is noted that most of the h-MREs in practice are fabricated with the Sylgard-184 (10:1) PDMS, having a shear modulus $G_m \sim 0.3 - 1.2$ MPa, depending on the curing conditions (Park et al., 2018; Wang et al., 2019; Kaidarova et al., 2018). Thus, the proposed models in Chapter 6 can be applied readily to the modeling of such composites without further modifications.

7.2 Future work

Starting from this point, further investigations can be carried out on several fronts to enrich the modeling frameworks and also to aid the design of the h-MRE components in the devices by full-field macroscopic numerical simulations. Here we discuss three such possible future works that may be carried out directly following this work.

(i) Modeling non-affine particle rotations **:** As discussed earlier in this chapter, the underlying non-affine particle rotations start affecting the present affine rotation model performances substantially. Thus, a natural extension of the present framework would be to incorporate the effect of non-affine particle rotations. Note, however, that the explicit estimates for $\mathbf{R}_p$ are not available and are extremely difficult to obtain for a general loading path. Nevertheless, from the detailed investigations in Chapter 6, we observe that the mechanical loading path, with or without a simultaneous magnetic loading, induce negligibly small non-affine particle rotations. Thus, the non-affine rotations resulting from a pre-defined magnetic loading path can be modeled empirically in terms of the local primary and remanent magnetic fields, c and G_m and, subsequently, the particle rotations can be modeled to be $\mathbf{R}_p = \mathbf{R}_{naf}\mathbf{R}$, where $\mathbf{R}_{naf}$ is the non-affine rotation tensor. Hence, definitions of the remanent variables in different configurations for the $\mathbf{F}-\mathbf{H}$ or $\mathbf{F}-\mathbf{h}$-based modeling can be modified from Fig. 6.2 to be Fig. 7.1. Notably, the pull-back transformations for the primary $\mathbf{h}$ and its conjugate $\mathbf{b}$ fields remain the same as defined via (2.40) and (2.45), respectively. In contrast, the pull-back transformation of $\mathbf{h}^r$ is now modified via $\mathcal{H}^r = \mathbf{R}^T\mathbf{R}_{naf}^T\mathbf{h}^r$. Consequently, the constitutive relations for $\boldsymbol{\sigma}$ and also the evolution equation of $\mathbf{h}^r$ would be modified, which can be obtained in the same way as derived in Chapter 6.

(ii) Viscous dissipation and rate-dependence **:** Although the commercially available Sylgard-184 PDMS exhibit negligibly small amount of viscous dissipation, some of the other commercial PDMS, e.g., Sylgard-186, exhibit considerable viscous dissipation and hence, a rate-dependent mechanical response (Wang et al., 2019). Evidently, the h-MREs fabricated from such viscous matrix materials are expected to exhibit rate-dependent, dissipative mechanical response along with the magnetic dissipation arising due to the hard-magnetic particles.

A similar microstructurally-guided modeling approach can be employed for viscous h-MREs, where a viscous matrix material must be considered in the microscopic modeling, whereas the magnetic hysteresis model for the particle phases would remain the same as in Chapter 4. A repre-

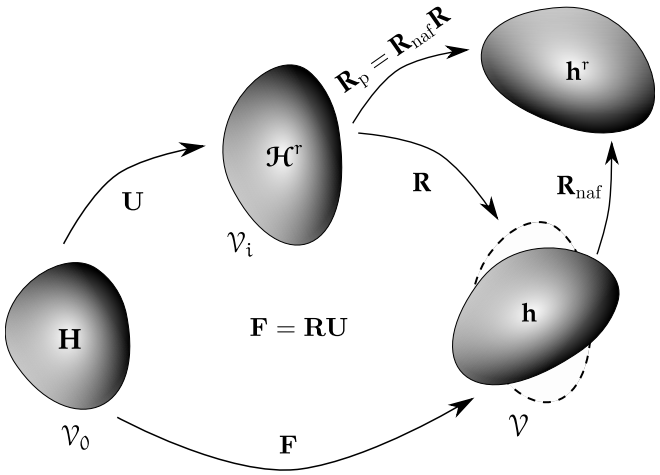

Figure 7.1: Definition of the intermediate internal variable $\mathcal{H}^r$ at the intermediate configuration $\mathcal{V}_i$ and the current internal variable $\mathbf{h}^r$ in a non-affine rotated configuration.

sentative 2D RVE computation considering the hysteresis response for NdFeB particles and the two potential-based visco-hyperelasticity model of Kumar and Lopez-Pamies (2016) for the matrix phase is shown in Fig. 7.2. We observe considerable rate-dependence in the resulting magnetostriction

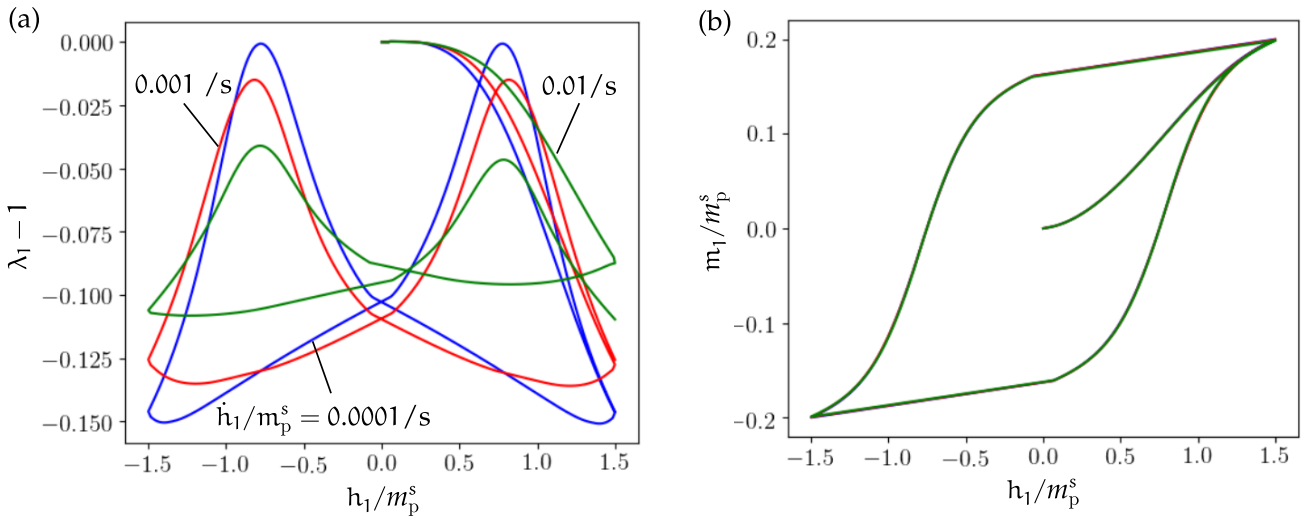

Figure 7.2: Rate-dependent effective (a) magnetostriction and (b) magnetization response of a h-MRE with $c = 0.2$, having a visco-hyperelastic matrix, subjected to proportional cyclic magnetic loading. Results for three loading/unloading rates, namely $\dot{h}_1/m_p^s = 0.0001$ /s, 0.001 /s and 0.01 /s, are shown.

response in Fig. 7.2a, whereas no effect of loading/unloading rate is observed in the computed magnetization hysteresis loops shown in Fig. 7.2b. Evidently, a microstructurally-guided macroscopic modeling would necessitate a number of very expensive 3D RVE computations, along with a crucial choice of the internal variables at the macroscale. In turn, the viscous deformation gradient $\mathbf{F}^v$ can be defined via a standard multiplicative decomposition to the total $\mathbf{F}$, such that $\mathbf{F} = \mathbf{F}^e\mathbf{F}^v$, where $\mathbf{F}^e$ is the elastic part of $\mathbf{F}$ (Reese and Govindjee, 1998; Kumar and Lopez-Pamies, 2016), whereas the remanent intermediate and current magnetic fields should be defined in the same fashion as in Chapter 6.

(iii) Numerical modeling of structural boundary value problems **:** Finally, the proposed s- and

ħ-MRE models can be used directly in the numerical realizations of the macroscopic, coupled boundary value problems (BVPs). In particular, the proposed *s*-MRE models can be used directly in the structural instabilities of thin magneto-active layers (Psarra et al., 2017, 2019), field-driven deflection of soft magnetic membranes, etc.

The macroscopic ħ-MRE models, on the other hand, can be applied directly to model the large structural deflections of *nearly inextensible* slender structures under small applied fields (Kim et al., 2018; Zhao et al., 2019), stretchable permanent magnetic devices (Sitti and Wiersma, 2020), bulk magneto-mechanical responses of 3D printed ħ-MREs (Huber et al., 2017), etc. Notably, the proposed fully coupled models for the ħ-MREs can be further simplified while modeling the large structural deflections of inextensible slender structures at small fields. Nevertheless, the thermodynamically-consistent constitutive relations for the stresses, conjugate magnetic and remanent fields remain identical to that in Chapter 6 for all the aforementioned structural BVPs. Eventually, one can derive the model of Zhao et al. (2019) from the proposed $\mathbf{F}-\mathbf{B}$-based ħ-MRE model under specific limiting conditions, i.e., small applied magnetic fields and inextensible, uniformly pre-magnetized structures having locally $\mathbf{b} \approx \mu_0 \mathbf{m}$. Although one should be extremely careful in assuming such an uniform filed distribution, which is *not* a general result even for the simplest possible MRE structures. In this context, our models do *not* assume any such distribution *a-priori* but provides the general modeling frameworks along with a set of equivalent ferromagnetic hysteresis models at finite strains for stiff to moderately-soft ħ-MREs. These models can then be simplified accordingly, depending on the BVPs of interest. Moreover, the proposed variational framework in Chapter 4, especially the local radial-return type update algorithm and the estimates for the algorithmically-consistent tangent stiffness matrices can be applied directly to the finite-element modeling of the aforementioned BVPs with little modifications.

Finally, the thermodynamically consistent Coleman-Noll-Gurtin approach, along with the suitable selection for the internal variables, presented in this work may also aid the future studies on the modeling of various dissipation mechanisms in the coupled electro-magneto-thermo-mechanical models, considering several internal variables and their evolutions.

Appendix

A Evolving switching surface model for hysteresis

Chapter summary: *This appendix provides an evolving switching surface model that is capable of modeling the initial magnetization response and the minor hysteresis loops. Phenomenological evolution laws for the switching surface are proposed by evolving suitably the coercive field b^c in terms of some history-dependent scalar variables. In this regard, the notion of a ferromagnetic bounding surface, that resembles closely to the well-known elasto-plastic bounding surface is proposed thereafter. Finally, we fit the proposed model with the measured minor loops of various permanent magnets and also probe the model performance against other experimental data. The model is observed to predict the key features of a measured first-order reversal curve (FORC) diagram considerably well.*

Chapter content

The switching surface (SS) model that is developed in Chapter 3 suffers from a drawback: it is unable to model the initial magnetization response and minor hysteresis loops accurately. In this appendix, we propose a generic extension to the SS model of Chapter 3, so that the initial magnetization response and the minor loops can be modeled accurately.

Here we develop an *evolving switching surface* (ESS) model that considers evolution of the switching surface in terms of N_{SS} history-dependent scalar variables. In particular, we now consider the

switching surface radius b^c to be a function of $\xi_{N_{SS}}$, where ξ is a set of N_{SS} independent scalar internal variables. Thus, the switching surface (3.17) now reads

$$\phi^h := \mathbf{b}^r \cdot \mathbf{b}^r - \{b^c(\xi_{N_{SS}})\}^2, \tag{A.1}$$

whereas the associated switching rule remains the same as (3.18). Specifically, here we propose this ESS model for the **h**-based model. Nonetheless, an equivalent **b**-based ESS framework can be proposed in a similar fashion. Notably, a similar framework for the history-dependent evolution of the yield surface is typically employed in mechanical elasto-plasticity in order to model the minor loops (Dafalias and Popov, 1975, 1976; Chaboche et al., 1979; Chaboche, 1986).

A.1 Isotropic hardening and symmetric cyclic loading

In this section, we discuss in detail the evolution of the coercive field $b^c(\xi_N)$ in terms of two history-dependent internal variables ($N = 2$), namely, $\xi_2 \equiv \{\overline{h}^r,\ R_{\mathbf{h}^r}\}$. The first element of ξ_2 is the accumulated remanent h-field (similar to the accumulated plastic strain in mechanical plasticity), defined as

$$\dot{\overline{h}}^r = \sqrt{\dot{\mathbf{h}}^r \cdot \dot{\mathbf{h}}^r} \qquad \text{with} \qquad \overline{h}^r = \int_t \dot{\overline{h}}^r dt. \tag{A.2}$$

The second element of ξ_2 is the radius of the memory surface, which is discussed later in this section.

A.1.1 Initial magnetization and hardening

It is important to note at this point that, in spite of exhibiting a qualitatively similar major hysteresis loop, the underlying mechanisms behind the ferroelectric and ferromagnetic switching differ significantly. The ferroelectrics undergo a phase transition upon loading beyond a critical electric field leading to switching of the polarization direction within a ferroelectric crystal (Huber and Fleck, 2001).

On the other hand, the ferromagnets consist of a large number of *magnetic domains* with different directions of magnetization, whereas domain nucleation and domain wall pinning are the two key mechanisms that cause coercivity. Experiments and micromagnetic theories suggest that the coercivity in the rare-earth (RE) magnets arise due to a combined effect of domain wall pinning and nucleation (Herbst, 1991). It is observed through advanced imaging techniques that reversed domains nucleate right from the beginning of magnetization of a virgin NdFeB specimen (Li et al., 2017). Thus, a combination of nucleation and pinning causes considerable amount of initial magnetization as compared to a solely pinning-type magnet. In order to capture this microscopic phenomena at the macroscopic level, we consider that the switching surface (3.17) evolves from a very small radius b_0^c to a constant *limiting surface* of radius b_{max}^c, which is the saturation coercive field, as shown in Fig. A.1a (inset). Motivated by experimental results the switching surface radius is a function of $\overline{h}^r$ (i.e., the first element of ξ_2) and can take the following form

$$b^c(\overline{h}^r) = b_{max}^c \left\{ \tanh\left[\left(\frac{\overline{h}^r}{\overline{h}_0^r} \right)^8 \right] \right\}^{1/q}. \tag{A.3}$$

In this expression, $\overline{h}_0^r$ is a reference accumulated remanent field (in analogy to the yield strain in

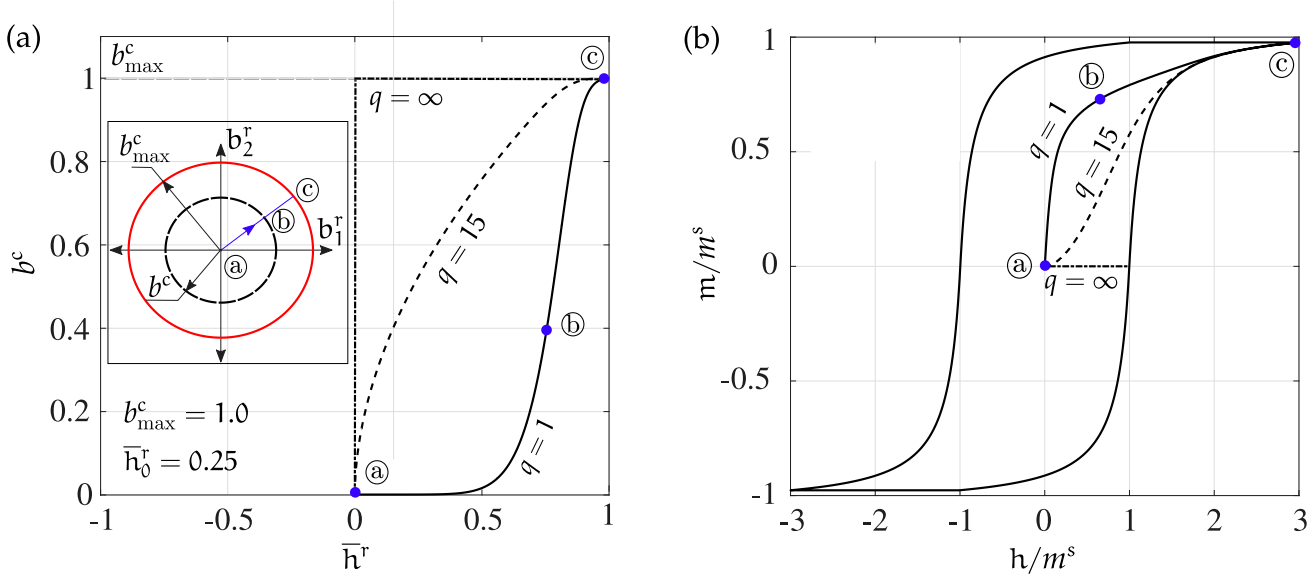

Figure A.1: (a)(inset) Evolving switching surface (in 2D) from a radius of b^c_0 to b^c_{max}. (a) Variation of b^c with $\bar{h}^r$ for different hardening exponents. (b) Effect of hardening exponent q on the initial magnetization curve.

mechanical plasticity) and q is a hardening exponent. The above evolution law for the switching surface is qualitatively similar to the isotropic hardening rules in mechanical plasticity (Chaboche et al., 1979; Chaboche, 1986). As a consequence of the constitutive relation (A.3), the magnetic domain nucleation is now captured by allowing switching right from the beginning. Obviously, the hardening exponent q plays a pivotal role in the modeling of different coercivity mechanisms at the macroscopic level. For a better understanding of this parameter, we discuss a few representative cases in the context of Fig. A.1. We note first that for $q \to \infty$, the coercive field $b^c(\bar{h}^r) \to b^c_{max}$, which, indeed, models the pinning type magnets. Thus, in the limit of $q \to \infty$, the proposed model reduces to the existing ferroelectric switching models (McMeeking and Landis, 2002; Landis, 2002; Klinkel, 2006; Linnemann et al., 2009; Miehe et al., 2011) with no isotropic hardening.

On the other hand, a pure nucleation-type response is obtained for $q = 1$. In this case, as depicted in Fig. A.1a and b, the switching surface starts growing from a radius $b^c \approx 0$ at ⓐ and then evolves through intermediate switching surfaces like ⓑ to finally saturate to the limiting surface of radius b^c_{max} at ⓒ. Practically, ferromagnets are modeled by choosing values in the range $1 \leqslant q < \infty$ as there exists no magnet that exhibits only pure domain pinning or only pure domain nucleation.

A.1.2 Cyclic loading and symmetric minor loops

The symmetric minor loops are obtained whenever the loading/unloading amplitude is kept *below* the saturation h-field h_s. Note that the magnetic domains do not become fully aligned to the loading direction before saturation. Thus, if a load reversal takes place at $|\mathbf{h}| < h_s$, then a lower h-field is required to reverse the specimen's magnetization direction. The minor loops during the initial magnetization of a specimen can be obtained in the proposed phenomenological framework by suitably defining the accumulated remanent field $\bar{h}^r$. Note further that $\bar{h}^r$ is a strictly increasing, history-dependent variable, which controls the evolution of the coercive field b^c. In order to capture the symmetric minor loops, we introduce a new history-dependent internal variable $R_{\mathbf{h}^r}$ (i.e., the

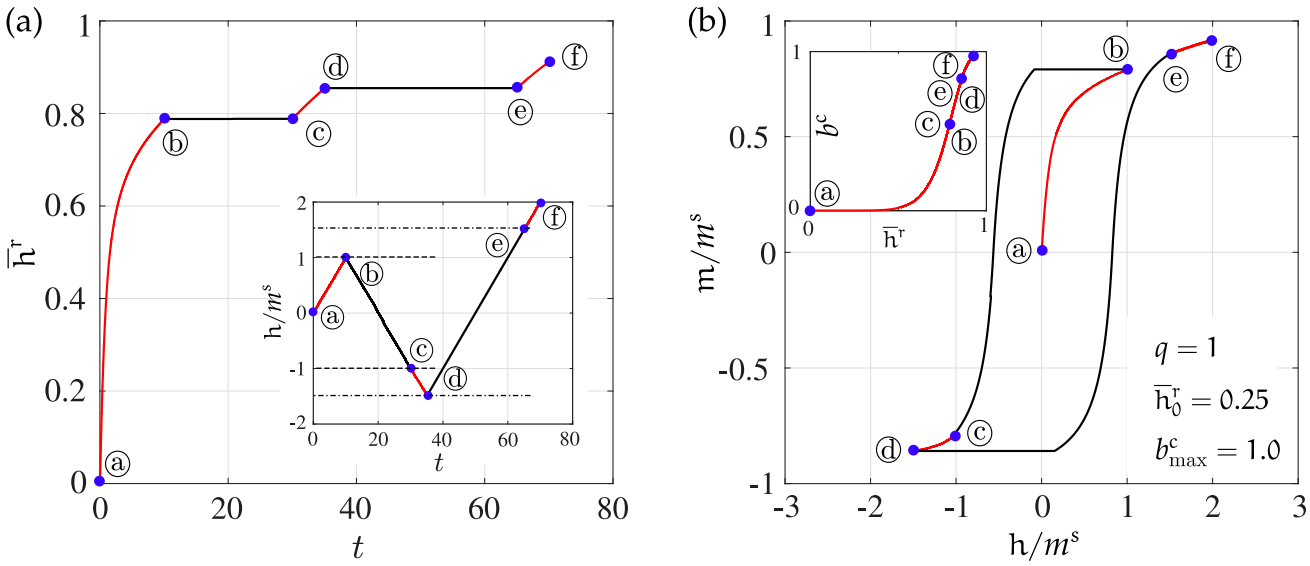

Figure A.2: (a) (inset) Cyclic loading profile. (a) Variation of $\bar{h}^r$ with time. (b) (inset) Evolution of b^c with $\bar{h}^r$. (b) Resulting hysteresis loop. Time scale is irrelevant for the rate-independent model.

second element of ξ_2) that *memorizes* the *prior maximum remanent field range*. The notion of such a remanent field range memory variable was first introduced by Chaboche et al. (1979) in the context of cyclic mechanical plasticity. Following Chaboche (1986), we allow $\dot{\bar{h}}^r$ to evolve following equation (A.3) only if the state of $\mathbf{h}^r$ lies on the *memory surface*. The latter is a spherical surface (for isotropic magnets) of radius $R_{\mathbf{h}^r}$ defined in the $\mathbf{h}^r$-space by

$$\phi_m := \mathbf{h}^r \cdot \mathbf{h}^r - R^2_{\mathbf{h}^r}. \tag{A.4}$$

At a given instant t_0, $R_{\mathbf{h}^r}$ corresponds to the maximum amplitude that $\mathbf{h}_r$ has reached over the entire loading history up to that time instant, i.e.,

$$R_{\mathbf{h}^r} = \max \|\mathbf{h}^r(t)\|, \qquad \forall\, 0 < t < t_0. \tag{A.5}$$

The isotropic hardening is effective only if the local state of $\mathbf{h}^r$ lies on the memory surface ϕ_m. This feature is incorporated in the hardening rule (A.3) by modifying (A.2) as

$$\dot{\bar{h}}^r = \begin{cases} \sqrt{\dot{\mathbf{h}}^r \cdot \dot{\mathbf{h}}^r}, & \text{if } \phi_m = 0 \\ 0, & \text{if } \phi_m < 0. \end{cases} \tag{A.6}$$

Note that b^c in (A.3) is not an explicit function of $R_{\mathbf{h}^r}$. However, $R_{\mathbf{h}^r}$ controls the evolution of $\bar{h}^r$ through (A.4) and (A.6). Thus, there exists an implicit dependence of b^c on the second element of ξ_2, i.e., $R_{\mathbf{h}^r}$.

For a better understanding of the modified isotropic hardening law, we discuss a representative example of magnetic cyclic loading with increasing amplitude in Fig. A.2. Temporal variation of h/m_s is shown in Fig. A.2a (inset). Specifically, we observe in Fig. A.2a that $\bar{h}^r$ increases from ⓐ to ⓑ. This increase in $\bar{h}^r$ results in the evolution of the switching surface radius b^c from ⓐ to ⓑ (see Fig. A.2b (inset)), which leads to the m– h response ⓐ – ⓑ in Fig. A.2b. Then, unloading from ⓑ to

ⓓ (beyond $|h^{ⓑ}| = |h^{ⓒ}|$) results in two distinct regimes. Firstly, from ⓑ to ⓒ, h/m^s remains less than the maximum loading amplitude of the previous half cycle ⓐ – ⓑ, i.e., $|h| < |h^{ⓑ}| = |h^{ⓒ}|$. Thus, $\bar{h}^r$ remains constant between ⓑ – ⓒ, which results in b^c to remain the same from ⓑ to ⓒ (see Fig. A.2b (inset)). In turn, going from ⓒ to ⓓ, $|h| > |h^{ⓑ}| = |h^{ⓒ}|$ of the previous half cycle ⓐ – ⓑ, $\bar{h}^r$ increases resulting to further increase of the switching surface radius in this regime (see Fig. A.2b (inset)). The switching surface radius continues to increase in a similar fashion during the subsequent half cycles, e.g., ⓓ – ⓕ, until eventually reaching b^c_{max}.

A.2 The extended constitutive model for asymmetric cyclic loading

So far in the proposed model, we incorporated the effect of isotropic hardening during the initial magnetization. However, experiments show existence of minor hysteresis loops under complex cyclic loading scenarios occuring *after* the initial magnetization. Clearly, from (A.3) and (A.6), we note that b^c evolves either during the initial magnetization or when h–field increases *beyond* the previously maximum absolute value of $|\mathbf{h}|$ attained at a preceding cycle (see e.g. Fig. A.2). Nevertheless, following available experimental observations, the switching surface can *shrink backwards* if more complex minor loop loadings are considered. In view of this, we attempt to enrich further the evolution law for b^c to model more complex cyclic loading cases, especially when load-reversals may take place *before* the local $|\mathbf{h}|$ reaches the maximum h–field values attained in the preceding cycles.

A.2.1 Notion of a bounding surface

The approach followed to model such complex minor loops is closely related to the bounding surface idea in mechanical plasticity. In particular, it has been observed by Dafalias and Popov (1975) (see also Chaboche (1986)) in the context of mechanical plasticity that kinematic and isotropic hardening is *not enough* to model cyclic plasticity under complex loading conditions. In that regard, Dafalias and Popov (1976) proposed a model where the evolution of the plastic internal variables (the remanent internal variable $\mathbf{h}^r$ in our case) depends additionally on some discrete, history-dependent parameters associated with loading/unloading of the material. These history parameters are obtained in the present work by constructing a *bounding surface* in the $\mathbf{h}^r$ space. In the following, we first develop the notion of the bounds in $\mathbf{h}^r$ for uniaxial loading/unloading and define the history-dependent parameters. Subsequently, the notion is extended in the context of general three-dimensional multiaxial loading/unloading cases.

A typical schematic representation of a h^r–h loop, observed in a uniaxial (1D) experiment is shown in Fig. A.3. In this figure, the h^r–h loop is observed to remain confined between two bounds: $|h^r| \leqslant h^r_s$, namely, an upper and a lower bound. In turn, the magnitude of h^r_s remains identical to the saturation magnetization m^s. Nonetheless, the notations h^r_s is used herein to explicitly indicate the range of variation of the remanent field $\mathbf{h}^r$.

It is observed that from an initial energetic regime ($|\dot{h}^r| = 0$), the remanent h-field switches and eventually saturates to the corresponding bound ($|h^r| = h^r_s$), i.e, the lower bound for the loading half-cycle and the upper bound for the unloading half-cycle, as shown in Fig. A.3 for an 1D loading example. Studying numerous uniaxial experiments and following Dafalias and Popov (1976) and Chaboche (1986), we conclude that the minor hysteresis loops can be modeled by considering b^c to be a function of the proximity of the current state of remanent field h^r to the corresponding bounding

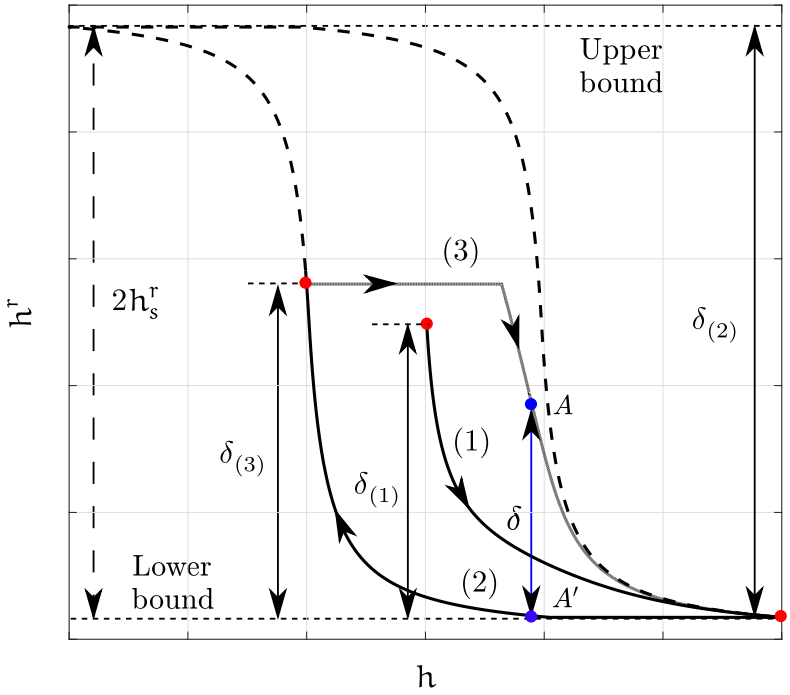

Figure A.3: Schematic illustration of upper and lower bounds, δ and $\delta_{(p)}$ for the uni-axial loading case.

(upper/lower) limit. This distance $\delta = AA'$, as shown in Fig. A.3 is computed by

$$\delta = h_s^r + \text{sign}(\dot{h})h^r. \tag{A.7}$$

The proximity of a state of h^r to the corresponding bounding limit at the beginning of the p^{th} half-cycle is denoted by $\delta_{(p)}$. The illustrative example of Fig.A.3 shows $\delta_{(p)}$ for three half-cycles, namely $p = 1, 2$ and 3, which together constitute a partially-reversed loading cycle. These *initial proximity* parameters, $\delta_{(p)}$, are the history-dependent terms, which play a pivotal role in modeling the evolution of b^c for complex loadings. It is worth noting that the initial local magnetization at the beginning of a new half-cycle also plays a crucial role in the micromagnetic model of Fulmek and Hauser (1996), which also models the minor loops by evolving a history-dependent material parameter. The same notion of evolving the history-dependent coercive field b^c is considered in our model, but within the framework of the bounding surface idea, which is by default a three-dimensional framework and in principle can also be extended to anisotropic magnetic responses.

In this regard, the computation of δ for the multiaxial case is a bit more involved but otherwise a direct extension of the above described 1D case. For simplicity, we assume an isotropic magnetic response to obtain a spherical *bounding surface* $\mathcal{B}$ in the $\mathbf{h}^r$ space of diameter $2h_s^r$ (see Fig. A.4a). To obtain δ, we first construct a plane containing both the vectors $\mathbf{h}^r$ and $\mathbf{n}_{\dot{\mathbf{h}}} = \dot{\mathbf{h}}/|\dot{\mathbf{h}}|$ and compute $\theta = \cos^{-1}(\mathbf{h}^r \cdot \mathbf{n}_{\dot{\mathbf{h}}}/|\mathbf{h}^r|)$. The intersection of this plane with $\mathcal{B}$ leads to a circle $\mathcal{C}$, whose 3D view and the 2D projection are shown in Fig. A.4a and b, respectively. Now, δ is obtained by computing the Eucledian distance between AA', where A represents the current state of $\mathbf{h}^r$ and A' is the corresponding point on $\mathcal{B}$ obtained by extending a straight line from A in the direction of $\mathbf{n}_{\dot{\mathbf{h}}}$ (see Fig. A.4b). From the planar geometry on the circle $\mathcal{C}$ (Fig. A.4b) with center O and radius h_s^r, we obtain δ using straightforward

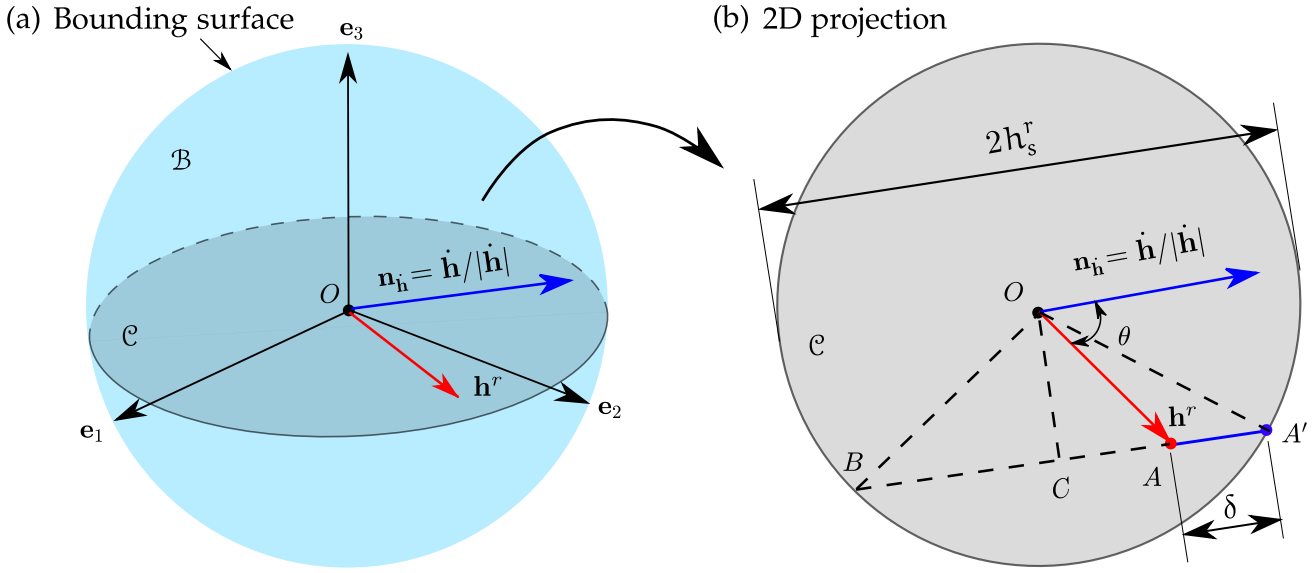

Figure A.4: (a) Schematic illustration of the bounding surface $\mathcal{B}$ and the circle $\mathcal{C}$ on the plane containing the vectors $\mathbf{n}_{\dot{\mathbf{h}}}$ and $\mathbf{h}^r$. (b) Estimation of $\delta_{(p)}$ from the planar geometry on $\mathcal{C}$.

geometrical arguments as

$$\delta = \sqrt{(h_s^r)^2 - |\mathbf{h}^r|^2 \sin^2\theta} + |\mathbf{h}^r| \cos\theta. \tag{A.8}$$

Figure A.4b shows that the uniaxial loading and unloading cases presented in Fig.A.3 and defined via the equation (A.7) are special cases of the more general three-dimensional framework that can be obtained by setting $\theta = 0$ and π, respectively, in equation (A.8).

By summarizing the above discussion, one may define the history-dependent variables to form a set of size $2p+4$, i.e.,

$$\xi_{2p+4} \equiv \{\overline{h}^r, R_{\mathbf{h}^r}, \overline{h}^e, \delta, \delta_{(p)}, \overline{h}^e_{(p)}, \delta_{(p-1)}, \overline{h}^e_{(p-1)}, ..., \delta_{(1)}, \overline{h}^e_{(1)}\},$$

where p is the number of half cycles (including the current one), and $\overline{h}^e$ is the accumulated energetic h-field (defined later in (A.12), similar to $\overline{h}^r$). Finally, $\overline{h}^e_{(p)}$ is the $\overline{h}^e$ at the beginning of the p^{th} half-cycle (similar to $\delta_{(p)}$). In principle, ξ is a set that has a continuously increasing number of elements, starting from $\xi_6 \equiv \{\overline{h}^r, R_{\mathbf{h}^r}, \overline{h}^e, \delta, \delta_{(1)}, \overline{h}^e_{(1)}\}$. Fortunately, real materials exhibit a fading memory (Dafalias and Popov, 1975, 1976). As a result, one can consider gradually increasing relative weights on $\delta_{(p)}$, $\delta_{(p-1)}$, $\delta_{(p-2)}$, and so on, and eventually discard the oldest history variables. A specific functional form of $b^c(\xi_{2p+4})$ is proposed next, based on available experimental observations.

It should be noted that, in the general context of magnetically anisotropic materials, the bounding surface $\mathcal{B}$ is expected to become non-spherical albeit remaining convex. The proposed framework can be readily extended for such cases but would probably require additional variables and anisotropic invariants.

A.2.2 First order minor loops

Typical experiments (Włodarski, 2007; Benabou et al., 2008; Martínez-García et al., 2013) show that the first order minor loops (FOMLs) exhibit, in a sense, two distinct features; (i) a low $|\mathbf{h}|$ switching

depends on the loading/unloading history while (ii) the switching surface radius increases from b_c to b_c^{max} during subsequent switching. When a load reversal takes place at a $|\mathbf{h}| < h_s$, both the rotation of the magnetic domains in the previous loading direction and the pinning of domain walls remain incomplete. Thus, one observes switching at a lower $|\mathbf{h}|$ during the current half cycle because of partial rotation of the magnetic domain walls during the previous half cycle (Hauser, 2004). Then, as switching proceeds during the current half cycle, the domain walls get rotated and pinned in the direction of $|\mathbf{h}|$, as usual. This micromagnetic phenomenon is captured in the present phenomenological model as follows; b^c is allowed to decrease during the energetic response of a partially-reversed half-cycle, whereby it may increase up to b^c_{max} during a subsequent switching. By recalling the observations (i) and (ii) done previously, we combine all the previous constitutive equations for b^c and extend them into three distinct evolution laws for the switching surface for the three different regimes: (i) the initial magnetization, (ii) the energetic part, and (iii) the switching part of a half cycle. Each one of these regimes is considered independently in the present work and their modeling can be carried separately depending on the level of complexity one is willing to reach.

Specifically, the initial magnetization regime is indicated by a function

$$\mathcal{K} = \mathcal{H}(\dot{\overline{h}}^r), \tag{A.9}$$

which is essentially a Heaviside step function with $\mathcal{K} = 1$ during the initial magnetization and 0 otherwise. Similarly, the energetic and the switching regimes of a half-cycle are written in terms of a Heaviside step function as

$$\mathcal{J} = 1 - \mathcal{H}\left(1 - \frac{\delta}{\delta_{(p)}}\right), \tag{A.10}$$

Recall from Section A.2.1 that $\delta = \delta_{(p)}$ during the energetic response and δ starts decreasing from $\delta_{(p)}$ when the switching starts. Thus, from definition (A.10), we have $\mathcal{J} = 1$ and 0 to represent the energetic and the switching regimes, respectively. We now propose a combined evolution law for b^c depending on the indicator functions $\mathcal{K}$ and $\mathcal{J}$ such that

$$b^c = \begin{cases} b^c_{max}\left\{\tanh\left[\left(\dfrac{\overline{h}^r}{\overline{h}^r_0}\right)^8\right]\right\}^{1/q} & \text{if} \quad \mathcal{K} = 1 \\ b^c_{(0)}\left\{1 - k_1\left(1 - \dfrac{\delta_{(p)}}{2h^r_s}\right)\dfrac{R_{\mathbf{h}^r}}{h^r_s}\mathscr{F}_1\right\} & \text{if} \quad \mathcal{K} = 0, \mathcal{J} = 1 \\ b^c_{(0)} + \left[b^c_{max}\left\{\tanh\left[\left(\dfrac{\overline{h}^r}{\overline{h}^r_0}\right)^8\right]\right\}^{1/q} - b^c_{(0)}\right]\mathscr{F}_2 & \text{if} \quad \mathcal{K} = 0, \mathcal{J} = 0, \end{cases} \tag{A.11}$$

where k_1 is a material parameter, $b^c_{(0)}$ is the initial b^c at the beginning of the energetic/switching regime, while the first law corresponding to the initial magnetization is the one proposed in (A.3).

The functions $\mathscr{F}_1$ and $\mathscr{F}_2$ are used to ensure a smooth decrease/increase in b^c during the energetic and switching parts, respectively, of a partially-reversed half-cycle. Note that during the energetic response, i.e., when the switching surface is modeled to shrink following $(A.11)_2$, both the accumulated remanent field $\overline{h}^r$ and the proximity parameter δ remain constant. Thus, the evolution of $\mathscr{F}_1$ during the energetic response may be carried out in terms of an accumulated energetic h-field,

defined as

$$\dot{\overline{h}}^{e} = \sqrt{\dot{\mathbf{h}}^{e} \cdot \dot{\mathbf{h}}^{e}}, \qquad \overline{h}^{e} = \int_{t} \dot{\overline{h}}^{e} dt. \tag{A.12}$$

A straightforward choice is to consider $\mathcal{F}_1$ to be a saturation function, which evolves from 0 and saturates at 1, such as

$$\mathscr{F}_1 = \tanh\left\{\frac{\delta^{D}_{(p)}}{2R_{\mathbf{h}^r}}\left(\frac{\overline{h}^{e}}{\overline{h}^{e}_{0}} - \frac{\overline{h}^{e}_{(p)}}{\overline{h}^{e}_{0}}\right)\right\}, \tag{A.13}$$

where the term $\overline{h}^{e}_{(p)}$ is a history-dependent parameter, that is $\overline{h}^{e}$ at the beginning of the p^{th} half cycle (similar to $\delta_{(p)}$) and $\delta^{D}_{(p)} = \delta_{(p)} + \delta_{(p-1)} - 2h^{r}_{s}$ is the proximity of the p^{th} half-cycle to the $(p-1)^{th}$ one, i.e., the proximity between two subsequent half-cycles. Finally, $\overline{h}^{e}_{0}$ in (A.13) is a material parameter that represents a reference accumulated energetic h-field (similar to $\overline{h}^{r}_{0}$ in (A.3)). Similarly, $\mathscr{F}_2$ is chosen to be a saturation function, that evolves from 0 to 1, such that

$$\mathscr{F}_2 = \tanh\left\{k_2 \frac{2h^{r}_{s}}{\delta^{M}}\left(1 - \frac{\delta}{\delta_{(p)}}\right)\left(\frac{\delta^{D}_{(p)}}{2h^{r}_{s}}\right)^{-k_3}\right\}, \tag{A.14}$$

where k_2 and k_3 are positive parameters that dictate the shape of the minor loop, and

$$\delta^{M} = \max\{\delta_{(1)}, \delta_{(2)}, ..., \delta_{(p)}\}.$$

Remark A.1. Note that $\mathscr{F}_2$ may become singular in the degenerate case of $\delta^{D}_{(p)} \to 0$, i.e., for tiny minor loops due to small fluctuations in the local **h**. This can be remedied by adding a correction term in $(A.11)_2$. Such a correction is shown in the following but is not necessary for well-defined cyclic loads. Specifically, one may augment $(A.11)_2$ with an additional term, such as

$$b^{c} = b^{c}_{(0)}\left\{1 - k_1\left(1 - \frac{\delta_{(p)}}{2h^{r}_{s}}\right)\frac{R_{\mathbf{h}^r}}{h^{r}_{s}}\mathscr{F}_3\mathscr{F}_1\right\} + \left[b^{c}_{max}\left\{\tanh\left(\frac{\overline{h}^{r}}{\overline{h}^{r}_{0}}\right)\right\}^{1/q} - b^{c}_{(0)}\right](1 - \mathscr{F}_3)\mathscr{F}_4, \tag{A.15}$$

where the functions $\mathscr{F}_3$ and $\mathscr{F}_4$ are now defined by

$$\mathscr{F}_3 = \tanh\left(6.0\frac{\delta^{D}_{(p)}}{h^{r}_{s}}\right), \tag{A.16}$$

$$\mathscr{F}_4 = \tanh\left\{\frac{2R_{\mathbf{h}^r}}{\delta^{D}_{(p)}}\left(\frac{\overline{h}^{e}}{\overline{h}^{e}_{0}} - \frac{\overline{h}^{e}_{(p)}}{\overline{h}^{e}_{0}}\right)\right\}, \tag{A.17}$$

respectively. Now, for $\delta^{D}_{(p)} = 0$, $\mathscr{F}_3$ vanishes, reducing (A.15) to its second term only. Therefore, instead of decreasing, the b^{c} rather increases to b^{c}_{max} during the energetic response by virtue of the saturation function $\mathscr{F}_4$.

The use of $(A.11)_{1,3}$ and (A.15) to model the FOMLs arising due to partially-reversed loading cycles are discussed next by use of two typical examples. A typical example of a first-order reversal curve is depicted in Fig. A.5. The inset of Fig. A.5a shows the uniaxial loading profile, where ⓐ – ⓑ represents the initial magnetization of a virgin sample followed by a *partially-reversed* cycle ⓑ – ⓓ –

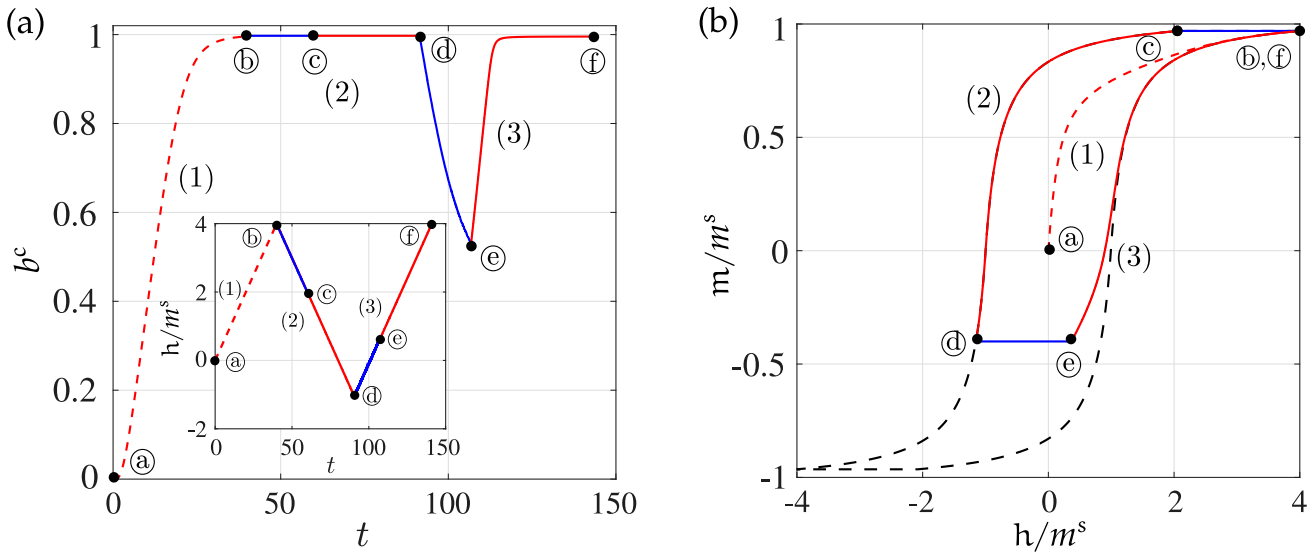

Figure A.5: (a) (inset) Cyclic loading profile. (a) Evolution of b^c in time. (b) Resulting $\mathfrak{m}-\mathfrak{h}$ loop. Time scale is irrelevant for the rate-independent model.

ⓕ. The initial magnetization from ⓐ to ⓑ results in the corresponding evolution of $\mathfrak{b}_c$ as evaluated from $(A.11)_1$ (see Fig. A.5a). The corresponding response in the $\mathfrak{m}-\mathfrak{h}$ space is shown for the same regime in Fig. A.5b.

At the beginning of the second half-cycle ⓑ – ⓓ, we have $\delta_{(2)} \approx 2\mathfrak{h}_s^r$ and $b^c_{(0)} = b^c_{max}\{\tanh[(\bar{\mathfrak{h}}^r/\bar{\mathfrak{h}}^r_0)^8]\}^{1/q}$. Thus, the evolution law for b^c, i.e, $(A.11)_2$ reduces to $b^c = b^c_{(0)}$, resulting in a constant b^c between ⓑ – ⓒ. During subsequent switching, b^c evolves following $(A.11)_3$. Note in $(A.11)_3$ that the coefficient of $\mathscr{F}_2$ now vanishes as b^c did not decrease from b^c_{max}. Hence, $(A.11)_2$ and $(A.11)_3$ together ensure a constant b^c on unloading if the preceding loading goes beyond saturation (see Fig. A.5a). Consequently in Fig. A.5b, we obtain a $\mathfrak{m}-\mathfrak{h}$ response in the interval ⓑ – ⓒ coinciding with the major loop.

The path ⓓ – ⓕ represents a partially-reversed half-cycle, where the load reversal takes place before saturation at ⓓ and thus, $\delta_{(3)} < 2\mathfrak{h}_s^r$. During the energetic response, ⓓ – ⓔ, b^c decreases to values lower than $b^c_{(0)} = b^c_{max}$ following the constitutive expression $(A.11)_2$ (see Fig. A.5a). Consequently, the switching is initiated at ⓔ at values lower than b^c_{max}. From that point on, b^c starts evolving following $(A.11)_3$ and hence increases from ⓔ to ⓕ approaching b^c_{max}. The resulting $\mathfrak{m}-\mathfrak{h}$ response is shown by the segment ⓓ – ⓔ in Fig. A.5b.

Note that the shape of the minor loop ⓓ – ⓔ depends explicitly on the choice of the minor loop shape parameters $\mathfrak{k}_1$, $\mathfrak{k}_2$ and $\mathfrak{k}_3$. The identification of $\mathfrak{k}_1$, $\mathfrak{k}_2$ and $\mathfrak{k}_3$ by use of a least-square fitting of the model with available experimental data is discussed in Section A.4. On the other hand, the proposed forms of the functions $\mathscr{F}_1$ and $\mathscr{F}_2$ will be shown to be sufficient to model a large number of different magnets.

For completeness, we also investigate a more complicated loading scenario where initially the magnet is *not* magnetized to saturation. That is a very important case in particle-filled magnetorheological elastomers, whereby not all particles attain the same level of magnetization given an external overall applied magnetic field.

In particular, the loading profile is depicted in the inset of Fig. A.6a. In this case, an initial loading

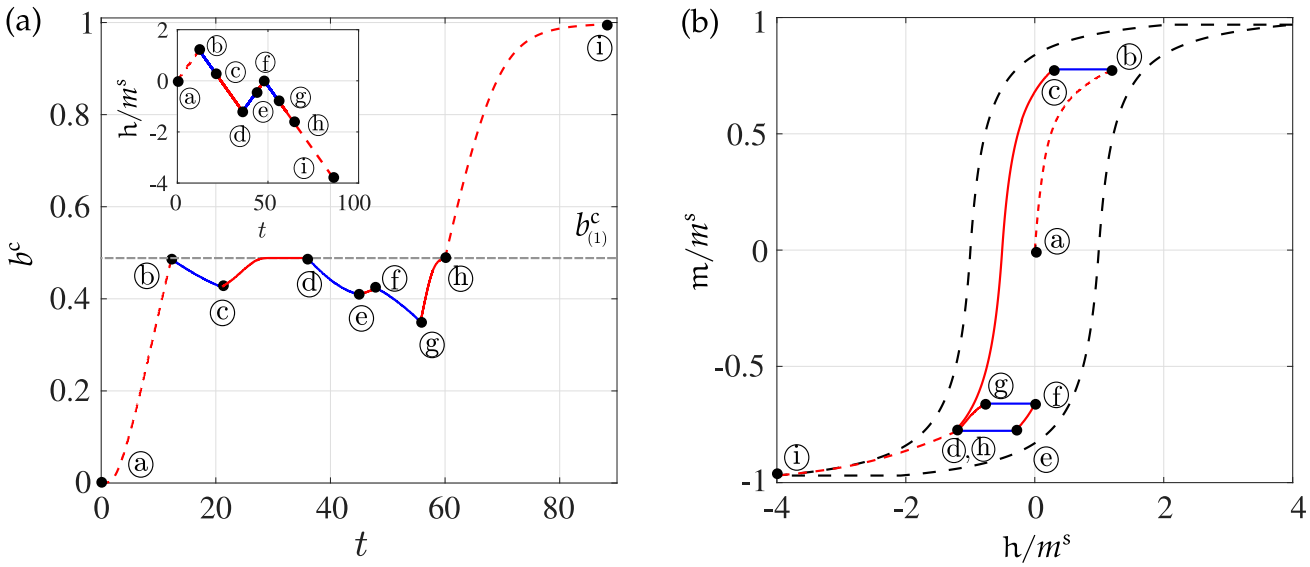

Figure A.6: (a) (inset) Cyclic loading profile. (a) Evolution of b^c in time. (b) Resulting $\mathfrak{m}$ – $\mathfrak{h}$ loop. Time scale is irrelevant for the rate-independent model.

from ⓐ to ⓑ increases b^c up to a given value $b^c_{(1)}$ resulting to an initial magnetization response in the same shown in Fig. A.6b. The subsequent two half cycles ⓑ – ⓓ and ⓓ – ⓕ follow the evolution equations $(A.11)_2$ and $(A.11)_3$ during the corresponding energetic and switching regimes, respectively, and result in a $\mathfrak{m}$ – $\mathfrak{h}$ response, shown in Fig. A.6b. An interesting observation can be made during the last unloading half-cycle ⓕ – ⓘ. We notice from Fig. A.6a (inset) that $|\mathfrak{h}|$ exceeds $\mathfrak{h}^{\max}$ when the magnet is unloaded beyond ⓗ. Thus, the shrinkage ⓕ – ⓖ of the switching surface is followed by its expansion in two steps. First, we get the expansion from ⓖ to ⓗ evaluated by equation $(A.11)_3$. This is followed by an expansion of b^c in the interval ⓗ to ⓘ as computed by equation $(A.11)_1$. As a result, we observe a two step magnetization response ⓖ – ⓘ in Fig. A.6b. Therefore, three different regimes are obtained from relation (A.11) during a half-cycle for a loading condition in the interval ⓕ – ⓘ.

Accurate prediction of the higher-order minor loops necessitates a more tedious definition of b^c and, in general, it requires a metric to identify the order of the minor loop. On the other hand, the nature of evolution of b^c remains the same for the higher order loops except for the need of additional history-dependent terms. Thus, an efficient storage of the order of the minor loop and the set ξ requires a suitable computational algorithm, which is beyond the scope of the present work. However, typically in engineering applications with magnets (Miyamoto et al., 1989) and MREs (Ginder et al., 1999), the material is *not* loaded with a highly fluctuating magnetic field that may cause secondary or higher order minor loops. Thus, the proposed model, that captures accurately the FOMLs, is expected to be sufficient for the applications at hand.

A.3 Identification of model parameters

The number of model parameters to be identified depends on the complexity of the experiment we intend to model. For the most general case, which involves modeling a magnet accurately up to its first-order minor loops, we need to specify thirteen parameters, namely, χ^e, χ, m^s, $b^c_{\max}$, $\kappa^{(1)}_{\mathfrak{h}}$, $\kappa^{(2)}_{\mathfrak{h}}$, $\kappa^{(3)}_{\mathfrak{h}}$,

$\overline{h}_0^r$, $\overline{h}_0^e$, q, k_1, k_2 and k_3. On the other hand, modeling only the major loop as carried out in Chapter 3 requires seven material parameters, namely χ^e, χ, m^s, b^c_{max}, $\kappa_h^{(1)}$, $\kappa_h^{(2)}$ and $\kappa_h^{(3)}$ with all others to remaining inconsequential. Arbitrary but non-singular values of some of those inconsequential parameters are reported in the tables of the following section. Subsequently, modeling the initial magnetization response along with the major loop requires two additional parameters $\overline{h}_0^r$ and q. Finally, for the modeling of the minor loops, we need to specify the remaining $\overline{h}_0^e$, k_1, k_2 and k_3 constants. Note that, only data for one representative first-order minor loop of the material are required to identify the four minor loop parameters. Any remaining first-order minor loop of the material will be predicted directly from the model *without* further change of the minor loop parameters. Specific examples of minor loop fitting and predictions are discussed in the next section.

The computed response is fitted to the corresponding experimental data using a standard least square method in three distinct steps:

- $\mathcal{S}1$ – *Calibration of major loop*: We first find the optimal major loop parameters χ^e, χ, m^s, b^c_{max}, $\kappa_h^{(1)}$, $\kappa_h^{(2)}$ and $\kappa_h^{(3)}$ (i.e. 7 parameters) by using the `lsqcurvefit` function of MATLAB (2017).

- $\mathcal{S}2$ – *Calibration of initial magnetization*: We then identify the parameters q and $\overline{h}_0^r$ (i.e. 2 parameters) that are necessary to fit the initial magnetization response.

- $\mathcal{S}3$ – *Calibration of a minor loop*: Finally, we identify the rest of the four minor loop parameters, namely $\overline{h}_0^e$, k_1, k_2, k_3 (i.e. 4 parameters) by fitting a single minor loop, if such information are available from the experiments analyzed.

At this point, it is worth discussing in more detail the necessity of the above three steps and thus the number of parameters needed to be identified in the context of four representative experimental cases reported in the literature:

i) Only the experimental major loop is available. In this case step $\mathcal{S}1$ is sufficient and hence, the corresponding seven parameters in this step need to be identified, while those in $\mathcal{S}2$ and $\mathcal{S}3$ remain inconsequential.

ii) The major loop with the initial magnetization response are reported. In this case we first carry out step $\mathcal{S}1$ followed by $\mathcal{S}2$, i.e., we identify nine parameters in total. The remaining four parameters of step $\mathcal{S}3$ remain inconsequential.

iii) The major loop and at least one asymmetric minor loop are reported. In this case, we first carry out step $\mathcal{S}1$ followed by $\mathcal{S}3$, i.e., we identify eleven parameters. The corresponding initial magnetization parameters remain inconsequential in this case.

iv) The major loop along with the initial magnetization and al least one symmetric or asymmetric minor loop are available. In this case, the fitting requires all three steps ($\mathcal{S}1 - \mathcal{S}3$) and has to be carried out sequentially. It is noted further that whenever we model the major loop and symmetric minor loops, all three steps and all thirteen parameters are required.

Hence, even if the complete theoretical model is described in terms of a total of thirteen parameters, the number of the parameters that needs to be identified may be much less in a large number of cases of practical interest. Specific examples involving all four cases discussed previously are investigated in the following section.

A.4 Assessment of the model with experiments

In the following, we compare the proposed model with the uniaxial tests of (a) sintered NdFeB magnets by Huang et al. (2016b) and (b) NdFeB powders by Deng et al. (2015) and Périgo et al. (2012). In those examples, we model the initial magnetization and the major loop. Subsequently, we compare the proposed model with the experimentally observed minor loops by Włodarski (2007) and Liu et al. (2010). Finally, we develop FORC diagram from the fitted model response and compare it with the FORC diagram generated by Pike et al. (1999) from the experimental data. It is important to mention that the polycrystalline magnets, used in the corresponding experiments, are typically isotropic. Anisotropic magnets may be manufactured through dedicated manufacturing techniques and will require additional constitutive parameters that will allow to describe properly the preferred magnetization directions.

A.4.1 Sintered NdFeB magnets

Sintered NdFeB magnets are the classical example of nucleation-type magnets with high initial susceptibility. In Fig. A.7, we obtain two sets of experimental data from Huang et al. (2016b): (a) the major hysteresis loop for spark plasma sintered NdFeB magnets, where the solid magnet is obtained by sintering very fine melt-spun NdFeB ribbons of less than 40 μm diameter, and (b) the major loop for sintered NdFeB, prepared by sintering coarse NdFeB ribbons (greater than 40 μm diameter).

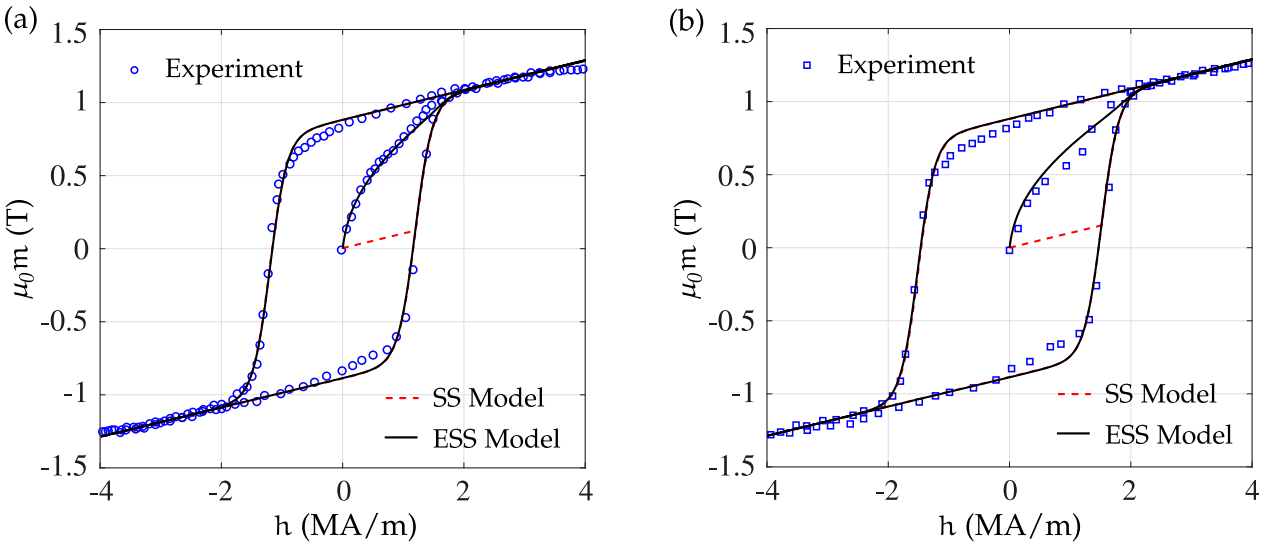

Figure A.7: Experimental m-h response of a NdFeB magnet (Huang et al., 2016b) with the fitted rate-independent SS and ESS models.

Specifically, following §1 and then §2, we obtain a least-square fit of our model with the experimental data in Fig. A.7a. First, we fix $\kappa_h^{(3)} = 1$ and carry out §1 to obtain the optimal χ^e, χ, m^s and b^c_{max}, as shown in Table A.1. Next, we carry out §2 to obtain q and $\bar{h}^r_0$. Due to unavailability of any minor loop data, the step §3 is inconsequential and hence, the minor loop parameters may be set to $\bar{h}^e_0 = 1.0$ MA/m and $k_1 = k_2 = k_3 = 0$.

We observe that the present ESS model is capable of probing accurately the experimental data in Fig. A.7a. Here, we note that in addition to modeling the major loops, the present model also traces

accurately the initial magnetization response. Note that the SS model, shown for comparison, as well as the pseudo-particle models only model the outer coercive loops accurately. Next, we probe the hysteresis loop for a coarse-grained sintered NdFeB magnet in Fig. A.7b.

Table A.1: Material parameters for sintered NdFeB magnets

§1: Major loop			
$\chi^e = 0.075$	$\chi = 4.0$	$m^s = 0.65$ MA/m	$b^c_{max} = 1.20\mu_0$(a) | $1.52\mu_0$(b) T
$\kappa_h^{(1)} = 0.0$	$\kappa_h^{(2)} = 0.0$	$\kappa_h^{(3)} = 1.0$	
§2: Initial magnetization			
$\bar{h}^r_0 = 0.58$ MA/m	$q = 3.35$		
§3: Minor loop			
$\bar{h}^e_0 = 1.0$ MA/m	$k_1 = 0.0$	$k_2 = 0.0$	$k_3 = 0.0$

The model is able to reproduce this second case by only re-identifying the parameter b^c_{max}, keeping the rest of the parameters the same. Thus, it is observed that different variants of magnets made of the same material (e.g., exhibiting different grain sizes) can be modeled by a small variation of the coercive field b^c_{max}.

A.4.2 NdFeB powder

In Fig. A.8, we consider the experimental data of Deng et al. (2015) and Périgo et al. (2012) for quasi-static, uniaxial loading of melt-spun NdFeB powder samples. In both cases, the proposed model is capable of reproducing extremely well the corresponding experimental data (see Table A.2 for corresponding parameters). Specifically, we first identify the model parameters using the experimental results of Deng et al. (2015). Then, the experiments of Périgo et al. (2012) are probed by re-adjusting χ^e and χ, which serve to describe the *shape* of the hysteresis loop. Table A.2 displays the values of the model parameters used to describe the major hysteresis loop. Note that in both experiments the maximum coersive field b^c_{max} is identical.

Table A.2: Material parameters for NdFeB powder

§1: Major loop			
$\chi^e = 0.095$(a) | 0.163(b)	$\chi = 8.0$(a) | 16.0(b)	$m^s = 0.67$ MA/m	$b^c_{max} = 0.845\mu_0$ T
$\kappa_h^{(1)} = 1.0$	$\kappa_h^{(2)} = 0.0$	$\kappa_h^{(3)} = 0.0$	
§2: Initial magnetization			
$\bar{h}^r_0 = 0.551$ MA/m	$q = 17.5$		
§3: Minor loop			
$\bar{h}^e_0 = 1.0$ MA/m	$k_1 = 0.0$	$k_2 = 0.0$	$k_3 = 0.0$

In addition, use of the same initial magnetization parameters $\bar{h}^r_0$ and q allows us to recover accurately the initial magnetization response in both samples. In Fig. A.8, the parameter q implies that the coercivity in NdFeB powder samples can be attributed to a combined effect of nucleation and pinning, which is in agreement with recent microscopic observations by Liu et al. (2013) in NdFeB ribbons (from which the NdFeB powders are obtained through grinding). Finally, the four minor loop parameters $\bar{h}^e_0$, k_1, k_2 and k_3 are inconsequential due to unavailability of any minor loop data and thus are set to $\bar{h}^e_0 = 1.0$ MA/m and $k_1 = k_2 = k_3 = 0$.

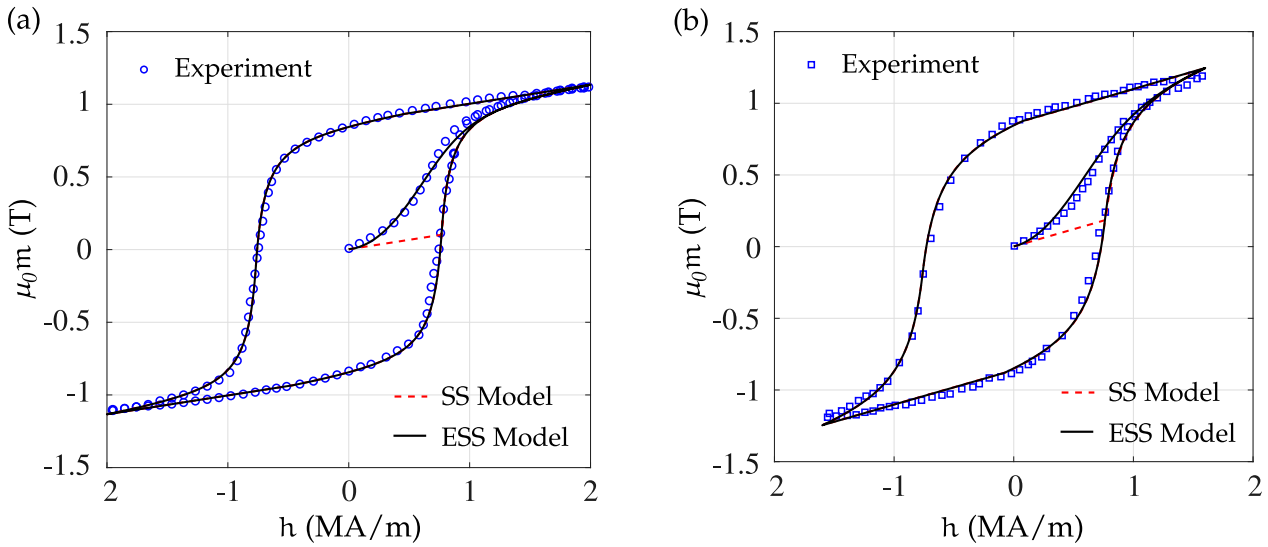

Figure A.8: Experimental m-h response of NdFeB powder from (a) Deng et al. (2015) and (b) Périgo et al. (2012) with the fitted rate-independent proposed model.

A.4.3 MgMn steel

In Fig A.9, we use the complete model to probe the experimental data of Włodarski (2007) for MgMn steel, which include several fully-reversed, uniaxial hysteresis loops with different amplitudes of loading. Thus, in addition to the initial magnetization and major coercive loop, the latter experiments provide also information on symmetric minor loops. We first identify b^c_{max}, χ^e, χ and m^s in order to probe the experimental major loop (see Table A.3).

Table A.3: Material parameters for MgMn Steel

$\mathcal{S}1$: Major loop			
$\chi^e = 0.9913$	$\chi = 0.03$	$m^s = 1.58$ kA/m	$b^c_{max} = 0.72\mu_0$ mT
$\kappa^{(1)}_h = 0.0$	$\kappa^{(2)}_h = 0.0$	$\kappa^{(3)}_h = 1.0$	
$\mathcal{S}2$: Initial magnetization			
$\bar{h}^r_0 = 1.45$ kA/m	$q = 45.6$		
$\mathcal{S}3$: Minor loop			
$\bar{h}^e_0 = 0.099$ kA/m	$k_1 = 3.0$	$k_2 = 5.0$	$k_3 = 0.1$

Subsequently, we fit the initial magnetization response by identifying the parameters q and $\bar{h}^r_0$. Finally, we fit the model with *one* of the minor loop data to obtain $\bar{h}^e_0$, k_1, k_2 and k_3 as shown in Table A.3. In Fig. A.9b, we use the already identified model to *predict* two additional experimental minor loops. We thus show that the model is able to reproduce but also to predict sufficiently well the major and minor hysteresis loops of MgMn steel.

A.4.4 Asymmetric minor loops

In Fig. A.10, we use our model to probe the experimental data for two different magnets; (a) annealed nanocrystalline Co alloy and (b) 3% silicon steel, subjected to uniaxial, partially-reversed loading, which results in asymmetric minor loops. The experimental $m - h$ response along with

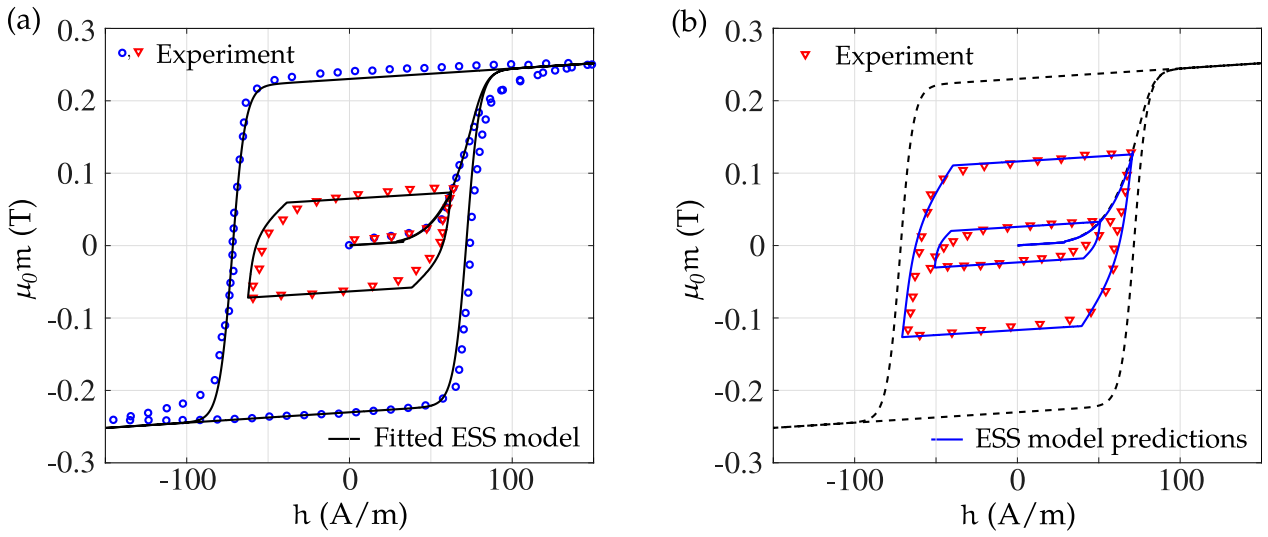

Figure A.9: Experimental m-h response of MgMn Steel by Włodarski (2007) with (a) the fitted model and (b) the model predictions.

three first-order reversal curves (FORCs) for the annealed nanocrystalline Co alloy magnet is obtained by Martínez-García et al. (2013). Similar to the previous figures, we carry out a two step fitting of our model. First, we fit the major loop data of Martínez-García et al. (2013) to obtain the model parameters except $\overline{h}_0^r$ and q, which are inconsequential due to unavailability of the initial magnetization data. We then use the model to probe one of the experimental FORC data thus identifying the parameters $\overline{h}_0^e$, k_1, k_2 and k_3. The resulting values for the model parameters are given in Table A.4.

Table A.4: Material parameters for annealed nanocrystalline Co alloy

$\mathcal{S}1$: Major loop			
$\chi^e = 0.855$	$\chi = 785.0$	$m^s = 51.5$ kA/m	$b^c_{max} = 12.0\mu_0$ mT
$\kappa_h^{(1)} = 1.0$	$\kappa_h^{(2)} = 0.0$	$\kappa_h^{(3)} = 0.0$	
$\mathcal{S}2$: Initial magnetization			
$\overline{h}_0^r = 1.0$ A/m	$q = 100.0$		
$\mathcal{S}3$: Minor loop			
$\overline{h}_0^e = 85.0$ A/m	$k_1 = 4.0$	$k_2 = 1.85$	$k_3 = 1.25$

In Fig. A.10a, the solid lines correspond to the model response that is fitted to the corresponding experimental data. The dashed lines correspond to predictions of the model without introduction of additional model parameters.

Finally, Fig. A.10b shows the experimental data of Benabou et al. (2008) corresponding to the b – h response of a 3% silicon steel sample that is subjected to a periodic h-field with the superposition of third harmonics. This type of loading gives rise to asymmetric minor loops. Again, a two-step fitting procedure, consisting of fitting the major loop and only one of the minor loops from the experimental data, yields the corresponding model parameters (see Table A.5). Note again that the initial magnetization parameters $\overline{h}_0^r$ and q remain inconsequential due to unavailability of the initial magnetization data and thus are set equal to 1 and 0, respectively. The second minor loop is then

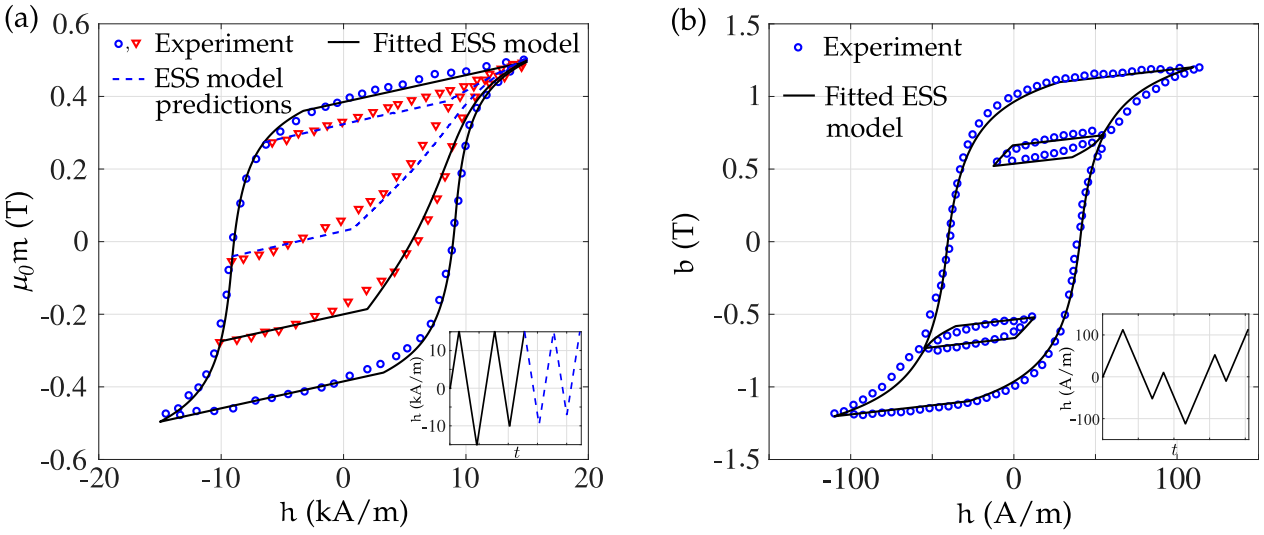

Figure A.10: (a)(inset) Loading profile for FORCs. (a) Experimental m-h response for nanocrystalline Co alloy from Martínez-García et al. (2013) with the model fitting and predictions. (b)(inset) Loading profile and (b) experimental b-h response for 0.3% silicon steel by Benabou et al. (2008) with the fitted model. Time scale is irrelevant for the rate-independent model.

found to be well predicted by the proposed model.

Table A.5: Material parameters for 3% silicon steel

§1: Major loop			
$\chi^e = 0.999$	$\chi = 126.3$	$m^s = 1000.0$ A/m	$b^c_{max} = 12.0\mu_0$ mT
$\kappa^{(1)}_h = 1.0$	$\kappa^{(2)}_h = 0.0$	$\kappa^{(3)}_h = 0.0$	
§2: Initial magnetization			
$\bar{h}^r_0 = 1.0$ A/m	$q = 0.0$		
§3: Minor loop			
$\bar{h}^e_0 = 100.0$ A/m	$k_1 = 8.0$	$k_2 = 4.0$	$k_3 = 1.34$

The examples presented in this section illustrate the capabilities of the model to reproduce an predict magnetic responses obtained by very complex loading histories and specifically resulting in asymmetric minor loops.

A.5 Construction of FORC diagrams

In this section, we use the proposed ESS model to probe a representative experimental FORC diagram. In particular, a set of FORCs, as shown in Fig. A.10a and Fig.A.11, enables us to construct the so called FORC diagram (Pike et al., 1999; Pike, 2003; Liu et al., 2013), which is essentially a contour plot showing the mixed derivative of the magnetization m with respect to the applied h-field h and the reversal h-field h_r. Specifically, the FORC distribution function ρ is defined by (Pike et al., 1999)

$$\rho(h, h_r) = -\frac{1}{2}\frac{\partial^2 m(h, h_r)}{\partial h \partial h_r}. \tag{A.18}$$

The FORC diagrams are typically plotted in the $h_c - h_u$ space, where $h_c = (h - h_r)/2$ is the coercive field[1] and $h_u = (h + h_r)/2$ is termed as the interaction field (Pike et al., 1999). The distribution of ρ as a function of h_c and h_u allows us to infer the characteristics of the micromagnetic interactions in the sample. For instance, a narrow distribution of ρ along h_u is typically obtained for single-domain (SD) magnets. The reader is referred to former representative studies (Pike et al., 1999; Pike and Fernandez, 1999; Pike, 2003; Roberts et al., 2000) for a more detailed description of a FORC diagram and its significance in inferring the micromagnetic properties of the material under study.

In order to obtain the FORC diagrams from the present ESS framework, we carry out a fitting methodology as proposed in Section A.4. We consider the classic example of a floppy disc material (Pike et al., 1999; Roberts et al., 2000; Newell, 2005) and consider fitting our model with the experimentally observed $m - h$ response (Pike et al., 1999). The calibrated model with the outer loop and with one of the representative FORCs is shown in Fig. A.11. The identified model parameters are given in Table A.6.

Table A.6: Material parameters for floppy disc material

$\mathcal{S}1$: Major loop			
$\chi^e = 0.999$	$\chi = 126.3$	$m^s = 1000.0$ A/m	$b^c_{max} = 12.0\mu_0$ mT
$\kappa^{(1)}_h = 1.0$	$\kappa^{(2)}_h = 0.0$	$\kappa^{(3)}_h = 0.0$	
$\mathcal{S}2$: Initial magnetization			
$\overline{h}^r_0 = 1.0$ A/m	$q = 0.0$		
$\mathcal{S}3$: Minor loop			
$\overline{h}^e_0 = 100.0$ A/m	$k_1 = 8.0$	$k_2 = 4.0$	$k_3 = 1.34$

Once the model parameters are identified, we then use the model to generate a data set of three hundred FORCs, a subset of which is shown in Fig. A.11.

One of the main characteristics of the proposed ESS model is that it generated sharp corners in the $m - h$ response at the point of transition from the energetic to switching regime (shown in Fig. A.11 by red line). This sharp corner in the $m - h$ space, which is an inherent feature of such phenomenological models, results in a discontinuity in the FORC distribution ρ. For the purpose of constructing a meaningful FORC diagram, we smooth out this discontinuity by considering a distribution (Pike et al., 1999) of the coercive field b^c around the identified b^c_{max} as given by Table. This distribution, chosen for simplicity to be Gaussian in the present case, serves to mimic in an approximate sense the collective response of a large number of grains in the material. In particular, we perform N different computations with $b^c_{max} = b^c_i$ $(\forall i \in [1, N])$ obtained from a Gaussian distribution $G(b^c_{mean}, \sigma_b)$, where the mean coercivity $b^c_{mean} = 89.3$ mT, as shown in Table A.11 by fitting of a constant coercive field model while $\sigma_b = 15.0$ mT is the standard deviation. Finally, the resulting m field is computed as $m = 1/N \sum_{i=1}^{N} m_i$. Considering $N = 20$, we obtain a sufficiently smooth FORC response as shown in Fig. A.11. Contrary to the Preisach (1935) - Pike et al. (1999) model of the floppy disc material, in the ESS framework, a small number of b^c_i with a narrow standard deviation is sufficient for accurate reproduction of the FORC diagram. This can be attributed to the observation that the proposed ESS framework contains *a-priori* the complex energetic-switching response during a partially-reversed half cycle via the use of non-trivial hardening functions.

[1]The coercive field $h_c = (h - h_r)/2$ should not be confused with the definition of the material parameter coercive field in Chapter 3. One should treat the present definition of h_c *exclusively* in the context of FORC diagrams.

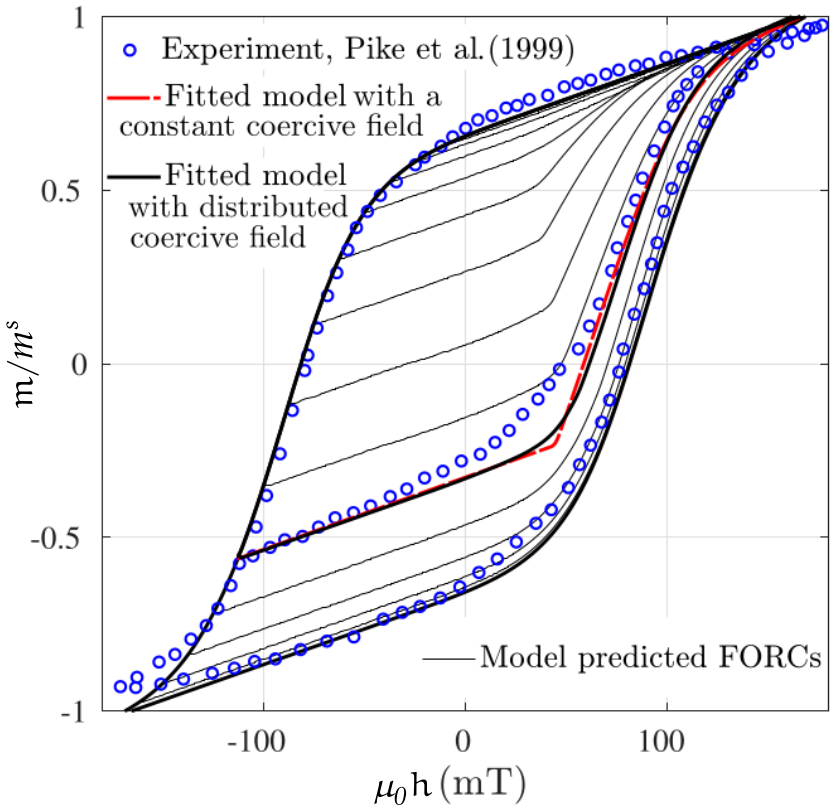

Figure A.11: Model parameter identification of the major loop and one of the representative FORC with the experimental hysteresis data for a floppy disc material (Pike et al., 1999).

Subsequently, by use of three hundred sufficiently smooth FORC data, we evaluate numerically the FORC distribution $\rho(h_c, h_u)$ by employing a backward Euler scheme. In such FORC diagrams, the distribution of ρ with respect to h_c and h_u plays a crucial role in inferring micromagnetic information of the material, whereas the magnitude of ρ is somewhat less significant. Thus, it is customary to normalize ρ with respect to its maximum ρ_{max} and represent the FORC distributions in a normalized scale of $(-\infty, 1]$ (Pike et al., 2005; Roberts et al., 2014; Pohlit et al., 2016). Figure A.12 shows the contour plot of the normalized ρ in the $\mu_0 h_c - \mu_0 h_u$ space. The FORC diagram in Fig. A.12 qualitatively matches the experimental FORC diagram developed by Pike (2003) (see inset of Fig. A.12). Our model successfully captures three major features of the experimental FORC diagram, namely, (a) an asymmetric reversible ridge near $\mu_0 h_c = 0$ mT, (b) an irreversible peak near $\mu_0 h_c = 87$ mT and $\mu_0 h_u = -5$ mT, and (c) a region with negative ρ below the irreversible peak (see Fig. 9 of Pike et al. (1999)). The reversible ridge near $\mu_0 h_c = 0$ mT and $\mu_0 h_u = -80$ mT is due to the change in the slope of the FORCs during their initiation at $h = h_r$, i.e., $\mu_0 h_c = 0$. Interestingly, the peak of the reversible ridge is asymmetric with respect to $\mu_0 h_u = 0$ axis. The irreversible peak in Fig. A.12 indicates the coercive and interaction fields at which the maximum irreversible changes take place in the micromagnetic domains. Our model accurately predicts the location of the irreversible peak for the floppy disk material.

Finally, we conduct a more quantitative analysis of the modeled FORC distribution in Fig. A.13a and b by probing the computed ρ versus the experimental observation and the Pike (2003) model.

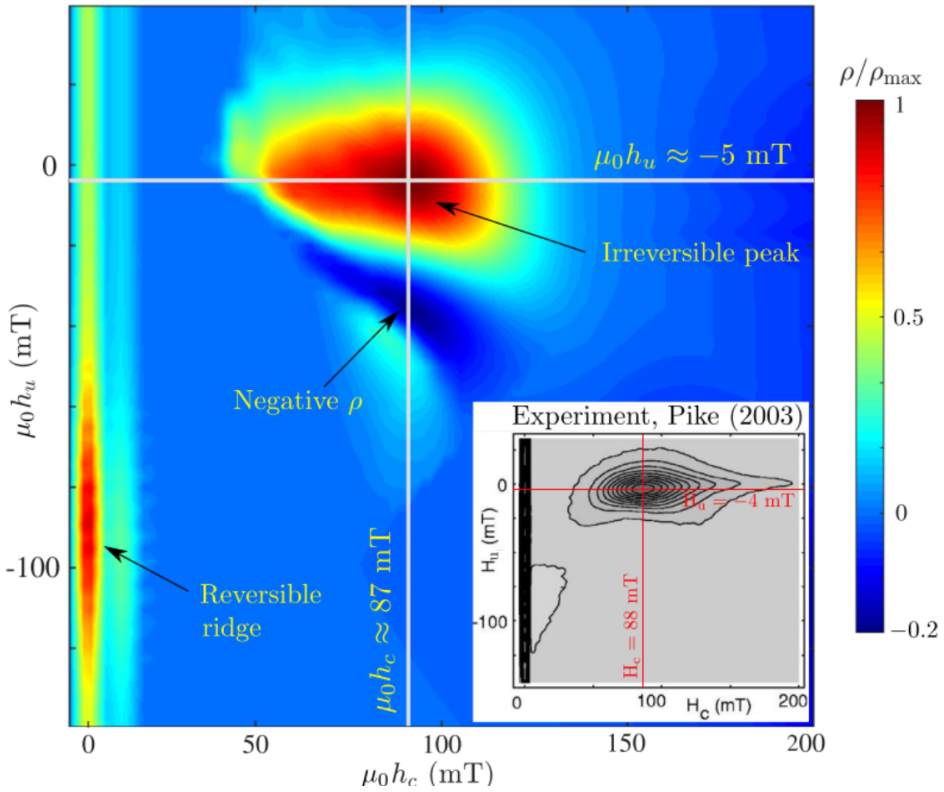

Figure A.12: Constructed FORC diagram for the floppy disc material from the modeled FORCs, a subset of which is shown in Fig.A.11. (inset) FORC diagram taken from Pike (2003) using the experimental FORC data of the floppy disc material. For consistency, the notation of the interaction field has been changed from H_b in the original paper to $H_u = \mu_0 h_u$, while $H_c = \mu_0 h_c$.

We observe in Fig. A.13a that our model predicts fairly well the distribution of ρ along $\mu_0 h_u = -5$ mT. In fact, the proposed framework makes a better prediction in this case than the existing Pike (2003) model. In turn, the Pike (2003) model is more accurate in predicting the peak of the reversible ridge. As depicted in Fig. A.13b, our model successfully predicts the asymmetric reversible ridge near $\mu_0 h_c = 0$ mT. However, the peak of the predicted ridge is slightly shifted from the experimental observation. Perhaps, a more involved model comprising multiple switching surfaces (François-Lavet et al., 2013) may be considered to model the reversible peak more accurately.

A.6 Concluding remarks

In this appendix, we introduce a simple yet effective framework for modeling the initial magnetization and minor loops of a permanent bulk magnet. Specifically, we incorporate the effect of initial magnetic hardening of a virgin specimen by introducing an isotropic hardening law, leading to the gradual growth of the switching surface until reaching a limiting surface, which encapsulates all the internal switching surfaces during the magnetization/demagnetization. Symmetric and asymmetric minor loops are modeled by introducing a set of discrete, history-dependent thermodynamic variables, that control the shrinkage and expansion of the switching surface depending on the loading history and the state of magnetization. In this context, we utilize the existing framework of the

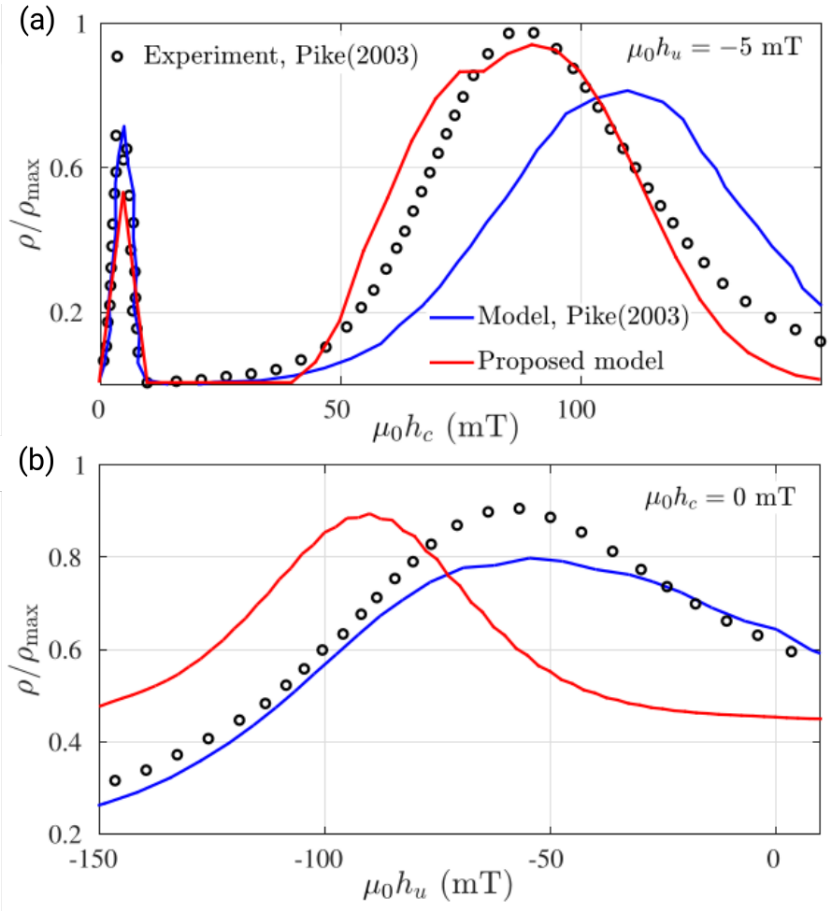

Figure A.13: Variation of ρ (a) with $\mu_0 h_{\mathrm{c}}$ for a constant $\mu_0 h_{\mathrm{u}} = -5$ mT and (b) with $\mu_0 h_{\mathrm{u}}$ for a constant $\mu_0 h_{\mathrm{c}} = 0$ mT.

bounding surface (originally used in the context of mechanical plasticity) and extend it to describe the macroscopic response of permanent magnets. In particular, the present natural extension of the existing switching surface framework of McMeeking and Landis (2002), Landis (2002) and Klinkel (2006) enables us to model accurately the initial magnetization and the symmetric and asymmetric minor loops up to first order.

One of the key advantage of the proposed ESS model is the sequential increase in the model complexity depending on the experiment we intend to model. Modeling only the major hysteresis loop does *not* require any isotropic hardening or shrinkage/expansion of the switching surface depending on the loading history. Hence, only the four material parameters related to the coercive field and the shape of the major loop are sufficient to describe the major hysteresis loop. On the other hand, if one needs to model also the initial magnetization response, two additional hardening parameters are further considered.

The modeling of the minor hysteresis loops necessitates a more tedious definition of the switching surface depending on the state of magnetization and the loading history, whereas it requires the determination of three additional material parameters. This sequential increase in the model complexity also allows us to probe various experimental data by identifying the model parameters in multiple *independent* steps. In the present work, we use at most eleven model parameters

to probe the most complex experimental loading history corresponding to first order asymmetric minor loops (FOMLs). This makes the corresponding parameter identification a well-controlled and fairly straightforward task contrary to the pseudo particle model (Bergqvist, 1997; Kalina et al., 2017), which requires 30 to 50 parameters that need to be identified all at once.

In particular, the model has been used to probe and predict several experimental data including the $\mathtt{m}$–$\mathtt{h}$ responses of the purely nucleation-type sintered NdFeB magnets, the combined nucleation-pinning-type NdFeB powder samples, the annealed nanocrystalline Co alloy and the $\mathtt{b}$–$\mathtt{h}$ responses of the MnMg steel and the 3% Si steel. Symmetric and asymmetric minor loop data from different experiments are used to probe the effectiveness of the proposed evolution/shrinkage law for the coercive field b^{c}. Excellent recovery and prediction of available experiments, whenever available are obtained in the present study.

Bibliography

ABAQUS. *CAE/2018*. Simulia, RI, USA, 2018.

Abramowitz, M. and Stegun, I. *Handbook of Mathematical Functions*. Dover, New York, 1972.

Ahamed, R., Choi, S.-B., and Ferdaus, M. M., 2018. A state of art on magneto-rheological materials and their potential applications. *Journal of Intelligent Material Systems and Structures*, 29(10):2051–2095.

Anoukou, K., Brenner, R., Hong, F., Pellerin, M., and Danas, K., 2018. Random distribution of polydisperse ellipsoidal inclusions and homogenization estimates for porous elastic materials. *Comp. Struct.*, 210:87 – 101.

Benabou, A., Leite, J., Clénet, S., Simão, C., and Sadowski, N., 2008. Minor loops modelling with a modified Jiles–Atherton model and comparison with the Preisach model. *Journal of magnetism and magnetic materials*, 320(20):e1034–e1038.

Bennett, K., Regueiro, R., and Borja, R., 2016. Finite strain elastoplasticity considering the Eshelby stress for materials undergoing plastic volume change. *International Journal of Plasticity*, 77:214–245.

Bergqvist, A., 1997. Magnetic vector hysteresis model with dry friction-like pinning. *Physica B: Condensed Matter*, 233(4):342–347.

Bodelot, L., Voropaieff, J.-P., and Pössinger, T., 2017. Experimental investigation of the coupled magneto-mechanical response in magnetorheological elastomers. *Experimental Mechanics*, 58(2):207–221.

Bottero, C. J. and Idiart, M. I., 2016. Influence of second-phase inclusions on the electro-deformation of ferroelectric ceramics. *International Journal of Solids and Structures*, 80:381–392.

Brown, W. F. *Magnetoelastic Interactions*, volume 9. Springer, 1966.

Bustamante, R., Dorfmann, A., and Ogden, R. W., 2008. Nonlinear electroelastostatics: a variational framework. *Zeitschrift für angewandte Mathematik und Physik*, 60(1):154–177.

Bustamante, R. and Ogden, R. W., 2012. Nonlinear magnetoelastostatics: Energy functionals and their second variations. *Mathematics and Mechanics of Solids*, 18(7):760–772.

Carstensen, C., Hackl, K., and Mielke, A., 2001. Non–convex potentials and microstructures in finite–strain plasticity. *Proceedings of the Royal Society of London. Series A: Mathematical, Physical and Engineering Sciences*, 458(2018):299–317.

Chaboche, J., Van, K. D., and Cordier, G., 1979. Modelization of the strain memory effect on the cyclic hardening of 316 stainless steel. *SMIRT-5, Division L. Berlin*.

Chaboche, J.-L., 1986. Time-independent constitutive theories for cyclic plasticity. *International Journal of plasticity*, 2(2):149–188.

Chatzigeorgiou, G., Javili, A., and Steinmann, P., 2012. Unified magnetomechanical homogenization framework with application to magnetorheological elastomers. *Mathematics and Mechanics of Solids*, 19(2):193–211.

Chen, Y.-C. and Wheeler, L., 1993. Derivatives of the stretch and rotation tensors. *Journal of Elasticity*, 32(3):175–182.

Choi, K. M. and Rogers, J. A., 2003. A photocurable poly(dimethylsiloxane) chemistry designed for soft lithographic molding and printing in the nanometer regime. *Journal of the American Chemical Society*, 125(14):4060–4061.

Coleman, B. D. and Gurtin, M. E., 1967. Thermodynamics with internal state variables. *The Journal of Chemical Physics*, 47(2):597–613.

Coleman, B. D. and Noll, W., 1959. On the thermostatics of continuous media. *Archive for Rational Mechanics and Analysis*, 4(1):97–128.

Coleman, B. D. and Noll, W., 1974. The thermodynamics of elastic materials with heat conduction and viscosity. In *The Foundations of Mechanics and Thermodynamics*, 145–156. Springer Berlin Heidelberg.

Dafalias, Y. F. and Popov, E. P., 1975. A model of nonlinearly hardening materials for complex loading. *Acta mechanica*, 21(3):173–192.

Dafalias, Y. F. and Popov, E. P., 1976. Plastic internal variables formalism of cyclic plasticity. *Journal of applied mechanics*, 43(4):645–651.

Danas, K., 2017. Effective response of classical, auxetic and chiral magnetoelastic materials by use of a new variational principle. *Journal of the Mechanics and Physics of Solids*, 105:25–53.

Danas, K., Deshpande, V. S., and Fleck, N. A., 2012a. Size effects in the conical indentation of an elasto-plastic solid. *Journal of the Mechanics and Physics of Solids*, 60(9):1605–1625.

Danas, K., Kankanala, S., and Triantafyllidis, N., 2012b. Experiments and modeling of iron-particle-filled magnetorheological elastomers. *Journal of the Mechanics and Physics of Solids*, 60(1):120 – 138.

Danas, K. and Triantafyllidis, N., 2014. Instability of a magnetoelastic layer resting on a non-magnetic substrate. *J. Mech. Phys. Solids*, 69:67 – 83.

Dashner, P. A., 1993. An objective kinematical formalism for the modeling of elastic-plastic materials subject to large deformation. *International Journal of Solids and Structures*, 30(19):2661–2672.

Deng, X., Liu, Z., Yu, H., Xiao, Z., and Zhang, G., 2015. Isotropic and anisotropic nanocrystalline NdFeB bulk magnets prepared by binder-free high-velocity compaction technique. *Journal of Magnetism and Magnetic Materials*, 390:26–30.

Dorfmann, A. and Ogden, R., 2003. Magnetoelastic modelling of elastomers. *European Journal of Mechanics-A/Solids*, 22(4):497–507.

Dorfmann, A. and Ogden, R., 2004. Nonlinear magnetoelastic deformations of elastomers. *Acta Mechanica*, 167(1-2):13–28.

Dorfmann, A. and Ogden, R., 2005. Some problems in nonlinear magnetoelasticity. *Zeitschrift für angewandte Mathematik und Physik ZAMP*, 56(4):718–745.

François-Lavet, V., Henrotte, F., Stainier, L., Noels, L., and Geuzaine, C., 2013. An energy-based variational model of ferromagnetic hysteresis for finite element computations. *Journal of Computational and Applied Mathematics*, 246:243–250.

Fulmek, P. L. and Hauser, H., 1996. Magnetization reversal in an energetic hysteresis model. *Journal of Magnetism and Magnetic Materials*, 160:35–37.

Galipeau, E. and Ponte Castañeda, P., 2013. A finite-strain constitutive model for magnetorheological elastomers: Magnetic torques and fiber rotations. *Journal of the Mechanics and Physics of Solids*, 61(4):1065–1090.

Garrell, M. G., Ma, B.-M., Shih, A. J., Lara-Curzio, E., and Scattergood, R. O., 2003. Mechanical properties of polyphenylene-sulfide (PPS) bonded Nd–Fe–B permanent magnets. *Materials Science and Engineering: A*, 359(1-2):375–383.

Ginder, J. M., Nichols, M. E., Elie, L. D., and Clark, S. M., 2000. Controllable-stiffness components based on magnetorheological elastomers. In N. M. Wereley (editor), *Smart Structures and Materials 2000: Smart Structures and Integrated Systems*. SPIE.

Ginder, J. M., Nichols, M. E., Elie, L. D., and Tardiff, J. L., 1999. Magnetorheological elastomers: properties and applications. In *Smart Structures and Materials 1999: Smart Materials Technologies*, volume 3675, 131–139. International Society for Optics and Photonics.

Green, A. E. and Naghdi, P. M., 1965. A general theory of an elastic-plastic continuum. *Archive for Rational Mechanics and Analysis*, 18(4):251–281.

Gurtin, M. E. *An Introduction to Continuum Mechanics*. Academic Press, 1982.

Halphen, B. and Nguyen, Q. S., 1975. Sur les matériaux standard généralisés. *Journal de Mécanique*, 14:39–63.

Hankin, R. K., 2015. Numerical evaluation of the gauss hypergeometric function with the hypergeo package. *The R Journal*, 7:81–88.

Hauser, H., 2004. Energetic model of ferromagnetic hysteresis: Isotropic magnetization. *Journal of Applied Physics*, 96(5):2753–2767.

Herbst, J., 1991. $R_2Fe_{14}B$ materials: Intrinsic properties and technological aspects. *Reviews of Modern Physics*, 63(4):819.

Hilber, W. and Jakoby, B., 2012. Controlled liquid flow in a microfluidic network with pressure sensitive valves based on polydimethylsiloxane (PDMS)/neodymium (NdFeB) composites. *Procedia Engineering*, 47:382–385.

Hoger, A. and Carlson, D. E., 1984. On the derivative of the square root of a tensor and Guo's rate theorems. *Journal of Elasticity*, 14(3):329–336.

Huang, S., Pessot, G., Cremer, P., Weeber, R., Holm, C., Nowak, J., Odenbach, S., Menzel, A. M., and Auernhammer, G. K., 2016a. Buckling of paramagnetic chains in soft gels. *Soft Matter*, 12(1):228–237.

Huang, Y., Wang, Y., Hou, Y., Wang, Y., Wu, Y., Ma, S., Liu, Z., Zeng, D., Tian, Y., Xia, W., et al., 2016b. Magnetic microstructure and magnetic properties of spark plasma sintered NdFeB magnets. *Journal of Magnetism and Magnetic Materials*, 399:175–178.

Huber, C., Abert, C., Bruckner, F., Groenefeld, M., Schuschnigg, S., Teliban, I., Vogler, C., Wautischer, G., Windl, R., and Suess, D., 2017. 3D printing of polymer-bonded rare-earth magnets with a variable magnetic compound fraction for a predefined stray field. *Scientific Reports*, 7(1).

Huber, J. E. and Fleck, N. A., 2001. Multi-axial electrical switching of a ferroelectric: theory versus experiment. *Journal of the Mechanics and Physics of Solids*, 49(4):785–811.

Huber, J. E., Fleck, N. A., Landis, C. M., and McMeeking, R. M., 1999. A constitutive model for ferroelectric polycrystals. *Journal of the Mechanics and Physics of Solids*, 47(8):1663–1697.

Hughes, T. J. R. and Winget, J., 1980. Finite rotation effects in numerical integration of rate constitutive equations arising in large-deformation analysis. *International Journal for Numerical Methods in Engineering*, 15(12):1862–1867.

Hütter, G., 2017. Coleman–Noll Procedure for Classical and Generalized Continuum Theories. In *Encyclopedia of Continuum Mechanics*, 1–8. Springer Berlin Heidelberg.

Hutter, K. and van de Ven, A., 1978. Field matter interactions in thermoelastic solids. Lectures Notes in Physics vol. 88.

Javili, A., Chatzigeorgiou, G., and Steinmann, P., 2013. Computational homogenization in magneto-mechanics. *International Journal of Solids and Structures*, 50(25-26):4197–4216.

Johnston, I. D., McCluskey, D. K., Tan, C. K. L., and Tracey, M. C., 2014. Mechanical characterization of bulk Sylgard 184 for microfluidics and microengineering. *Journal of Micromechanics and Microengineering*, 24(3):035017.

Jolly, M. R., Carlson, J. D., Muñoz, B. C., and Bullions, T. A., 1996. The magnetoviscoelastic response of elastomer composites consisting of ferrous particles embedded in a polymer matrix. *Journal of Intelligent Material Systems and Structures*, 7(6):613–622.

Kaidarova, A., Khan, M. A., Amara, S., Geraldi, N. R., Karimi, M. A., Shamim, A., Wilson, R. P., Duarte, C. M., and Kosel, J., 2018. Tunable, flexible composite magnets for marine monitoring applications. *Advanced Engineering Materials*, 20(9):1800229.

Kalina, K. A., Brummund, J., Metsch, P., Kästner, M., Borin, D. Y., Linke, J. M., and Odenbach, S., 2017. Modeling of magnetic hystereses in soft MREs filled with NdFeB particles. *Smart Materials and Structures*, 26(10):105019.

Kalina, K. A., Metsch, P., Brummund, J., and Kästner, M., 2020. A macroscopic model for magnetorheological elastomers based on microscopic simulations. *International Journal of Solids and Structures*, 193-194:200–212.

Kalina, K. A., Metsch, P., and Kästner, M., 2016. Microscale modeling and simulation of magnetorheological elastomers at finite strains: A study on the influence of mechanical preloads. *International Journal of Solids and Structures*, 102-103:286–296.

Kankanala, S. and Triantafyllidis, N., 2004. On finitely strained magnetorheological elastomers. *Journal of the Mechanics and Physics of Solids*, 52(12):2869–2908.

Kankanala, S. and Triantafyllidis, N., 2008. Magnetoelastic buckling of a rectangular block in plane strain. *Journal of the Mechanics and Physics of Solids*, 56(4):1147–1169.

Kankanala, S. V., 2007. On finitely strained magnetoelastic solids. *PhD Thesis*.

Keip, M.-A. and Rambausek, M., 2016. A multiscale approach to the computational characterization of magnetorheological elastomers. *International Journal for Numerical Methods in Engineering*, 107(4):338–360.

Keip, M.-A. and Rambausek, M., 2017. Computational and analytical investigations of shape effects in the experimental characterization of magnetorheological elastomers. *International Journal of Solids and Structures*, 121:1–20.

Keip, M.-A. and Sridhar, A., 2018. A variationally consistent phase-field approach for micro-magnetic domain evolution at finite deformations. *Journal of the Mechanics and Physics of Solids*.

Kim, Y., Yuk, H., Zhao, R., Chester, S. A., and Zhao, X., 2018. Printing ferromagnetic domains for untethered fast-transforming soft materials. *Nature*, 558(7709):274–279.

Klinkel, S., 2006. A phenomenological constitutive model for ferroelastic and ferroelectric hysteresis effects in ferroelectric ceramics. *International Journal of Solids and Structures*, 43(22):7197–7222.

Kovetz, A. *Electromagnetic Theory*, volume 975. Oxford University Press Oxford, 2000.

Kumar, A. and Lopez-Pamies, O., 2016. On the two-potential constitutive modeling of rubber viscoelastic materials. *Comptes Rendus Mécanique*, 344(2):102–112.

Landis, C. M., 2002. Fully coupled, multi-axial, symmetric constitutive laws for polycrystalline ferroelectric ceramics. *Journal of the Mechanics and Physics of Solids*, 50(1):127–152.

Lantean, S., Barrera, G., Pirri, C. F., Tiberto, P., Sangermano, M., Roppolo, I., and Rizza, G., 2019. 3D printing of magnetoresponsive polymeric materials with tunable mechanical and magnetic properties by digital light processing. *Advanced Materials Technologies*, 4(11):1900505.

Lefèvre, V., Danas, K., and Lopez-Pamies, O., 2017. A general result for the magnetoelastic response of isotropic suspensions of iron and ferrofluid particles in rubber, with applications to spherical and cylindrical specimens. *Journal of the Mechanics and Physics of Solids*, 107:343–364.

Lefèvre, V., Danas, K., and Lopez-Pamies, O., 2019. Two families of explicit models constructed from a homogenization solution for the magnetoelastic response of mres containing iron and ferrofluid particles. *International Journal of Non-Linear Mechanics*.

Lefèvre, V. and Lopez-Pamies, O., 2016. Nonlinear electroelastic deformations of dielectric elastomer composites: I — ideal elastic dielectrics. *J Mech Phys Solids*, 99:409–437.

Lerner, A. A. and Cunefare, K., 2007. Performance of MRE-based vibration absorbers. *Journal of Intelligent Material Systems and Structures*, 19(5):551–563.

Li, H., Liang, Y., Tan, X., Xu, H., Hu, P., and Ren, K., 2017. Coercivity mechanism of $(Nd_{0.8}Ce_{0.2})_{2.4}Fe_{12}Co_2B$ ribbons with ferromagnetic grain boundary phase. *Materials*, 10(9):1062.

Li, Y., Li, J., Li, W., and Du, H., 2014. A state-of-the-art review on magnetorheological elastomer devices. *Smart Materials and Structures*, 23(12):123001.

Linke, J. M., Borin, D. Y., and Odenbach, S., 2016. First-order reversal curve analysis of magnetoactive elastomers. *RSC Advances*, 6(102):100407–100416.

Linnemann, K., Klinkel, S., and Wagner, W., 2009. A constitutive model for magnetostrictive and piezoelectric materials. *International Journal of Solids and Structures*, 46(5):1149–1166.

Liu, J., Sepehri-Amin, H., Ohkubo, T., Hioki, K., Hattori, A., Schrefl, T., and Hono, K., 2013. Effect of Nd content on the microstructure and coercivity of hot-deformed Nd–Fe–B permanent magnets. *Acta Materialia*, 61(14):5387–5399.

Liu, Z., Huang, H., Gao, X., Yu, H., Zhong, X., Zhu, J., and Zeng, D., 2010. Microstructure and property evolution of isotropic and anisotropic NdFeB magnets fabricated from nanocrystalline ribbons by spark

plasma sintering and hot deformation. *Journal of Physics D: Applied Physics*, 44(2):025003.

Lokander, M. and Stenberg, B., 2003. Performance of isotropic magnetorheological rubber materials. *Polymer Testing*, 22(3):245–251.

Lopez-Pamies, O., Goudarzi, T., and Danas, K., 2013. The nonlinear elastic response of suspensions of rigid inclusions in rubber: II—a simple explicit approximation for finite-concentration suspensions. *Journal of the Mechanics and Physics of Solids*, 61(1):19–37.

Lubliner, J., 1986. Normality rules in large-deformation plasticity. *Mechanics of Materials*, 5(1):29–34.

Lubliner, J. *Plasticity Theory*. Courier Corporation, 2008.

Malvern, L. E. *Introduction to the Mechanics of a Continuous Medium*. Prentice-Hall, Inc., 1969.

Manti, M., Cacucciolo, V., and Cianchetti, M., 2016. Stiffening in soft robotics: A review of the state of the art. *IEEE Robotics & Automation Magazine*, 23(3):93–106.

Martínez-García, J. C., Rivas, M., Lago-Cachón, D., and García, J., 2013. First-order reversal curves analysis in nanocrystalline ribbons. *Journal of Physics D: Applied Physics*, 47(1):015001.

MATLAB. *version 9.2.0.538062 (R2017a)*. The MathWorks Inc., Natick, Massachusetts, 2017.

McMeeking, R. M. and Landis, C. M., 2002. A phenomenological multi-axial constitutive law for switching in polycrystalline ferroelectric ceramics. *International Journal of Engineering Science*, 40(14):1553–1577.

McMeeking, R. M. and Landis, C. M., 2005. Electrostatic forces and stored energy for deformable dielectric materials. *Journal of Applied Mechanics*, 72(4):581–590.

McMeeking, R. M., Landis, C. M., and Jimenez, S. M., 2007. A principle of virtual work for combined electrostatic and mechanical loading of materials. *International Journal of Non-Linear Mechanics*, 42(6):831–838.

Miehe, C., 2002. Strain-driven homogenization of inelastic microstructures and composites based on an incremental variational formulation. *International Journal for Numerical Methods in Engineering*, 55(11):1285–1322.

Miehe, C., Rosato, D., and Kiefer, B., 2011. Variational principles in dissipative electro-magneto-mechanics: A framework for the macro-modeling of functional materials. *International Journal for Numerical Methods in Engineering*, 86(10):1225–1276.

Miehe, C., Schotte, J., and Lambrecht, M., 2002. Homogenization of inelastic solid materials at finite strains based on incremental minimization principles. application to the texture analysis of polycrystals. *Journal of the Mechanics and Physics of Solids*, 50(10):2123–2167.

Miyamoto, T., Sakurai, H., Takabayashi, H., and Aoki, M., 1989. A development of a permanent magnet assembly for mri devices using Nd-Fe-B material. *IEEE Transactions on Magnetics*, 25(5):3907–3909.

Mukherjee, D., Bodelot, L., and Danas, K., 2020. Microstructurally-guided explicit continuum models for isotropic magnetorheological elastomers with iron particles. *International Journal of Non-Linear Mechanics*, 103380.

Mukherjee, D. and Danas, K., 2019. An evolving switching surface model for ferromagnetic hysteresis. *Journal of Applied Physics*, 125(3):033902.

Newell, A. J., 2005. A high-precision model of first-order reversal curve (FORC) functions for single-domain ferromagnets with uniaxial anisotropy. *Geochemistry, Geophysics, Geosystems*, 6(5).

Ogden, R. W. *Non-Linear Elastic Deformations*. Courier Corporation, 1997.

Ortiz, M. and Simo, J., 1986. An analysis of a new class of integration algorithms for elastoplastic constitutive relations. *International Journal for Numerical Methods in Engineering*, 23(3):353–366.

Pao, Y.-H. and Hutter, K., 1975. Electrodynamics for moving elastic solids and viscous fluids. *Proceedings of the IEEE*, 63(7):1011–1021.

Park, S., Mondal, K., Treadway, R. M., Kumar, V., Ma, S., Holbery, J. D., and Dickey, M. D., 2018. Silicones for stretchable and durable soft devices: Beyond Sylgard-184. *ACS Applied Materials & Interfaces*, 10(13):11261–11268.

Perales-Martínez, I. A., Palacios-Pineda, L. M., Lozano-Sánchez, L. M., Martínez-Romero, O., Puente-Cordova, J. G., and Elías-Zúñiga, A., 2017. Enhancement of a magnetorheological PDMS elastomer with carbonyl iron

particles. *Polymer Testing*, 57:78–86.

Perger, W. F., Bhalla, A., and Nardin, M., 1993. A numerical evaluator for the generalized hypergeometric series. *Computer physics communications*, 77(2):249–254.

Périgo, E., de Campos, M., Faria, R., and Landgraf, F., 2012. The effects of the pressing step on the microstructure and aging of NdFeB bonded magnets. *Powder technology*, 224:291–296.

Pigliaru, L., Rinaldi, M., Ciccacci, L., Norman, A., Rohr, T., Ghidini, T., and Nanni, F., 2020. 3D printing of high performance polymer-bonded PEEK-NdFeB magnetic composite materials. *Functional Composite Materials*, 1(1).

Pike, C. and Fernandez, A., 1999. An investigation of magnetic reversal in submicron-scale Co dots using first order reversal curve diagrams. *Journal of Applied Physics*, 85(9):6668–6676.

Pike, C. R., 2003. First-order reversal-curve diagrams and reversible magnetization. *Physical Review B*, 68(10).

Pike, C. R., Roberts, A. P., and Verosub, K. L., 1999. Characterizing interactions in fine magnetic particle systems using first order reversal curves. *Journal of Applied Physics*, 85(9):6660–6667.

Pike, C. R., Ross, C. A., Scalettar, R. T., and Zimanyi, G., 2005. First-order reversal curve diagram analysis of a perpendicular nickel nanopillar array. *Physical Review B*, 71(13).

Pinsky, P. M., Ortiz, M., and Pister, K. S., 1983. Numerical integration of rate constitutive equations in finite deformation analysis. *Computer Methods in Applied Mechanics and Engineering*, 40(2):137–158.

Pohlit, M., Eibisch, P., Akbari, M., Porrati, F., Huth, M., and Müller, J., 2016. First order reversal curves (FORC) analysis of individual magnetic nanostructures using micro-hall magnetometry. *Review of Scientific Instruments*, 87(11):113907.

Ponte Castañeda, P. and Galipeau, E., 2011. Homogenization-based constitutive models for magnetorheological elastomers at finite strain. *Journal of the Mechanics and Physics of Solids*, 59(2):194–215.

Preisach, F., 1935. Über die magnetische Nachwirkung. *Zeitschrift für physik*, 94(5-6):277–302.

Psarra, E., Bodelot, L., and Danas, K., 2017. Two-field surface pattern control via marginally stable magnetorheological elastomers. *Soft Matter*, 13(37):6576–6584.

Psarra, E., Bodelot, L., and Danas, K., 2019. Wrinkling to crinkling transitions and curvature localization in a magnetoelastic film bonded to a non-magnetic substrate. *Journal of the Mechanics and Physics of Solids*, 133:103734.

Reese, S. and Govindjee, S., 1998. A theory of finite viscoelasticity and numerical aspects. *International Journal of Solids and Structures*, 35(26-27):3455–3482.

Rigbi, Z. and Jilkén, L., 1983. The response of an elastomer filled with soft ferrite to mechanical and magnetic influences. *Journal of Magnetism and Magnetic Materials*, 37(3):267–276.

Roberts, A. P., Heslop, D., Zhao, X., and Pike, C. R., 2014. Understanding fine magnetic particle systems through use of first-order reversal curve diagrams. *Reviews of Geophysics*, 52(4):557–602.

Roberts, A. P., Pike, C. R., and Verosub, K. L., 2000. First-order reversal curve diagrams: A new tool for characterizing the magnetic properties of natural samples. *Journal of Geophysical Research: Solid Earth*, 105(B12):28461–28475.

Robinson, F., 1975. Electromagnetic stress and momentum in matter. *Physics Reports*, 16(6):313–354.

Rosato, D. and Miehe, C., 2014. Dissipative ferroelectricity at finite strains. variational principles, constitutive assumptions and algorithms. *International Journal of Engineering Science*, 74:162–189.

Royet, D., Hériveaux, Y., Marchalot, J., Scorretti, R., Dias, A., Dempsey, N. M., Bonfim, M., Simonet, P., and Frénéa-Robin, M., 2017. Using injection molding and reversible bonding for easy fabrication of magnetic cell trapping and sorting devices. *Journal of Magnetism and Magnetic Materials*, 427:306–313.

Sánchez, P. A., Gundermann, T., Dobroserdova, A., Kantorovich, S. S., and Odenbach, S., 2018. Importance of matrix inelastic deformations in the initial response of magnetic elastomers. *Soft Matter*.

Schümann, M., Borin, D., Huang, S., Auernhammer, G., Müller, R., and Odenbach, S., 2017. A characterisation of the magnetically induced movement of NdFeB-particles in magnetorheological elastomers. *Smart Materials*

and Structures, 26(9):095018.

Schümann, M. and Odenbach, S., 2017. In-situ observation of the particle microstructure of magnetorheological elastomers in presence of mechanical strain and magnetic fields. *Journal of Magnetism and Magnetic Materials*, 441:88–92.

Semisalova, A. S., Perov, N. S., Stepanov, G. V., Kramarenko, E. Y., and Khokhlov, A. R., 2013. Strong magnetodielectric effects in magnetorheological elastomers. *Soft Matter*, 9(47):11318.

Sitti, M. and Wiersma, D. S., 2020. Pros and cons: Magnetic versus optical microrobots. *Advanced Materials*, 1906766.

Steigmann, D. J., 2004. Equilibrium theory for magnetic elastomers and magnetoelastic membranes. *International Journal of Non-Linear Mechanics*, 39(7):1193–1216.

Steigmann, D. J., 2010. Applications of polyconvexity and strong ellipticity to nonlinear elasticity and elastic plate theory. In *CISM International Centre for Mechanical Sciences*, 265–299. Springer Vienna.

Stepanov, G. V., Borin, D. Y., Bakhtiiarov, A. V., and Storozhenko, P. A., 2017. Magnetic properties of hybrid elastomers with magnetically hard fillers: rotation of particles. *Smart Materials and Structures*, 26(3):035060.

Sugawa, Y., Ishidate, K., Sonehara, M., and Sato, T., 2013. Carbonyl-iron/epoxy composite magnetic core for planar power inductor used in package-level power grid. *IEEE Transactions on Magnetics*, 49(7):4172–4175.

Suo, Z., Zhao, X., and Greene, W., 2008. A nonlinear field theory of deformable dielectrics. *Journal of the Mechanics and Physics of Solids*, 56(2):467–486.

Szabó, L. and Balla, M., 1989. Comparison of some stress rates. *International Journal of Solids and Structures*, 25(3):279–297.

Tarantino, M., Zerhouni, O., and Danas, K., 2019. Random 3D-printed isotropic composites with high volume fraction of pore-like polydisperse inclusions and near-optimal elastic stiffness. *Acta Materialia*, 175:331–340.

Taylor, A. P., Cuervo, C. V., Arnold, D. P., and Velasquez-Garcia, L. F., 2019. Fully 3D-printed, monolithic, mini magnetic actuators for low-cost, compact systems. *Journal of Microelectromechanical Systems*, 28(3):481–493.

Wang, Z., Xiang, C., Yao, X., Floch, P. L., Mendez, J., and Suo, Z., 2019. Stretchable materials of high toughness and low hysteresis. *Proceedings of the National Academy of Sciences*, 116(13):5967–5972.

Włodarski, Z., 2007. Extraction of hysteresis loops from main magnetization curves. *Journal of magnetism and magnetic materials*, 308(1):15–19.

Zabihyan, R., Mergheim, J., Pelteret, J., Brands, B., and Steinmann, P., 2020. FE^2 simulations of magnetorheological elastomers: influence of microscopic boundary conditions, microstructures and free space on the macroscopic responses of MREs. *International Journal of Solids and Structures*, 193-194:338–356.

Zerhouni, O., Tarantino, M., and Danas, K., 2019. Numerically-aided 3D printed random isotropic porous materials approaching the Hashin-Shtrikman bounds. *Composites Part B: Engineering*, 156:344–354.

Zhao, R., Kim, Y., Chester, S. A., Sharma, P., and Zhao, X., 2019. Mechanics of hard-magnetic soft materials. *Journal of the Mechanics and Physics of Solids*, 124:244–263.

Zhou, R., Surendran, A. N., Mejulu, M., and Lin, Y., 2020. Rapid microfluidic mixer based on ferrofluid and integrated microscale NdFeB-PDMS magnet. *Micromachines*, 11(1):29.

Zienkiewicz, O. and Taylor, R. *The Finite Element Method, Volume 1: The Basis*. 2000.

ECOLE DOCTORALE

Titre : Modélisation théorique et numérique des élastomères magnéto-rhéologiques contenant des particules ferromagnétiques douces et dures

Mots clés : Magnéto élasticité,elements finis,mécanique des matériaux,polymeres.

Résumé : Les élastomères magnétorhéologiques (MREs) sont composites à deux phases comprenant des inclusions métalliques magnéto-actives dans une matrice d'élastomère mécaniquement souple. Ce travail fournit un ensemble de modèles constitutifs équivalents guidés microstructurellement pour les MREs isotropes dans les espaces de variables F-H, F-h, F-b et F-b. En fonction des propriétés magnétiques des phases d'inclusion, les MREs sont appelés doux (s-MREs) ou durs (h-MREs), s'ils contiennent, respectivement, des particules magnéto-actives (par exemple, fer) ou des particules magnétisables de façon permanente (par exemple, NdFeB). À leur tour, les particules magnéto-actives "douces" non-coercitives présentent une réponse de magnétisation de type saturation, tandis que les particules magnétiques "dures" fortement coercitives présentent une hystérésis ferromagnétique.
Deux modèles équivalents, basés sur h et b, thermodynamiquement cohérents et indépendants de la vitesse sont proposés ici pour l'hystérésis ferromagnétique. Une homogénéisation numérique à champ complet est ensuite réalisée afin d'estimer la réponse macroscopique des s- et h-MREs. Ces estimates d'homogénéisation pour les s- et h-MREs fournissent des informations cruciales sur les réarrangements et les rotations.
Des modèles macroscopiques explicites et entièrement objectifs, qui deviennent identiques aux estimations analytiques d'homogénéisation dans certaines limites, sont proposés pour les s-MREs dans les deux espaces de variables F-H et F-B. Étant donné que la plupart des propriétés effectives sont estimées à partir des cas limites d'homogénéisation analytique, le nombre de paramètres du modèle à estimer via l'ajustement de la réponse du modèle se réduit à un. De la même manière, des modèles constitutifs entièrement objectifs et équivalents dans les espaces de variables F-H, F-h, F-B et F-b, avec un seul paramètre supplémentaire, sont proposés pour les h-MREs, où les variables internes dans le Lagrangien F-H et F-B sont considérées comme étant dans une configuration intermédiaire sans étirement.
D'excellents accords sont obtenus entre les modèles proposés pour les s- et h-MREs et les estimations numériques d'homogénéisation pour des matrices ayant des modules de cisaillement $G_{\mathrm{m}} >$ 0,3 MPa et pour les fractions volumiques $c \leq 30\%$.

Title : Theoretical and numerical modeling of magnetorheological elastomers comprising magnetically soft and hard particles

Keywords : Magnetoelasticity, finite elements, mechanics of materials, polymers

Abstract : Magnetorheological elastomers (MREs) are two phase composites comprising magneto-active metallic inclusions in a mechanically soft elastomer matrix. This work provides a set of equivalent microstructurally-guided constitutive models for isotropic MREs in the F-H, F-h, F-B and F-b variable spaces. Depending on the magnetic properties of the inclusion phases, the MREs are referred to be the soft (s-MRE) and hard (h-MRE), comprising of, respectively, magneto-active (e.g., iron) and permanently magnetizable (e.g., NdFeB) particles. In turn, the non-coercive, "soft" magneto-active particles exhibit a saturation-type magnetization response, whereas, highly coercive "hard" magnetic particles exhibit ferromagnetic hysteresis.
Two equivalent, h and b-based, thermodynamically consistent, rate-independent models for the ferromagnetic hysteresis are proposed herein. A full field numerical homogenization is carried out subsequently, in order to estimate the macroscopic response of the s- and h-MREs. These estimates for both s- and h-MREs provide crucial insights on the particle rearrangements and rotations.
Fully objective, explicit macroscopic models, those become exact to the analytical homogenization estimates in certain limits, are proposed for the s-MREs in both F-H and F-B variable spaces. Since most of the effective properties are estimated from the limiting cases of analytical homogenization, the number of model parameters to be estimated via model response fitting reduces to one. Similarly, fully objective, equivalent constitutive models in the F-H, F-h, F-B and F-b variable spaces, having only one additional model parameter, are proposed for the h-MREs, where the internal variables in the Lagrangian F-H and F-B-based formulations are considered to be in a stretch-free, intermediate configuration.
Excellent agreements of the proposed models for the s- and h-MREs are obtained with the numerical homogenization estimates for moderately-soft to relatively stiff matrix phases having shear moduli $G_{\mathrm{m}} > 0.3$ MPa and for particle volume fractions $c \leq 30\%$.

Institut Polytechnique de Paris
91120 Palaiseau, France